

Applied Hydrogeophysics

Edited by

Harry Vereecken, Andrew Binley, Giorgio Cassiani,
André Revil and Konstantin Titov

NATO Science Series

Applied Hydrogeophysics

NATO Science Series

A Series presenting the results of scientific meetings supported under the NATO Science Programme.

The Series is published by IOS Press, Amsterdam, and Springer in conjunction with the NATO Public Diplomacy Division

Sub-Series

I. Life and Behavioural Sciences	IOS Press
II. Mathematics, Physics and Chemistry	Springer
III. Computer and Systems Science	IOS Press
IV. Earth and Environmental Sciences	Springer

The NATO Science Series continues the series of books published formerly as the NATO ASI Series.

The NATO Science Programme offers support for collaboration in civil science between scientists of countries of the Euro-Atlantic Partnership Council. The types of scientific meeting generally supported are "Advanced Study Institutes" and "Advanced Research Workshops", and the NATO Science Series collects together the results of these meetings. The meetings are co-organized by scientists from NATO countries and scientists from NATO's Partner countries – countries of the CIS and Central and Eastern Europe.

Advanced Study Institutes are high-level tutorial courses offering in-depth study of latest advances in a field.

Advanced Research Workshops are expert meetings aimed at critical assessment of a field, and identification of directions for future action.

As a consequence of the restructuring of the NATO Science Programme in 1999, the NATO Science Series was re-organised to the four sub-series noted above. Please consult the following web sites for information on previous volumes published in the Series.

<http://www.nato.int/science>
<http://www.springer.com>
<http://www.iospress.nl>



Series IV: Earth and Environmental Sciences – Vol. 71

Applied Hydrogeophysics

edited by

Harry Vereecken

Forschungszentrum Jülich GmbH,
Germany

Andrew Binley

Lancaster University, UK

Giorgio Cassiani

Università di Milano Bicocca, Italy

Andre Revil

Université Aix-Marseille, Aix-en-Provence, France

and

Konstantin Titov

State University of St. Petersburg, Russia

 Springer

Published in cooperation with NATO Public Diplomacy Division

Proceedings of the NATO Advanced Research Workshop on
Soils and Groundwater Contamination: Improved Risk Assessment
St. Petersburg, Russia
25-29 July 2004

A C.I.P. Catalogue record for this book is available from the Library of Congress.

ISBN-10 1-4020-4911-0 (PB)
ISBN-13 978-1-4020-4911-8 (PB)
ISBN-10 1-4020-4910-2 (HB)
ISBN-13 978-1-4020-4910-1 (HB)
ISBN-10 1-4020-4912-9 (e-book)
ISBN-13 978-1-4020-4912-5 (e-book)

Published by Springer,
P.O. Box 17, 3300 AA Dordrecht, The Netherlands.

www.springer.com

Printed on acid-free paper

All Rights Reserved
© 2006 Springer

No part of this work may be reproduced, stored in a retrieval system, or transmitted in any form or by any means, electronic, mechanical, photocopying, microfilming, recording or otherwise, without written permission from the Publisher, with the exception of any material supplied specifically for the purpose of being entered and executed on a computer system, for exclusive use by the purchaser of the work.

CONTENTS

Acknowledgements	vii
List of Contributors	ix
1. Applied Hydrogeophysics	1
Harry Vereecken, Andrew Binley, Giorgio Cassiani, André Revil, and Konstantin Titov	
2. Hydrogeophysical Parameter Estimation Approaches for Field Scale Characterization	9
Niklas Linde, Jinsong Chen, Michael B. Kowalsky, and Susan Hubbard	
3. A Successive Linear Estimator for Electrical Resistivity Tomography	45
Tian-Chyi J. Yeh, Junfeng Zhu, Andreas Englert, Amado Guzman, and Steve Flaherty	
4. Unsaturated Zone Processes	75
Giorgio Cassiani, Andrew Binley, and Ty P.A. Ferré	
5. Solute Transport Processes	117
Andreas Kemna, Andrew Binley, Frederick Day-Lewis, Andreas Englert, Bülent Tezkan, Jan Vanderborgh, Harry Vereecken, and Peter Winship	
6. Biogeophysics: The Effects of Microbial Processes on Geophysical Properties of the Shallow Subsurface	161
Estella A. Atekwana, D. Dale Werkema, and Eliot A. Atekwana	
7. Cold Regions Hydrogeophysics: Physical Characterization and Monitoring	195
Helen K. French, Andrew Binley, Ivan Kharkhordin, Bernd Kulessa, and Sergey S. Krylov	

8. Hydrogeophysical Applications in Coastal Aquifers Mark Goldman and Uri Kafri	233
9. Applications of the Self-Potential Method to Hydrological Problems André Revil, Konstantin Titov, Claude Doussan, and Vincenzo Lapenna	255
10. Engineered Barriers for Pollutant Containment and Remediation Lee Slater and Andrew Binley	293
11. Geoelectrical Characterisation of Covered Landfill Sites: A Process-Oriented Model and Investigative Approach Maxwell Meju	319
12. Chernobyl-Born Radionuclides: Groundwater Protectability with Respect to Preferential Flow Zones Vyacheslav M. Shestopalov, Yuriy F. Rudenko, Alexander S. Bohuslavsky, and Volodymir N. Bublias	341
Index	377

ACKNOWLEDGEMENTS

The book “Applied Hydrogeophysics” presents the outcome of a successful NATO Advanced Research Workshop which was held in St. Petersburg, 25–29 July, 2004 and entitled “Soils and groundwater contamination: Improved risk assessment.” We thank NATO for supporting and funding this workshop.

We are grateful to all reviewers who helped to increase the quality of the scientific information contained in this book: Alberto Bellin, Fred Day-Lewis, Claudio Gallo, Alberto Godio, Sander Huisman, Ivan Kharkhordin, Sébastien Lambot, Maxwell Meju, Véronique Naudet, Jirka Simunek, Heiner Stoffregen, Andreas Weller and Paul Wilkinson.

We particularly thank Gaby Pillert for the administrative and technical support in preparing the workshop but especially for her support in organisation and preparation of this book and for maintaining good contact with all authors.

Andrew Binley
Giorgio Cassiani
André Revil
Konstantin Titov
Harry Vereecken
Editors

LIST OF CONTRIBUTORS

Atekwana Estella

Dep. of Geological Sciences and
Engineering
University of Missouri-Rolla
125 McNutt Hall
65409 Rolla, Missouri
MO, USA

Atekwana Eliot

University of Missouri-Rolla
Dep. of Geological Sciences
and Engineering
125 McNutt Hall
65409 Rolla, Missouri
MO, USA

Binley Andrew

Lancaster University
Dep. of Environmental Science
Bailrigg
LA1 4YQ Lancaster
UK

Bohuslavsky Alexander

National Academy of Sciences
of Ukraine
Radioenvironmental Center
O.Gonchar Str.
1054 Kyiv
Ukraine

Bublias Volodymir

National Academy of Sciences
of Ukraine
Radioenvironmental Center
O.Gonchar Str.
1054 Kyiv
Ukraine

Cassiani Giorgio

Università di Milano
Dipartimento di Scienze Geologiche
e Geotecnologiche
Piazza della Scienza 4
20126 Biocca
Italy

Chen Jingsong

Earth Science Division
Lawrence Berkeley National
Laboratory
1 Cyclotron Rd.
MS 90-1116 Berkeley
CA, USA

Day-Lewis Frederick

U.S. Geological Survey
Office of Ground Water, Branch
of Geophysics
11 Sherman Place, Unit 5015,
Storrs
CT, USA

Doussan Claude

INRA
Unité Climat Sol Environnement
Domaine St Paul, Site Agroparc,
84914 Avignon Cedex 9
France

Englert Andreas

Forschungszentrum Jülich GmbH
Agrosphere (ICG-IV)
52425 Jülich
Germany

Ferré Ty P.A.

Dep. of Hydrology and Water Resources
 The University of Arizona
 1133 E. James E. Roger Way
 85721 Tuscon
 Arizona, USA

French Helen

Norwegian Institute for Agricultural and Environmental Research
 Soil, Water and Environment Division
 Frederik A. Dahlsv. 20
 1432 As
 Norway

Flaherty Steve

ARCADIS
 3777 E. Broadway Blvd. Suite 100
 85716 Tuscon
 Arizona, USA

Goldman Mark

The Geophysical Institute of Israel
 PO Box 182. Industrial Zone North
 71100 Lod
 Israel

Guzman Amado

ARCADIS
 3777 E. Broadway Blvd. Suite 100
 85716 Tuscon
 Arizona, USA

Hubbard Susan

Earth Science Division
 Lawrence Berkeley National Laboratory
 1 Cyclotron Rd., MS 90-1116
 Berkeley
 CA, USA

Kafri Uri

Geological Survey of Israel
 PO Box 182. Industrial Zone North
 95501 Jerusalem
 Israel

Kemna Andreas

Forschungszentrum Jülich GmbH
 Agrosphere (ICG-IV)
 52425 Jülich
 Germany

Kharkhordin Ivan

Inst. of Environmental Geosciences
 St. Petersburg Division
 14-th Line, 29
 199178 St. Petersburg
 Russia

Kowalsky Michael

Earth Science Division
 Lawrence Berkeley National Laboratory
 1 Cyclotron Rd., MS 90-1116
 Berkeley
 CA, USA

Krylov Sergey

Dep. of Earth Physics,
 Inst. of Physics
 St. Petersburg University
 Ulyanovskaya 1, Petershof
 198904 St. Petersburg
 Russia

Kulessa Bernd

University of Wales Swansea
 School of the Environment and Society
 Singleton Park
 SA2 8pp Swansea
 Wales, UK

Lapenna Vincenzo

Institute of Methodology for
Environment Analysis
(IMAA-CNR)
Potenza I 85050
Italy

Linde Niklas

Dep. of Earth Sciences/Geophysics
Uppsala University
Villav. 16
75236 Uppsala
Sweden

Meju Maxwell

Dep. of Environmental Science
Lancaster University
Bailrigg
LA1 4YQ Lancaster
UK

Revil André

CNRS-CEREGE, Dept. Geophysics
BP 80
13545 Aix-en-Provence, Cedex 4
France

Rudenko Yuriy

National Academy of Sciences
of Ukraine
Radioenvironmental Center
O.Gonchar Str.
1054 Kyiv
Ukraine

Shestopalov Vyacheslav

Radioenvironmental Center
National Academy of Sciences
of Ukraine
O.Gonchar Str.
1054 Kyiv
Ukraine

Slater Lee

Dep. of Earth & Environmental
Sciences
Rutgers University
101 Warren Street
7102 Newark
NJ

Tezkan Bülent

Inst. of Geophysics and
Meteorology
Cologne University
Albertus-Magnus-Platz
50923 Köln
Germany

Titov Konstantin

Russian Institute of Exploration
Geophysics
20 Fayansovaya St.
193019 St. Petersburg
Russia

Vanderborght Jan

Forschungszentrum Jülich GmbH
Agrosphere (ICG-IV)
52425 Jülich
Germany

Vereecken Harry

Forschungszentrum
Jülich GmbH
Agrosphere (ICG-IV)
52425 Jülich
Germany

Werkema Dale

U.S. EPA, ORD, NERL, ESD,
CMB
944 E. Harmon Ave
89119 Las Vegas
Nevada, USA

Winship Peter Lancaster University Dep. of Environmental Science Bailrigg LA1 4YQ Lancaster UK	1133 E. James E. Roger Way 85721 Tuscon Arizona, USA
Yeh Tian-Chyi J. Dep. of Hydrology and Water Resources The University of Arizona	Zhu Junfeng The University of Arizona Dep. of Hydrology and Water Resources 1133 E. James E. Roger Way 85721 Tuscon Arizona, USA

1. APPLIED HYDROGEOPHYSICS

Harry Vereecken, Andrew Binley, Giorgio Cassiani, Andre Revil,
and Konstantin Titov

1.1. Introduction

Soils and groundwater are important natural resources that sustain life on Earth. In the last century, the enormous expansion of industrial and agricultural activities has led to an increased environmental pressure on these systems. Soils and groundwater are extremely important because they yield much of our water resources and sustain food production for humanity. Agricultural activities consume nearly 80% of the fresh water used throughout the world, and the majority of this water is used for irrigation. In many countries aquifers are used as the major source of water for this purpose. Irrigation of cropland has greatly increased food production, but has also had some drawbacks due to the amount of water drawn from aquifers. Some of the major problems related with irrigation are excessive leaching of nutrients and pesticides, depletion of aquifers, ground subsidence, and soil salinization.

The vadose zone, being the subsurface environment between soil surface and groundwater, also serves as the repository for municipal, industrial and government waste. In Europe, more than 1.5 million sites are estimated to be potentially contaminated (EEA, 2000). These sites consist of military, industrial and waste disposal sites that are either abandoned or still under operation. The total number of identified sites that have been explicitly identified is about 21,000. The estimated total clean-up costs are at least in the order of 100 billion Euros.

As safe and effective use of the subsurface environment is a major challenge facing our society, there is a great need to improve our understanding of the shallow subsurface and the groundwater systems. As the subsurface is impossible to 'observe' directly, methods are needed to reveal its physical and hydrological properties, in addition to the hydrochemical characteristics of fluids stored and flowing through it. Traditional borehole-based sampling is often limited because of the localized knowledge often derived from such measurements and the disturbance induced to samples. As in the oil and mining industry, geophysical methods may offer a means of addressing this problem, by providing a spatially extensive, non-invasive means of investigating the subsurface. In the past, applications of geophysical methods in

groundwater and vadose zone hydrology have mainly focused on mapping geological structures (e.g. clay/sand layers, bedrock valleys, etc), delineation of aquifer boundaries, mapping of fracture zones, etc. In summary, the focus has been for a long time on the “geometrical” characterization of the subsurface. For such purposes standard methods are presently available and well-documented in the literature.

Recently, increased attention has been given to the use of geophysical methods to derive parameters and state variables characterizing especially surface near groundwater systems and soils (Vereecken et al., 2002, 2004; Rubin and Hubbard, 2005). This approach has also similarities with the experience of the oil industry, having as an objective the “petrophysical” characterization of the subsurface. Research in this direction is mainly driven by the fact that geophysical methods allow continuous mapping in space and time of geophysical properties which can be transferred to parameters or variables characterizing the aquifer system (e.g. water content, porosity, flow velocity). Classical approaches like drilling and coring have shown their limitations in capturing this spatial and temporal variability. Characterizing spatial and temporal variability of aquifers is, however, a key factor determining e.g. success of water management strategies or predicting pollution risks to water supply systems.

Hydrogeophysical methods and approaches are presented in the recent book *Hydrogeophysics* edited by Yoram Rubin and Susan Hubbard (2005). That book is the first to deal explicitly with geophysical methods for hydrological and hydrogeological processes. It addresses in depth the fundamentals of hydrogeological characterization as well as the fundamentals of geophysical characterization. A series of case studies and emerging technologies in the field of hydrogeophysics are also presented.

In *Applied Hydrogeophysics* we follow up on the material presented in *Hydrogeophysics* but focus on the applications of hydrogeophysical methods to the understanding of hydrological processes and environmental problems dealing with the flow of water and the transport of contaminants. This book, unlike its predecessor, is therefore organized mainly in hydrological process-driven chapters, rather than in methodological chapters. We feel that this structure is suitable particularly to the understanding of the end user and the professionals that want to make use of the new hydrogeophysical techniques for their specific field of application. In addition, this structure gives a more pronounced practical touch to the book. Hence the title *Applied Hydrogeophysics*.

The book is the outcome of a successful NATO Advanced Research Workshop held in St. Petersburg, 25–29 July, 2004 entitled “Soils and groundwater contamination: Improved risk assessment based on integrated hydrogeological and geophysical methods.” The objectives of the meeting were to critically evaluate the state of the art in hydrogeophysics for the assessment of

risks related to soil/groundwater contamination, to promote the interaction between soil scientists, hydrologists, hydrogeologists and geophysicists from all over the world; and to identify goals for future research. Specific attention was given to the applications of hydrogeophysical methods and techniques to problems arising in the use and management of soil and groundwater systems.

In the following we present a brief summary of the context and content of the various chapters.

1.2. Brief Overview

The book is organised in 12 chapters. The chapter of Linde et al. (Chapter 2) discusses the choices that must be made in estimating hydrogeophysical parameters. The authors identify three different methods presently available in the literature: direct mapping, integration methods and joint inversion methods. Direct mapping refers to the transformation of a geophysical model into hydrogeological model. A typical example is the estimation of water content data using ground penetrating radar. In integration methods the geophysical inversion is performed independently from the hydrogeological data and it includes the well-known methods such as cokriging and Bayesian estimation. The joint inversion methods aim to simultaneously invert geophysical and hydrogeophysical data. In their chapter, Linde et al. present the state of the art cases for each of these three methods.

The chapter by Yeh et al. on the hydrogeophysical use of sequential successive linear estimator (SSLE) and electrical resistivity tomography (ERT) introduces the SSLE as a promising alternative procedure for the inversion of ERT measurements. The SSLE is a geostatistically based cokriging-like approach. However, unlike the classical cokriging, the SSLE is able to tackle the nonlinear relationship between electrical potentials and the electrical conductivity. After a description of the SSLE, several synthetic case studies and a field application using the SSLE are given. The examples show the ability of the SSLE to condition the inverse procedure by a priori knowledge about the structure of the electrical conductivity as well as independent point measurements of the electrical conductivity in the subsurface. As expected, the conditioning of the inverse procedure reduces the ill-posedness of the inverse problem and therefore enhances the quality of the inversion results. Furthermore the SSLE features a quantification of the estimate of the electrical conductivity that is essential for decision making based on inversion results.

The chapter by Cassiani and others on unsaturated zone processes presents the basic concepts of non-invasive determination and monitoring of the

temporal and spatial variation of volumetric moisture content in soils under natural and experimental conditions. Knowledge of soil moisture dynamics and its spatial distribution is important in many hydrological processes such as soil water flow, infiltration, surface runoff, and soil evaporation. Moreover, soil water content and water flow play a critical role in a number of environmental processes such as soil and subsoil contamination, catchment hydrology, flood generation, slope stability, water resources and agricultural management. Typical measurements techniques of soil water content such as soil coring combined with gravimetric determination and time domain reflectometry (TDR) only provide local and spatial discontinuous information of soil moisture content and are often destructive and highly invasive. The authors illustrate in their chapter the value of ground-penetrating radar (GPR) and electrical resistivity tomography for investigating water flow and soil water content dynamics in a non-invasive and spatially distributed manner. In particular, the analysis of time lapse measurements, provides a means of determining vadose zone structural properties from dynamic hydrogeophysical signals. The authors present examples dealing with the use of cross-hole GPR and vertical radar profiling to monitor natural infiltration, and cross-hole monitoring of a tracer injection using GPR and ERT.

Chapter 5 (Kemna et al.) deals with the use of hydrogeophysical methods to characterize solute transport in soils and groundwater. It gives an outline of the conceptual and mathematical models that are generally used for the description and modelling of transport processes in porous media such as soils, aquifer sediment and karstic and fractured media. The relationship between the spatial and temporal moments of solute concentrations to transport parameters and heterogeneity of the hydraulic conductivity is outlined. The chapter focuses on hydrogeophysical approaches to characterize solute transport and solute mapping such as ERT, GPR and Radio-Magnetic Tellurics (RMT). Results are shown for a tracer monitoring experiment at the Krauthausen test site in Germany. At this site tracer tests with high and low conductive tracer solutions were performed to study the role of heterogeneity on solute transport. Applications of hydrogeophysical methods are also presented for the case of solute transport in fractured aquifers at various sites in the US, Switzerland and UK. For the unsaturated zone, applications of hydrogeophysical methods, such as cross-borehole radar tomography, high-resolution borehole resistivity and radar profiling are presented for studying the temporal dynamics and spatial variation of moisture content in a sandstone aquifer at a UK site. Finally, the chapter presents current developments and an outlook in the development and use of hydrogeophysical methods and techniques for improving our understanding of solute transport processes.

The chapter by Atekwana et al. (Chapter 6) presents research in a novel discipline aimed at understanding the impact of microbial activity and processes

on geophysical properties of earth materials. The chapter demonstrates the effect of microbial activity on properties such as texture, surface area, pore size and pore geometry, tortuosity, cementation, formation factor and elastic moduli. In addition, chemical properties may be changed by microbial activity and that may lead to alteration of e.g. ionic strength, ionic charge density and ionic mobility of the fluid phase, leading to variations in electrical conductivity. The chapter presents results from laboratory experiments exploring microbe-sediment-geophysical relationships using direct current resistivity, induced polarization, self-potential and seismic methods. Examples of the applications of these geophysical methods to detect microbial activity are presented for different field sites that are contaminated with hydrocarbons.

French et al. present in Chapter 7 various examples of geophysical methods that have been used to characterize water flow and transport processes in the subsurface environments located in the cold regions of Russia, Norway and Switzerland. In permafrost areas, water supply and changes in mechanical properties due to changes in permafrost are major issues. Applications of electromagnetic sounding are presented for the case of leakage from frozen dams, the detection of taliks, cryopegs and ground ice at Yamal Peninsula, and saltwater injection into permafrost areas. Surface tomographic electrical resistivity methods are presented that allow the determination of infiltration and the characterization of solute transport. Studies on the drainage conditions beneath a glacier conducted with resistivity techniques are also discussed. The authors address the difficulties encountered when applying these geophysical methods to characterize hydrological processes in cold regions. These problems are, for example, related to the grounding and calibration of geophysical measurements with respect to hydrological state variables, such as water content, but also to variations in temperature and phase transitions that may affect geophysical properties. A combination of all these elements may hamper the interpretation of geophysical measurements. The authors suggest that combining conventional methods with geophysical methods may overcome these problems.

Goldman and Kafri (Chapter 8) discuss the applications of time domain electromagnetic (TDEM) measurements for detecting the geometry and bulk resistivity of seawater intrusion into granular and carbonate coastal aquifers. Many of these aquifer systems are located in the Mediterranean coastal areas of southern Spain, southern France, Greece, the Adriatic coastal areas but also the southern Atlantic coast of the USA. The authors provide evidence that TDEM permits more reliable estimates of the porosity of those parts of the aquifers where saltwater has intruded. The method, however, requires calibration with respect to available hydrological data such as water levels, salinities and porosities.

In Chapter 9, Revil et al. discuss the theory and application of self-potential (SP) methods to environmental problems. The physics underlying the self-potential signals are associated with both ground water flow (streaming potential) and redox processes (electro-redox effect). The authors present various applications of the self-potential method, including the determination of hydraulic conductivity and storativity of aquifers using the electrical response during a pumping test, the monitoring of water flow in the vadose zone, the study of landslides, and the delineation of contaminant plumes in shallow aquifers. Recently, self-potential tomography (or electrography) methods have been developed, allowing imaging of subsurface properties. The inversion of self-potential signals is similar to that developed in medical imaging where electro-encephalographic signals are inverted to locate the source of epilepsy and electrophysiological activity of the brain.

Geophysical methods for investigating subsurface engineered barriers, used for containment and remediation, are presented in the Chapter 10 by Slater and Binley. These structures provide unique geophysical targets and are typically characterized by strong geophysical signatures associated either with the barrier itself, or the flow of liquids through them. The authors discuss the use of geophysical methods for the investigation of subsurface engineered containment structures (landfill liners/covers, waste tanks/storage ponds, containment barriers and caps) and flow through structures (permeable reactive barriers). Characterization and monitoring requirements are first introduced, followed by an in-depth analysis of the applicability of geophysical measurements for the following purposes: (1) verification that design specifications are met during installation; (2) characterization of variation in the physical properties of such barriers; (3) monitoring of liquids (leaks) through containment barriers; (4) evaluation and monitoring of geochemical processes occurring in flow through reactive barriers. Recent examples of the application of geophysical technologies to such studies of engineered barriers are presented. The authors present recommendations for future geophysical research on these unique targets.

In the chapter of Meju a consistent and process-based geoelectrical framework for the investigation of non-engineered landfill sites is presented. His approach is based on concepts derived from geotechnics and contaminant biogeochemistry and takes into account the complex geometry of landfill sites, the heterogeneous material composition and the attendant biogeochemical processes occurring in landfills. The main tenet of the approach is that geoelectrical response of landfill sites will vary in relation to significant changes in the chemistry of subsurface pore fluids and that these responses can be observed with hydrogeophysical methods such as electrical and electromagnetic methods (e.g. DC-resistivity techniques, Transient Electromagnetics (TEM) and Radio Magnetic Telluric soundings (RMT)). The chapter provides various

interesting case studies that illustrate the various aspects of the proposed conceptual geoelectrical model as well as a discussion of emerging methods and challenges in the field of land-fill characterization.

In Chapter 12, Shestopalov et al. present data on groundwater contamination from Chernobyl-sourced radionuclides (^{137}Cs and ^{90}Sr) within the Chernobyl Exclusion Zone and Kyiv region. Measurable concentrations of these radioisotopes exist not only in the soil water and shallow groundwater, but also in regional aquifers down to a depth of 100 m and more. Experimental and modeling studies have shown that groundwater contamination mainly enters the upper aquifer by preferential pathways occurring at different scales. Depression-related vertical preferential flow zones occur widely in the floodplain terraces of the Dnieper and Ukrainian Polesye regions, and their role in the penetration of Chernobyl-sourced radionuclides through the soil-unsaturated zone into the aquifer system has been studied in detail. An experimental study of radionuclide distribution in deposits and groundwater also reveals the influence of other types of preferential flow zones on the total contamination in the geological environment. To account for the preferential flow zones it is necessary to obtain more reliable assessments of possible groundwater contamination and protectability. A new concept is proposed to assess groundwater protectability and vulnerability, based on a typology approach, using field experiment assessments and modeling. Application of this methodology enables maps to be drawn of groundwater protectability and vulnerability for ^{137}Cs within the Kyiv region of the Dnieper basin. The relative share of the input from depressions in the overall groundwater recharge and radionuclide contamination is assessed.

1.3. Outlook

Throughout *Applied Hydrogeophysics*, current limitations and future challenges are highlighted. Given the rapid development of the field of hydrogeophysics, we anticipate significant advances in the near future. The development of improved joint-inversion approaches will allow better constraints of hydrological models using geophysical methods; Chapters 2 and 3 point towards a number of such approaches. This will require comprehensive datasets containing both hydro-geological and geophysical information at high spatial and temporal resolution in order to develop and validate such approaches. The appreciation of links between biogeochemical and geophysical properties of the subsurface, as outlined in Chapter 6, has immense future potential for understanding groundwater contamination mechanisms, including the monitoring of contamination and remediation. Examples illustrated in Chapters 5, 7, 8, 10, 11 and 12 also illustrate how hydrogeophysics may offer new tools for

monitoring subsurface processes, particularly for the determination of vulnerability of important groundwater resources. Methodological development, driven by the hydrological community, is likely to offer better tools for determining hydrological properties of the subsurface. Chapter 9 reveals how new approaches using self potential may give insight into water and chemical fluxes within the subsurface, i.e., quantities of direct value to the hydrologist. New methods, also targeting directly the hydrological processes and properties, such as surface magnetic resonance imaging, are advancing in their development and we anticipate exciting new findings in the near future.

References

EEA, 2000. Management of contaminated sites in Europe. Topic Report 13/1999, p. 171.
http://reports.eea.eu.int/Topic_report_No_131999/en/tab_content_RLR.

Rubin, Y., and S.S. Hubbard (eds), 2005. Hydrogeophysics, Springer, The Netherlands.

Verreecken H., U. Yaramanci, and A. Kemna, 2002. Non-invasive methods in hydrology. Special issue. *J. Hydrol.*, 267, 125–299.

Verreecken H., S. Hubbard, A. Binley, and T. Ferre, 2004. Hydrogeophysics: An introduction from guest editors. *Vadose Zone J.*, 3, 1060–1062.

2. HYDROGEOPHYSICAL PARAMETER ESTIMATION APPROACHES FOR FIELD SCALE CHARACTERIZATION

Niklas Linde, Jinsong Chen, Michael B. Kowalsky, and Susan Hubbard

2.1. Introduction

The potential benefits of including geophysical data in hydrogeological site characterization have been stated numerous times (e.g. Ezzedine et al., 1999; Hubbard et al., 1999; Chen et al., 2001; Hubbard and Rubin, 2005). The principle reason for the growing interest in using geophysical methods in hydrogeological studies is that geophysics may provide spatially distributed models of physical properties in regions that are difficult to sample using conventional hydrological wellbore methods (e.g. Butler, 2005). The geophysical models often reveal more details compared with hydrogeological models derived from hydrogeological data, such as pump tests and observations of hydraulic heads. Furthermore, geophysical methods are less invasive compared with hydrogeological methods and they are comparatively cheap. Therefore, geophysical surveys can improve hydrogeological characterization if we could relate the geophysical and hydrogeological properties in an appropriate way. The added value of including geophysics in hydrogeological characterization has become increasingly accepted and several published case studies clearly show the worth of including geophysics for different applications and data types (e.g. see reviews by Hyndman and Tronicke, 2005; Goldman et al., 2005; Daniels et al., 2005). However, the success of a given hydrogeophysical case-study is dependent on many different factors and it is often difficult to develop an opinion *a priori* about the applicability of a method at another site or for another application. Here, we discuss some of the choices that need to be considered in a characterization effort and point out similarities and fundamental differences between different hydrogeophysical parameter estimation approaches presented in the literature.

The integration of hydrogeological and geophysical data sets is a complex process that often entails consideration of several different factors, such as:

- the measurement support volume is dependent on the characterization method;
- the models have space-varying resolution that depend on the data type, survey design, geological characteristics, and other factors;

- the effects of measurement errors and simplified assumptions are difficult to assess;
- an infinite number of models can often explain a finite number of noisy data.

Because of non-uniqueness, we need to state a preference for a certain type of model (e.g. the smoothest, the least number of model parameters, etc.) and it is not always clear how this preference affect the outcome of an investigation. Our problem of hydrogeophysical parameter estimation is further complicated because relationships between geophysical and hydrogeological parameters are often:

- non-unique;
- poorly understood; and
- non-stationary.

Reviews of petrophysical relationships for hydrogeophysical investigations are given by Lesmes and Friedman (2005) and Pride (2005).

In Section 2.2, we discuss some critical choices that should be considered prior to the hydrogeophysical parameter estimation effort, such as: project objectives and available data (Section 2.2.1); model parameterization (Section 2.2.2); petrophysical relationships (Section 2.2.3); a priori information (Section 2.2.4); optimization or Monte Carlo methods (Section 2.2.5), objective functions (Section 2.2.6); and at which stage to establish the link between geophysics and hydrogeology (Section 2.2.7). We discuss three categories of hydrogeophysical parameter estimation, which we refer to as direct mapping (Section 2.3), integration methods (Section 2.4), and joint inversion methods (Section 2.5). We acknowledge that not all research falls cleanly into a single category. For example, McKenna and Poeter (1995) used a geostatistical indicator simulation to define zonation. Nonetheless, we find that this classification scheme is useful for the purposes of this review, and we give several case-studies to illustrate the merits and limitations of these categories (Section 2.3–2.5). We conclude this chapter with a summary and outlook discussion (Section 2.6).

We hope that this chapter will help the reader in considering the factors important for hydrogeophysical characterization, and in developing a hydrogeophysical parameter estimation approach for their specific problem of interest.

2.2. Critical Choices

Throughout this chapter we group available data into geophysical and hydrogeological data. These data are further grouped into measurements of system

properties (e.g. permeability) and measurements of state variables (e.g. apparent resistivity, seismic travel-times, hydraulic head, and breakthrough times of tracer). Strictly speaking, measurements of system properties in hydrogeological site-characterization do not exist because these measurements are typically obtained by measuring other state variables from which an estimate is derived using a relationship that is valid under certain conditions (e.g. Butler, 2005). Rather, measurements of system properties denote estimates that have been made outside our estimation procedure and we must assume that they are known to a certain degree of accuracy.

2.2.1. PROJECT OBJECTIVES AND AVAILABLE DATA

The need for information about the structure of hydrogeological system properties occurs in many applications and at different scales. The objectives, site characteristics, and available geophysical and hydrogeological data vary on a case-by-case basis, and attempts to estimate hydrogeological system properties using geophysical data must take these characteristics into account. In this chapter, we consider these characteristics as given (e.g. we do not consider experimental design). Instead, we attempt to provide some guidance on how to formulate a hydrogeophysical parameter estimation method that matches specific objectives and provides a level of detail that can be resolved given the available data. In practice, other factors related to available budget, expertise, and computational facilities will be influential in determining the approach taken.

2.2.2. MODEL PARAMETERIZATION

Model parameterization depends on the research objectives and the available data. Regularization is a necessary step towards defining a well-posed inverse problem (e.g. Tikhonov and Arsenin, 1977). We must find ways to constrain model space in order to obtain meaningful results. We consider three approaches to model parameterization: zonation (e.g. Carrerra and Neuman, 1986a, b, c); geostatistical (e.g. Hoeksema and Kitanidis, 1984; Dagan, 1985); and Tikhonov regularization approaches (e.g. Tikhonov and Arsenin, 1977; Constable et al., 1987).

Zonation is used in applications where we assume that the earth can be divided into a number of zones where the variations of a property within the zones are small compared with the variations between the zones. Possible applications where a zonation approach could be justified are the delineation of sand from interbedded clay layers or sediments from the underlying bedrock. The advantage of the zonation approach is that the number of model parameters can be relatively small and smoothness constraints in the inver-

sion may thus be avoided. Auken and Christensen (2004) demonstrated that this approach is preferable when mapping large-scale hydrogeological units in sedimentary environments using electrical methods. Such an approach also allows straightforward incorporation of borehole logs (Auken and Christensen, 2004). The zonation approach is probably the best approach when geological structure is apparent and formation boundaries are distinct (McLaughlin and Townley, 1996). However, the influence of the model parameterization is strong in zonation approaches and it might be difficult to reach conclusive results (e.g. Constable et al., 1987). Hydrogeological inversion codes that fall into this category are non-linear regression models such as the freely available UCODE (Hill, 1992) and MODFLOWP (Poeter and Hill, 1998), where regularization is imposed through model parameterization and/or by keeping certain model parameters fixed.

The geostatistical parameterization assumes that the parameter of interest is a spatial random variable with a certain correlation structure and sometimes a deterministic trend (e.g. Gómez-Hernández, 2005). This correlation structure typically includes a variance and integral scales that might vary in different directions (i.e., anisotropy). The geostatistical approach thereby decreases the number of effective parameters through spatial correlations and a known variance. A geostatistical parameterization is probably preferable when the parameters of interest vary in more or less random fashion and there is no clearly defined structure (McLaughlin and Townley, 1996).

The dominant approach to geophysical inversion is to use a fine grid discretization, where regularization is achieved through smoothing (i.e., finding the model that fits the data with minimum structure), damping (i.e., finding the model that fits the data and is the closest to an initial model) or a combination of smoothing and damping (Tikhonov and Arsenin, 1977; Maurer et al., 1998). Maurer et al. (1998) showed that a known mean and spatial correlation structure of a system property can be described by a combination of smoothing and damping; thereby, indicating a strong similarity between Tikhonov regularization approaches and geostatistics. However, the perspective is quite different. Tikhonov regularization is imposed to find a unique model (i.e., to make an ill-posed inverse problem well-posed). However, in geostatistical formulations the model covariance structure is honoured because it is assumed to describe real characteristics of the site. Damping has recently also been introduced in geostatistics (Kitanidis, 1999).

Our brief discussion on model parameterization shows that some understanding of the site characteristics is helpful in determining an appropriate model parameterization (e.g. Auken and Christensen, 2004). From this we can infer that the resulting models are not just determined by the data, but also by seemingly innocent choices of model parameterization and regularization.

2.2.3. THE PETROPHYSICAL RELATIONSHIP

How are geophysical and hydrogeological properties related? This is one of the most difficult questions in the efforts of hydrogeophysical parameter estimation. We should strive to choose a representation of the petrophysical relationship that reflects our understanding. This leads us to consider petrophysical relationships that are either:

- physically or empirically based;
- intrinsic or model-based;
- parameterizable or non-parameterizable;
- unique or non-unique; and
- stationary or non-stationary.

Below we briefly describe these petrophysical relationship characteristics. Since it is not within the scope of this chapter to provide detailed descriptions of physically based and empirical petrophysical relationships, the reader is referred to reviews given by Mavko et al. (1998), Lesmes and Friedman (2005), and references therein.

2.2.3.1. *Physically or Empirically Based Petrophysical Relationship*

Let us consider the problem of inferring water saturation in the vadose zone using radar data. In low loss material and for radar frequencies the EM wave velocity v (m/s) is related to the dielectric constant through (Davis and Annan, 1989):

$$v \approx \frac{c}{\sqrt{\kappa}}, \quad (1)$$

where c is the EM wave velocity in free space (3×10^8 m/s) and κ is the effective dielectric constant. An approximate value of the effective dielectric constant can be calculated using the so-called complex resistive index method (CRIM) (Tinga et al., 1973; Alharthi and Lange, 1987; Roth et al., 1990):

$$\kappa = [(1 - \phi)\sqrt{\kappa_s} + S_w\phi\sqrt{\kappa_w} + (1 - S_w)\phi\sqrt{\kappa_a}]^2, \quad (2)$$

where ϕ is porosity, S_w is water saturation, κ_s , κ_w , and κ_a are the dielectric constants for the solid, water, and air components of the soil, respectively. By combining Equations (1–2) we can estimate the water saturation if we have an estimate of porosity, radar velocity, and the permittivity of the earth material:

$$S_w = \frac{\left(\frac{c}{v} + (\phi - 1)\sqrt{\kappa_s} - \phi\sqrt{\kappa_a}\right)}{\phi(\sqrt{\kappa_w} - \sqrt{\kappa_a})}. \quad (3)$$

Using a physically based approach, it is straightforward to relate uncertainties in the petrophysical models' parameters with uncertainties in the resulting models. As an example, we show confidence limits of water saturation for the

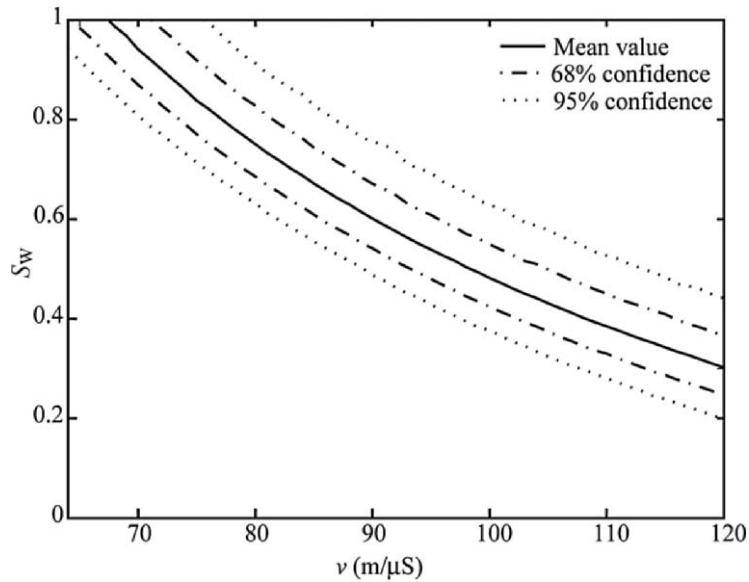


Figure 1. A petrophysical model between radar velocity v and water saturation S_w based on the CRIM model. The resulting confidence intervals are shown assuming normally distributed random errors in the radar velocity, porosity, and the effective dielectric constant of the solid

case where it is assumed that κ_s , ϕ , and v are normally distributed, where κ_s has a mean of 4 and a standard deviation of 1, ϕ has a mean of 0.35 and a standard deviation of 0.02, and that v has a standard deviation of 1 m/μs (Figure 1). We see that substantial prediction errors in the estimation of saturation occur, even when parameters are well-defined and the structure of the petrophysical model is assumed to be known. For this example, the dominating cause of uncertainty is the uncertainty of κ_s .

Most often, we rely on semi-empirical relationships (such as Archie's law; Archie, 1942) or purely empirical relationships (such as a linear regression between log electrical conductivity and log permeability measurements; Purvance and Andricevic, 2000a). These relationships are much more difficult to work with because (1) we need to estimate a site-specific relationship and (2) we have limited understanding of the validity of this relationship away from the calibration points. However, this is often the only possibility and several successful case studies are given in the literature (e.g. Purvance and Andricevic, 2000b; Hubbard et al., 2001).

2.2.3.2. Intrinsic or Model-Based Petrophysical Relationship

We define the intrinsic petrophysical relationship as the relationship between the true geophysical and hydrogeological system properties; and we define the

model-based petrophysical relationship as the relationship between our geophysical and hydrogeological model parameters. The intrinsic relationship is unknown to us. Laboratory analysis might provide a good estimate, although it may be difficult to scale the relationship for use at the field scale (e.g. Moysey and Knight, 2004). Day-Lewis and Lane (2004) compared the correlation between a synthetic slowness (i.e., the inverse of velocity) structure and the estimated slowness structure derived from a hypothetical radar survey. They showed that the linear correlation coefficients between these two structures were space-varying, significantly less than one, a function of acquisition errors, survey geometry, and regularization. This implies that the model-based petrophysical relationship is different from the intrinsic petrophysical relationship and that it might be non-stationary even if the intrinsic petrophysical relationship is stationary. This is problematic, because:

- if we use a physically based relationship, such as Equation (3), or a close approximation of the intrinsic relationship based on laboratory analysis, its predictive power will be significantly decreased if we use it to relate our estimated geophysical model with hydrogeological properties and it might give biased results;
- an empirical relationship estimated by regression of collocated hydrogeological data and estimated geophysical parameters will not be strictly valid throughout the model domain even if all properties except the geophysical and hydrogeological system properties of interest are kept constant; and
- relationships that we establish in the field are not only a function of hydrogeological characteristics, but also of acquisition errors, survey geometry, and regularization of the inverse problem. These campaign-related errors reduce the validity of the developed relationships for use at other sites.

How large are these potential errors compared with other error sources and with regard to the accuracy needed to meet specific project objectives? It is not always necessary to have very detailed models and the effects discussed above might be insignificant in certain applications, such as mapping of the interface between salt and freshwater in coastal aquifers where the electrical formation factor is determined using borehole information and applied to large scale resistivity models. However, these effects are probably significant if we attempt to provide high-resolution characterization at the local scale in order to predict solute transport.

2.2.3.3. *Weak or No Parameterization of the Petrophysical Relationship*

In some cases, a relationship between a geophysical and a hydrogeological system property may not exist or it may be very weak. For example, Pride (2005) stated that there is no theoretical basis for a universal relationship between seismic velocity and permeability in porous media. However, site

specific models may exist (Pride, 2005; Hubbard et al., 2001; Hyndman et al., 2000), although they may vary within short distances (Prasad, 2003). It has been argued that the logarithm of electrical conductivity and the logarithm of permeability have a linear relationship, but the slope is site-specific and it is very sensitive to clay content (Purvance and Andricevic, 2000a).

In cases where the petrophysical relationships are weak, zonation approaches (see Section 2.2.2) can potentially be useful to determine the geometry of hydrofacies. Borehole information and tracer test data can subsequently be used to estimate the hydrogeological system properties of these zones (e.g. Hyndman et al., 1994; Hyndman and Gorelick, 1996; McKenna and Poeter, 1995, see also Section 2.5.1). Such an approach is useful when different facies have distinctly different geophysical properties because under such circumstances the determination of facies becomes relatively insensitive to errors in the geophysical data acquisition and the subsequent inversion. Alternatively, if we use a geostatistical parameterization or an Occam type of inversion we could impose restrictions on the model space. An example was provided by Gallardo and Meju (2004) who jointly inverted seismic refraction data and surface dc resistivity data by restricting the model space of the two models to models where the cross-gradients, \mathbf{t} , of the models were zero. The cross-gradient in the case of one geophysical model, \mathbf{m}_g , and one hydrogeological model, \mathbf{m}_h , is defined as

$$\boldsymbol{\tau} = \nabla \mathbf{m}_g \times \nabla \mathbf{m}_h \quad (4)$$

This approach has yet not been incorporated in hydrogeophysics, but it is promising because structural similarity between models is emphasized instead of a petrophysical relationship that is difficult to justify in many applications.

In short, the representation of the petrophysical relationship is one of the most difficult tasks in hydrogeophysical parameter estimation. A precautionary attitude is recommended.

2.2.4. A PRIORI INFORMATION

A priori information is information about characteristics of the models that we get from other sources of information rather than the actual geophysical or hydrogeological data. Prior information in deterministic inversions is used to define bounds of possible models, such as ensuring that velocities are positive, or that the electrical resistivities are below 10,000 Ohm-m in a sedimentary basin. These bounds should ideally represent information that is known without doubt. Stochastic inversion theory takes an additional step by assigning a probability distribution of the possible values of the model parameters before any measurements are made (e.g. Tarantola, 1987).

A priori information is sometimes used to tune the model to get agreeable features of the solution or make it well-posed. This violates a pure use of a priori information, but might be a good place to incorporate subjectivity, if needed. We agree with the ironic comment made by Jackson (1979) in discussing the use of a priori information to resolve non-uniqueness: “One disadvantage of the technique is that the assumptions which lie hidden in the abstractness of most methods are in this method left naked for the world to see.” An excellent tutorial to the use of a priori information is Scales and Tenorio (2001), and Malinverno and Briggs (2004) provided a discussion on how hierarchical and empirical Bayes can be used to avoid assuming that the probability distribution function is known.

2.2.5. OPTIMIZATION OR MONTE CARLO METHODS

Local optimization methods are the most common parameter estimation approaches and model uncertainties are typically evaluated around the solutions that minimize the objective function. Uncertainty is thus often described in terms of a standard deviation of the estimated model parameters or through sensitivity analysis of what parameters are better resolved than others. Furthermore, in a deterministic approach only uncertainties in the data are assumed. Uncertainty estimates performed in this way are often over-optimistic. Another form of uncertainty arises if the problem is strongly non-linear because it might result in local minima. There are ways to decrease non-linearity, such as transformation of the data, weighting, and alternative parameterizations of the models. We can also assess the existence of local minima by trying different initial and prior models (e.g. Oldenburg and Li, 1999). Even if we find the global minimum it does not mean that we can disregard other local minima. An alternative is to carry out a global search to derive the posterior pdf of all model parameters. Markov chain Monte Carlo Methods (MCMC) are often performed for computational efficiency using the Metropolis-Hastings algorithm (e.g. Mosegaard and Tarantola, 1995) or Gibb’s sampling (e.g. Chen et al., 2003), as will be described in Sections 2.4.3 and 2.5.3.

2.2.6. OBJECTIVE FUNCTIONS

In this section, we discuss common objective functions used in different estimation procedures. The treatment is cursory and it is mainly given to illustrate in a simple fashion how different methods are interconnected and to provide relevant references. We also spend some time discussing Occam’s inversion because of its widespread use in geophysical inversion. Geophysical inverse theory is treated by Menke (1984), Parker (1994), and Tarantola (1987); an excellent review of hydrogeological inversion is given by McLaughlin and

Townley (1996). A formalized treatment of stochastic forward and inverse modeling in hydrogeophysics is given by Rubin and Hubbard (2005).

The data fit χ_d^2 is often defined as

$$\chi_d^2 = (\mathbf{d} - \mathbf{F}[\mathbf{m}])^\top \mathbf{C}_d^{-1} (\mathbf{d} - \mathbf{F}[\mathbf{m}]), \quad (5)$$

where \mathbf{d} is an $N \times 1$ data vector (e.g. seismic travel times, mass fractions of tracer); \mathbf{F} is a forward model operator; \mathbf{C}_d^{-1} is the inverse of the data covariance matrix. It is commonly assumed that the data are uncorrelated, rendering the \mathbf{C}_d^{-1} a diagonal matrix that contains the inverses of the estimated variances of the observation errors; thus, more reliable data carry larger weight when evaluating the data fit. Our data covariance matrix can either be estimated or assumed to take certain values if the method does not allow an error estimate. There is an implicit assumption of Gaussian errors in this formulation of the data fit. This is neither the only nor necessarily the best description of data fit, but it is without doubt the most commonly used. Huber (2003) provided a review of robust statistics and Finsterle and Najita (1998) discussed robust estimation in hydrogeology.

A general description of the model norm assuming that the model parameters have a Gaussian distribution is

$$\chi_m^2 = (\mathbf{m} - \mathbf{m}_0)^\top \mathbf{C}_m^{-1} (\mathbf{m} - \mathbf{m}_0), \quad (6)$$

where \mathbf{m}_0 is an a priori model of size $M \times 1$; and \mathbf{C}_m^{-1} is the inverse of the model covariance matrix, which characterizes the expected variability and correlation of model parameters. However, the model covariance matrix is often unknown and it might be restrictive to damp the model to be close to an a priori model, if no good a priori model exists. Therefore, other model norms are typically defined using different measures of roughness (Constable et al., 1987), e.g. based on the first derivatives of the model

$$R_1 = (\partial \mathbf{m})^\top (\partial \mathbf{m}), \quad (7)$$

where ∂ is an $M \times M$ matrix, which for 1-D models is given by

$$\partial = \begin{bmatrix} 1 & & & \\ -1 & 1 & & 0 \\ & \dots & \dots & \\ & 0 & -1 & 1 \end{bmatrix} \quad (8)$$

The data fit and measures of model structure can be combined to formulate the most common objective functions.

A weighted least-squares objective function (Equation (5)) is used when we do not have any a priori information and when the inverse problem is well-posed without adding a regularization term. However, this is typically

not the case and we must impose a priori information, justified or not. The corresponding objective function corresponds with the maximum a posteriori (MAP) estimate (e.g. Menke, 1984):

$$\phi_{\text{MAP}} = (\mathbf{m} - \mathbf{m}_0)^T \mathbf{C}_m^{-1} (\mathbf{m} - \mathbf{m}_0) + (\mathbf{d} - \mathbf{F}[\mathbf{m}])^T \mathbf{C}_d^{-1} (\mathbf{d} - \mathbf{F}[\mathbf{m}]). \quad (9)$$

This is a weighting of a priori assumptions and data fit. However, we do not always have a good estimate of the model covariance and the data errors. Furthermore, the inverse problem may still not have a unique solution (e.g. the integral scales are extremely short). This is the reason why Occam types of inversion are so popular in geophysical applications. We briefly review Occam's inversion (Constable et al., 1987), which was originally developed for plane-wave electromagnetic data, but has been applied to diverse problems, including resistivity tomography (e.g. the commercial software Res2DInv of Loke (1997)). The goal of Occam inversion is to minimize R_1 (or any other measure of model roughness) subject to $\chi_d^2 = \chi_*^2$, where χ_*^2 is the desired level of data misfit. We solve the problem by minimizing the penalty functional $W_\lambda(\mathbf{m})$

$$W_\lambda(\mathbf{m}) = (\partial \mathbf{m})^T (\partial \mathbf{m}) + \lambda^{-1} \{ (\mathbf{d} - \mathbf{F}[\mathbf{m}])^T \mathbf{C}_d^{-1} (\mathbf{d} - \mathbf{F}[\mathbf{m}]) \}, \quad (10)$$

where λ^{-1} acts as a trade-off parameter between the smooth well-conditioned problem defined by a heavy penalty of model roughness (i.e., λ is large) and the ill-conditioned problem defined by the data fit (i.e., λ is small). For each iteration a line search for the λ that minimize χ_d^2 if $\chi_d^2 > \chi_*^2$, or else for the maximum λ for which $\chi_d^2 \leq \chi_*^2$, is made.

Occam approaches fit the data to the level of the estimated data errors with the smoothest possible model. Thus, we must be careful in adopting Occam types of inversion in environmental applications. Occam's inversion was developed for interpretation of magnetotelluric data, which is a technique that provides actual data error estimates and where we, due to the large depth of investigation, often have very limited a priori information. Therefore, it is sensible to be as conservative as possible. However, this method provides only a single model that might have little useful relations to the earth that gave rise to the observed data (Ellis and Oldenburg, 1994) and our prior knowledge. For example, it might be of little value to try to infer the spatial correlation structure of the estimated system property from an Occam inversion. In short, Occam's inversion invariably provides models that are smoother than the true Earth structure. Ellis and Oldenburg (1994) argued that we should construct alternative approaches that emphasizes the prior information and includes the observed data as a supplementary constraint. Please note that any a priori model or model covariance matrix in principle could be included in the Occam formulation if the objective function to minimize is defined as (Siripunvaraporn and

Egbert, 2000)

$$W_\lambda(\mathbf{m}) = (\mathbf{m} - \mathbf{m}_0)^T \mathbf{C}_m^{-1} (\mathbf{m} - \mathbf{m}_0) + \lambda^{-1} \{(\mathbf{d} - \mathbf{F}[\mathbf{m}])^T \mathbf{C}_d^{-1} (\mathbf{d} - \mathbf{F}[\mathbf{m}])\}, \quad (11)$$

which is identical to the MAP estimate (Equation (9)) if $\chi_d^2 = \chi_*^2$ is reached for $\lambda = 1$.

2.2.7. DIRECT MAPPING, INTEGRATION METHODS, OR JOINT INVERSION METHODS

We divide hydrogeophysical parameter estimation approaches into three broad categories: (1) direct mapping; (2) integration methods; and (3) joint inversion methods. We define *direct mapping* as a transformation of a geophysical model into a hydrogeological model, where hydrogeological data are only used to develop a petrophysical relationship or provide a qualitative understanding of the relationship between the geophysical and hydrogeological property of interest. Direct mapping is discussed in Section 2.3. *Integration methods* refer to cases where the geophysical inversion is performed independently of hydrogeological data, and vice versa. The task is to interpolate available data or inverse models given their uncertainties, petrophysical relationships, and a priori information. This group includes well-known geostatistical approaches such as co-kriging and Bayesian formulations; they are discussed in Section 2.4. Finally, *joint inversion methods* refer to cases where geophysical or hydrogeological inversion also utilizes hydrogeological or geophysical data, respectively. This diverse group is discussed in Section 2.5. There are large differences within each category and significant overlaps exist in many published studies (e.g. McKenna and Poeter, 1995; Hyndman and Gorelick, 1996). The critical choices discussed in Section 2.2 must be made regardless of our choice between direct mapping, integration methods and joint inversion methods. These choices are of fundamental importance and an attempt to provide some guidance was made in Section 2.2.

Relying on a set of case studies, we now discuss the strengths and limitations of these three different categories of hydrogeophysical parameter estimation methods. The categories refer to the stage in which hydrogeological and geophysical properties are related. There are advantages in inferring this relation at an early stage, but it comes at a price, as is discussed in the following sections. Our primary focus is on joint inversion methods, because interesting developments are taking place in this area and they are much less reviewed than direct mapping and integration methods in the hydrogeophysical literature.

The following discussion focuses only on applications within hydrogeophysics. We do not review the vast literature on data integration and joint inversion in other fields, such as in the petroleum (e.g. Deutsch, 2002) and mining engineering (e.g. Journel and Kyriakis, 2004) fields.

2.3. Direct Mapping

The simplest approach to hydrogeophysical parameter estimation is to transform the geophysical model into a hydrogeological model using a petrophysical relationship. This is the only possibility if we do not have any hydrogeological data. Hydrogeological data are absent or scarce in many applications, e.g. if we want to map a fracture zone for a potential well in sub-Saharan Africa (e.g. Caruthers and Smith, 1992); if we want to make preliminary investigations to find a site that meets our research objectives (e.g. Hubbard et al., 2001); or if we want to map salt-water intrusion (e.g. Yang et al., 1999). Such examples probably make up most applications in environmental geophysics. In such cases, it is important to use all available information and geological understanding to obtain the best possible geophysical model; ideally by performing joint inversion of different geophysical data sets (e.g. Meju, 1996; Gallardo and Meju, 2004). However, it is generally not advisable to transform a geophysical model into a hydrogeological model if no petrophysical relationship with reasonably high predictive power is available. It is often better to acknowledge our ignorance about the relation between our geophysical model and the underlying hydrogeological system and instead give qualitative interpretations, such as locations of possible clay lenses or fracture zones. Quantitative models could potentially be developed at a later stage if hydrogeological data become available. However, there are cases where direct mapping can be used for high-resolution studies of hydrogeological parameters. Water content estimation using Ground Penetrating Radar (GPR) is one example where direct mapping is often acceptable, and it is discussed in the next section.

2.3.1. EXAMPLE 1: ESTIMATION OF WATER CONTENT

In recent years, GPR has developed as a tool for mapping water content and movement within the vadose zone. A review of GPR concepts and applications in hydrogeological applications is provided by Annan (2005).

As recently summarized by Huisman et al. (2003), a variety of GPR approaches have been successfully used to estimate soil water content, including the use of ground-based GPR ground-wave and reflection data, and GPR crosshole tomographic direct wave travel time data. With most approaches, the velocity is first estimated and is then converted to a dielectric constant using Equation (1), which is then converted to water content using relationships such as Equation (3). For example, Grote et al. (2003) used the GPR ground-wave travel time data to estimate volumetric water content, and reported a volumetric water content RMS error of 0.011 to 0.017 using 900 and 450 MHz antennas, respectively. Fisher (1992), Greaves et al., (1996), and van Overmeeren et al. (1997) used common midpoint (CMP) approaches

to estimate water content. In general, the time required to collect CMP data makes this approach prohibitive for water content estimation over large areas, and the error associated with CMP velocity analysis is typically on the order of 10% (Tillard and Dubois, 1995, Greaves et al., 1996). Common-offset GPR data are faster and easier to collect, although in order to estimate the velocity of the reflected wave, one must have information about the depth of the reflector. Grote et al. (2002) investigated the utility of the GPR common-offset approach using reflectors buried at a known depth, and found that this approach was accurate to within 0.01. More recently, Lunt et al. (2004) used wellbore information together with common offset GPR reflection data to assess the error associated with the GPR water content reflection method under natural conditions. Lunt et al. (2004) found that the RMS water content error under natural conditions was 0.018. Hubbard et al. (2005) used the GPR reflection travel time data of Lunt et al. (2004), together with wellbore soil layer depth information within a Bayesian framework to estimate water content associated with an interface located 0.5–1.4 m below ground surface over a 2.5 acre field site.

Crosshole radar methods are now used quite frequently to map or monitor water content (Hubbard et al., 1997; Binley et al., 2001; Peterson, 2001; Alumbaugh et al., 2002). For tomographic acquisition, the transmitter and receiver position are varied until the entire interwell area is traversed by electromagnetic waves. Inversion algorithms are used to invert the GPR travel time data into velocity (e.g. Peterson, 2001), which are then translated into dielectric constant using Equation (1) and water content estimates using relations such as Equation (3). It should be noted that ray-based tomographic techniques invert for slowness (i.e., the inverse of velocity). Alumbaugh et al. (2002) showed that water content estimates obtained from crosshole GPR have an RMS error of 0.03. Crosshole surveys are useful in that they can provide high-resolution two-dimensional images of water content at one point in time, or, when measured in a time-lapse sense, as a function of time (Hubbard et al., 1997; Eppstein and Dougherty, 1998; Binley et al., 2002; Day-Lewis et al., 2003). Although crosshole tomographic radar data are becoming more commonly used for moisture monitoring, the maximum borehole separation distance of about 15 m generally limits this technique to very local-scale investigations.

An example of the use of crosshole radar data for estimating volumetric water content is illustrated using data collected within the porous granular vadose zone of the DOE Hanford Site in Washington (Ward et al., 2000; Gee and Ward, 2001). Neutron probe data were collected at this site, calibrated using gravimetric techniques, and interpreted in terms of volumetric water content (Ward et al., 2000). Tomographic GPR data were collected using the PulseEKKO 100 GPR system and 200 MHz antennas (Majer et al.,

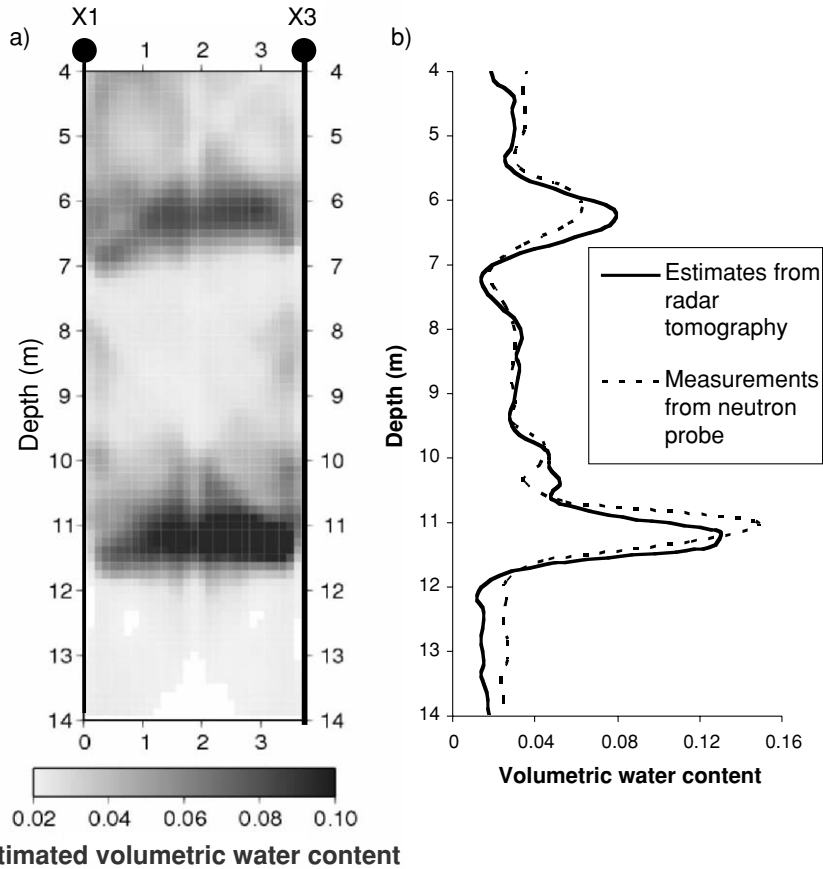


Figure 2. (a) Volumetric water content estimated using tomographic radar data, (b) comparison of tomographic estimates and neutron probe measurements of water content near borehole X3

2002). Inversion of the tomographic travel time data was performed following Peterson (2001), and used with Equation (1) to estimate dielectric constants. Equation (3) was used to convert the dielectric constant estimates to water content, with $\kappa_s = 5.6$ (Kowalsky, 2004b), and $\phi = 0.345$ (inferred from saturated water content values of Zhang et al. (2004)). Figure 2a shows the 2-D distribution of estimated volumetric water content between two wells, and Figure 2b shows a comparison of neutron probe values collected from an access tube located close to X3 with the estimates of water content obtained from the tomographic pixels along the column located approximately 0.25 m away from X3 wellbore (to avoid the geophysical distortion commonly encountered at the wellbore location). Figure 2 illustrates that a simple mixing model was sufficient for estimating water content in multiple directions with a reasonable

accuracy, and thus highlights the use of GPR for direct mapping of water content.

2.4. Integration Methods

By integration methods, we refer to approaches where the geophysical inversion is carried out independently of the hydrogeological data or where the hydrogeological inversion is carried out independently of the geophysical data. Integration methods are widely used and we discuss two types: co-kriging and Bayesian approaches.

2.4.1. CO-KRIGING

Co-kriging (Deutsch and Journel, 1992) is a widely used method in geostatistics; it is essentially kriging conditioned on secondary information. Co-kriging is valid if we can represent the data such that measurement errors are Gaussian with a known variance; the area under study is stationary or stationary within large areas; and if the relation between the attributes is linear and known. The estimate is an expected mean behavior and it should not be considered as a realistic model of the true system properties. A classical application of co-kriging is to infer the transmissivity distribution of an aquifer using transmissivity estimates and hydraulic head data (e.g. Clifton and Neuman, 1982). Applications of co-kriging using hydrogeological and geophysical data include Doyen (1988), Parks and Bentley (1996), Cassiani and Medina (1997), Lesch et al. (1995), Cassiani et al. (1998), and Gloaguen et al. (2001).

Co-kriging is a straightforward method to apply and it is useful when the assumptions behind the method are valid and the type of information obtained is sufficient for project objectives. Drawbacks with the method are that the estimation variance only gives a qualitative estimate of model uncertainty and the estimated model is unrealistically smooth.

2.4.2. BAYESIAN METHODS

Bayes' theorem is an appealing framework for integration of different types of data and a priori information. General literature on Bayesian methods includes Press (1989) and Sivia (1996).

A Bayesian formulation of data integration is more general than co-kriging because it allows any prior distribution as well as non-linear petrophysical relationships. Chen et al. (2001) combined collocated geophysical models of GPR velocity, GPR attenuation, and seismic velocity with permeability estimates

from flowmeter data to estimate the likelihood functions for the case of three geophysical data types. The likelihood functions were estimated through a normal linear regression method. The prior was a kriged estimate of the permeability structure based on flowmeter data where the correlation structure was estimated using available geophysical models and flowmeter data. This approach was used to estimate the permeability structure at the South Oyster Bacterial Transport Site (Chen et al., 2001; Hubbard et al., 2001). In the next section, we will give an example of an integration method for geochemical characterization.

2.4.3. EXAMPLE 2: GEOCHEMICAL CHARACTERIZATION

Traditional methods for characterizing geochemical heterogeneity typically involve drilling a borehole and either retrieving a soil sample for laboratory analysis or collecting borehole logs within the hole. Although these methods are deemed necessary for collecting data to understand field-scale bacterial transport processes, it is prohibitive to use them intensively for collecting dense data to estimate geochemical parameters in a multi-dimensional domain. Borehole-sampling methods combined with geophysical methods, hold potential for improved geochemical characterization, as is discussed below.

This study demonstrates the use of GPR tomographic data collected at the DOE South Oyster Bacterial Transport Site in Virginia for estimating solid-phase Fe(II) and Fe(III) concentrations using a sampling-based Bayesian model. By exploiting the site-specific mutual dependence of GPR attenuation and extractable Fe(II) and Fe(III) concentrations on lithofacies (developed using collocated GPR attenuation pixel values and soil sample measurements), a Bayesian model was developed. Within the model, lithofacies and Fe(II) and Fe(III) concentrations at each pixel between the boreholes were considered as random variables. The borehole lithofacies measurements and crosshole GPR tomograms (Figure 3a) were considered as independent parameters. By conditioning all the unknowns to the available datasets, a joint posterior probability distribution function of those variables was defined at each location. Using a Markov chain Monte Carlo (MCMC) method, many samples of each unknown were obtained, which were subsequently used to calculate mean, variance, and predictive intervals for each unknown variable.

Cross validation was performed based on data at the three wells, shown as wells D1, D2, and D3 in Figure 3, to assess the accuracy of the developed estimation method. Each well in turn was considered as a testing well and the other two wells as training wells. Cross validation results show that the geophysical data, constrained by lithofacies, have the potential

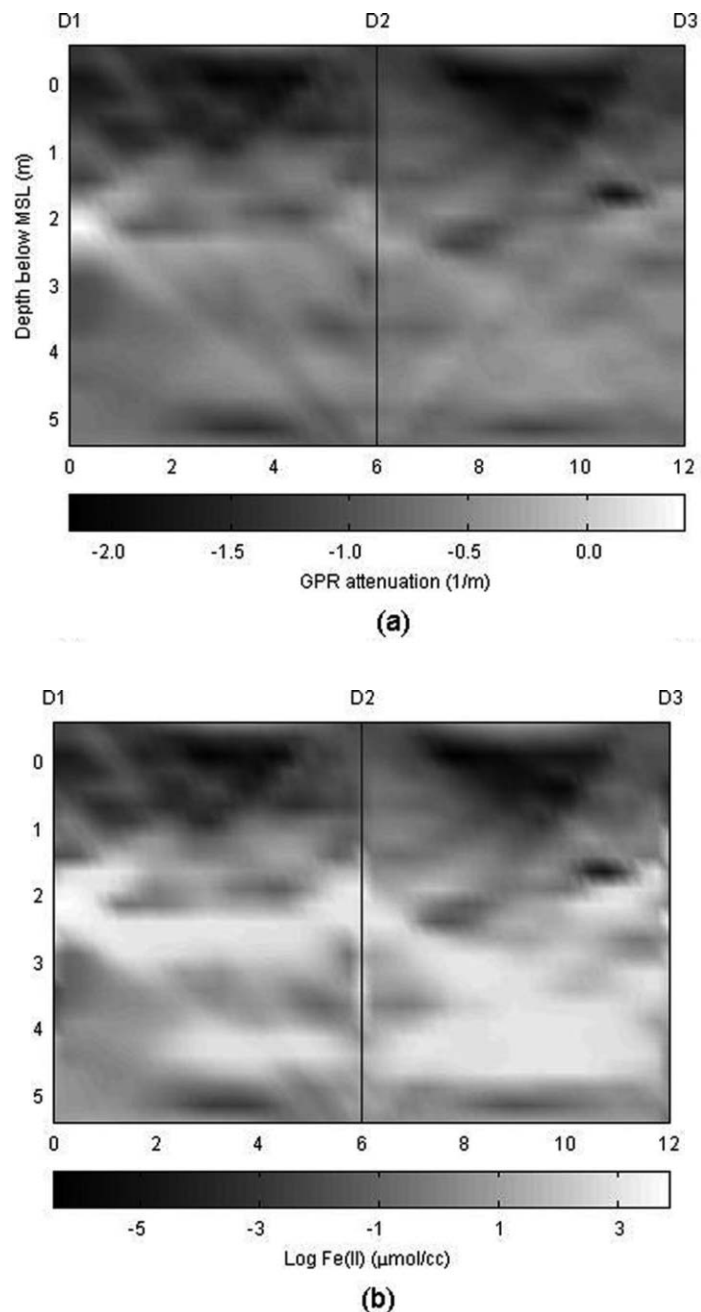


Figure 3. (a) GPR attenuation; (b) estimated mean natural logarithmic Fe(II) concentrations; (c) frequency of sand (a frequency of 0.0 implies that lithofacies is mud, whereas a frequency of 1.0 implies that lithofacies is sand); (d) estimated mean natural logarithmic Fe(III) concentrations (from Chen et al., 2004)

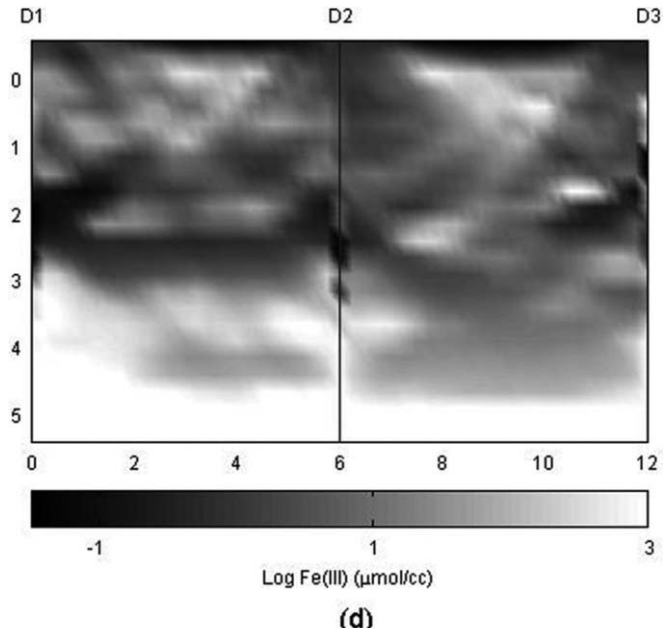
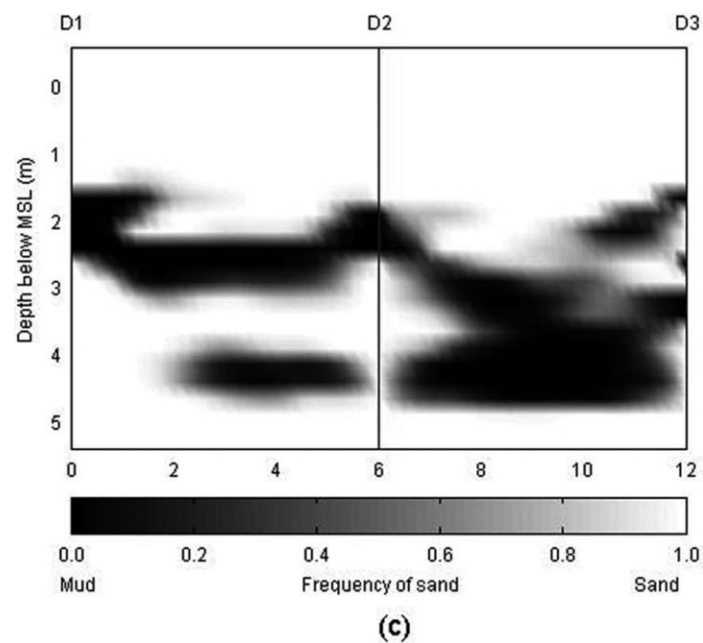


Figure 3. (Continued)

for providing high-resolution, multi-dimensional information on extractable Fe(II) and Fe(III) concentrations at the South Oyster site.

Figures 3 (b–d) show the two dimensional images of the estimated mean logarithmic extractable Fe(II) concentrations, the probability of sand lithofacies, and the mean logarithmic extractable Fe(III) concentrations, respectively. It is evident that with the help of high-resolution GPR tomograms, the measurements of extractable Fe(II) and Fe(III) as well as lithofacies measurements can be extended to locations where direct measurements are not available. For details, see Chen et al. (2004).

2.4.4. DISCUSSION OF INTEGRATION METHODS

Integration methods are relatively easy to implement because geophysical inversion and hydrogeological data processing are carried out separately. Furthermore, they rely on well-established techniques to integrate different types of data. This category of parameter estimation methods is relatively mature, and many successful case-histories exist (e.g. Cassiani and Medina, 1997; Chen et al., 2001; Hubbard et al., 2001; Chen and Rubin, 2003; Chen et al., 2004). However, they have some inherent limitations.

- The geophysical inverse models used in the estimation could potentially be improved if we incorporate hydrogeological data in the geophysical inverse procedure because of information sharing. Integration methods do not take advantage of this opportunity.
- Geophysical models typically have a space-varying resolution. We should strive to constrain our hydrogeological models to the features that are well constrained in the geophysical inversion, and avoid interpreting phantom structures or features that are not related to hydrogeological system properties. In principle, it may be possible to assign different weights to areas with different resolution. In practice, however, it is difficult to estimate those weights. This is a common problem in the interpretation of any geophysical model. One way to decrease the effects of this problem is to incorporate the geophysical inversion (Hyndman et al., 1994; Hyndman and Gorelick, 1996) or the geophysical model (Hyndman et al., 2000; Linde et al., 2006) as a part of the hydrogeological inversion (see Section 2.6.1).
- We often assume that the petrophysical relationship is stationary and use it over the entire spatial domain. In practice, non-stationary petrophysical relationships are common. For example, we know that intrinsic petrophysical relationships might show non-stationary behavior under certain conditions (e.g. Prasad, 2003; Yeh et al., 2002). Even a perfect stationary intrinsic relationship may break down in the geophysical inversion (Day-Lewis

and Lane, 2004). More discussion of stationarity was provided in Section 2.2.2.

- How should we estimate the model-based petrophysical relationships? The natural choice is to compare collocated tomographic pixels and nearby borehole information (e.g. Chen et al., 2001; Hubbard et al., 2001). However, for ray-based tomography (GPR and seismic), the resolution of the inverted geophysical data at or near boreholes is worse than the resolution in the central parts of the tomograms (e.g. Day-Lewis and Lane, 2004), whereas the resolution is best close to the borehole in ERT applications. Thus, the location where collocated data are used to develop a site-specific relationship can impact the resulting hydrogeological model. In addition, the environment around the boreholes may be disturbed by the drilling, altering both the hydrogeological and the geophysical measurements and thus further complicating the task of estimating a valid petrophysical relationship throughout the tomogram.
- In integration methods, we often assume that the resolution of the geophysical models is fine enough that the resulting hydrogeological models capture all important variations of the hydrogeological system properties. This assumption might not be valid in some applications because we know that the tomograms are smooth estimates of the true geophysical structure and that they have a limited resolution (e.g. Day-Lewis and Lane, 2004).

Moysey et al. (2005) developed a framework to address some of the limitations associated with the development of petrophysical relationships. In their study, a stochastic calibration method was developed to estimate field-scale estimates of petrophysical relationships given a petrophysical relationship at the core scale. Conditional realizations of the system property of interest were generated (e.g. water content) using petrophysical relationships and geostatistical information. These realizations were mapped into geophysical realizations (e.g. dielectric constant) using the appropriate petrophysical relationship at the core scale (e.g. the CRIM formula). Synthetic geophysical surveys were performed and inversions of these realizations were made. Using this approach, average or pixel-specific field-scale petrophysical relationship could be developed that takes scaling, measurement errors, uncertainties in the petrophysical relationship, and the inversion process into account. Moysey et al. (2005) illustrated for a synthetic example how the methodology improved water content estimation using radar tomograms compared with the case where the intrinsic relationship was applied to map the tomographic estimate into water content. However, a priori knowledge is needed about the spatial correlation structure of the system property of interest, the errors of the data, and the intrinsic petrophysical relationship. Nonetheless, the study indicates how the hydrogeophysical community has recognized some of the

limitations involved in earlier estimation approaches and how efforts are underway to overcome these obstacles.

In the next section, we discuss how joint inversion methods can improve estimates compared with integration methods. However, the limitations listed above will always apply to some degree.

2.5. Joint Inversion Methods

In Section 2.2.7, we gave the following definition: “by joint inversion methods we refer to cases where geophysical or hydrogeological inversion also utilizes hydrogeological or geophysical data, respectively.” Thus, joint inversion includes many different approaches for hydrogeophysical parameter estimation, including:

- geophysical inverse modeling that incorporates measurements of hydrogeological system properties;
- geophysical inverse modeling that incorporates both measurements of hydrogeological system properties and measurements of dependent hydrogeological variables;
- hydrogeological inversion that is regularized by geophysical models, and maybe also by measurements of hydrogeological system properties; or
- both hydrogeological and geophysical inverse modeling are conditioned to both measurements of hydrogeological and geophysical system properties, as well as dependent hydrogeological and geophysical variables. These joint inversion models can either be updated simultaneously or in a sequential fashion.

Joint inversion of hydrogeological and geophysical data sets is a current topic of research (e.g. Yeh and Simunek, 2002). In the following, we present several examples in which joint inversion models were applied, including the zonation of a 3-D structure in a sandy aquifer (see Section 2.5.1); estimation of flow parameters in the vadose zone (see Section 2.5.2); and delineation of fracture zones (see Section 2.5.3). Finally, we gather the experiences from these examples and other studies to make some concluding remarks on joint inversion methods.

2.5.1. EXAMPLE 3: ZONATION OF PERMEABILITY

Hyndman et al. (1994) performed coupled seismic and tracer test inversion in a 2-D synthetic aquifer in order to estimate zones of high and low permeability. The motivation for this study was that geophysical information might help in estimating the permeability structure, but that it is sometimes

not justified to impose a known petrophysical relationship. The assumption behind their approach was that changes in lithology manifest as large changes in seismic velocity. Furthermore, they argued that groundwater flow is often predominantly controlled by large-scale heterogeneities. Their approach was based on a division of the seismic velocities into two classes. They applied their split inversion methodology (SIM), which essentially estimates a tomogram with zones delineating the spatial distribution of two lithological classes. The permeabilities of the classes were determined using tracer test data. The zonation was updated by minimizing the squared misfit of seismic travel times and tracer test data. The permeabilities within the classes were updated. This procedure was repeated in an iterative fashion.

Hyndman and Gorelick (1996) extended this analysis to 3-D and three unique lithological classes. They applied their method to the Kesterson aquifer. They observed a reasonably good data fit to the tracer test data. Hyndman et al. (2000) established a linear field scale model-based petrophysical relationship between seismic velocity and permeability. They did this by transforming realizations of the seismic velocity structure at Kesterson into permeability. The relationship between seismic velocity and permeability had a correlation factor of 0.74, which can be compared with a relationship of 0.16 using borehole data. The tracer test data were better explained when the permeability realizations were obtained using both hard permeability data and soft seismic slowness models (Figure 4b) compared with only permeability data (Figure 4a).

2.5.2. EXAMPLE 4: VADOSE ZONE PARAMETER ESTIMATION USING TIME-LAPSE GPR TRAVEL TIME DATA

Crosshole GPR measurements are being used increasingly for monitoring transient flow processes in the vadose zone, thanks to their high sensitivity to pore water distribution in the subsurface (see Equation (2)). As described in Section 2.3.1, tomographic inversion techniques (e.g. Peterson et al., 2001) are typically applied to crosshole GPR data sets to infer spatial distributions of electromagnetic velocity or dielectric constant, which can be related to water saturation through a petrophysical relationship, such as Equation (3). However, while tomographic techniques are useful for gaining a qualitative understanding of flow processes (such as identifying flow directions and preferential flow paths), in general they cannot be used to obtain quantitative estimates of vadose zone flow parameters, such as permeability and the soil hydraulic parameters of the capillary pressure and relative permeability functions.

In the present section, we describe an alternative approach for using cross-hole GPR data that allows flow parameter distributions to be estimated in the vadose zone. This approach, described in detail by Kowalsky et al. (2004),

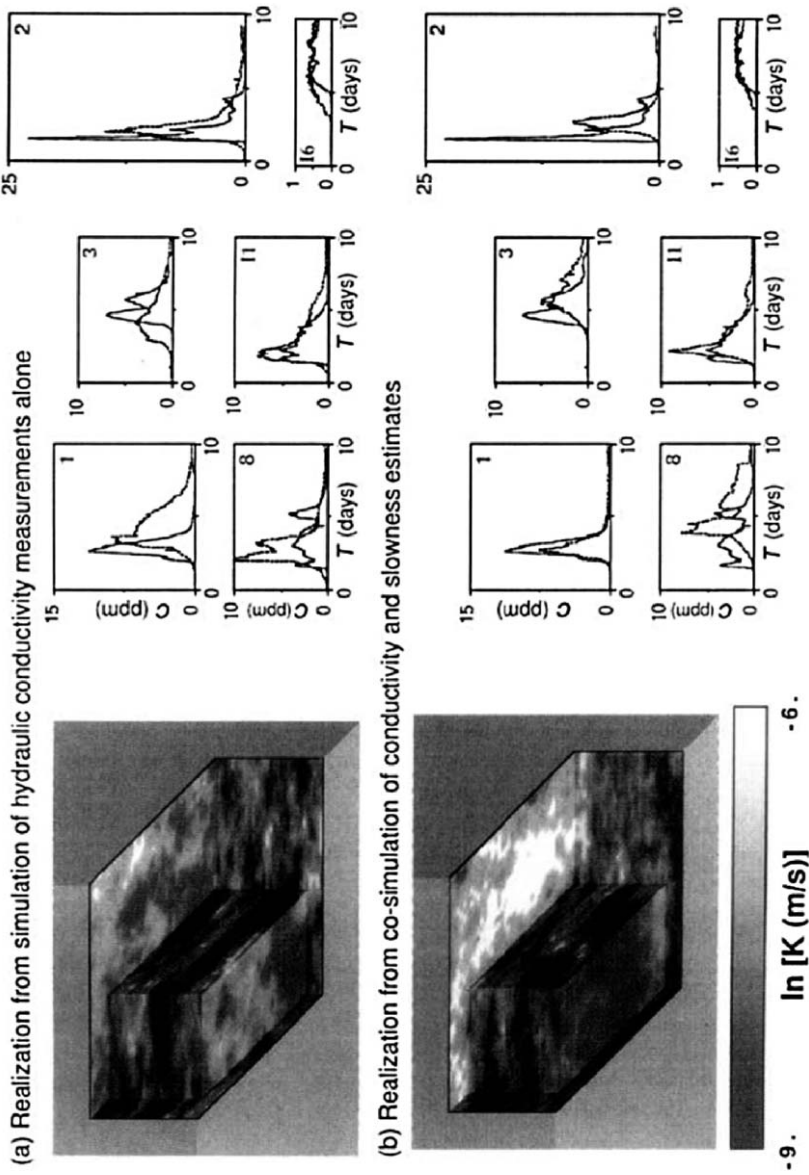


Figure 4. Comparison of tracer concentration histories for the 1986 fluorescein test at the Kesterson aquifer simulated through permeability realizations (a) generated using permeability measurements alone and (b) generated using sequential Gaussian cosimulation with hard permeability data and soft seismic slowness data from a seismic realization (adopted from Hyndman et al., 2000)

involves the joint inversion of hydrological and geophysical measurements collected during transient flow events. Geophysical observations are indirectly related to the hydraulic system properties: for any given soil hydraulic parameter estimates, a flow experiment is simulated and the resulting distributions of water saturation are used as input to simulate dependent geophysical state variables. Inversion proceeds by perturbing the hydraulic parameters – which causes changes in the simulated water distributions and the subsequent dependent geophysical state variables – until a good match between simulated and measured geophysical and hydrological data is achieved.

The example considered by Kowalsky et al. (2004) involved the case where the only non-uniform flow parameter is the permeability, and it can be treated as a log normally distributed space random function (SRF) with known patterns of spatial correlation. Through a maximum a posteriori (MAP) inversion framework that employs concepts from the pilot point method, the log permeability distribution and additional flow parameters can be estimated. This methodology allows for the generation of multiple parameter distributions that reproduce measurements of permeability, that contain the specified patterns of spatial correlation, and that are consistent with the hydrological and geophysical data; these parameter distributions can be used for hydrological modeling and also to calculate parameter probability density functions, which provide a measure of parameter uncertainty.

The GPR measurements considered in this example were those corresponding to the zero-offset profile (ZOP). In this case, the GPR antennae are kept in their respective wells at equal depths, and a single measurement is taken at each depth as the antennae are simultaneously lowered, yielding a data set that can be collected quickly but that does not contain as much information as if collected for two-dimensional tomographic reconstruction. One complication with multiple-offset gathers (MOG), where the antennae positions are varied such that a large number of angles pass the volume between the boreholes, is that data collection take a lot of time in relation to the infiltration processes under study.

Results of the synthetic example indicate that inversion with ZOP GPR measurements allows for accurate prediction of the soil hydraulic parameters, even with moderate noise (assumed normally distributed) present in the GPR data. While GPR measurements offer the benefit of non-intrusively monitoring changes in water saturation over large distances, measurements collected using ZOP are insensitive to lateral variations in flow. However, the combined use of ZOP measurements with local borehole saturation measurements greatly improves the accuracy and reduces the uncertainty of parameter estimates (see Figure 5).

A main limitation in this example, but not in the approach itself, lies in the assumption that the permeability is the only non-uniform parameter,

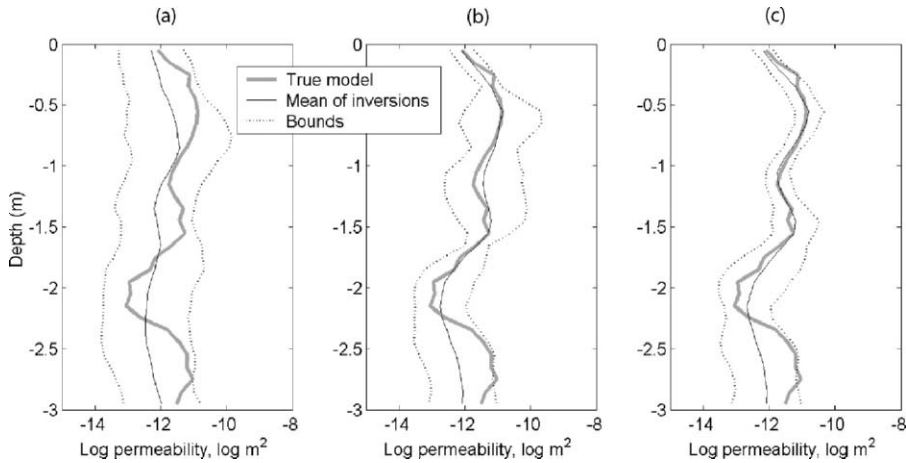


Figure 5. Vertical cross-section (within 2-D model) showing true log permeability (gray) and mean surfaces obtained from 20 inversion realizations (black lines) for (a) conditional simulation (no inversion performed), (b) inversion using only ZOP GPR measurements, and (c) inversion using ZOP GPR measurements and local borehole saturation measurements. The estimation bounds are shown with dotted lines (from Kowalsky et al., 2004)

since in reality additional flow parameters can be non-uniform. (It should be noted that information describing the spatial variability of soil hydraulic parameters is limited.) Additionally, it was assumed that the spatial correlation patterns of log permeability were known, as was the petrophysical model. The possibility of jointly estimating the parameters of the petrophysical model, using travel time measurements for arbitrary GPR antennae positions (data collection configurations other than the ZOP), and using real field data are addressed elsewhere (Kowalsky et al., 2005).

2.5.3. EXAMPLE 5: FRACTURE DELINEATION USING SEISMIC SLOWNESS

Characterization of fractured aquifers is important for contaminant remediation and water resources investigations. Due to the complexity of fracture formations, such characterization is very challenging using conventional methods, such as borehole logging. For successful characterization, integration of multiple sources of information is often needed.

Crosshole seismic techniques have, among many other geophysical methods been found to be useful for fracture characterization. For instance, Cohen et al. (1995) showed that seismic tomography could be used to map permeable fracture zones based on data collected from the Raymond site in Virginia. Majer et al. (1997) used time-lapse seismic tomographic data before and after

air injection to detect fracture channels at the Newkirk site in Oklahoma. Ellefsen et al. (2002) used seismic tomograms to map hydrogeological zonation at the Mirror Lake site in New Hampshire. Daley et al. (2003) demonstrated the potential of using seismic tomograms to monitor contaminant transport in fractured aquifers at the Idaho National Laboratory site. The main reason for the success of these examples is that seismic velocity is a function of the stiffness and density of the medium and fractures often cause a decrease of the stiffness of the medium and hence a reduction in seismic velocity.

However, in all those applications seismic travel times were first inverted and the resulting seismic velocity values were then used for hydrogeological characterization. This approach is limited for quantitative fracture characterization. First, the inverted seismic velocity is subject to uncertainty because of many reasons, such as source and receiver locations, measurement errors, deviations of boreholes, and choice of inversion methods. Second, petrophysical relations between seismic velocity and hydrogeological properties are non-unique. This is because seismic methods measure effective mechanical properties of the medium, and hydraulic behavior is not governed by the mechanical properties of the medium, although it is related (Majer et al., 1990). As indicated by many studies of fractured rock (e.g. Majer et al., 1990), only a part of the fractures are hydraulically conductive. Therefore, low seismic velocity does not necessarily correspond to high permeability.

To circumvent these limitations, Chen et al. (2003) developed a new approach to integrate crosshole seismic and borehole flowmeter data for characterizing fractured aquifers. They considered seismic travel time (rather than inverted seismic velocity) as data and considered seismic velocity and hydrogeological zonation indicator at each pixel as unknown random variables. They used a probabilistic petrophysical model with unknown parameters to link seismic velocity to hydrogeological properties. Within a Bayesian framework, the unknown variables and parameters were simultaneously estimated using a Markov chain Monte Carlo method by conditioning to crosshole seismic travel time and borehole flowmeter data. Data collected at the US DOE NABIR Field Research Center (FRC) at the Oak Ridge National Laboratory in Tennessee were used to test the methodology.

Figure 6 shows the estimated probabilities of being in the high permeability fracture zone along the cross-section between two wells. The black color represents high probability and the white color represents low probability of being in the fracture zone. This image provides more information about hydrogeological zonation than using borehole flowmeter data only. If we use some cutoff value, for example 0.5 or 0.75, we can obtain an estimate of hydrogeological zonation in the fractured aquifer. We have also quantitatively compared our estimated results with the field tracer experiments, and they are consistent. For details, please see Chen et al. (2003).

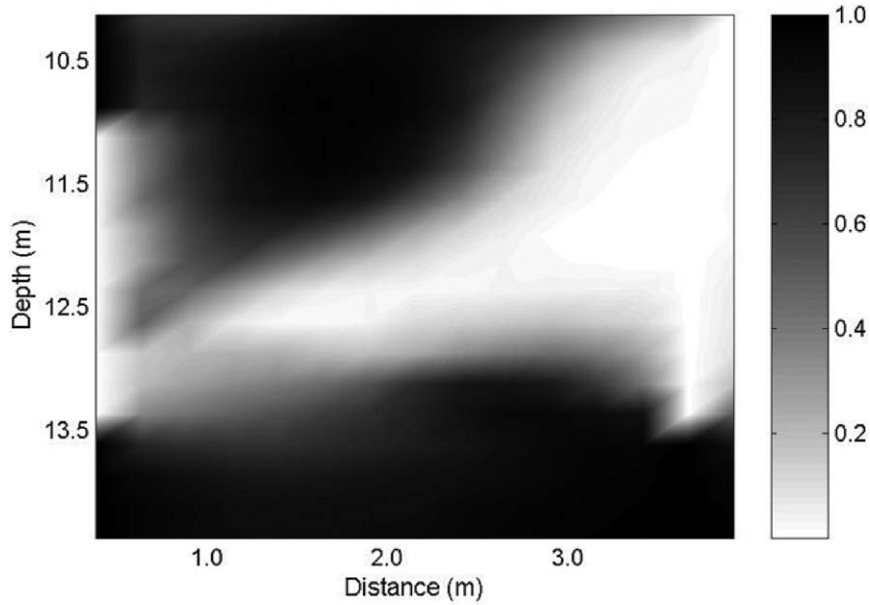


Figure 6. The probability of high permeability fracture zone along a cross section (from Chen et al., 2003)

2.5.4. DISCUSSION OF JOINT INVERSION METHODS

Our wide definition of joint inversion methods includes all inversions where both hydrogeological and geophysical data are used. Advantages arise in joint inversion methods compared with integration methods because well-posedness of the inverse problem generally improves when we add additional sources of information. A further advantage is that we can be very flexible in handling the petrophysical relationship within the inversion. Thus, we can test the influence of assuming a known petrophysical relationship by letting the parameters in the petrophysical relationship be free parameters in the inversion. We partially avoid scaling problems, and we can develop the petrophysical relationship at the field scale. However, we must note that measurements of hydrogeological system properties are also included in integration methods (see Section 2.4) and the improvements in including them in the inversion remains to be tested. However, more fundamental improvements can be obtained through joint inversion using measurements of both geophysical and hydrogeological state variables. The reason is simply that if no measurements of dependent hydrogeological state variables are included (e.g. tracer test data), all resolved structure away from measurements of hydrogeological system properties (e.g. permeability in boreholes) is due to what we resolve in the geophysical inversion. This means that we

must assume stationary petrophysical relationships without any good means of testing this assumption, and we must assume that all relevant hydrogeological structure has a geophysical signature. On the other hand, measurements of hydrogeological state variables give us the opportunity to simultaneously minimize the misfit of both the hydrogeological and geophysical data.

2.6. Summary and Outlook

Because geophysical data provide additional information for hydrogeological parameter estimation, even if there is uncertainty in the geophysical data and models, hydrogeophysics offers the potential for improved subsurface characterization. The choice of the appropriate hydrogeophysical parameter estimation approach largely depends on the problem. Each method is based on assumptions, which should be acknowledged and examined. No method is good for all applications at the current stage. There is much room to improve our current methods as hydrogeophysics is a new and interdisciplinary field.

In this chapter, we have discussed choices that must be made in hydrogeophysical parameter estimation. We have also attempted to classify hydrogeophysical parameter estimation into three classes: direct mapping; integration methods, and joint inversion methods. We do not advocate one particular approach, but we emphasize the importance of stating our assumptions and have realistic expectations on the estimates. These expectations should be formed with regards to the available data, the project objectives, and the hydrogeophysical parameter estimation approach. The justification of assumptions becomes very important when we want to estimate quantitative and detailed hydrogeological models, for example, that are to be used as input to flow simulations in a risk analysis.

For a quantitative analysis, we should ideally know, among other factors: the errors of our data, the intrinsic petrophysical relationships, the space-varying resolution of our individual inversion models, scaling laws, the spatial correlation of different properties, discretization effects, effects of physical simplifications in the forward operators, and the small-scale variability. Naturally, sometimes the resulting estimates are relatively insensitive to errors in the description of these effects, and it might be justified to assume that we have a correct description. However, this needs to be checked, for example, by using synthetic examples or by studying similar cases in the literature.

How can fundamental improvements in hydrogeophysical parameter estimation be realized? In this work we have focused on a given data set and

problem. We have discussed how we could treat uncertain petrophysical relationships, and in a qualitative manner discussed how different choices of for example objective functions or parameterization influence our estimate. We have also discussed different approaches to parameter estimation. However, careful survey design and surveying, together with a good conceptual understanding of the problem, of the petrophysical relationships, and the dominant processes are probably the most important factors in successful hydrogeophysical parameter estimation efforts. Obviously, even the most sophisticated approach cannot give a detailed estimate based on very noisy data, but it can provide reasonable error bounds. As hydrogeophysics evolves we must put more emphasis on minimizing, estimating, and parameterization of the errors in our measurements in order to improve the estimations and their uncertainty bounds. We need to improve our understanding of the validity of petrophysical relationships and maybe put more emphasis on methods that are more closely linked to groundwater flow and permeability, such as induced polarization (IP) and self-potential (SP) methods.

In conclusion, our challenge is not only to develop new parameter estimation methods, but also to make sure that the assumptions we make are valid for a given application, or at least that they do not severely bias results. We will never obtain a true model of the Earth's structure, but hopefully we can obtain models that sufficiently meet our needs, even if they provide only limited information, such as bounds around the true system properties. For this to happen, we must improve our estimations of measurement and modeling errors. We believe that approaches that we term joint inversion methods are well suited to increase our knowledge about the worth of different data types and to design field campaigns that have the potential to give the best characterization for a given budget. However, joint inversion methods are in their infancy and the solution to many problems of practical importance can be adequately addressed using direct mapping or integration methods.

Acknowledgements

This study was partly funded by DE-AC03-76SF00098 to Susan Hubbard. Some of the computations were carried out at the Center for Computational Seismology (CCS), supported by DOE's office of Basic Energy Sciences at Lawrence Berkeley National Laboratory. We are thankful to Laust Pedersen (Uppsala University) for commenting on the draft manuscript. Comments from one anonymous reviewer and J.A. Huisman helped to significantly improve this chapter.

References

Alharthi, A., and J. Lange, 1987. Soil water saturation: Dielectric determination, *Water Resour. Res.*, 23 (4), 591–595.

Alumbaugh, D., P. Chang, L. Paprocki, J. Brainard, R.J. Glass, and C.A. Rautman, 2002. Estimating moisture contents in the vadose zone using cross-borehole ground penetrating radar: A study of accuracy and repeatability, *Water Resour. Res.*, 38 (12), 1309.

Annan, A.P., 2005. GPR methods for hydrogeological studies, in *Hydrogeophysics*, edited by Y. Rubin and S.S. Hubbard, Springer, The Netherlands, pp. 185–214.

Archie, G.E., 1942. The electrical resistivity log as an aid in determining some reservoir characteristics, *Trans. AIME*, 146, 54–62.

Auken, A., and A.V. Christiansen, 2004. Layered and laterally constrained 2D inversion of resistivity data, *Geophysics*, 69 (3), 752–761.

Binley, A., P. Winship, R. Middleton, M. Pokar, and J. West, 2001. High-resolution characterization of vadose zone dynamics using cross-borehole radar, *Water Resour. Res.*, 37 (11), 2639–2652.

Binley, A., P. Winship, L.J. West, M. Pokar, and R. Middleton, 2002. Seasonal variation of moisture content in unsaturated sandstone inferred from borehole radar and resistivity profiles, *J. Hydrol.*, 267 (3–4), 160–172.

Butler, J.J., Jr., 2005. Hydrogeological methods for estimation of spatial variations in hydraulic conductivity, in *Hydrogeophysics*, edited by Y. Rubin and S.S. Hubbard, Springer, The Netherlands, pp. 23–58.

Carrera, J., and S.P. Neuman, 1986a. Estimation of aquifer properties under transient and steady state conditions, 1, Maximum likelihood method incorporating prior information, *Water Resour. Res.*, 22 (2), 199–210.

Carrera, J., and S.P. Neuman, 1986b. Estimation of aquifer properties under transient and steady state conditions, 2, Uniqueness, stability and steady state conditions, 2, *Water Resour. Res.*, 22 (2), 211–227.

Carrera, J., and S.P. Neuman, 1986c. Estimation of aquifer properties under transient and steady state conditions, 3, Application to synthetic and field data, *Water Resour. Res.*, 22 (2), 228–242.

Caruthers, R.M., and I.F. Smith, 1992. The use of ground electrical survey methods for siting water-supply boreholes in shallow crystalline basement terrains, in *Hydrogeology of Crystalline Basement Aquifers in Africa*, edited by E.P. Wright and W.G. Burgess, Geological Society Special Publication No. 66, pp. 203–220.

Cassiani, G., G. Bohm, A. Vesnaver, and R. Nicolich, 1998. A geostatistical framework for incorporating seismic tomography auxiliary data into hydraulic conductivity, *J. Hydrol.*, 206 (1–2), 58–74.

Cassiani G., and M.A. Medina, 1997. Incorporating auxiliary geophysical data into ground-water estimation, *Ground Water*, 35 (12), 79–91.

Chen, J., S. Hubbard, and Y. Rubin, 2001. Estimating the hydraulic conductivity at the South Oyster Site from geophysical tomographic data using Bayesian techniques based on the normal linear regression model, *Water Resour. Res.*, 37 (6), 1603–1613.

Chen, J., and Y. Rubin, 2003. An effective Bayesian model for lithofacies estimation using geophysical data, *Water Resour. Res.*, 39 (5), 1118, doi: 10.1029/2002WR001666.

Chen, J., S. Hubbard, M. Fienan, T. Mehlhorn, and D. Watson, 2003. Estimation of hydrogeological zonation at the NABIR Field Research Center using high-resolution geophysical data and Markov Chain Monte Carlo methods, *EOS Transaction*, 84 (46).

Chen, J., S. Hubbard, Y. Rubin, C. Murray, E. Roden, and E. Majer, 2004. Geochemical characterization using geophysical data and Markov Chain Monte Carlo methods: A case study at the South Oyster Bacterial Transport Site in Virginia, *Water Resour. Res.*, 40 (12), W12412, doi: 10.1029/2003WR002883.

Clifton, P., and S. Neuman, 1982. Effects of kriging and inverse modeling on conditional simulation of the Avra Valley aquifer in Southern Arizona, *Water Resour. Res.*, 18 (4), 1215–1234.

Cohen, A.J.B., 1995. Hydrogeological characterization of fractured rock formations: A guide for groundwater remediation, Technical Report, Lawrence Berkeley National Laboratory, Berkeley, California.

Constable, S.C., R.L. Parker, and C.G. Constable, 1987. Occam's inversion: A practical algorithm for generating smooth models from EM sounding data, *Geophysics*, 52 (3), 289–300.

Dagan, G., 1985. Stochastic modeling of groundwater flow by unconditional and conditional probabilities: The inverse problem, *Water Resour. Res.*, 21 (1), 65–72.

Daley, T.M., E.L. Majer, and J.E. Peterson, 2003. Crosswell seismic imaging in a contaminated basalt aquifer, *Geophysics*, 69 (1), 16–24.

Daniels, J.J., B. Allred, A. Binley, D. LaBrecque, and D. Alumbaugh, 2005. Hydrogeophysical case studies in the vadose zone, in *Hydrogeophysics*, edited by Y. Rubin and S.S. Hubbard, Springer, The Netherlands, pp. 413–440.

Day-Lewis, F.D., J.W. Lane, Jr., J.M. Harris, and S.M. Gorelick, 2003. Time-lapse imaging of saline tracer tests using cross-borehole radar tomography, *Water Resour. Res.*, 39 (10), doi: 10.1029/2002WR001722.

Day-Lewis, F.D., and J.W. Lane, Jr., 2004. Assessing the resolution-dependent utility of tomograms for geostatistics, *Geophys. Res. Lett.*, 31 (7), L07503, doi: 10.1029/2004GL019617.

Davis, J.L., and A.P. Annan, 1989. Ground-penetrating radar for high-resolution mapping of soil and rock stratigraphy, *Geophys. Prosp.*, 37 (5), 531–551.

Deutsch, C. and A. Journel, 1992. *GSLIB: Geostatistical Software Library and User's Guide*, Oxford University Press.

Deutsch, C.V., 2002. *Geostatistical Reservoir Modeling*, Oxford University Press.

Doyen, P.M., 1988. Porosity from seismic data: A geostatistical approach, *Geophysics*, 53 (10), 1263–1275.

Ellefsen, K.J., P.A. Hsieh, A.M. Shapiro, 2002. Crosswell seismic investigation of hydraulically conductive, fractured bedrock near Mirror Lake, New Hampshire, *J. Appl. Geophys.*, 50 (3), 299–317.

Ellis, R.G., and D.W. Oldenburg, 1994. Applied geophysical inversion, *Geophys. J. Int.*, 116 (1), 5–11.

Eppstein, M.J., and D.E. Dougherty, 1998. Efficient three-dimensional data inversion: Soil characterization and moisture monitoring from cross-well ground-penetrating radar at a Vermont test site, *Water Resour. Res.*, 34 (8), 1889–1900.

Ezzedine, S., Y. Rubin, and J. Chen, 1999. Bayesian method for hydrogeological site characterization using borehole and geophysical survey data: Theory and application to the Lawrence Livermore National Laboratory Superfund site, *Water Resour. Res.*, 35 (9), 2671–2683.

Finsterle, S., and J. Najita, 1998. Robust estimation of hydrogeologic model parameters, *Water Resour. Res.*, 34 (11), 2939–2947.

Fisher, E., G.A. McMechan, and A.P. Annan, 1992. Acquisition and processing of wide-aperture ground-penetrating radar data, *Geophysics*, 57 (3), 495–503.

Gallardo, L.A., and M.A. Meju, 2004. Joint two-dimensional DC resistivity and seismic travel time inversion with cross-gradient constraints, *J. Geophys. Res.*, 109 (B3), B03311, doi: 10.1029/2003JB002716.

Gee, G.W., and A.L. Ward, 2001. Vadose Zone Transport Field Study, Status Report, PNNL-13679, Pacific Northwest National Laboratory, Richland, WA.

Gloaguen, E., M. Chouteau, D. Marcotte, and R. Chapuis, 2001. Estimation of hydraulic conductivity of an unconfined aquifer using cokriging of GPR and hydrostratigraphic data, *J. Appl. Geophys.*, 47 (2), 135–152.

Goldman, M., H. Gvirtzman, M.A. Meju, and V. Shtivelman, 2005. Hydrogeophysical case studies at the regional scale, in *Hydrogeophysics*, edited by Y. Rubin and S.S. Hubbard, Springer, The Netherlands, pp. 361–390.

Gómez-Hernández, J.J., 2005. Geostatistics, in *Hydrogeophysics*, edited by Y. Rubin and S.S. Hubbard, Springer, The Netherlands, pp. 59–86.

Greaves, R.J., D.P. Lesmes, J.M. Lee, and M.N. Toksoz, 1996. Velocity variations and water content estimated from multi-offset, ground-penetrating radar, *Geophysics*, 61 (3), 683–695.

Grote, K., S.S. Hubbard, and Y. Rubin, 2002. GPR monitoring of volumetric water content in soils applied to highway construction and maintenance, *Leading Edge*, 21 (5), 482–485.

Grote, K., S. Hubbard, and Y. Rubin, 2003. Field-scale estimation of volumetric water content using GPR groundwave techniques, *Water Resour. Res.*, 39, 1321, doi: 10.1029/2003WR002045.

Hill, M.C., 1992. A computer program (MODFLOWP) for estimating parameters of a transient three-dimensional, ground-water flow model using nonlinear regression, U.S. Geological Survey Open-File Report 91-484, 358 pp.

Hoeksema, R.J., and P.K. Kitanidis, 1984. An application of the geostatistical approach to the inverse problem in two-dimensional groundwater modeling, *Water Resour. Res.*, 20, 1003–1020.

Hubbard, S.S., J.E. Peterson Jr, E.L. Majer, P.T. Zawislanski, K.H. Williams, J. Roberts, and F. Wobber, 1997. Estimation of permeable pathways and water content using tomographic radar data, *Leading Edge*, 16 (11), 1623–1630.

Hubbard, S.S., Y. Rubin, and E. Majer, 1999. Spatial correlation structure estimation using geophysical and hydrogeological data, *Water Resour. Res.*, 35 (6), 1809–1825.

Hubbard, S.S., J. Chen, J. Peterson, E.L. Majer, K.H., Williams, D.J. Swift, B. Mailloux, and Y. Rubin, 2001. Hydrogeological characterization of the South Oyster Bacterial Transport Site using geophysical data, *Water Resour. Res.*, 37 (10), 2431–2456.

Hubbard, S., I. Lunt, K. Grote, and Y. Rubin, 2006. Vineyard soil water content: Mapping small scale variability using ground penetrating radar, in *Geoscience Canada Geology and Wine series*, edited by R.W. Macqueen and L.D. Meinert, in press.

Hubbard, S.S. and Y. Rubin, 2005. Introduction to Hydrogeophysics, in *Hydrogeophysics*, edited by Y. Rubin and S.S. Hubbard, Springer, The Netherlands, pp. 3–21.

Huber, P., 2003. *Robust Statistics*, Wiley.

Huisman, J.A., S. Hubbard, D. Redman, P. Annan, Monitoring soil water content with ground-penetrating radar: A review, *Vadose Zone J.*, 2, 476–491.

Hyndman, D.W., J.M. Harris, and S.M. Gorelick, 1994. Coupled seismic and tracer test inversion for aquifer property characterization, *Water Resour. Res.*, 30 (7), 1965–1977.

Hyndman, D.W., and S.M. Gorelick, 1996. Estimating lithologic and transport properties in three dimensions using seismic and tracer data: The Kesterson aquifer, *Water Resour. Res.*, 32 (9), 2659–2670.

Hyndman, D.W., J.M. Harris, and S.M. Gorelick, 2000. Inferring the relation between seismic slowness and hydraulic conductivity in heterogeneous aquifers, *Water Resour. Res.*, 36 (8), 2121–2132.

Hyndman, D., and J. Tronicke, 2005. Hydrogeophysical case studies at the local scale: The saturated zone, in *Hydrogeophysics*, edited by Y. Rubin and S.S. Hubbard, Springer, The Netherlands, pp. 391–412.

Jackson, D.D., 1979. The use of *a priori* data to resolve non-uniqueness in linear inversion, *Geophys. J. R. Astron. Soc.*, 57, 137–157.

Journel, A.G., and P. Kyriakis, 2004. *Evaluation of Mineral Reserves: A Simulation Approach*, Oxford University Press.

Kitanidis, P.K., 1999. Generalized covariance functions associated with the Laplace equation and their use in interpolation and inverse problems, *Water Resour. Res.*, 35 (5), 1361–1367.

Kowalsky, M.B., S. Finsterle, and Y. Rubin, 2004. Estimating flow parameter distributions using ground-penetrating radar and hydrological measurements during transient flow in the vadose zone, *Adv. Water Resour.*, 27 (6), 583–599.

Kowalsky, M.B., S. Finsterle, J. Peterson, S. Hubbard, Y. Rubin, E. Majer, A. Ward, and G. Gee, 2005. Estimation of field-scale soil hydraulic and dielectric parameters through joint inversion of GPR and hydrological data, *Water Resour. Res.*, 41 (11), W11425, doi: 10.1029/2005WR004237.

Lesch, S.M., D.J. Strauss, and J.D. Rhoades, 1995. Spatial prediction of soil-salinity using electromagnetic induction techniques. 1. Statistical prediction models – a comparison of multiple linear-regression and cokriging, *Water Resour. Res.*, 31 (2), 373–386.

Lesmes, D., and S. Friedman, 2005. Relationships between the electrical and hydrogeological properties of soils and rocks, in *Hydrogeophysics*, edited by Y. Rubin and S.S. Hubbard, Springer, The Netherlands, pp. 87–128.

Linde, N., S. Finsterle, and S. Hubbard, 2006. Inversion of tracer test data using tomographic constraints, *Water Resour. Res.*, 42, W04410, doi: 10.1029/2004WR003806.

Loke, M.H., 1997. Rapid 2D resistivity inversion using the least-squares method, *RES2DINV* Program manual, Penang, Malaysia.

Lunt, I., S. Hubbard and Y. Rubin, 2004. Soil moisture content estimation using ground penetrating radar reflection data, *J. Hydrol.*, doi: 10.1016/j.jhydrol.2004.10.014.

Malinverno, A. and V.A. Briggs, 2004. Expanded uncertainty quantification in inverse problems: hierarchical Bayes and empirical Bayes, *Geophysics*, 69 (4), 1005–1016.

Majer, E.L., L.R. Myer, J.E. Peterson, K. Karasaki, J.C.S. Long, S.J. Martel, P. Blumling, and S. Vomvoris, 1990. Joint seismic, hydrogeological, and geomechanical investigations of a fractured zone in the Grimsel rock laboratory, Switzerland, Technical Report, Lawrence Berkeley National Laboratory, Berkeley, California.

Majer, E.L., J.E. Peterson, T. Daley, B. Kaelin, L. Myer, J. Queen, P. D'Onfro, and W. Rizer, 1997. Fracture detection using crosswell and single well surveys, *Geophysics*, 62 (2), 495–504.

Majer, E.L., K.H. Williams, J.E. Peterson, and T.M. Daley, 2002. High resolution imaging of vadose zone transport using crosswell radar and seismic methods, Lawrence Berkeley National Laboratory Report LBNL 49022.

Maurer, H., K. Holliger, and D.E. Boerner, 1998. Stochastic regularization: Smoothness or similarity? *Geophys. Res. Lett.*, 25 (15), 2889–2892.

Mavko, G., T. Mukerji, and J. Dvorkin, 1998. *The Rock Physics Handbook*, Cambridge University Press.

McKenna, S.A., and E.P. Poeter, 1995. Field example of data fusion in site characterization, *Water Resour. Res.*, 31 (12), 3229–3240.

McLaughlin, D., and L.R. Townley, 1996. A reassessment of the groundwater inverse problem, *Water Resour. Res.*, 32 (5), 1131–1161.

Meju, M.A., 1996. Joint inversion of TEM and distorted MT soundings: Some effective practical considerations, *Geophysics*, 61 (1), 56–65.

Menke, W., 1984. *Geophysical Data Analysis – Discrete Inverse Theory*, Academic Press, New York.

Mosegaard, K., and A. Tarantola, 1995. Monte Carlo sampling of solutions to inverse problems, *J. Geophys. Res.*, 100 (B7), 12,431–12,447.

Moysey, S., and R.J. Knight, 2004. Modeling the field-scale relationship between dielectric constant and water content in heterogeneous systems, *Water Resour. Res.*, 40 (3), 3510, doi: 10.1029/2003WRR002589.

Moysey, S., K. Singha, and R. Knight, 2005. A framework for inferring field-scale rock physics relationships through numerical simulation, *Geophys. Res. Lett.*, 32, L08304, doi: 10.1029/2004GL022152.

Oldenburg, D.W., and Y. Li, 1999. Estimating the depth of investigation in dc resistivity and IP surveys, *Geophysics*, 64 (2), 403–416.

van Overmeeren, R.A., S.V. Sariowan, and J.C. Gehrels, 1997. Ground penetrating radar for determining volumetric soil water content: Results of comparative measurements at two sites. *J. Hydrol.* 197 (1–4), 316–338.

Parker, R.L., 1994. *Geophysical Inverse Theory*, Princeton University Press, Princeton.

Parks, K.P., and L.R. Bentley, 1996. Enhancing data worth of EM survey in site assessment by cokriging, *Ground Water*, 34 (4), 597–604.

Peterson, J.E., Jr., 2001. Pre-inversion corrections and analysis of radar tomographic data. *JEEG*, 6 (1), 1–18.

Poeter, E.P., and M.C. Hill, 1998. Documentation of UCODE, a computer code for universal inverse modeling, U.S. Geological Survey Water Resources Investigations Report 98-4080, 116 pp.

Prasad, M., 2003. Velocity-permeability relations within hydraulic units, *Geophysics*, 68 (1), 108–117.

Press, S.J., 1989. *Bayesian Statistics: Principles, Models, and Applications*, Wiley.

Pride, S.R., 2005. Relationships between seismic and hydrological properties, in *Hydrogeophysics*, edited by Y. Rubin and S.S. Hubbard, Springer, The Netherlands, pp. 253–290.

Purvance, D.T., and R. Andricevic, 2000a. On the electrical-hydraulic conductivity correlation in aquifers, *Water Resour. Res.*, 36 (10), 2905–2913.

Purvance, D.T., and R. Andricevic, 2000b. Geoelectrical characterization of the hydraulic conductivity field and its spatial structure at variable scales, *Water Resour. Res.*, 36 (10), 2915–2924.

Roth, K.R., R. Schulin, H. Fluhler, and W. Attinger, 1990. Calibration of time domain reflectometry for water content measurement using a composite dielectric approach, *Water Resour. Res.*, 26 (10), 2267–2273.

Rubin, Y., and S. Hubbard, 2005. Stochastic forward and inverse modeling: The “hydrogeophysical” challenge, in *Hydrogeophysics*, edited by Y. Rubin and S.S. Hubbard, Springer, The Netherlands, pp. 487–512.

Scales, J.A., and L. Tenorio, 2001. Prior information and uncertainty in inverse problems, *Geophysics*, 66 (2), 389–397, 2001.

Siripunvaraporn, W., and G. Egbert, 2000. An efficient data-subspace inversion method for 2-D magnetotelluric data, *Geophysics*, 65 (3), 791–803.

Sivia, D.S., 1996. *Data Analysis: A Bayesian Tutorial*, Clarendon Press, Oxford.

Tarantola, A., 1987. *Inverse Problem Theory*, Elsevier, The Netherlands.

Tinga, W.R., W.A.G. Voss, and D.F. Blossey, 1973. Generalized approach to multiphase mixing theory, *J. Appl. Phys.*, 44 (9), 3897–3902.

Tikhonov, A.N., and V.Y. Arsenin, 1977. *Solutions of Ill-Posed Problems*, Halsted Press/Wiley.
Cited by McLaughlin and Townley (1996).

Tillard, S., and J.-C. Dubois, 1995. Analysis of GPR data: Wave propagation velocity determination. *J. Appl. Geophys.*, 33 (1–3), 77–91.

Ward, A.L., T.G. Caldwell, and G.W. Gee, 2000. Vadose zone transport field study: Soil water content distribution by neutron moderation, PNNL-13795, Pacific Northwest National Laboratory, Richland, WA.

Yang, C.H., L.T. Tong, and C.F. Huang, 1999. Combined application of dc and TEM to seawater intrusion mapping, *Geophysics*, 64 (2), 417–425.

Yeh, T.-C. J., and J. Simunek, 2002. Stochastic fusion of information for characterization and monitoring the vadose zone, *Vadose Zone J.*, 1, 207–221.

Yeh, T.-C. J., S. Liu, R.J. Glass, K. Barker, J.R. Brainard, D.L. Alumbaugh, and D. LaBrecque, 2002. A geostatistically based inverse model for electrical resistivity surveys and its application to vadose zone hydrology, *Water Resour. Res.*, 38 (12), 1278.

Zhang, Z.F., A.L. Ward, and G.W. Gee, 2004. A combined parameter scaling and inverse technique to upscale the unsaturated hydraulic parameters for heterogeneous soils, *Water Resour. Res.*, 40 (8), W08306, doi: 10.1029/2003WR002925.

3. A SUCCESSIVE LINEAR ESTIMATOR FOR ELECTRICAL RESISTIVITY TOMOGRAPHY

Tian-Chyi J. Yeh, Junfeng Zhu, Andreas Englert, Amado Guzman, and Steve Flaherty

3.1. Introduction

A dc resistivity survey is an inexpensive and widely used technique for investigation of near surface resistivity anomalies. It recently has become popular for the investigation of subsurface pollution problems (NRC, 2000). In principle, it measures the electric potential field generated by a transmission of dc electric current between electrodes implanted at the ground surface. Then, an apparent (bulk or effective) electrical resistivity for a particular set of measurement electrodes is calculated using formulas that assume homogeneous earth. Many pairs of current transmission and electric potential measurements are used to “map” subsurface electrical resistivity anomalies.

This conventional resistivity survey is analogous to classical aquifer test in which an aquifer is excited by pumping at one well and the response of the aquifer (e.g. drawdown-time relation or well hydrograph) is observed at another well. The theoretical well hydrograph from an analytical solution that assumes aquifer homogeneity and infinite domain (e.g. Theis' solution, 1935) is then used to match the observed hydrograph to obtain apparent or effective aquifer transmissivity and storage coefficient. Due to the homogeneity assumption, the theoretical drawdown represents a spatially averaged drawdown in a heterogeneous aquifer. This average drawdown is unequivocally different from the one observed at a well in a heterogeneous aquifer, although the difference may be small due to diffusive nature of the flow process. Thus, applying Theis' solution to aquifer tests in a heterogeneous aquifer is tantamount to comparing apples to oranges (Wu et al., 2005). They suggested that the apparent transmissivity represents a weighted average of transmissivity anomalies over the cone of depression. High weights are given to transmissivity anomalies near the observation and the pumping well. The apparent transmissivity reflects, as a consequence, local geology but it can also be affected by significant geologic anomalies within the cone of depression. In other words, the physical meaning of the apparent transmissivity can be highly dubious.

The strong similarity between traditional aquifer and apparent resistivity analysis leads us to conclude that conventional analysis of electrical resistivity

survey is another example of comparison between apples and oranges. In fact, the apparent resistivity approach has been found virtually ineffective for environmental applications, where electrical resistivity anomalies are subtle, complex, and multi-scale (Yeh et al., 2002).

Meanwhile, a contemporary electrical resistivity survey (electrical resistivity tomography, ERT) has been designed to collect extensive electric current and electric potential data sets in multi-dimensions. The resistivity field is estimated from the inversion of the data set using, a mathematical computer model based on a regularized optimization approach and without the assumption of subsurface homogeneity (e.g. Daily et al., 1992; Ellis and Oldenburg, 1994; Li and Oldenburg, 1994; and Zhang et al., 1995). However, the general uniqueness and resolution of the three-dimensional electrical resistivity inversion have not been investigated sufficiently thus far (NRC, 2000).

While the physical process is different between electric current and groundwater flow, the governing equation for electric current and potential field created by an electrical resistivity survey is similar to that for steady flow in saturated porous media induced by pumping or injection. The mathematical inversion of an electrical resistivity survey is thus analogous to that of a groundwater aquifer test. Groundwater hydrologists and reservoir engineers have attempted to solve the inverse problem of flow through multidimensional, heterogeneous porous media for the last few decades (e.g. Gavalas et al., 1976). Reviews of the inverse problem of subsurface hydrology and various solution techniques can be found in Yeh (1986), Sun (1994), and McLaughlin and Townley (1996). The general consensus is that prior information on geological structure, and some point measurements of parameters to be estimated are necessary to better constrain solution of the inverse problem. A similar finding was also reported by Oldenburg and Li (1999) and Li and Oldenburg (2000) for the inverse problems in geophysics.

A multi-variate linear estimator (cokriging) has been widely used by groundwater hydrologists to estimate the hydraulic conductivity field from scattered measurements of pressure head and hydraulic conductivity in aquifers (e.g. Kitanidis and Vomvoris, 1983; Hoeksema and Kitanidis, 1984; Yeh and Zhang, 1996). The popularity of cokriging is attributed to its ability to incorporate spatial statistics, point measurements of hydraulic conductivity and hydraulic head into the estimation, and its ability to yield conditional mean estimates. Cokriging is also known for its ability to quantify the uncertainty associated with its estimate due to limited information and heterogeneity. Kitanidis (1997) discussed the differences between cokriging and classical inverse methods in subsurface hydrology and showed cokriging is a Bayesian formalism. Nevertheless, cokriging is a linear estimator and it is limited to mildly nonlinear systems, such as aquifers of mild heterogeneity, where the variance of the natural logarithm of hydraulic conductivity, $\sigma_{\ln K}^2$, is less than

0.1. When the degree of aquifer heterogeneity is large ($\sigma_{\ln K}^2 > 1$), the linear assumption becomes inadequate and cokriging cannot take full advantage of the hydraulic head information (Yeh et al., 1996).

To overcome this shortcoming, Yeh et al. (1995, 1996), Gutjahr et al. (1994), and Zhang and Yeh (1997) developed an iterative geostatistical technique, referred to as a successive linear estimator (SLE). This technique uses a linear estimator successively to incorporate the nonlinear relation between hydraulic properties and the hydraulic head in inverse modeling. It also successively updates conditional covariances to quantify reductions in uncertainty due to successive improvements of the estimate. Yeh et al. (1995 and 1996), and Zhang and Yeh (1997) demonstrated that using the same amount of information, SLE revealed a more detailed hydraulic conductivity field than cokriging. Hughson and Yeh (2000) successfully applied SLE to the inverse problem in three-dimensional, variably saturated, heterogeneous porous media.

Based on the SLE algorithm, Yeh and Liu (2000) developed a sequential successive linear estimator (SSLE) to process the large amount of data sets created by steady-state hydraulic tomography for imaging aquifer heterogeneity. In addition, they investigated effects of monitoring intervals, pumping intervals, and the number of pumping locations on the final estimate of hydraulic conductivity. Subsequently, guidelines for design of hydraulic tomography tests were established, which are also applicable to ERT. The SSLE algorithm for hydraulic tomography was subsequently validated by Liu et al. (2002) using sandbox experiments. Robustness of SSLE compelled Zhu and Yeh (2005) to develop three-dimensional (3-D) transient hydraulic tomography, which can be used to image 3-D hydraulic conductivity and the specific storage fields in heterogeneous aquifers.

Successes of SSLE for hydraulic tomography have motivated its application to ERT. In particular, Yeh et al. (2002) developed a SSLE algorithm for ERT and investigated the effectiveness of surface and downhole electrode arrays in stratified geological media. They concluded that surface electrode arrays detect only anomalies near the surface and downhole arrays provide more accurate mapping of the anomalies at great depths. More importantly, using field core samples Baker (2001) and Yeh et al. (2002) investigated the spatial variability of Archie's law that relates moisture content to electrical resistivity. Significant spatial variability of the parameters of the law was found in a 20 m \times 20 m \times 15 m vadose zone in an alluvium deposit. Thereafter, numerical experiments were undertaken to demonstrate effects of the variability on ERT estimation of moisture content in the vadose zone. Finally, they cautioned interpretation of ERT for mapping changes in moisture content in the vadose zone if the variability of Archie's parameter is ignored.

To resolve the variability problem, Liu and Yeh (2004) developed an integrative ERT inversion approach based on SSLE. This integrative approach allows inclusion of prior knowledge of spatial statistics of the parameters of Archie's law and the resistivity field to be estimated as well as direct measurements of the parameters, resistivity, and moisture content values. They demonstrated how the new approach can be used to determine moisture content distribution directly without using time-lapse ERT surveys.

Since SSLE, a geostatistically based inverse model, is relatively new in geophysics, the aim of this chapter is to introduce the SSLE algorithm for ERT and to demonstrate its usefulness. Specifically, we first discuss in Section 3.2 the basic concept of stochastic representation of ERT inverse problems and then explain why the analysis of ERT survey should be viewed as a conditional mean estimation of a spatially stochastic resistivity field. In Section 3.3, the mathematical formulation of SSLE for ERT inversion is presented. Next, numerical examples are used to illustrate the robustness of the algorithm and the concept of ERT (namely, an intelligent data collection scheme to resolve the ill-posedness of electrical resistivity inversion problem) in Section 3.4. Examples of applications of ERT to monitoring solute distributions in aquifers and moisture content distributions in the vadose zone then follow. Using these examples, we show effects on the quality of ERT inversion by conditioning with direct measurements of concentration and moisture content. Lastly, the application of the SSLE algorithm to an ERT survey in a mine leaching field is presented (Section 3.5), where a stochastic approach for eliminating biased and noisy ERT data – an important step in ERT analysis – is presented.

3.2. Stochastic Conceptualization of ERT Inverse Problems

Assume that in a geological formation, the electric current flow induced by an electrical resistivity survey can be described by

$$\nabla \cdot [\xi(\mathbf{x}) \nabla \phi(\mathbf{x})] + I(\mathbf{x}) = 0 \quad (1)$$

where \mathbf{x} is the location vector (x, y, z) , ϕ is the electric potential [V], $I(\mathbf{x})$ represents the electric current source per volume [A/m^3], and ξ is the electrical conductivity [S/m] within a previously defined volume, a reciprocal of the electrical resistivity, ρ [$\text{ohm}\cdot\text{m}$], which is assumed to be locally isotropic. The boundary conditions associated with Equation (1) are

$$\phi|_{G_1} = \phi^* \quad \text{and} \quad \xi(x) \nabla \phi \cdot \mathbf{n}|_{G_2} = q \quad (2)$$

where ϕ^* is the electric potential specified at boundary G_1 , q denotes the

prescribed electric current per unit area (current density), and \mathbf{n} is the unit vector normal to the boundary G_2 .

The electrical conductivity or resistivity of geologic media varies spatially due to inherent heterogeneous geologic processes (Sharma, 1997). One way to describe the spatial variability of electrical conductivity is the stochastic representation approach, similar to that used in geohydrology for the variability of hydraulic properties of aquifers and vadose zones (see Gelhar, 1993; Yeh, 1992, 1998). Specifically, the electrical conductivity field of a geologic formation is considered as a stochastic process, $\xi(\mathbf{x}, \pi)$, where π is the ensemble index, ranging from one to infinity. That is, the value of $\xi(\mathbf{x})$ at each location \mathbf{x} in the formation is a random variable regardless if the value is known or unknown. The electrical conductivity field of the formation, therefore, is visualized as a collection of an infinite number of random variables in space. This stochastic process can be described by a mean, $\langle \xi(\mathbf{x}) \rangle = \Omega$ (where $\langle \cdot \rangle$ denotes the expected value, i.e., ensemble average or the average over the infinite number of possible realizations or π in ensemble space) and perturbations around the mean, $\omega(\mathbf{x}, \pi)$, characterized by a joint probability distribution. For simplicity, the ensemble index, π , will be dropped hereafter.

Assuming that the perturbation is a second-order stationary stochastic process (that is, the stochastic process has a stationary mean and variance as well as its covariance depends on the separation distance only), its joint probability distribution can thus be adequately represented by its mean and covariance function, $\mathbf{R}_{\omega\omega}(\boldsymbol{\eta})$, where $\boldsymbol{\eta}$ is the separation vector between electrical conductivity values at two locations. The covariance function represents in a statistical sense the spatial correlation structure (pattern) of the electrical conductivity of a geologic formation. More specifically, the spatial correlation structure states the likelihood of occurrence of the same electrical conductivity value at two different locations. Because of this stochastic representation of the electrical conductivity, the electric potential field induced during an electrical resistivity survey can also be considered as a stochastic process. It can be described by $\phi(\mathbf{x}) = V(\mathbf{x}) + v(\mathbf{x})$, where $V(\mathbf{x}) = \langle \phi(\mathbf{x}) \rangle$ and $v(\mathbf{x})$ is the perturbation of the electric potential.

Suppose that electrical conductivity measurements (referred to as the primary variable or primary information), ξ_i^* (where $i = 1, \dots, n$, and n is the total number of electrical conductivity measurements) are available from borehole electrical resistivity surveys. From these measurements, we have estimated the mean and covariance function of the electrical conductivity field of the geologic formation. Now, suppose that an ERT survey is then conducted. For each transmission of electric current during the survey, we have collected k electric potential values, v_j^* , where $j = n + 1, n + 2, \dots, n + k$. Hereafter, the electric potential measurements are referred to as secondary information. Now, our goal is to exploit the primary and secondary information available

to estimate the electrical conductivity distribution over the volume of the geologic formation. Mathematically, we are seeking an inverse model that can produce the electric potential and electrical conductivity fields that satisfy the following conditions. That is, they must preserve the observed electric potential and electrical conductivity values at sample locations and also satisfy underlying physical processes (i.e., the governing electric potential equation). In a conditional probability context, such electric potential field and electrical conductivity field are conditional realizations of $\phi(\mathbf{x})$ and $\xi(\mathbf{x})$ fields, respectively, among many possible realizations of the ensemble. In other words, they are a subset of the ensemble of each field, which meets the prescribed conditions.

These conditional realization of the electrical conductivity field can also be expressed as the sum of the conditional mean electrical conductivity field and its conditional perturbation field, i.e., $\xi_c(\mathbf{x}) = \Omega_c(\mathbf{x}) + \omega_c(\mathbf{x})$. The subscript c denotes the state of being conditioned. Similarly, the conditional electric potential fields can be written as $\phi_c(\mathbf{x}) = V_c(\mathbf{x}) + v_c(\mathbf{x})$. It should be noticed that as more independent data or constrains are used to condition the stochastic processes, the processes should approach particular realizations of the processes (i.e., the reality). Transmission of electric current at different locations and recording of electric potentials using the same sampling network (i.e., a tomographic survey) as in an ERT survey is tantamount to creating many independent constraints to condition the stochastic processes. Nevertheless, many possible realizations of such conditional $\xi(\mathbf{x})$ and $\phi(\mathbf{x})$ fields remain in spite of the tomographic survey. The means of these conditional fields (i.e., conditional means of $\Omega_c(\mathbf{x})$ and $V_c(\mathbf{x})$) on the other hand are unique, although not necessarily reflective of the true fields.

One way to obtain these conditional mean fields is to solve the inverse problem for all possible conditional realizations of the electrical resistivity field. An average of all of the possible realizations then yields the conditional mean electrical resistivity field (see Hanna and Yeh, 1998 and others for geohydrology applications). An alternative approach is to solve the inverse problem in terms of the conditional mean equation, as described below.

In order to formulate the conditional mean equation, we first substitute the conditional stochastic variables into the governing electric potential Equation (1) and then take the expected value of the resultant equation. The conditional-mean equation thus takes the following form

$$\nabla \cdot [\Omega_c(\mathbf{x}) \nabla V_c(\mathbf{x})] + \nabla \cdot \langle \omega_c(\mathbf{x}) \nabla v_c(\mathbf{x}) \rangle + I(\mathbf{x}) = 0 \quad (3)$$

In Equation (3), the current source, $I(\mathbf{x})$, is treated as a deterministic constant that is known. According to Equation (3), the true conditional mean $\Omega_c(\mathbf{x})$ and $V_c(\mathbf{x})$ fields do not satisfy the continuity Equation (3) unless the second term involving the product of perturbations is zero. This term represents the

uncertainty due to a lack of information of the two variables at locations where measurements are not available. The uncertainty will vanish under two conditions, namely: 1) all the electrical conductivity values in the domain (i.e., the geologic formation) are specified exactly (i.e., $\omega_c(\mathbf{x}) = 0$); or 2) all the electric potential values in the domain are known perfectly (i.e., $v_c(\mathbf{x}) = 0$) as are the electric fluxes at the boundaries. In practice, these two conditions will never be met and evaluation of this term is intractable at this moment. Consequently, in the subsequent analysis we will assume this term is proportional to the conditional mean electric potential gradient such that we can rewrite the mean equation as

$$\nabla \cdot [\Omega_{\text{ceff}}(\mathbf{x}) \nabla V_c(\mathbf{x})] + I(\mathbf{x}) = 0 \quad (4)$$

This conditional mean equation has the same form as Equation (1) but variables are expressed as the conditional effective electrical conductivity, $\Omega_{\text{ceff}}(\mathbf{x})$, and conditional mean electric potential field, $V_c(\mathbf{x})$. The conditional effective electrical conductivity thus is a parameter field that combines the conditional mean electrical conductivity, $\Omega_c(\mathbf{x})$, and $\langle \omega_c(\mathbf{x}) \nabla v_c(\mathbf{x}) \rangle (\nabla V_c(\mathbf{x}))^{-1}$. According to this concept, the conditional effective electrical conductivity field will agree with the electrical conductivity measurements at sample locations. It yields a conditional mean electric potential field that preserves values of electric potential measurements when it is employed in the forward model, Equation (4), subject to the prescribed boundary conditions. Following this concept, an optimal inverse solution to Equation (4) seeks the conditional effective electrical conductivity field. The sequential successive linear estimator (SSLE) approach to be introduced below is designed for this purpose.

3.3. Sequential Successive Linear Estimator for ERT

Suppose that a geologic medium to be investigated is discretized into M elements and each element has an electrical conductivity value, $\xi(\mathbf{x})$. For mathematical convenience, the natural logarithm of the electrical conductivity, $\ln \xi(\mathbf{x})$, instead of $\xi(\mathbf{x})$, will be used as the stochastic process for our analysis. That is, $\ln \xi(\mathbf{x}) = F + f(\mathbf{x})$ and $\langle \ln \xi(\mathbf{x}) \rangle = F$, which is assumed to be spatially invariant (although it is not necessary). One of the advantages of using $\ln \xi(\mathbf{x})$ is that this approach avoids negative value of estimated $\xi(\mathbf{x})$ values during the inverse procedure.

To derive the conditional effective electrical conductivity that will produce a conditional mean potential field in Equation (4), SSLE starts with the classical cokriging technique to construct a cokriged, mean-removed log conductivity field. The technique uses observed electrical conductivity perturbations,

f_i^* , and the observed electric potential perturbations, v_j^* , caused by one transmission of electric current during the tomography. That is,

$$\hat{f}(\mathbf{x}_0) = \sum_{i=1}^n \lambda_{i0} f^*(\mathbf{x}_i) + \sum_{j=n+1}^{n+k} \mu_{j0} v^*(\mathbf{x}_j) \quad (5)$$

where $\hat{f}(\mathbf{x}_0)$ is the cokriged f value at location, \mathbf{x}_0 . Then, we define $\hat{Y}_k(\mathbf{x}_0) = [F + \hat{f}(\mathbf{x}_0)]$ and the cokriged electrical conductivity, $\hat{\xi}_k(\mathbf{x}_0)$, is given as $\exp[\hat{Y}_k(\mathbf{x}_0)]$. The cokriging weights, λ_{i0} and μ_{j0} , in Equation (5) represent influences of observations, $f^*(\mathbf{x}_i)$ and $v^*(\mathbf{x}_j)$, at locations \mathbf{x}_i and \mathbf{x}_j on the estimate $\hat{f}(\mathbf{x}_0)$ at \mathbf{x}_0 . They are evaluated from solving the following system of equations

$$\begin{aligned} \sum_{i=1}^n \lambda_{i0} R_{ff}(\mathbf{x}_\ell, \mathbf{x}_i) + \sum_{j=n+1}^{n+k} \mu_{j0} R_{fv}(\mathbf{x}_\ell, \mathbf{x}_j) &= R_{ff}(\mathbf{x}_0, \mathbf{x}_\ell) \quad \ell = 1, 2, \dots, n \\ \sum_{i=1}^n \lambda_{i0} R_{vf}(\mathbf{x}_\ell, \mathbf{x}_i) + \sum_{j=n+1}^{n+k} \mu_{j0} R_{vv}(\mathbf{x}_\ell, \mathbf{x}_j) &= R_{vf}(\mathbf{x}_0, \mathbf{x}_\ell) \quad \ell = n+1, \dots, n+k \end{aligned} \quad (6)$$

where R_{ff} , R_{vv} , and R_{fv} , are the covariance between f 's and that between v 's, and the cross-covariance between f 's and v 's, respectively. Equations (5) and (6) are applied to every location, \mathbf{x} , in the solution domain to estimate the $f(\mathbf{x})$ field and in turn, the $\xi(\mathbf{x})$ field. The weights in equation, in essence, ensure the estimate fields obey the statistical correlation relations of f 's and v 's as well as the spatial cross correlation between f 's and v 's. In theory, the covariance, R_{vv} , and the cross-covariance, R_{fv} , in Equation (6) can be estimated from field data sets. But good estimates require a large number of measurements. As a consequence, they are derived from a first-order numerical approximation (to be discussed later: see Equations (9)–(11)) that involves the governing equation (Equation 1) for the electric potential field induced by the ERT survey. Therefore, the cokriging estimation procedure implicitly considers the physical process of propagation of electric currents.

As mentioned in the introduction, the information of electric potential measurements is not fully utilized by cokriging because the relation between f 's and v 's is nonlinear while it is assumed to be linear in cokriging. To resolve this problem, a successive linear estimator is used. That is,

$$\hat{Y}_c^{(r+1)}(\mathbf{x}_0) = \hat{Y}_c^{(r)}(\mathbf{x}_0) + \sum_{j=n+1}^{n+k} \beta_{j0}^{(r)} [\phi^*(\mathbf{x}_j) - \phi^{(r)}(\mathbf{x}_j)] \quad (7)$$

where $\hat{Y}_c^{(r)}(\mathbf{x}_0)$ is the estimate of the conditional mean of $\ln \xi(\mathbf{x}_0)$ at iteration r , which is the iteration index. The estimate is equal to the cokriged log conductivity field, \hat{Y}_k , at $r = 0$. The residual about the mean estimate at

iteration r is defined as $y^{(r)}(\mathbf{x}_0) = \ln \xi(\mathbf{x}_0) - \hat{Y}_c^{(r)}(\mathbf{x}_0)$. In Equation (7), the terms within the bracket on the right-hand side of the equation denotes the difference between $\phi^{(r)}(\mathbf{x}_j)$, the simulated electric potential at \mathbf{x}_j (i.e., the solution to Equation (4)) at iteration r , and $\phi^*(\mathbf{x}_j)$, the observed potential at the same location. The weighting coefficients, $\beta_{j0}^{(r)}$'s, similar to the cokriging weights, represent the influence of the differences between simulated and observed electric potentials at location, \mathbf{x}_j , to the improvement of the electrical conductivity estimate at \mathbf{x}_0 . To ensure the improved estimate obeys the spatial correlation structure, the values of $\beta_{0j}^{(r)}$'s are determined by solving the following system of equations:

$$\sum_{j=n+1}^{n+k} \beta_{j0}^{(r)} \Lambda_{vv}^{(r)}(\mathbf{x}_\ell, \mathbf{x}_j) + \theta \delta_{j\ell} = \Lambda_{vy}^{(r)}(\mathbf{x}_0, \mathbf{x}_\ell) \text{ and } \ell = n+1, \dots, n+k \quad (8)$$

where $\Lambda_{vv}^{(r)}$ and $\Lambda_{vy}^{(r)}$, are the residual covariance (or conditional covariance function) of v_c and cross-covariance (or conditional cross-covariance) at iteration r between v_c and y_c , respectively. In Equation (8), θ is used as a stabilizing factor and $\delta_{\ell j}$ is a Kronecker delta. Specifically, during an iteration, the stabilizing factor is added to the diagonal terms of the covariance on the left-hand side of Equation (8) to numerically condition the system of equations. This makes the matrix of the equations diagonally dominant and thus assures stability and convergence of the solution. A larger term can result in a slower convergence rate, and a smaller θ value tends to expedite the convergence but often lead to numerical instability. During each iteration, the product of a constant weighting factor of user's choice and the maximum value of the diagonal terms of $\Lambda_{vv}^{(r)}$ is assigned to be this stabilizing term. Since the maximum value of the diagonal terms of $\Lambda_{vv}^{(r)}$ changes during each iteration, the θ value changes accordingly.

The solution to Equations (6) and (8) requires knowledge of the covariance of the electric potential and its cross covariance with the electrical conductivity. We approximate them by a first-order analysis. The first-order analysis (e.g. Dettinger and Wilson, 1981) expands the electric potential at location \mathbf{x}_i at the r th iteration as a first-order Taylor series:

$$\phi(\mathbf{x}_i) = \hat{V}_c^{(r)}(\mathbf{x}_i) + v_c^{(r)}(\mathbf{x}_i) \approx G(\mathbf{x}_i) + \frac{\partial G(\mathbf{x}_i)}{\partial \ln \xi(\mathbf{x}_j^{-1})} y^{(r)}(\mathbf{x}_j) \quad (9)$$

where G is a mathematical function that represents Equation (1) and associated boundary conditions. $G(\mathbf{x}_i)$, therefore, represents $\hat{V}_c^{(r)}$ at location \mathbf{x}_i , which is evaluated using the conductivity field, $\hat{Y}_c^{(r)}(\mathbf{x})$. The term $\frac{\partial G(\mathbf{x}_i)}{\partial \ln \xi(\mathbf{x}_j^{-1})}$ denotes the sensitivity of $\hat{V}_c^{(r)}$ at location \mathbf{x}_i to change of $\ln \xi$ at location \mathbf{x}_j . The Einstein convention is adopted in Equation (9): the repeated subscript implies

summation over its entire range. The first-order approximation of the residual $v^{(r)}(\mathbf{x}_i)$ can then be written as

$$v^r(\mathbf{x}_i) = \frac{\partial G(\mathbf{x}_i)}{\partial \ln \xi(\mathbf{x}_j)} y^{(r)}(\mathbf{x}_j) = \mathbf{J}^{(r)} \mathbf{y}^{(r)} \quad (10)$$

where $\mathbf{J}^{(r)}$, the sensitivity matrix, can be evaluated using many different methods. We here choose the adjoint state sensitivity method (Sykes et al., 1985; Sun and Yeh, 1992; Li and Yeh, 1998; Yeh et al., 2002; Liu and Yeh, 2004) for its computational efficiency.

Using Equation (10), we then derive the approximate covariance of $v^{(r)}$ and the cross-covariance between $y^{(r)}$ and $v^{(r)}$. That is,

$$\begin{aligned} \Lambda_{vv}^{(r)} &= \mathbf{J}^{(r)} \Lambda_{yy}^{(r)} \mathbf{J}^{T(r)} \\ \Lambda_{vy}^{(r)} &= \mathbf{J}^{(r)} \Lambda_{yy}^{(r)} \end{aligned} \quad (11)$$

where \mathbf{J} is the sensitivity matrix ($k \times M$), and superscript T stands for the transpose. Λ_{yy} is the covariance matrix of y , in which each component is given by

$$\Lambda_{yy}^{(1)}(\mathbf{x}_0, \mathbf{x}_\ell) = R_{ff}(\mathbf{x}_0, \mathbf{x}_\ell) - \sum_{i=1}^{n_f} \lambda_{io} R_{fi}(\mathbf{x}_o, \mathbf{x}_\ell) - \sum_{j=n+1}^{n+k} \mu_{jo} R_{fj}(\mathbf{x}_j, \mathbf{x}_\ell) \quad (12)$$

at iteration $r = 0$, where $\ell = 1, 2, \dots, M$, and λ and μ are the cokriging coefficients. Equation (12) is the cokriging variance if $\mathbf{x}_0 = \mathbf{x}_k$, a measure of the uncertainty associated with the cokriging estimate at location \mathbf{x}_0 . For $r \geq 1$, the covariance is evaluated according to

$$\Lambda_{yy}^{(r+1)}(\mathbf{x}_0, \mathbf{x}_\ell) = \Lambda_{yy}^{(r)}(\mathbf{x}_0, \mathbf{x}_\ell) - \sum_{i=n+1}^{n+k} \beta_{io}^{(r)} \Lambda_{yy}^{(r)}(\mathbf{x}_i, \mathbf{x}_\ell) \quad (13)$$

Notice that these covariances are merely approximate conditional covariances because of its first order nature. The accuracy of this approximation was investigated by Hanna and Yeh (1998).

Upon completing updating the $\hat{Y}_c^{(r)}(\mathbf{x})$ field, the mean electric flow equation is solved again with the newly estimated $\hat{Y}_c^{(r+1)}(\mathbf{x})$ field for a new electric potential field, $\phi(\mathbf{x})$. Then, the change of σ_f^2 (the variance of the estimated electrical conductivity field) and the change of the largest misfit in the electric potential among all the monitoring locations between two successive iterations are evaluated. If both changes are smaller than some prescribed tolerances, the iteration stops. Otherwise, new Λ_{vy} and Λ_{vv} are evaluated using Equation (11) and Equation (8) is solved again to obtain a new set of weights. The new weights are subsequently used in Equation (7) in conjunction with $\phi^*(\mathbf{x}_j) - \phi^{(r)}(\mathbf{x}_j)$ to obtain a new estimate of $\hat{Y}_c^{(r+1)}(\mathbf{x})$.

The above discussion describes the SLE for only one set of primary and secondary information during one electric current transmission. Of course, this algorithm can simultaneously include all of the electric potential measurements collected during all the electric current transmissions during ERT. Nevertheless, the system of Equations in (6) and (8) can become extremely large and ill conditioned, and stable solutions to the equations can become difficult to obtain (Hughson and Yeh, 2000).

To avoid this problem, the electric potential data sets are analyzed sequentially. Specifically, SSLE starts the iterative process with the available electrical conductivity measurements and the electric potential data set collected from one of the electric current transmissions. Once the estimated field converges to the given criteria, the newly estimated electrical conductivity field is the effective electrical conductivity conditioned on the electric potential data due to the current transmission at the first location, and the residual electrical conductivity covariance is the corresponding conditional electrical conductivity covariance.

Subsequently, the conditional effective electrical conductivity is used to evaluate the conditional mean electric potential and sensitivity matrix, associated with the electric current transmission at the next location. Based on Equation (11), the sensitivity matrix in conjunction with the conditional electrical conductivity covariance then yields the electric potential covariance and the cross-covariance of the electric potential and the electrical conductivity fields that correspond to the current transmission at this new location. These covariance and cross-covariance are subsequently employed in (8) to derive the new weights. With the conditional mean electric potential, new weights, and the observed electric potential, Equation (7) yields the electrical conductivity estimate, representing the estimate at the first iteration based on the information from the electric current injection at this new location as well as the previous transmission. The iterative process then proceeds to include the nonlinear relation between electric potential and electrical conductivity.

The same procedure is repeated for the next electric current transmission until all of the transmissions are considered. In essence, our sequential approach uses the estimated electrical conductivity field and its covariance, conditioned on previous sets of electric potential measurements, as prior information for the next estimation based on a new set of ERT survey data. It continues until all the data sets are fully utilized. A flow chart of the SSLE algorithm is illustrated in Figure 1. Such a sequential approach allows accumulation of high-density secondary information obtained from the electrical resistivity tomography, while maintaining the covariance matrix at a manageable size that can be solved with the least numerical difficulties. Vargas-Guzman and Yeh (1999 and 2002) provided a theoretical proof to show that such a sequential approach is identical to the simultaneous approach for linear systems. For

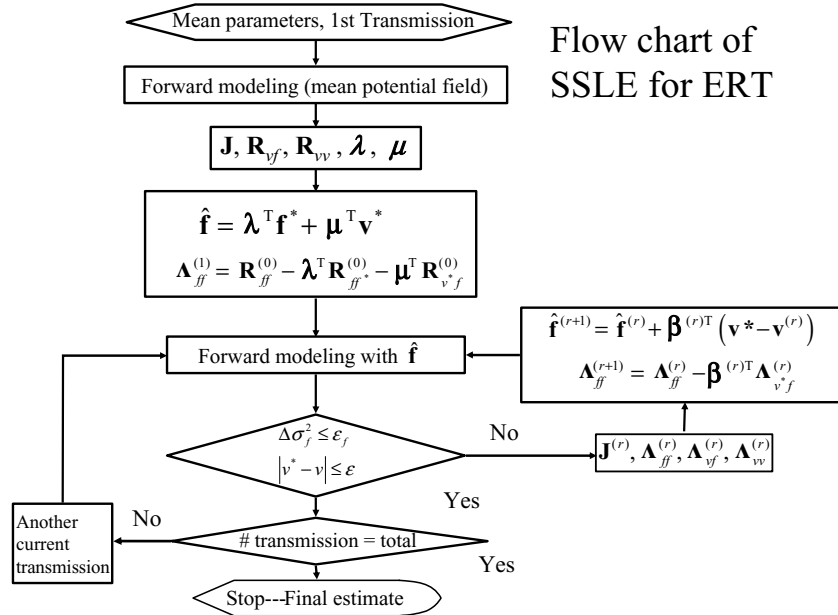


Figure 1. Flow chart showing the algorithm of SSLE for ERT

nonlinear problem as ERT, analysis of the data set in different sequence can lead to different estimates. If a large number of data are used, however, the difference is small. To avoid this problem, the final estimate can be fed back to the SSLE algorithm to ensure a global consistency (Zhu and Yeh, 2005).

The approach is different from classical regularized optimization (Tikhonov and Arsenin, 1977) approaches that have been widely used in many engineering fields. The regularization approach seeks the smoothest parameter estimate using a somewhat “arbitrary” Tikhonov factor, ignoring our prior knowledge of the spatial structure of the parameter field. On the other hand, SSLE seeks a smooth estimate of the primary variable field that is conditioned on the spatial statistical structure representing our prior knowledge of the field.

Specifically, with a prescribed spatial mean and covariance function of the primary variable field, SSLE uses 3-D partial differential equations that govern the physics of electric flow to approximate spatial first and second moments of the secondary variable. The spatial auto-correlation of the primary and the secondary variable and their cross-correlation are subsequently derived. With measured primary and secondary variables at sample locations and the approximate auto-correlation and the cross-correlation, a linear estimator is then used to derive the estimate at any location in space – the best linear

unbiased estimates. Because of the nonlinear relation between the primary and secondary variables, the linear estimation is carried out iteratively to maximize the effectiveness of available secondary information. As a result, the estimated secondary variable satisfies the governing partial differential equations; and both estimated primary and secondary variables agree with the data (measured voltage, current, and resistivity values if any) at sampling locations. Whereas at locations where no measurements are available, the estimates are merely the approximate conditional means for the given measurements. Therefore, it is expected that SSLE will yield less smooth and more realistic estimates than the regularization approach. SSLE is a Bayesian formalism and is conceptually the same as but methodologically different from the maximum a posterior (McLaughlin and Townley, 1996) and the quasi-linear geostatistical inverse approach (Kitanidis, 1995). Lastly, we want to point out that SSLE is not limited to stationary processes; only the uncertainty estimate will be affected (i.e., less accurate) by this assumption.

3.4. Numerical Examples

In this section, we use three numerical examples to illustrate the robustness of ERT and our SSLE approach. The first example demonstrates the concept of tomographic survey under two different scenarios: a) a homogeneous resistivity field with a rectangular anomalous resistivity inclusion; b) a rectangular anomaly embedded in a randomly distributed resistivity field. The second example illustrates effects of conditioning using point measurements on ERT inversion. The last example demonstrates an integrative approach using SSLE (Liu and Yeh, 2004) and ERT to directly estimate a moisture content distribution in a 3-D heterogeneous vadose zone, where the constitutive relation between the moisture content and resistivity is spatially random.

3.4.1. EXAMPLE 1

The size of the domain examined in this example was 0.29 m in the x direction (horizontal) by 0.21 m in y direction (vertical). The domain was discretized into 609 elements with a uniform element size of 0.01 m \times 0.01 m. All the boundaries were assigned as Neumann (no flow) types except at the location (0.15 m, 0.0 m) where a constant voltage of zero was assigned. The two scenarios were investigated: a) a rectangular-shape anomaly with a low electrical conductivity of 3.4000E-07 S/m was embedded in the domain of a homogeneous electrical conductivity of 0.0034 S/m. The size of the anomaly was

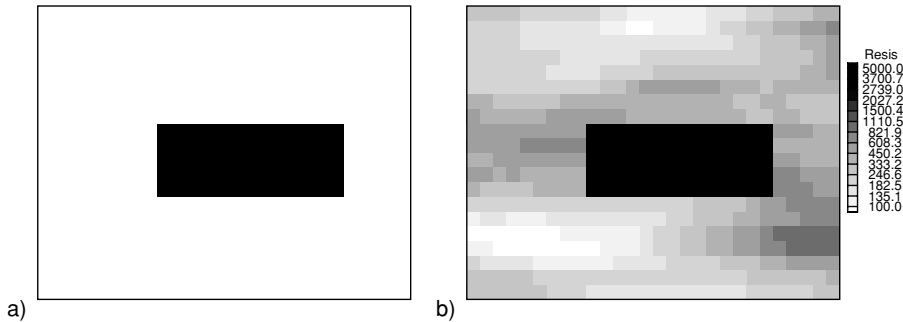
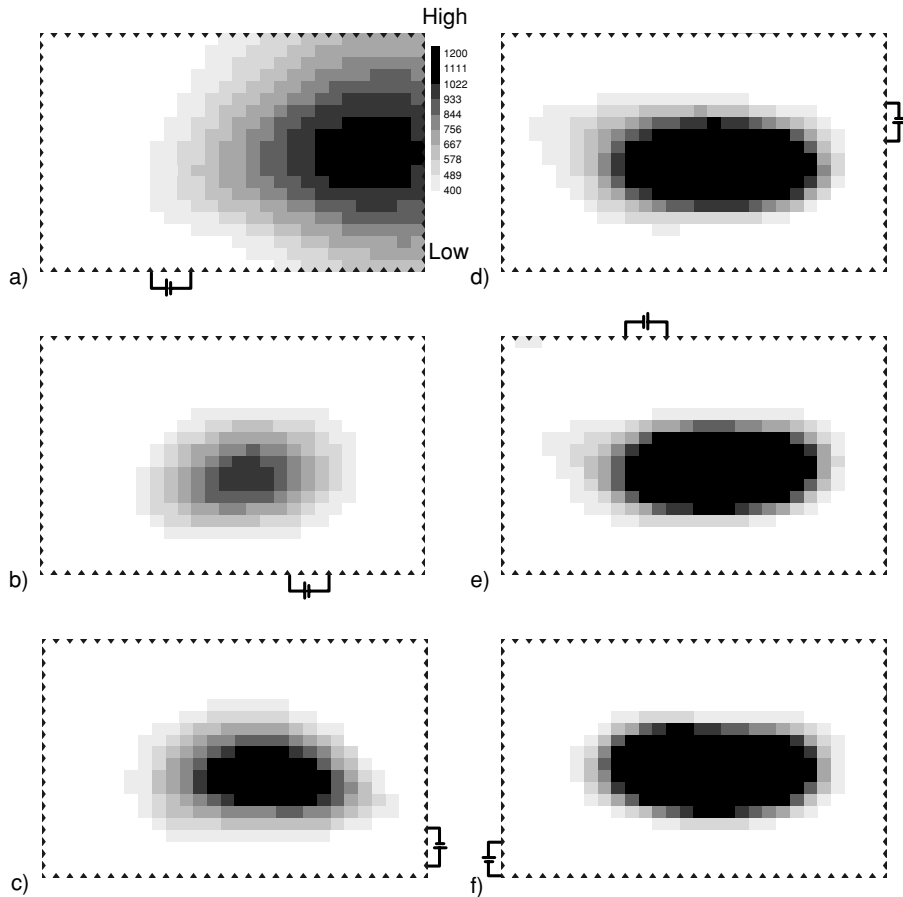


Figure 2. Two synthetic resistivity fields for Example 1: a) A high resistivity rectangle inclusion in a homogeneous resistivity field, and b) a high resistivity rectangle embedded in a random resistivity field

0.14 m by 0.05 m. The left corner of the anomaly was located at (0.09, 0.07) (see Figure 2a); b) instead of embedding it in a homogeneous background electrical conductivity field, the rectangular anomaly was placed in a randomly distributed electrical conductivity field. The mean electrical conductivity of the random field was set to be 0.0034 S/m and the variance of the natural log of the electrical conductivity field was given as 0.3. Its correlation structure was exponential with a correlation of 0.2 m and 0.005 m in the x and y directions, respectively (see Figure 2b). Notice that these electrical conductivity fields of the two scenarios can be considered as nonstationary stochastic fields.

For the two scenarios, ninety six electrodes were placed in each of the elements located around the perimeter of the domain (Figure 3). The ERT survey consisted of 43 transmissions of electric current from a pair of electrodes at different location around the perimeter. During each test, a constant electric current of 0.0001 A was introduced into the domain by one pair of electrodes (transmitting electrodes). The transmitting electrodes were 0.03 m apart. The voltages were then measured in all the 96 electrodes (receiving electrodes). Each voltage measurement was measured from one receiving electrode (a dipole-dipole configuration). In total, 43 tests were performed numerically which resulted into 4128 voltage measurements.

Numerical inversions of the transmission current data and voltage measurements were then carried out with the SSLE algorithm. Figures 3 and 4 show the estimated electrical conductivity fields for scenarios a) and b), respectively. As illustrated in these figures, as more current transmissions around the perimeter of the domain are conducted and more pairs of source and resultant voltage field are collected and analyzed, the shape of the anomaly as well as the background conductivity field inside the domain becomes better defined. On the other hand, the rate of the improvement on the estimated



After a) 5, b) 10, c) 15, d) 20, e) 30, and f) 43 surveys.

Figure 3. Progression of the estimated resistivity field for case a in example 1 after various numbers of surveys. The battery symbols indicate the location of the source pair

electrical conductivity field diminishes as the number of current transmissions increases.

This example illustrates the intuitive nature of the ERT concept. In essence, ERT is analogous to the human approach inspecting an object: we examine the object from different angles and perspectives – around the perimeter of the object. Light is the source, our eyes are the sensors, and our brain provides the inversion algorithm. Unlike the human brain which provides a “deterministic” rendering of the object, SSLE interprets signals to yield a statistically unbiased image of the object and an uncertainty estimate. This simple example also demonstrates that an inverse problem can be made better posed if sufficient and necessary data are collected. Finally, it should be pointed out

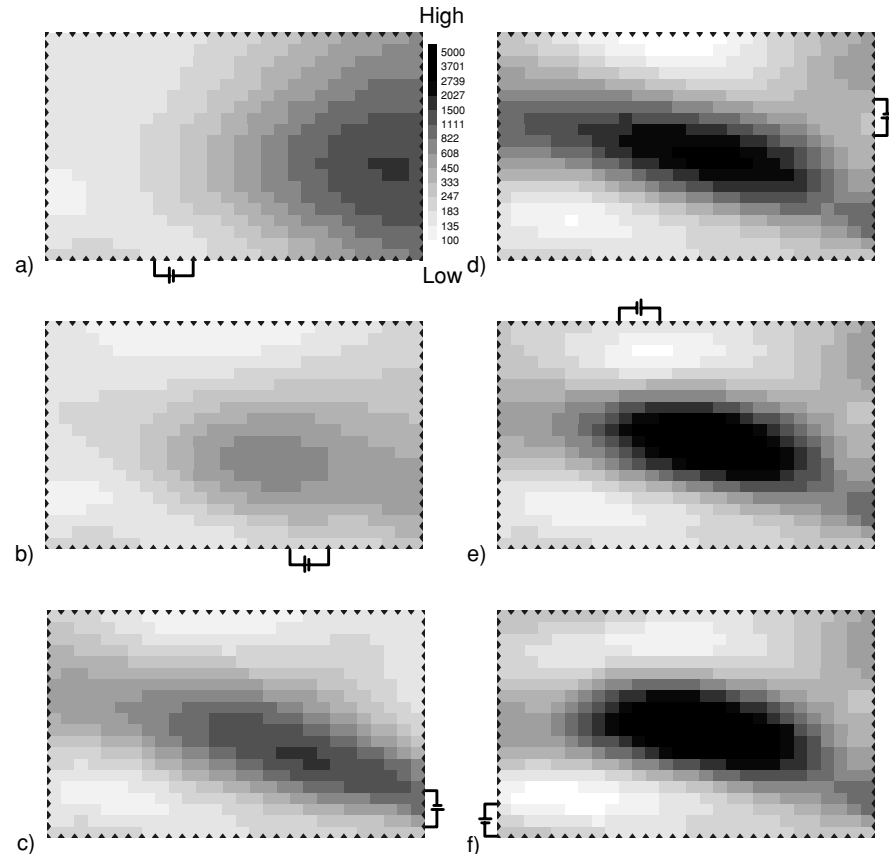


Figure 4. Progression of the estimated resistivity field for case b in example 1 after various numbers of surveys. The battery symbols indicate the location of the source pair

that a tomographic survey is a technique that allows collection of the necessary data set, without invasive probing into the domain.

A similar type of survey called electrical impedance tomography (EIT) has been used as a medical imaging device to “seeing” into human bodies (e.g. Mueller et al., 2002). While the concepts of ERT and EIT are similar, the scales of problems and resolution required in these sciences are significantly different. ERT in subsurface is limited by the number of electric potential sensors and our ability to deploy the sensors to completely surround a geologic medium to be investigated. The variability of electrical resistivity field in geologic media is also more complex and larger in magnitude. Therefore, it is expected that uncertainty in ERT is much greater than that in EIT used in medical sciences.

3.4.2. EXAMPLE 2

Example 2 illustrates the utility of ERT for characterizing migration of contaminants in large-scale geological media. Generally speaking, characterization of transport processes at a field scale based on few local measurements of contaminant concentrations is highly uncertain. Recent field and numerical experiments (e.g. Kemna et al., 2002; Vanderborgh et al., 2005) studying transport processes have shown promising results for reducing this uncertainty using ERT. The following synthetic 2D study demonstrates the potential of a joint inversion approach using local concentrations and electrical resistivity measurements for reducing uncertainty and enhancing our ability to characterize and monitor contaminant movements without extensive invasive and costly drilling operations.

In this example, migration of a highly electrically conductive solute plume was simulated in a 2D highly stratified, heterogeneous aquifer with a randomly distributed hydraulic conductivity field. The aquifer was assumed to be free of the solute initially and the aquifer had a uniform electrical conductivity field. A snapshot of the solute plume was then acquired. The concentration distribution of the plume was subsequently converted to a bulk electrical conductivity, σ , distribution based on a linear relation:

$$\sigma = 0.01 \text{ S/m} + c \cdot 0.18 \text{ S/m} \quad (14)$$

where c is the concentration. This conversion led to an electrical conductivity field with a maximum at 0.1 S/m and a background of 0.01 S/m (Figure 5a).

This electrical conductivity field was used to simulate the ERT survey using electrodes located within three boreholes (see Figures 5b or 5c). There were 10 electrodes for each borehole. During the ERT survey a “skip one” dipole-dipole source and measurement array was employed. For each transmission, a current of +1 Am or -1 Am is assigned to each electrode of the source pair. The voltage measurements during each current transmission from a source pair were taken at locations starting from one dipole length (1 m) away from the source along the borehole. In the neighboring borehole, the dipole measurements were started from the bottom electrodes, resulting in eight measurements for each borehole. The survey started with the current transmission along the borehole near $y = 5$ m and voltage measurements along the boreholes near $y = 5$ m and 15 m. The source was then moved to the borehole near $y = 15$ m and measurements were taken from the three boreholes. Lastly, the source was moved to the borehole near $y = 25$ m and measurements were taken along the boreholes near $y = 15$ m and 25 m. Altogether this survey consisted of 8 current transmissions at each borehole and 316 dipole-dipole measurements. During the simulation as well as the inversion, no flux boundaries were assumed at the right, left and top of the

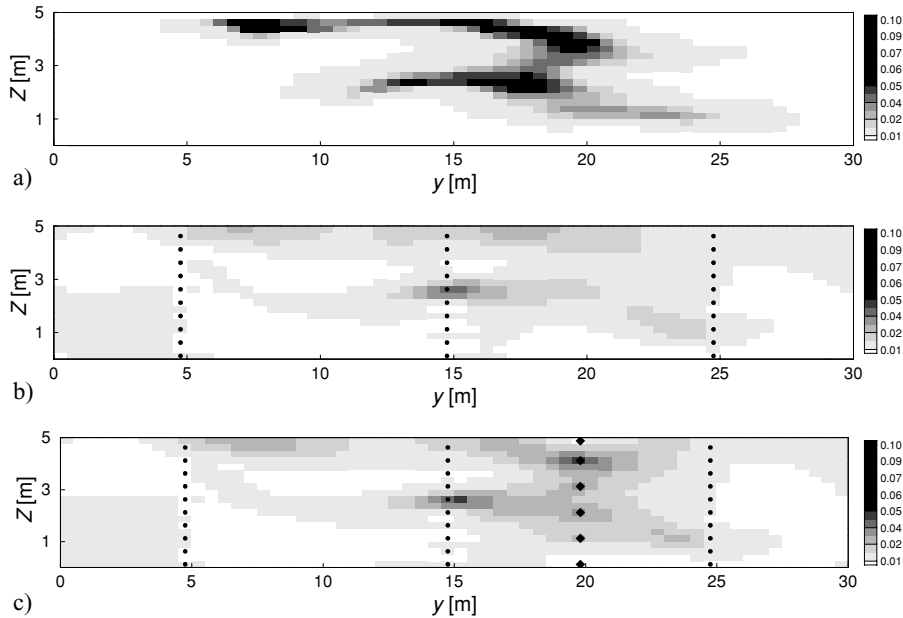


Figure 5. Two dimensional electrical conductivity distributions (S/m): a) synthetically simulated tracer plume, b) inversion results without conditioning, c) inversion results including conditioning. Electrode positions are denoted by dots. Locations of a priori known electrical conductivities are denoted by diamonds

domain. The bottom boundary was set to a constant voltage of 1 V. In an additional borehole the electrical conductivity was assumed to be known a priori at six locations (black diamonds at $y = 20$ m in Figure 5c), representing the result of a borehole resistivity survey.

The SSLE algorithm was subsequently employed to interpret the voltage measurements from the simulated ERT survey. In the first case, the inversion was conducted without point measurements of the resistivity from the six locations along the borehole. Figure 5b depicts the estimated conductivity field for this case. In the second case, the inversion includes the electrical conductivities from the six locations and the resultant conductivity field is shown in Figure 5c. An inspection of Figures 5a–c reveals that the survey captures the general pattern of the electrical conductivity distribution caused by the tracer plume quite satisfactorily. The electrical conductivity anomalies between wells in particular are well represented (Figure 5b) even though no direct concentration measurements are used and the voltage sampling array of the ERT survey is sparse (10 m apart in the horizontal direction) – ERT is indeed a potentially less invasive tool to monitor solute movement in the subsurface. Nonetheless, the estimated electrical conductivity fields are smoother

than those of the true field in Figure 5a. This is attributed to the fact that SSLE seeks a conditional effective parameter field (see Equation 4), which is smooth if insufficient number of conditioning data sets are included. In other words, had more source/voltage measurements been conducted, the estimated field would have been closer to the true field. This finding also supports results of field experiments by Singha and Gorelick (2005).

Figure 5c shows effects of incorporation of the six point electrical conductivity samples from the borehole survey. A comparison of this figure with the other two clearly indicates that inclusion of the point measurements (conditioning using the primary variable) enhances the quality of the inversion results in terms of the pattern and resistivity values significantly. As a result, the example advocates the integration of ERT surveys with direct point measurements.

3.4.3. EXAMPLE 3

The utility of ERT and the SSLE algorithm is demonstrated for monitoring transient water infiltration through 3-D vadose zones in this example. Here, water movement was simulated in a 3-D synthetic vadose zone corresponding to an infiltration event. The vadose zone was assumed to be a cube (2 m on each side) consisting of 2,000 elements in size of $0.2 \text{ m} \times 0.2 \text{ m} \times 0.1 \text{ m}$. Random values of the heterogeneous unsaturated hydraulic parameters were generated and assigned to each element using the spectral method (see Liu and Yeh, 2004). The simulated moisture content distribution at 50,000 minutes after the infiltration commenced, $\theta_{50,000}$, (Figure 6a) was used as the true moisture content fields for this demonstration. A power law constitutive relation then related the moisture content to the resistivity (e.g. Yeh et al., 2002):

$$\rho = \rho_0 \theta^{-m} \quad (15)$$

where ρ is bulk electrical resistivity, ρ_0 is a fitting parameter that is related to the electrical resistivity of pore water, m is a dimensionless fitting parameter, and θ denotes volumetric moisture content. We assumed that ρ_0 did not change during the infiltration event.

This constitutive relation (Equation 15) or a similar type of relation has frequently been used by practitioners to translate a resistivity field to a moisture content field as well. In addition, a single constitutive relation is often assumed for a given entire field. Yeh et al. (2002), however, found that the parameters of Equation (15), ρ_0 and m , varied significantly in space under field conditions. They showed that without considering the spatial variability of these parameters, interpretation of moisture content distribution based on Equation (15) can be misleading. In this example, to describe spatial variability in the parameters of the resistivity and moisture content relation in the vadose

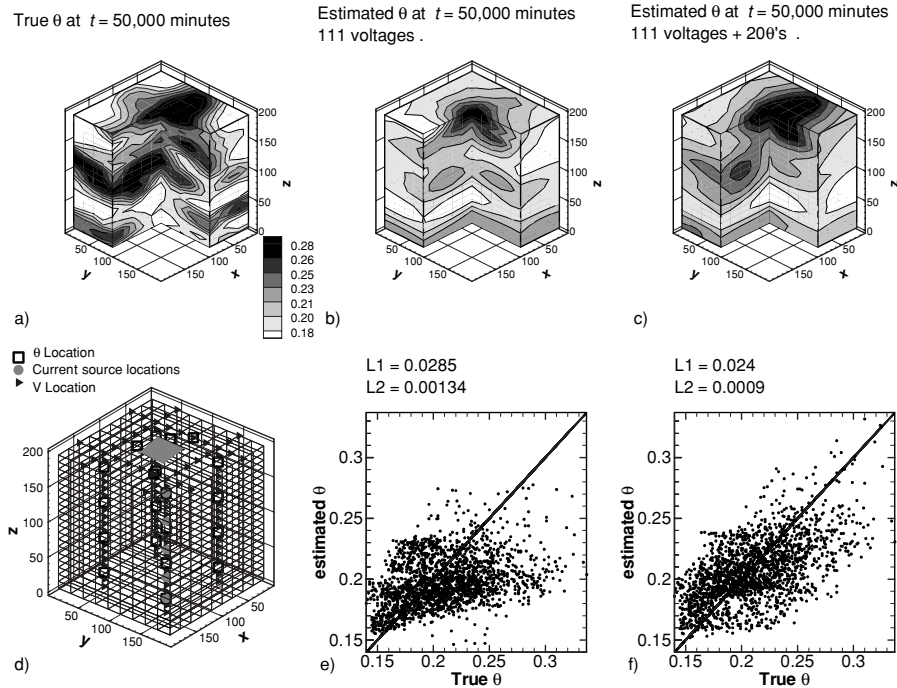


Figure 6. a) true moisture distribution, θ , at time = 50,000 minutes after infiltration; b) estimated moisture content distribution using 111 voltage measurements from the ERT; c) estimated moisture content distribution using the 111 voltage measurements plus 20 direct moisture content measurements; d) the layout for the ERT survey; e) a scatter plot showing the estimated moisture content vs. the true moisture content distribution, corresponding to Figure 6b; f) the scatter plot corresponding to Figure 6c

zone, the two parameters, ρ_0 and m , were considered as random fields with geometric means of 7.036 Ωm and 1.336, respectively. Variances of $\ln\rho_0$ and $\ln m$ were assumed to be 0.633 and 0.034, respectively. We further assumed that both parameters possessed the same exponential correlation structure with a horizontal correlation scale of 0.8 m and a vertical correlation scale of 0.2 m.

Based on these synthetic ρ_0 , m and $\theta_{50,000}$ fields, a true resistivity field at 50,000 minutes ($\rho_{50,000}$) after infiltration were calculated using Equation (15). ERT surveys were then simulated using this resistivity field. Figure 6d displays the 3-D layout of the ERT surveys. The design of the ERT survey layout included four boreholes penetrating the entire depth of the simulation domain. The x and y coordinate pairs, in meters, of the four bore holes were (0.5, 0.5), (1.5, 1.5), (0.5, 1.5), and (1.5, 1.5). Each borehole had twenty electrodes. Additional 31 electrodes were deployed along the surface in four lines with endpoints at the above $x-y$ coordinates. Currents were then transmitted

sequentially at the five depths of 0.25, 0.55, 0.95, 1.35, and 1.75 m along the upper right bore hole (1.5, 1.5). The ERT surveys resulted in five current/voltage data sets of 111 voltage measurements each. In addition, we also sampled 20 ρ_0 and m values along each of the four bore holes (a total of 80 measurements). The moisture content θ was sampled at 20 locations indicated by squares in Figure 6d.

To estimate the θ field directly based on the data from the ERT survey, the SSLE algorithm was modified by Liu and Yeh (2004) to include Equation (15), as well as the sample values of ρ_0 , m , and θ 's. This SSLE is called the integrative SSLE. For the purpose of demonstrating the effect of the direct θ measurements on the estimated moisture content field, we estimated the moisture content distribution at 50,000 minutes for two cases; a) without using any θ measurement and b) with 20 θ measurements in addition to the voltage measurements.

Figures 6a and 6b show the true moisture content distribution at 50,000 minutes and the corresponding estimated moisture content distribution using 111×5 voltage measurements, and 80 pairs of ρ_0 and m measurements, respectively. The estimated field using the same number of voltage, ρ_0 and m measurements, but including 20 direct θ measurements, is illustrated in Figure 6c. An inspection of the three figures reveals that the integrative SSLE algorithm reproduces the general pattern of the simulated true moisture content distribution, even though the constitutive relation between resistivity and moisture content varies spatially. Again, the estimated moisture content fields in Figures 6b and 6c are smoother than that in Figure 6a. The inclusion of the 20 θ measurements, on the other hand, greatly improves the estimate of the θ distribution. Figures 6e and 6f are scatter plots that correspond to Figures 6b and 6c, respectively. A 45° line indicates perfect estimation (unbiasedness and zero variance); scattering (variance) around the line is indicative of smoothness of the estimates. According to these two scatter plots, the inclusion of the 20 θ measurements reduces the biasedness of the ERT inversion for moisture content. The goodness of fit was also evaluated using L1 and L2 norms. The reductions in the L1 and L2 norms from Figures 6e to 6f indicate that the addition of moisture content measurements dramatically improve the estimate.

The conditional variance of the estimate from our SSLE approach can be used to assess the uncertainty associated with the estimate: a smaller conditional variance indicates less uncertainty in the estimate. The conditional variances corresponding to the estimates obtained when using zero and 20 θ measurements are shown on Figures 7a and 7b, respectively. Small conditional variances are located closely to the four boreholes where secondary information is measured. At locations where moisture content measurements were collected, the conditional variance is zero, indicating that these observations are honored in the inverse model and that no uncertainty exists.

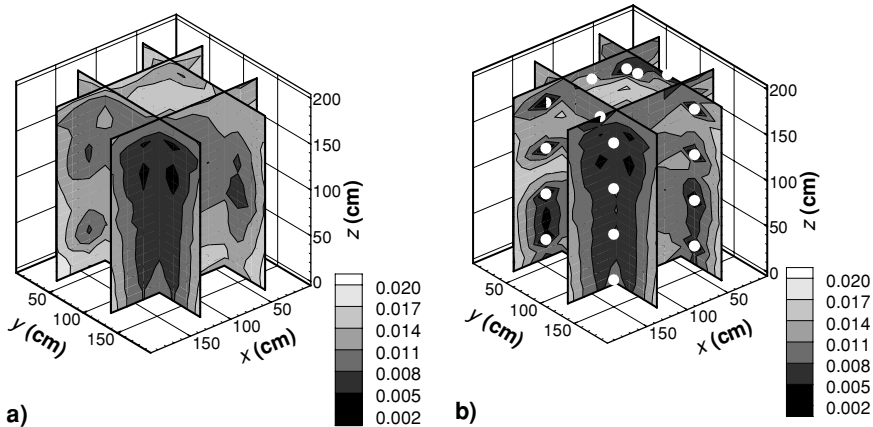


Figure 7. Estimation variance maps corresponding to the estimates in Figures 6b and 6c

3.5. Field Study

Previous numerical examples illustrate the ERT concept and robustness of SSLE. These examples however exclude measurement error and noise. Measurement error and noise are associated to equipment resolution and external electromagnetic sources (natural or induced) and they are inherent in the real-world applications of ERT. In this section we show an application of ERT to monitoring leaching operation in a mine site and demonstrate ways to tackle measurement error and noise, using our stochastic approach.

As a part of the operation of a test module in the Quebrada Blanca (QB) leaching operation in Northern Chile (see Guzman et al., 2006 for a complete description of the experimental setting), an ERT monitoring system was installed early January, 2004. Leaching consists of applying a dilute acid solution on the surface of the heap using a drip irrigation system to promote the removal of metal values. The application rate ranged from 4.2×10^{-4} cm/s to 8.4×10^{-4} cm/s. The duration of the leach cycle is defined as the time at which the desire level of metal extraction (e.g. 80%) is attained. The monitoring system was used to track operational variables (i.e., moisture content, temperature, and oxidation/reduction potential; ORP) for evaluation of the leaching mechanisms within the test module. The system operated during the first half of the leach cycle to 12 June 2004 when the system was dismantled. The monitoring system consisted of 34 probes, emplaced at the site with a horizontal spacing of 1.5 m. Twenty-four probes were installed along the centerline of the eastern cell of the test module with dimensions of 80 m by 40 m by 8 m depth; six along a line perpendicular to the centerline on the center of the cell; and two probes on each of the NW and SE quadrants of the cell.

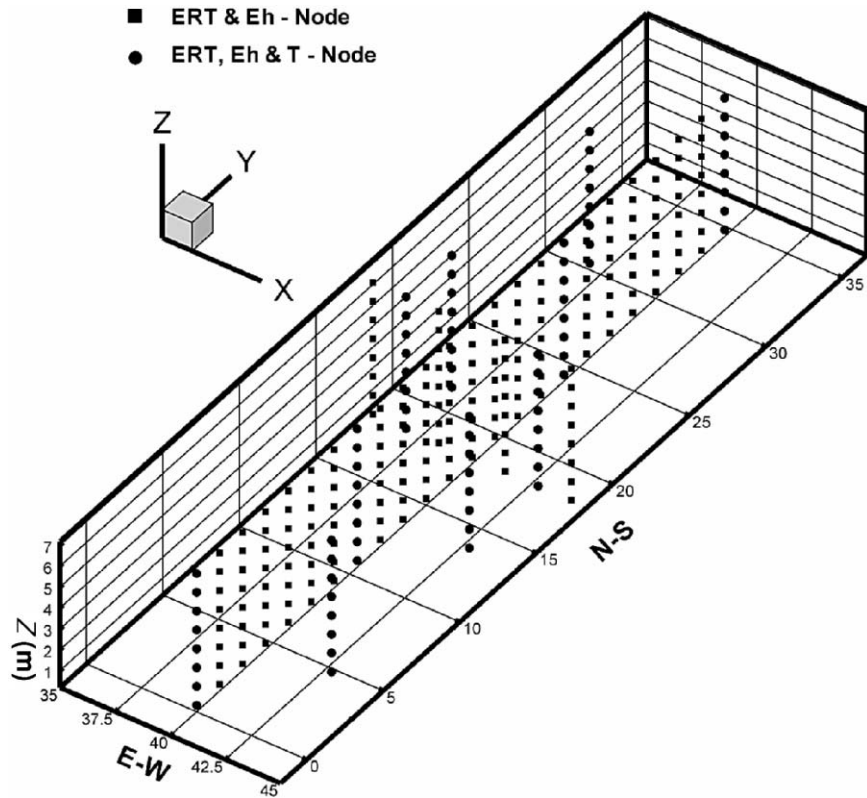


Figure 8. Spatial distribution of ERT electrodes at the QB leaching test module

Each probe was equipped with 8 multi-purpose sensors at a vertical interval of 0.9 m. Figure 8 presents a perspective view of the layout of the monitoring system.

To preprocess the voltage data collected from the ERT survey, a systematic approach similar to the structured groundwater model calibration approach proposed by Yeh and Mock (1996) was used. Specifically, the forward model (Equation 4) is first used to simulate the electric potential field in a homogeneous resistivity field at the site, corresponding to an electric current transmission (one pair of source electrodes). The initial value for the homogeneous electrical resistivity field was obtained based on the rock type of the site. The simulated electric potential field was then considered as the mean electric potential field, $\mu(\mathbf{x})$. This mean field was compared with the measured potential field, constructed by interpolation and extrapolation using the measured electric potential values. This comparison allowed us to diagnose possible systematic errors in the measurements and/or our incorrect estimated mean resistivity field. A scatter plot (Figure 9) of the

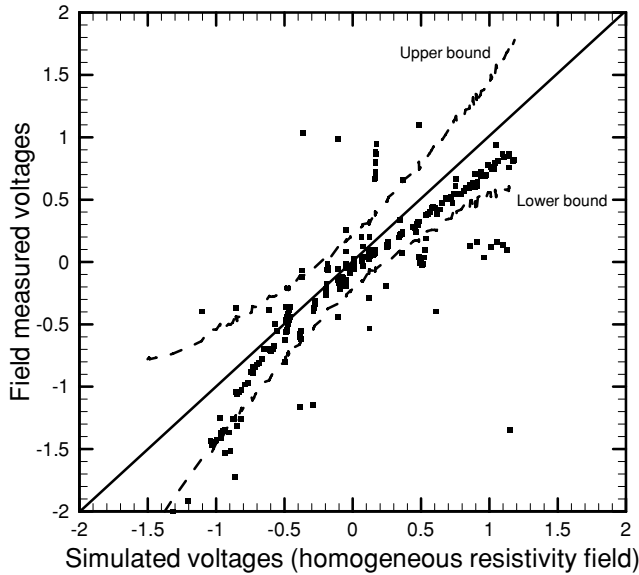


Figure 9. The scatter plot illustrating how the theoretical voltage variance is used to remove noisy measurements

measured values versus the observed ones at all of the measurement locations was also utilized for this purpose. After this diagnostic procedure, measurements of transmissions with systematic errors were eliminated from the following inversion steps. The variance of the electric potential (σ^2) at each measurement location was determined using Equation (11) afterward. The required covariance of the electrical resistivity field in Equation (11) again was specified using prior information. In this example, the prior information was merely an initial guess although the covariance could have been estimated had some borehole resistivity measurements been taken. Notice that the mean and variance calculation process is embedded in the SSLE algorithm.

Next, the estimated standard deviation of the potential value at each measurement location was used to define a low and an upper bound of the electric potential measurements (i.e., $\mu - k\sigma$ and $\mu + k\sigma$, respectively, in which k is an arbitrary integer). Measurements within the upper and the low bound were considered to be statistically reliable given prior knowledge of the spatial variability of the resistivity field at the site. These measurements were selected for the inversion process. Figure 9 illustrates this procedure for a selected transmission of the electric current.

The simulation domain used for the inversion was 34 m in West-East direction, 57 m in North-south direction, and 9.9 m in vertical direction. The domain was discretized into 7106 elements. The corresponding number of

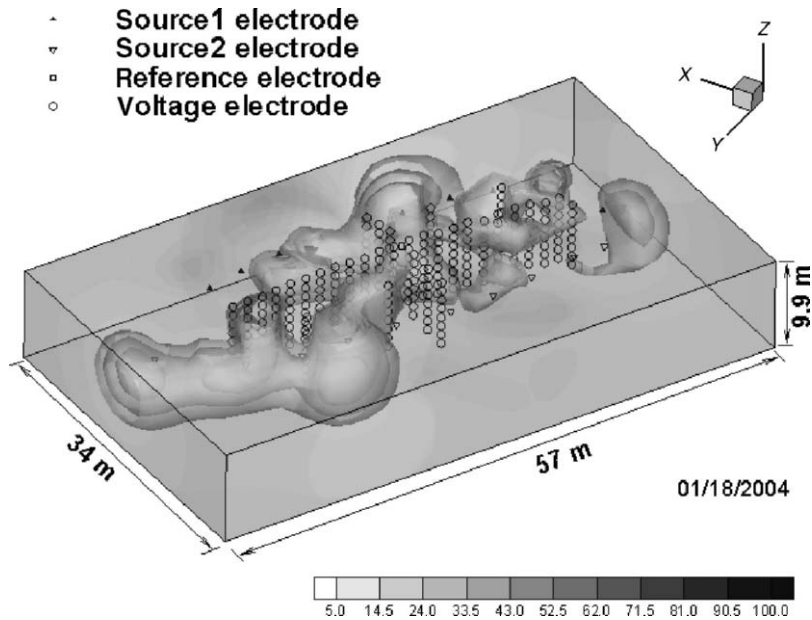


Figure 10a. Estimated resistivity field at the QB site on 18 Jan. 2004

nodes is 8424. The size of each element was 1.5 m (N-S) by 2.0 m (W-E) by 0.9 m (V). The top and bottom surfaces were assumed to be no-flow and the other four sides were considered to be constant voltage boundaries with a value of zero volts. Using the above discretization and boundary conditions, the preprocessed ERT data collected from three different times were analyzed. Figure 10a shows the estimated resistivity field at the site on 18 Jan. 2004. The estimated field for 24 Feb. 2004 is given in Figure 10b and for 22 March, 2004 is in Figure 10c. The total number of measurements used for each inversion was 2700. The computational time for each case was about 4 hours on a cluster consisting of four PCs.

While there were no immediate measurements of in-situ moisture content available to validate our estimated resistivity fields, Figures 10a–c shows increases in volume of low resistivity zones (a general indicator of high moisture content) as the irrigation progressed with time. Measurements of moisture content during the dismantling of the monitoring system showed good correspondence with estimates of moisture content based on the resistivity measurements and lab calibration (Guzman et al., 2006). The evolution of the estimated resistivity fields illustrates the progression of the infiltration process. Moreover, the resistivity measurements delineated the strong correspondence between moisture distribution and surface topography (i.e., zone of high resistivity near the surface correspond to topographic highs while

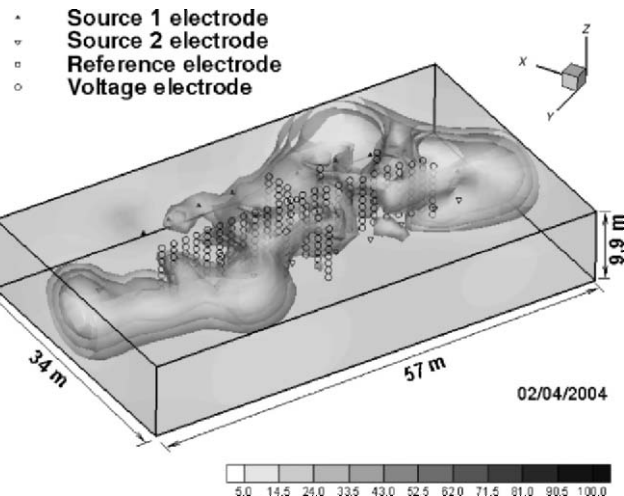


Figure 10b. Estimated resistivity field at the QB site on 24 Feb. 2004

low resistivity areas, wetter zones, correspond to topographic lows). This is quite encouraging since the topographic relief across the surface of the test module is of the order of ± 0.5 m. Other factors and procedures as discussed in Example 3 could have possibly improved the accuracy of our estimates.

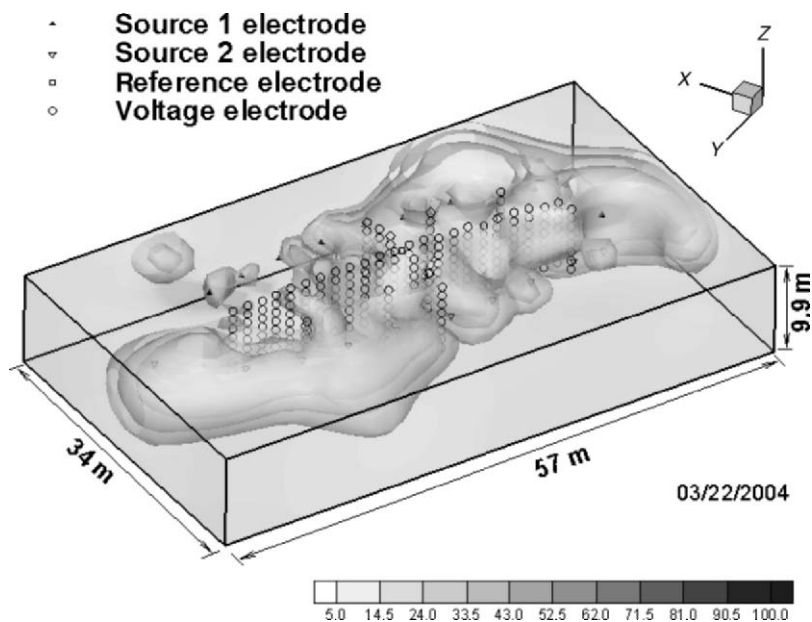


Figure 10c. Estimated resistivity field at the QB site on 22 March 2004

Nevertheless, this field case demonstrates the applicability of our SSLE procedure to a real-world ERT data set.

3.6. Discussions and Conclusion

ERT, instead of the traditional resistivity survey, is an inexpensive and viable technique for the investigation of subsurface resistivity anomalies. It has been listed as one of the most promising near-term science technology targets by a National Technical Working Group of DOE (NTWG, 2004).

Once a resolution of subsurface electrical resistivity anomalies is defined and necessary and sufficient conditions (Yeh and Šimunek, 2002) are given, a 3-D ERT inversion problem can be well posed at least mathematically. While for most field problems, the necessary and sufficient conditions may be difficult and costly to acquire. A tomographic survey nonetheless offers an intelligent way – common sense – to collect information to make the problem better posed and the estimate as such increases its resolution. For ill- or better-posed problems, a stochastic estimator (such as SSLE) that seeks the condition mean estimate and yields an estimate of its uncertainty is an appropriate choice. Note that stationarity and normality are not required for SSLE to derive good estimates but accurate and dense data sets are. However, the implicit stationarity and normality assumptions do affect the uncertainty derived from SSLE. The uncertainty estimate from any stochastic models, nevertheless, is uncertain itself – statistics is never wrong but can be imprecise. More importantly, the goal of a stochastic estimator is not to predict absolute uncertainty but to provide a quantitative means to assess effectiveness of different sampling strategies.

ERT combined with SSLE or an appropriate stochastic estimator is useful for environmental applications. However, cautions must be taken if an estimated resistivity field is translated to other environmental attributes (such as moisture content, solute concentration, or hydraulic properties of the subsurface). The ambiguity and the spatial variability of the relation between geophysical and other environmental attributes must be considered. For this purpose, an integrative approach (e.g. Liu and Yeh, 2004) or a stochastic information fusion approach (e.g. Yeh and Šimunek, 2002) is deemed necessary. Likewise, fusion of an ERT survey with a high frequency radar (e.g. ground penetrating radar) survey may enhance our ability to detect subsurface environmental anomalies at higher resolutions and greater depths than either survey by itself.

Lastly, expanding the concept of ERT to basin- or continental-scale electrical resistivity tomographic surveys appears to be logical and feasible although it requires high energy sources. Magnetotellurics (e.g. Vozoff, 1991;

White et al., 2001) in effect is a low frequency, electromagnetic method for continental-scale surveys, which has been used for imaging the electrical conductivity of the Earth. But it does not have the element of the tomographic survey (i.e., examination of the Earth at different angles and perspectives) and its image as such is often equivocal and non-unique. Exploiting cloud-to-ground, direct lightning strikes as a possible energy source (i.e., lightning tomography) for the basin- or continental-scale electromagnetic tomographic surveys as proposed by Yeh (2005) appears to be a logical future research topic in hydrogeophysics.

References

Baker, K., 2001. Investigation of direct and indirect hydraulic property laboratory characterization methods for heterogeneous alluvial deposits: Application to the Sandia-Tech Vadose Zone infiltration test site, Masters Thesis, New Mexico Institute of Mining and Technology, Socorro, NM.

Daily, W., A. Ramirez, D. LaBrecque, and J. Nitao, 1992. Electrical resistivity tomography of vadose water movement, *Water Resour. Res.*, 28 (5), 1429–1442.

Dettinger, M.D., and J.L. Wilson, 1981. First-order analysis of uncertainty in numerical models of groundwater flow, 1, Mathematical development, *Water Resour. Res.*, 17, 149–161.

Ellis, R.G., and S.W. Oldenburg, 1994. The pole-pole 3-D dc resistivity inverse problem: A conjugate gradient approach, *Geophys. J. Int.*, 119, 187–194.

Gavalas, G.R., P.C. Shan, and J.H. Seinfeld, 1976. Reservoir history matching by Bayesian estimation, *Soc. Pet. Eng. J.*, 337–350.

Gelhar, L.W., 1993. *Stochastic Subsurface Hydrology*, Prentice Hall, Englewood Cliffs, New Jersey.

Gutjahr, A., B. Bullard, S. Hatch, and D.L. Hughson, 1994. Joint conditional simulations and the spectral approach to flow modeling. *Stochastic Hydrol. Hydraul.*, 8 (1), 79–108.

Guzman, A., R.E. Scheffel, and S.M. Flaherty, 2006. Geochemical Profiling of a Sulfide Leaching OperationA Case Study, SME Annual Convention, March 28–31, 2006, St. Louis, MO, USA.

Hanna, S., and T.-C.J. Yeh, 1998. Estimation of co-conditional moments of transmissivity, hydraulic head, and velocity fields, *Adv. Water Resour.*, 22 (1), 87–93.

Hoeksema, R.J., and P.K. Kitanidis, 1984. An application of the geostatistical approach to the inverse problem in two-dimensional groundwater modeling, *Water Resour. Res.*, 20 (7), 1003–1020.

Hughson, D.L., and T.-C.J. Yeh, 2000. An inverse model for three-dimensional flow in variably saturated porous media, *Water Resour. Res.*, 36 (4), 829–839.

Kemna, A., J. Vanderborght, B. Kulessa, and H. Vereecken, 2002. Imaging and characterization of subsurface solute transport using electrical resistivity tomography (ERT) and equivalent transport models, *J. Hydrol.*, 267, 125–146.

Kitanidis, P.K., 1995. Quasi-linear geostatistical theory for inversing, *Water Resour. Res.*, 31 (10), 2411–2519.

Kitanidis, P.K., 1997. Comment on “A reassessment of the groundwater inverse problem” by D. McLaughlin and L.R. Townley, *Water Resour. Res.*, 33(9), 2199–2202.

Kitanidis, P.K., and E.G. Vomvoris, 1983. A geostatistical approach to the inverse problem in groundwater modeling and one-dimensional simulations, *Water Resour. Res.*, 19 (3), 677–690.

Li, B., and T.-C.J. Yeh, 1998. Sensitivity and moment analysis of head in variably saturated regimes, *Adv. Water Resour.*, 21 (6), 477–485.

Li, Y., and D.W. Oldenburg, 1994. Inversion of 3D dc-resistivity data using an approximate inverse mapping, *Geophys. J. Int.*, 116, 527–537.

Li, Y., and D.W. Oldenburg, 2000. Incorporating geological dip information into geophysical inversions, *Geophysics*, 65 (1), 148–157.

Liu, S., and T.-C.J. Yeh, 2004. An integrative approach for monitoring water movement in the vadose zone, *Vadose Zone J.*, 3, 681–692.

Liu, S., T.-C.J. Yeh, and R. Gardiner, 2002. Effectiveness of hydraulic tomography: Sandbox experiments, *Water Resour. Res.*, 38(4), doi: 10.1029/2001WR000338.

McLaughlin, D., and L. R. Townley, 1996. A reassessment of the groundwater inverse problem, *Water Resour. Res.*, 32 (5), 1131–1161.

Mueller, J.L., S. Siltanen, and D. Isaacson. A direct reconstruction algorithm for electrical impedance tomography. *IEEE Trans. Med. Imaging*, 21 (6), 555–559.

National Research Council (NRC), 2000. Seeing into the earth: noninvasive characterization of the shallow subsurface for environmental and engineering application, Board on Earth Sciences and Resources, Water Science and Technology Board, Commission on Geoscience, Environment, and Resources, National Academy Press, Washington, DC.

National Technical Working Group (NTWG), 2004. Natural and passive remediation of chlorinate solvents: Critical evaluation of science and technology targets, WSRC-TR-2003-00328, Westinghouse Savannah River Company, Savannah River Site, Aiken, SC 29808, February 19, 2004.

Oldenburg, D.W., and Y. Li, 1999. Estimating depth of investigation in dc resistivity and Ip surveys, *Geophysics*, 64 (2), 403–416.

Sharma, Perm V., 1997. Environmental and Engineering Geophysics, Cambridge University Press, Cambridge.

Singha, K., and S. Gorelick, 2005. Saline tracer visualized with three-dimensional electrical resistivity tomography: Field-scale spatial moment analysis. *Water Resour. Res.*, 41, W05023, doi: 10.1029/2004WR003460.

Sun, N.Z., 1994. Inverse Problems in Groundwater Modeling, Kluwer Academic Press, Norwell, MA.

Sun, N.-Z., and W.W.-G. Yeh, 1992. A stochastic inverse solution for transient groundwater flow: Parameter identification and reliability analysis, *Water Resour. Res.*, 28 (12), 3269–3280.

Sykes, J.F., J.L. Wilson, and R.W. Anderews, 1985. Sensitivity analysis for steady state groundwater flow using adjoint operators, *Water Resour. Res.*, 21 (3), 359–371.

Theis, C.V., 1935. The relation between lowering the piezometric surface and the rate and duration of discharge of a well using ground water storage, in 16th Annual Meeting of the Transactions of the American Geophysical Union, Part 2, 519–524.

Tikhonov, A.N., and V.A. Arsenin, 1977. Solutions of Ill-posed Problems. Winston, Washington.

Vanderborght, J., A. Kemna, H. Hardelauf, and H. Vereecken, 2005. Potential of electrical resistivity tomography to infer aquifer transport characteristics from tracer studies: A synthetic case study, *Water Resour. Res.*, 41, W06013, doi: 10.1029/2004WR003774.

Vargas-Guzman, J.A., and T.-C.J. Yeh, 1999. Sequential kriging and cokriging: Two powerful geostatistical approaches, *Stochastic Environ. Res. Risk Assess.*, 13, 416–435.

Vargas-Guzmán, J.A., and T.-C.J. Yeh, 2002. The successive linear estimator: A revisit, *Adv. Water Resour.*, 25, 773–781.

Vozoff, K., 1991. The magnetotelluric method, in *Electromagnetic Methods in Applied Geophysics – Applications*, Chapter 8, edited by M.N. Nabighia, Society of Exploration Geophysicists.

White, B.S., W.E. Kohler, and L.J. Srnka, 2001. Random scattering in magnetotellurics, *Geophysics*, 1, 188–204.

Wu, C.-M., T.-C.J. Yeh, J. Zhu, T.H. Lee, N.-S. Hsu, C.-H. Chen, and A.F. Sancho, 2005. Traditional analysis of aquifer tests: Comparing apples to oranges?, *Water Resour. Res.*, 41, W09402, doi: 10.1029/2004WR003717.

Yeh, T.-C.J., 1992. Stochastic modeling of groundwater flow and solute transport in aquifers, *J. Hydrol. Process.*, 6, 369–395.

Yeh, T.-C.J., 1998. Scale issues of heterogeneity in vadose-zone hydrology, in *Scale Dependence and Scale Invariance in Hydrology*, edited by G. Sposito, Cambridge Press, Cambridge, MA.

Yeh, T.-C.J., 2005. Exploiting natural recurrent stimuli for “seeing” into groundwater basins, in Fall AGU Meeting, SF.

Yeh, T.-C.J., A.L. Gutjahr, and M. Jin, 1995. An iterative cokriging-like technique for groundwater flow modeling, *Groundwater*, 33 (1), 33–41.

Yeh, T.-C.J., and J. Šimůnek, 2002. Stochastic fusion of information for characterizing and monitoring the vadose zone, *Vadose Zone J.*, 1, 207–221.

Yeh, T.-C.J., M. Jin, and S. Hanna, 1996. An iterative stochastic inverse method: Conditional effective transmissivity and hydraulic head fields, *Water Resour. Res.*, 32 (1), 85–92.

Yeh, T.-C.J., and S.Y. Liu, 2000. Hydraulic tomography: Development of a new aquifer test method, *Water Resour. Res.*, 36 (8), 2095–2105.

Yeh, T.-C.J., S. Liu, R.J. Glass, K. Baker, J.R. Brainard, D. Alumbaugh, and D. LaBrecque, 2002. A geostatistically based inverse model for electrical resistivity surveys and its applications to vadose zone hydrology, *Water Resour. Res.*, 38 (12), 1278, doi: 10.1029/2001WR001024.

Yeh, T.-C.J., and P.A. Mock, 1996. A structured approach for calibrating steady-state ground water flow models, *Groundwater*, 34 (3), 444–450.

Yeh, T.-C.J., and J. Zhang, 1996. A geostatistical inverse method for variably saturated flow in vadose zone, *Water Resour. Res.*, 32 (9), 2757–2766.

Yeh, W.W.-G., 1986. Review of parameter identification procedures in groundwater hydrology: The inverse problem, *Water Resour. Res.*, 22 (1), 95–108.

Zhang, J., and T.-C.J. Yeh, 1997. An iterative geostatistical inverse method for steady flow in the vadose zone, *Water Resour. Res.*, 33 (1), 63–71.

Zhang, J., R.L. Mackie, and T. Madden, 1995. 3-D resistivity forward modeling and inversion using conjugate gradients, *Geophysics*, 60, 1313–1325.

Zhu, J., and T.-C.J. Yeh, 2005. Characterization of aquifer heterogeneity using transient hydraulic tomography, *Water Resour. Res.*, 41, W07028, doi: 10.1029/2004WR003790.

4. UNSATURATED ZONE PROCESSES

Giorgio Cassiani, Andrew Binley, and Ty P.A. Ferré

4.1. Introduction

The vadose zone, i.e., the part of subsurface above the water table, is home to a number of key processes that control the mass and energy exchanges between the subsurface and the atmosphere. Vadose zone hydrology provides boundary conditions for both atmospheric processes, including micro-meteorology and climatic changes, and subsurface water migration, with strong implications in water resources management. The rates, timing, and patterns of aquifer recharge are controlled by percolation through the vadose zone. Contaminants released near the ground surface can be altered, retarded or wholly removed by biological, chemical and physical processes in the vadose zone before reaching underlying aquifers. Unsaturated processes control also the availability of water for agriculture, and are the driving mechanisms in slope stability, floods and other major engineering geology problems. Few hydrological problems of practical interest can neglect the importance of the complex, non linear dynamics of vadose zone processes. However, in practice, the impact of the vadose zone on hydrologic problems is often ignored or treated using highly simplified approximations, mainly because of limited available data in this region. A proper characterization of the vadose zone should also account for the natural variability of the soil properties at different scales.

Hydrologic characterization of the vadose zone is challenging, particularly when the investigation extends deeper than one or two meters below ground. Advances have been made in the design of tensiometers to allow for direct measurement of water pressure, even to great depths. However, direct measurement of water content still requires the recovery of soil samples for laboratory analyses. Both of these direct measurements are invasive, based on drilling. In addition, direct measurement of water content is destructive, requiring sampling. As a result of their need for drilling, direct measurements are generally inadequate to yield sufficient spatial coverage for basin-scale investigations. In addition, direct sampling disturbs the soil, restricting the ability to monitor transient processes. Finally, it is difficult to use small-scale samples to describe representative field-scale properties, particularly in loose sediments. At present, only gypsum block probes (and related instruments) provide indirect measurements of water pressure. However, these probes are invasive,

difficult to use for quantitative investigations and do not permit continuous recording of moisture contents. A leap forward in our ability to make rapid and inexpensive time-lapse measurements of volumetric water content was provided by the introduction of time domain reflectometry (TDR) in the early 1980s (see Section 4.3.1). TDR paved the way for the general acceptance of indirect measurements of soil volumetric water content. However, TDR is limited in both its depth and spatial coverage. These limitations have led to the development of other geophysical techniques for hydrological monitoring.

From a practical standpoint, two compartments can be identified in the subsurface that require different approaches for indirect monitoring. The *shallow* vadose zone, no deeper than a few meters below ground, can be successfully imaged, with extensive spatial coverage, by taking measurements from the ground surface. In contrast, the *deep* vadose zone, requires measurements in single-boreholes, between boreholes, or from the surface to boreholes to achieve sufficient vertical resolution for quantitative hydrologic interpretation.

The development of geophysical techniques for the characterization of the subsurface has been very rapid over the past couple of decades. Ground-penetrating radar (GPR) and electrical resistivity tomography (ERT) have seen the most widespread use to date. This rapid development has been due to the growing demand for data to constrain distributed hydrologic models and simultaneous advances in instrument design, providing the opportunity to collect, store, and process large quantities of high-quality field data. Of particular importance to hydrologic characterization and monitoring are the abilities of geophysical methods to describe two aspects of the subsurface:

- a. *static* aspects, which *do not* change over time, principally related to physical and chemical properties of the medium;
- b. *dynamic* aspects, which *do* change over time in response to changes in fluid saturations and water chemistry.

Similar developments are taking place in the petroleum industry, where petroleum geophysics is seen more and more often as a means for understanding the nature of a site *and* its evolution in terms of fluid-dynamics. For example, indirect measurements of changes in fluid saturation are being used as a key supporting technique for a site's management during petroleum production.

This successful use of geophysical data for hydrologic investigations requires:

- a. that the collected geophysical data have a clear, identifiable and quantitative petrophysical relationship to environmental variables of interest;

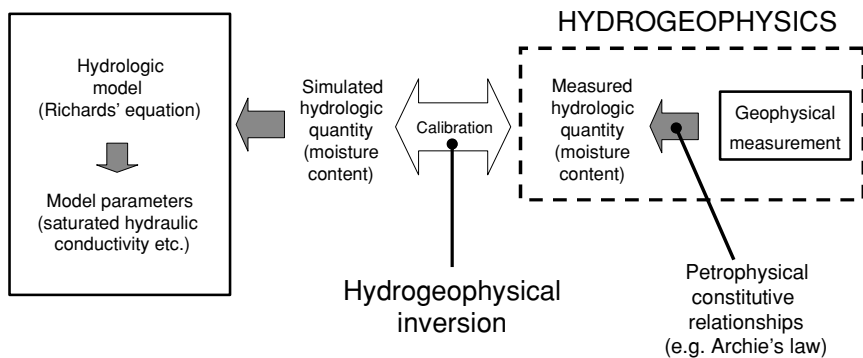


Figure 1. Conceptual scheme for the use of geophysical data to calibrate (invert for) unsaturated flow parameters

- b. that the resolution and sensitivity of geophysical methods in space and time is fully understood and is appropriate to constrain the hydrologic process of interest;
- c. that indirect measurements be incorporated into hydrologic models in the most effective way, (i.e., accounting for resolution, sensitivity and scale effects).

The efforts aimed at fulfilling these requirements constitute the body of a fascinating and diversified area of research known as “hydrogeophysics”. Ideally (Figure 1), geophysical data and hydrologic modeling should be linked through a quantitative calibration based upon the dependent physical variable—generally the soil moisture content. This procedure is theoretically capable of providing estimates of the governing parameters of the hydrologic model, i.e., in the case of Richards’ equation, saturated hydraulic conductivity and the other unsaturated flow parameters.

This chapter provides some background regarding the physical processes (mainly water flow) in the vadose zone (Section 4.2.1), the available geophysical techniques (Section 4.2.2), and the petrophysical relationships linking volumetric water content and geophysical response (Section 4.2.3). Section 4.3 will discuss the applications in the shallow vadose zone, with reference to TDR (Section 4.3.1), GPR in surface-to-surface configuration (Section 4.3.2), and ERT applied at the small scale particularly with the use of surface electrodes only (Section 4.3.3). Section 4.4 will cover applications in the deep vadose zone, specifically cross-hole GPR (Section 4.4.1) and cross-hole ERT (Section 4.4.2). For each technique, a brief summary of the methodology is given, pointing to more detailed references, together with some application examples.

4.2. Principles and Methods

4.2.1. UNSATURATED FLOW IN POROUS MEDIA

The flow of water in unsaturated porous media is controlled by differences in hydraulic head – H [L] defined as the sum of a pressure head ψ and an elevation head z :

$$H = \psi(\theta) + z \quad (1)$$

The relationship between pressure head ψ and volumetric water content, θ [–], commonly referred to as the water retention curve, depends on the soil physical characteristics. Several empirical expressions exist that describe this relationship, each depending on a limited number of constitutive parameters. One of the most widely accepted models is van Genuchten's (1980). This four-parameter relationship between pressure head ψ and volumetric water content θ is:

$$\theta = \theta_r + \frac{\theta_s - \theta_r}{[1 + (\alpha |\psi|)^n]^m} \quad (2)$$

where θ_r is the residual water content at very high suction (asymptotically at infinite suction), θ_s is the water content at full saturation (approximately equal to porosity), $\alpha [L^{-1}]$ is inversely related to the mean soil grain size, and n is an exponent with larger values associated to a wider grain (and pore) size distribution. The relationship is often simplified by taking $m = 1 - 1/n$.

Note that, in general, the pressure saturation curve during drainage is different from the corresponding curve during imbibition (hysteresis). In addition, if drainage or imbibition is reversed at some stage, the system follows generally an intermediate behaviour (scanning curve). In spite of this complexity, a van Genuchten parameterization can be adopted for drainage, imbibition or scanning conditions, albeit using different parameter values.

If a gradient of total head ∇H exists in the porous medium, a consequent flow of water is induced, according to Darcy's law. As first introduced by Buckingham, and later described by Richards (1928):

$$q = -K(\psi)\nabla H \quad (3)$$

where q is water flux [L/T] and $K(\psi)$ is the unsaturated hydraulic conductivity [L/T] at a given pressure head ψ . By assuming that the air phase is infinitely mobile, the flow of water can be described based only on water phase properties. Then, by combining the Darcy-Buckingham law (3) with the principle of mass conservation, one can derive the so called Richards'

equation:

$$\frac{\partial}{\partial x_i} \left(K(\psi) \frac{\partial H}{\partial x_i} \right) = \frac{\partial \theta(\psi)}{\partial t}, \quad i = 1, 2, 3 \quad (4)$$

where x_i are the spatial coordinates and t is time. More complete, multi-phase flow models have been developed to account for variations in temperature, fluid compressibility, and a deformable soil matrix, similar to state-of-the art models in petroleum engineering.

Application of the Richards' equation is dependent on determination of the highly non-linear hydraulic properties $K(\psi)$ (or $K(\theta)$) and $\theta(\psi)$. Laboratory measurements (see Klute and Dirksen, 1986) can provide valuable information on the soil characteristics at sampling locations, where pressure-saturation relationships can be determined and hydraulic conductivity dependence on saturation can either be measured or inferred from theoretical considerations (Mualem, 1976). However, as described above, direct sampling has limitations related to spatial and temporal coverage, especially for investigations in the deep vadose zone. Inverse estimation of hydraulic properties from spatially and temporally distributed measurements of water content provide an alternative to these direct methods (e.g. Lambot et al., 2002; Linde et al., 2006). In this chapter we will show how geophysical data can be used to provide quantitative estimates of the unsaturated hydraulic properties of a porous medium.

4.2.2. APPLICABLE GEOPHYSICAL METHODS

A range of field geophysical techniques are available to assist with understanding of unsaturated zone processes. The methods permit either static structural characterization (e.g. the definition of lithological boundaries, fracture zones, etc.) or estimation of volumetric or mass water content (or dynamic changes in these properties). The range of methods allows determination of the following properties: seismic velocity (elastic properties), electrical conductivity (or its inverse, resistivity), dielectric permittivity, mass density. Applicable techniques are seismic (refraction, reflection and transmission) (e.g. Steeples, 2005), electromagnetic induction, dc resistivity and induced polarization (e.g. Binley and Kemna, 2005), TDR, GPR (e.g. Annan, 2005). Other techniques, such as Nuclear Magnetic Resonance (NMR) are still in a development stage (Valla and Yaramanci, 2002). In addition, a number of geophysical well logging methods, based on the same physical principles, allow the determination of properties in the unsaturated zone (e.g. Kibr et al., 2005). While all the methods above can have some use in vadose zone studies, they vary considerably in complexity and, most important, in actual usefulness.

The seismic velocity depends on the elastic properties and density of the soil matrix and only weakly on the volumetric water content. Seismic methods are traditionally used to determine structural information about the subsurface and thus may assist in zonation of properties within a hydrological model. However, the principal seismic method – multicoverage reflection – is not suitable for shallow applications. Seismic refraction can only give low-resolution images of the subsurface, and borehole-to-borehole transmission tomography requires considerable effort in comparison to the information it can provide for unsaturated zone studies.

Electrical conductivity may be measured using a range of geophysical techniques: frequency domain electromagnetic conductivity, time domain electromagnetic conductivity, dc resistivity. In addition, induced polarization (IP) allows measurement of properties related to the conductivity at the fluid – grain interface.

Inductive electromagnetic techniques may be used to determine geologic structure or hydrological response through time lapse monitoring. Specifically, frequency domain methods are particularly useful for mapping lateral changes in hydrogeologic structure because the lack of direct contact of the instrument with the ground allows for rapid instrument deployment over large areas. However, depth profiling with frequency domain methods requires the use of different frequencies and different coil separations, limiting the practically achievable temporal and spatial resolution of the electrical conductivity profile. Time domain methods measure over a wide range of frequencies in a short time, allowing for efficient depth profiling. However, because these methods typically require the use of relatively large antenna loops, they are difficult to deploy quickly at many surface locations, limiting spatial coverage. The ability of time domain electromagnetic methods to make rapid, nondestructive measurements of electrical conductivity suggests that these methods could contribute to monitoring transient infiltration and to calibrating numerical models describing water flow throughout the vadose zone. A general weakness of inductive methods is that they provide low resolution images of the subsurface resistivity structure.

Direct contact with electrical sources and receivers through electrodes is required with DC resistivity methods and thus achieving wide spatial coverage is considerably more labor intensive than for inductive methods. Measurements are typically carried out using four electrodes, two for current injection and two for potential measurement, in order to avoid the problems caused by contact resistance between soil and electrodes. DC resistivity allows the determination of spatial variation in electrical conductivity with resolution principally controlled by electrode spacing. In addition, the dynamic range of the method is broad, permitting application in highly resistive and highly conductive environments. This latter property makes DC resistivity ideally

suited to mapping spatial changes in conductivity which result from changes in volumetric water content in the soil. When DC current is switched on or off, a transient phenomenon known as induced polarization (IP) is observed: the measured voltage does not go to zero instantly, but at a fairly slow rate (slower than the transient due to electromagnetic induction). IP is caused by ionic transport in the pore water, and polarization phenomena at the grain-water interfaces.

Dielectric permittivity is directly related to volumetric water content and is measured in the field using TDR at small scale, or GPR at larger scales. Both methods rely on the fact that the velocity of an electromagnetic wave in a soil is related to the dielectric permittivity. TDR measures this velocity directly using guided waves, whereas GPR can be used to measure the velocity of an unguided wave between two antennas, for example positioned at the ground surface or in different boreholes. GPR is also used to map lithological or hydrological (e.g. water table) boundaries from reflected signals in surface profiling mode.

In this chapter we focus on the application of DC resistivity and GPR for unsaturated zone studies. For more details of other techniques the reader is referred to Rubin and Hubbard (2005). Before illustrating examples of how these methods are applied it is necessary to examine the relationships between measured geophysical properties and fundamental hydrological parameters.

4.2.3. PETROPHYSICAL CONSTITUTIVE RELATIONSHIPS

Electromagnetic geophysical techniques have seen the most widespread use for the investigation of the vadose zone. Typically, these techniques measure the electrical resistivity ρ (Ωm) (or its reciprocal, electrical conductivity σ in S/m) and/or the dielectric constant (or relative dielectric permittivity) $\kappa(-)$. Our ability to infer hydrologically relevant properties from electrical properties is key to quantitative hydrogeophysical applications in the vadose zone. The assumption is usually made that it is possible to identify a unique monotonic relationship linking soil volumetric water content with either soil dielectric permittivity or electric conductivity. These relationships are generally dependent on the geological formation, so that site calibration is needed. Calibration is particularly important for electrical conductivity, while many common unconsolidated media require little or no calibration to infer water content from dielectric permittivity. The need for medium-specific calibration means that different parameter values could be needed for different geological formations at the same site.

The relationships between water saturation and electrical resistivity, originally developed for the interpretation of well logs for the petroleum industry, date back by many decades. Such are the empirical relationships devised by

Archie (1942) and Waxman and Smits (1968), which relate effective electrical conductivity to porous medium properties, as well as to water saturation. More recent are the developments on dielectric models, mostly triggered by the need to interpret TDR data. Most notable are the commonly used relationship by Topp et al. (1980) and the Complex Refractive Index Model (CRIM) discussed by Roth et al. (1990). Many other empirical, semi-empirical and theoretical models exist, but we will restrict our discussion to the models above, by far the most widely adopted in field applications.

4.2.3.1. Electrical Conductivity

Experimental evidence shows that the bulk electrical resistivity of a rock sample increases with increasing electrical resistivity of the saturating fluid. At full saturation, and when the fluid conductivity is overwhelmingly larger than the solid matrix or the internal surface conductivity, bulk conductivity σ_b and fluid conductivity σ_w are proportional, according to Archie's (1942) law:

$$\sigma_b = \frac{\sigma_w}{F} \quad (5)$$

where F is named the formation factor, which is a function of porosity ϕ :

$$F = \frac{a}{\phi^m} \quad (6)$$

where a and m are empirical constants. Theoretically, a should be equal to 1. The cementation exponent m depends on the internal structure of the pore space, which can be described in terms of tortuosity. The typical range for m is 1.0–2.5.

If matrix conductivity is non-negligible, Equation (5) can be generalized to:

$$\sigma_b = \frac{\sigma_w}{F} + \sigma_s \quad (7)$$

where σ_s is the effective solid matrix conductivity, another medium-specific parameter. The matrix electrical conductivity is related to the properties of the grain coating, mainly composed of clay and oxides, and of the electrical double layer in contact with an aqueous solution. Note that the formulation (7) assumes that fluid and solid act as conductors in parallel (see also Rhoades et al., 1976). Some evidence indicates that this may not be universally true (Brovelli et al., 2005).

As water saturation decreases, electrical resistivity increases. This can be represented by extending Archie's law (5) to account for water saturation S_w [–]:

$$\sigma_b = \frac{\sigma_w}{F} S_w^n \quad (8)$$

where n is another empirical exponent having in general values close to 2. Similarly, Equation (7) can be generalized into the Waxman and Smits (1968) model, originally developed for shaly sandstones:

$$\sigma_b = \frac{S_w^n}{F} \left(\sigma_w + \frac{\sigma_s}{S_w} \right) \quad (9)$$

Given the functional form of Equation (8), time-lapse measurements of electrical conductivity can yield directly variations of water saturation in terms of ratios in the absence of significant surface electrical conductivity:

$$\frac{\sigma_b(t_2)}{\sigma_b(t_1)} = \left[\frac{S_w(t_2)}{S_w(t_1)} \right]^n \quad (10)$$

where t_1 and t_2 are two measurement time instants; note that Equation (10) does not require knowledge of the formation factor F .

4.2.3.2. Dielectric Constant

Many studies have been carried out to investigate the relationship between the bulk relative dielectric permittivity κ of a porous medium and its volumetric water content. The Maxwell-Garnett mixing model is based on the effective medium approach (EMA) and is not generally valid (i.e., it can only be applied to high porosity systems), but it provides the upper/lower bound for the bulk dielectric permittivity (Robinson and Friedman, 2003). Modifications of the EMA leads to the self-consistent and self similar consistent models or Hanai-Bruggeman theory; for a review see Chelidze and Guéguen (1999).

Two empirical approaches have gained popularity in practical applications: one is the complex refractive index method (CRIM), which is a volume averaging relationship and explicitly incorporates porosity ϕ , volumetric water content θ , and the dielectric constant of solid matrix (κ_s), air (κ_a) and water phase (κ_w) (Roth et al., 1990; Chan and Knight, 1999):

$$\kappa^\alpha = (1 - \phi)\kappa_s^\alpha + \theta\kappa_w^\alpha + (\phi - \theta)\kappa_a^\alpha \quad (11)$$

where α is an exponent generally taken equal to $1/2$. If time-lapse measurements of bulk dielectric constant are collected, CRIM provides a convenient means of estimating changes in soil volumetric water content with no need to account for the dielectric permittivity of the solid phase:

$$\theta(t_2) - \theta(t_1) = \frac{\kappa(t_2)^\alpha - \kappa(t_1)^\alpha}{\kappa_w^\alpha - \kappa_a^\alpha} \quad (12)$$

The second empirical approach was developed for the interpretation of TDR data. Topp et al. (1980), using a large set of different soils, developed an empirical relationship to relate the effective permittivity to the volumetric water content, which takes no explicit account of variations in the properties

of the solid matrix (e.g. permittivity, porosity, connectivity, etc.):

$$\theta = -5.3 \times 10^{-2} + 2.92 \times 10^{-2}\kappa - 5.5 \times 10^{-4}\kappa^2 + 4.3 \times 10^{-6}\kappa^3 \quad (13)$$

The *Topp* model is generally applied unless the medium has properties (e.g. porosity, magnetic susceptibility, high clay content) that differ from typical agricultural soils. Unusual soils require calibration and are better served by the CRIM model.

4.3. Shallow Vadose Zone

It is relatively easy to make measurements in the shallowest couple of meters below ground. Despite this relatively easy access, direct monitoring techniques have several important limitations:

- a. Direct techniques typically require soil sampling (e.g. gravimetric water content measurement) – or controlled application of water (e.g. saturated hydraulic conductivity measurement). Both of these approaches disturb the natural water flow regime;
- b. It is difficult to achieve high temporal and spatial resolution using destructive gravimetric sampling to monitor transient processes;
- c. Direct methods are typically time consuming and labor intensive, limiting the number of samples that can be collected within a given monitoring budget.
- d. Direct techniques have a limited characterization scale (usually $<0.1\text{--}1\text{ m}$), which may not be relevant for the modeling and management scales of interest (usually $>1\text{--}100\text{ m}$), given the inherent variability of the soil properties.

Nondestructive, indirect techniques (e.g. TDR) can overcome many of these limitations. Noninvasive, nondestructive, indirect techniques (e.g. GPR) offer even better solutions, where applicable. However, these surface-to-surface methods have resolution that quickly degrades with depth limits and, for some methods, poorly understood sample volumes and sensitivity distributions. Ideally, indirect methods should be used together with direct, invasive methods to provide *in situ* calibration of petrophysical relationships and acceptable spatial and temporal resolution and coverage.

4.3.1. TDR

4.3.1.1. *Methodology*

TDR is not always classified as a geophysical method, partly because, unlike most other hydrogeophysical methods, it was developed by soil scientists and hydrologists. The method gained wide acceptance in these communities

when it was demonstrated that: (a) TDR can make rapid, non-destructive, minimally invasive measurements of volumetric water content; and (b) the method can be applied in a wide range of soils without the need for medium specific calibration. The method advanced further due to its ability to measure both volumetric water content and bulk electrical conductivity in the same sample volume. Finally, the method has seen broad use both in the field and in the laboratory because users can design probes to have sample volumes and spatial sensitivities to satisfy specific monitoring needs. Several recent reviews provide a comprehensive overview of the theory and application of the method (e.g. Noborio, 2001; Robinson et al., 2003).

Although several researchers have applied borehole-based TDR (e.g. Ferré et al., 1996; Dahan et al., 2003), the method is most commonly applied by inserting two or three parallel metal rods directly into the soil. The rods can be inserted vertically or sub-vertically, from the ground surface, or horizontally in excavated trenches. The rods can be inserted and removed immediately after measurement when conducting areal surveys. Alternatively, many probes can be connected to a common TDR instrument through a multiplexer to allow for automated sampling. Because TDR measurements are rapid, generally requiring only a few seconds once the rods are installed, very high temporal resolution of dynamic hydrologic processes is possible.

A fast rise-time voltage step is applied to the rods through connecting (coaxial) cables. The difference in two-way travel times of the step to the top and bottom of the rods, together with the known length of the probes, is used to determine the propagation velocity. This is used to infer the dielectric permittivity, and thereby the water content, as described in Section 4.2.3. The accuracy of travel time determinations relies on the preservation of sufficient high frequency energy in the travelling wave to reliably identify the reflection from the end of the probe. Therefore, like GPR, the primary limitation on the depth of investigation of TDR from the ground surface is signal loss. For electrically conductive soils, the maximum depth of investigation may be only a few centimetres; for dry sand, measurements can be made to several meters depth. Typically, TDR probes range from 10 cm to 2 m in length. Electrically resistive coatings have been used to propagate signal through lossy media, but these coatings have deleterious effects on the calibration of TDR probes (Ferré et al., 1996). Final advantage of TDR is that the guided wave has well understood properties, allowing for combination of travel time and signal attenuation measurements to infer the complex dielectric permittivity (e.g. Heimovaara et al., 1995; Das et al., 1999).

4.3.1.2. *Example*

Thousands of positive examples of TDR can be found in the literature. We present a counter example to demonstrate that any geophysical method, even

one as widely successful as TDR, must be used and interpreted with caution. The example application is based on one of the advantages of TDR measurements made with uncoated rods: the unique relationship between the measured travel time and the length-weighted average water content along the TDR probes. Based on this property, the volumetric water content measured with vertically installed adjacent probes of different length can be used to monitor infiltration, redistribution, and drainage. This application assumes, as is widely done, that vertical heterogeneity is more pronounced than horizontal variability, allowing for the differencing of laterally adjacent cumulative water storage values to produce vertical water content profiles. The method is applied in a highly homogeneous environment.

Experiments were conducted on an field site on Canadian Forces Base Borden, Ontario. The site material is a homogeneous, well-sorted, fine- to medium-grained sand with no significant clay fraction. The top meter of soil was excavated to provide an undisturbed surface and the entire site was covered with a greenhouse to eliminate natural recharge. Finally, a 3 m by 3 m drip-line irrigation system with drip points located on a 15 cm by 15 cm grid was placed on the surface of the site to provide controlled infiltration.

Six pairs of continuous-rod waveguides were installed. The lengths of the continuous-rod pairs were 40, 60, 80, 100, 120 and 140 cm. Each rod had a diameter of 0.4 cm and a separation of 3 cm. Measurements were made with a Tektronix 1502B cable tester (Beaverton, OR) connected to a personal computer through an RS-232 serial interface. Automated analysis software was written by the authors to analyze the TDR waveforms based on the straight-line intersection method used by Topp et al. (1982). Waveforms were collected under fully drained conditions and during the advance of a wetting front. Once the water content profile showed no measurable change with time, the infiltration system was turned off and drainage was monitored.

The volumetric water contents determined for each continuous-rod pair, determined using the *Topp* equation are plotted against the length of the rod-pair on Figure 2 for profiles collected during infiltration. Each rod-pair measures the average water content from the ground surface to the end of the rods; therefore, the water content measured with each pair increases immediately with the onset of infiltration. The water content increases in time for all of the rod-pairs until late time, when the profiles become nearly constant in time. At each depth, the water content increases continuously in time until steady-state flow is established.

To produce an interval-differenced water content profile, the water contents measured by any two continuous-rod pairs differing in length by 20 cm were used to calculated the water content of the nonoverlapping depth interval.

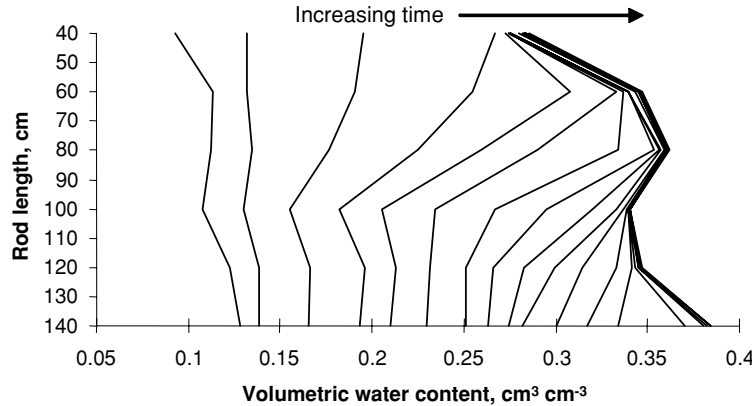


Figure 2. Average water content estimated from TDR measurements at the Borden site

The interval-differenced water content is defined as,

$$\theta_n = \frac{\theta_l L_l - \theta_s L_s}{L_l - L_s}, \quad (14)$$

where θ is the water content, L is the probe length and the subscripts n , s and l denote the non-overlapping region and the short and long rod-pairs, respectively. Interval-differenced profiles determined from the continuous-rod measured water contents are shown in Figure 3.

The water content is unreasonably low at 90 cm depth after 70 minutes of infiltration. This error is likely due to lateral variations in water content

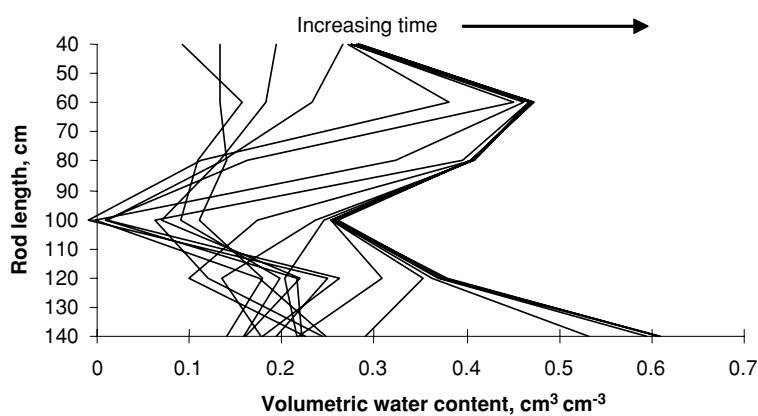


Figure 3. Water content along individual depth intervals estimated from TDR measurements at the Borden site

between probes and points out the potential errors that can occur when comparing measurements with different sample volumes. Similar errors would apply to any method that mixes lateral and vertical variations to produce a vertical profile of hydrologic conditions, such as common midpoint profiling with electrical methods, vertical seismic profiling, or wide angle reflection and refraction ground penetrating radar. Unlike these other methods, each TDR probe can be examined independently as well. For example, before the wetting front reaches the end of the rods, the cumulative flux is equal to the local infiltration rate at each probe. Assuming that the flux remains constant, the change in stored water as a function of time as the water passes the ends of the rods can be used to infer the hydraulic properties of the medium (Parkin et al., 1995). Assuming unit gradient conditions, the flux can be equated to the hydraulic conductivity at the final water content; this can be repeated to characterize the K - θ relationship. Finally, measurements made during free drainage can be used to infer the hydraulic properties in a manner similar to a one-step outflow experiment (Kool et al., 1985).

4.3.2. RADAR FROM THE SOIL SURFACE

4.3.2.1. *Methodology*

The identification of the water table using GPR has been a goal frequently pursued with varying degrees of success (e.g. Nakashima et al., 2001). Any method that relies on measurement of the water content cannot identify the water table directly, except in very coarse soils, due to the formation of a saturated capillary fringe above the water table. The water table elevation is very continuous in space, unless the area shows substantial changes in hydraulic properties over a small scale, allowing for interpolation of the water table elevation from borehole-based measurements. In contrast, the top of the capillary fringe is likely highly irregular, even above a flat-lying water table. As a result, GPR can probably be more useful as a means to identify temporal changes in volumetric water content above the capillary fringe e.g. as an effect of pumping (Bevan et al., 2003; Ferré et al., 2003).

In shallow investigations volumetric water content can be estimated from GPR velocity measurements using both transmitter and receiver antennas deployed at the ground surface (see Huisman et al., 2003). The energy transmitted through the ground follows multiple pathways simultaneously (Figure 4a). The determination of the propagation velocity is key to estimates of volumetric water content. While other techniques have been proposed (e.g. full-wave electromagnetic inversion – Lambot et al. (2004a,b)) the general approach is to identify distinct arrivals on the radargram (e.g. Figure 4b) and pick traveltimes for such events, to be used for velocity calculation.

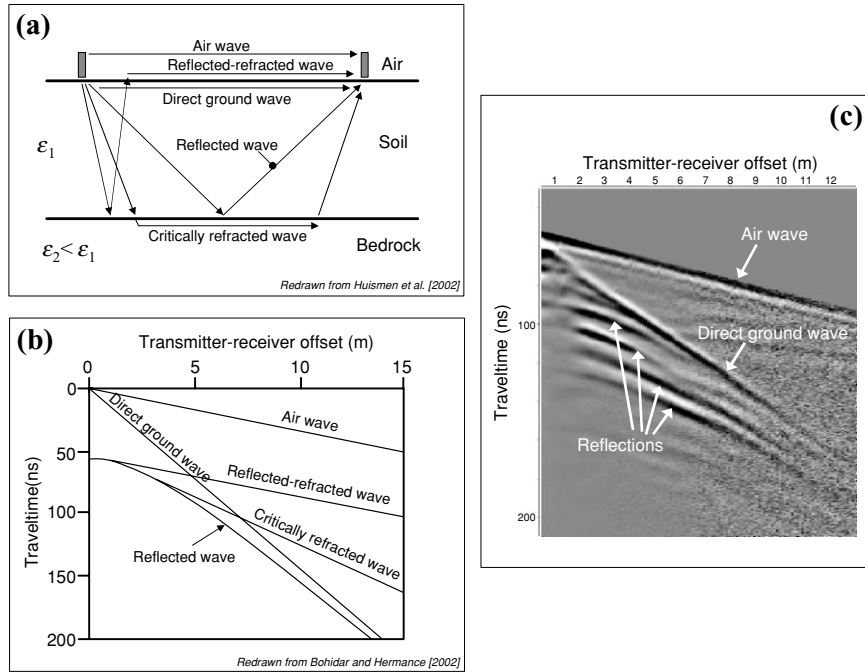


Figure 4. (a) Expected GPR wave propagation pathways in surface-to-surface configuration; (b) corresponding time-offset relationships; (c) example field data: Grugliasco (Turin, Italy), acquisition with 200 MHz antennas – 19 March 2004

The acquisition procedure largely dictates the events that can be used for velocity determination. Running a single-offset profile (both antennas are moved simultaneously while maintaining a constant separation) allows for velocity determination from reflections, only if they come from a horizon or a body at a known depth. If the correct antenna separation is used, then the volumetric water content can be mapped quickly over large areas and averaged over a fairly large scale from velocity determinations based on the direct ground wave as well (Huisman et al., 2001). It should also be kept in mind that velocity information from direct ground wave is potentially fraught with difficulties, especially if other events than the direct ground wave manifest themselves in the radargram, such as refracted waves (Bohidar and Hermance, 2002) and guided waves (Arcane et al., 2003).

Single-offset transects allow for rapid coverage of large areas. However, under some conditions, multiple measurements must be made and interpreted simultaneously. Either the Wide Angle Reflection and Refraction (WARR) mode, where one antenna is kept fixed while the other is moved, or the Common Mid Point (CMP) mode, where both antennas are moved simultaneously to keep the same mid-point, can be adopted. Both WARR and CMP

allow generally for a good identification of direct waves through the air and the ground (Figure 4c). The slope of the direct ground wave dromocrone yields the GPR velocity for volumetric water content determination. Alternatively, a number of CMP gathers can be collected, similar to seismic reflection processing, and velocity analysis can be performed on reflection events. The information coming from different offsets is sufficient to give velocity estimates even in absence of independent knowledge of the depth of selected reflectors. However, unlike in seismic processing, this velocity analysis from the reflected waves does not generally give very accurate estimates, partly because some of the hypotheses underlying velocity analysis in seismic reflection, such that velocity is generally increasing with depth, are not satisfied for GPR (Becht et al., 2005).

Off-ground GPR reflection is also a rapidly developing method for the measurement of volumetric moisture content in the very shallow soil layers. The method has been used by Chanzy et al. (1996) and, particularly in the field of hydrogeophysics, by Lambot et al. (2004c) who used GPR reflection data to identify simultaneously the water retention curve and hydraulic conductivity function of a sandy soil using electromagnetic and hydrodynamic inversion techniques.

4.3.2.2. *Example 1: WARR GPR Time-Lapse Monitoring During Surface Irrigation*

An experimental plot was located adjacent to the campus of the Agricultural Faculty of the University of Turin, Italy. Depth to the water table is approximately 20 m below ground. Sediments in this area are largely eolian. The soil is sandy, mixed (calcareous), mesic Arenic Eutrudepts. Two distinct horizons are identifiable: an upper horizon, approximately 1 m thick, with finer sand overlying a lower layer of coarser sediments. Vegetation is composed of natural grass.

An irrigation experiment was performed at the site on 28 Sept. 2004 by means of a line of sprayers. The soil was initially extremely dry as a consequence of an exceptionally dry summer period. The irrigation intensity was always lower than the infiltration capacity of the soil, so no ponding was observed on the soil surface. Soil water content was monitored by means of surface-to-surface GPR using a PulseEkko 100 radar system with 200 MHz antennas. The sampling interval was 0.2 ns, 64-fold vertical stacking was used, and WARR offset increments equal to 10 cm over a 14 m line were sampled. A GPR WARR survey was acquired before the start of irrigation, and roughly every two hours thereafter over the six-hour irrigation period. TDR rods ranging in length between 0.15 m and 2 m, spread along the irrigated line, were monitored using a Tektronix 1502 B. Point excavation to a depth of about 1.5 m was performed in the irrigated plot, and visual inspection was used to support indirect evidence of the contact between wet and dry soil.

The very homogenous structure of the soil is ideal for identifying a sharp infiltration front on a WARR radargram. As the front infiltrates, a low-velocity layer develops that is sandwiched between the air above, with the fastest possible GPR velocity $c = 0.3$ m/ns, and a fast half-space below having the GPR velocity of the dry soil. Under such conditions, a critically refracted GPR wave coming from the interface between the wet layer and the dry layer below is recorded at earlier arrival times than the direct GPR wave through the low-velocity wet layer. Figure 5 shows the evolution of WARR surveys over time, clearly showing the presence of the critically refracted event, and the growth of the intercept time (at zero offset) of such refracted event as a consequence of wet layer thickening as irrigation progresses. Note in Figure 5 also the presence of multiple reflected-refracted events that manifest themselves as multiples of the critically refracted event at larger arrival times. The presence of multiples is in fact a transition towards a waveguide phenomenon – see Example 2 – not quite fully developed under the conditions at Grugliasco.

A classical analysis of critically refracted events (e.g. Bohidar and Hermance, 2002) leads to the estimation of both velocity of the dry and wet soil layers, and of the thickness of the wet layer (Table 1). Using the Topp et al. (1980) relationship, the estimated volumetric water content of the dry and wet soil are respectively 5 % and 38 %. These values are fully supported by the TDR data. The depth of the infiltration front estimated by GPR refraction analysis is also confirmed by direct inspection, even though some discrepancy is observed at the beginning of infiltration.

4.3.2.3. *Example 2: GPR Guided Waves in Soil Layers Along a Mountain Slope*

A study area was located at the north-western tip of the Como Lake, Italy, to study the use of GPR for water content mapping along mountain slopes. The investigated site is part of a small catchment (the S. Vincenzo Creek basin). The slope parcel selected for detailed monitoring is located close to Monte-mezzo, at an elevation of 1150 m a.s.l., its size is roughly 40 m × 40 m, with a dip varying between 30° and 40°. The slope is characterized by extended unconsolidated deposits, with medium to large blocks of different nature in a sandy-gravelly matrix, usually interpreted as moraine deposits. The highly friable paragneiss bedrock outcrops only in small areas and shows subvertical foliation. The test site is mainly covered with grass. Infiltration can potentially cause, under very intense rainfall, soil saturation with interflow and possible triggering of shallow landslides in the soil cover and/or partly in the underlying bedrock. Both direct (piezometers, tensiometers, etc.) and indirect (geophysical) methods have been used to characterize slope and bedrock morphology as well as changes in soil volumetric water content over time. Here we focus on the use of ground-penetrating radar (GPR) in surface-to-surface configuration. The monitoring has been performed using a PulseEkko

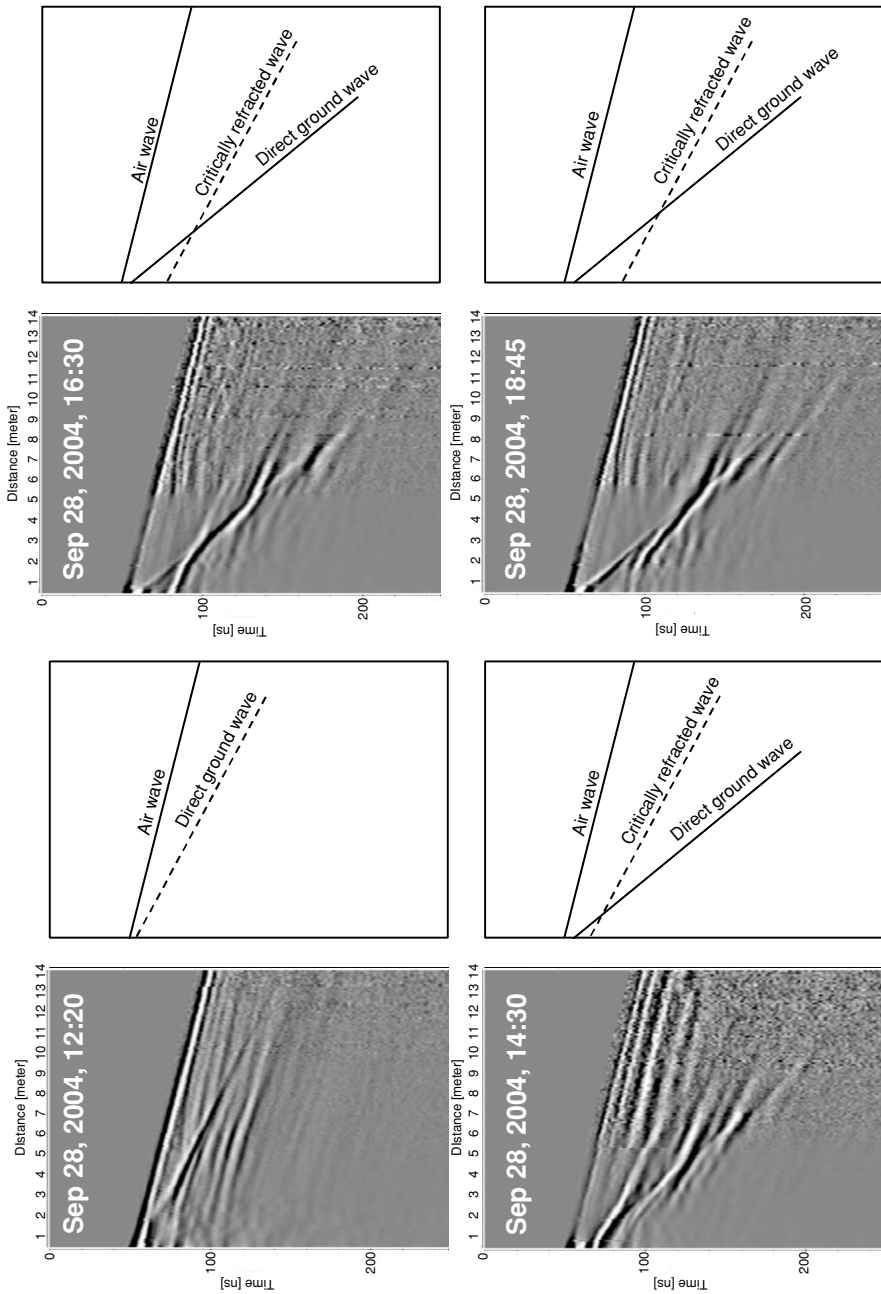


Figure 5. GPR time-lapse WARR acquisition at the Grugliasco (Turin, Italy) site during a controlled irrigation experiment at the ground surface.

TABLE 1. Grugliasco site: estimates of GPR velocities and infiltration front depth during the irrigation experiment of 28 Sept. 2004

Time	Velocity of the wet layer v_1 (m/ns)	Velocity of the dry layer v_2 (m/ns)	Depth from refracted GPR (m)	Depth from excavation (m)
12:20	—	0.156	—	—
14:30	0.063	0.154	0.49	0.35
16:30	0.062	0.154	0.88	0.8
18:45	0.064	0.151	1.28	1.25

100 radar system with 100 MHz antennas, with a sampling interval of 0.2 ns and offset increments equal to 10 cm over the 20 m line. At each station, the signal was stacked 64 times to improve the signal/noise ratio.

A typical dataset collected using a WARR configuration at the Montemezzo site is shown in Figure 6. The character of these data is distinctively different from data in the same configuration collected over a

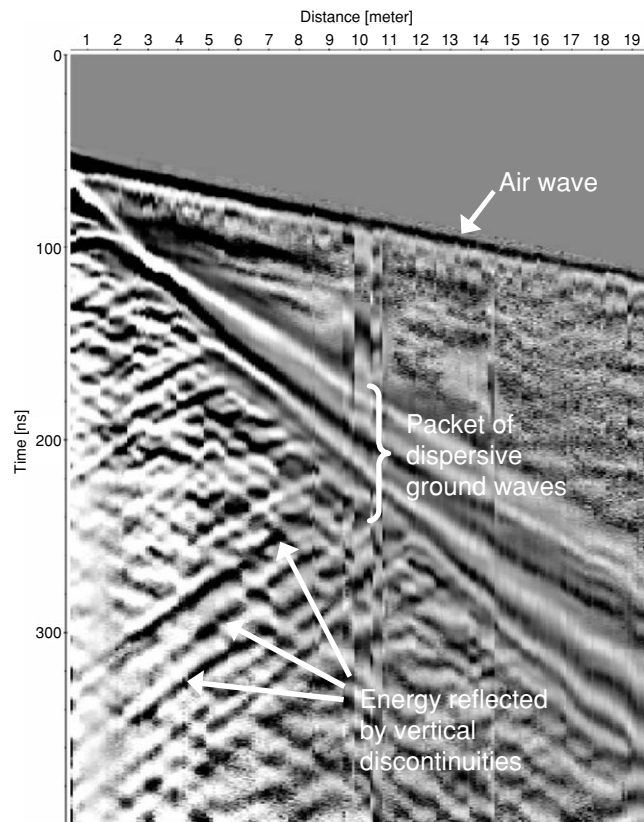


Figure 6. WARR with 100 MHz antennas Montemezzo – line 1–22 April, 2004

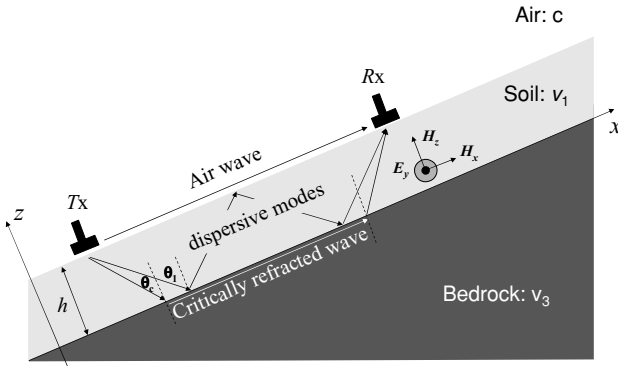


Figure 7. Scheme of slope with radar propagation pathways in a thin waveguide

fairly homogeneous subsoil – see Figures 4c and 5. In particular, the direct ground wave at Montemezzo is composed of a wavetrain that becomes longer at larger offset, with a clear dispersive nature: lower frequencies travel faster than higher frequencies. Consequently, the change in first arrival travel time with changing offset cannot be directly related to the GPR velocity of the shallow soil layer.

A schematic representation of the case of a thin soil layer resting on the top of bedrock, as observed at this site, is shown in Figure 7. The GPR velocity in the soil cover is much lower than in the bedrock, primarily because the soil has a much higher porosity, and can attain a much higher volumetric water content than the underlying rock. If, in addition, the thickness of the soil layer is comparable to the dominant GPR wavelength at the frequencies of interest, the geological structure becomes a refractive waveguide. Such a structure allows the modal propagation of guided waves in addition to the propagation of direct, refracted, reflected, and reflected-refracted waves (Arcone et al., 2003). The data interpretation requires the definition of a model relating the properties of this propagation to the guide parameters (thickness, soil and bedrock velocities). The simplest model that can describe this physical system is an asymmetric slab waveguide, with two infinite parallel planes that define the interfaces between a core of velocity v_1 and two cladding layers (the air and the bedrock) with higher velocities v_2 and v_3 . The deployment of antennas (electrical dipoles) parallel to each other justifies the assumption of propagation of TE polarized waves, in which the electric field is everywhere perpendicular to the direction of propagation (Figure 7).

A very robust technique for dispersion analysis is based on the wavefield transformation widely adopted in seismic processing and in the surface wave methods to infer the dispersion characteristics of Rayleigh waves (Strobbia, 2003). The data are transformed from the time-offset domain ($t-x$) into the frequency-wavenumber ($f-k$) domain; an automatic search algorithm identifies

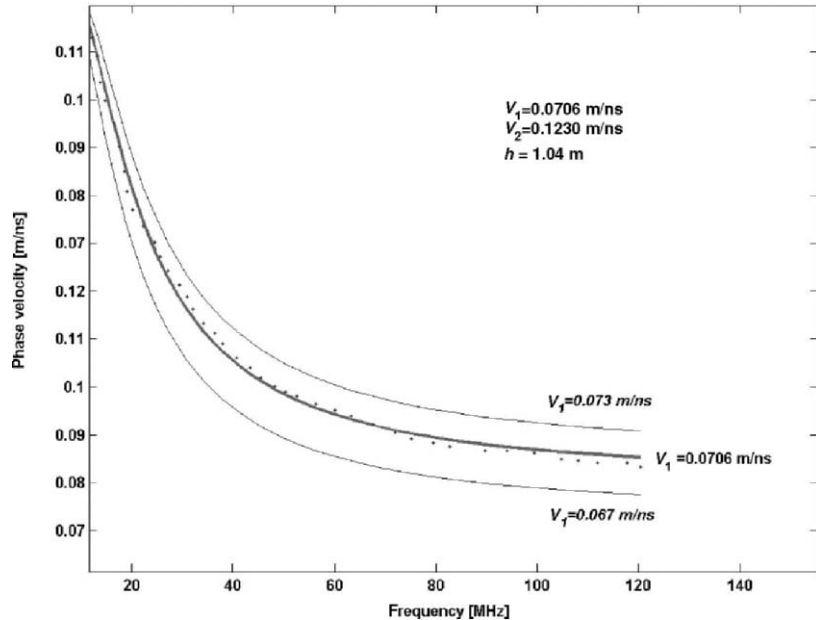


Figure 8. Montemezzo site: example of experimental dispersion curve inverted for GPR velocities and soil thickness: note the excellent sensitivity of the forward model to changes in soil velocity v_1

the wavenumber corresponding to the maximum of spectral density at each frequency, and the f - k graphs are easily converted in f - v curves by considering that $v = 2\pi f/k$. The resulting dispersion curve is the final product of the processing phase; an inversion algorithm transforms the dispersion curve into estimates of the three governing parameters (thickness, velocity of the soil layer and velocity of the bedrock). The computed dispersion curves are very sensitive to the model parameters – see in particular Figure 8 for sensitivity to the velocity in the soil layer.

The Topp et al. (1980) relationship was used to convert bulk dielectric constant into volumetric water content values (Table 2). Volumetric water

TABLE 2. Estimates of soil and bedrock properties as derived from GPR guided wave inversion, Montemezzo site

	v_{soil} (m/ns)	v_{bedrock} (m/ns)	h (m)	θ_{soil} [-]	θ_{bedrock} [-]
Oct. 03	0.075	0.106	1.01	0.29	0.15
Apr. 04	0.078	0.11	0.95	0.27	0.14
Oct. 04	0.068	0.102	0.68	0.34	0.16
Dec. 04	0.065	0.098	0.65	0.36	0.18
Feb. 05	0.071	0.111	0.75	0.32	0.13

content in soil and bedrock follow the same time pattern, even though changes are relatively small. Note that the estimate of soil thickness changes over time: this is probably due to the use of a single-layer forward model (Figure 7) in a situation where wetting and drying of the underlying bedrock may require the use of more complex, multi-layer waveguide models. Figure 6 shows also that substantial backscattered energy travel horizontally with a velocity close to the bedrock velocity. This evidence seems to confirm that the bedrock is broken into blocks, and is therefore permeable and subjected to volumetric water content changes.

4.3.3. DC RESISTIVITY

4.3.3.1. *Methodology*

The DC resistivity method (see Binley and Kemna, 2005) determines the spatial variation of resistivity (in 1-D, 2-D or 3-D) using four electrode measurements. Two of the electrodes are used as transmitter electrodes to create an electrical circuit and the other two are used to measure the potential difference which results from the potential field created by the transmitter electrodes. The measured potential difference relative to the injected current is an integrated measure of the resistivity within the vicinity of the four electrode array. By varying the positions of the four electrodes the user gains more lateral or vertical coverage. Surveys are often carried out in sounding mode or imaging mode, the latter often being referred to as electrical resistivity tomography.

A vertical electrical sounding (VES) is used to determine the vertical variation of resistivity, i.e., no lateral variation is assumed. Four-electrode measurements are made on the soil surface with progressively larger spacing, centered at the same position. The resulting series of measurements (a sounding curve) are then modeled to determine a series of layers of varying resistivity that is consistent with the observed response. This approach is widely used to determine lithological boundaries in hydrogeological studies, over large horizontal and depth scales, some cases with a focus on the study of vadose zone processes (for example, Chand et al., 2004; Kalinski et al., 1993). The method has, however, been utilized for investigation of shallow vadose zone processes. Kean et al. (1987), for example, carried out VES surveys to study changes in volumetric water content over depths of a few meters following addition of a water tracer. Frohlich and Parke (1989) used VES to infer changes in volumetric water content to a depth of 3 m during natural recharge.

Resistivity imaging is more commonly used today for investigating the shallow subsurface following the introduction in the 1980s and now widespread availability of computer controlled multi-electrode switching in

dc resistivity instruments. Surface imaging combines a lateral profile and vertical sounding and data are processed using appropriate inverse methods (see Binley and Kemna, 2005) to produce a 2-D or 3-D image of the subsurface. Surveys are carried out by performing profiles along a transect (or transects) at different electrode spacing.

Surface resistivity imaging is ideal for shallow vadose zone studies as the depth of penetration does not suffer in the same way as GPR. Electrical contact between electrodes and soil surface is required, however, which may limit application in particular environments. In addition, installation of electrodes, layout of cables and data collection is relatively time consuming (in comparison to electromagnetic induction methods) and thus lateral coverage may be limited in order to minimize survey times. Survey lengths are typically tens of meters with data coverage to depths of a few meters.

4.3.3.2. *Examples*

Surface resistivity has been widely used for mapping changes in volumetric water content in the shallow subsurface. Barker and Moore (1998) show two examples of time-lapse imaging using resistivity. In their first example, the distribution of moisture following injection of a water tracer on the ground surface is mapped to a depth of 4 meters and their results show clearly the impact of the roots of a nearby tree on the lateral redistribution of moisture. In their second example, they show changes in resistivity to a depth of 5 meters caused by water table lowering during abstraction of water from a pumping well.

Benderitter and Schott (1999) and Zhou et al. (2001) have used surface resistivity imaging to study lateral variability in infiltration under natural loading. Other examples of shallow vadose zone studies using dc resistivity imaging include: Hagrey and Michaelsen (1999), who claim the identification of preferential flow under forced (irrigation) loading using resistivity imaging at their site; Panissod et al. (2001), who used resistivity images to map changes in volumetric water content due to crop water uptake and French and Binley (2004), who used time-lapse 3-D resistivity imaging to monitor changes in resistivity to a depth of 0.5 m caused by localised infiltration following snowmelt (see also Chapter 7 for more details).

The wide range of applications, such as those listed, demonstrates the flexibility of resistivity imaging for monitoring spatial and temporal variation in resistivity in the shallow vadose zone due to natural and forced loading. The determination of moisture contents from resistivity measurements alone is often difficult because of the impact of other factors (clay content, salinity, temperature) on bulk resistivity. However, changes in moisture content may be estimated from time-lapse measurements, provided appropriate petrophysical relationships are available, although few authors have attempted to make such quantitative estimates.

4.4. Deep Vadose Zone

The vadose zone becomes more difficult to investigate with increasing depth. Boreholes provide useful points of access to the soil, especially below the water table, where water samples can be recovered more easily. Similarly, pressure head can be measured more easily below the water table than in the deep vadose zone. Direct sampling in the deep vadose zone faces the same limitations with respect to spatial and temporal coverage as in the shallow vadose zone. In fact, these limitations increase due to increased drilling and sampling costs with depth. As a result, the dynamics of hydrologic processes in deep vadose zones is poorly characterized, even though this zone plays a critical role in determining the travel times and fates of contaminants travelling to deep unconfined aquifers.

Unfortunately, the surface-based non-invasive methods described above are less effective for monitoring the deep vadose zone. Specifically, the resolution and accuracy of these methods degrade with depth of investigation. In general, it is more appropriate to use boreholes as access points for these non-invasive techniques to characterize the deep vadose zone.

4.4.1. BOREHOLE RADAR

4.4.1.1. *Methodology*

The increasing availability of commercial borehole GPR systems has led to a number of recent hydrogeological applications of the technique in unsaturated systems (for example, Hubbard et al., 1997; Eppstein and Dougherty, 1998; Alumbaugh et al., 2002). Note that most hydrological applications are conducted in transmission mode, while other uses – e.g. geotechnical in fractured rocks – exploit reflected events. Borehole transmission surveys may be conducted in three different configurations, depending on the survey goals and practical constraints, in order to determine dielectric properties at the field scale. In two modes, a GPR signal is transmitted from one antenna placed in the first borehole, and received by a second antenna in the other borehole. Measurement of the received electromagnetic wave permits determination of the first arrival and hence velocity of the wave (v). In one mode, using a multiple offset gather (MOG), the receiver is moved to different locations in one borehole whilst the transmitter remains fixed. The transmitter is then moved and the process repeated. Following collection of all data in this mode and determination of the travel time for each wave path-line it is possible to derive a tomogram of velocity within the plane of the borehole pair. In contrast, a zero offset profile (ZOP) may be determined by keeping transmitter and receiver at equal depth. By systematically lowering or raising the pair of antennas in the two boreholes it is possible to build a one-dimensional profile

of average inter-borehole travel time over the entire borehole length. If only one borehole is available, a profile of cumulative travel time to a given depth can be obtained by laying the transmitter antenna at the ground surface next to the borehole and lowering the receiver antenna at progressively larger depth (vertical radar profiling or VRP).

Each of the three considered transmission modes has advantages and disadvantages. MOG has the greatest information content, and can represent the actual (2D) distribution of dielectric properties. However, at least with currently available borehole GPR systems, acquisition is slow and cumbersome, and may require many hours for each pair of holes. In addition, tomographic inversion is required to reconstruct the velocity image. ZOP is fast to acquire and easy to interpret, but only provides 1D information. Both MOG and ZOP require two closely spaced and parallel boreholes (generally less than 10 m even under ideal conditions). Typically, this requires that holes be drilled specifically for this purpose. If only one plastic-cased borehole is available, VRP is still feasible, and can provide a 1D vertical profile of GPR velocity. However, unlike ZOP, VRP requires that some regularized inversion of travel time data be performed, and consequently some information must be gathered on the error structure in the data.

The images of relative permittivity can be converted into volumetric water content, or volumetric water content changes over time, as described in Section 4.2.3. These 1D or 2D datasets can then be used to calibrate unsaturated flow models, as discussed in Section 4.1 (Figure 1) to yield estimates of hydraulic conductivity and other unsaturated flow field parameters.

Example 1: Cross-Hole GPR Monitoring of Natural Infiltration. Time-lapse ZOP borehole GPR profiles can supply important information on the hydrologic behavior of the deep vadose zone under natural infiltration conditions. These data can be used to constrain a mathematical model of unsaturated flow to provide more quantitative information.

A field site was located near Eggborough, North Yorkshire, UK, adjacent to a small sand quarry. The field site is one of two selected for detailed study of the vadose zone in the Sherwood Sandstone – Example 3 in this section will present results from the other site. The research program aims to utilize cross-borehole geophysical methods to improve models of vadose zone recharge dynamics. Twelve boreholes were drilled at the Eggborough site, seven of which were used for deployment of borehole GPR. The other boreholes were installed for DC resistivity measurements in both cross-hole and single-hole mode. From analyses of the cores (West et al., 2003), the sandstone sequence at the site consists of fluvially derived fining upwards sequences 1 to 3 m thick, grading from medium grained to fine grained sandstone. The glacial drift cover (mainly gravels and cobbles in fine matrix) is typically 1–2 m

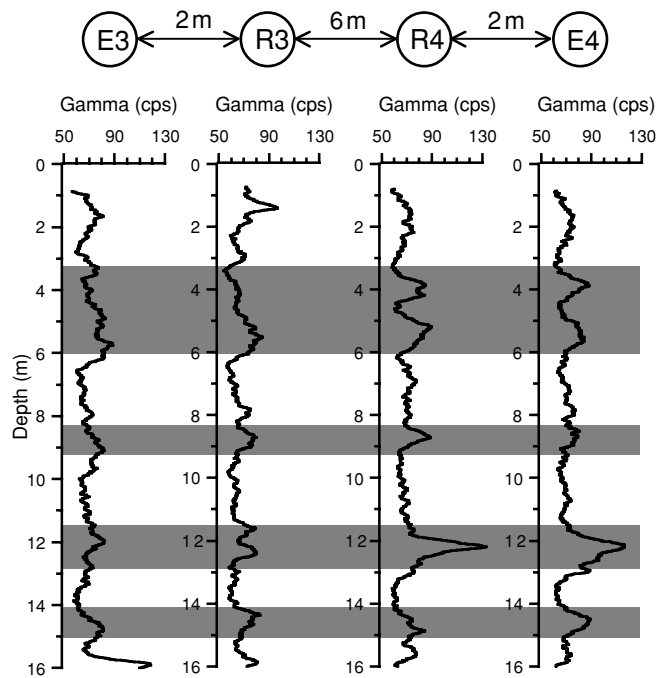


Figure 9. Natural gamma logs from boreholes E3, R3, R4, E4 (surveys carried out June 1999). The horizontal bands indicate zones of relatively high gamma count (inferred layers of finer sandstone/siltstone)

thick. In each of the GPR boreholes, a 76 mm diameter PVC casing was installed, surrounded by a sand/cement backfill. The boreholes were logged using natural gamma and electromagnetic conductivity sondes. The layered sequence at the site is clearly evident from the cores and from the well logs (Figure 9). For the purpose of this study two types of sandstone were identified (medium and laminated).

In order to determine changes in bulk dielectric properties at the Eggborough site, borehole-to-borehole radar surveys were conducted in ZOP mode. This type of borehole data acquisition is suitable for situations where the variations of physical properties in the subsurface are mainly in the vertical direction. Such is the case for infiltration-dominated volumetric water content distribution, as in the case presented herewith. Care must be taken to ensure that critical refraction at the soil/air interface does not produce the first arrival of energy at the receiver antenna. If such first arrival is mistaken for a direct wave through the soil, serious errors can be made in the estimation of soil dielectric properties (Siggins, 1992). Also, critical refractions could occur at the interface between high and low velocity layers in the sequence (Rucker and Ferré, 2004). Monthly cross-hole radar monitoring was

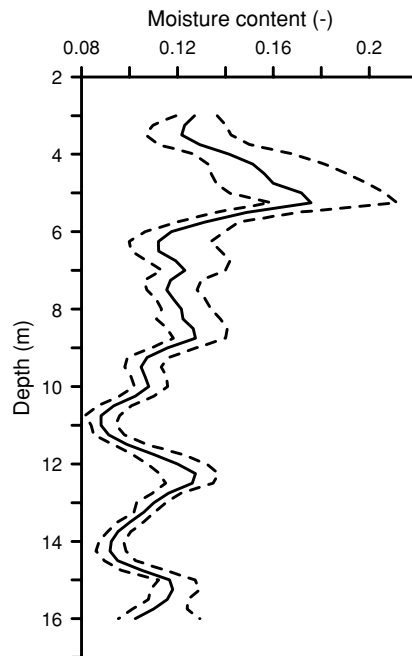


Figure 10. Volumetric water content data derived from GPR profiles at Eggborough between Aug 1999 and Feb 2001. Solid line indicates average profile, dashed lines show minimum and maximum observed values at each depth

performed from August 1999 to February 2001. GPR velocity was converted into volumetric water content using a calibrated CRIM formulation. The data show small changes of volumetric water content over time and fairly large spatial variability with depth (Figure 10). It could be concluded that the infiltration at the site takes place under quasi-steady state conditions. Knowledge of effective precipitation (rainfall minus evapotranspiration) together with the volumetric water content profile in Figure 10 ensures that the travel time of water – and potential contaminants – from the ground surface to the water table can be computed: at the Eggborough site this is roughly equal to 4500 days. However, in order to estimate the unsaturated hydraulic properties of the Sherwood Sandstone the above information must be analyzed by means of the mathematical models based on the formulation in Section 4.2.1.

One-dimensional Richards' equation modeling of the infiltration process was performed under spatially heterogeneous (layered), steady-state conditions. Both layer structure (composed of the upper drift, and a sequence of medium and laminated sandstone), derived from stochastic geostatistical simulation of gamma ray counts obtained from borehole logs, and Richards' equation parameters were simulated using a Monte Carlo (stochastic) approach,

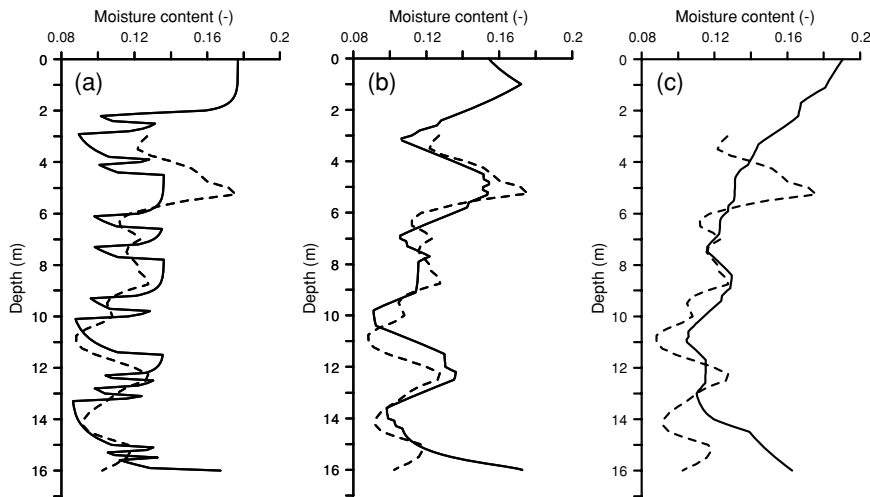


Figure 11. (a) Best simulation with no window averaging and comparison with time-averaged data, (b) Best simulation with vertical averaging window = 2 m, (c) Best simulation with vertical averaging window = 5 m. Data profile is shown by the dashed line, simulated profiles by solid lines

constrained on a priori information regarding the possible range of hydraulic parameters. The results of the Monte Carlo analysis show that, in order to match the GPR-derived volumetric water content profiles, it is necessary to take into account the vertical scale of measurements, with an averaging window size of the order of the antenna length and the Fresnel zone width (2–3 m – see Figure 11).

Example 2: Vertical Radar Profile Monitoring of Natural Infiltration. One-dimensional profiles of volumetric water content with depth can be obtained using either a ZOP (Example 1) or a VRP configuration, as shown in this example. VRPs carry information on (1) the distribution of radar velocity as a function of depth, from which volumetric water content distributions can be inferred, and (2) the presence of reflecting horizons within the formation, often associated with lithological contacts.

High-resolution, time-lapse VRPs were acquired at a crude oil contaminated site in Trecate, Piemonte, Northern Italy, on a few existing boreholes originally developed for groundwater monitoring and remediation. In 1994, the site was the scene of an inland crude oil spill following an oil well blowout. Details of the incident have been reported elsewhere (Burberry et al., 2004). The Po river plain aquifer at Trecate comprises an extensive, unconfined silty sand and gravel unit in excess of 60 m thickness beneath the site. Groundwater levels at the site show seasonal fluctuations of 5 to 6 m, with higher levels experienced during the summer period due to irrigation. Information

on site stratigraphy can be derived from drilling logs and *Geoprobe* (Salina, Kansas, USA) cores. A thick sequence of poorly sorted silty sands and gravels in extensive lenses, typical of braided river sediments, characterizes the site stratigraphy. An artificial layer of clayey-silty material, less than 1 m thick, originally placed as a liner for rice paddies overlies most of the site.

Periodic VRP acquisition was performed in 5 different boreholes with approximately one survey per fortnight, from October 2002 to December 2003, using a PulseEKKO 100 system with 100 MHz borehole antennas. The transmitter was laid on the ground radially, its centre positioned at 0.70 m from the borehole axis; the receiver antenna was lowered at 5 cm steps, starting at 0.75 m below ground. We adopted a 64-fold vertical stack and a time sampling interval equal to 0.4 ns. Periodically, a test was made on the VRP signal quality by repeating a whole VRP at short time distance: an average error of roughly 0.5 ns was measured with the receiver antenna above the water table (consistent with results by Alumbaugh et al. (2002)), 4 ns below the water table. Note that a link exists between the travel time picking errors and the vertical resolution of VRP: the latter depends on our ability to distinguish travel time values of neighbouring traces, which is strongly linked to the travel time picking error discussed above. On this basis, the VRP vertical resolution at the Trecate site has been estimated around 0.25 m.

VRP data processing is relatively simple, involving: (a) careful calibration of the system time zero via walkaway tests in air, possibly repeated before and after the VRP acquisition (*time zero correction*); and (b) careful *dewowing* to remove the low frequency noise (“wow”) induced by dynamic range limitations in the radar equipment. The problem caused by the “wow” becomes more severe as the receiver antenna is lowered deeper into the subsurface. This happens because, while the “wow” has the same energy at all depths, the radar wavelet signal becomes weaker with depth. In order to preserve the timing of the first break, Gerlitz et al. (1993) suggested using a residual *median* filter, and provided relevant rules for calculating the median filter length. According to this approach, a filter length of 80 ns was applied to the Trecate VRP data. Examples of processed VRP data are shown in Figure 12.

Travel times, as derived from picking of first arrivals, must be inverted into interval radar velocity values. Such inversion involves as many unknowns as equations. However, the apparent simplicity of the problem hides the inherent instability of the solution caused by errors in the data (travel times). If such errors are not accounted for, erratic non-physical radar velocity values will appear in the solution. The problem requires some form of regularization based on the estimated errors in the data. We adopted an Occam inversion, similar to that proposed by Lizarralde and Swift (1999). The amount of regularization in this formulation is a function of the error level in the data. An example of

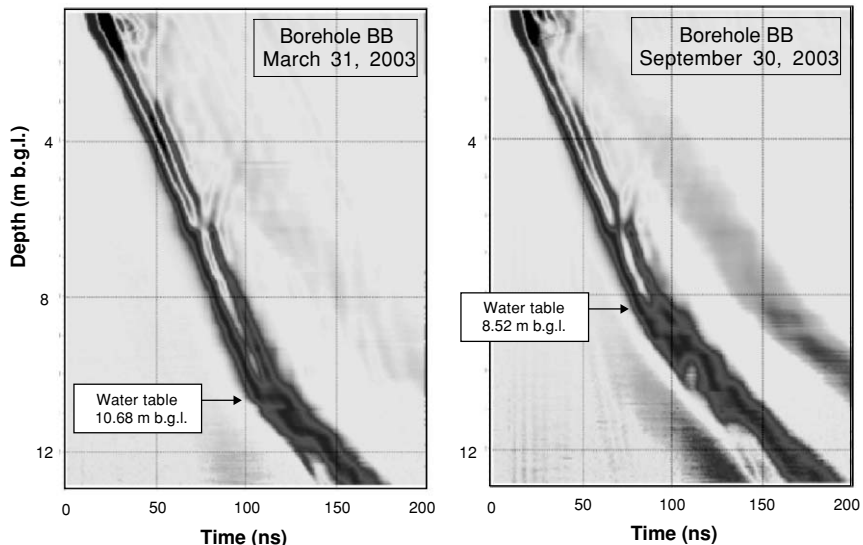


Figure 12. Examples of VRP data acquired at the Trecate site at the end of Winter and at the end of Summer, showing (a) the sharp change in slope corresponding to the location of the water table; (b) the pronounced water table oscillations due to regional irrigation; and (c) the presence of clearly identifiable reflections at about 2 m and 6.5 m below ground

volumetric water content profiles derived by inversion of VRP and utilization of Topp et al. (1980) relationship are shown in Figure 13.

More information can be extracted from VRP data than only first arrivals. The energy arriving after the first break is often generated by reflections at lithological interfaces (see Figure 12) that are associated with sharp changes in the electromagnetic impedance and, ultimately, in permittivity values and radar velocities. The interfaces below the downhole antenna produce reflections of the direct signal (down-going wavefield), and the upward traveling wave is detected by the receiver antenna. This up-going wavefield can be easily identified in records since its slope is opposite to the down-going, direct wavefield. Processing the records can enhance the reflections and produce an image of the interfaces in the subsoil, as in conventional VSP processing (Hardage, 2000) – see Figure 14. The information derived from VRP reflections has been correlated with information from drilling logs, and interfaces have been corrected, when needed, to their actual depth location.

The VRP-derived volumetric water content profiles have been used to calibrate a dynamic Richards' equation model via a Monte Carlo inversion approach, similar to that described in Example 1. It has been possible to identify the value of subsurface hydraulic parameters, in particular hydraulic

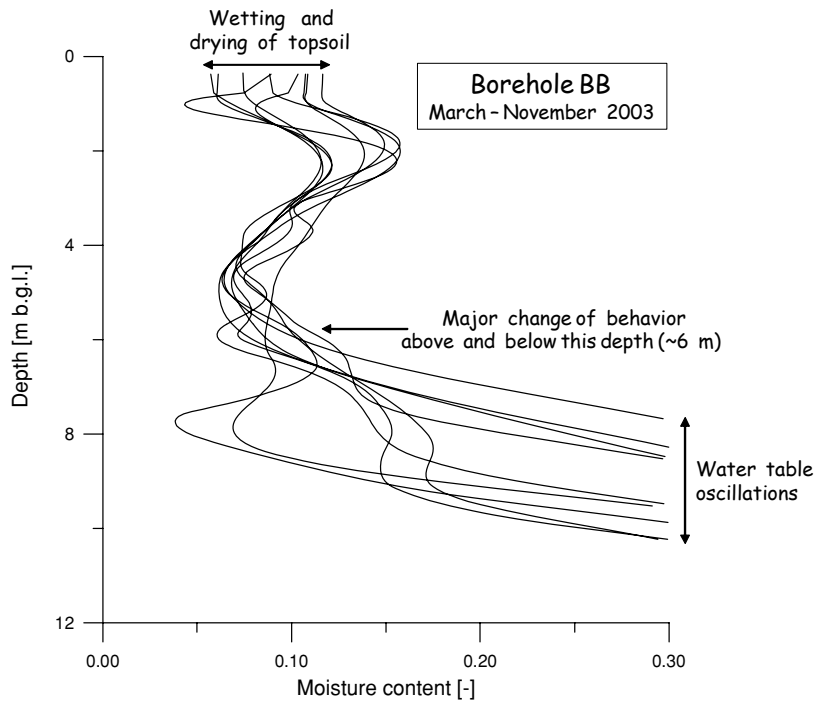


Figure 13. Examples of volumetric water content profiles derived from VRP data at the Trecate site. Each line corresponds to a date between March and November 2003. The dynamics due to water table oscillations and precipitation/evaporation is clearly visible, together with the effect of lithological control around 6 m b.g.l.

conductivity, of the main lithological units. The volumetric water content profiles at this site are highly dynamic and vary over a larger range, thus stressing the system sufficiently to identify its governing parameters and increasing the signal to noise ratio of the measurements.

Example 3: Cross-Hole GPR Monitoring of a Tracer Injection. Monitoring of natural flow in the vadose zone is useful in many respects, but is both time-consuming and potentially inconclusive in terms of identification of unsaturated flow parameters. The latter problem may arise because under natural conditions the porous medium may never be stressed sufficiently to deliver information on the governing parameters (see Example 1). An obvious way around this problem is to conduct tracer experiments by introducing a known volume of water in the vadose zone, and monitoring its time-space evolution. Binley et al. (2002b) present results from a water tracer experiment carried out at a UK sandstone site. Here we focus on how borehole GPR data were used to help determine the hydraulic conductivity of the sandstone.

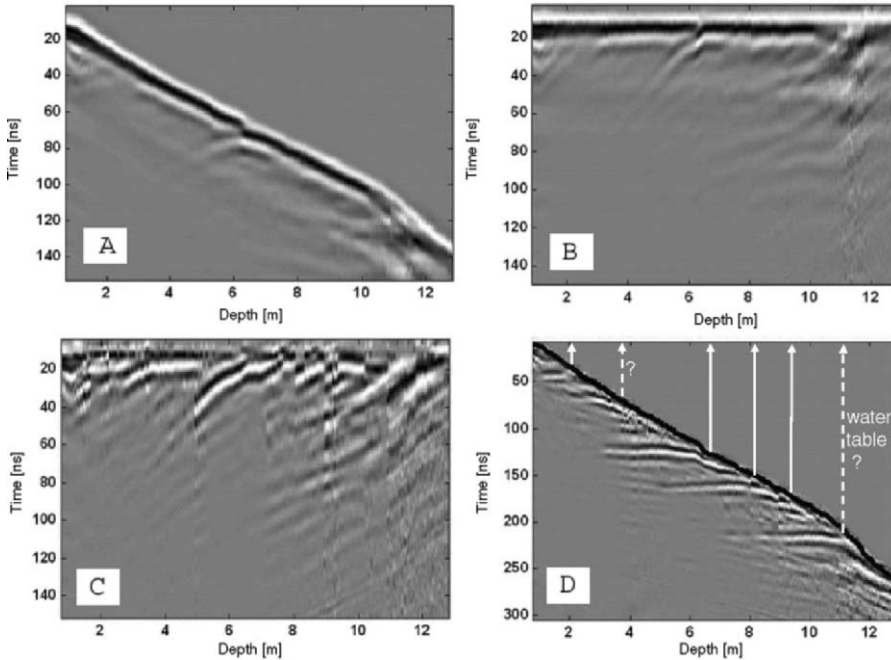


Figure 14. Sequence of VRP processing to extract up-going reflections from VRP data: (a) data after dewowing and static shift for instrument time-zero; (b) corrected for statics computed on first arrivals; (c) reflection enhancement via residual median filtering; and (d) reflections double corrected back with statics from first arrivals

At a field site in Hatfield, South Yorkshire, UK, six boreholes were installed in June/July 1998 to a depth below the water table (approximately 12 m) as part of a project (run by the UK universities of Lancaster and Leeds) aimed at characterizing the unsaturated properties of the Permo-Triassic Sherwood Sandstone – see also Example 1. The boreholes were drilled in order to monitor the migration of injected water tracers using cross-borehole (transmission) radar and cross-borehole 2- and 3-D electrical resistivity tomography (ERT). In addition, a tracer injection borehole was drilled to a depth of 3.5 m at the centre of the borehole array. The site lithology is similar to that at the Eggborough site (Example 1) but slightly less heterogeneous. Drift thickness at the site is typically 2 to 3 m. The sandstone underneath is composed of two main sub-lithologies: medium grained sandstone, which comprises most of the soil column, and sub-horizontally laminated fine to medium sandstone. Laboratory experiments were conducted (West et al., 2003) to identify the parameters of a CRIM: porosity $\phi = 0.32$, dielectric constant of the grains $\kappa_s = 5$.

Approximately 2.1 m^3 of tracer was introduced in the injection borehole over 3 days. The injected water was prepared using mains supply water, with

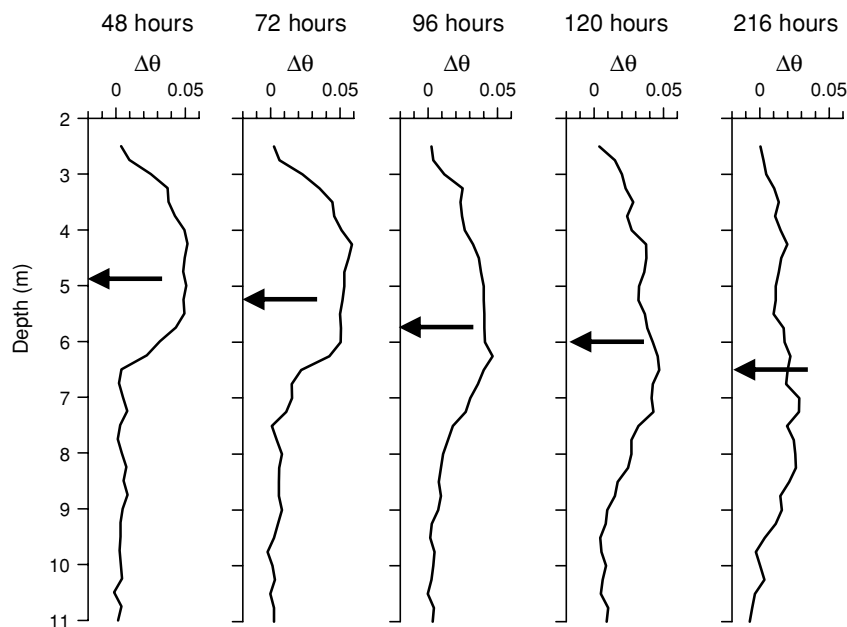


Figure 15. Cross-borehole radar zero offset profile results for borehole pair showing change in volumetric water content ($\Delta\theta$) using CRIM model at various times following injection of tracer. Horizontal arrow shows position of centre of mass of change in volumetric water content

the addition of a small quantity of NaCl to maintain an electrical conductivity of approximately $660 \mu\text{S}/\text{cm}$, equivalent to observed local groundwater conductivity. Injection of the tracer was performed using a constant head device.

Before, during and after injection, ZOP transmission radar measurements were collected between the two radar boreholes, 5 m apart, using the Sensors and Software PulseEKKO radar system equipped with 100 MHz borehole antennas. Figure 15 shows changes in volumetric water content with respect to background (before injection) as a function of depth at increasing elapsed time after the end of injection. The injected bulb and its evolution over time is clearly identified by ZOP cross-hole GPR.

A 3D, finite element, Richards' equation model was run to reproduce the tracer experiment. Trial and error fitting of the vertical saturated hydraulic conductivity of the medium sandstone was performed on this model, while the remaining van Genuchten (1980) parameters were kept constant during the exercise, their values estimated from the literature. The vertical motion of the slug centre of mass, as illustrated by the ZOP radar, was chosen as the key feature describing the injection experiment. As shown in Figure 16, the centre of mass motion is extremely sensitive to changes in the saturated hydraulic conductivity of the sandstone, as selected in the numerical model.

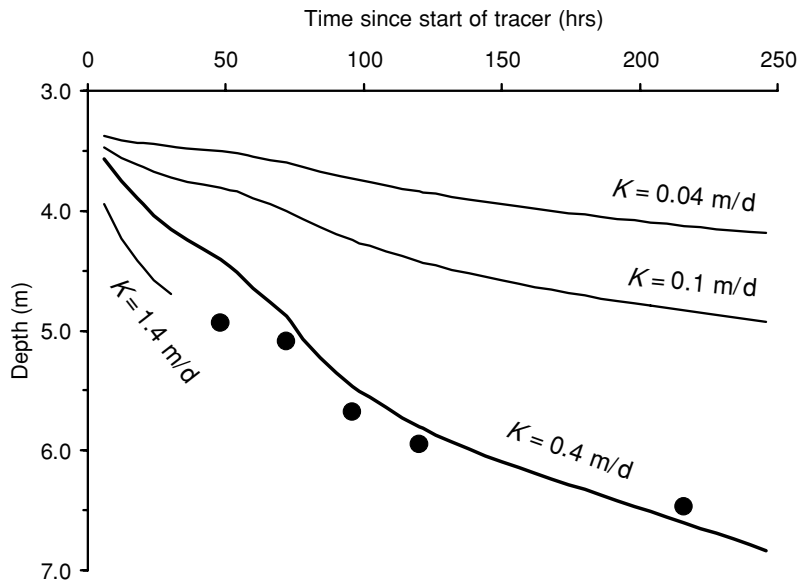


Figure 16. Comparison of measured (based on ZOP radar) and simulated movement of the centre of mass of the tracer

This phenomenon can be explained as follows: (a) the higher the hydraulic conductivity, the faster the vertical downward movement of the bulb (gravity dominates capillary forces); but (b) the higher the hydraulic conductivity, the quicker the disappearance of the bulb itself (flow rates are higher and water escapes from the bulb more quickly). As a result, an effective (field) saturated hydraulic conductivity of the sandstone can be identified to be 0.4 m/d . Varying this value by only a few tenths of m d^{-1} changes the simulation behavior substantially (see, for example, the case in Figure 16 with $K_s = 0.1 \text{ m d}^{-1}$) adding confidence to the discriminatory power of the calibration. It is worth noting that knowledge of the antecedent water content prior to tracer injection (obtained from the pre-tracer ZOP surveys) was critical in calibrating the unsaturated flow model.

4.4.2. BOREHOLE RESISTIVITY IMAGING

4.4.2.1. Methodology

Surface resistivity imaging is rarely applied to the study of deep vadose zone processes because of the limited sensitivity at depth. Park (1998) is perhaps the only published study that uses surface arrays to examine flow in the unsaturated zone at a depth of over 10 m, albeit under forced loading. Under natural loading, changes in volumetric water content at depths of over a few meters are

likely to be small and surface imaging techniques limited in use. To enhance sensitivity with depth, electrodes may be installed in boreholes. Recognising this Binley et al. (2002) demonstrated how borehole-based electrode arrays may be used to characterise seasonal variation in volumetric water content to depths of 10 m over a period of over two years at a sandstone site in the UK.

Single borehole arrays have limited lateral coverage, however, electrode arrays in pairs of borehole may be utilized using cross-borehole electrical resistivity tomography to obtain high resolution images of resistivity at depth. Cross-borehole resistivity is an extension of conventional surface resistivity imaging and uses similar inverse modelling techniques (see Daily et al., 2004a). Daily et al. (1992) is the first demonstration of how this technique can be applied in hydrogeophysics, in their study of vadose zone flow. Other vadose zone studies using cross-borehole resistivity include Ramirez et al. (1996), Slater et al. (1997), Zaidman et al. (1999), Binley et al. (2002b), French et al. (2002) and Daily et al. (2004b).

As pointed out by Binley and Kemna (2005), the main advantages of cross-borehole resistivity imaging, in comparison to surface resistivity imaging, are: (1) high resolution at depth is possible and (2) investigations can be made without the need for surface access (for example, surveys under buildings are possible). The method suffers from a number of disadvantages, however. These are: (1) boreholes are required (which often need to be purpose drilled), (2) the images cover only the region between the boreholes, (3) the boreholes must not be too far apart otherwise sensitivity is reduced, (4) data acquisition often requires more sophisticated instrumentation and is often more time consuming, (5) data noise levels are usually higher than those using surface electrodes, and (6) data processing techniques are more complex.

Example: Cross-Borehole Electrical Resistivity Tomography Monitoring of Tracer Migration. The vadose zone tracer test reported earlier – Example 3 in Section 4.3 – and fully described in Binley et al (2002b), also included application of cross-borehole electrical resistivity tomography. Borehole electrodes were installed at 0.73 m intervals between 2 and 13 m in four boreholes at the site and supplemented by a number of surface electrodes. Binley et al. (2002b) show results from 3-D resistivity imaging (using all four boreholes) and 2-D imaging (using pairs of boreholes). Here, we illustrate sample results from one pair of boreholes in order to show comparison with borehole GPR results (Figure 15). Resistivity data were collected under background (pre-tracer) conditions and then regularly for a period of five days following injection of the 2.1 m³ volume of tracer (injected continuously for three days).

Figure 17 shows development of the water tracer as it migrates vertically through the unsaturated zone. In Figure 17a only two thirds of the tracer

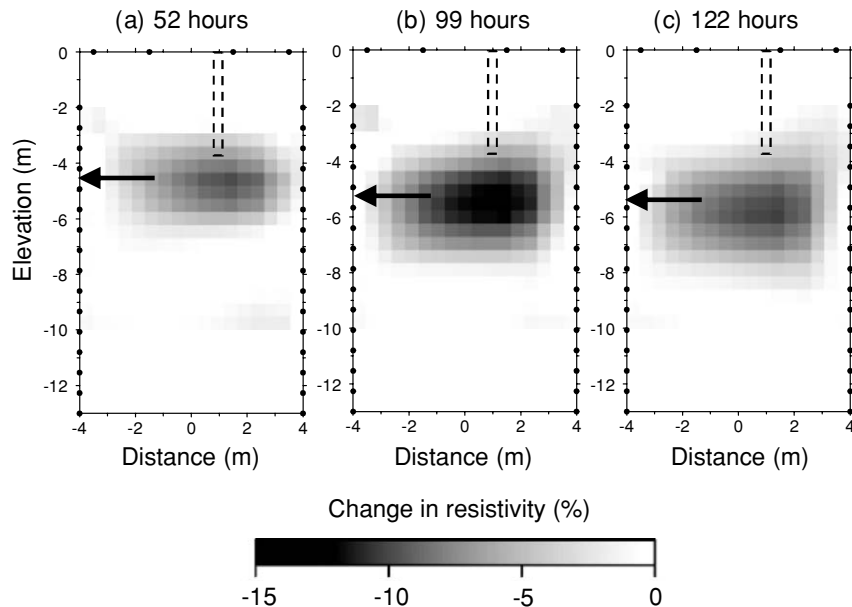


Figure 17. Changes in resistivity following injection of a tracer. Images show changes relative to pre-tracer conditions at times after the start of injection. Filled circles show location of electrodes. Horizontal arrow shows position of centre of mass of change in resistivity. The tracer injection borehole is shown as a broken line

has been injected and therefore changes in resistivity are smaller than those observed after end of injection (for example, Figure 17b). The sequence in Figure 17 shows vertical migration of the tracer plume at a similar rate to that inferred from borehole GPR measurements (see Figure 15). In fact, Binley et al. (2002b) confirmed similarity between GPR, 2-D resistivity and 3-D resistivity responses. Note, however, that the resistivity images suggest significant lateral spreading of the tracer. It is unclear if this is real (perhaps a result of spreading caused by a hydraulically impeding layer just below tracer injection) or simply an artefact of over-smoothing of the data inversion.

Using the 3-D resistivity images Binley et al. (2002b) carried out a test of mass balance in the resistivity images, that is, the additional water volume inferred from the resistivity images using petrophysical relationships was compared to the known injected volume. They reported a 50% mass balance error – an under-prediction from the resistivity images and concluded that this is a result of limited sensitivity near the centre of the image (where much of the tracer volume would be). Such errors demonstrate a serious limitation in using geophysical data for such purposes. It is clear that an appreciation of errors and uncertainty in the geophysical images is necessary if they are to be used in a quantitative manner, that is as hydrological data sources.

4.5. Conclusion and Outlook

In this chapter we presented the basic concepts and a few examples of non-invasive monitoring of volumetric moisture content evolution in soils under natural and forced conditions. The techniques considered are TDR, ERT and GPR, that can all provide quantitative estimations of water content, that in turn can be used for the calibration of unsaturated flow models. Note that these geophysical techniques provide also information on the electric conductivity, which can be related to texture, salinity. Preference given to one technique may depend on local conditions, with particular attention to the depth of investigation. With the exception of TDR, the use of these non-invasive techniques requires a precise understanding of issues relating to their penetration, resolution and information content as a function of acquisition geometry and other field parameters. For successful application of ERT and GPR, knowledge of petrophysical relationships between hydrological and geophysical parameters is essential. In many cases, site specific relationships should be determined, rather than relying on assumed universal models. The use of ERT for moisture content determination in static systems is particularly problematic as other factors (pore water salinity, clay content, temperature) affect bulk resistivity. ERT does, however, offer a means of monitoring changes in moisture content through time-lapse measurements.

The future development of these techniques for the monitoring of unsaturated zone processes is likely to include:

- a. data integration from several sources, e.g. GPR and ERT, in order to improve resolution and accuracy – see e.g. Chapter 2 of this book;
- b. a systematized use of data from geophysical methods as a way to calibrate hydrological models;
- c. the joint analysis of water flow and solute transport in the vadose zone by means of a combination of GPR and ERT;
- d. the use of induced polarization especially in multi-frequency (spectral) mode (SIP);
- e. better recognition of the non-uniqueness of tomographic processing and greater appreciation of the limited resolution and sensitivity of geophysical imaging techniques – see e.g. Day-Lewis et al. (2005).

Acknowledgements

We are indebted to Stefano Ferraris (for the Grugliasco case study), Michela Giustiniani (for help in field work and data processing of the Grugliasco and Montemezzo sites), Claudio Strobbia (for data analysis of the Montemezzo e

Trecate cases). Much of the data for the UK Hatfield site was collected and processed by Peter Winship and Roy Middleton at Lancaster. Peter Winship also led field-based activities at the UK Eggborough site.

References

Alumbaugh, D.L., P.Y. Chang, L. Paprocki, J.R. Brainard, R.J. Glass, and C.A. Rautman, 2002. Estimating moisture contents in the vadose zone using cross-borehole ground penetrating radar: A study of accuracy and repeatability, *Water Resour. Res.* 38(12), 1309, doi: 10.1029/2001WR000754.

Annan, A.P., 2005. GPR methods for hydrogeological studies, in *Hydrogeophysics*, edited by Y. Rubin and S.S. Hubbard, Springer, Series: Water Science and Technology Library, Vol. 50, 523 pp.

Archie, G.E., 1942. The electrical resistivity log as an aid in determining some reservoir characteristics, *Trans. AIME*, 146, 54–67.

Arcone, S.A., P.R. Peapples, and L. Liu, 2003. Propagation of a ground-penetrating radar (GPR) pulse in a thin surface waveguide, *Geophysics*, 68 (3), 1922–1933.

Barker, R., and J. Moore, 1998. The application of time-lapse electrical tomography in ground-water studies, *The Leading Edge*, 1454–1458.

Becht A., E. Appel, and P. Dietrich, in press. Analysis of multi-offset GPR data: a case study in a coarse-grained gravel aquifer, *Near Surface Geophysics*.

Benderitter, Y., and J.J. Schott, 1999. Short time variation of the resistivity in an unsaturated soil: The relationship with rainfall, *European J. Environ. Eng. Geophys.*, 4, 37–49.

Bevan, M.J., A.L. Endres, D.L. Rudolph, and G. Parkin, 2003. The non-invasive characterization of pumping-induced dewatering using ground-penetrating radar, *J. Hydrol.*, 281, 55–69.

Binley, A., S. Henry-Poulter, and B. Shaw, 1996. Examination of solute transport in an undisturbed soil column using electrical resistance tomography, *Water Resour. Res.*, 32(4), 763–769.

Binley, A., P. Winship, R. Middleton, M. Pokar, and J. West, 2001. High resolution characterization of vadose zone dynamics using cross-borehole radar, *Water Resour. Res.* 37 (11), 2639–2652.

Binley, A., P. Winship, L.J. West, M. Pokar, and R. Middleton, 2002a. Seasonal variation of moisture content in unsaturated sandstone inferred from borehole radar and resistivity profiles, *J. Hydrol.*, 267 (3–4), 160–172.

Binley, A.M., G. Cassiani, R. Middleton, and P. Winship, 2002b. Vadose zone flow model parameterisation using cross-borehole radar and resistivity imaging, *J. Hydrol.*, 267, 147–159.

Binley, A.M., G. Cassiani, and P. Winship, 2004. Characterization of Heterogeneity in Unsaturated Sandstone Using Borehole Logs and Cross Borehole Tomography, edited by J. Bridge and D. W. Hyndman, SEPM (Society for Sedimentary Geology), Special Publication No. 80, Aquifer characterization, 176 pp.

Binley, A.M., and A. Kemna, 2005. DC Resistivity and Induced Polarization methods, in edited by Y. Rubin and S.S. Hubbard, *Hydrogeophysics*, Springer, Series: Water Science and Technology Library, Vol. 50, 523 pp.

Bohidar, R.N., and J.F. Hermance, 2002. The GPR refraction method, *Geophysics*, Vol. 67, No. 5, pp. 1474–1485.

Brovelli, A., G. Cassiani, E. Dalla, F. Bergamini, D. Pitea, and A.M. Binley, 2005. Electrical properties of partially saturated sandstones: novel computational approach with hydro-geophysical applications, *Water Resour. Res.*, 41 (3), W03005, doi: 10.1029/2004WR003382.

Burberry L., G. Cassiani, G. Andreotti, T. Ricchiuto, and K.T. Semple, 2004. Well test and stable isotope analysis for the determination of sulphate-reducing activity in a fast aquifer contaminated by hydrocarbons, *Environ. Pollut.*, 129 (2), 321–330.

Chan, C. Y., and R. J. Knight, 1999. Determining water content from dielectric measurements in layered materials, *Water Resour. Res.*, 35, 85–93.

Chand, R., S. Chandra, V.A. Rao, V.S. Singh, and S.C. Jain, 2004. Estimation of natural recharge and its dependency on sub-surface geoelectric parameters, *J. Hydrol.*, 299, 67–83.

Chanzy, A., A. Tarussov, A. Judge, and F. Bonn, 1996. Soil water content determination using digital ground penetrating radar, *Soil Sci. Soc. Am. J.*, 60, 1318–1326.

Chelidze, T., and Y. Guéguen, 1999. Electrical spectroscopy of porous rocks: a review – I. theoretical models, *Geophys. J. Int.*, 137, 1–15.

Dahan, O., E.V. McDonald, and M.H. Young, 2003. Flexible time domain reflectometry probe for deep vadose zone monitoring, *Vadose Zone J.*, 2, 270–275.

Daily, W.D., A.L. Ramirez, D.J. LaBrecque, and J. Nitao, 1992. Electrical resistivity tomography of vadose water movement, *Water Resour. Res.*, 28, 1429–1442.

Daily, W., A. Ramirez, A. Binley, and D. LaBrecque, 2004a. Electrical resistance tomography, *The Leading Edge*, 23 (5), 438–442.

Daily, W., A. Ramirez, and A. Binley, 2004b. Remote Monitoring of Leaks in Storage Tanks using Electrical Resistance Tomography: Application at the Hanford Site, *J. Environ. Eng. Geophys.*, 9(1), 11–24.

Das, B.S., J.M. Wraith, and W.P. Inskeep, 1999. Nitrate concentrations in root zone estimated using time domain reflectometry, *Soil Sci. Soc. Am. J.*, 63, 1561–1570.

Day-Lewis, F., K. Singha, and A. Binley, 2005. On the Limitations of Applying Petrophysical Models to Tomograms: A Comparison of Correlation Loss for Cross-Hole Electrical-Resistivity and Radar Tomography, *J. Geophys. Res.*, 110 (B8), B08206, doi: 10.1029/2004JB003569.

Eppstein, M.J., and D.E. Dougherty, 1998. Efficient three-dimensional data inversion: Soil characterization and moisture monitoring from cross-well ground-penetrating radar at the Vermont test site, *Water Resour. Res.*, 34 (8), 1889–1900.

Ferré, T.P.A., G. von Glinski, and L.A. Ferré, 2003. Monitoring the maximum depth of drainage in response to pumping using borehole ground penetrating radar, *Vadose Zone J.*, 2, 511–518.

French, H.K., C. Hardbattle, A. Binley, P. Winship, and L. Jakobsen, 2002. Monitoring snowmelt induced unsaturated flow and transport using electrical resistivity tomography, *J. Hydrol.*, 267 (3–4), 273–284.

French, H., and A. Binley, 2004. Snowmelt infiltration: Monitoring temporal and spatial variability using time-lapse geophysics, *J. Hydrol.*, 297, 174–186.

Frohlich, R.K., and C.D. Parke, 1989. The electrical resistivity of the vadose zone – field survey, *Ground Water*, 27 (4), 524–530.

Gerlitz, K., M.D. Knoll, G.M. Cross, R.D. Lutzano, and R. Knight, 1993. Processing ground penetrating radar data to improve resolution of near-surface targets, in *Symposium on the Application of Geophysics to Engineering and Environmental Problems (SA GEEP'93)*, San Diego, CA, pp. 561–574.

Hagrey, S.A. al, and J. Michaelsen, 1999. Resistivity and percolation study of preferential flow in vadose zone at Bokhorst, Germany, *Geophysics*, 64 (3), 746–753.

Hardage, B.A., 2000. Vertical Seismic Profiling: Principles, Third updated and revised edition, Handbook of Geophysical Exploration, Vol. 14, Pergamon.

Heimovaara, T.J., A.G. Focke, W. Bouten, and J.M. Verstraten, 1995. Assessing temporal variations in soil water composition with time domain reflectometry, *Soil Sci. Soc. Am. J.*, 59, 689–698.

Hubbard, S.S., J.E. Peterson Jr., E.L. Majer, P.T. Zawislanski, K.H. Williams, J. Roberts, and F. Wobber, 1997. Estimation of permeable pathways and water content using tomographic radar data, *The Leading Edge*, 16 (11), 1623–1628.

Huisman, J.A., C. Sperl, W. Bouten, and J.M. Verstraten, 2001. Soil water content measurements at different scales: Accuracy of time domain reflectometry and ground-penetrating radar, *J. Hydrol.*, 245, 48–58.

Huisman, J.A., S.S. Hubbard, J.D. Redman, and A.P. Annan, 2003. Measuring soil water content with ground penetrating radar: A review, *Vadose Zone J.*, 2, 476–491.

Kalinski, R.J., W.E. Kelly, I. Bogardi, and G. Pesti, 1993. Electrical-resistivity measurements to estimate travel-times through unsaturated ground-water protective layers, *J. Appl. Geophys.*, 30 (3), 161–173.

Kean, W.F., M.J. Waller, and H.R. Layson, 1987. Monitoring moisture migration in the vadose zone with resistivity, *Ground Water*, 27 (5), 562–561.

Klute, A., and C. Dirksen, 1986. Methods of Soil Analysis, Part I, in edited by A. Klute and C. Dirksen, ASA and SSSA, Madison, WIpp. 771–798.

Knoll, M.D., and W.P. Clement, 1999. Vertical radar profiling to determine dielectric constant, water content and porosity values at well locations, *Symposium on the Application of Geophysics to Engineering and Environmental Problems (SAGEEP'99)*, pp. 821–830.

Kobr, M., S. Mares, and F. Paillet, 2005. Geophysical well logging, in *Hydrogeophysics*, edited by Y. Rubin and S.S. Hubbard, Springer, Series: Water Science and Technology Library, Vol. 50, 523 pp.

Kool, J.B., J.C. Parker, and M.T. van Genuchten, 1985. Determining soil hydraulic properties from one-step outflow experiments by parameter estimation: Theory and numerical studies, *Soil Sci. Soc. Am. J.*, 49, 1348–1354.

Lambot, S., M. Javaux, F. Hupet, and M. Vanclooster, 2002. A global multilevel coordinate search procedure for estimating the unsaturated soil hydraulic properties, *Water Resour. Res.*, 38 (11), 1224, doi: 10.1029/2001WR001224.

Lambot, S., E.C. Slob, I. van den Bosch, B. Stockbroeckx, B. Scheers, and M. Vanclooster, 2004. Estimating soil electric properties from monostatic ground-penetrating radar signal inversion in the frequency domain, *Water Resour. Res.*, 40, W04205, doi: 10.1029/2003WR002095.

Lambot, S., E.C. Slob, I. van den Bosch, B. Stockbroeckx, and M. Vanclooster, 2004b. Modeling of ground-penetrating radar for accurate characterization of subsurface electric properties, *IEEE Trans. Geosci. Remote Sens.*, 42, 2555–2568.

Lambot, S., M. Antoine, I. van den Bosch, E.C. Slob, and M. Vanclooster, 2004c. Electromagnetic inversion of GPR signals and subsequent hydrodynamic inversion to estimate effective vadose zone hydraulic properties, *Vadose Zone J.*, 3, 1072–1081.

Linde, N.J., J. Chen, M. Kowalsky, and S. Hubbard, 2006. Hydrogeophysical parameter estimation for field characterization, in this book.

Lizarralde, D., and S. Swift, 1999. Smooth inversion of VSP traveltimes data, *Geophysics*, 64 (3), 659–661.

Mualem, Y., 1976. A new model for predicting the hydraulic conductivity of unsaturated porous media, *Water Resour. Res.*, 12, 513–522.

Nakashima, Y., H. Zhou, and M. Sato, 2001. Estimation of groundwater level by GPR in an area with multiple ambiguous reflections, *J. Appl. Geophys.*, 47, 241–249.

Noborio, K., 2001. Measurement of soil water content and electrical conductivity by time domain reflectometry: A review, *Comput. Electronics Agric.*, 31, 213–237.

Panissod, C., D. Michot, Y. Benderitter, and A. Tabbagh, 2001. On the effectiveness of 2D electrical inversion results: An agricultural case study, *Geophys. Prospect.*, 49, 570–576.

Park, S., 1998. Fluid migration in the vadose zone from 3-D inversion of resistivity monitoring data, *Geophysics*, 63 (1), 41–51.

Parkin, G.W., R.G. Kachanowski, D.E. Elrick, and R.G. Gibson, 1995. Unsaturated hydraulic conductivity measured by time-domain reflectometry under a rainfall simulator, *Water Resour. Res.*, 31 (3), 447–454.

Ramirez, A., and W. Daily, 2001. Electrical imaging at the large block test – Yucca Mountain, Nevada, *J. Appl. Geophys.*, 46, 85–100.

Rhoades, J.D., P.A.C. Raats, and R.J. Prather, 1976. Effects of liquid-phase electrical conductivity, water content, and surface conductivity on bulk soil electrical conductivity, *Soil Sci. Soc. Am. J.*, 40, 651–655.

Richards, L.A., 1928. The usefulness of capillary potential to soil-moisture and plant investigators, *J. Agric. Res.*, 37, 719–742.

Robinson, D.A., and S.P. Friedman, 2003. A method for measuring the solid particle permittivity or electrical conductivity of rocks, sediments, and granular materials, *J. Geophys. Res. B*, 108 (B2), 2076.

Robinson, D.A., S.B. Jones, J.W. Wraith, D. Or, and S.P. Friedman, 2003. A review of advances in dielectric and electrical conductivity measurement in soils using time domain reflectometry, *Vadose Zone J.*, 2, 444–475.

Roth, K., R. Schulin, H. Fluhler, and W. Hattinger, 1990. Calibration of time domain reflectometry for water content measurements using a composite dielectric approach, *Water Resour. Res.*, 26 (10), 2267–2273.

Rucker, D.F., and Ty P. A. Ferre, 2004. Correcting water content measurement errors associated with critically refracted first arrivals on zero offset profiling borehole ground penetrating radar profiles, *Vadose Zone J.*, 3, 278–287.

Rubin, Y. and S.S. Hubbard (eds.), 2005. *Hydrogeophysics*, Springer Series: Water Science and Technology Library, Vol. 50, 523 pp.

Siggins, A.F., 1992. Limitations of shallow cross-hole radar investigations, Fourth Intern. Conf. on GPR, Rovaniemi, Finland, Geological survey of Finland, special paper 16, pp. 307–315.

Slater, L., Zaidman, M.D., Binley, A.M., and West, L.J., 1997. Electrical imaging of saline tracer migration for the investigation of unsaturated zone transport mechanisms, *Hydrol. Earth Syst. Sci.*, 1, 291–302.

Steeple, D., 2005. *Shallow Seismic Methods*, in edited by Y. Rubin and S.S. Hubbard, *Hydrogeophysics*, Springer, Series: Water Science and Technology Library, Vol. 50, 523 pp.

Strobbia, C., 2003. Surface wave method. Acquisition, processing and inversion, PhD Thesis, Politecnico di Torino, Turin, Italy.

Topp, G.C., J.L. Davis, and A.P. Annan, 1980. Electromagnetic determination of soil water content: Measurements in coaxial transmission lines, *Water Resour. Res.*, 16, 574–582.

Topp, G.C., J.L. Davis, and A.P. Annan, 1982. Electromagnetic determination of soil water content using TDR, 2: Evaluation of installation and configuration of parallel transmission lines, *Soil Sci. Soc. Am. J.*, 46 (4), 678–684.

Valla, P., and U. Yaramanci, 2002. Surface nuclear magnetic resonance: What is possible?, *J. Appl. Geophys.*, 50(1–2), Special Issue, May 2002.

van Genuchten, M.Th., 1980. A closed-form equation for predicting the hydraulic conductivity of unsaturated soils, *Soil Sci. Soc. Am. J.*, 44, 892–898.

Waxman, M., and L. Smits, 1968. Electrical conductivities in oil-bearing shaly sands, *Soc. Pet. Eng. J.*, 107–122.

West, L.J., K. Handley, Y. Huang, and M. Pokar, 2003. Radar frequency dielectric dispersion in sandstone: Implications for determination of moisture and clay content, *Water Resour. Res.*, 39 (2), 1026, doi: 10.1029/2001WR000923.

Zaidman, M.D., R.T. Middleton, L.J. West, and A.M. Binley, 1999. Geophysical investigation of unsaturated zone transport in the Chalk in Yorkshire. Part 2, *Q. J. Eng. Geol. Hydrogeol.*, 32, 185–198, .

Zhou, Q.Y., J. Shimada, and A. Sato, 2001. Three-dimensional spatial and temporal monitoring of soil water content using electrical resistivity tomography, *Water Resour. Res.*, 37 (2), 273–285.

5. SOLUTE TRANSPORT PROCESSES

Andreas Kemna, Andrew Binley, Frederick Day-Lewis, Andreas Englert, Bülent Tezkan, Jan Vanderborght, Harry Vereecken, and Peter Winship

5.1. Introduction

Soils and aquifers are major compartments of the subsurface environment, which together control the terrestrial hydrological cycle. This subsurface is important for water resources and also as repository for municipal, industrial, and government waste. Aquifers are typically recharged by natural rainfall entering the soil profile and leaching into deeper soil layers. Due to intensive agricultural or industrial activities the leachate leaving the soil profile and entering the aquifer may contain concentrations of toxic substances such as agrochemicals, heavy metals, and polycyclic aromatic hydrocarbons. At contaminated industrial sites light and dense non-aqueous phase liquids (LNAPLs, DNAPLs) may be transported as a separate phase to the underlying aquifer systems. Once any of these chemicals have entered the aquifer they can be transported over large horizontal distances thus contaminating large parts of the aquifer and threatening water supply wells. Remediation of highly contaminated aquifer systems is commonly a long-term and expensive proposition. As safe and effective use of the subsurface environment is a major challenge facing our society, there is a great need to improve our understanding of the shallow subsurface and the groundwater systems. This particularly includes the understanding of transport processes, which are responsible for the fate of contaminants.

Transport processes in the subsurface are strongly controlled by the underlying soil or rock structure. Structural characteristics can vary considerably depending on geologic setting. For instance, in granular aquifers solutes in the groundwater may be transported relatively uniformly within individual lithological units, whereas fractured-rock aquifers typically exhibit distinct flow and transport paths along joints and fissures. Preferential flow may occur also in soils, for example along macropores, which can rapidly transmit soluble pollutants from the surface into groundwater. Generally, subsurface transport properties are characterized by substantial heterogeneity, depending in particular on rock texture, pore-space geometry, and mineralogy. Correspondingly, solute transport processes also show a heterogeneous behavior, associated with strong spatio-temporal variability of solute concentrations.

Due to the strong heterogeneity of the subsurface, conventional measurement techniques, such as local sediment or water sampling, are generally incapable of capturing the variability of transport properties, as well as the complexity of transport processes. Therefore, in recent years increasing attention has been paid to geophysical methods that can provide spatially highly resolved information on subsurface parameters; thus geophysical methods represent powerful tools for subsurface transport characterization. This is particularly true if geophysical imaging methods are applied in an automated, time-lapse manner, using modern data acquisition systems and processing techniques. Typical of hydrogeophysical approaches for transport characterization is the incorporation of relationships between transport related parameters and geophysical properties; these petrophysical relationships provide important links between geophysical imaging techniques and hydrological models. Such an integrated approach leads to improved characterization of solute transport processes in heterogeneous soils and aquifers.

The present chapter gives an overview of the state of the art of using hydrogeophysical methods to characterize subsurface solute transport processes. The next section provides the basic quantities and equations used for the description of solute transport processes. In the following sections, general methodological aspects of hydrogeophysical characterization approaches are outlined, published field applications are briefly reviewed, and selected case studies are presented in detail to illustrate the potential and also the limitations of the approaches in different subsurface environments (granular/fractured, saturated/unsaturated). The last section is dedicated to current methodological developments and perspectives on future advances.

5.2. Fundamentals of Solute Transport

The purpose of this section is to outline equations, parameters, and concepts that are used for the description and modeling of transport processes in soils and aquifers. For a more in depth treatment we refer to textbooks and review papers on this subject, such as Bear (1972), Fetter (2001), and Zheng and Bennett (2002) for groundwater flow and transport; Dagan (1989), Gelhar (1993), Rubin (2003), and Zhang (2002) for flow and transport in heterogeneous media; and Jury and Flühler (1992), Feyen et al. (1998), and Vanclooster et al. (2005) for transport in the unsaturated zone.

5.2.1. CONSTITUTIVE EQUATIONS FOR TRANSPORT MODELING

5.2.1.1. Definition of Concentrations

A bulk volume of sediment, soil, aquifer, or rock is composed of different phases: solid or mineral phase, water phase, and gaseous phase. The presence

or absence of the gaseous phase generally demarcates the unsaturated or vadose zone from the water-saturated zone or aquifer. In aquifers, the (connected) pore space is completely filled with water and the volumetric water content, θ , equals the (effective) porosity, ϕ , whereas in the vadose zone θ changes with time in reaction to changing boundary conditions at the soil-atmosphere surface and is less than ϕ .

Chemical substances can be present in different phases of the soil. The volume averaged total concentration, C_t , is defined as the mass storage of the chemical substance per unit bulk volume of the sediment or soil and is equal to the volume weighted sum of the concentrations in the separate phases:

$$C_t = \theta C_d + \rho_b C_a + (\phi - \theta) C_g, \quad (1)$$

where ρ_b is the bulk density of the sediment, and the subscripts d, a, and g denote respectively the dissolved, adsorbed, and gaseous phases. Note that C_a is defined as mass of adsorbed substance per mass of dry sediment. The fate and transport processes of chemical substances will be influenced by interface phenomena and the partitioning of the chemical between liquid, solid, and gaseous phases. For aquifers, and for non-volatile substances in the unsaturated zone, transport only takes place in the liquid phase; hence we focus this chapter on transport in the liquid phase (water).

The definitions of ϕ , θ , ρ_b , and C_t require a support volume. The representative elementary volume (REV) represents a macroscopic support volume which is sufficiently large to average out microscopic variations of ϕ , θ , ρ_b , and C_t that result from the microscopic structure of the phase distribution, i.e., the pore network. As a consequence, the functions that determine the spatial distributions of ϕ , θ , ρ_b , and C_t , which are defined at the scale of an REV, are not explicitly dependent on the microscopic structure of the pore network but rather represent the macroscopic variation of these variables. Similarly, averaged water and solute fluxes through the surface of an REV can be defined.

5.2.1.2. Transport in Sediments and Granular Media

Solute concentrations in granular media or sediments are described at the macroscopic scale using the convection (or advection) dispersion equation. This equation is a continuum mass balance equation which relates the rate of change of mass in an infinitesimal bulk volume (left hand side of Eq. (2)) to the divergence of the solute fluxes and solute production or loss in that volume (right hand side of Eq. (2)):

$$\theta \frac{\partial C_d}{\partial t} + \rho_b \frac{\partial C_a}{\partial t} = \nabla \cdot (\theta \mathbf{D} \nabla C_d) - \mathbf{q} \nabla C_d + \gamma, \quad (2)$$

where \mathbf{D} is the hydrodynamic dispersion tensor, \mathbf{q} the water flux vector, and γ a source/sink term which is used to implement processes like injection, (bio)degradation, or decay of solutes.

The water flux divided by the volumetric water content (in the saturated zone equal to porosity), \mathbf{q}/θ , is the pore water velocity, \mathbf{v} , which represents the velocity at which an “inert” substance, i.e., a substance which does not interact with the solid phase and does not react, is carried by the water flow through the porous medium.

The hydrodynamic dispersion tensor accounts for a solute flux due to a concentration gradient. The dispersive solute flux leads to a decrease of peak solute concentrations with time and a smoothing of concentration gradients. Two mechanisms are responsible for the dispersive solute flux: molecular diffusion and hydromechanical dispersion (the combined effect of which is also referred to as local or pore-scale dispersion). The former represents the effect of thermal agitation and molecular collisions, referred to as Brownian motion; the latter represents the effect of variations of the advection velocity that exist at a scale smaller than the scale of the averaging volume. The hydrodynamic dispersion is related to the molecular diffusion constant of the substance in bulk water, D_0 , and the macroscopic pore water velocity, \mathbf{v} , as:

$$D_{ij} = \tau \delta_{ij} D_0 + \alpha_T \delta_{ij} |\mathbf{v}| + (\alpha_L - \alpha_T) \frac{v_i v_j}{|\mathbf{v}|}, \quad (3)$$

where δ_{ij} is the Kronecker delta ($\delta_{ij} = 0$ for $i \neq j$, $\delta_{ij} = 1$ for $i = j$); τ is a tortuosity factor accounting for the decreased diffusion in a porous medium as compared with the diffusion in the bulk fluid; and α_L and α_T are the longitudinal and transverse dispersivities. Unlike molecular diffusion, hydromechanical dispersion depends on direction: it is larger in the direction of the mean flow than in the direction transverse to it, with α_L being approximately a factor of 10 larger than α_T . As a consequence, solute plumes tend to elongate in the direction of flow. The dispersivity lengths can be related to the variance of the subscale advection velocities and the spatial scale of these variations. For transport in well-sorted saturated sediments, this scale corresponds to the grain size.

An additional equation is required to relate the sorbed concentration to the concentration in solution. When sorption and desorption are instantaneous, C_a and C_d can be directly related through a sorption isotherm. For the case of rate-limited sorption/desorption, an additional equation describing the sorption kinetics is included.

5.2.1.3. Transport in Fractured and Karstic Media

The use of continuum equations to describe flow and transport in fractured media may be problematic since the scale of an REV for a network of fractures

may be considerably larger than the scale of the transport process that is of interest or the scale at which flow rates, porosities, and concentrations can be determined using in-situ techniques.

Flow and transport in fractured rock can be described using different conceptual models that span a range of data requirement and mathematical complexity. The end members of this spectrum include the discrete fracture network (DFN) and the equivalent porous medium (EPM) models. The DFN approach (e.g. de Marsily et al., 2005) represents the most complexity, with the geometry of discrete fractures explicitly considered, and flow and transport described in a spatially explicit way in the fracture network. The mass exchange between the rock matrix and fracture network is described by a three-dimensional (3-D) diffusion equation. Application of this approach requires information about the distribution of the fracture widths, lengths, apertures, and orientations; the fracture density; the connectivity of the fracture network; and the geometry and size of the matrix blocks. The spatial discretization of the flow and transport equations should be sufficiently fine to represent the fracture network structure.

The EPM represents the least complexity (e.g. Tiedeman et al., 1998; Hsieh et al., 1999), with transport in the fracture network described by a convection-dispersion equation (Eq. (2)). In this concept, the flow and concentrations are not predicted in each single fracture but the average concentrations and flow velocities in the fracture network are sought. In an EPM, a single flow and transport equation applies throughout the continuum model; however, heterogeneity can be incorporated to describe fracture-controlled variations in hydraulic properties. Indeed, stochastic continuum models (Neuman, 1987; Tsang et al., 1996) can account for substantial spatial variability consistent with fracture zones and fracture-controlled hydraulics (Day-Lewis et al., 2000).

Intermediate between the complexity of the DFN and simplicity of the EPM are multi-region representations, which describe flow and transport as occurring in multiple, interacting media. For example, in bi-continuum models (e.g. the mobile-immobile domain model) (e.g. Gerke and van Genuchten, 1993), the pore space is divided into two domains: one representing the volume occupied by small pores in the rock matrix (the immobile domain) and one representing the pore volume of the fractures (the mobile domain). Pressure heads, water fluxes, and solute concentrations are predicted for each pore domain using a pore domain specific flow and transport model and model parameterization. The equations for the two pore domains are coupled to describe mass exchange between them, e.g. due to matrix diffusion, often modeled as a first-order kinetic process. The effects of the geometry and size of the rock matrix blocks and the effective diffusion constant on the solute mass exchange are therefore lumped in an exchange rate parameter.

5.2.1.4. Transport in the unsaturated zone

Transport in the unsaturated or vadose zone is generally described by the same continuity equations as those that are used for transport in saturated sediments. However, due to the strong temporal dynamics of atmospheric forcing, i.e., rainfall and evapotranspiration, of the water flow in the subsurface, the water content and the flow velocity vary considerably with time. The water contents and fluxes in response to atmospheric forcing are described by the unsaturated flow equation, Richards Equation, which is, in contrast with the flow equation for the saturated zone, a strongly non-linear equation because the hydraulic conductivity and the volumetric water content are non-linear functions of the water pressure head (see Chapter 4 of this volume).

The hydrodynamic dispersion in unsaturated media depends on the volumetric water content. First, the tortuosity of the pathways for molecular diffusion increases with decreasing soil water content. Second, the water-filled pore network and therefore the variance of the local advection velocities change with changing water content. As a consequence, dispersivity is not a material constant for unsaturated media.

Flow in the vadose zone is generally in the vertical direction. A common simplification is that of one-dimensional (1-D) transport, i.e., solute fluxes and concentration gradients in the horizontal direction are neglected. This assumption follows from the generally widespread application of chemicals or pollutants at the soil surface, i.e., diffuse, or non-point source, pollution.

5.2.2. SOLUTE PLUME DESCRIPTION BY MEANS OF SPATIAL AND TEMPORAL MOMENTS

To parameterize transport models, tracer experiments are commonly performed (see, e.g. Ptak et al., 2004). A tracer solution is applied at the soil surface or injected in a well and the movement of the tracer solution in the subsurface is monitored. Either the evolution of solute fluxes at a certain point or plane, i.e., the breakthrough curve (BTC), is monitored, or the spatial concentration distribution at a certain time is observed. These BTCs and spatial distributions are characterized by their temporal and spatial moments, respectively.

The 0th order temporal, T^0 , and spatial, X^0 , moments are defined as

$$T^0(x) = \int_0^{\infty} C^f(x, t) dt \quad \text{and} \quad X^0(t) = \int C(x, t) dx, \quad (4)$$

where $C^f(x, t)$ is a flux concentration, which is defined as the solute flux divided by the water flux, and C is the solute concentration (corresponding with C_d in Section 5.2.1 – the subscript d is dropped here and in the following

for simplicity). The 0th order moments represent the tracer mass that is measured and can be compared with the injected solute mass to determine a mass balance or recovery. For the temporal moments, the 0th time moment of an averaged solute flux in a reference plane can be measured to determine the mass recovery. This solute flux can be directly measured in laterally confined systems from which the effluent can be collected, such as for cores or soil lysimeters, but its measurement in aquifers or fields is highly problematic.

The n th normalized temporal, \bar{T}^n , and spatial, \bar{x}_{ijk}^n , moments are defined as

$$\bar{T}^n(\mathbf{x}) = \frac{\int_0^\infty t^n C^f(\mathbf{x}, t) dt}{T^0(\mathbf{x})} \quad \text{and} \quad \bar{x}_{ijk}^n(t) = \frac{\int x_i^{n_i} x_j^{n_j} x_k^{n_k} C(\mathbf{x}, t) dx}{X^0(t)}, \quad (5)$$

where $n_i + n_j + n_k = n$. For an instantaneous solute injection, the 1st normalized moments of an inert tracer represent the mean travel time and travel distance, respectively, and can be used to derive the transport velocity v_1 according to

$$v_1 = x_1 / \bar{T}^1 \quad \text{or} \quad v_1 = \bar{x}_1^1(t) / t, \quad (6)$$

where x_1 is assumed to be distance along the mean flow direction.

Because of spatial variability in hydraulic properties, water velocities are also variable at a macroscopic scale. This spatial variability leads to an additional spreading of a solute plume beyond that caused by microscopic variations of the pore-scale velocity and molecular diffusion. Figure 1 illustrates the spreading of a solute plume predicted in a macroscopically homogeneous flow field by a convection-dispersion model. The effect of spatial variability in the hydraulic conductivity on solute spreading is illustrated in Figure 2.



Figure 1. Solute transport in a homogeneous medium. Top: Hydraulic conductivity distribution. Bottom: "Snapshot" of a solute plume being transported through the homogeneous medium (the black rectangle on the left denotes the initial solute distribution). Spreading and mixing processes are due to local dispersion

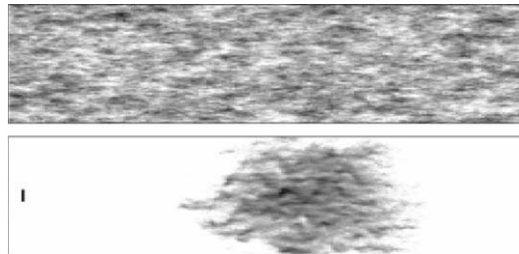


Figure 2. Solute transport in a heterogeneous medium. Top: Hydraulic conductivity distribution. Bottom: "Snapshot" of a solute plume being transported through the heterogeneous medium (the black rectangle on the left denotes the initial solute distribution). Spreading and mixing processes are due to local dispersion and the heterogeneity in the flow field

The spreading of the tracer plume can be quantified in terms of its second centralized temporal, σ_t^2 , and spatial $\sigma_{x_i}^2$, moments, given as

$$\sigma_t^2(x) = \bar{T}^2 - (\bar{T}^1)^2 \quad \text{and} \quad \sigma_{x_i}^2(t) = \bar{x}_i^2 - (\bar{x}_i^1)^2. \quad (7)$$

These centralized moments can be used to define an effective dispersion coefficient, D_{eff} :

$$D_{\text{eff},11}(x_i) = \frac{\sigma_t^2(x_i) v_1^3}{2x_i} \quad \text{or} \quad D_{\text{eff},ii}(t) = \frac{\sigma_{x_i}^2(t)}{2v_1 t}. \quad (8)$$

When the effective dispersion coefficient is used in Equation (2), the spreading of a tracer plume in a heterogeneous aquifer can be predicted without explicitly describing the smaller spatial variability of the flow field, i.e., assuming a homogeneous flow field. The effective dispersion coefficient is directly related to geostatistical parameters that characterize the variance (i.e., the contrast in the top panel of Figure 2) and the structure (i.e., the spatial extent of the regions with similar grayscales in the top panel of Figure 2) of the hydraulic conductivity field (e.g. Dagan, 1989).

It should be noted that the use of Equation (2) to predict the spreading of a solute plume in a heterogeneous medium, implies the assumption that the effective dispersion parameter is an intrinsic property of the material which does not depend on the travel time or travel distance of the solute plume. According to Equation (8), this implies that σ_t^2 and $\sigma_{x_i}^2$ increase linearly with x_i and t , respectively, i.e., that the transport process is "Fickian." There is a large body of literature showing that in most practical cases transport is non-Fickian, and "Fickianity" is reached asymptotically at exceedingly large times (e.g. Gelhar et al., 1992). Therefore, monitoring the temporal and spatial evolution of, respectively, the spatial and temporal moments of a solute plume

gives essential information about the transport process in a heterogeneous medium.

5.3. Hydrogeophysical Approaches for Solute Transport Characterization

5.3.1. GENERAL ASPECTS

Conventional measurement techniques, such as local sediment or water sampling, are generally incapable of capturing the variability of structural parameters as well as the complexity of solute transport processes in heterogeneous soils and aquifers. Therefore, in recent years geophysical methods have been used increasingly as non- to minimally invasive tools for subsurface structure and transport process characterization (see, e.g. Vereecken et al., 2002; Rubin and Hubbard, 2005). They can provide spatially and temporally highly resolved information on subsurface parameters which are closely linked to both structural and transport properties.

Depending on the purpose of investigation, different geophysical techniques are normally applied (for example Nobes, 1996, contains many references on early hydrological applications). For structural aquifer characterization, seismic as well as electrical or electromagnetic (including ground penetrating radar) methods represent appropriate tools (see, e.g. Hyndman and Tronicke, 2005; Vereecken et al., 2005). For the imaging of subsurface flow and transport processes, electrical and electromagnetic (EM) methods are especially well suited (see, e.g. Tezkan, 1999; Binley and Kemna, 2005), since the relevant state variables associated with these processes – water content and solute concentration – give rise to measurable electrical signatures. Whereas electrical and low-frequency EM methods are predominantly used to infer information on water chemistry from the measured bulk electrical conductivity (EC) of the porous medium, ground penetrating radar (GPR) (a high-frequency EM surveying method) represents a standard tool to estimate water content from the measured bulk dielectric permittivity (see, e.g. Huisman et al., 2003).

In contrast to structural hydrogeological characterization, where “static” properties of the subsurface are explored which can be considered constant with time (e.g. delineation of lithological boundaries, estimation of hydraulic conductivity, assessment of aquifer heterogeneity), transport characterization involves the monitoring of “dynamic” processes associated with spatio-temporal variations of subsurface state variables. The mapping and monitoring of transport processes therefore requires application of time-lapse geophysical methodologies. In solute tracer experiments, the presence of tracer “illuminates” flow and transport paths for subsequent geophysical

identification using electrical or EM methods. Corresponding time-lapse data are used as surrogate concentration data to infer the timing and location of tracer breakthrough. In conjunction with transport models, such data can be directly interpreted in terms of transport parameters, such as flow velocity and dispersivity.

5.3.2. HYDROGEOPHYSICAL PARAMETER RELATIONSHIPS

In hydrogeophysical applications for solute transport characterization, the measured geophysical properties are linked to hydrological state variables through petrophysical relationships (see, e.g. Lesmes and Friedman, 2005, as for electrical properties).

The bulk EC (inverse of resistivity), σ_b , of soils or rocks (without electronically conductive minerals) derives from electrolytic conduction in the pore fluid (water) and surface conduction along electrically charged mineral-fluid interfaces (most importantly along clay mineral surfaces in sedimentary environments). Both mechanisms are usually assumed to act in parallel, i.e.,

$$\sigma_b = \sigma_{el} + \sigma_s, \quad (9)$$

where σ_{el} and σ_s denote electrolytic and surface conductivity, respectively (see, e.g. Brovelli et al., 2005, for discussion about the validity of this assumption). If surface conductivity can be neglected ($\sigma_s \approx 0$), such as for clay-free sand and gravel aquifers, the bulk EC can be expressed as a function of porosity ϕ , water saturation, $S = \theta/\phi$, and water EC, σ_w , according to Archie's Law (Archie, 1942):

$$\sigma_b \approx \sigma_{el} = \frac{\phi^m}{a} S^n \sigma_w, \quad (10)$$

with m and n being two empirical parameters referred to as, respectively, cementation exponent and saturation exponent, and a being a proportionality constant of the order of one.

Equation (10) represents the basis for the sensitivity of electrical and EM measurements to water chemistry, since the water EC is proportional to the amount of total dissolved solids (TDS) (e.g. Todd, 1980). In tracer experiments with inert solutes, changes in water EC can thus be directly attributed to changes in tracer concentration:

$$\sigma_w \sim C \quad \text{or} \quad \Delta\sigma_w \sim \Delta C, \quad (11)$$

where the proportionality constant is normally obtained from water sample analyses. Since σ_w also depends on temperature (see, e.g. Sen and Goode, 1992) any temperature effects must be corrected for before applying

Equation (11). Combining Equations (10) and (11) yields for the relative changes between time t and a reference time t_0 :

$$\frac{\sigma_b(t)}{\sigma_b(t_0)} = \frac{\theta^n(t)C(t)}{\theta^n(t_0)C(t_0)}. \quad (12)$$

It is important to emphasize that inference of TDS or a specific solute concentration from measured bulk EC (e.g. using Eq. (12)) is based on the assumption of negligible clay mineral content; such inference is hindered by the presence of surface conductivity. Since σ_s is typically a non-linear and spatially variable function of salinity, it is usually difficult to establish a relation between σ_b and σ_w even if using site-specific calibrations.

The basis for GPR monitoring of transport lies in the sensitivity of EM waves to changes in bulk EC and/or dielectric permittivity. EM wave attenuation increases with EC, so that corresponding measurements offer, in principle, similar access to water salinity as discussed above. Attenuation is relatively difficult to measure, particularly due to often unknown antenna characteristics; however, analysis of time-lapse difference data eliminates some of these issues. Much more common is the use of GPR to determine the dielectric permittivity from EM wave velocity, which increases with water content (and is practically independent of solute concentration).

The dielectric permittivity, ε , or the dielectric constant $\kappa = \varepsilon/\varepsilon_0$ (where ε_0 is the permittivity in vacuum), can be related to water content using different petrophysical models. An often used empirical relationship for soils and loose sediments was established by Topp et al. (1980):

$$\theta = -5.3 \times 10^{-2} + 2.92 \times 10^{-2} \kappa_b - 5.5 \times 10^{-4} \kappa_b^2 + 4.3 \times 10^{-6} \kappa_b^3, \quad (13)$$

where κ_b is the bulk dielectric constant. Alternatively, volumetric mixing formulas may be used, where soils or rocks are considered as multi-phase mixtures and κ_b is calculated from the dielectric constants and volume fractions of the individual phases. For a three-phase mixture of solid matrix, water, and air, the so-called complex refractive index method (CRIM) yields (e.g. Shen et al., 1985)

$$\sqrt{\kappa_b} = (1 - \phi)\sqrt{\kappa_m} + \theta\sqrt{\kappa_w} + (\phi - \theta)\sqrt{\kappa_a}, \quad (14)$$

where κ_m is the dielectric constant of the solid matrix, κ_w is the dielectric constant of water (assumed to be 81), and κ_a is the dielectric constant of air (assumed to be 1).

5.3.3. HYDROGEOPHYSICAL IMAGING

Hydrogeophysical imaging involves tomographic inversion of geophysical data to produce subsurface images of the measured physical property. The resultant images, or “tomograms”, are then linked to the hydrological property of interest using hydrogeophysical parameter relationships. Electrical imaging, also referred to as electrical resistivity (or resistance) tomography (ERT) (see, e.g. Daily et al., 2005), provides images of bulk EC which may be converted into solute concentration maps on the basis of Equations (10) and (11), for instance allowing solute plume delineation in aquifers. GPR, if applied in tomographic mode (see, e.g. Hubbard et al., 1997; Peterson, 2001; Binley et al., 2001; Alumbaugh et al., 2002; Schmalholz et al., 2004), offers the possibility to obtain soil moisture maps from imaged permittivity distributions using petrophysical relationships such as Equation (13) or (14) (see also Chapter 4 of this volume).

In time-lapse geophysical imaging, difference tomograms are generated by either inverting difference data or differencing tomograms inverted from absolute data. Besides the ability to capture dynamic processes, time-lapse imaging offers other methodological advantages. For instance, systematic measurement errors (for example due to inaccurate electrode positions in ERT, or uncertain antenna radiation patterns in GPR) or numerical modeling (discretization) errors which are correlated in time may partially cancel out in the difference inversion process, which can lead to more reliable imaging results (see, e.g. Ramirez and Lytle, 1986; Daily et al., 1992; LaBrecque and Yang, 2001).

Time-lapse hydrogeophysical imaging represents a powerful tool for solute transport characterization since a full picture of the spatio-temporal evolution of the process can be obtained (see Figure 3). For instance, solute plume movement and spreading may be quantified by performing a spatial moment analysis of the concentration distributions derived from 3-D electrical imaging results (Singha and Gorelick, 2005). Binley et al. (1996) proposed to interpret time-lapse electrical images locally as solute concentration BTCs, from which temporal moments may be computed, or which may be analyzed by means of equivalent convection-dispersion models to quantify transport properties (Kemna et al., 2002). The evolution of the spatial and temporal moments of a plume with time and travel distance, respectively, contains important information about the transport process in heterogeneous media (see again Section 5.2.2 of this chapter).

Equivalent transport models represent a simplification of the general 3-D convection-dispersion equation (Eq. (2)) on the basis of equivalent parameters for an idealized homogeneous medium. The equivalent parameters are defined such that parameters of predicted solute plumes in the equivalent

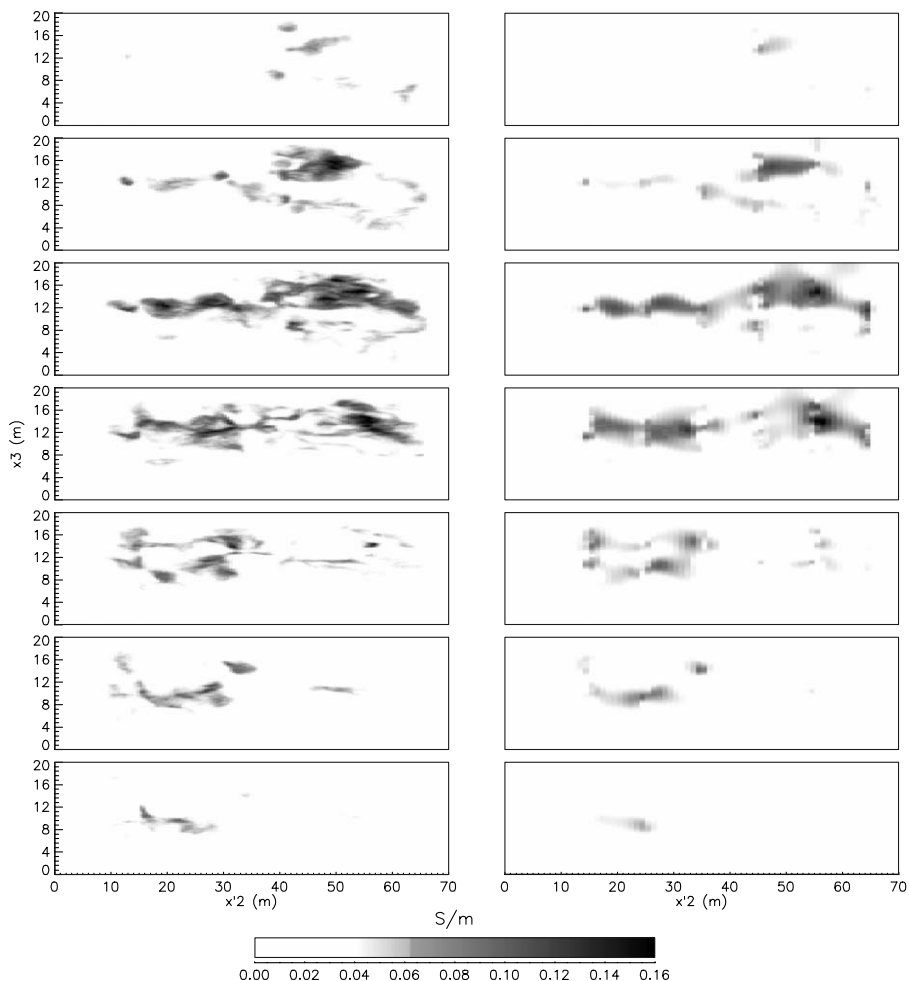


Figure 3. Results from a synthetic experiment where 2-D ERT imaging was simulated on the basis of simulated solute transport in a 3-D heterogeneous medium. Shown are original (left panels) and ERT inverted (right panels) EC changes associated with solute concentration changes in an image plane perpendicular to the mean flow direction at selected time intervals (time evolves from top to bottom). ERT data are based on seven vertical electrode strings (boreholes) evenly distributed across the image plane (from Vanderborgh et al., 2005, by permission of the American Geophysical Union)

homogeneous medium match those of plumes in a heterogeneous medium. For instance, the spreading of a solute plume resulting from flow heterogeneities in the longitudinal and transverse directions (i.e., parallel and orthogonal to the flow direction, respectively) can be quantified in terms of dispersivity parameters of an equivalent model (e.g. Dagan, 1989). Using for instance an equivalent stream tube model, which conceptualizes the medium as a bundle

of independent stream tubes parallel to the mean flow direction (i.e., lateral mixing between stream tubes is neglected) (Simmons, 1982), the heterogeneity of transport and the local mixing within a plume can be quantified across a perpendicular two-dimensional (2-D) ERT image plane (Kemna et al., 2002). Transport in each stream tube is described by a 1-D convection-dispersion model:

$$\frac{\partial C}{\partial \tau} = -v_s \frac{\partial C}{\partial \xi} + v_s \lambda_s \frac{\partial^2 C}{\partial \xi^2}, \quad (15)$$

where v_s is the equivalent convection (or advection, for horizontal mean flow) velocity, λ_s the equivalent longitudinal dispersivity, and ξ the stream tube coordinate. Whereas the heterogeneity of transport is represented by the spatial variability of v_s , local mixing is described by λ_s (e.g. Cirpka and Kitanidis, 2000; Vanderborght and Vereecken, 2002). The heterogeneity of transport also contains information about the spatial structure of the hydraulic conductivity field (e.g. Rubin and Ezzedine, 1997; Vanderborght and Vereecken, 2001; Bellin and Rubin, 2004).

Vanderborght et al. (2005) investigated the potential and limitations of the above approach in a numerical simulation where heterogeneous transport in a 3-D flow field was imaged with 2-D ERT (see Figure 3). Figure 4 shows that for the assumed cross-borehole measurement geometry, ERT-derived local BTCs provide correct estimates of (stream tube model equivalent) tracer mass (Figures 4a,b) and advection velocity (Figures 4c,d), corresponding to the 0th and 1st temporal moments, at reasonable spatial resolution. However, the recovery of the corresponding longitudinal dispersivity (Figures 4e,f), related to the 2nd temporal moment, is poor. This reflects the general problem of resolving the breakthrough of a 3-D heterogeneous tracer plume in a 2-D ERT image plane, where dispersivities in the direction perpendicular to the image plane tend to be overestimated due to the 3-D sensitivity characteristics of electrical measurements.

Geophysical imaging is a very attractive approach since it provides high spatial resolution in between wells, where no direct hydrologic information is available. However, depending on the physical nature of the measurement method applied, the resolution varies in a characteristic way across the imaging plane or volume. Variable tomographic resolution must be considered if tomograms are to be used for quantitative interpretation, as in hydrogeophysical approaches. Spatial resolution in ERT continuously decreases with increasing distance from the electrodes. For surface electrode arrays, image resolution decreases primarily with depth, while for cross-borehole electrode arrays resolution is poorest in the middle between the boreholes (see, e.g. Daily et al., 2005). Image resolution in GPR tomography is complementary to ERT; here the coverage with radar waves in cross-borehole transmission

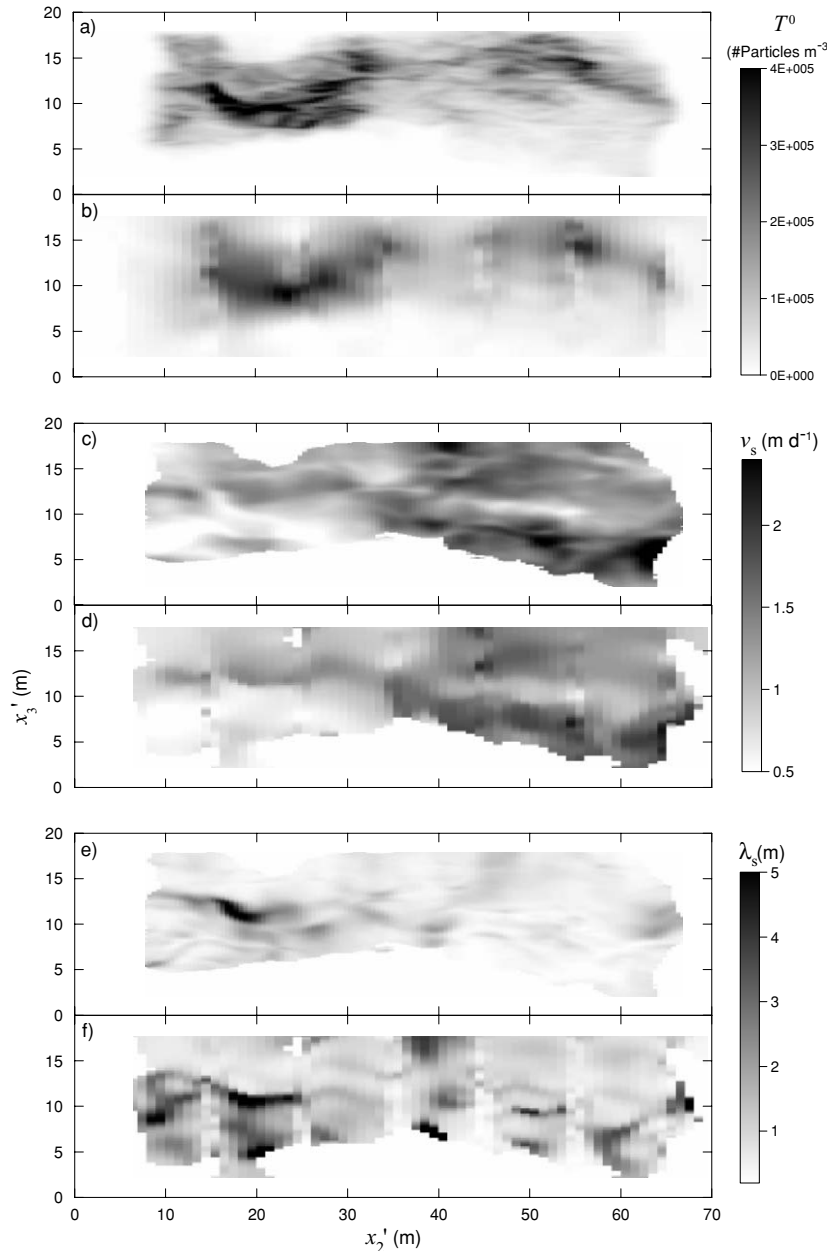


Figure 4. Equivalent stream tube model analysis (Eq. (15)) of the images in Figure 3 showing spatial distribution of parameters derived from the original (panels a, c, and e) and ERT inverted (panels b, d, f) local BTCs in the image plane: 0th moment of the BTCs, corresponding to T^0 in Equation (4) (panels a and b); stream tube velocity, v_s , corresponding to v_1 in Equation (6) (panels c and d); and stream tube dispersivity, λ_s , related to $D_{eff,11}$, in Equation (8) (panels e and f) (from Vanderborgh et al., 2005, by permission of the American Geophysical Union)

surveys is typically greatest in the middle of the image plane, while resolution can be relatively poor close to the antenna positions (see, e.g. Day-Lewis et al., 2004).

The resolution (i.e., sharpness and contrast) of geophysical images is limited by measurement sensitivity, measurement error, regularization criteria (e.g. damping or spatial-derivative filters for flatness or smoothness), and inconsistencies between the modeled and true measurement physics. If the imaging algorithm is based on a model smoothness constraint (which is widely used for ill-posed imaging problems such as ERT), high resolution regions normally show good (i.e., close to true) model contrast, while model contrast can be very poor (i.e., far from true) in areas with low resolution. If, as usual in hydrogeophysical imaging, hydrologic-geophysical parameter relationships are applied to the geophysical images, the derived images of, for example, water content or solute concentration are likewise affected by the limited and spatially variable image resolution. For instance, solute tracer concentrations in low resolution areas may be considerably underestimated in ERT surveys, which may lead to a poor tracer mass balance (e.g. Singha and Gorelick, 2005). This means, in other words, that the apparent petrophysical model mapping an imaged geophysical parameter to a true hydrological quantity is no longer the same as the original core-scale relationship, but is a modified one which is dependent on image resolution (and thus varies spatially).

Recently, Day-Lewis et al. (2005) studied this problem in numerical experiments for ERT and GPR tomography, respectively, and the corresponding standard petrophysical model used for water content determination (see Eqs. (12) and (13)). They point out that image resolution, as estimated for instance by calculating the model resolution matrix according to linear inverse theory (see, e.g. Alumbaugh and Newman, 2000), could actually be used to calibrate for the resultant breakdown of the core-scale petrophysical model. Such an approach was also promoted recently by Moysey et al. (2005) on the basis of numerical analogs to geophysical surveys derived from Monte Carlo simulation, which can be used to infer field-scale (i.e., post-imaging) petrophysical relationships.

5.4. Solute Transport Characterization Studies

In this section the use of hydrogeophysical methods for the characterization of solute transport processes in different subsurface environments (granular aquifers, fractured aquifers, vadose zone) will be reviewed. After providing a brief overview of published work in the respective area, each subsection will focus on a selected case study to demonstrate the state of the methodology in typical field-scale applications.

It may be noted that we here only focus on solute transport studies. As for the delineation and monitoring of non-aqueous contaminant plumes, where likewise numerous successful applications of electrical and GPR methods exist, we refer to the review articles by Nobes (1996) and Pellerin (2002), as well as to the textbooks edited by Ward (1990) and Butler (2005).

5.4.1. SOLUTE TRANSPORT IN GRANULAR AQUIFERS

5.4.1.1. Overview

Mapping of subsurface solute plumes in granular aquifers has been a common application of electrical and EM methods for many years (see, e.g. Nobes, 1996; Pellerin, 2002; Rubin and Hubbard, 2005). With these methods the bulk electrical conductivity (EC) in the subsurface is measured, which is highly influenced by pore fluid chemistry. Accordingly, there have been numerous successful applications in the environmental and hydrological field.

Earlier granular aquifer studies include the monitoring of saline water plumes (e.g. solute tracer, seawater) by profiling or mapping the associated electrical signature by means of electrical measurements at the surface (e.g. White, 1988; Hagemeyer and Stewart, 1990; Osiensky and Donaldson, 1995; Morris et al., 1996) or in boreholes (e.g. Bevc and Morrison, 1991), as well as by means of surface EM measurements (e.g. Goldstein et al., 1990; Goldman et al., 1991; Merrick, 1997). With the advance of tomographic inversion procedures, the imaging of transport processes with relatively high spatial resolution became possible, leading to numerous applications in this regard in granular aquifers. For example, Slater et al. (2000, 2002) demonstrated the potential of ERT for solute transport imaging in controlled tank experiments. Corresponding field-scale applications of ERT include monitoring of solute tracer experiments (e.g. Kemna et al., 2002; Singha and Gorelick, 2005) and monitoring of saltwater-freshwater dynamics (e.g. Slater and Sandberg, 2000; Acworth and Dasey, 2003).

5.4.1.2. Selected Example Krauthausen, Germany

In order to investigate solute transport in heterogeneous granular aquifers, several groundwater tracer experiments were conducted at the Krauthausen test site of the Jülich Research Center in Germany. The experiments were monitored using time-lapse ERT and, in a single case, radio-magnetotellurics (RMT). RMT is an EM method where the response of the subsurface to EM waves from available civilian and military transmitters is measured.

At the Krauthausen test site 72 observation wells were installed for monitoring purposes, allowing multi-level groundwater sampling every 0.3 m down to a depth of 10 m. The aquifer at the site can be divided into a bottom layer of sand and gravel between 4.5 and 11 m depth, and an overlying gravel layer

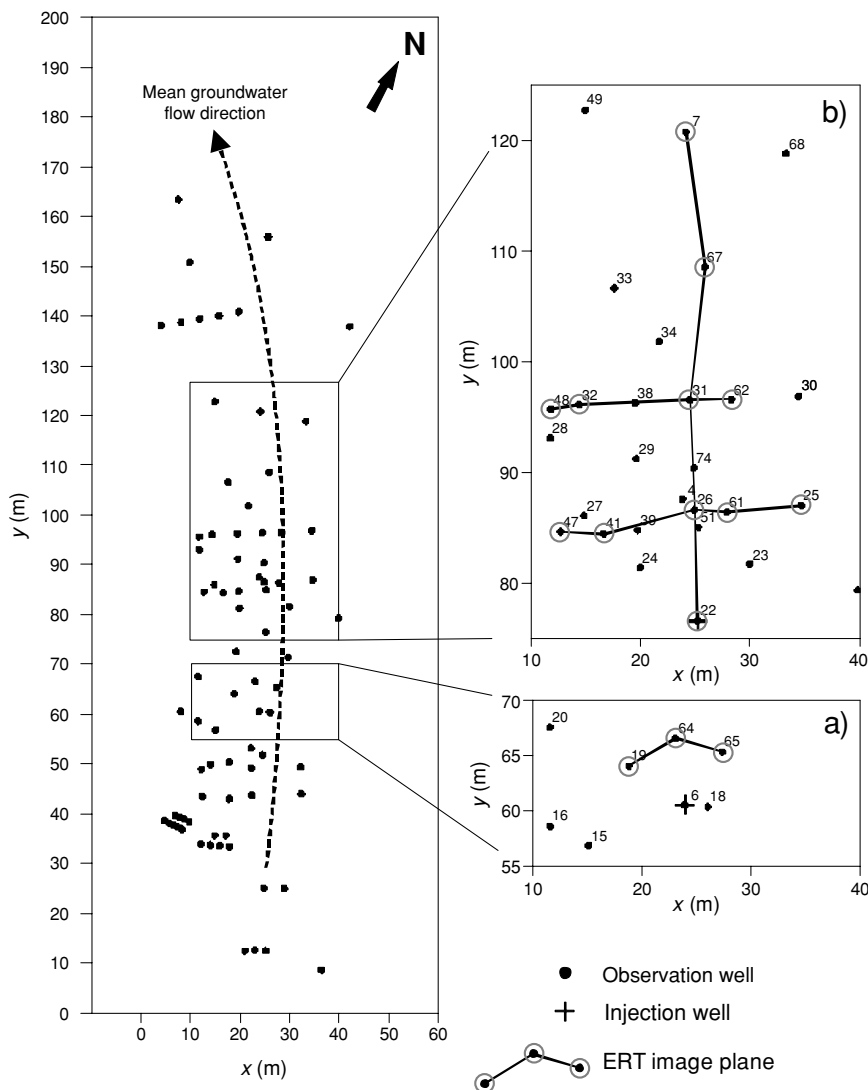


Figure 5. Map view of the Krauthausen test site showing the locations of monitoring wells (solid circles). The two areas shown in insets on the right-hand side were selected for tracer experiments carried out in conjunction with geophysical imaging in (a) 2000, and (b) 2002 and 2003. Crosses indicate the position of respective tracer injection wells; open circles indicate the position of ERT boreholes, defining (a) one and (b) three vertical image planes

extending from 1.3 to 4.5 m depth. The aquifer base consists of thin clay and silt layers extending from 11 to 13 m depth. The groundwater table typically fluctuates between 1 and 2.5 m depth. A detailed description of the site can be found in Vereecken et al. (2000). Figure 5 provides an overview of the test

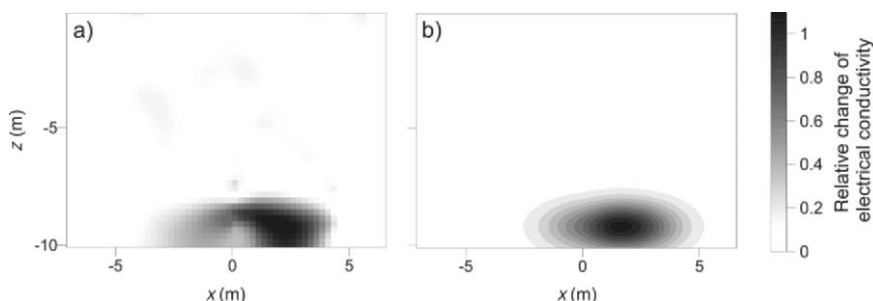


Figure 6. (a) Snapshot of tracer breakthrough (five days after injection) as imaged with time-lapse ERT in the 2000 experiment approximately 5 m down-gradient of the injection well. (b) Corresponding result of an equivalent 3-D convection-dispersion model fit, assuming a linear relation between relative EC change and tracer concentration. The shown cross-section corresponds to the ERT profile indicated in Figure 5 at approximately $y = 65$ m (from Kemna et al., 2002, by permission of Elsevier)

site showing the locations of monitoring wells and the regions selected for the tracer tests.

In September–December 2000, a first study was carried out using 2,000 L of a NaBr solution with a concentration of 15 g/L as an electrically conductive tracer (Kemna et al., 2002). The tracer was injected between 6 and 7 m depth in the screened section of a monitoring well (at a rate of 500 L/h), and monitored down-gradient in an ERT image plane perpendicular to the known mean flow direction (see Figure 5). The image plane was spanned by electrodes in three boreholes and additional electrodes at the surface (see Kemna et al., 2002, for details on ERT survey design). Although gravitational sinking of the tracer plume resulted in solute breakthrough in a less sensitive region of the ERT image plane, the principal part of the plume was detected (see Figure 6a). A calibration relation between water EC and tracer concentration obtained from multi-level sampling results provided the basis for a quantitative analysis in terms of transport model parameters. Since the tracer in this experiment only “sensed” a relatively small portion of the aquifer, the observed breakthrough could be reasonably well described by a 3-D convection-dispersion model with homogeneous equivalent parameters (see Figure 6b) (Kemna et al., 2002).

As a continuation of the smaller-scale tracer test conducted in 2000, two larger-scale experiments were carried out in the years 2002 and 2003, respectively (Kemna et al., 2004a; Müller et al., 2005), where it was expected that geophysical imaging could reveal more significant characteristics of heterogeneous transport. “Up-scaling” was accomplished by (i) injecting larger tracer volumes over longer time periods (140,000 L over seven days), (ii) injecting tracer solution over almost the entire aquifer depth (between 3 and 10 m depth), and (iii) monitoring tracer breakthrough at cross-hole reference

planes further away from the injection well (see Figure 5). In the 2002 experiment, a CaCl_2 tracer solution (2.9 g/L) with a higher EC than that of the native groundwater (contrast 7:1) was injected, whereas a “negative” tracer solution (partly deionized water) with a lower EC than that of the native groundwater (contrast 1:4) was injected in the 2003 experiment. In both experiments the same volume of tracer solution was injected in the same well and at the same time of the year (September–December) to ensure similar hydrological boundary conditions and facilitate direct comparison of both experiments; however, different plume evolution scenarios were expected due to density contrasts between the tracers. During both tracer experiments, multi-level groundwater samples were taken. Calibration relations between bulk EC and groundwater EC were determined on the basis of laboratory measurements on columns packed with aquifer material using different solutions of known EC (see Müller et al., 2005).

Down-gradient of the tracer injection well, three transects – two perpendicular and one parallel to the mean flow direction – were selected for ERT measurements (see Figure 5). The image planes were spanned by four to five boreholes, each equipped with 13 equally spaced electrodes along the screened interval between 3 and 10 m depth. Additional surface electrodes were used for the majority of surveys in order to increase subsurface coverage. For ERT data collection, a combination of standard “skip-1” and “skip-2” dipole-dipole protocols was used (i.e., all possible dipole-dipole configurations with a fixed dipole “length” of respectively two and three electrode spacings). For both positive and negative tracer experiments, measurements were conducted over almost four months at more than 40 days using the Resecs instrument by Geoserve. The time-lapse ERT data were inverted to produce images of bulk EC changes using a 2-D smoothness-constrained difference inversion approach described in Kemna et al. (2002). It was shown in a synthetic experiment, the design of which followed the present application, that the approach is actually capable of resolving 3-D solute transport characteristics (Vanderborght et al., 2005).

Figure 7 shows the time-lapse ERT results for both experiments at selected days after tracer injection in one of the image planes. The displayed cross-section corresponds to the transect perpendicular to the mean flow direction with a distance of about 10 m from the tracer injection well (see Figure 5). The breakthroughs of both the conductive and resistive plumes are clearly resolved in the middle part of the image plane. Remarkably, two vertically separated zones of tracer breakthrough are observed between days 10 and 17 in both experiments, representing an effect of larger-scale aquifer heterogeneity. However, the ERT results also reveal differences in the behavior of the two plumes. The density-driven downward drift of the conductive plume leads to a more lateral spreading of the lower part of the plume on top of the aquifer base,

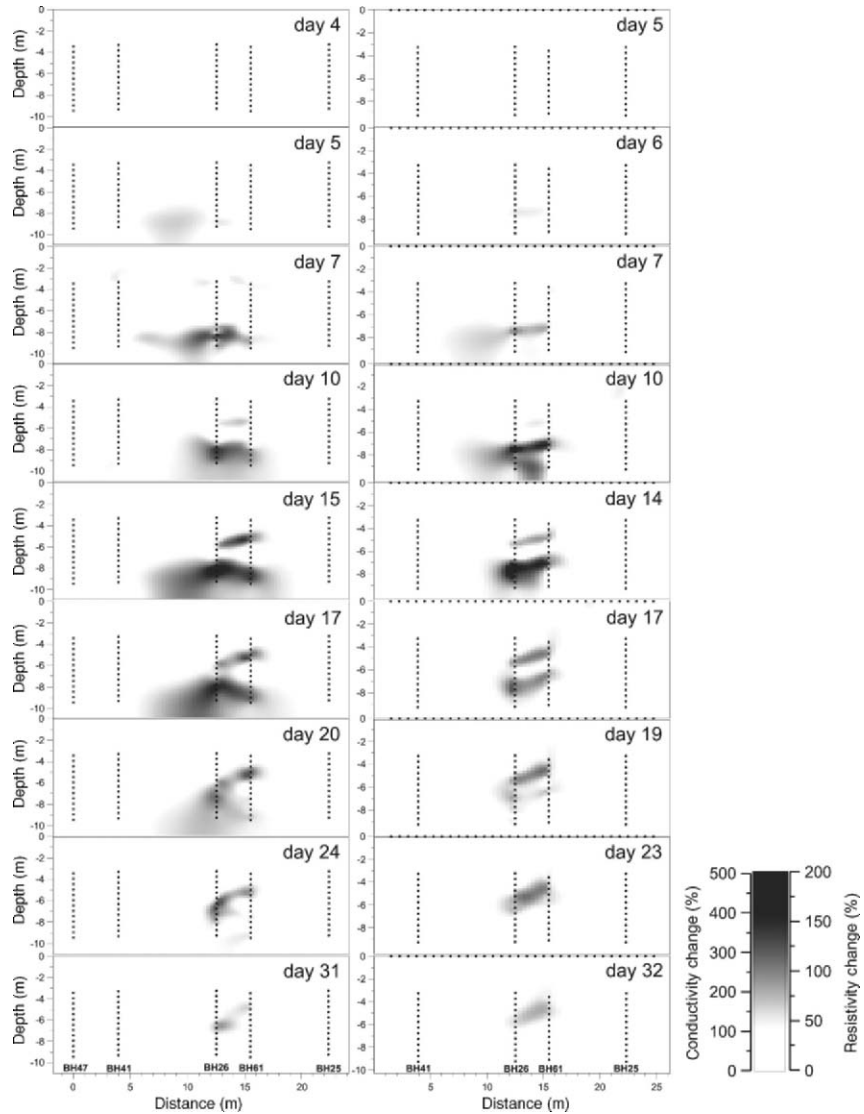


Figure 7. Time-lapse ERT results of the positive (2002) (left panels) and negative (2003) (right panels) tracer experiments showing relative changes of, respectively, electrical conductivity (left) and resistivity (right) in a cross-section perpendicular to the mean flow direction at selected days after tracer injection. Solid circles indicate the position of electrodes. The shown cross-section corresponds to the ERT profile indicated in Figure 5 at approximately $y = 85$ m

while the corresponding part of the resistive plume slowly moves upwards until it eventually merges into the upper plume branch. For both experiments tracer breakthrough in this upper part is delayed and exhibits longer tailing compared to the breakthrough in the lower zone.

On the basis of the obtained calibration relations between bulk EC, water EC, and tracer concentration, the time-lapse ERT results can be interpreted in terms of transport parameters. Using for instance a stream tube model analysis (see Section 5.3.3), equivalent flow velocities and longitudinal dispersivities in the breakthrough region of the image plane can be quantified. The spatial variability of these parameters contains information about the spatial structure of the flow field, which in turn can be used to infer information about the structure of the hydraulic conductivity field.

For the positive tracer experiment in 2002, the spatio-temporal evolution of the tracer plume was also monitored by time-lapse radio-magnetotelluric measurements at the surface (Nix et al., 2005). While ERT focused primarily on vertical image planes perpendicular to the mean flow direction, the RMT survey was designed to especially help in the characterization of plume movement in the direction parallel to the mean flow, and by this the RMT complemented the ERT survey.

The RMT method (see, e.g. Tezkan, 1999) uses EM fields from high-power civilian and military transmitters operating in a frequency range between 10 and 300 kHz, which, at great distances from the transmitters, can be considered as planar waves. These waves are associated with orthogonal horizontal electric and magnetic field components at the surface of the earth which are measured in an RMT survey. The ratio of these electric and magnetic horizontal components defines an EM impedance which contains information about the subsurface resistivity distribution.

In the present study, multi-frequency RMT data were collected every 2.5 m on a 35 m by 20 m measurement grid at the surface covering the tracer injection well and the first 30 m of the down-gradient region. Four frequencies between 16 and 234 kHz were used, corresponding to exploration depths of about 5 to 30 m for the expected background resistivity values in this depth range. The horizontal magnetic field component was measured with a coil of 0.4 m diameter, and the horizontal electric field component was measured with two grounded electrodes at 1 m separation, using a light-weighted instrument (Müller, 1983). The RMT measurements were repeated one to three times per week over a period of ten weeks to enable a quasi-monitoring of the conductive anomaly associated with the tracer plume.

For selected transects parallel to the mean groundwater flow direction (see Figure 5), the time-lapse RMT data were inverted into images of bulk EC using a 2-D smoothness-constrained inversion approach (for details, see Nix, 2005). Figure 8 shows the inversion results for three time intervals as difference images relative to the background distribution. Clearly the tracer plume is revealed as a conductive anomaly which progresses with time in the flow direction. The observed plume behavior is overall consistent with the tracer breakthrough as observed with ERT (cf. Figure 7), taking the different

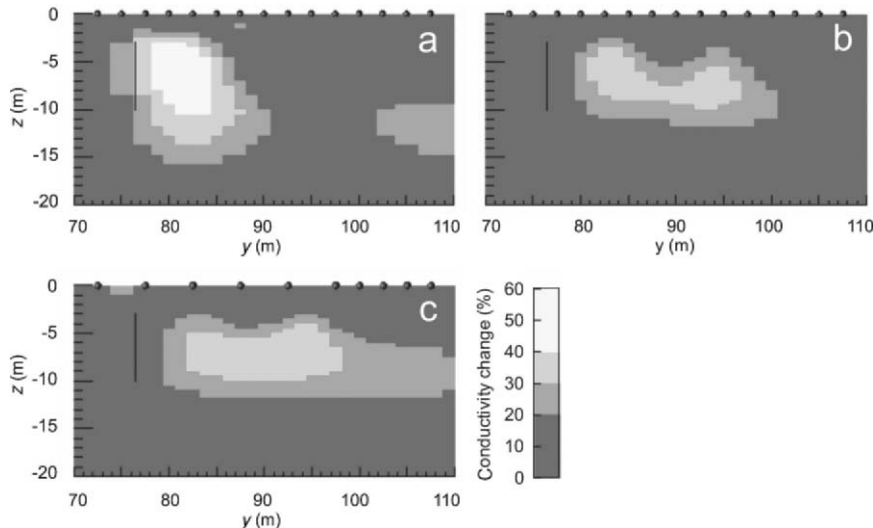


Figure 8. Difference images of 2-D RMT inversion results showing EC changes relative to the background at (a) one week, (b) three weeks, and (c) five weeks after tracer injection. The shown cross-section corresponds to $x = 25$ m (cf. Fig. 5) (from Nix et al., 2005, by permission of the European Association of Geoscientists and Engineers)

spatial resolution capabilities of the two methods into account. Flow velocity estimates derived from tracer arrival times on the basis of the RMT results are in good agreement with those obtained from the ERT results (Nix, 2005).

Figures 7 and 8 also illustrate the complementary character of ERT and RMT results in the present case. While ERT captures the spatial extent of the tracer plume in a plane perpendicular to the flow direction, RMT delineates the plume in a vertical plane parallel to the flow direction. A combined interpretation results in a better picture of the spatio-temporal plume evolution, which may provide the basis for improved characterization and moment analyses.

5.4.2. SOLUTE TRANSPORT IN FRACTURED AQUIFERS

5.4.2.1. Overview

Monitoring and predicting solute transport in fractured rock remains a major hydrologic challenge. The permeability structure of fractured-rock aquifers is difficult to identify because conventional hydrologic measurements are sparse, commonly sample poorly defined aquifer volumes local to boreholes, and do not provide insight into the 3-D architecture of fracture networks away from boreholes; moreover, fractures can act as either flow conduits or barriers, resulting in extreme heterogeneity.

In static mode, geophysical methods have been used to characterize near-surface structures in fractured rock. Cross-hole GPR tomography (e.g. Olsson et al., 1992), seismic tomography (e.g. Ellefsen et al., 2002), borehole reflection-mode GPR (e.g. Lane et al., 1998a), surface reflection-mode GPR (e.g. Grasmueck, 1996), and acoustic and optical televiewer logs can provide insight into the locations and orientations of fractures and fracture zones. Furthermore, azimuthal electrical resistivity (e.g. Lane et al., 1995) and seismic refraction (e.g. Lieblich et al., 1991) have been used to identify principal axes of electrical and seismic anisotropy, which in turn have been related to dominant fracture-strike direction. Although knowledge of fracture location, orientation, and extent is useful, researchers working at numerous sites have concluded that a small percentage of high-permeability fractures can dominate flow and transport. Discriminating permeable from non-permeable fractures is critical to developing reliable conceptual and numerical groundwater models.

Time-lapse geophysical tomography is used increasingly to monitor transport in fractured rock. Of particular utility are GPR and ERT, which, conducted in combination with tracer tests, can reveal permeable fractures and fracture zones. GPR tomography was used to monitor tracer tests in several landmark fractured-rock hydrology studies, including the Oracle, Arizona site (Ramirez and Lytle, 1986); the Grimsel test site in Switzerland (Niva et al., 1988); and the Stripa Mine in Sweden (Olsson et al., 1991). ERT, similarly, has been used to monitor transport in fractured rock, including salt-water intrusion at a limestone quarry in the UK (Slater et al., 1997a). We now provide a focused review of a recent investigation in which cross-hole GPR tomography was used to monitor saline tracer tests in fractured, crystalline rock.

5.4.2.2. Select Example: Mirror Lake Site, United States
A series of cross-hole radar experiments were performed in conjunction with saline tracer tests at the US Geological Survey's fractured-rock hydrology research site, near Mirror Lake, New Hampshire, in the United States. The bedrock at the site is schist intruded by granite, pegmatite, and lamprophyre. The tracer tests discussed here were conducted in a fracture zone identified previously using hydraulic and tracer data (e.g. Hsieh et al., 1999; Day-Lewis et al., 2000). In early GPR tomography efforts at the site (Wright et al., 1996; Lane et al., 1998b, 2000), tracer was injected into packed-off zones of boreholes and tomography was performed in several image planes. These studies produced one-to-several time-lapse snapshots of tracer migration, using independent inversion of each time-lapse dataset. Although results from these early studies provided valuable qualitative information, more quantitative information was sought to calibrate flow and transport models for the site. This review focuses primarily on work by Day-Lewis et al. (2003, 2004); the goal

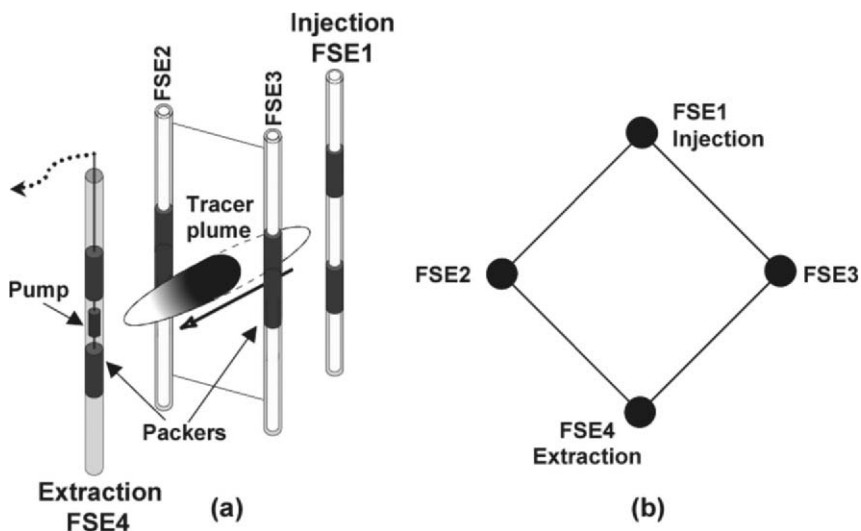


Figure 9. (a) Schematic cross-section and (b) plan view of the experimental setup for the cross-hole radar and tracer experiments. Tracer injection was in FSE1, extraction was from FSE4, and tomographic imaging was in the FSE1-FSE2, FSE2-FSE3, and FSE3-FSE1 planes. The distance between injection and extraction wells is about 13 m. Not to scale (from Day-Lewis et al., 2003, by permission of the American Geophysical Union)

of these studies was to improve the link between geophysical inversion and calibration of groundwater models.

Day-Lewis et al. (2003) conducted “sequential-injection and scanning” (SIS), a novel cross-hole data acquisition procedure first proposed by Lane et al. (1998b). In SIS, a different set of common-source or common-receiver gathers is acquired during each of a series of identical tracer tests, so that a different section of the interwell region is scanned during each test. Prior to each tracer injection, a full background GPR dataset is collected for differencing. Figure 9 provides a schematic of the experimental setup in the FSE1-FSE4 well cluster at the Mirror Lake site. A 5-hr doublet tracer test was repeated 12 times with the same injection rate (1.9 L/min in FSE1) and pumping rate (3.8 L/min in FSE4). After achieving a steady-state flow field, the injection was switched from native groundwater to the saline-tracer solution of 50 g/L (NaCl) for a 10-min period; injection was then switched back to native groundwater.

GPR data were collected from antennas in FSE1, FSE2, and FSE3; log-through PVC packers were used in these wells, but the presence of the pump precluded data collection in FSE4. Data for the twelve tests were combined to assemble 30 time-lapse datasets on a 10-min interval throughout the experiment. The presence of tracer was seen in a small subset of the difference

attenuation data. Over time, the tracer migrates through different portions of the aquifer and was detected along different raypaths.

Previous analyses of time-lapse geophysical data relied on the assumption that changes in the imaged property during data collection were negligible. For long-duration tracer tests (e.g. Olsson et al., 1991), this assumption can be justified; however, tracer-test design is often based on hydrologic and not geophysical concerns, and solute concentrations may change quickly relative to geophysical data collection during shorter duration tracer tests. Day-Lewis et al. (2002) demonstrated how the static-image assumption can result in systematic errors in tomograms, with the spatial pattern of errors controlled by the acquisition geometry and schedule. To overcome this problem, Day-Lewis et al. (2003) inverted the time-lapse difference attenuation data on a 4-D space-time nodal mesh, accounting for data acquisition time and allowing for image changes during data collection. In effect, another axis (time) was introduced into the inversion. To enhance resolution of the tomograms and suppress artifacts, inversion constraints were applied to restrict the target anomaly to the region of the 3-D mesh traversed by raypaths along which amplitude changes were observed.

Six of the 31 time-lapse tomograms are shown in Figure 10. Inspection of the tomograms indicates that the tracer moved quickly away from the injection borehole (FSE1) and out of the FSE1-FSE3 and FSE2-FSE3 planes. Difference-attenuation histories for nodes in the three image planes are plotted in Figure 11. Although the estimated difference attenuation can be considered surrogate concentration data, it should be noted that the regularization used for inversion results in smoothness in both space and time; hence the actual solute breakthrough curves (BTCs) may be less disperse and more irregular. The concentration history at the outlet (Figure 11d) showed two peaks – the first sharper and higher concentration.

Inspection of Figure 11 reveals apparent inconsistencies between the geophysical results and the measured tracer breakthrough at the outlet. The first detection of tracer in the FSE2-FSE3 plane (between 30 and 40 minutes) is reasonable given the first direct detection in discharge at FSE4 (about 50 minutes); however, the timing of the peak difference attenuation shows an apparent inconsistency with the timing of peak discharge concentration. Difference-attenuation histories indicate that peak tracer concentration occurs in the FSE2-FSE3 plane between 90 and 100 minutes after the start of injection, whereas the peak tracer concentration arrived earlier at the outlet, at about 77 minutes. Furthermore, the attenuation BTCs in the image plane are broader than the concentration history at the outlet, yet the effect of dispersion ought to be less at intermediate points in the interwell region.

There are valid hydrologic reasons to expect that time-lapse radar and solute breakthrough data would differ. First, there is a discrepancy between the

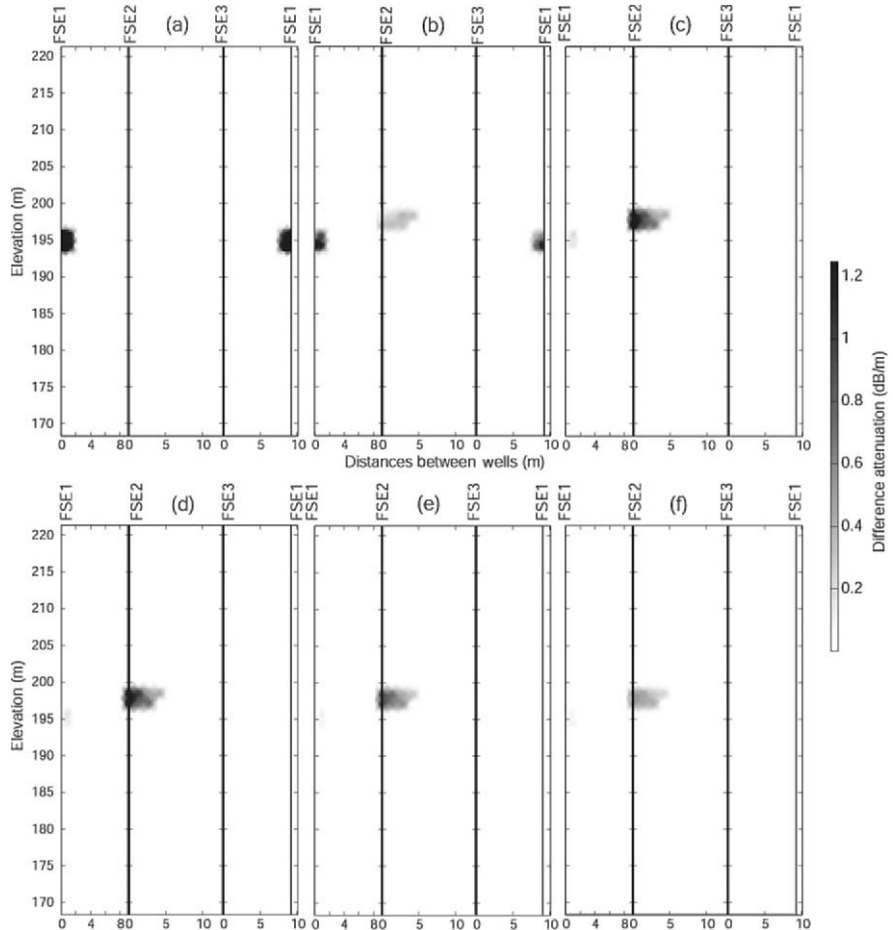


Figure 10. (a) 20-minute, (b) 50-minute, (c) 90-minute, (d) 120-minute, (e) 150-minute, and (f) 200-minute difference-attenuation tomograms from constrained inversion (from Day-Lewis et al., 2003, by permission of the American Geophysical Union)

measurement support volumes for tomography and tracer sampling. Tomographic estimates commonly represent spatial averages over multiple flow-paths with different arrival times and BTCs. Such local averaging may result in (i) a time lag between peak concentration and peak radar attenuation, and (ii) greater spread in the difference-attenuation history compared to the solute BTC (Figure 12), as explained previously in Section 5.3.3. Second, comparison of tomographic estimates with tracer concentrations is complicated in the presence of rate-limited mass transfer (RLMT). Under RLMT, solute mass is divided between mobile and immobile domains, i.e., permeable, connected fractures and dead-end fractures or matrix porosity. Here, the geophysical

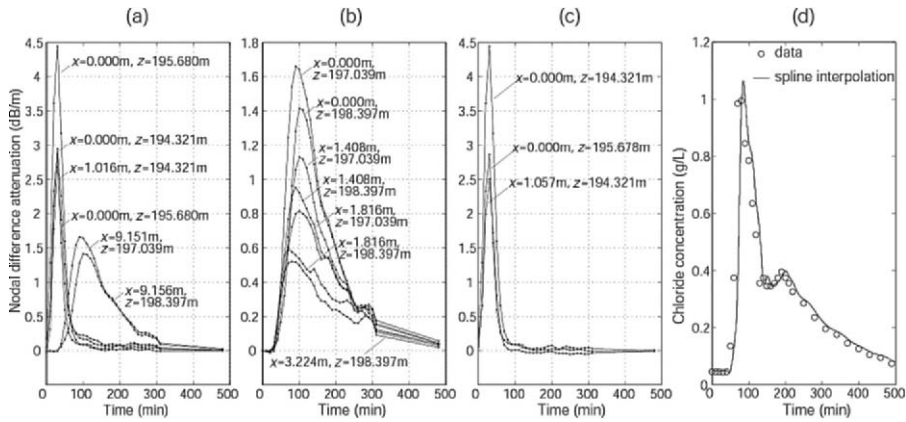


Figure 11. Nodal difference-attenuation histories in the (a) FSE1-FSE2, (b) FSE2-FSE3, and (c) FSE3-FSE1 image planes. Node locations are indicated as distance between wells (m) and elevation (m), for comparison with Figure 10. (d) Discharge concentration at FSE4 (from Day-Lewis et al., 2003, by permission of the American Geophysical Union)

measurements will sample total solute mass, whereas pumped discharge will sample preferentially from the mobile domain.

Day-Lewis et al. (2004) investigated the apparent discrepancies between solute and geophysical data. Conceptual models involving different patterns of heterogeneity and RLMT were proposed as possible explanations, and a suite of corresponding numerical models were calibrated to the hydrologic data. To address the problem of support volume, and to facilitate comparison

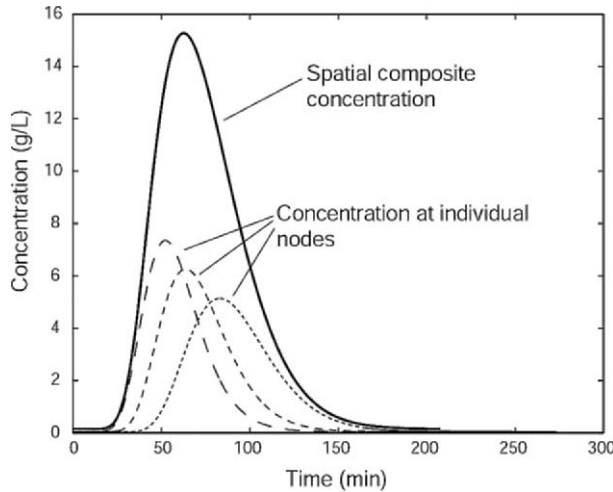


Figure 12. Schematic diagram showing hypothetical tracer concentration BTCs at points on several flow paths, and the spatial composite (sum) BTC (from Day-Lewis et al., 2004)

between the GPR tomograms and tracer concentration, Day-Lewis et al. (2004) proposed an upscaling procedure based on the spatial and temporal averaging described by the model resolution matrix for the inversion. The authors found that simple zonal heterogeneity could divert tracer outside the three-well prism; hence the observed peak in the interwell region might be at the edge of a preferential pathway, and tracer could move to the outlet along a faster path unseen by the GPR.

5.4.3. SOLUTE TRANSPORT IN THE UNSATURATED ZONE

5.4.3.1. Overview

As illustrated earlier, time-lapse electrical conductivity (or resistivity) imaging can be used to infer pathways of solutes in saturated aquifers; however, in the vadose zone changes in moisture content will also affect electrical conductivity (EC). This is particularly important in vadose zone tracer studies as moisture contents may change significantly as the plume evolves, and the water front may advance the tracer front due to redistribution of “old” pore water in the system. These effects must be removed in order to determine the solute pathway. Since the dielectric constant is not affected by changes in solute concentration, any redistribution of water mass may be determined using cross-borehole GPR. Radar may also be used to determine changes in signal attenuation, and hence EC (see, e.g. Chang et al., 2004); however, estimates of conductivity in this way are often subject to high uncertainty. Time-lapse ERT provides a more reliable means of determining conductivity changes and, when combined with radar surveys, the evolution of a solute plume in the unsaturated zone may be assessed.

There are few examples in the literature of vadose zone solute transport investigations using hydrogeophysical methods. Most hydrogeophysical vadose zone studies have concentrated on mapping moisture content (see, e.g. Chapter 4 of this volume and Daniels et al., 2005). In some cases the migration of saline tracers has been tracked using ERT to infer flow pathways, particularly where residual moisture content is high (e.g. Slater et al., 1997b; Zaidman et al., 1999). ERT has also been used effectively by Ramirez et al. (1996) to monitor leakage into the vadose zone from underground storage tanks (see also Daily et al., 2004, for further developments of this work). French et al. (2002) (see also Chapter 7 of this volume) monitored, using ERT, the movement of a bromide tracer in the unsaturated zone to determine likely travel times of contaminants following snowmelt. Hagrey and Michaelsen (1999) also studied the role of preferential pathways in the shallow vadose zone, in their case using surface ERT to map changes in resistivity following injection of a saline tracer. Using Mise-à-la-masse and self-potential measurements, Nimmer and Osiensky (2002) attempted to delineate a saline tracer injected

into unsaturated fractured rock. Hall et al. (2004) demonstrate how EM logging may be used to track saline tracers in the vadose zone.

The contrast in EC, due to saline tracer injection, has been the focus of much of the past work on solute transport in the unsaturated zone using hydrogeophysics. In most cases, however, the effect on EC due to changes in moisture content has been neglected. In the example below we illustrate how combined radar and resistivity surveys may be utilized to address this.

5.4.3.2. Selected Example Hatfield Site, UK

Here, we illustrate combined time-lapse ERT and GPR imaging in an application to a sandstone site in the UK. The site, in Hatfield, South Yorkshire, UK, has been the focus of a number of studies of vadose zone processes using geophysical methods, for example, cross-borehole radar tomography for monitoring changes in moisture content in the unsaturated zone due to natural and forced (tracer) inputs (Binley et al., 2001); the evaluation of seasonal variation of moisture content profiles using high-resolution borehole resistivity and radar profiling (Binley et al., 2002a); attempts to utilize the geophysical data to develop numerical predictive models of unsaturated flow (Binley et al., 2002b); and development of petrophysical models relating geophysical data to hydrological properties (West et al., 2003).

In 1998, a number of boreholes were drilled at the Hatfield site, six of which were developed for monitoring tracer migration in the sandstone (see Figure 13). Four of these boreholes were designed for cross-borehole resistivity measurements and two were developed for cross-borehole radar acquisition. In addition, a shallow borehole was installed to allow injection of tracers between a depth of 3 and 3.5 m below ground level, i.e., directly

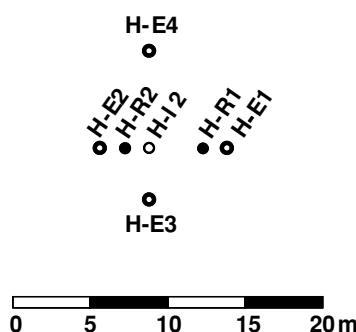


Figure 13. Layout of the tracer array boreholes at the Hatfield site. H-E1, H-E2, H-E3, and H-E4 are electrode array boreholes (each contains sixteen stainless steel mesh electrodes equally spaced between 2 and 13 m depth); H-R1 and H-R2 are cased to 12 m with 75 mm PVC casing for borehole radar acquisition; H-I2 is a shallow borehole for injection of tracer into the sandstone between 3 and 3.5 m depth. The water table at the site is typically 10 to 12 m below ground level

into the sandstone. Cores extracted from the site and geophysical logs (natural gamma and EM induction) show evidence of layers of fine sandstone/siltstone at depths of 6 m and 9 m. These layers may act as local flow-impeding layers and may thus affect the vertical transport of solutes (e.g. from agrochemicals applied on the ground surface).

During March 2003, 1,200 liters of a saline tracer (conductivity 2200 $\mu\text{S}/\text{cm}$) were injected into the sandstone using borehole H-I2, and changes in bulk resistivity and dielectric constant of the sandstone were then monitored using GPR and ERT. The tracer was injected over a period of three days, from 14th March 2003 to 17th March 2003 at a steady rate of approximately 17 liters per hour.

ERT data were collected using a six-channel Geoserve Resecs instrument with current and potential electrode pairs chosen so that one of the electrodes in each dipole was in one borehole, and the other being in any of the remaining three boreholes. A total of 6,372 measurements were made in this manner (acquisition time was approximately two and a half hours) for each “snapshot.” Reciprocal data (i.e., current and potential electrodes swapped) were collected to assess error level; a maximum of 3,186 measurements were used for data inversion. Inversion of the data in order to produce a 3-D resistivity image was based on a regularized least squares algorithm.

Using boreholes H-R1 and H-R2 (see Figure 13), transmission radar data were collected in multiple offset gathers (MOG) using a Sensors and Software PulseEKKO PE100 system with 100 MHz antennas. The MOG surveys carried out used transmitter locations at 1 m increments between depths of 1 m and 10 m in H-R1, with receiver positions at 0.25 m increments between 1 m and 10 m depth in H-R2. MOG data were inverted using the MIGRATOM code (Jackson and Tweeton, 1994) to produce an image of dielectric constant between H-R1 and H-R2.

The changes in resistivity, relative to pre-tracer conditions, at four times are shown in Figure 14. The images show clearly the vertical migration of the tracer and evidence of lateral spreading of pore fluid between 8 and 9 m depth (due to existence of lower permeability layers). The observed resistivity changes are due to changes in pore water salinity (new water) and redistribution of moisture (old water).

In order to determine the extent to which the added tracer has migrated through the profile we must remove the effect of changes in moisture content from the resistivity signal. If we assume that bulk conductivity, σ_b , (inverse of bulk resistivity) varies with moisture content (θ) and water conductivity (σ_w) according to Equation (10) (Archie’s Law), and water conductivity in turn is linearly related to solute concentration (C) (Eq. (11)), then, in each parameter cell of the ERT image, the ratio of bulk conductivity at time t to the pre-tracer bulk conductivity at time t_0 is given by Equation (12).

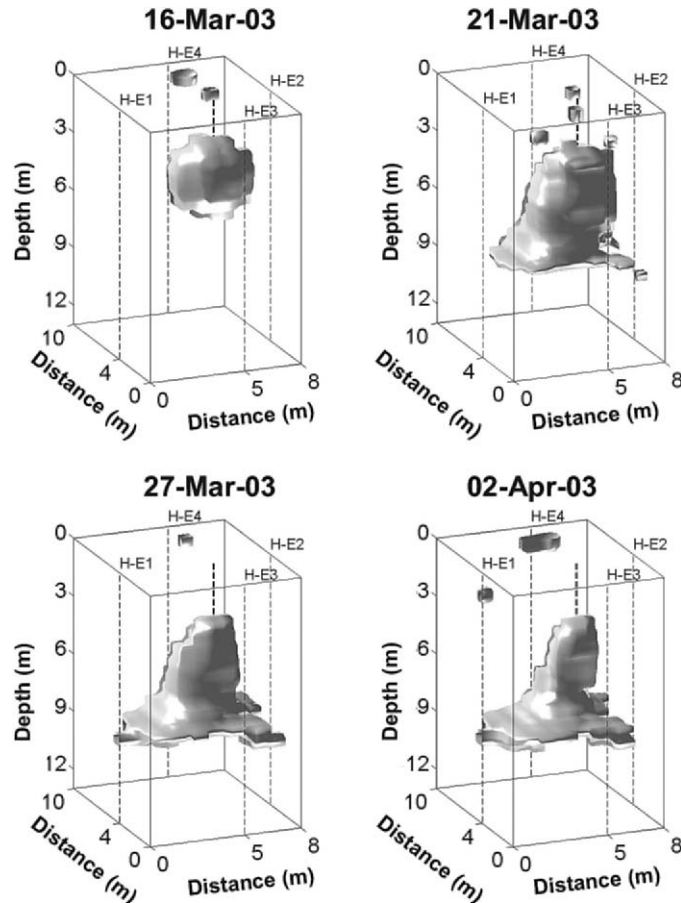


Figure 14. Changes in resistivity during tracer test at the Hatfield site shown as isosurfaces of 7.5% reduction in resistivity relative to pre-tracer conditions. Shading is used to illustrate the shape of the moisture bulb that develops during the test

In the plane of the boreholes H-R1 and H-R2 the moisture content may be determined allowing Equation (12) to be utilized to compute changes in pore water salinity. The 2-D radar tomogram provides images of bulk dielectric constant (κ_b). We here used the complex refractive index method (CRIM) (Eq. (14)) to relate the bulk dielectric constant to moisture content. Combining equations (12) and (14) gives an expression for the solute concentration at time t relative to the background (pre-tracer) levels at time t_0 (Eq. 16). West et al. (2003) carried out measurements of dielectric properties at different levels of water saturation in core samples extracted from the site. Based on these measurements we assumed here that $\kappa_m = 5$ and $\phi = 0.32$. Moreover

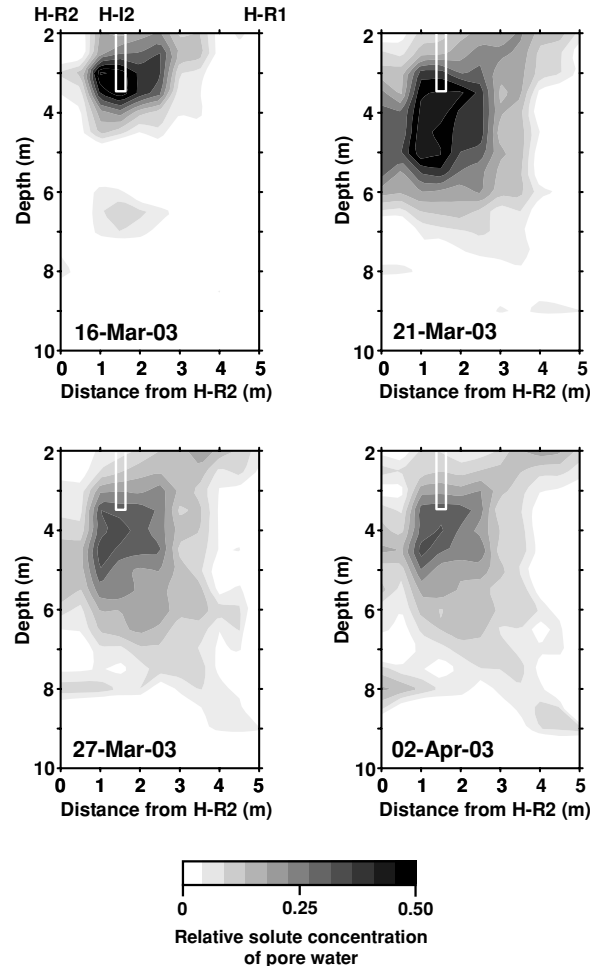


Figure 15. Changes in pore water solute concentration during the tracer test at the Hatfield site, inferred from radar and resistivity images

we assumed a value of $n = 1.13$ (Binley et al., 2002a).

$$\frac{C(t)}{C(t_0)} = \frac{\sigma_b(t)}{\sigma_b(t_0)} \left(\frac{\sqrt{\kappa_b(t_0)} + \phi(\sqrt{\kappa_m} - \sqrt{\kappa_a}) - \sqrt{\kappa_m}}{\sqrt{\kappa_b(t)} + \phi(\sqrt{\kappa_m} - \sqrt{\kappa_a}) - \sqrt{\kappa_m}} \right)^n. \quad (16)$$

The conductivity quotients $\sigma_b(t)/\sigma_b(t_0)$ were interpolated from the ERT images onto the vertical plane between radar boreholes H-R1 and H-R2. Then, using changes in dielectric constant obtained from the radar tomograms, changes in pore water solute concentrations relative to pre-tracer conditions were computed on a pixel by pixel basis according to Equation (16). The results for selected times are shown in Figure 15. By comparing with the bulk

resistivity response in Figure 14 it is apparent that a moisture front advances the solute plume, i.e., the addition of the tracer displaces pre-tracer pore fluid, which moves vertically ahead of the added saline water. Early transport of the tracer is relatively rapid to a depth of 6 m, at which point vertical transport is impeded (probably due to a fine grained horizon at this depth). We note that the diagonal feature at greater depths apparent in the lower (i.e., advanced time) panels of Figure 15 could be artifacts, which are characteristic in ray tracing tomography (such as that used here for analysis of the GPR signals).

Equation (16) is subject to errors from a number of sources: (i) errors in the petrophysical model, (ii) non-uniqueness in the geophysical inversions, (iii) poor resolution and lack of sensor sensitivity in the geophysical methods, and (iv) contrasting measurement support volumes of the two geophysical modalities. The apparent upward migration of the tracer (see Figure 15), for example, is clearly erroneous. Nevertheless, this analysis offers some insight into solute transport processes in the unsaturated zone that could not have been achieved without joint application of radar and resistivity. Such an approach is unlikely to offer a reliable means of determining solute transport dispersion coefficients but may offer a means of estimating pore water velocities in unsaturated soils.

5.5. Concluding Remarks

As demonstrated by the field examples presented in the previous section, geophysical imaging methods offer enormous potential for the characterization of subsurface solute transport processes in different geologic environments. High-resolution images of solute concentration distributions can be obtained, and their change with time monitored if the methods are applied in a time-lapse manner. By integrating geophysically derived solute data with transport models, quantitative information on transport properties can be derived.

The interpretation of electrical resistivity or dielectric permittivity (i.e., the parameters measured in electrical/EM and GPR surveys) depends on petrophysical models relating geophysical data to solute concentration. As mentioned in Section 5.3.2, there exists no readily available relationship between solute concentration and measured bulk electrical conductivity if electric surface conduction along mineral-fluid interfaces exists; thus in many geologic environments, bulk electrical conductivity can not be considered a reliable surrogate for concentration and the application of transport models for quantitative analysis is not possible. To overcome this problem, new approaches are needed to discriminate lithology from water content and/or salinity effects in the measured geophysical data. This might be accomplished by jointly applying different geophysical methods, each sensitive to a different property,

to resolve the ambiguity involved in interpreting a single data type. As for electrical data, a promising approach in this respect is the measurement of induced polarization (IP) (see, e.g. Kemna et al., 2004b), as a complement to standard resistivity. IP measurements offer the potential for an improved characterization of porous rocks (see, e.g. Lesmes and Friedman, 2005), which can be expected to help in reducing ambiguities in the observed geophysical response with respect to texture, mineralogy, and fluid chemistry on the basis of improved petrophysical models.

Hydrogeophysical studies rely on petrophysical relationships to translate geophysical images into cross-sections, maps, or volumes of solute concentration or other parameters of hydrologic interest. Commonly, petrophysical relations are derived empirically in the lab or at boreholes where co-located geophysical and hydrologic measurements are available. That such petrophysical relations apply uniformly over tomograms is a critical assumption implicit in many hydrogeophysical studies. This assumption has been called into question, given that tomograms are the products of regularized inverse problems, and therefore blunted and blurry versions of reality. Section 5.3.3 reviewed recent, first attempts at modeling and accounting for tomographic resolution in hydrogeophysical estimation; however, the behavior of these relationships under the imaging process, as well as their effect on overall error propagation remain important topics for future work.

Closely related to the issue of resolution limitations is the general scaling behavior of both hydrologic and geophysical parameters. Hydrogeophysical studies commonly combine data and/or petrophysical relations from multiple scales. For example, empirical or theoretically derived petrophysical relations defined at a small (e.g. core) scale, are used to convert geophysical properties estimated at a second, larger scale (e.g. cross-hole), to define hydrologic transport parameters for modeling at a third, larger scale. However, it is well known that hydraulic and transport properties are scale-dependent quantities (e.g. Neuman, 1990; Yeh, 1998; Russo, 1998; and Beckie, 1998). The applicability of core-scale relationships at larger scales where effective properties are determined in field applications remains an open question. Additional research is needed to develop frameworks to integrate geophysical and hydrologic data defined for different scales.

The most important aspect in hydrogeophysical approaches is the integration of geophysical methods and hydrological models. In this chapter we presented examples where estimated geophysical images were used to infer parameters of equivalent transport models, such as equivalent advection velocities and longitudinal dispersivities of a stream tube model. Here geophysical imaging, hydrologic-geophysical parameter conversion, and inverse transport parameter determination represented separate steps. Conceptually it is straightforward to merge all three steps into a single procedure, with the

obvious advantage that in such an approach, parameter estimation would be directly controlled from a structure or process point of view. A priori knowledge on structure or process characteristics, as well as any additionally available hydrological data, may then be easily incorporated to constrain the overall hydrogeophysical inversion process.

Very promising in the latter regard are stochastic inverse frameworks based on geostatistical concepts, which offer great flexibility for the incorporation of different types of data (geophysical, hydrological) and model parameter constraints. These methods constrain the inversion procedure using spatial covariance functions that characterize the spatial structure of the inverted variable field. Kitanidis (1999) showed that the smoothness constraint commonly used to regularize the ERT inverse problem is identical to a specific spatial covariance function used in the geostatistically based inverse formulation. Therefore, the geostatistically based approach offers the possibility to include a priori information about the structure of the medium through spatial covariance functions. It also provides a framework to incorporate additional information about local-scale geophysical and hydrological data in the inversion process. Yeh et al. (2002) and Liu and Yeh (2004) demonstrated the use of such an approach, based on sequential linear estimation, for the inversion of ERT data. More details on approaches for the integration of geophysical and hydrological data, and the use of geostatistically based inversion schemes for hydrogeophysical purposes can be found in Chapters 2 and 3, respectively, of this volume.

With this chapter we intended to give an overview of the state of the art of the characterization of subsurface solute transport processes using hydrogeophysical methods. By (i) reviewing underlying concepts and physics, such as hydrogeophysical parameter relationships and hydrogeophysical imaging, and (ii) presenting a variety of field applications in different geologic environments, we hoped to provide the reader with a fair idea about the potential, current limitations, and future challenges in this field. Given the rapid development in hydrogeophysics, as documented by this book, this chapter undoubtedly represents only a snapshot in the evolution of hydrogeophysical methods and approaches for reliable characterization of subsurface transport processes. Future advances will undoubtedly lead to a better understanding of these processes in different hydrogeological settings.

References

Acworth, R.I., and G.R. Dasey, 2003. Mapping of the hyporheic zone around a tidal creek using a combination of borehole logging, borehole electrical tomography and cross-creek electrical imaging, New South Wales, Australia, *Hydrogeol. J.*, 11, 368–377.

Alumbaugh, D.L., and G.A. Newman, 2000. Image appraisal for 2-D and 3-D electromagnetic inversion, *Geophysics*, 65, 1455–1467.

Alumbaugh, D., P.Y. Chang, L. Paprocki, J.R. Brainard, R.J. Glass, and C.A. Rautman, 2002. Estimating moisture contents in the vadose zone using cross-borehole ground penetrating radar: A study of accuracy and repeatability, *Water Resour. Res.*, 38, 1309, 12 p., Doi: 10.1029/2001WR000754.

Archie, G.E., 1942. The electrical resistivity log as an aid in determining some reservoir characteristics, *Trans. Am. Inst. Min. Metall. Eng.*, 146, 54–62.

Bear, J., 1972. *Dynamics of Fluids in Porous Media*, Elsevier, New York.

Beckie, J., 1998. Analysis of scale effects in large-scale solute transport models, in *Scale Dependence and Scale Invariance in Hydrology*, edited by G. Sposito, Cambridge University Press, Cambridge, UK, pp. 314–334.

Bellin, A., and Y. Rubin, 2004. On the use of peak concentration arrival times for the inference of hydrogeological parameters, *Water Resour. Res.*, 40, W07401, 13 p., Doi: 10.1029/2003WR002179.

Bevc, D., and H.F. Morrison, 1991. Borehole-to-surface electrical resistivity monitoring of a salt water injection experiment, *Geophysics*, 56, 769–777.

Binley, A., S. Henry-Poulter, and B. Shaw, 1996. Examination of solute transport in an undisturbed soil column using electrical resistance tomography, *Water Resour. Res.*, 32, 763–769.

Binley, A., P. Winship, R. Middleton, M. Pokar, and J. West, 2001. High resolution characterization of vadose zone dynamics using cross-borehole radar, *Water Resour. Res.*, 37, 2639–2652.

Binley, A., P. Winship, L.J. West, M. Pokar, and R. Middleton, 2002a. Seasonal variation of moisture content in unsaturated sandstone inferred from borehole radar and resistivity profiles, *J. Hydrol.*, 267, 160–172.

Binley, A., G. Cassiani, R. Middleton, and P. Winship, 2002b. Vadose zone flow model parameterisation using cross-borehole radar and resistivity imaging, *J. Hydrol.*, 267, 147–159.

Binley, A., and A. Kemna, 2005. DC resistivity and induced polarization methods, in *Hydrogeophysics*, edited by Y. Rubin and S.S. Hubbard, Springer, Dordrecht, pp. 129–156.

Brovelli, A., G. Cassiani, E. Dalla, F. Bergamini, D. Pitea, and A.M. Binley, 2005. Electrical properties of partially saturated sandstones: Novel computational approach with hydrogeophysical applications, *Water Resour. Res.*, 41, W08411, 12 p., Doi/10.1029/2004WR003628.

Butler, D.K. (ed), 2005. *Near-Surface Geophysics*, Investigations in Geophysics, Vol. 13, Society of Exploration Geophysicists, Tulsa, OK.

Chang, P.-Y., D. Alumbaugh, J. Brainard, and L. Hall, 2004. The application of ground penetrating radar attenuation tomography in a vadose zone infiltration experiment, *J. Contam. Hydrol.*, 71, 67–87.

Cirpka, O.A., and P.K. Kitanidis, 2000. Characterization of mixing and dilution in heterogeneous aquifers by means of local temporal moments, *Water Resour. Res.*, 36, 1221–1236.

Dagan, G., 1989. *Flow and Transport in Porous Formations*, Springer, Berlin.

Daily, W.D., A.L. Ramirez, D.J. LaBrecque, and J. Nitao, 1992. Electrical resistivity tomography of vadose water movement, *Water Resour. Res.*, 28, 1429–1442.

Daily, W., A. Ramirez, and A. Binley, 2004. Remote monitoring of leaks in storage tanks using electrical resistance tomography: Application at the Hanford site, *J. Environ. Eng. Geophys.*, 9, 11–24.

Daily, W., A. Ramirez, A. Binley, and D. LaBrecque, 2005. Electrical resistance tomography – theory and practice, in *Near-Surface Geophysics*, Investigations in Geophysics, Vol.

13, edited by D.K. Butler, Society of Exploration Geophysicists, Tulsa, OK, pp. 525–550.

Daniels, J.J., B. Allred, A. Binley, D. LaBrecque, and D. Alumbaugh, 2005. Hydrogeophysical case studies in the vadose zone, in *Hydrogeophysics*, edited by Y. Rubin and S.S. Hubbard, Springer, Dordrecht, pp. 413–440.

Day-Lewis, F.D., P.A. Hsieh, and S.M. Gorelick, 2000. Identifying fracture-zone geometry using simulated annealing and hydraulic-connection data, *Water Resour. Res.*, 36, 1707–1721.

Day-Lewis, F.D., J.M. Harris, and S.M. Gorelick, 2002. Time-lapse inversion of crosswell radar data, *Geophysics*, 67, 1740–1752.

Day-Lewis, F.D., J.W. Lane, Jr., J.M. Harris, and S.M. Gorelick, 2003. Time-lapse imaging of saline-tracer transport in fractured rock using difference-attenuation radar tomography, *Water Resour. Res.*, 39, 1290, 14 p., Doi: 10.1029/2002WR001722.

Day-Lewis, F.D., J.W. Lane, Jr., and S.M. Gorelick, 2004. Combined interpretation of radar, hydraulic and tracer data from a fractured-rock aquifer, *Hydrogeol. J.*, 14, 1–14. Doi: 10.1007/s10040-004-0372-y,

Day-Lewis, F.D., K. Singha, and A.M. Binley, 2005. Applying petrophysical models to radar traveltimes and electrical resistivity tomograms: Resolution-dependent limitations, *J. Geophys. Res.*, B08206, 17 p., Doi: 10.1029/2004JB005369.

de Marsily, G., F. Delay, J. Goncalves, P. Renard, V. Teles, and S. Violette, 2005. Dealing with spatial heterogeneity, *Hydrogeol. J.*, 13, 161–183, Doi: 10.1007/s10040-004-0432-3.

Ellefsen, K.J., P.A. Hsieh, and A.M. Shapiro, 2002. Crosswell seismic investigation of hydraulically conductive, fractured bedrock near Mirror Lake, New Hampshire, *J. Appl. Geophys.*, 50, 299–317.

Fetter, C.W., 2001. *Applied Hydrogeology*, 4th Ed., Prentice-Hall, New York.

Feyen, J., D. Jacques, A. Timmerman, and J. Vanderborgh, 1998. Modelling water flow and solute transport in heterogeneous soils: A review of recent approaches, *J. Agric. Eng. Res.*, 70, 231–256.

French, H.K., C. Hardbattle, A. Binley, P. Winship, and L. Jakobsen, 2002. Monitoring snowmelt induced unsaturated flow and transport using electrical resistivity tomography, *J. Hydrol.*, 267, 273–284.

Gelhar, L.W., C. Welty, and K.R. Rehfeldt, 1992. A critical review of data on field scale dispersion in aquifers, *Water Resour. Res.*, 28, 1955–1974.

Gelhar, L.W., 1993. *Stochastic Subsurface Hydrology*, Prentice-Hall, Englewood Cliffs, NJ.

Gerke, H.H., and M.T. van Genuchten, 1993. A dual-porosity model for simulating preferential movement of water and solutes in structured porous media, *Water Resour. Res.*, 29, 305–319.

Goldman, M., D. Gilard, A. Ronen, and A. Melloul, 1991. Mapping of seawater intrusion into the coastal aquifer of Israel by the time-domain electromagnetic method, *Geoexploration*, 28, 153–174.

Goldstein, N.E., S.M. Benson, and D. Alumbaugh, 1990. Saline groundwater plume mapping with electromagnetics, in *Geotechnical and Environmental Geophysics*, Vol. II – Environmental and Groundwater, *Investigations in Geophysics*, Vol. 5, edited by S.H. Ward, Society of Exploration Geophysicists, Tulsa, OK, pp. 17–25.

Grasmueck, M., 1996. 3-D ground-penetrating radar applied to fracture imaging in gneiss, *Geophysics*, 61, 1050–1064.

Hagemeyer, R.T., and M. Stewart, 1990. Resistivity investigation of salt-water intrusion near a major sea-level canal, in *Geotechnical and Environmental Geophysics*, Vol. II –

Environmental and Groundwater, Investigations in Geophysics, Vol. 5, edited by S.H. Ward, Society of Exploration Geophysicists, Tulsa, OK, pp. 67–77.

Hagrey, S.A. al, and J. Michaelsen, 1999. Resistivity and percolation study of preferential flow in the vadose zone at Bokhorst, Germany, *Geophysics*, 64, 746–753.

Hall, L.M., J.R. Brainard, R.S. Bowman, and J.M.H. Hendrickx, 2004. Determination of solute distributions in the vadose zone using downhole electromagnetic induction, *Vadose Zone J.*, 3, 1207–1214.

Hsieh, P.A., A.M. Shapiro, and C.R. Tiedeman, 1999. Computer simulation of fluid flow in fractured rocks at the Mirror Lake FSE well field, in U.S. Geological Survey Toxic Substances Hydrology Program – Proceedings of the Technical Meeting, Charleston, SC, March 8–12, 1999, Subsurface Contamination from Point Sources, edited by D.W. Morganwalp and H.T. Buxton, U.S. Geological Survey Water-Resources Investigations Report 99-4018C, pp. 777–781.

Hubbard, S.S., J.E. Peterson Jr., E.L. Majer, P.T. Zawislanski, K.H. Williams, J. Roberts, and F. Wobber, 1997. Estimation of permeable pathways and water content using tomographic radar data, *The Leading Edge*, 16, 1623–1628.

Huisman, J.A., S.S. Hubbard, J.D. Redman, and J.P. Annan, 2003. Measuring soil water content with ground penetrating radar: A review, *Vadose Zone J.*, 2, 476–491.

Hyndman, D., and J. Tronicke, 2005. Hydrogeophysical case studies at the local scale: The saturated zone, in *Hydrogeophysics*, edited by Y. Rubin and S.S. Hubbard, Springer, Dordrecht, pp. 391–412.

Jackson, M.J., and D.R. Tweeton, 1994. MIGRATOM – Geophysical tomography using wave-front migration and fuzzy constraints, Bureau of Mines Report RI9497, 35p.

Jury, W.A., and H. Flühler, 1992. Transport of chemicals through soil – mechanisms, models, and field applications, *Adv. Agron.*, 47, 141–201.

Kemna, A., J. Vanderborght, B. Kulessa, and H. Vereecken, 2002. Imaging and characterisation of subsurface solute transport using electrical resistivity tomography (ERT) and equivalent transport models, *J. Hydrol.*, 267, 125–146.

Kemna, A., J. Vanderborght, K. Borgers, K. Gößling, A. Verweerd, A. Englert, K. Müller, and H. Vereecken, 2004a. Monitoring tracer experiments at the Krauthausen test site using time-lapse ERT, Extended Abstract Book “Near Surface 2004” – 10th European Meeting of Environmental and Engineering Geophysics, Eur. Assoc. Geosci. Eng., P007, 4 p.

Kemna, A., A. Binley, and L. Slater, 2004b. Crosshole IP imaging for engineering and environmental applications, *Geophysics*, 69, 97–107.

Kitanidis, P.K., 1999. Generalized covariance functions associated with the Laplace equation and their use in interpolation and inverse problems, *Water Resour. Res.*, 35, 1361–1367.

LaBrecque, D.J., and X. Yang, 2001. Difference inversion of ERT data: A fast inversion method for 3D in situ monitoring, *J. Environ. Eng. Geophys.*, 5, 83–90.

Lane, J.W., Jr., F.P. Haeni, and W.M. Watson, 1995. Use of a square-array direct-current resistivity method to detect fractures in crystalline bedrock in New Hampshire, *Ground Water*, 33, 476–485.

Lane, J.W., Jr., F.P. Haeni, and R. Versteeg, 1998a. Use of multi-offset borehole-radar reflection method in fractured crystalline bedrock at Mirror Lake, Grafton County, New Hampshire, in *Symposium on the Application of Geophysics to Engineering and Environmental Problems*, March 22–26, 1998, Chicago, IL, Proceedings, Wheat Ridge, CO, Environmental and Engineering Geophysical Society, pp. 359–368.

Lane, J.W., Jr., F.P. Haeni, and F.D. Day-Lewis, 1998b. Use of time-lapse attenuation-difference radar tomography methods to monitor saline tracer transport in fractured crystalline bedrock, in *7th International Conference on Ground-Penetrating Radar (GPR’98)*,

Lawrence, KS, May 27–30, 1998, Proceedings, Lawrence, KS, University of Kansas, pp. 533–538.

Lane, J.W., Jr., F.D. Day-Lewis, J.M. Harris, F.P. Haeni, and S.M. Gorelick, 2000. Attenuation-difference radar tomography: Results of a multiple-plan experiment at the U.S. Geological Survey fractured rock research site, Mirror Lake, New Hampshire, in GPR 2000 – Proceedings of the 8th International Conference on Ground Penetrating Radar, edited by D.A. Noon, G.F. Stickley, and D. Longstaff, University of Queensland, Queensland, Australia, pp. 666–675.

Lesmes, D.P., and S.P. Friedman, 2005. Relationships between the electrical and hydrogeological properties of rocks and soils, in Hydrogeophysics, edited by Y. Rubin and S.S. Hubbard, Springer, Dordrecht, pp. 87–128.

Lieblich, D.A., J.W. Lane Jr., and F.P. Haeni, 1991. Results of integrated surface-geophysical studies for shallow subsurface fracture detection at three New Hampshire sites, in Expanded Abstracts with Biographies, SEG 61st Annual International Meeting, Houston, TX, November 10–14, 1991, Society of Exploration Geophysicists, pp. 553–556.

Liu, S., and T.-C.J. Yeh, 2004. An integrative approach for monitoring water movement in the vadose zone, *Vadose Zone J.*, 3, 681–692.

Merrick, N.P., 1997. An experiment in geophysical monitoring of a contaminated site, in *Groundwater in the Urban Environment – Problems, Processes and Management*, edited by J. Chilton, Balkema, Rotterdam, The Netherlands, pp. 487–490.

Morris, M., J.S. Rønning, and O.B. Lile, 1996. Geoelectric monitoring of a tracer injection experiment: Modeling and interpretation, *Eur. J. Environ. Eng. Geophys.*, 1, 15–34.

Moysey, S., K. Singha, and R. Knight, 2005. Inferring field-scale rock physics relations through numerical simulation, *Geophys. Res. Lett.*, 32, L08304, 4 p., Doi: 10.1029/2004GL022152.

Müller, I., 1983. Anisotropic properties of rocks detected with electromagnetic VLF (very low frequency), in Proceedings of the International Symposium on Field Measurements in Geomechanics, Zürich, Sept. 1983, Special Publication, pp. 273–282.

Müller, K., J. Vanderborght, A. Englert, A. Kemna, and H. Vereecken, 2005. Characterization of transport processes in a heterogeneous aquifer using electrical resistivity tomography (ERT), in Bringing Groundwater Quality Research to the Watershed Scale, Proceedings of GQ2004, 4th International Groundwater Quality Conference, held at Waterloo, Canada, July 2004, IAHS Publication, Vol. 297, pp. 182–190.

Neuman, S.P., 1987. Stochastic continuum representation of fractured rock permeability as an alternative to the REV and fracture network concepts, in Proceedings of the 28th US Symposium on Rock Mechanics, New York, American Institute of Minerals, Metallic and Petroleum Engineering, pp. 533–561.

Neuman, S.P., 1990. Universal scaling of hydraulic conductivities and dispersivities in geologic media, *Water Resour. Res.*, 26, 1749–1758.

Nimmer, R.E., and J.L. Osiensky, 2002. Direct current and self potential monitoring of an evolving plume in partially saturated fractured rock, *J. Hydrol.*, 267, 258–272.

Niva, B., O. Olsson, and P. Blumlung, 1988. Grimsel test site: Radar crosshole tomography with application to migration of saline tracer through fracture zones, TR88-31, Swedish Geological Co., Uppsala, Sweden.

Nix, B., 2005. Radiomagnetotellurik-Messungen zur räumlichen und zeitlichen Ausbreitung eines Grundwasser-Tracers. Diploma thesis, Institute of Geophysics and Meteorology, University of Cologne.

Nix, B., B. Tezkan, K. Müller, and A. Kemna, 2005. Monitoring of a groundwater tracer using radiomagnetotellurics (RMT): Extended Abstracts “Near Surface 2005” – 11th European

Meeting of Environmental and Engineering Geophysics, Eur. Assoc. Geosci. Eng., A014, 4 p.

Nobes, D.C., 1996. Troubled waters: Environmental applications of electrical and electromagnetic methods, *Surv. Geophys.*, 17, 393–454.

Olsson, O., P. Anderson, and E. Gustafsson, 1991. Site characterization and validation – monitoring of saline tracer transport by borehole radar measurements, Final Report, Stripa Project TR91-18, Swedish Nuclear Fuel and Waste Management Co., Stockholm, Sweden.

Olsson, O., L. Falk, O. Forslund, L. Lundmark, and E. Sandberg, 1992. Borehole radar applied to the characterization of hydraulically conductive fracture zones in crystalline rock, *Geophys. Prospect.*, 40, 109–142.

Osiensky, J.L., and P.R. Donaldson, 1995. Electrical flow through an aquifer for contaminant source leak detection and delineation of plume evolution, *J. Hydrol.*, 169, 243–263.

Pellerin, L., 2002. Applications of electrical and electromagnetic methods for environmental and geotechnical investigations, *Surv. Geophys.*, 23, 101–132.

Peterson, J.E., Jr., 2001. Pre-inversion corrections and analysis of radar tomographic data, *J. Environ. Eng. Geophys.*, 6, 1–18.

Ptak, T., M. Piepenbrink, and E. Martac, 2004. Tracer tests for the investigation of heterogeneous porous media and stochastic modelling of flow and transport – a review of some recent developments, *J. Hydrol.*, 294, 122–163.

Ramirez, A.L., and R.J. Lytle, 1986. Investigation of fracture flow paths using alterant geophysical tomography, *Int. J. Rock Mech. Miner. Sci. Geomech. Abstr.*, 23 (2), 165–169.

Ramirez, A., W. Daily, A. Binley, D. LaBrecque, and D. Roelant, 1996. Detection of leaks in underground storage tanks using electrical resistance methods, *J. Environ. Eng. Geophys.*, 1, 189–203.

Rubin, Y., and S. Ezzedine, 1997. The travel time of solutes at the Cape Cod tracer experiment: Data analysis, modeling, and structural parameter inference, *Water Resour. Res.*, 33, 1537–1547.

Rubin, Y., 2003. Applied Stochastic Hydrogeology, Oxford University Press, New York.

Rubin, Y., and S.S. Hubbard (eds), 2005. Hydrogeophysics, Springer, Dordrecht.

Russo, D., 1998. Stochastic modeling of scale-dependent macrodispersion in the vadose zone, in *Scale Dependence and Scale Invariance in Hydrology*, edited by G. Sposito, Cambridge University Press, Cambridge, UK, pp. 266–290.

Schmalholz, J., H. Stoffregen, A. Kemna, and U. Yaramanci, 2004. Imaging of water content distributions inside a lysimeter using GPR tomography, *Vadose Zone J.*, 3, 1106–1115.

Sen, P.N., and P.A. Goode, 1992. Influence of temperature on electrical conductivity shaly sands, *Geophysics*, 57, 89–96.

Shen, L.C., W.C. Savre, J.M. Price, and K. Athavale, 1985. Dielectric properties of reservoir rocks at ultra-high frequencies, *Geophysics*, 50, 692–704.

Simmons, C.S., 1982. A stochastic-convective transport representation of dispersion in one-dimensional porous media systems, *Water Resour. Res.*, 18, 1193–1214.

Singha, K., and S.M. Gorelick, 2005. Saline tracer visualized with three-dimensional electrical resistivity tomography: Field-scale spatial moment analysis, *Water Resour. Res.*, 41, W05023, 17 p., Doi: 10.1029/2004WR003460.

Slater, L., A. Binley, and D. Brown, 1997a. Electrical imaging of fractures using ground-water salinity change, *Ground Water*, 35, 436–442.

Slater, L., M.D. Zaidman, A.M. Binley, and L.J. West, 1997b. Electrical imaging of saline tracer migration for the investigation of unsaturated zone transport mechanisms, *Hydrol. Earth Syst. Sci.*, 1, 291–302.

Slater, L., A. Binley, W.D. Daily, and R. Johnson, 2000. Cross-hole electrical imaging of a controlled saline tracer injection, *J. Appl. Geophys.*, 44, 85–102.

Slater, L.D., and S.K. Sandberg, 2000. Resistivity and induced polarization monitoring of salt transport under natural hydraulic gradients, *Geophysics*, 65, 408–420.

Slater, L., A. Binley, R. Versteeg, G. Cassiani, R. Birken, and S. Sandberg, 2002. A 3D ERT study of solute transport in a large experimental tank, *J. Appl. Geophys.*, 49, 211–229.

Tezkan, B., 1999. A review of environmental applications of quasi-stationary electromagnetic techniques, *Surv. Geophys.*, 20, 279–308.

Tiedeman, C.R., D.J. Goode, and P.A. Hsieh, 1998. Characterizing a ground water basin in a New England mountain and valley terrain, *Ground Water*, 36, 611–620.

Todd, D.K., 1980. *Groundwater Hydrology*, 2nd Ed., Wiley, New York.

Topp, G.C., J.L. Davis, and A.P. Annan, 1980. Soil water content: Measurements in coaxial transmission lines, *Water Resour. Res.*, 574–582.

Tsang, Y.W., C.F. Tsang, F.V. Hale, and B. Dverstorp, 1996. Tracer transport in a stochastic continuum model of fractured media, *Water Resour. Res.*, 32, 3077–3092.

Vanclooster, M., M. Javaux, and J. Vanderborght, 2005. Solute transport in soil at the core and field scale, in *Encyclopedia of Hydrological Sciences*, edited by M.G. Anderson, Wiley, New York, pp. 1041–1055.

Vanderborght, J., and H. Vereecken, 2001. Analyses of locally measured bromide breakthrough curves from a natural gradient tracer experiment at Krauthausen, *J. Contam. Hydrol.*, 48, 23–43.

Vanderborght, J., and H. Vereecken, 2002. Estimation of local scale dispersion from local breakthrough curves during a tracer test in a heterogeneous aquifer: The Lagrangian approach, *J. Contam. Hydrol.*, 54, 141–171.

Vanderborght, J., A. Kemna, H. Hardelauf, and H. Vereecken, 2005. Potential of electrical resistivity tomography to infer aquifer transport characteristics from tracer studies: A synthetic case study, *Water Resour. Res.*, 41, W06013, 23 p., Doi: 10.1029/2004WR003774.

Vereecken, H., U. Döring, H. Hardelauf, U. Jaekel, U. Hashagen, O. Neuendorf, H. Schwarze, and R. Seidemann, 2000. Analysis of solute transport in a heterogeneous aquifer: The Krauthausen field experiment, *J. Contam. Hydrol.*, 45, 329–358.

Vereecken, H., U. Yaramanci, and A. Kemna (eds), 2002. *Non-invasive Methods in Hydrology*, *J. Hydrol.*, Special Issue, 267/3-4, 175 p.

Vereecken, H., A. Kemna, H.-M. Münch, A. Tillmann, and A. Verweerd, 2005. Aquifer characterization by geophysical methods, in *Encyclopedia of Hydrological Sciences*, edited by M.G. Anderson, Wiley, New York, pp. 2265–2283.

Ward, S.H. (ed), 1990. *Geotechnical and Environmental Geophysics*, Vol. II – Environmental and Groundwater, *Investigations in Geophysics*, Vol. 5, Society of Exploration Geophysicists, Tulsa, OK.

West, L.J., K. Handley, Y. Huang, and M. Pokar, 2003. Radar frequency dielectric dispersion in sand and sandstone: Implications for determination of moisture content and clay content, *Water Resour. Res.*, 39, 1026, 12 p., Doi: 10.1029/2001WR000923.

White, P.A., 1988. Measurement of ground-water parameters using salt-water injection and surface resistivity, *Ground Water*, 26, 179–186.

Wright, D.L., T.P. Grover, K.J. Ellefsen, J.W. Lane Jr., and P.G. Kase, 1996. Radar tomograms at Mirror Lake, New Hampshire – 3D visualization and a brine tracer experiment, in *Symposium on the Application of Geophysics to Engineering and Environmental Problems*, Keystone, CO, April 28–May 2, 1996, *Proceedings*, edited by R.S. Bell and M.H. Cramer, Environmental and Engineering Geophysical Society, Wheat Ridge, CO, pp. 565–575.

Yeh, T.-C.J., 1998. Scale issues of heterogeneity in vadose-zone hydrology, in *Scale Dependence and Scale Invariance in Hydrology*, edited by G. Sposito, Cambridge University Press, Cambridge, UK, pp. 224–265.

Yeh, T.-C.J., S. Liu, R.J. Glass, K. Baker, J.R. Brainard, D. Alumbaugh, and D. LaBrecque, 2002. A geostatistically based inverse model for electrical resistivity surveys and its application to vadose zone hydrology, *Water Resour. Res.*, 38, 1278, 13 p., Doi: 10.1029/2001WR001204.

Zaidman, M., R.T. Middleton, L.J. West, and A.M. Binley, 1999. Geophysical investigation of unsaturated zone transport in the Chalk in Yorkshire, *Q. J. Eng. Geol.*, 32, 185–198.

Zhang, D.X., 2002. *Stochastic Methods for Flow in Porous Media*, Academic, London.

Zheng, C., and G.D. Bennett, 2002. *Applied Contaminant Transport Modeling*, 2nd Ed., Wiley, New York.

6. BIOGEOPHYSICS: THE EFFECTS OF MICROBIAL PROCESSES ON GEOPHYSICAL PROPERTIES OF THE SHALLOW SUBSURFACE

Estella A. Atekwana, D. Dale Werkema, and Eliot A. Atekwana

6.1. Introduction

The geologic record suggests the presence of microbes on Earth as early as the Precambrian (Hall-Stoodley et al., 2004). Microbes are involved in practically every aspect of earth evolution. The term microbe is a general descriptor for tiny organisms that individually are too small to be seen with the unaided eye. Microbes may include bacteria, archaea, fungi, and protists. Viruses are also included as a major type of microbe, although there is some debate whether viruses can be classified as living organisms. The role microbes play in altering environmental systems is well documented in many biogeochemical studies. Notable is the role of microbes in water-rock interactions (Chapelle and Bradley, 1997). Field observations and laboratory experiments suggest that bacteria can accelerate silicate weathering either by direct contact with minerals or by producing organic and inorganic acids that enhance the dissolution of silicates (Heibert and Bennett, 1992). Thus, microbes are able to directly alter mineral surface chemistry and pore water chemistry over short to geologic time scales. Microbial induced changes in water-rock-regolith environments over variable time scales cause changes in the physical properties of these environments that may be detected and measured using geophysical methodologies.

The reader should take note that we have used the term regolith instead of sediment or soil to distinguish between these terms. As determined from a classical geologic definition we use regolith to describe fragmental and unconsolidated rock derived material, whether residual or transported, and overlies bedrock. This definition includes rock debris of all origins such as volcanic ash, glacial drift, alluvium, loess, vegetal accumulations and soil. In the text, the use of sediment or sediments will refer to the more general term representing solid fragmental material transported and deposited by wind, water or ice, chemically precipitated from solution or secreted by organisms, and forms in layers in loose unconsolidated form. We use the definition of soil as the natural medium for the growth of land plants.

Attempts to understand the role of microbes in altering the physical properties in water-rock environments has resulted in the development of a new sub-discipline in geophysics called biogeophysics, which combines the fields of microbiology, geology, and geophysics. Biogeophysics studies the interaction between microorganisms and subsurface geologic media and possibly the direct geophysical detection of microbes and microbial cell concentrations. Research in this subdiscipline presents a potential for the development and utility of geophysical techniques to measure not only the subsurface physical and chemical properties, as geophysics is conventionally used, but also these properties as related to biological activities, processes, and interactions.

Links between biological processes and changes in geophysical properties were first suggested by Bermejo et al. (1997) and Sauck et al. (1998). Bermejo et al. (1997) and Sauck et al. (1998) documented in field investigations that glacial sediments impacted by petroleum hydrocarbons and undergoing biodegradation developed regions where the bulk electrical conductivity was elevated and ground penetrating radar reflections were attenuated. Since these studies were published, there has been a growing interest in investigating biological interactions with geologic media and the accompanying changes in geophysical properties in both laboratory and field studies. This chapter provides a brief review of how microbial interactions with the geologic media may translate to changes in the bulk physical properties of the subsurface which are potentially measurable by geophysical techniques. The results of select laboratory and field investigations, utilizing mostly electrical and some seismic methods that have been completed in this new field of biogeophysics, are presented.

6.2. Physical Properties and Processes of the Shallow Subsurface Environment Measured by Geophysical Methods

The shallow subsurface environment is affected by both geologic, biologic, chemical, and anthropogenic processes and effects. This environment extends from the surface to depths of tens of meters and contains rocks, regolith, air, and water. Generally, the water saturation profile is used to categorize the shallow subsurface into the vadose, transition, and saturated zones. Biological processes are somewhat dependent on the water saturation profile, and the physical properties of these zones are markedly different. Therefore, the typical physical properties of the vadose, transition, and saturated zones may in part be governed by the microbial ecology.

The physical properties of the shallow subsurface detected by geophysical techniques depend on the mineralogy of the rock or regolith, the type and nature of pore spaces (grain porosity versus fracture porosity) which control the

volume of pore fluids, and the interconnectedness (i.e., permeability) of pores, which control the ability of pore fluids to flow through the material. Additionally, the pores could be occupied entirely by air, water, and solids in different proportions. Unlike air, which may not significantly vary in composition in the subsurface unless organic vapors are present, the chemical composition of the water and solids may vary significantly in both the unsaturated and the saturated zone. Variation in the chemical composition of the water and solids is mostly governed by mineral-water interaction and fate and transport processes.

Understanding the effects of microbial processes on geophysical properties requires knowledge of how the physical properties of the shallow subsurface are changed by microbial processes. Microbial processes may occur at the scale of the cell surface, and thus detectable at variable scale from nanometer to meter scale or greater depending on the extent of microbial alteration of the media. For instance, in the absence of microbial processes, the physical properties of the subsurface environment are mainly related to the physical and electrical character of the geologic media and the chemical and electrical characteristic of the fluids in the media. Add microbes and their metabolic processes, then the interactions between the media, fluid, and microbes become significant. In summary, the important questions to consider in relation to microbial alteration of the subsurface geologic environment are: 1) to what extent do microbial processes alter the solid media and fluids in the geologic environment, 2) to what extent do the microbes themselves alter the physical properties due to the unique properties of the cell surfaces, and 3) which geophysical techniques are sensitive to these microbial dependent alterations.

6.3. Microbial Controls on Subsurface Environments/Processes

6.3.1. DISTRIBUTION OF MICROBES IN THE NEAR SUBSURFACE

Microbe distribution in the near subsurface environment varies and is closely related to substrate, water, and nutrient availability. Substrate is defined as the substance on or in which microorganisms live and grow, or the surface to which a fixed microorganism is attached (e.g. soil, rock, regolith, or leaf tissue). A nutrient is any substance that an organism digests or metabolizes as food for energy. In natural systems, the main substrate utilized by microbes is organic matter (e.g. humic and fulvic acids, organic debris). Subsurface organic matter is generated mainly by plants at the surface making the soil zone rich in organic matter. Below the soil zone, organic matter can be physically transported to deeper depths; however, concentration usually declines with depth. Because of the abundance and diversity of organic matter, the soil zone has large numbers

of microorganisms that range from 10^6 to 10^9 organisms per gram of soil for bacteria and 10^4 to 10^6 organisms per gram of soil for fungi (Balkwill and Boone, 1997; Turco and Sadowsky, 1995). Microbial population numbers decline with depth below the soil zone mirroring the decrease of organic matter with increasing depth. Due to the low abundance of organic carbon substrate in the lower unsaturated and saturated zone, most of the microbes are dormant, although they are viable. This viable population can quickly adapt and grow with the introduction of organic carbon substrate and nutrients.

6.3.2. ENHANCEMENT OF MICROBIAL ACTIVITY IN THE SUBSURFACE

Enhanced microbial activity in the shallow subsurface beneath the soil zone has resulted mainly from anthropogenic activities. Anthropogenic activities supply nutrients and/or organic carbon substrate not readily available at depths greater than the soil zone. For example, agricultural activities release nitrates into the subsurface. With adequate organic carbon substrate, these nitrates can stimulate the growth of microbes. Also, petroleum hydrocarbons (e.g. from surface oil spills, leaking pipelines, or leaking underground storage tanks) supply enormous amounts of carbon in regions of the subsurface that would otherwise be carbon poor. Additionally, landfilling operations alter the subsurface microbial system, because high concentrations of carbon and nutrients are available within landfills. The interaction of landfill leachate and groundwater supplies organic carbon and nutrients to the subsurface.

It is important to note that the supply of nutrients and carbon to the shallow subsurface stimulate microbial growth. The presence of nutrients, carbon, and the microbial growth activity change the natural composition of the solids, liquids, and gases. As a result, the physical and chemical properties of the subsurface environment will move toward a new equilibrium. When sufficient contrast exists between the natural and the disturbed system, it is possible to record these changes using geophysical techniques. For instance, the production of gasses such as N_2 and CH_4 potentially decrease acoustic wave amplitudes (Williams et al., 2004).

6.3.3. IMPACT OF MICROBIAL PROCESSES ON THE GEOPHYSICAL PROPERTIES OF THE SUBSURFACE ENVIRONMENT

The geologic processes responsible for the formation of earth materials (rocks, regolith, sediments, soils, and fluids) in the shallow subsurface occur over several thousands to millions of years. Broadly speaking, even surficial processes such as hydrologic cycling which occur over shorter time scales are somewhat constant or in nearly steady state. Thus, the physical properties of the shallow subsurface are generally characterized by geophysical methods assuming a good understanding of geologic, hydrologic, and chemical

changes that occur naturally in the system. Considering that the distribution and abundance of microbes below the soil zone are minimal, and that the substrate and nutrient availability is nearly constant over time, the geophysical properties of the subsurface rarely change (or change only slowly in human scale time for which measurements are made) due to normal microbial processes. However, if the numbers of microbes in the subsurface increase or microbial communities change due to increased nutrients or organic carbon, their growth and proliferation have the potential to chemically and physically alter the subsurface environment.

6.3.3.1. Bio-Physicochemical Changes Induced in the Rock Environment by Microbial Processes

A schematic representation of the important bio-physicochemical changes induced in the geologic media by microbes is shown in Figure 1. Microbes provided with an organic carbon source and nutrients will grow, proliferate, and develop biofilms. The biofilms grow on the surfaces of the substrate and between pore openings in rocks and sediments which induce physical changes in the rock environment. During microbial growth, consumption of the carbon substrate, utilization of nutrients, and the production of byproducts alter the chemistry of the pore fluids in profound ways (Chapelle and Bradley, 1997). In addition, some of the metabolic byproducts such as carbon dioxide and organic acids chemically interact with the rock or sediment matrix, further altering the chemistry of the pore fluid. The electrical properties of the rock or sediment matrix are also altered because microbes electrically interact with the surfaces of solids. The important aspect of the schematic shown in Figure 1 is that the physical and chemical properties of the subsurface environment can be altered by microbial processes. How the subsurface environment is altered physically, chemically, and geophysically by microbial processes is the subject of much research.

6.3.3.2. Microbial Growth and the Formation of Biofilms

Microbial growth, attachment to mineral surfaces, and formation of biofilms also have the potential to affect the physical, chemical, and electrical properties of the subsurface environment. The nature of this alteration in the subsurface environment by microbes can be examined by how microbial growth interacts with the solid, liquid, and gas phases. Locations in the subsurface conducive for microbial growth are those suitable for duplication and with readily available nutrients and organic substrate. This environment where microbes readily grow can be considered a microenvironment because of its scale (micrometer to nanometer scale) relative to that of the solid surfaces (nanometer to millimeter or larger). Within this microenvironment, microorganisms create a niche consisting of the microorganism, its physical habitat, and the nutrients and substrate required for growth and function. Microorganisms create their

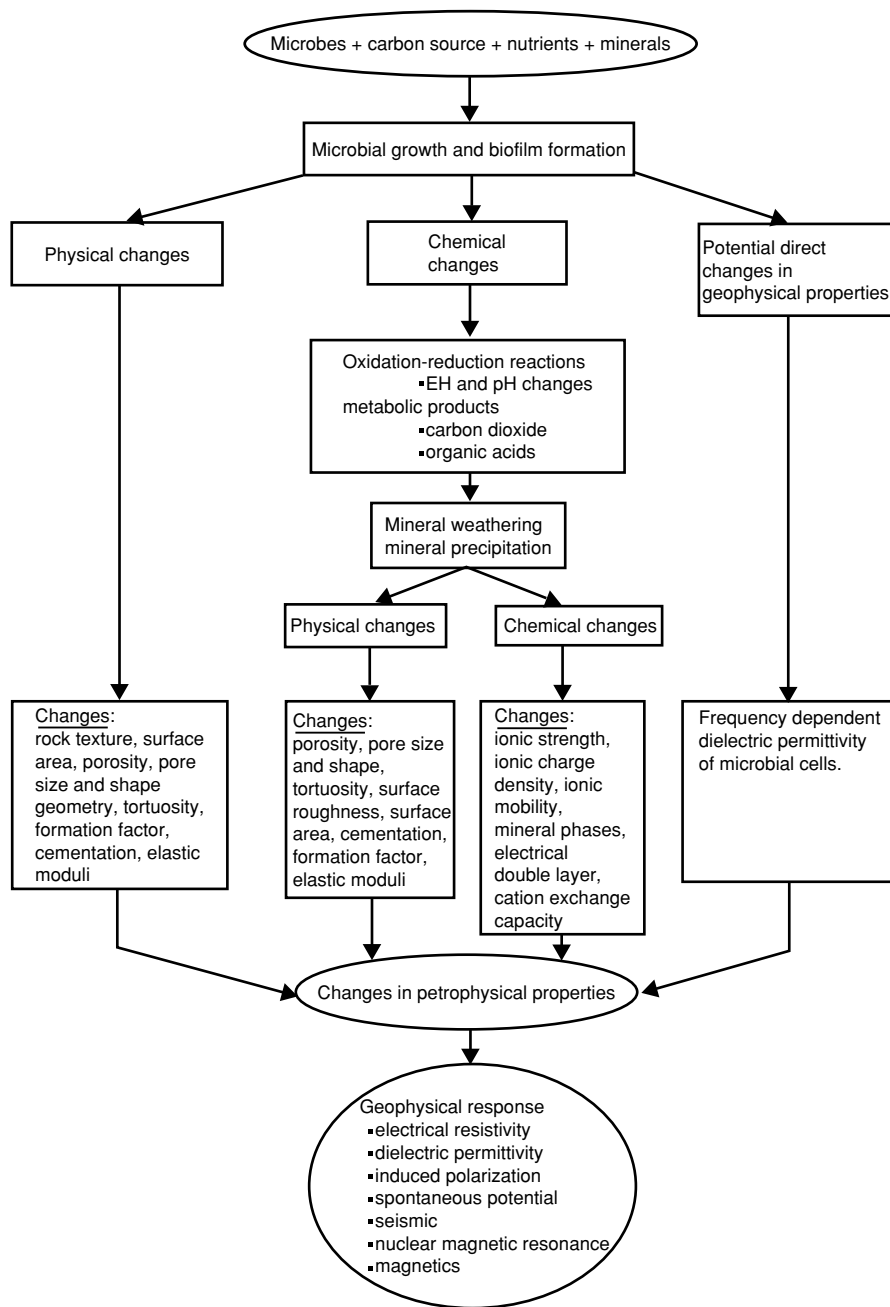


Figure 1. Schematic representation of microbial-mineral interactions and how the resulting changes in the subsurface environment impact different geophysical responses

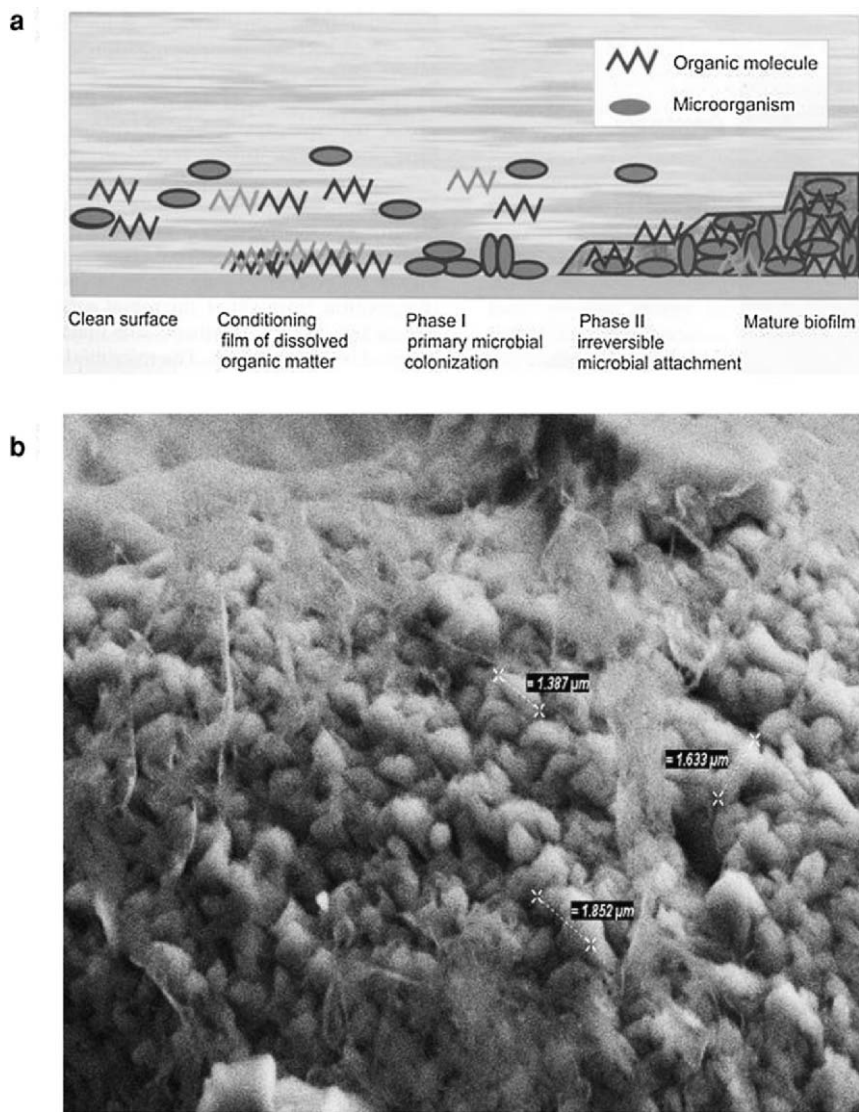


Figure 2. a. Schematic representation of biofilm development and attachment to substrate (Modified & adapted from Marshall, 1992 and Marshall, 1976); b. Environmental scanning electron microscope image of biofilm from a sand column inoculated with mixed microbial culture (Courtesy, C. Davis (unpublished data))

own microenvironments and niches by forming biofilms. Biofilms are organized microbial systems consisting of microbial cells, microbial by-products, nutrients, substrates, and solid surfaces (Marshall, 1992). Biofilms are created by the attachment, growth, and proliferation of microorganisms on the surfaces of minerals (Figures 2a and b). Attachment of microbes to mineral

surfaces is governed by the hydrophobicity of the solid surface usually controlled by organic molecules attached to the surface, electrostatic interaction, and van der Waals forces. For more information on biofilms and microbial growth on solid surface, the interested reader can consult additional research findings (Marshall, 1985; van Loosdrecht et al., 1990; Wolfaardt et al., 1994).

Biofilm formation requires the irreversible attachment of microbes to solid surfaces. Irreversible attachment occurs through the secretion of extracellular polymers that provide a strong bond to the solid surface that creates a matrix which surrounds the cells and forms the internal architecture of microbial communities. The initial formation of biofilms can be a simple form with a single layer of cells. Biofilms mature by continuous proliferation and growth of the attached cells and by continuous deposition of new cells from the fluid surrounding the surface. In more mature systems, biofilms have a complex internal architecture consisting of several layers of cell aggregates, interstitial pores, and conduits in a three dimensional network (Figure 2). Biofilm development provides the microbial community with the means to filter and collect essential nutrients. In addition, it protects the community from abiotic environmental stresses such as temperature fluctuations, drastic pH changes in the pore fluids, and from predation by protozoans. In environmental settings with altered physicochemical conditions or alteration of biofilm conditions, gene expressions that are beneficial to the microbial community adaptation are easily transferred within the biofilm community (Goodman and Marshall, 1995).

6.3.3.3. Physical Changes in the Subsurface Environment Resulting from Microbial Growth

During microbial growth and biofilm formation, the pore environment is altered in many ways as depicted in Figures 3a and b. Physical changes due to microbial growth and biofilm formation includes modification of sediment texture, pore size, pore shape, and grain surface roughness. As microbes grow on the surfaces of sediment grains in colonies, they form a “pseudoglue” called exopolysaccharides, which helps bind particles into larger aggregates, thus altering sediment structure and texture (Figure 3c). When fine particles such as clay are available, microorganisms cause the particles to orient along the microbial surfaces, which aids in the formation of large sediment aggregates (Robert and Chenu, 1992).

The aggregation of sediments resulting from the growth of a microbial community alters the sediment texture at sub-centimeter scale. This may cause the sediment properties to differ from adjacent environments not affected by microbial processes. The formation of a network of hyphae by filamentous microbes will tend to reduce the pore throats between adjacent sediment grains, altering the pore geometry thus reducing the overall porosity (Figures 3a–c), and enhancing sediment grain cementation. Biofilm growth has been found to

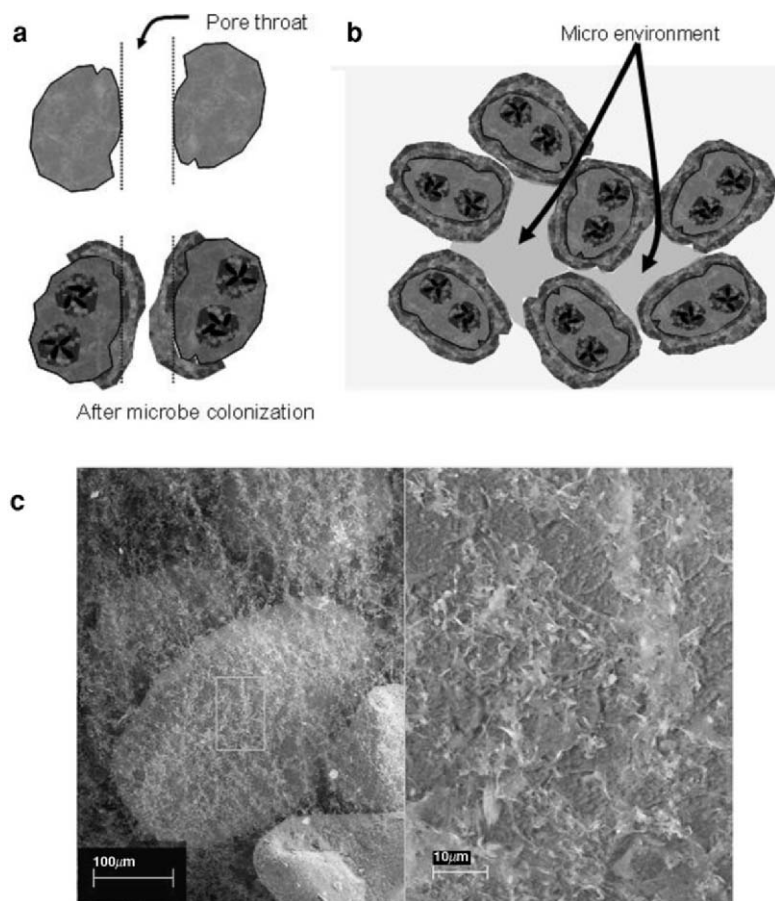


Figure 3. a and b. Schematic representation of how changes in microbial growth and proliferation impact pore structure; c. Environmental scanning electron microscope image of biofilm within sand column covering sand grains. Right image is close up view of green box on left image

significantly reduce the porosity and permeability of porous media (Dunsmore et al., 2004; Bouwer et al., 2000). If the phenomenon of biofilm growth occurs on an extensive scale, it can result in bioclogging which increases rock and sediment stiffness, decreases porosity and permeability, and possibly the rock's elastic moduli. The increased growth of the biomass and biofilm production that alters the pore throat geometry also alters the bulk density, thereby potentially impacting acoustic wave amplitudes and velocities (Williams et al., 2005). Microbes have large relative surface area (Van Der Wal et al., 1997a). Hence, microorganisms that grow in colonies may increase the surface roughness of relatively smooth sediment grains thereby enhancing the effective surface area and their electrical conductivity. For relatively rough sediment

surfaces, growth of microbes in intra-grain pore spaces may effectively smoothen the grains causing a reduction of the overall sediment grain surface area. Very little is known about the mechanical properties of biofilm, however, some studies suggest that they are hydrogels (Hall-Soodley et al., 2004). Recently, it has been suggested that biofilms exhibit classic visco-elastic behavior with a shear modulus of 10^{-1} – 10^5 Pa (Stoodley et al., 2002). Thus, microbial growth and attachment to sediments can potentially alter the physical properties of the media. Alterations in the texture, pore properties, permeability, rock or sediment stiffness, and elastic moduli are specific physical properties that are measured by electrical and seismic geophysical methods.

6.3.3.4. Chemical Changes in the Subsurface Environment Resulting from Microbial Activity-Sediment-Water Interaction

The chemistry of the fluid within the pores where microbial growth occurs is significantly different relative to the chemistry of the fluid in pores where microbial growth is absent. As a result of microbial utilization, the concentration of the organic carbon substrate and nutrients decrease with time, while the metabolic by-products and waste products accumulate in the pore fluid. The abundance of terminal electron acceptors (TEA's) governs nutrient utilization by microbes during the breakdown of organic carbon (Bekins et al., 2001; Cozzarelli et al., 2001). Terminal electron acceptors are sequentially utilized from O_2 , NO_3^- , Fe(III), Mn (IV), SO_4^{2-} and CO_2 . As the TEAs are consumed, the breakdown of organic carbon produces organic acids and carbon dioxide (Bollinger et al., 1999; Aggarwal and Hinchee, 1991). For example, the pH of the pore fluid decreases as the carbon dioxide dissolves to form carbonic acid. Carbonic acid and organic acids enhance the dissolution of the sediment minerals (Bennett et al., 1996). Thus, significant changes in the chemical conditions of the subsurface environment may result from mineral weathering (Figure 1).

The bio-chemical weathering processes in subsurface sediments potentially induce physical changes (e.g. formation factor, tortuosity, and pore geometry) in the subsurface environment. In cemented sediments, calcite, iron oxide, or silica cement can be dissolved by aggressive acids, changing the cementation factor of the rock and ultimately altering the porosity and the formation factor. Surfaces of minerals may become etched and pitted (Figures 4a and b) perhaps due to differential mineral weathering, the concentration of weathering along crystal defects, or by direct microbial colonization of mineral surfaces. To grow, microbes optimize the pH (between 6.0–6.5) which leads to direct mineral weathering producing etches and pits on mineral surfaces (Bennett et al., 1996; McMahon et al., 1995). Pits and etches caused by either water-mineral interaction or by direct colonization of microbes may change the surface characteristics of minerals by enhancing surface roughness and increasing the relative surface area of sediment grains.

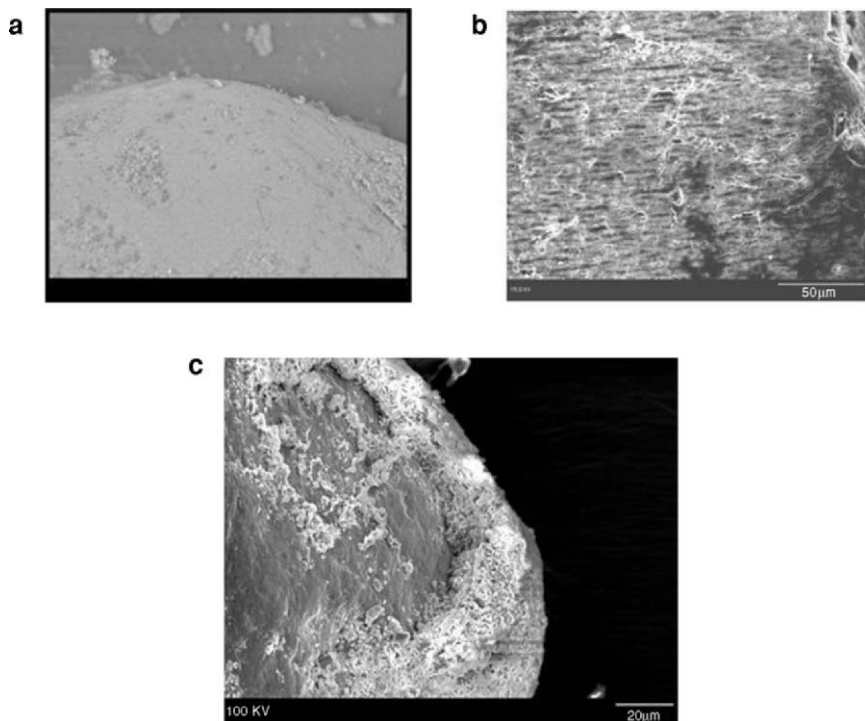


Figure 4. a. Smooth sand grain from an uncontaminated location compared to b. Highly weathered and etched grain from a hydrocarbon impacted location at a field site in Carson City Michigan. c. Scanning electron microscope image showing unknown chemical precipitates on sand grains from a microbially active sand column (Atekwana E.A., unpublished data)

The pore fluid chemistry in the subsurface may change from conditions that promote mineral dissolution to those that cause the precipitation of mineral phases from solution (e.g. Figure 4c). Significant changes in the pH and Eh in the sediment environment may occur as a result of microbial activity. Such pH and Eh changes can result in new mineral stability fields in which some minerals become unstable and are dissolved and mobilized (e.g. Fe^{2+}), while others are precipitated from solution (e.g. sulfide and magnetite). The process of precipitation is complex and governed by mineral saturation indices (Stumm and Morgan, 1995). As ions in solution exceed their saturation indices, minerals begin to precipitate from solution. Minerals that are commonly precipitated from solution may include but are not limited to calcite, silica, manganese, iron oxyhydroxides, iron sulfide, and zinc sulfide. The precipitates usually occur on or between sediment. Depending on the chemical character of the precipitates, the relative surface area, formation porosity, pore throat diameter, and the formation factor may change with significant impact on electric current flow and seismic wave propagation. For example,

decreasing matrix porosity may strengthen the sediment matrix and causing an increase in seismic wave velocity and a decrease in seismic energy attenuation.

Biologically induced mineralization (BIM), in which an organism modifies its local microenvironment creating conditions suitable for the chemical precipitation of extracellular mineral phases has been documented in many studies (Mann et al., 1989). For example, sulfate-reducing bacteria can induced precipitation of magnetite, siderite, vivianite, and iron-sulfides by BIM (Lovely, 1990). The precipitation of these minerals in sediments may change the magnetic properties of the altered subsurface environment which are potentially detectable by the magnetic method. It is suggested that biogenic magnetic minerals deposited in sediments can acquire a natural remnant magnetization that preserves a record of the ancient geomagnetic field (Moskowitz et al., 1993).

6.3.4. EFFECT OF CHEMICAL CHANGES IN SEDIMENTS RESULTING FROM MICROBIAL ACTIVITY-MINERAL-WATER INTERACTION ON ELECTRICAL PROPERTIES

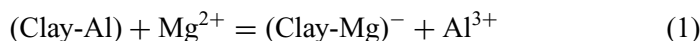
6.3.4.1. *Electrolytic and Surface Conduction*

The same chemical changes (direct microbial action and mineral-water interaction) in the subsurface environment that alters the physical properties also cause measurable changes in the chemistry of the pore fluid. During microbial metabolism of organic carbon, the consumption of TEAs, and the production of intermediates and byproducts are expected to cause temporal changes in the ionic content of the pore fluid. Electrical current is partially transmitted in sediments via pore fluids. The electric current propagation in the pore fluids depends on the electrolytic properties that are governed by ion strength, ionic charge density, and ionic mobility. During mineral weathering, the dissolved ions are released into solution in varying concentration, generally higher in the immediate vicinity of microbial colonies and mineral surfaces. The increase in the ionic strength and ionic charge density at the mineral-fluid interface enhances electrical conductivity at the mineral surfaces within the electric double layer (EDL) (e.g. Lesmes and Frye, 2001) while the increased ionic strength in the bulk solution enhances the electrical conduction through the fluid.

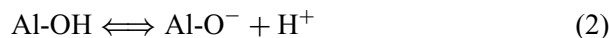
6.3.4.2. *Electrical Interactions Between Microbes and the Subsurface Environment*

Geologic materials posses surface electrical charges associated with fine sediment particles such as clays and organic particles. This surface electrical charge is best described as the bulk sediment capacity to exchange cations between solids and solution, commonly described as the cation exchange

capacity (CEC). Thus the CEC is the total amount of negative charge in the sediment due to clay and organic matter, and is reported in millimoles of positive charge per kilogram of sediment. For fine particles such as clays, CEC is the result of either isomorphic substitution or ionization. In isomorphic substitution, there is a loss of one positive charge (gain of one negative charge) when a divalent cation (e.g. Mg^{2+}) is substituted for a trivalent cation (e.g. Al^{3+}) within the clay lattice.



Ionization on the other hand occurs in hydroxyl groups from metal oxides, oxyhydroxides, and hydroxides interacting with surfaces of clays.



Ionization reaction on clay surfaces are pH dependent and increase with increase in pH. Microbial growth, which generally decreases pH, does not favor or induce ionization reactions. Both isomeric substitution and ionization cause clays to exhibit a net negative charge on the clay surfaces that can attract additional positive charges by cation exchange.

Microbial adhesion to mineral surfaces affects electrical interactions between the mineral particles and the microbial cell surfaces. The important parameters that govern microbial cell attachment to mineral surfaces are related to electrostatic attraction, hydrophobic interaction, and van der Waals forces and have been described in detail by van Loosdrecht et al. (1990). Since both microbial cells and mineral surfaces are negatively charged, electrostatic interactions are repulsive. With appropriate counterions such as K^+ , Na^+ , Mg^{2+} , Fe^{3+} and Al^{3+} , microbes can attach themselves to mineral particles such as clays via cation bridging (Figure 5). This attachment of microbes to

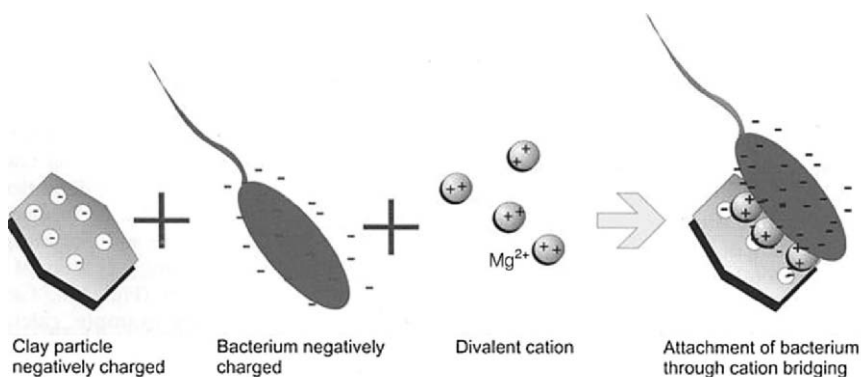


Figure 5. Schematic representation of microbial interactions with clay surfaces and attachment to clay surfaces through cation bridging (modified from Maier et al., 2000)

surfaces of clays alters the EDL. Since the EDLs of microbes and clays repel each other, the thinner the EDL layers, the less the repulsion between the clays and the cell surfaces. Higher valence cations between the clays and increased cation concentrations in the pore fluids tend to minimize the thickness of the EDL (Newby et al., 2000). With minimal repulsive forces for thinner layers, other attractive forces such as van der Waals and electrostatic forces allow for increased microbial attachment to mineral surfaces (Gammack et al., 1992).

Additionally, it has recently been recognized that the ion selectivity of the outer cellular membrane of live bacterial cells in solution can generate a large low frequency polarization (e.g. Prodan et al., 2004). Thus, the microbes themselves have electrical properties that may impact the bulk electrical properties of the subsurface environment.

6.4. Laboratory Studies of the Effects of Microbial Processes on Geophysical Properties

6.4.1. INTRODUCTION

To reduce the complexity and the variability of the natural environment, experiments are conducted in laboratory settings. In this section, laboratory experiments that have been conducted to explore microbe-sediment-geophysical relationships using geophysical techniques of direct current (dc) resistivity, induced polarization (IP), self potential (SP), and seismic are described. These investigations have furthered the understanding of the effects of microbial processes on the geophysical signatures.

6.4.2. DIRECT CURRENT RESISTIVITY STUDIES

Geoelectrical investigations conducted at aged hydrocarbon spill sites have documented attenuation of ground penetrating radar signals (Bermejo et al., 1997; Bradford, 2003) and higher bulk electrical conductivities (Sauck et al., 1998; Atekwana et al., 2000; Atekwana et al., 2002; Shevlin et al., 2003; Werkema et al., 2003) coincident with subsurface regions of hydrocarbon impact. A model proposed by Sauck (2000) attributes the higher bulk electrical conductivity at hydrocarbon contaminated sites to biodegradation and increase in the total dissolved solids (TDS). TDS increases in groundwater are from enhanced weathering of minerals by acids produced as byproducts of the microbial degradation process. While TDS is a likely parameter that closely links the bulk electrical conductivity to microbial degradation of hydrocarbons, anthropogenic effects (e.g. salt application during de-icing of streets) can also result in increases in TDS in groundwater. At the time of the Sauck (2000) study, there were no controlled studies that showed: 1) higher TDS

resulted from biodegradation, and 2) microbial degradation in hydrocarbon contaminated sediments actually caused increases in the bulk electrical properties. However, laboratory slurry experiments showed a direct relationship between aerobic microbial mineralization of a petroleum hydrocarbon and an increase in pore water conductivity, volatile organic acids, and total dissolved solids (Cassidy et al., 2001).

To investigate whether bulk conductivity increase measured at field sites contaminated by hydrocarbon was due to biodegradation, Atekwana et al. (2004a) used dc resistivity to investigate changes in electrical conductivity during biodegradation in a column experiment (Figure 6). The experimental columns were designed to simulate typical field conditions with a water saturated zone, a transition zone, and a vadose zone. The columns which were 80 cm in length and 30.48 cm in diameter were filled with fine-medium grain sand that was collected from a hydrocarbon contaminated site. The microbes used in the experiments were cultured from contaminated sediments from the same hydrocarbon contaminated site. Both contaminated (amended with four liters of diesel fuel) and uncontaminated columns were maintained. The distribution of the different phases of diesel contamination is shown schematically in Figure 6. Microbial activity was verified by monitoring microbial population growth and the production of carbon dioxide (measured as dissolved inorganic carbon). A change in the bulk chemistry of the pore fluid which may result from mineral weathering was assessed by measuring Ca^{2+} . Bulk electrical conductivity of the sediments (σ_b) was measured using a 2 cm Wenner array. Microbial population capable of mineralizing the diesel was determined by the Most Probable Number (MPN) technique. Pore water was extracted at four discrete depths and analyzed for dissolved inorganic carbon (DIC) and Ca^{2+} .

Figure 6a shows the relative increase in alkane degraders, which are the microbes that degraded the diesel fuel in the contaminated column. Notable is the large increase in alkane degraders in the contaminated column from 35 cm to 60 cm depth compared to the uncontaminated column (Figure 6b). Sediments in the uncontaminated column (Figure 6b) show relatively low Most Probable Number throughout all depths, with only a slight increase over time and no apparent depth stratification.

The relative change in the magnitude of the bulk electrical conductivity (σ_b) is presented as percent change $(100(\sigma_{bti} - \sigma_{btb})/\sigma_{btb})$ for select time intervals t_i relative to the baseline value t_b (time at which the σ_b stabilized). During the experiment, the contaminated column showed an increase in σ_b (Figure 6a) compared to the uncontaminated column which showed a decrease with time (Figure 6b). Higher DIC in the contaminated column (up to 110 mg/l) compared to the uncontaminated column (up to 80 mg C/l) was attributed to mineralization of diesel fuel and the production of carbon dioxide

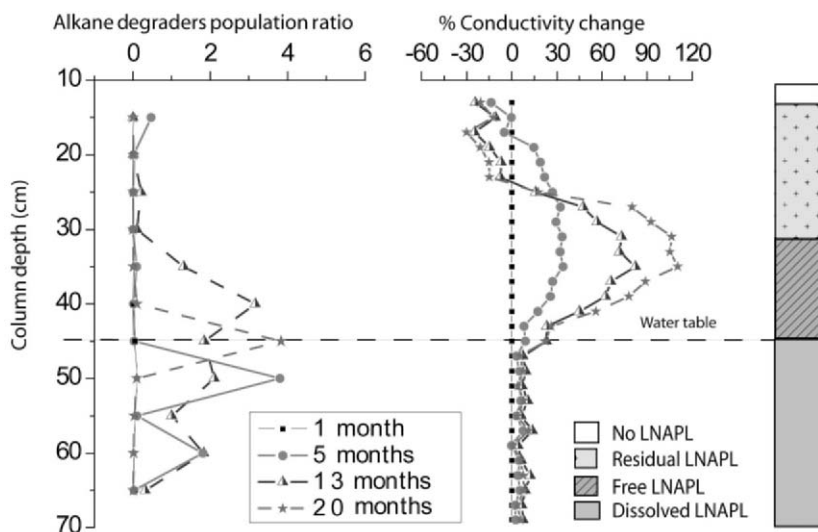
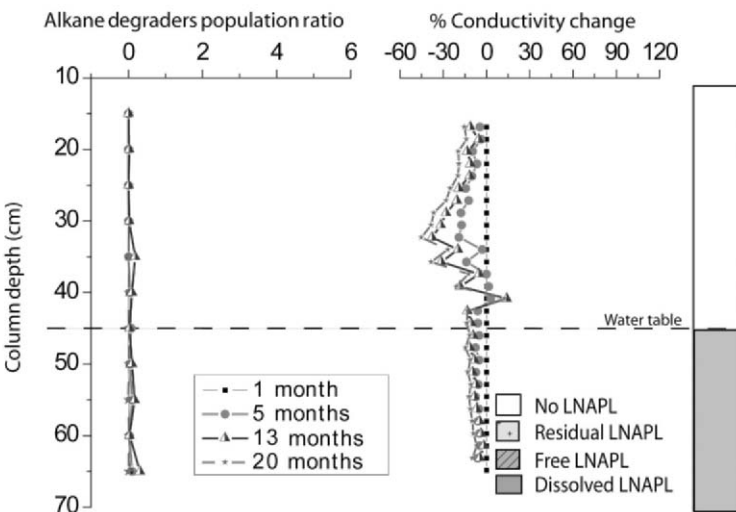
A**B**

Figure 6. Temporal change alkane degrading population in bulk conductivity (σ_b) and sediment profile in (a) contaminated column and (b) uncontaminated column. Four time periods have been plotted to illustrate temporal changes. Also shown is the vertical distribution of diesel fuel and sediment profile in the columns (modified from Atekwana et al., 2004b)

by microbes (Figures 7a and b). The contaminated column showed a greater temporal increase in Ca^{2+} (change of ~ 20 mg/l) and higher overall concentration (up to 40 mg/l) than the uncontaminated column which showed an 8 mg/l increase (Figures 7c and d).

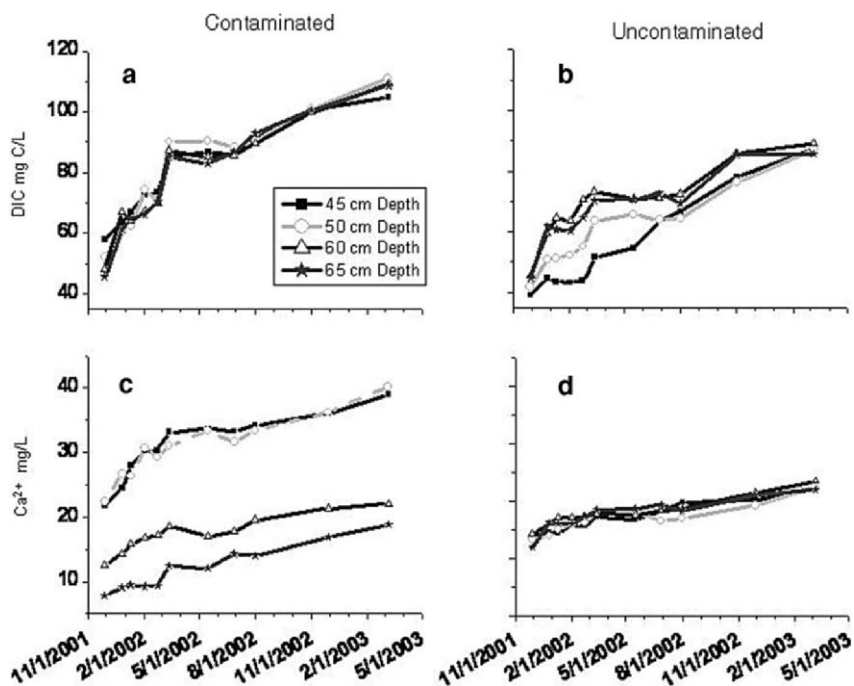


Figure 7. Temporal changes in the concentration of dissolved inorganic carbon (DIC) and Ca^{2+} (a) and (c) contaminated column and (b) and (d) uncontaminated column (modified from Atekwana et al., 2004b)

The results from this laboratory experiment provide the first indirect link between microbial processes and higher σ_b in a controlled laboratory experiment. These results support observations made in field settings. The increase in σ_b , which the authors attribute to increasing ionic strength from enhancement of microbial growth and activity that is stimulated by an excess organic source, is in part consistent with the Sauck (2000) model and the Cassidy et al. (2001) study.

6.4.3. INDUCED POLARIZATION STUDIES

In the absence of high clay content sediments, dc resistivity is primarily sensitive to the pore fluid conductivity. Furthermore, dc resistivity cannot be used to differentiate electrical responses due to chemical changes, electrical interaction occurring at the mineral-fluid interface, or changes in the sediment texture (e.g. pore throat geometry, surface area, or porosity). The sensitivity of the induced polarization (IP) method to changes in the surface chemical properties of rocks and soils (Lesmes and Frye, 2001) makes it a suitable

technique for investigating changes on electrical properties of sediments due to microbial activity.

Abdel Aal et al. (2004) have measured the effects of microbial processes on the complex (real and imaginary) conductivity of sediments in laboratory sand columns. In this experiment, the sand columns were 50 cm long and constructed of 7.6 cm ID polyvinyl chloride pipe. The columns were filled with fine-grained (0.45–0.65 mm) sand that was collected from a field site contaminated with diesel fuel. The microbial inoculum was cultured from the same site from which the sands were collected. The column treatments included a biotic column containing mineral nutrients (25% Bushnell Hass medium), diesel fuel, and bacteria, and two abiotic columns with one containing only nutrients and the other containing nutrients and diesel fuel.

Temporal microbial population and chemical measurements calculated as relative percent change from values measured at the start of the experiment are shown in Figure 8a. Microbial growth expressed as Most Probable Number (MPN) in the columns showed relative increases only in the biotic column. Utilization of organic carbon by microbes determined as temporal decrease of benzene, toluene, ethyl benzene, and xylenes (BTEX) components of diesel was consistent with depletion of terminal electron acceptors (e.g. nitrates) in the biotic column. As carbon dioxide produced during diesel mineralization dissolved in the pore fluid, the carbonic acid formed decreases the pH. The continuous decrease in pH in the biotic column suggests pH conditions that are conducive for mineral weathering. The weathering of minerals in the biotic column was expressed as temporal increase in Ca^{2+} in the biotic compared to the abiotic columns. The weathering of minerals in the biotic column increases the ionic content of the solution and caused temporal increases of the electrical conductivity of the pore fluid (fluid conductivity).

Complex conductivity measurements showed a temporal increase in the real (σ') and imaginary (σ'') conductivity in the biotic columns, while the abiotic columns showed no significant changes (Figure 8b). Interestingly, the real conductivity response was similar to that observed in some biological and chemical parameters (e.g. MPN, Ca^{2+} , and fluid conductivity) which rapidly increased in the early stages (<20 weeks) of the experiment. This was attributed to the sensitivity of the real conductivity to the electrolyte composition (fluid conductivity). In contrast, the imaginary conductivity response, which is a measure of interfacial polarization, changed slowly during the first 14 weeks and increased more rapidly thereafter. The authors suggest that the delayed response of the imaginary conductivity may have been due to progressive changes in the surface area of the mineral grains induced by microbial growth and perhaps the formation of biofilms. Alternatively, as the ionic strength of the pore solution increased, this may have reduced the

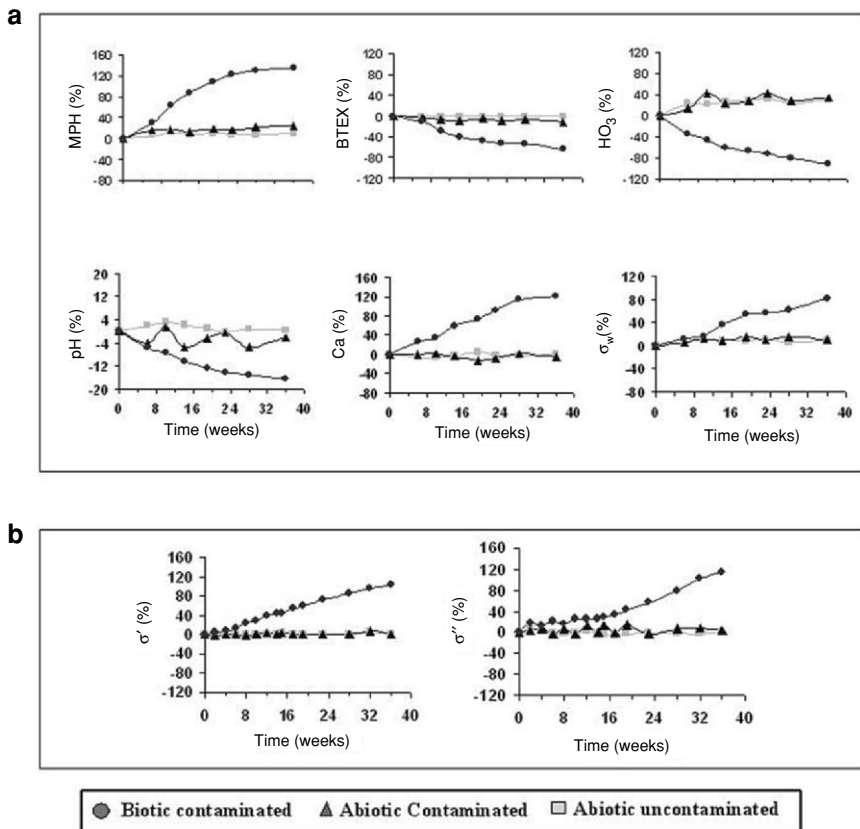


Figure 8. a. Temporal percent change in biogeochemical parameters (microbial population numbers (MPN), benzene+toluene+ethylbenzene+xylene (BTEX), nitrate, pH, calcium, and fluid conductivity from pore water from biotic and abiotic sand columns. b. Temporal percent change in real and imaginary conductivity in biotic and abiotic sand columns (modified from Abdel Aal et al., in review)

thickness of the electrical double layer and induced greater attachment of microbes to mineral surfaces.

In another study, Ntarlagiannis et al. (2005a) used the IP method to monitor microbial induced metal sulfide precipitation for a period of seventy days. Bacteria (*Desulfovibrio vulgaris*) were injected into sand columns packed with Ottawa II sand. The columns were 30.5 cm in length with a 5.08 cm diameter. The experiment was conducted under anaerobic conditions. Nurtients (lactate and sulfate) and a metal solution consisting of iron and zinc were introduced into the columns.

The biostimulation resulted in the precipitation of Fe and Zn sulfide. IP measurements along the length of the column were used to assess the electrical

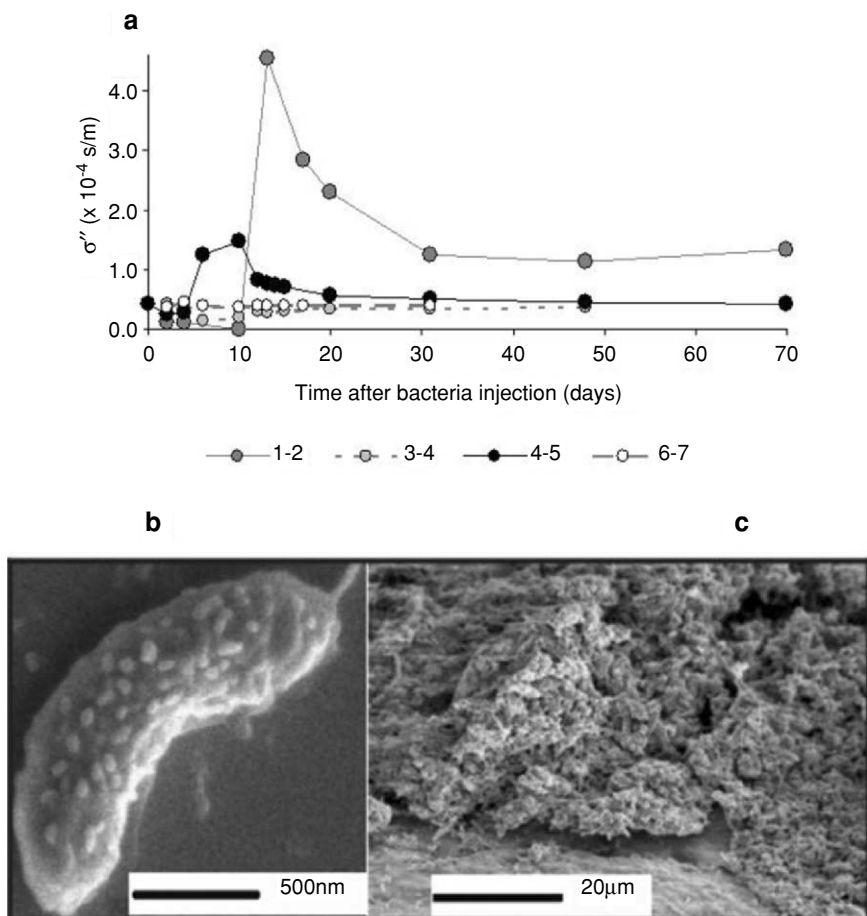


Figure 9. Imaginary conductivity (σ'') as a function of time for different electrode pairs (1–2, 3–4, 4–5 and 6–7) at 35 Hz for the experiment run with metals; Scanning electron microscope (SEM) images of samples obtained from two locations within the inoculated, metals-amended electrical column after 78 days, (b) biomineral and, (c) quartz grain encrusted with a mineralized biofilms (modified from Ntarlagiannis et al., 2005a)

response of the bio-induced mineral precipitation. Changes in the electrical measurements, primarily the interfacial polarization, were observed (Figure 9). Polarization anomalies up to 14 mrad were coincident with regions of lactate consumption, metal reduction, and higher microbial population numbers. At the end of the experiment, temporal changes in polarization and conduction correlated with a geometrical rearrangement of metal coated bacterial cells (Figure 9b). The authors attributed the polarization increase to a metal–fluid interfacial mechanism that develops as metal sulfides precipitated

onto microbial cells and form biominerals. The above study demonstrates the potential for using IP parameters to monitor microbial induced mineral precipitation.

We note that in another study, Ntarlagiannis et al. (2005b) have been able to detect the presence of microbial cells in sand columns using the IP method. High concentrations of bacterial cells in the sand column resulted in a higher imaginary conductivity response when compared to sand control columns with no bacteria. The authors relate the higher imaginary conductivity response in the bacteria columns to higher total available surface area and alterations on the electrical double layer of mineral grains and bacteria cells.

The above studies support the fact that of the IP parameters, the real conductivity is controlled by fluid conductivity, while the imaginary conductivity is sensitive to the interface conductivity. This distinction may ultimately permit discrimination between the relative contributions of microbial activity to changes in the pore fluid chemistry versus changes in the physical and chemical properties at interfaces.

6.4.4. SELF POTENTIAL STUDIES

The self potential (SP) method may be a good sensor of redox conditions in contaminated aquifers. This method is based on the measurement of naturally occurring potentials in the subsurface resulting from electrokinetic potentials (due to groundwater flow) and oxidation-reduction phenomena (Naudet et al., 2003). It has been hypothesized that biofilms may act as conduits for electron transfer from the reduced portions to the oxidized portions of contaminant plumes (Naudet et al., 2003). To further investigate this geobattery concept, Naudet and Revil (2005) conducted a laboratory experiment to investigate the influence of microbial processes on self potential signals in a sandbox experiment treated with sulfate reducing bacteria and organic nutrients. The Plexiglas tank (2 m long, 0.5 m high, and 6 cm thick) was filled with sediments (mostly quartz sand) obtained from the Scarpe River (France) containing heavy metals (Zn, Cd, Pb). Indigenous microorganisms cultured from the sands were used as the inoculum for this experiment. In the treated areas of the sandbox, a decrease in the redox potential (-50 mV) was observed, whereas, values outside the treated area remained stable at 160 mV. The data show a good linear correlation between the temporal variation of self potential signals and redox potential. To explain this observation, Naudet and Revil (2005) proposed a geobattery concept akin to those of ore deposits in which biofilms and possible metallic precipitates at the redox front allow for the transfer of electrons between the reduced and oxidized portions of the system, resulting in a net driving current density. Thus, in addition to the ability of microbes to degrade contaminants (e.g. at hydrocarbon contaminated sites or landfill

sites) bacteria can also serve as conduits for the transfer of electrons from oxidized zones to the reduced portions of contaminated aquifers (See also Chapter 9).

6.4.5. ACOUSTIC WAVE STUDIES

Seismic techniques are sensitive to changes in the elastic/viscoelastic properties of material as well as its mechanical properties. Hence, microbial alterations of sediment such as mineral dissolution, mineral precipitation, and biofilm formation that impact the mechanical properties of the sediment and the fluids in the pores (Figure 2), can also impact the propagation of acoustic waves. In the same experiment by Ntarlagiannis et al. (2005a), Williams et al. (2005) investigated the effect of alterations in sediment characteristics resulting from microbe-mediated sulfide mineral precipitation on acoustic wave propagation. Acoustic wave measurements were made using two fluid-coupled 1000 kHz piezoelectric transducers connected to a high-voltage pulse-receiver. Velocity and amplitude measurements were made on the columns for the duration of the experiment. Their data show that when compared to control columns, acoustic wave signatures of biologically active columns were increasingly attenuated over time (amplitudes decreased by up to 86%) with only modest increases in wave velocity. The changes in velocity were shown to be concomitant with the accumulation of mineral precipitates. Williams et al. (2005) suggested that the decreases in acoustic wave amplitude resulted from the development of differential elastic moduli due to the accumulation of metal sulfide-encrusted microbes within the pore space, with the sulfide aggregates representing a distinct porous material embedded within the main pores between the sand grains. They further suggested that differences between the elastic moduli of the sulfide bearing pores and those not containing appreciable precipitates may have enhanced this attenuation mechanism. Acoustic signals were also observed to exhibit a time-varying response, with wave amplitudes rebounding slightly from their most attenuated levels. The rebound in acoustic wave amplitudes is suggested to have resulted from increasing homogeneity in the distribution of mineral precipitates within the pores as time elapsed, or alternatively, from the loss of secondary porosity due to coarsening of the metal sulfides within the pores.

The above laboratory investigations suggest the potential for the geophysical monitoring of biological activity and resulting geomicrobiology processes in field settings. However, more sophisticated controlled experiments than those presented here are needed to unravel these interrelated processes and their effects on geophysical measurements.

6.5. Field Studies of the Effects of Microbial Processes on Geophysical Properties

6.5.1. DIRECT CURRENT RESISTIVITY STUDIES

Good examples of microbial impact on geophysical properties come from studies made at hydrocarbon impacted sites (Sauck et al., 1998; Werkema et al., 2003; Atekwana et al., 2004a; Atekwana et al., 2004b). These sites can be considered natural laboratories where excess organic substrates stimulate microbial activity. With petroleum hydrocarbons impacting or contaminating the subsurface, the presence of terminal electron acceptors (e.g. NO_3^- , SO_4^{2-}) stimulate microbially mediated reactions resulting in measurable geoelectrical changes, if enough time elapses.

Atekwana et al. (2004b) investigated the bulk electrical conductivity and microbial population distribution in sediments at a site contaminated with light non-aqueous phase liquid (LNAPL). The study was conducted at a former refinery site where continuous hydrocarbon (mostly JP-4 jet and diesel fuel) releases occurred, impacting soils and groundwater for more than 50 years. Intrinsic bioremediation is known to occur at the site (Legall, 2002).

Downhole resistivity measurements were made from in-situ vertical resistivity probes, while the MPN method was used to characterize the spatial distribution of aerobic heterotrophic and oil degrading microbial populations. At the background location (Figure 10a), the heterotrophic microbes and microbes capable of degrading hydrocarbon (oil degraders) ranged from 10^2 to 10^6 and 10^2 to 10^5 MPN/g of soil, respectively. The oil degrading microbial population in the uncontaminated location represented, on average, less than 5% of the total heterotrophic microbial community. At the contaminated location (Figure 10b), the heterotrophic microorganisms ranged from 10^3 to 10^6 MPN/g of soil, and the oil degrading microorganisms from 10^2 to 10^5 MPN/g of soil. The oil degrading microorganisms accounted for 55% of the total heterotrophic microbial community within the contaminated zones. When compared to the background location (Figure 10a), the contaminated location showed peaks in oil-degrading microbial populations within regions where the bulk conductivity was elevated (Figure 10b). The higher bulk conductivity was coincident with LNAPL-impacted zones, in contrast to geoelectrical models that predict lower conductivity in such zones. The highest bulk conductivity was observed to be associated with depth zones impacted by residual and free phase LNAPL (Figure 10b). These observations are consistent with previous work at this site (Werkema et al., 2003; Atekwana et al., 2004, 2004c).

The coincidence of a higher percentage of oil degrading microbial populations in zones of higher bulk conductivity suggests that the higher conductivity

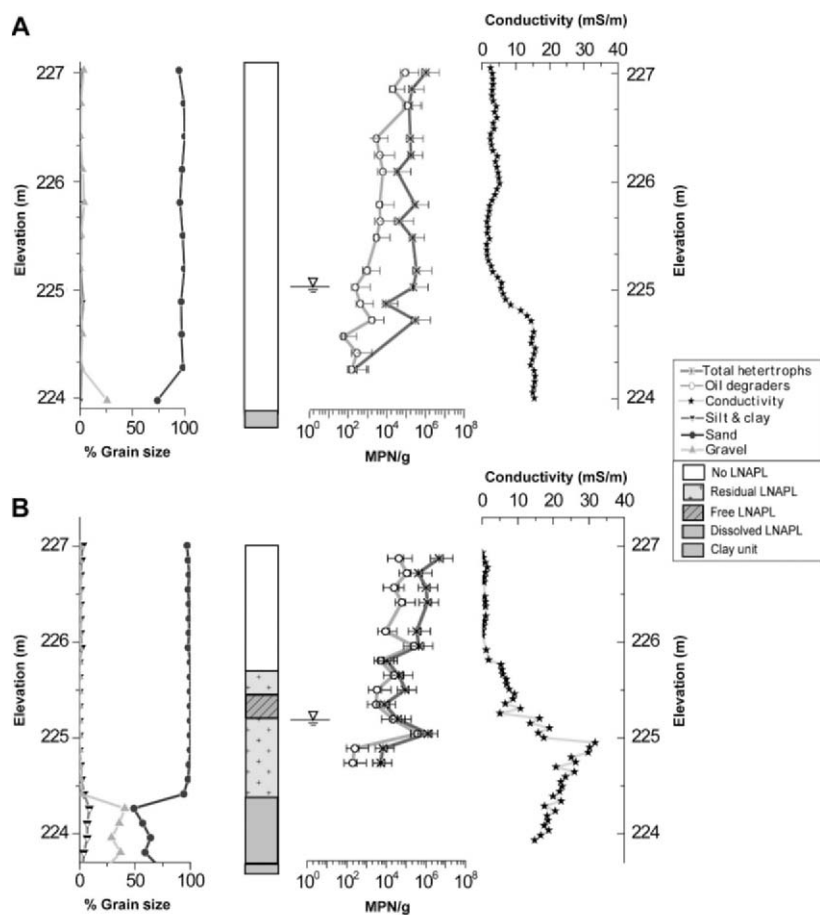


Figure 10. Grain size distribution, LNAPL distribution, microbial population distribution and *in situ* conductivity variation from (a) an uncontaminated location and (b) LNAPL-contaminated location (modified from Atekwana et al., 2004c)

in these zones may be due to increased fluid conductivity related to microbial degradation of LNAPL, consistent with geochemical studies that indicated intrinsic biodegradation at the site. Using a simple Archie's Law analysis, Werkema et al. (2003) show that a 5.5 fold increase in pore water conductivity over equivalent uncontaminated locations, was necessary to reproduce the bulk electrical conductivity measured at the contaminated location. Other studies at this site using microbial community dynamics from ribosomal DNA intergenic spacer analysis (RISA) show microbial communities adapted and thriving at depth interfaces coincident with higher concentrations of hydrocarbon, higher bulk conductivity, and where extensive etching and pitting of mineral grains were observed (Duris, 2002; Burton et al., 2003). The

conductivity increase correlated with locations of LNAPL contamination was also observed from surface geophysical measurements (Atekwana et al., 2000; 2002).

6.5.2. GROUND PENETRATING RADAR STUDIES

Sauck et al. (1998) provide another good example of surface resistivity and ground penetrating radar (GPR) measurements over a hydrocarbon contaminated site. The study was conducted at the decommissioned Wurtsmith Air force Base in Oscoda, Michigan, USA, where fire training exercises using JP-4 jet fuel for more than 30 years resulted in groundwater contamination. Figure 11a shows a GPR section from a bistatic 100 MHz antenna over the contamination plume. The GPR section shows a zone of attenuated GPR reflection labeled, 'shadow zone,' between 290–342 m. The zone of attenuated GPR reflections is coincident with a region of lower resistivity (Figure 11b). This suggests that the attenuated GPR reflections may be due to elevated groundwater conductivity from the enhanced mineral dissolution due

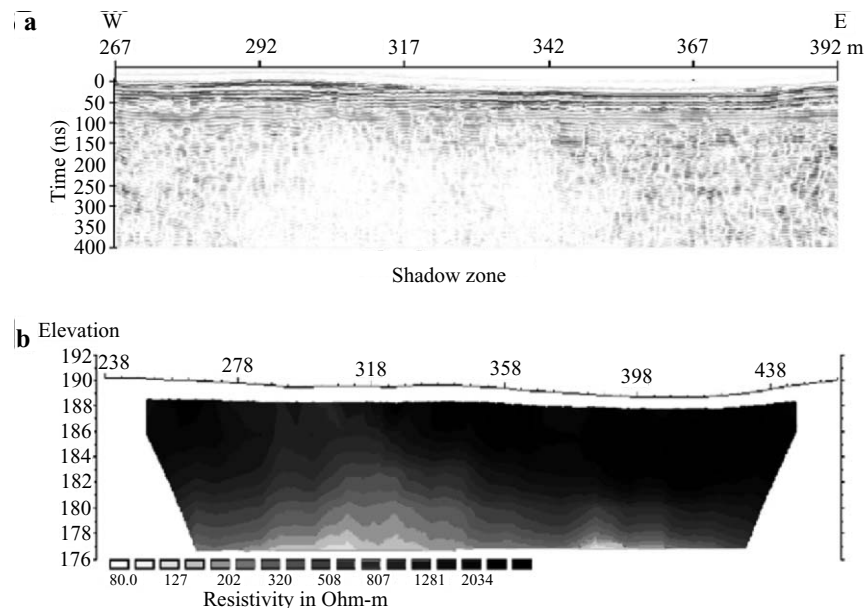


Figure 11. a) Ground penetrating radar (GPR) profile over a hydrocarbon contaminated zone at the Wurtsmith Air Force Base, Oscoda, MI; b) dipole-dipole resistivity profile over the same area as in A. Note that the zone of attenuated GPR reflections delineated as shadow zone is coincident with area of lower resistivity on the resistivity profiles (modified from Sauck et al., 1998)

to microbial degradational activity. Reported groundwater conductivity within the contaminated zones were two times the background values, providing further support for enhanced mineral weathering and consistent intrinsic bioremediation at the site (Dojka et al., 1998). The attenuated GPR reflections observed by Sauck et al. (1998) have been confirmed by GPR investigations over the same site by Bradford (2003). Thus, conductive zones observed at many hydrocarbon contaminated sites may represent areas of active biodegradation and demonstrate the potential for geoelectrical techniques to be used in conjunction with other traditional techniques in investigating intrinsic microbial degradation of hydrocarbons at contaminated sites (Atekwana et al., 2002; Shevlin et al., 2003).

6.5.3. SELF POTENTIAL STUDIES

Enhanced microbial activity in the subsurface requires a carbon source and terminal electron acceptors utilized by microbes to mineralize carbon. Hence, redox processes are quite active in organic rich groundwaters making them ideal settings for SP investigations. As such, strong self potential anomalies have been observed over anaerobic groundwater plumes in association with hydrocarbon plumes (e.g. Sauck et al., 1998; Vichabian et al., 1999) and food waste (Nyquist and Cory, 2002). Similarly, Naudet et al. (2003) have reported large SP anomalies over landfill leachate plumes which are in part derived from microbial degradation of organic matter and other substances in landfills. At the Entressen municipal landfill in the southeast of France, Naudet et al. (2003) have documented large SP anomalies of ~ 400 mV. The authors attribute this large SP anomaly to the presence of a redox front as the SP anomaly decreased significantly within the anaerobic zone. The residual SP anomalies were further shown to be linear with in situ measurements of redox potential and consistent with the laboratory results by Naudet and Revil (2005) discussed above (see section on laboratory SP studies). As discussed in this laboratory study, microbial biofilms may be playing an important role in transferring electrons from oxidized zones to reduced zones. Such microbial processes are the basis of producing electricity via microbial fuel cells (Van Der Wal et al., 1997b; Park and Zeikus, 2000; Redman et al., 2004).

6.5.4. INDUCED POLARIZATION STUDIES

The induced bio-physicochemical changes by microorganisms summarized in Figure 2 and described in Section 6.3, as well as the unique electrical

characteristics of bacteria themselves, may have a profound effect on induced polarization (IP) measurements. The laboratory work of Abdel Aal et al. (2006) provides the first evidence suggesting that microbial activity may impact both the electrolytic and interfacial electrical properties of unconsolidated sediments measurable by IP techniques. The question then arises as to whether or not the effects of biodegradation processes observed in laboratory columns are significant enough to be observed at field sites contaminated by petroleum hydrocarbons.

Abdel Aal et al. (2006) investigated the effects of microbial activity on IP parameters from field samples. In their study, IP measurements in the frequency range of 0.1 to 1000 Hz were acquired on sediment cores retrieved from an aged-hydrocarbon contaminated site where intrinsic biodegradation was occurring. In general, they recorded higher real and imaginary conductivity for samples obtained from the contaminated locations compared to uncontaminated locations (Figure 12a). At the uncontaminated location, the imaginary conductivity of sediments was higher in the saturated zone compared to the unsaturated zone as expected (Figure 12b). However, they report higher imaginary conductivity values for samples from the smear zone, where contamination is present as residual phase hydrocarbon compared to values obtained for samples contaminated with dissolved phase hydrocarbons below the water table. The real conductivity, although generally elevated for samples from contaminated locations, did not show a strong correlation with contamination, suggesting that the imaginary conductivity parameter was able to better distinguish between contaminated and uncontaminated samples (Figures 12a and b). Furthermore, these results corroborate very well with the results from the Werkema et al. (2003) study which showed that the depth zone where the largest conductivity magnitude occurred was in the residual contaminated smear zone, not in the dissolved contaminated zone. Abdel Aal et al. (2006) attribute the enhanced IP response observed at contaminated locations to enhanced microbial activity. They suggested that the high imaginary conductivity response was due to an increase in the ionic strength of the pore fluid and an increase in the surface area of the mineral or sediment surfaces. These increases were attributed to the attachment of microbes which were enhanced due to mineral weathering from metabolic byproducts such as organic and carbonic acids. Additionally, the accumulation of charged cells in the electrical double layer (EDL) at the mineral-electrolyte interface, coupled with possible ion transport through cellular membranes, might also contribute to the IP response. The above findings illustrate the potential utility of electrical measurements for monitoring enhanced microbial activity such as occurs at sites undergoing natural hydrocarbon degradation.

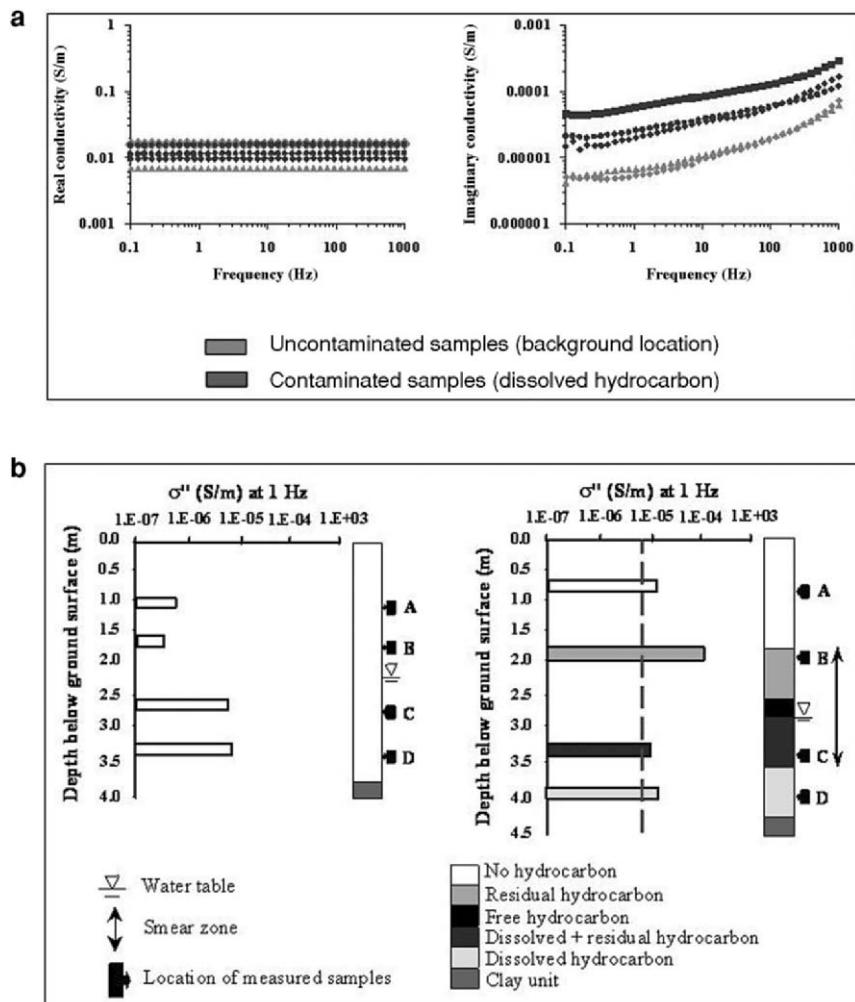


Figure 12. Induced polarization data obtained on core samples from a hydrocarbon contaminated site a) real and imaginary conductivity and b) Bar plots of the 1 Hz imaginary (σ'') conductivity. Samples from the unsaturated part of the smear zone (contaminated with residual phase hydrocarbon) show relatively higher σ'' magnitudes compared to dissolved hydrocarbon contaminated and uncontaminated samples. Vertical, dashed line represents maximum σ'' magnitudes obtained at the uncontaminated location (Modified from Abdel Aal et al., 2006)

6.5.5. OTHER METHODS

Finally, although we do not discuss the impact of microbial activity on other geophysical methods such as nuclear magnetic resonance (NMR) or magnetic field strength measurements, laboratory investigations by Bryar and Knight (2002) suggest that nuclear magnetic resonance relaxation measurements are

sensitive to changing soil redox conditions. Since microbial activity is sensitive to redox conditions it is possible that NMR measurements may be used to detect and monitor microbial activity.

6.6. Conclusions

Biogeophysics is an emerging discipline aimed at understanding the impact of microbial activity and processes on geophysical properties of earth materials. Microbes modify the physical properties of their environment through growth, proliferation, and biofilm formation or due to their metabolic by-products. In shallow subsurface environments where microbial activity is greater than natural conditions (e.g. organic contamination), geophysical methods have been used to detect and characterize zones of microbial activity. The laboratory studies presented above suggest that changes in the geologic media resulting from direct and indirect microbial alteration of the petrophysical and chemical properties can be detected by different geophysical methods. Alterations of the geologic media occur when microbes directly colonize sediment surfaces forming biofilms that alter such properties as texture, surface area, pore size and pore geometry, tortuosity, cementation, formation factor, and elastic moduli. Chemical changes in the microbial environment may result from the development of pH sensitive environment conducive to microbial survival or through secondary mineral-water reactions enhanced by byproducts of organic carbon metabolism. The mineral-water interaction driven by changing pH and redox conditions may result in mineral weathering and cause physical changes in the subsurface environment. Changing chemical conditions, some induced by microbial activity may result in mineral precipitation which changes the physical conditions of the subsurface environment and the groundwater chemistry. When the chemistry of the pore fluids change, the ionic strength, ionic charge density, and ionic mobility of the fluid phase also change, resulting in the alteration of the electrical conductivity. In addition, the interaction of the electrical properties of the pore fluids with that of the mineral surfaces may affect the condition of the electric double layer. The electric double layer may be altered directly by microbial colonization since microbes carry a net negative charge. The challenge therefore is to use geophysics and microbiology to shed light on these important microbial alterations of the subsurface environment.

The implications of the geophysical detection of subsurface microbial processes may have far reaching implications in other fields such as astrobiology, geomicrobiology, biogeochemistry, and remediation studies. But knowing how microbes affect geophysical signatures and which physical parameters and geophysical methodologies are most suited for investigating microbial

activity remains a subject of much interest and a fertile area for further research. Thus, more studies at the laboratory and the field scale are needed to better understand the influence of microbial processes on geophysical signatures and to further this new discipline of biogeophysics.

Acknowledgements

We acknowledge contributions from our other colleagues (L. Slater, S. Rossbach, W. Sauck, T. Endres, and D. Cassidy) and graduate students (F. Legall and G. Abdel Aal) who helped shape the development of the ideas presented in this chapter. Additionally, the review by Eric Koglin helped to improve the clarity and focus of the manuscript. Review comments by Slater and Naudet also helped improve this manuscript. The U.S. Environmental Protection Agency through its Office of Research and Development collaborated in the research for this chapter. It has been subjected to the Agency's review and approved for publication. Mention of trade names or commercial products does not constitute an endorsement or recommendation for use.

References

Abdel Aal, G.Z., E.A. Atekwana, L.D. Slater, and E.A. Atekwana, 2004. Effects of microbial processes on electrolytic and interfacial electrical properties of unconsolidated sediments, *Geophys. Res. Lett.*, 31 (12), L12505, doi: 10.1029/2004GL020030.

Abdel Aal, G.Z., L.D. Slater, and E.A. Atekwana, 2006. Induced-polarization measurements on unconsolidated sediments from a site of active hydrocarbon biodegradation, *Geophys.*, 71, H13–H24, doi: 10.1190/1.2187760.

Aggarwal, P.K., and R.E. Hinchee, 1991. Monitoring in situ biodegradation of hydrocarbons by using carbon isotopes, *Environ. Sci. Technol.*, 25, 1178–1180.

Atekwana, E., E.A. Atekwana, R.S. Rowe, D.D. Werkema, Jr., and F.D. Legall, 2004a. The relationship of total dissolved solids measurements to the bulk electrical conductivity in an aquifer contaminated with hydrocarbon, *J. Appl. Geophys.*, 56, 281–294.

Atekwana, E.A., E.A. Atekwana, D.D. Werkema, J.P. Allen, L.A. Smart, J.W. Duris, D.P. Cassidy, W.A. Sauck, and S. Rossbach, 2004b. Evidence for microbial enhanced electrical conductivity in hydrocarbon-contaminated sediments, *Geophys. Res. Lett.*, 31, L2350.

Atekwana, E.A., W.A. Sauck, G.Z. Abdel Aal, and D.D. Werkema, Jr., 2002. Geophysical investigation of vadose zone conductivity anomalies at a hydrocarbon contaminated site: Implications for the assessment of intrinsic bioremediation, *J. Environ. Eng. Geophys.*, 7 (3), 102–110.

Atekwana, E.A., W.A. Sauck, and D.D. Werkema, Jr., 2000. Investigations of geoelectrical signatures at a hydrocarbon contaminated site, *J. Appl. Geophys.*, 44, 167–180.

Atekwana, E.A., D.D. Werkema, Jr., J.D. Duris, S. Rossbach, E.A. Atekwana, W.A. Sauck, D.P. Cassidy, J. Means, and F.D. Legall, 2004c. In situ apparent resistivity measurements and microbial population distribution at a hydrocarbon contaminated site: Implications for assessing natural attenuation, *Geophysics*, 69 (1), 56–63.

Balkwill, D.L., and D.R. Boone, 1997. Identity and diversity of microorganisms cultured from subsurface environments, in *The Microbiology of the Terrestrial Deep Surface*, edited by P.S. Amy and D.L. Haldeman, CRC, Boca Raton, FL, pp. 105–117.

Bekins, B., B.E. Rittmann, and J.A. Macdonald, 2001. Natural attenuation strategy for groundwater cleanup focuses on demonstrating cause and effect, *Eos, Trans, Am. Geophys. Union*, 82 (5), 53–58.

Bennett, P.C., F.K. Hiebert, and W. Joo Choi, 1996. Microbial colonization and weathering of silicates in a petroleum-contaminated groundwater, *Chem. Geol.*, 132, 45–53.

Bermejo, J.L., W.A. Sauck, and E.A. Atekwana, 1997. Geophysical discovery of a new Inapl plume at the former Wurtsmith Afb, Oscoda, Michigan, *Ground Water Monit. Rem.*, 17 (4), 131–137.

Bollinger, C., P. Hohener, D. Hunkeler, K. Haberli, and J. Zeyer, 1999. Intrinsic bioremediation of a petroleum hydrocarbon-contaminated aquifer and assessment of mineralization based on stable carbon isotopes, *Biodegradation*, 10 (201), 217.

Bouwer, E.J., H.H.M. Rijnaarts, A.B. Cunningham, and R. Gerlach, 2000. Biofilms in porous media, in *Biofilms II: Process Analysis And Applications*, edited by J.D. Bryers, Wiley-Liss, pp. 123–158.

Bradford, J.H., 2003. GPR offset dependent reflectivity analysis for characterization of a high-conductivity Inapl plume, in *Proceedings of the Symposium on the Application of Geophysics to Engineering and Environmental Problems (Sageep '03)*, April 6–10, San Antonio, TX, pp. 238–252.

Bryar, T.R., and R. Knight, 2002. Sensitivity of nuclear magnetic relaxation measurements to changing soil redox conditions, *Geophys. Res. Lett.* 29, 2197.

Burton, M., E.A. Atekwana, and E. Atekwana, 2003. Mineral grain surface observations at hydrocarbon-contaminated aquifer: Implications for the electrical properties of soils, in *Proceedings of the Symposium on the Application of Geophysics to Engineering and Environmental Problems (Sageep '03)*, April 6–10, San Antonio, TX., pp. 271–280.

Cassidy, D.P., D.D. Werkema, W.A. Sauck, E.A. Atekwana, S. Rossbach, and J. Duris, 2001. The effects of LNAPL biodegradation products on electrical conductivity measurements, *J. Environ. Eng. Geophys.*, 6, 47–52.

Chapelle, F.H., and P.M. Bradley, 1997. Alteration of aquifer geochemistry by microorganisms, in Hurst, 56Hurst, C.J., G.R. Knudsen, M.J. McInerney, L.D. Stetzenbach, and M.V. Walter (eds.), *Manual of Environmental Microbiology*, American Society for Microbiology, pp. 558–564. ASM Press, Washington, D.C.

Cozzarelli, I.M., B.A. Bekins, M.J. Baedecker, G.R. Aiken, R.P. Eganhouse, and M.E. Tuccillo, 2001. Progression of natural attenuation processes at a crude oil spill site: I. Geochemical evolution of the plume, *J. Contam. Hydrogeol.*, 53, 369–385.

Dojka, M.A., P. Hugenholtz, S.K. Haack, and P. Norman, 1998. Microbial diversity in a hydrocarbon- and chlorinated-solvent-contaminated aquifer undergoing intrinsic bioremediation, *Appl. Environ. Microbiol.*, 3869–3877.

Dunsmore, B.C., C.J Bass., and Lappin-ScottH.M., 2004. A novel approach to investigate biofilm accumulation and bacterial transport in porous matrices, *Environ. Microbiol.*, 6 (2), 183–187.

Duris, J.W., 2002. Microbial community structure in hydrocarbon impacted sediment associated with anomalous geophysical signatures, M.S.Thesis, Western Michigan University, Kalamazoo, MI, 1–72.

Gammack, S.M., E. Paterson, J. Kemp, M.S. Cresser, and K. Killham, 1992. Factors affecting the movement of microorganisms in soils, in *Soil Biochemistry*, edited by G. Stotzky and J.M. Bollag, Vol. 7, Marcel Dekker, New York, pp. 304–418.

Goodman, A.E., and K.C. Marshall, 1995. Genetic responses of bacteria at surfaces, in *Microbial Biofilms*, edited by H.M. Lappin-Scott and J.W. Costerton, Cambridge University Press, Cambridge, UK, pp. 80–98.

Hall-Stoodley, L., W.J. Costerton, and P. Stoodley, 2004. Bacterial biofilms: From the natural environment to infectious diseases, *Nat. Rev./Microbiol.*, 2, 95–108, doi: 10.1038/nrmicro821.

Heibert, F.K., and P.C. Bennett, 1992. Microbial control of silicate weathering in organic-rich ground water, *Science*, 258, 278–281.

Legall, F.D., 2002. Geochemical and isotopic characteristics associated with high conductivities in a shallow hydrocarbon-contaminated aquifer, Ph.D. Dissertation, Western Michigan University, Kalamazoo, MI, 1–85.

Lesmes, D.P., and K.M. Frye, 2001. Influence of pore fluid chemistry on the complex conductivity and induced polarization responses of Berea Sandstone, *J. Geophys. Res.*, 106 (B3), 4079–4090.

Lovely, D.R., 1990. Magnetite Formation During Microbial Dissimilatory Iron Reduction, *Iron Biominerals*, edited by R.B. Frankel and R.P. Blakemore, Plenum, New York, pp. 151–166.

Maier, R.M., I.L. Pepper, and C.P. Gerba, 2000. *Environmental Microbiology*, Academic, San Diego, CA, pp. 156–157.

Mann, S., J. Webb, and R.J.P. Williams (eds), 1989. *Biomineralization: Chemical and Biochemical Perspectives*, VCH, New York, pp. 1–385.

Marshall, K.C., 1976. *Interfaces in Microbial Ecology*, Harvard University Press, Cambridge, Mass, pp. 44–47.

Marshall, K.C., 1985. Mechanisms of bacterial adhesion at solid–water interfaces, in *Bacterial Adhesion*, edited by D.C. Savage and M. Fletcher, Plenum, New York, pp. 133–161.

Marshall, K.C., 1992. Biofilms: An overview of bacterial adhesion, activity, and control at surfaces, *Am. Soc. Microbiol. News*, 58, 202–207.

Mcmahon, P.B., D.A. Vroblesky, P.M. Bradely, F.H. Chapelle, and C.D. Gullet, 1995. Evidence for enhanced mineral dissolution in organic acid-rich shallow ground water, *Ground Water*, 33 (2), 207–216.

Moskowitz, B.M., R.B. Frankel, and D.A. Bazylinski, 1993. Rock magnetic criteria for the detection of biogenic magnetite, *Earth Planet. Sci. Lett.*, 120, 283–300.

Naudet, V., A. Revil, J.Y. Bottero, and P. Begassat, 2003. Relationship between self-potential (sp) signals and redox conditions in contaminated groundwater, *Geophys. Res. Lett.*, 30 (21), 2091.

Naudet, V., and A. Revil, 2005. A sandbox experiment to investigate bacteria-mediated redox processes on self-potential signals, *Geophys. Res. Lett.*, 32, doi: 10.1029/2005gl022735.

Newby, D.T., I.L. Pepper, and R.M. Maier, 2000. *Microbial Transport in Environmental Microbiology*, edited by R.M. Maier, I.L. Pepper, and C.P. Gerba, Academic, New York, 585 p.

Ntarlagiannis, D., K.H. Williams, L.D. Slater, and S.S. Hubbard, 2005a. Low frequency electrical response to microbial induced sulfide precipitation, *J. Geophys. Res.*, 110, G02009, doi: 10.1029/2005JG000024.

Ntarlagiannis, D., N. Yee, L. Slater, and E.A. Atekwana, 2005b. Electrical measurements on microbial cells in suspension and in sand columns, *Eos Trans. AGU*, 86 (18), Jt. Assem. Suppl., May 23–27, Abstract Ns51b-06.

Nyquist, J.E., and C.E. Corry, 2002. Self-potential: The ugly duckling of environmental geophysics, *The Leading Edge*, 21, 446–451.

Park, D.H., and J.G. Zeikus, 2000. Electricity generation in microbial fuel cells using neutral red as an electronophore, *Appl. Environ. Microbiol.*, 66 (4), 1292–1297.

Prodan, C., F. Mayo, J.R. Claycomb, J.H. Miller, and M.J. Benedik, 2004. Low frequency, low-field dielectric spectroscopy of living cell suspensions, *J. Appl. Phys.* 95 (7), 3754–3756.

Redman, J.A., S. Walker, and M. Elimelech, 2004. Bacterial adhesion and transport in porous media: Role of the secondary energy minimum, *Environ. Sci. Technol.*, 38, 1777–1785.

Robert, M., and C. Chenu, 1992. Interactions between soil minerals and microorganisms, in *Soil Biochemistry*, edited by G. Stotzky and J.M. Bollag, Vol. 7, Marcel Dekker, New York, pp. 307–418.

Sauck, W.A., E.A. Atekwana, and M.S. Nash, 1998. High conductivities associated with an Inapl plume imaged by integrated geophysical techniques, *J. Environ. Eng. Geophys.*, 2 (3), 203–212.

Sauck, W.A., 2000. A conceptual model for the geoelectrical response of LNAPL plumes in granular sediments. *J. Appl. Geophys.*, 44, 151–165.

Shevlin, V., A. Mousatov, E. Nakamura-Labastida, O. Elgado-Rodriguez, J. Sanche-Osi, and H. Sanchez-Osio, 2003. Study of oil pollution in airports with resistivity sounding, in *Proceedings of the Symposium on the Application of Geophysics to Engineering and Environmental Problems* (Sageep 2003), San Antonio, TX., Paper Con02, pp. 180–189.

Stoodley, P., R. Cargo, C.J. Rupp, S. Wilson, and I. Klapper, 2002. Biofilm mechanics and shear-induced deformation and detachment. *J. Ind. Microbiol. Biotechnol.* 29, 361–368.

Stumm, W., and J.J. Morgan, 1995. *Aquatic Chemistry: Chemical Equilibria and Rates in Natural Waters*, 3rd edition. New York: John Wiley and Sons.

Turco, R.F., and M. Sadowsky, 1995. The microfloral of bioremediation, in *Bioremediation: Science and Applications*, edited by H.D. Skipper and R.F. Turco, Special Publication No. 43, Soil Science Society of America, Madison, WI., pp. 87–102.

Van Der Wal, A., M. Minor, W. Norde, A.J.B. Zehnder, and J. Lyklema, 1997a. Conductivity and dielectric dispersion of gram-positive bacterial cells, *J. Colloidal Interfacial Sci.*, 186, 71–79.

Van Der Wal, A., M. Minor, W. Norde, A.J.B. Zehnder, and J. Lylkema, 1997b. Electrokinetic potential of bacterial cells, *Langmuir*, 13, 165–271.

Van Loosdrecht, M.C.M., J. Lyklema, A.J. Norde, and B. Zehnder, 1990. Influence of interfaces on microbial activity, *Microbiol. Rev.*, 54, 75–87.

Werkema, D.D., E.A. Atekwana, A.L. Endres, W.A. Sauck, and D.P. Cassidy, 2003. Investigating the geoelectrical response of hydrocarbon contamination undergoing biodegradation, *Geophys. Res. Lett.*, 30 (12), 1647.

Williams, K.H., D. Ntarlagiannis, L.D. Slater, P. Long, A. Dohnalkova, S.S. Hubbard, and J.F. Banfield, 2004. Remote sensing of subsurface microbial transformations, *Eos Trans., AGU*, Abstract B51f-01.

Williams, K.H., D. Ntarlagiannis, L.D. Slater, A. Dohnalkova, S.S. Hubbard, and J.F. Banfield, 2005. Geophysical imaging of stimulated microbial mineralization, *Environ. Sci. Technol.*, 39, 7592–7600.

Wolfaardt, G.M., J.R. Lawrence, R.D. Robarts, S.J. Caldwell, and D.E. Caldwell, 1994. Multicellular organization in a degradative biofilm community, *Appl. Environ. Microbiol.*, 60, 434–446.

7. COLD REGIONS HYDROGEOPHYSICS: PHYSICAL CHARACTERISATION AND MONITORING

Helen K. French, Andrew Binley, Ivan Kharkhordin, Bernd Kulessa, and Sergey S. Krylov

7.1. Introduction

The use of geophysical methods to characterize distribution of continuous and discontinuous permafrost has been widely applied (e.g. Arcone et al., 1998; Sullivan et al., 2000; Hauck et al., 2001; Hinkel et al., 2001; Moorman et al., 2003) including ground penetrating radar (GPR), electrical resistivity (ER) and electromagnetic (EM) sounding. Different methods have been employed to study water movement in frozen soils: time domain reflectrometry (TDR), electrical resistivity (ER), EM soundings and self potential (SP). In this chapter the main focus is on the use of geophysical methods to solve hydrological problems in areas with frozen conditions, but also includes examples of characterisation of structures in the permafrost which have an importance for hydrogeological processes in these regions. Frozen and thawed structures in the subsurface may cause water and contaminant pathways which are not intuitively based on traditional soil stratification procedures. Because these structures are temperature dependent there may also be a need to monitor spatio-temporal changes in these structures in order to assess how they may affect flow paths in the ground. Time-lapse measurements may hence be required. To study changes in the soil water system under frozen or partially frozen conditions can be a challenge; soil water sampling equipment may freeze and destructive methods such as conventional soil sampling is impossible under frozen conditions. The objective of conducting various geophysical methods in a hydrological perspective is to describe flow paths and to improve models for water and solute transport under partially frozen conditions.

The next section of this chapter describes the physical properties of permafrost, seasonally frozen soils and glaciers, and is followed by descriptions of how these affect the hydrology in the respective systems. A description of applicable geophysical methods and properties obtained under frozen conditions are given in part 2. Some of the methods are described in more detail than others due to limited space. A new book on application of geophysical methods on glacial and periglacial terrain edited by Hauck and Kneisel

will, however, be published in the near future and should be a more complete description of applicable methods in cold regions. In part 3 case studies providing examples of some of the applicable geophysical methods are presented. Conclusions and a substantial list of references finalize this chapter.

7.1.1. DESCRIPTION OF FROZEN SYSTEMS

7.1.1.1. *Permafrost*

Permafrost is a widespread phenomena in the world and can be encountered in any cold or mountainous region. In about 25% of the continental areas, frozen ground is the foundation for buildings, dams, waste sites, and other engineering constructions. More than 60% of Russia is affected by permafrost conditions. Permafrost is defined as any rock or soil material containing frozen water that has remained below 0°C continuously for two or more years. Another type of material is frozen ground without ice due to high salinity of pore fluid. The maximum thickness of permafrost can be up to 600–800 m (Taimyr, Russia) while rocks at negative temperatures can be 1000–1500 m thick (Anabarskiy Shield, Russia). Generally, these rocks underlie the massive permafrost zone in Eastern Siberia. A conceptual model of a permafrost zone is shown in Figure 1.

The overlying ground surface layer affected by seasonal frost, i.e. which freezes every winter and thaws every summer, is called the 'active layer.' The thickness of the active layer generally ranges from 1 to 4 m and depends on a number of factors such as average summer temperature, slope exposition, soil type, drainage conditions, etc (Kiryukhin et al., 1989). A deviation of about 20% from a mean value of long-term observations of seasonal melting depth has been observed.

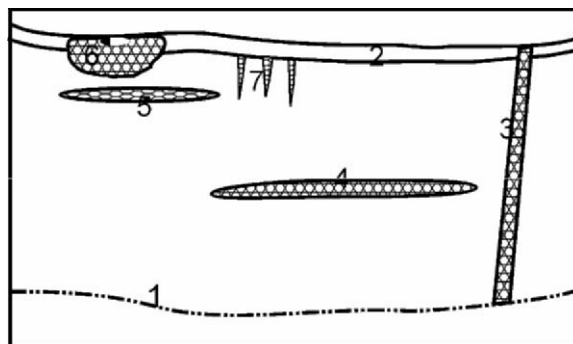


Figure 1. Cryostructure of permafrost zone (not to scale). 1 – bottom permafrost boundary, 2 – seasonally active layer, 3 – penetrating talik along fault, 4 – interpermafrost talik with saline water (cryopeg), 5 – subsurface ice lens, 6 – local talik under river, 7 – ice veins

Not only seasonally melted layers can be detected in the permafrost zone, 'taliks' are another type of thawed soil or rock material found near rivers. These thawed zones are caused by the heating effect of rivers, and generally contain fresh groundwater. These zones are very important for water supply (Ponomariov, 1960; Kulakov, 1990). Fresh water resources in areas of permafrost are extremely restricted. In the coldest regions, when the temperature of permafrost under the active layer is below -5°C , thawed zones do not generally penetrate through all the permafrost. Close to the southern boundary of these areas the permafrost becomes discontinuous.

Intensive water circulation along faults sometimes produces thawed zones. In winter such zones can be delineated at the land surface by frazils formed due to freezing of discharging water. A frazil is an ice body on the ground surface caused by freezing of discharging groundwater or water flow through ice covered rivers. Water in the fractured zones inside the permafrost can also be used for water supply. 'Cryopegs' (Tolstikhin, 1941), or lenses of saline water captured during freezing, is the last type of thawed zones within the permafrost. This solution is in thermodynamic equilibrium with ice at a given temperature and pressure. Frequently such lenses are under cryogenic water head, which may exceed the hydrostatic head. Cryogenic water head is the pressure created during water freezing.

Two areas of application of geophysical methods in cold regions for hydrologic and engineering purposes can be defined: (1) exploration of groundwater resources and (2) long-term monitoring of natural and man-made changes to the permafrost state. Hydrogeophysical methods help to solve a number of hydrogeological and engineering problems such as: mapping the melting zones near rivers and faults; monitoring of permafrost state under engineering constructions; forecasting of contaminant transport and monitoring at waste disposal sites; monitoring of cryogenic processes like frost heaving, thermal karst, and freeze fracturing.

7.1.1.2. *Seasonally Frozen Soils*

Seasonally frozen soils have temperatures below 0°C during winter time, but thaw completely during summer. In contrast to the active layer described above they are not underlain by permafrost. Seasonally frozen soils are found near the ground surface and are usually unsaturated (see also chapter by G. Cassiani), but is also found in areas with shallow groundwater systems e.g. in bog areas. The freezing process itself will have effect on water movement in the unsaturated soil, leading to movement of unfrozen water towards the freezing zone which eventually is filled up by ice. This process can cause mechanical changes in the soil such as frost heave. The freezing and thawing process may also have chemical effects because ion-rich water remains unfrozen at lower temperatures than pure water, in addition the freezing and thawing process

may provoke e.g. the release of, for instance, dissolved organic carbon from organic litter (Lewis and Grant, 1979; Boyer et al., 2000). The depth of the ground frost is largely dependent on the time of freezing and snow fall. The infiltration capacity in seasonally frozen soils will also be affected by the water contents at the time of freezing. Impermeable ice cover often formed on the ground surface may prevent feeding of groundwater during snowmelt. The cumulative infiltration of meltwater released by a melting snow cover varies directly with the snow water equivalent and inversely with the total water content (ice and liquid water) of the soil at the time of melt (Kane and Stein, 1983; Granger et al., 1984; Gray et al., 1985; Woo and Marsh, 1990). The snow cover serves as an insulation layer and may prevent soil frost development. Zhao et al. (2002) showed that seasonal amounts of snowmelt infiltration are relatively insensitive to variations in soil texture. At a fixed sub-zero temperature and water content the more sandy soils have higher ice content than the more clayey soils, hence the hydraulic conductivity is reduced relatively more in the sandy soils than in the clayey soils.

7.1.1.3. *Glaciers*

As described in many popular textbooks (Hambrey and Alean, 1992; Patterson, 1994; Bennett and Glasser, 1996; Benn and Evans, 1997; Post and LaChapelle, 2000), glaciers form by gradual transformation of snow to ice as a result of progressive burial and compaction, and cover approximately 10% of the earth's surface. Approximately 75% of the earth's freshwater resources are frozen within glaciers, ranging dramatically in size from small mountain ice masses a few hundred meters across to large continental glaciers, such as e.g. the Greenland and Antarctic ice sheets. Driven by gravity, all glaciers flow, their long-term health being determined by the rate of ice accumulation in their upper reaches relative to the rate of ice wasting in the lower reaches. Depending on whether ice masses terminate on land or on water, wasting respectively involves melting (*ablation*) or mechanical disintegration (*calving*) in variable proportions. Glacier flow can occur by internal (*englacial*) ice deformation, sliding over the glacier bed, or by deformation of unconsolidated *subglacial* sediments where they are present between the ice base and the bedrock. Glaciers are either temperate or cold if they contain significant amounts of or no liquid water, respectively, or polythermal if they contain both temperate and cold ice. Polar glaciers are typically composed of cold ice, often with temperate ice near the base as a result of geothermal heating, while mountain glaciers in warmer climates are often entirely temperate. Apart from the geometrical and structural properties of glaciers and the underlying substrate, their thermal regimes and heat budgets have a strong impact on ice flow and response to climatic change. In the light of ongoing global warming it is vital to understand such responses since the accelerated melting of the world's glaciers threatens to contribute

significantly to sea level rise, negatively impact water resources and increase glacial hazards on a global scale, and potentially cause feed back on the climate itself.

7.1.2. HYDROLOGICAL PROCESSES IN COLD REGIONS

7.1.2.1. *Hydrogeological and Cryological Processes in Permafrost Areas*

The most important processes for hydrologists in permafrost zone are related to phase transitions as well as water and solute transport in frozen ground. A number of phenomena related to the freezing processes are observed in cold regions: the presence and formation of frozen and thawed structures in soils, e.g. taliks (Figure 1); freeze fracturing; frost heaving; thermal karst (i.e., subsidence caused by melting of buried ice); contaminant transport. A description of conceptual and mathematical models for these processes have been published by Ershov (1979), Grechishev et al. (1984), Feldman (1988), Gorelic and Kulinin (2002), Grant and Iskandar (2000) and Washburn (1979). An advanced petrographical study of frozen rocks was performed by Solomatkin (1986).

To understand the development of frozen ground properties it is important to take into account that liquid water may be present in frozen ground due to three reasons: (1) freezing point depression of pore water caused by increased ion concentration of remaining pore liquid during freezing; (2) lowering of freezing point in thin capillaries; (3) freezing point depression in the vicinity of charged mineral surfaces.

There is only a limited number of contributions to the modeling of brine (saline water), minerals and ice equilibrium at temperatures below 0°C, but some examples may be found in Marion and Farren (1999) and Charykova and Charykov (2003). Experimental data on salt solubility at temperatures below 0°C are also available (Pelsh, 1973). Both experiments and calculations have shown that the observed quantity of unfrozen water can not only be explained by the lowering of freezing temperature in concentrated salt solutions.

The effect of pore size distribution on temperature dependency of freezing of solutions in pores was analyzed by Gorelic and Kulinin (2002). It was shown that the lowering of freezing temperature in silts and clays could not be quantitatively explained by the effect of capillary forces alone. The quantity of unfrozen water correlates with specific surface of porous media. There is experimental evidence of ice melting nearby hydrophilic surface (Anisimov and Tankaev, 1981). At present we do not have a valid theoretical description of this effect, but it is likely that it could be derived from the theory of double electrical layer. The idea is similar to the theory of surface super conductivity. The ion concentration near the particle surface depends on surface charge and zeta-potential. As the freezing temperature is a function of ion concentration, the freezing temperature will also be affected by these properties.

7.1.2.2. *Hydrology in Seasonally Frozen Soils*

Seasonal ground frost greatly affects the hydrology in the Boreal zone in the Northern Hemisphere. Ground frost and the formation of impermeable ice on the ground surface redistribute melt water during the snowmelt period, and inhibit infiltration in sediments with otherwise high infiltration capacity (sandy aquifers). Some numerical groundwater models that include freezing and phase change have been developed (Ippisch, 2001; Jansson, 1991; White and Oostrom 2000) but this is uncommon in most commercial groundwater software. Physical processes occurring at cm and m scale near the surface, as described by e.g. Stähli et al. (1996) and Granger et al. (1984) are important controls of the flow of meltwater and can also affect the hydrology at a catchment scale (response time, etc.). As a result of impermeable ground surface, a large amount of melt water collects in depressions or becomes surface runoff. According to Baker and Spaans (1997); Derby and Knighton (1997); French and van der Zee, (1999); Hayashi et al., (2003); Johnsson and Lundin (1991) ponding (melt water collected on the surface), redistribution of meltwater and focussed infiltration during snowmelt are commonly observed. The focussed infiltration affects the flow pattern in the unsaturated zone (French et al., 1999). This may cause higher velocities through the unsaturated zone than during evenly distributed infiltration on the surface, hence reducing potential for contaminant degradation. Flow paths in shallow groundwater may also be affected by temporarily frozen ground (Titov et al., 2000). Organic pollutants such as de-icing chemicals near roads and airports (French et al., 2001), and excess nutrients and pesticides in agricultural areas, increase the risk of polluting the groundwater. Increased surface runoff during snowmelt may also contribute strongly to pollution of surface waters. Redistribution of meltwater may also cause infiltration along buildings into the insulation layer affecting heat capacity and exchange below these buildings.

7.1.2.3. *Glacier Hydrology*

Understanding the hydrological properties and processes of glaciers is important because the presence of *englacial* water within and *subglacial* water beneath glaciers exerts a strong control on ice mass dynamics and thus response to climatic change. Sudden rapid discharge of surface (*supraglacial*) melt water ponds through the ice body is a mechanism by which polar ice shelves can disintegrate catastrophically, and do so increasingly as a result of ongoing global warming. Catastrophic glacier lake outburst floods (GLOFs) represent an increasingly common environmental hazard e.g. in the Himalayas and South America, posing a severe threat to downstream infrastructure and communities. In mountainous regions, head-catchment hydrology is often controlled by the presence of glaciers, with key implications for downstream water resources (e.g. for hydroelectric power generation, agricultural irrigation,

and more general human use) and their long-term availability in the light of sustained glacier retreat. Future predictions of human impacts of cryospheric change thus critically depends on thorough understanding of glacier hydrology and whether these impacts are direct, e.g. through GLOFs, or indirect, e.g. through sea level rise or feedback of cryospheric processes on the global climate.

The extent of a glacier's hydrological system depends on its heat budget, and therefore differs between temperate, polythermal, and cold ice masses. As reviewed e.g. by Hooke (1989), Hubbard and Nienow (1997), and Fountain and Walder (1998), temperate glaciers in warmer climates are at the pressure melting point through most of the year, supporting well-developed hydrological systems during the summer melt season. The water system of such glaciers may be divided into supraglacial, englacial, and subglacial hydrology, all of which are intimately linked with each other. During the summer melt season when the snow cover (*snowpack*) has melted, supraglacial melt water flow typically accumulates in, and is rapidly evacuated via, river-like, meandering channels incised downward into the ice. Melt water can enter the ice body through moulin (sub-vertical passageways created by melt water action) or crevasses (sub-vertical fractures created by mechanical action e.g. as glacier flow around obstacles). A variety of englacial flow passageways have been proposed to exist, ranging in size from very small-scale flow along ice grain intersections to much larger scale, englacial conduits originating e.g. as crevasse-bottom streams are pinched off by ice creep. Although several theoretical and conceptual models of such passageways have been developed, little compelling field evidence reflecting their relative frequency of occurrence and spatial distribution has so far been reported. In contrast, subglacial hydrological systems at temperate glaciers have been studied comparatively well, both on a theoretical basis and from a field-based perspective. Widespread, *distributed* drainage is dominant subglacially, taking the form of either (i) a water film between the ice base and the subglacial substrate, (ii) a system of linked cavities, or (iii) Darcian flow through subglacial sediments, where they are present. During the summer melt season distributed drainage is intersected by an arterial network of subglacial channels, bifurcating frequently from large trunk tunnels near the glacier terminus to progressively smaller, upglacier feeder channels. Such channels are effective in evacuating large quantities of melt water, while the relatively inefficient distributed system controls water storage at the bed. During winter, channels are absent and subglacial drainage is predominantly distributed, since little melt water can percolate through the commonly meter-thick snowpack to enter the ice body or reach the glacier bed. While water pressure and discharge in subglacial channels scale inversely, they are directly related in distributed drainage systems.

7.2. Applicable Geophysical Methods in Cold Regions

Data on geophysical properties of frozen media are scarcer in literature than unfrozen properties, but necessary for interpretation of measurements performed under such conditions. Different geophysical methods have different challenges with respect to their applicability under frozen conditions. Methods for calibrating geophysical measurements in cold areas may be more cumbersome than under thawed conditions, as frozen ground is difficult to sample. A practical guide to periglacial field methods is given in e.g. Humlum and Matsuoka (2004). Methods that require grounding, e.g. through electrodes, may have problems obtaining the necessary electrical contact with the frozen media due to the lack of free ions, while methods such as ground penetrating radar and capacitively coupled systems do not have this problem. A proposed method to reduce the grounding resistance problem is to supply current to the electrode during freezing (Merrian, 2004). The next sections, give examples of measured geophysical properties and highlights challenges for various methods under frozen conditions.

7.2.1. ELECTRICAL RESISTIVITY (ER)

The electrical resistivity of frozen materials is usually much higher than their resistivity in the unfrozen state. This can be explained by reduced liquid water contents and/or changed geometry due to frost heave. The electric charge in frozen rocks is mainly borne by the ions in the diffuse part of the electric double layer. The resistivity depends on the ice content in the porous media and particularly on the cryotexture. Table 1 shows some DC-resistivity values obtained *in situ* for unfrozen and frozen rocks in some regions in the North (adapted from Frolov, 1998).

The contact resistance is large in frozen environments because the number of free water molecules is limited. In temporarily frozen soils, however, there is usually some liquid water present. Time-lapse studies can be conducted by placing the electrodes below the ground frost. In permafrost areas surveys can be conducted in the active layer during summer. A general rule of thumb states that when temperature falls from 0°C to -1°C , the resistivity increases sharply by one to two orders of magnitude (step 1); if the temperature decreases to -8°C , the resistivity follows by one additional order of magnitude (step 2). At lower temperatures, the resistivity stabilizes (step 3). The change in resistivity versus temperature depends on the salinity of the pore liquid. When the salinity increases, the freezing temperature is reduced. In addition, salinity has a large influence on the cryogenic structure (Figure 1). Humid materials containing no ice are called “cool” and have low resistivity. After freezing the resistivity of these materials increases further and depends

TABLE 1. DC-resistivity values obtained in situ for unfrozen and frozen rocks in different regions of Northern Siberia

		Resistivity, kΩm	Cryostructure	Temperature, °C
Rocks				
Granite, gneiss, shale	Cracked	0.15–1.0	Frozen pore	–2
	Monolithic	12–30	50–100	–2
Limestone, marl.	Cracked	0.5–2.0	5–10	–2
	Monolithic	6–9	19–36	–2
Sandstone	Cracked	0.1–0.5	0.9–10	–2
	Monolithic	1–1.5	3–15	–2
Deposits				
Loamy sand		0.1–0.12	0.7–1.0	–0.5
Gravel, debris		0.07–0.18	3–15	–5
Clay loam		0.05–0.1	2–5 Layered recticulate	–1
Loam		0.02–0.1	0.2–3 0.2–40 3–100	–0.2 to –8 –1 to –8 –1 to –8
Sand		0.05–0.1	0.8–100 20–300	–0.2 to –7 –0.2 to –6
Peat			0.2–40	–0.2 to –3
Ground ice			3000	–2

* Schlieren is a piece of ice within the soil or rock material.

strongly on the cryogenic structure. If the salinity of the porous liquid is high ($>5\text{ g/l}$), the resistivity of sand and clay does not depend on the mineral composition and its dependence on the salinity obeys a power law (Frolov et al., 1997). In this particular study an exponent of 1.85 was suggested. Unfrozen deposits below 0°C possessing extremely low resistivity ($0.5–1\text{ }\Omega\text{m}$) are called cryopegs.

Direct current methods can be successfully applied to map permafrost, search for taliks and for exploring water flow paths through artificially frozen dams. As a rule, the stepwise increase in resistivity described above, correspond to a three-layer section. In summer the active layer has low resistivity, the second layer (frozen ground) has high resistivity, and the bottom layer with relatively low resistivity is usually composed of unfrozen or “cool” deposits with high salinity. It is challenging to separate lithological units within the frozen layer with the use of DC-methods. Sometimes rocks with high ice content or slab ice prevent the investigation of deeper layers. Shallow inhomogeneities like ice-wedges may also distort the resistivity response; this problem may be resolved with high spatial resolution ER tomography.

7.2.2. SELF POTENTIAL (SP)

Self potential (SP) is produced by different types of phenomena; one is the water flow in porous media (see Revil et al., 2006). Low salinity and low temperature are responsible for a low electrical conductivity of the pore water hence a high value of the streaming potential coupling coefficient. In a system with preferential flow of water with low ionic strengths and low temperature, typical for meltwater, extremely high electrical potential fluctuations (several hundreds millivolts) can be expected. Hence SP has the potential to reveal flow in thawed zones of a frozen layer. Titov et al. (2000) employed a combination of ER and SP methods to study water seepage from a reservoir under variable freezing conditions. Measurements were performed during spring floods (April–May 1998) before and after snowmelt near St., Petersburg, between a reservoir and a river. Strong bipolar anomaly in part of the vertical section was interpreted as large volumes of water seepage through only limited volume from the pond to the river. The seasonally frozen soil represented a temporary surficial barrier which caused the flow pattern to change completely from frozen to thawed conditions. Another example of SP application in glaciers is given in a later section.

7.2.3. ELECTROMAGNETIC SOUNDINGS (EM)

Frozen medium can be considered as non-ideal dielectric. Both frequency-domain (FEM) and time-domain (TEM) electromagnetic methods have been applied to permafrost areas (section 7.3.1.1. and e.g. Hoekstra and McNeil, 1973; Hauck et al., 2001). The penetration depth is mainly a function of the distance between transmitter and receiver but the use of appropriate frequency may optimise the signal strength for a specific target (Geonics, undated). The applicability of different FEM and TEM methods for mountain permafrost studies is described in Hauck et al. (2001).

If time varying electromagnetic field is applied, the AC-resistivity and dielectric permittivity become complex frequency-dependent functions. Sometimes it is more convenient to deal with conductivity, which is the reciprocal of resistivity. We can consider either effective conductivity $\sigma_e(\omega) = \sigma_1(\omega) + i\sigma_2(\omega)$, or effective dielectric permittivity: $\varepsilon_e(\omega) = \varepsilon_1(\omega) - i\varepsilon_2(\omega)$. Here, $\sigma_2 = \omega\varepsilon_1$, $\varepsilon_2 = \sigma_1/\omega$, $i = \sqrt{-1}$.

Dispersion (i.e. change with excitation frequency) of dielectric permittivity in ice and frozen media is considered in the literature (Olhoeft, 1985; Maeno et al., 1992; Frolov, 1998). Although dispersion of ε is discussed here, similar issues will apply to dispersion of conductivity. The dispersion of dielectric permittivity of ice can be described by the Debye formula (Debye, 1929). The results of laboratory experiments and detailed review of fresh ice

dielectric properties are given in Hobbs (1974); Petrenko (1993); Fujita et al. (1993).

It is established, that ε_1 of fresh ice varies from $100\text{--}130 \varepsilon_0$ (where ε_0 is the permittivity of the free space $= (1/36\pi)10^{-9}\text{F/m}$) at low frequencies to $3.2\varepsilon_0$ at high frequencies. The main change of the fresh ice permittivity occurs at frequencies $10^3\text{--}10^4$ Hz, and this range moves towards low frequencies when the temperature falls.

Frequency dispersion of electrical properties in ice-containing frozen materials was thoroughly documented in laboratory (Olhoeft, 1985; Maeno et al., 1992; Frolov, 1998) and in field experiments. Olhoeft (1985) and Maeno et al. (1985) carried out experiments with naturally frozen clays, whereas Frolov (1998) worked with artificially frozen samples. The results of the experiments with artificial samples demonstrated that in most cases the frequency dispersion can be described by the Cole–Cole formula (Cole and Cole, 1941). The Debye formula (a special case of the Cole–Cole formula) is suitable for ice, while the Cole–Cole formula describes the dispersion of dielectric permittivity of frozen materials and rocks. Permittivity reaches a high frequency limit ($\sim 2.5\varepsilon_0$) at frequencies of $10^5\text{--}10^7$ Hz. At low frequencies the permittivity tends to values of $200\text{--}300\varepsilon_0$. The frequency range of dispersion shifts to low frequencies when the temperature or salinity decreases.

The frequency dependency of electrical properties of *natural* frozen materials appears to be much more complicated. Olhoeft (1985) investigated the samples of frozen sediments sampled from the borehole drilled near Tuktoyaktuk at 10 m depth, North-Western Territories of Canada. The samples were kept in frozen state when transported and stored in the laboratory. The measurements of electrical properties were carried out at -10.2°C , the in-situ temperature, and under varying confining pressure. The confining pressure range corresponded to depths of 0–10 m. In the frequency range $10^1\text{--}10^6$ Hz five areas of frequency dispersion with different relaxation times were detected. Olhoeft (1985) attributed them to five different physical reasons for dielectric relaxation. The resistivity of investigated samples was reduced from 10^5 to $5 \times 10^2 \Omega\text{m}$ when frequency increased from 10^1 to 10^6 Hz, and relative permittivity was reduced from 10^4 to approximately 30.

Maeno et al. (1992) conducted experiments with the samples of humid clayey sediments at temperatures above and below zero. The obtained frequency dependencies of conductivity and permittivity demonstrate smooth change of these parameters within a frequency range of $30\text{--}10^5$ Hz. When the humidity is high (above 20%) and the temperatures are about 0°C , the dielectric permittivity at frequencies $10^3\text{--}10^5$ Hz is changed by two orders of magnitude, exceeding $2000 \varepsilon_0$ at low frequencies.

Similar behaviour of a medium's electric parameters is typical for the so called “anomalous low frequency dispersion” (ALFD) (Jonscher, 1990).

There is no fixed relaxation time in a wide frequency range for the ALFD, unlike the dispersion described by the Cole–Cole formula. The permittivity does not reach the low-frequency limit tending to the extremely high values, while the loss tangent remains constant. This type of electric polarization is often called CPA (constant phase angle) process, and it was observed for a set of natural and artificial materials such as ionic glasses, polymers, a porous ceramic catalyst, humid sand, granite etc. Corresponding frequency dependence of permittivity was named “universal dielectric function:”

$$\tilde{\epsilon} \sim (i\omega/\omega_p)^{n-1}, \quad \omega > \omega_p,$$

$$\tilde{\epsilon} \sim (i\omega/\omega_p)^{-m}, \quad \omega < \omega_p,$$

where $0 < n < 1$, $0 < m < 1$, and $m > (1 - n)$ in most of the experiments, and ω_p is crossover frequency. Concluding from this, laboratory measurements show a frequency dispersion of resistivity and permittivity of frozen fine-grained and coarse-grained sediments in the frequency range 10^1 – 10^6 Hz. In this range the resistivity is reduced by two-three orders of magnitude when frequency increases, and low-frequency permittivity can reach anomalously high values of 10^3 – $10^4 \epsilon_0$ (Maeno et al., 1992).

Exemplified by several field tests conducted both with transient and frequency electromagnetic (TEM, FEM) soundings in permafrost regions the frequency dispersion of resistivity and permittivity has been documented. In TEM soundings the polarization phenomena lead to sign change of transient process (Walker and Kawasaki, 1988), whereas in FEM the characteristic distortions of apparent resistivity curves can be observed (Krylov and Bobrov, 1998). Some results of dispersion parameters based on field electromagnetic soundings, are given in Table 2 (dispersion was approximated by the Cole–Cole formula).

TABLE 2. Dispersion parameters

Reference	Region	Type of frozen sediments	Relaxation time, μ s	Chargeability	Resistivity at high freq., Ohmm	Resistivity at low freq., Ohmm
Walker and Kawasaki, 1988	Alaska	Sand	700	0.5	500	1000
Kozevnikov & Nikiforov, 1995	Buryatia	Sand	—	—	—	10^3 – 10^4
Krylov and Bobrov, 1998	Yamal peninsula	Loam	10	0.4–0.6	20–40	50–100
Zadoroznaya and Lepeshkin, 1998	Tazovsky peninsula	Loamy sand	80	0.2	40–200	50–225

Frequency dispersion of the electrical properties of frozen sediments makes it complicated to interpret EM investigations, but it can serve as valuable additional information. For example, the dispersion phenomena allows one to detect geological sections of the loams with high ice content, having DC-resistivity equal to that of frozen sand or fresh slab ice.

7.2.4. CAPACITIVELY COUPLED SYSTEMS

A capacitively-coupled resistivity meter (Tomifeev et al., 1994) consists of a simple coaxial-cable array with transmitter and receiver sections. A transmitter electrifies two coaxial cables (transmitter dipole) with an AC current. Current is thus coupled to the earth through the capacitance of the cable. A matched receiver, automatically tuned to the transmitter frequency, measures the associated voltage picked up on the receiver's dipole cables. The receiver then transmits a voltage measurement, normalized to current, to a logging console. No grounding is required and the system works best in resistive environments, hence it is very suitable for monitoring frozen systems. The electrical properties of the ground are measured without any galvanic electrodes used in traditional resistivity surveys. The OhmMapper TR1 (Geometrics) and the CORIM (Iris instruments) are two examples of capacitively-coupled resistivity systems designed to measure subsurface resistivity in areas where exploration using a traditional galvanically coupled (DC) resistivity system is non-applicable. The system is pulled along the ground either by a single person or attached to a small all-terrain vehicle. In order to collect a 2D depth section, the OhmMapper can be set up with a number of receivers, hence with several different transmitter-receiver. Similarly to other resistivity methods, 3D images can also be achieved. Typical depths of investigation are 10–20 m. The OhmMapper operates in the range from <3 to $>100,000$ Ωm . The CORIM has been designed for shallow investigations (few meters). Hauck and Kneisel (2003) compared measurements of electrical resistivity obtained along the same partially frozen ground profile. They found more noise in the capacitively coupled system measurements than the traditional DC measurements. They also found that the apparent resistivities were lower for the OhmMapper than the DC measurements, possibly explained by higher contact resistance when grounding is necessary. There are so far few publications on the application of this system in frozen environments, possibly explained by the fact that commercial systems have not been available until recently.

7.2.5. GROUND PENETRATING RADAR (GPR)

Ground penetrating radar has been widely used in different frozen environments because different types of ice and non-frozen ground vary in their

TABLE 3. Soil dielectric permittivity (Sullivan et al., 2000)

Material	Permittivity value
Pure ice	3.1–3.2
Permanently frozen materials	4.4–5.6
Unfrozen saturated sediments	12.0–45.0
Dry soil	4.0–8.0
Weathered bedrock	> 11.0
Bedrock: granite: sandstone	7.0–9.0, 10.0
Sand: dry, 15% moisture, 25% moisture	≈3.0, ≈9.0, ≈25.0

response to radar sounding. The GPR system transmits a short electromagnetic (EM) pulse (frequency range from 10 to 1000 MHz) into the ground and the reflection is recorded by the receiving antenna. The greater the contrast in dielectric permeability the larger is the amplitude of the reflected pulse. Propagation of EM waves in an isotropic medium is a function of the dielectric permittivity (ϵ , which affects the wave propagation time) and the electric conductivity (σ , which affects the loss factor). Both values are very sensitive to soil moisture content (Parkhomenko, 1967; Arcone et al., 1998). For more general information see e.g. Sharma, (1997) and Reynolds, (1997). Some examples of soil dielectric permittivity values at high frequencies, > 1 MHz, are given in Table 3.

Frozen ground has distinct dielectric properties. There are several examples of GPR being used to identify horizontal and lateral distribution of permafrost zones, the water table and bedrock (e.g. Hinkel, et al., 2001; Moorman et al., 2003; Bradford et al., 2005). Sullivan et al. (2000) provided an objective method of GPR data interpretation of partially frozen ground, including permafrost zones crossing between the unsaturated and saturated zones, using neural network methods.

In some cases, the small scales of depth and lateral variations of permafrost make GPR a more appropriate method than seismic and EM induction methods (Arcone et al., 1998). Because of the low signal attenuation in frozen ground GPR can extend to greater depths than in unfrozen environments, for one location 25 m in frozen ground compared to 10 m under unfrozen conditions (Moorman et al., 2003). The temperature gradient near the base of the permafrost is generally smaller than the top of the permafrost, which can lead to a very broad frozen fringe that in addition to noise and signal attenuation causing the base of permafrost seldom to be imaged. Another important issue in frozen ground mapping is that there is great lateral variation in propagation velocity. At the edge of a frozen zone the propagation velocity can change by 300% (Moorman, 2003).

Both surface and borehole based geophysical methods can be used to investigate subglacial hydrological properties and processes, although both are still

very sparsely documented in the literature. Copland and Sharp (2001) demonstrated that reconstructing the bed reflection power at polythermal glaciers using surface-based radar measurements can support mapping of subglacial hydrological conditions, allowing delineation of distributed and channelised subglacial drainage systems in particular.

7.2.6. SEISMIC REFLECTION PROFILING

The use particularly of seismic reflection methods in studying hydrological properties of frozen and glacial materials has recently increased in popularity. Röthlisberger (1972) reviews early seismic work on glaciers and in frozen ground, and provides a guide for solving the practical problems particular to seismic field work in cold regions. A key observation is that seismic velocity decreases with increasing temperature in all frozen materials by up to 80–90%, which indeed is supported by seismic theory (Zimmerman and King, 1986; Jacoby et al., 1996; Johansen et al., 2003). The decrease becomes increasingly more pronounced as the 0°C isotherm is approached and the material progressively melts. Seismic velocity is therefore a sensitive proxy for the liquid water content in frozen materials, and consequently can support studies of permafrost hydrology and deformation of glacial ice. In contrast, little is currently known about the attenuation of seismic waves in dependency of liquid water content.

Deriving reflection coefficients from seismic data recorded on glaciers and ice sheets has recently become popular in inferring the acoustic impedance of unlithified sediments sandwiched between overlying basal ice and underlying bedrock (Vaughan et al., 2003). This allows assessment of whether such subglacial sediments are water-saturated and actively deforming (Atre and Bentley, 1993; Smith, 1997; Anandakrishnan, 2003), subglacial permafrost is present (e.g. Smith et al., 2002a,b), pooled water or even a preferential water flow pathway are present at the ice-sediment interface (Atre and Bentley, 1994; King et al., 2004), or sediment hydro-mechanical properties are changing over time (Nolan and Echelmeyer, 1999). These observations are particularly important because motion and hydrology of the world's ice masses and their response to climatic forcing is strongly controlled by mechanical and hydrological processes interacting at the glacier bed.

7.3. Case Studies

7.3.1. PERMAFROST

7.3.1.1. *EM Soundings of Saline Permafrost and Anomalous Polarization*

Electromagnetic (EM) methods were employed to investigate saline permafrost at Bovanenkovo gas field, Yamal Peninsula, North-Western

Siberia. The objective of the investigation was to detect taliks, cryopegs and ground ice.

Yamal Peninsula is located between the Kara Sea and River Ob estuary north of Western Siberia. The area of investigation consists of flat marsh with numerous thermokarst lakes. Tundra plant cover is dominated by mosses, lichens, grasses and low shrubs. The upper part of the geological section was mainly formed in the Pleistocene. It is built by a sequence of intercalated saline and freshwater sediments. The thickness of permafrost is 185 m and the active layer is 0.5–2 m thick at the field site. Figure 2 shows a bore-hole section in one of the field sites and the corresponding generalized

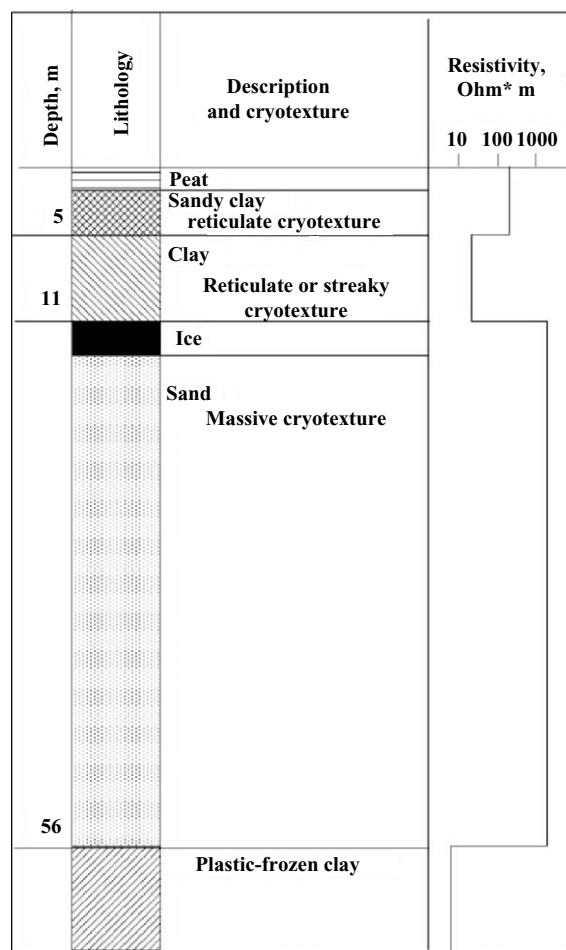


Figure 2. The stratigraphic borehole section at platform # 64 with description of the volume ice content and the cryotexture (drilling data from "Cryos" firm, 1991) and the generalised geoelectrical section obtained from EM soundings

vertical electrical sounding from the electrical logging and EM sounding with the description of ice texture and ice content for every geological unit.

The deepest and most ancient deposits at Bovanenkovo field are clays (salinity 6 g/kg) in the plastic-frozen (cool) state. Their upper boundary is located at 35–70 m below surface. These clays have high electric conductivity and because of the strong attenuation of electromagnetic field they are not permeable to EM soundings. Higher up in the profile there is a layer of frozen sand which is not saline but sometimes contains cryopegs. Lenses of slab ice (up to 10 m thick) often occur at the upper boundary of sand spit. The next layer is composed of marine clay or loam (salinity varies between 2.3–16 g/kg from one site to another), which has high ice-content and low electrical resistivity for alternating current at high frequencies. The combination of high salinity and high ice-content plays an important role for the electrical properties of permafrost. The top layer of the section consists of loamy sand covered by peat that is not saline.

The “Yamal-4” system developed at St. Petersburg University, is specialized equipment for conducting electromagnetic soundings for solving geotechnical problems in permafrost regions. The equipment allows for both frequency (FEM) and transient (TEM) soundings. A horizontal loop of 25 × 25 m was used as a primary source of EM field both in FEM and TEM techniques. Forty frequencies, ranging from 16 Hz to 160 kHz, were used in the FEM soundings. The resultant EM field was sensed by a ferrite antenna mounted on a tripod. The instrument for TEM soundings provides measurement of transient process at time delays from 10 μ s to 10 ms. A separate loop was used as the receiver of the induced signal.

It is well known, that in TEM soundings with coinciding loops, performed over a medium with frequency dispersion of electrical properties, the value of the time derivative of the transient voltage response could be changed, and negative values of the signal may occur (Flis et al., 1989). The sign change of the transient process has previously been observed in permafrost regions (Walker and Kawasaki, 1988).

TEM sounding with coinciding loops, carried out at the Bovanenkovo gas field, produced negative values of measured transient voltage at 16–25 μ s. The resistivity of the medium with the frequency dispersion should be considered as complex. It is usually described by the Cole-Cole formula (Pelton et al., 1978).

$$\tilde{\rho}(i\omega) = \rho_\infty \left(1 + \frac{m}{1 - m + (i\omega\tau)^c} \right) \quad (1)$$

where ω is the angular frequency, m is chargeability, $m = (\rho_c - \rho_\infty)/\rho_c$,

τ : relaxation time of polarisation process, ρ_∞ : resistivity at high frequencies, ρ_c : resistivity at low frequencies.

Mathematical simulations of TEM soundings using the model including the frequency dispersion in the second layer were carried out. The results showed that the observed distortions of the sounding curves could only be explained if dispersion described by the formula (1) with $c \cong 1$ is assumed. The parameters of the Cole-Cole formula (m, τ, ρ_∞) for the second layer, which provided the best fit of theoretical curve to experimental data, were determined.

The chargeability of clayey deposits commonly does not exceed 0.1, the measured value of 0.4 seems to be anomalously high. If we introduce a frequency dependent relative effective permittivity ε as $\varepsilon = \text{Im} \tilde{\sigma} / \omega \varepsilon_0$, where $\tilde{\sigma} = 1/\tilde{\rho}$ is the complex conductivity and ε_0 is the dielectric constant of vacuum, the low-frequency value of permittivity (ε_c), corresponding to the above parameters m, τ, ρ_∞ , will also be extremely high. For this particular case $\varepsilon_c = 1.8 \times 10^4$. Frequency dispersion characterized by such extreme values of chargeability and permittivity must be considered as anomalous.

Because the instant of sign change depends only on the relaxation time of induced polarization process, the effect of the dispersion in the second layer appears in the sounding curve at the moment corresponding to the electromagnetic response of the fourth layer. In Figure 3 the theoretical curve of TEM sounding is shown. There is good agreement between the calculated curve and the field data, justifying the choice of Eq. (1) to describe the observed frequency dispersion.

The results demonstrate that the frequency dispersion of electrical properties have to be taken into account in shallow permafrost EM-investigations. Any particular sedimentary material (clay, clayey sand or sand) can not be classified as non-frozen only on the basis of the low resistivity values obtained in alternate electromagnetic field. Unless polarization effects can be ruled out, joint interpretation of AC and DC results is necessary. Searches for talik zones are typically solved by joint interpretation. Contaminants in frozen sediments may be challenging to find with DC methods due presence of high-resistivity screens. If that is the case, EM soundings can be a more effective tool for solving hydrogeological problems, especially TEM soundings, which are highly sensitive to polarization effects. Moreover, high-frequency (fast) polarization is related to cryostructure of the rocks and can be used both for determination of ice-content and for monitoring of the state of frozen sediments. There are good reasons for assuming that polarization effects are "sensitive" to various types of technological pollution, but no experimental work has yet been performed and investigations of these effects will be undertaken in the future.

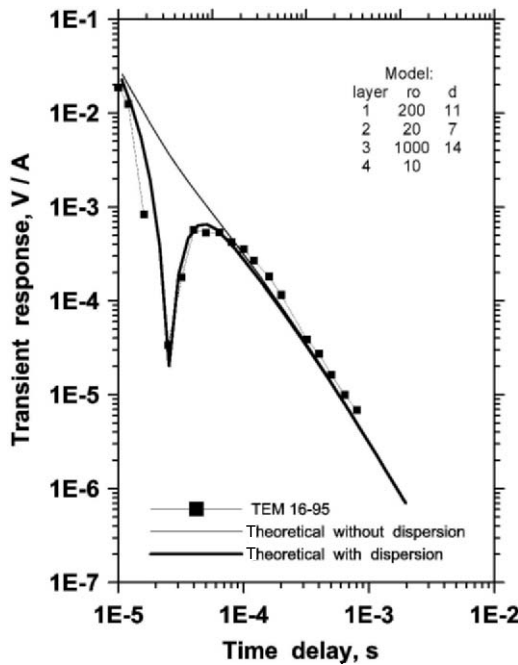


Figure 3. The field curve of TEM sounding from the platform #64 (TEM 16-95) and theoretical curves for the presented model. Parameters of the model and parameters of dispersion in the 2-d layer are same as for FEM soundings

7.3.1.2. Model of Salt Water Injection Into Permafrost Zone, Sakha Yakutia, Russia

Yakutia is the largest diamond-bearing region in Russia. A number of pits are used for diamond pipe development. The main environmental problems at these sites were described by Mironenko and Atroschenko (2000). Most important is utilization of drainage brines of extremely high salinity. A detailed description of natural brine composition and hydrochemical zonality can be found in Alexeev and Alexeeva (2003). At present brines being buried into permeable layers (marls, limestones) are found in the upper part of the permafrost zone. These layers were frozen under unsaturated conditions and contain open porosity, which is necessary to initiate brine injection. Further development of brine spreading is accompanied by ice melting. A simplified cross-section is shown in Figure 4.

Monitoring brine spreading is of interest in order to protect the local surface water from contamination. Geophysical methods are preferred to conventional well monitoring, as these methods are capable of capturing the complex pattern of flow pathways and heterogeneity of the permafrost. The first experience in this area was described by Blokh et al. (1996). They applied low

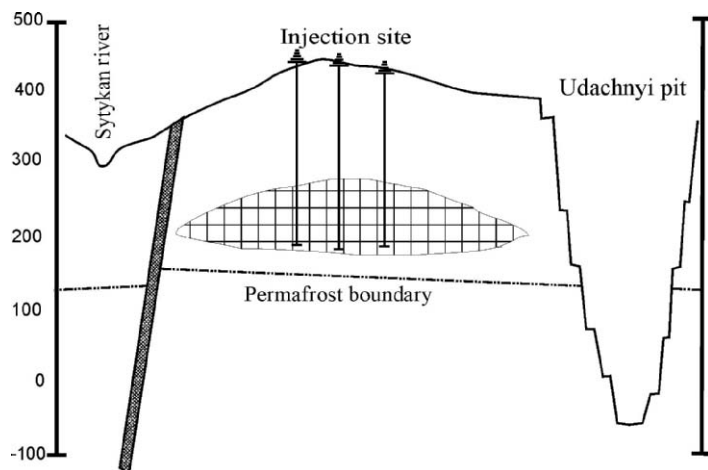


Figure 4. Cross-section of injection site area (left axis is altitude, m)

frequency inductive method with an ungrounded loop. For the interpretation it was assumed that permafrost with saline water is a perfect conductor and that the permafrost outside plume is a perfect insulator.

To get a better understanding of brine spreading in the permafrost zone a 1D (radial) numerical code (SALWAT) for solute transport in permafrost zone was developed. The main purpose of developing this code was to quantitatively investigate possible regimes of brine and salt water distribution in frozen ground. A number of assumptions were made: constant injection rate is the boundary condition on the central well;

- thermal and chemical equilibrium is maintained inside each cell;
- saturated flow (all pores are filled with ice or liquid);
- negligible conductive heat exchange through top and bottom of the aquifer;
- no salts are included in the ice structure;
- the liquidus line (i.e., freezing temperature as a function of salinity) is approximated by a linear equation;
- heat capacity is independent of temperature.

The following cases were considered: (1) a brine injection (the freezing point of the injected solute is below the initial temperature of permafrost zone); (2) a slightly saline water injection (freezing point is above the temperature of permafrost zone). The governing equations for the two component system include mass balance equations for water and dissolved compound, energy balance, and equilibrium phase distribution. Parameters of the model can be divided into two groups: basic physical and chemical constants (Table 4) and site specific data and characteristics of injection technology (Table 5).

A number of numerical experiments were performed to investigate the solute spreading in the permafrost. Two scenarios were considered either

TABLE 4. Physical and chemical constants

Parameter	Value
Ice heat capacity, kJ/m^3	1840
Rock heat capacity, kJ/m^3	2000
Brine heat capacity, kJ/m^3	4000
Coefficient for liquidus curve, K l/g	-0.06
Relative volume changes during ice melting	0.91

(1) the salinity of the injected solution is higher or (2) the salinity of the injected solution is lower than the equilibrium concentration at the initial temperature of permafrost. Scenario (1) corresponds to brine salinity of more than 70–100 g/L. An example of brine migration calculation for concentrated brine injection is shown in Figure 5. The following zones can be distinguished:

1. The zone without ice formed near the injection well. Temperatures are in the range of (-12 to -8°C) in the frontal part to above 0°C close to the well. Salinity in this zone is the same as salinity of the injected brine.
2. A transition zone with melting ice. The temperature is below the initial temperature of permafrost. Salinity changes from salinity of initial brines to that which is in equilibrium with ice at initial temperature of layer.
3. The zone near the front of the spreading solute is characterized by temperatures very close to initial temperature of permafrost. Solution initially fills the available open porosity and its salinity is in equilibrium with ice at temperature of layer.

In the case of slightly saline water injection (scenario 2), zones *a* and *c* remain the same but the temperature in zone *b* is higher than the initial temperature of the layer and the free porosity is smaller. Based on these findings the conceptual model of brine spreading in permafrost can not be considered a brine plume (conductor) in unchanged permafrost (insulator). Complex zones of the plume have to be considered. Electrical conductivity of the frontal zone can be low when there is little open porosity initially.

TABLE 5. Site data and injection parameters

Parameter	Value
Initial temperature of aquifer, °C	-3
Aquifer thickness, m	5
Total porosity	0.06
Initial free porosity	0.015
Volume of injected brine, m^3	10000
Brine salinity, g/l	240

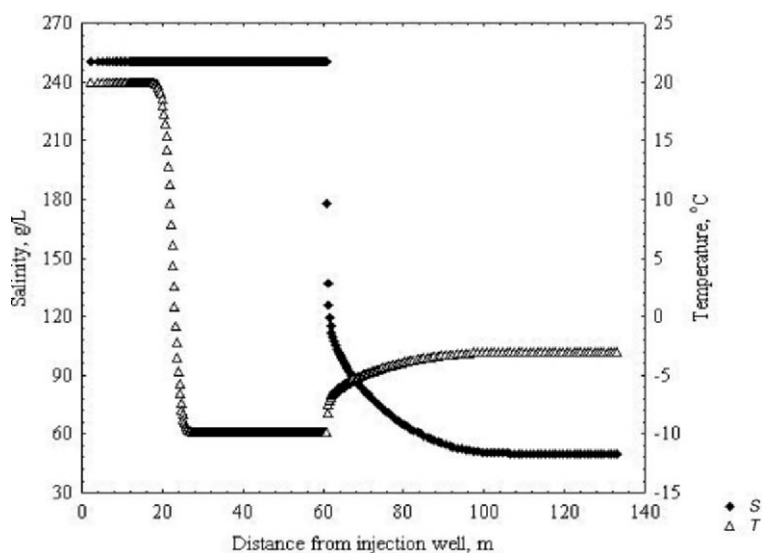


Figure 5. Salinity and temperature changes during brine injection into permafrost zone

Additional information might be provided from induced polarization; such tests have not yet been performed.

7.3.2. SEASONALLY FROZEN SOILS

The objectives of the two next case studies were (1) to examine the presence of preferential pathways in the unsaturated zone during snowmelt and (2) to quantify the spatial variability of the infiltration process during snowmelt. A better understanding of the hydrology during winter and snowmelt in seasonally frozen soils is important to be able to improve models for flow and transport under these conditions. The fieldwork for both experiments was carried out at Moreppen, Gardermoen (French et al., 1994) in southeastern Norway. The Gardermoen glacial-contact delta is an aquifer composed of sand and gravel underlain by silty glaciomarine deposits. The unsaturated zone (1–30 m thick) is heterogeneous, with sediments of fine to coarse sand and gravel. In its natural state, the ground surface is mostly forested (mainly spruce) with open areas of pioneer vegetation (grass, bushes, young birch). The annual precipitation is approximately 800 mm and the evapotranspiration is about 400 mm. More than 50% of the groundwater recharge occurs during the snowmelt period (3–5 weeks). Oslo airport was opened here in 1998 and, as it is situated on the largest unconfined precipitation fed aquifer in Norway, has received much attention with respect to groundwater protection. The examples given below are results of electrical resistivity measurements performed under snowmelting conditions.

7.3.2.1. *Solute Transport in Partially Frozen Soil*

Electrical resistivity tomography (ERT) as well as conventional suction cup techniques were employed to study the transport of an inactive tracer NaBr in the unsaturated zone (French et al., 2002). A frozen solution of NaBr in water was supplied as a line source on the ground surface above two parallel vertical profiles monitored by the two measurement systems prior to the onset of snowmelt. Two boreholes situated 1.8 m apart, were used for ERT data collection. Each borehole contained a set of 25 stainless steel mesh electrodes mounted, at 0.16 m intervals, on 4 cm diameter PVC pipes. The top electrode was situated near the surface, the bottom electrode at a depth of 3.84 m. A dipole-dipole configuration, using an electrode separation of 0.32 m, was used to collect the ERT data. This dipole-dipole configuration resulted in a total of 1172 resistance measurements. In order to assess data quality all measurements were repeated in a reciprocal dipole arrangement. Here, potential and current electrodes are swapped (see Binley et al., 1995). Such an assessment permits removal of outliers prior to data inversion and also allows characterisation of data weights for the inversion process. Collection of the complete set of 2344 measurements, took several hours using the Campus Geopulse (note that several more modern instruments allow much higher data collection rates). These measurements were repeated throughout the whole melting period (April 2001). A common set of measurements which had acceptable reciprocity in all data-sets for the whole experiment was then selected. This ensured that image sensitivity was not biased by different measurements. Inversion of ERT data produces images of resistivity that should be consistent with the measured resistances. The procedure adopted here was the well-established Occam's approach (see LaBrecque et al., 1996). The biggest challenge in conducting these experiments was to obtain sufficient contact between electrodes near the surface and the surrounding soil because of the extremely high electrical resistivity under frozen conditions, which was present down to about 0.4 m depth, also the soil is well drained. In order to overcome this problem silica flour was wrapped around the electrodes in order to retain higher water content near the electrode and a very low current, in the order of 1 mA, was applied (maximising input voltage across transmitter electrodes). Using the image produced from pre-tracer data collected on 24 March 2001 as a background (reference) state, images of changes in bulk electrical conductivity were produced to examine migration of the tracer and increased soil water content due to the snowmelt process (Figure 6).

On the first image we see an increased conductivity on the surface, explained by initial snowmelt and infiltration. On April 9 there is an early breakthrough of solute and water down at about 1.5 m indicating preferential flow. This was also observed by increased bromide concentration in soil water from (30) lysimeter suction cups. It is likely that the snowmelt and ice formation

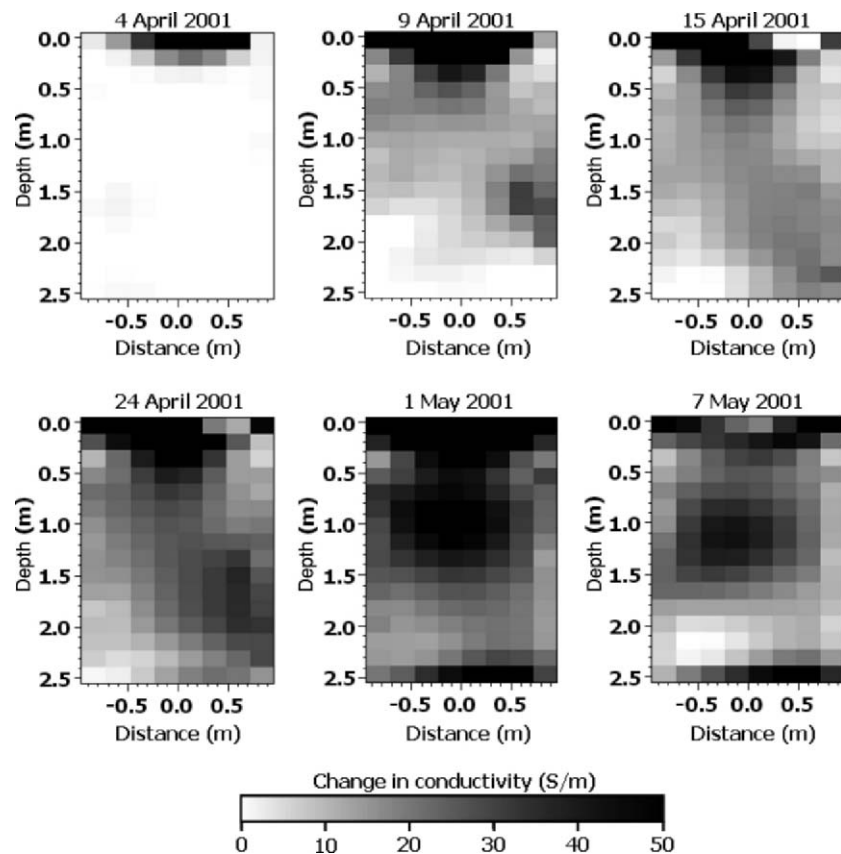


Figure 6. ERT images showing change in bulk electrical conductivity between two boreholes using ERT data collected on 24 March 2001 as a reference

the surface plays an important role in the initiation of preferential flow paths. Although measurements were conducted under high contact resistance conditions the ERT survey gave images of plume movement which was similar to conventional soil water sampling methods. The water percolation velocities through the unsaturated zone could possibly have been calculated by filtering out the effect of increased water conductivity due to the bromide concentration (found in soil water samples), but has not yet been tested. Similarly, solute velocity calculation only based on ERT measurements would require independent measurements of liquid water saturation, e.g. by the use of TDR and neutron probes. The disadvantage of calibration with these methods, however is that they only provide local values. Other hydrogeophysical studies of contaminant transport are described in depth in chapter by A. Kemna (Chapter 5).

7.3.2.2. *Melt Water Infiltration Into a Partially Frozen Soil*

The experiment described here took place simultaneously as that described above, but was conducted about 15 m from the lysimeter trench and had a different lay-out of the electrodes. While the other study focussed on solute transport, the objective here was to quantify horizontal variability of infiltration during the snowmelt (French and Binley, 2004) for better definition of flux boundary conditions in unsaturated zone modelling. In order to examine the spatial and temporal variability of snowmelt infiltration, a series of electrical resistivity surveys in 6 lines covering an area of 3.75 m by 1 m were carried out using electrodes installed at 0.2 m below the ground surface. There were also 4 boreholes down to 2.4 m depth with 16 electrodes in each. The area is fairly flat (elevation differences of about 20 cm) and consequently it is logical to expect uniform infiltration. Electrical resistivity data were collected from 25 March 2001, before snowmelt had started, on a regular basis until 4 May, some days after all the snow had melted. Thus, changes in the resistivity distribution, caused by the infiltration of water, could be imaged as a function of time. Electrical resistivity was measured in a Wenner configuration (see for example, Telford et al., 1990). The data set collected 1 April was used as the background image for the surface lines.

The results from time-lapse survey, shown as horizontal slices, for April 8–30 (Figure 7) reveal significant changes over time, and suggest that localised infiltration takes place. There were only minor changes in soil temperature during the experiment, thus conductivity changes can be explained by changes in water content due to infiltration of melting snow. The patterns of inferred increases in saturation are consistent with observed reductions in snow cover and appear to be principally controlled by variations in microtopography. Resistivity changes observed at depth, using borehole-based electrodes show rapid percolation through the unsaturated profile. Such behaviour is consistent with observed rapid changes in local ground water levels. The results confirm the potential threat to groundwater quality during snowmelt and illustrate the spatial scale of processes that require adequate attention in groundwater management in vulnerable areas.

7.3.3. GLACIERS

7.3.3.1. *Drainage Conditions Beneath Haut Glacier d'Arolla*

Haut Glacier d'Arolla, Valais, Switzerland has a surface area of $\sim 6 \text{ km}^2$ and extends from $\sim 2600 \text{ m a.s.l.}$ at its snout to $\sim 3500 \text{ m a.s.l.}$ at its headwall (see e.g. Figure 1 in Kulessa et al., 2003a). The glacier typifies a temperate Alpine ice mass, and has been subject to intensive scientific study especially in the 1990s. Previous work demonstrated that a major subglacial drainage channel is active ephemerally during the late melt season in the eastern part of the

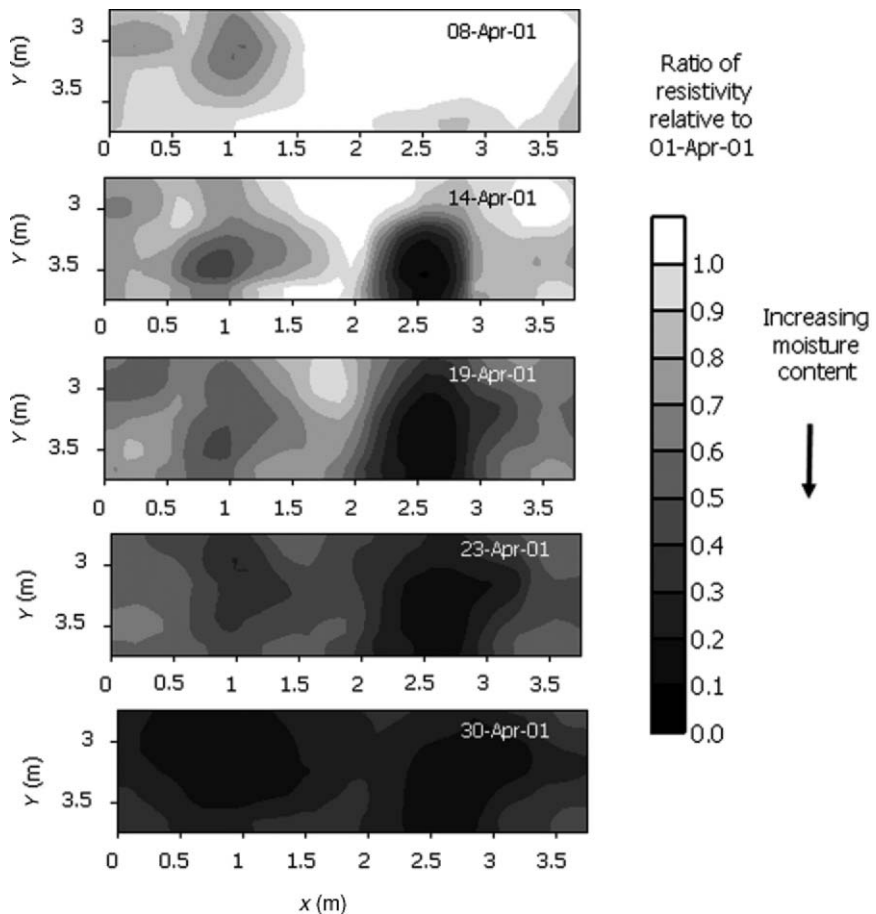


Figure 7. Horizontal sections showing changes in 2D resistivity relative to April 1 monitored by 5 parallel lines of 16 electrodes with 25 cm spacing in both directions.

glacier's ablation area (Sharp et al., 1993; Hubbard et al., 1995; Gordon et al., 1998), interacting with the surrounding, distributed drainage system on a diurnal basis: during the day water pressure is high in the channel due to increased delivery of surface melt water, forcing water out into the distributed system, and vice versa during the night when melt water delivery is low (Hubbard et al., 1995). A layer of unconsolidated sediments is sandwiched between overlying ice and underlying bedrock, with sediment thickness increasing from a few centimetres near the channel to >25 cm some tens of meters away from it (Harbor et al., 1997; Mair et al., 2002). The diurnally reversing hydraulic gradient is believed to cause systematic flushing of fines from the subglacial sediments near the channel (Hubbard et al., 1995). Prior to the work at Haut

Glacier d'Arolla, temporal and spatial variations in interpreted electrical resistivity (Brand et al., 1987) and in apparent resistivity and electrical self-potential (*SP*) (Blake and Clarke, 1999) were qualitatively related to changes in subglacial water quality, water saturation, and drainage structure. As part of the 1994–97 summer field campaigns (July–August), *SP* (Kulessa et al., 2003a) and time-lapse electrical resistivity data (Kulessa et al., 2006) were acquired in the 1996 melt season, and more than 100 slug tests were conducted in the 1994 and 1995 melt seasons (Kulessa and Hubbard, 1997; Kulessa et al., 2005). Multi-annual subglacial *SP* (1996–97), water pressure (1995–97), and water electrical conductivity (*EC*) (1995–97) measurements were made with an automated data logger (Kulessa, 2000; Kulessa et al., 2003b).

Time series of the latter three parameters, collected near the major subglacial drainage channel and covering the period between the 1996 and 1997 melt seasons, are shown in Figure 8. At the end of the 1996 melt season, channelized drainage gradually collapses as melt water delivery to the glacier bed becomes insufficient, as marked by a progressive increase in water pressure until ice overburden pressure is reached ($\sim 90\%$ of ice thickness; Figure 8a). This pressure persists until the *spring event* in June 1997, when the first significant delivery of surface water to the glacier bed in the new melt season re-opens the subglacial channel, and large water pressure fluctuations result (Figure 8a). The exact subglacial hydrological processes operating during spring events and their implications for ice deformation and glacier motion are complex (e.g. Mair et al., 2002, 2003).

Of particular interest here are the large *SP* cycles which persist through the whole inter-melt season period, reaching a maximum peak-to-peak amplitude of +2.62 V during the spring event in June (Figure 8c). Corresponding cycles also persist in the water pressure and *EC* data (see inlays in Figures 8a and 8b). Fourier analysis revealed that these cycles correspond to characteristic solar and lunar constituents of the diurnal and semi-diurnal earth and atmospheric spectra (Kulessa et al., 2003b), representing the first unequivocal evidence of the impact of such tides on the subglacial hydraulic system beneath any ice mass. Detailed analysis of signal phasing and correlation with gravity and atmospheric pressure data suggest that the glacier substrate is deformed particularly as bedrock expands, periodically forcing water to flow from the ice body into the subglacial sediments (Kulessa et al., 2003b). The exact tidally-forced hydro-mechanical processes operating at the glacier bed, including the origin of the extremely large subglacial *SP* amplitudes, are subject to ongoing research, with potentially global significance for glacier drainage and motion.

Kulessa et al. (2003a) found that the *SP* data collected during the 1996 melt season were caused by coinciding streaming and electrochemical potentials, respectively driven by subglacial water flow (both along the subglacial channel

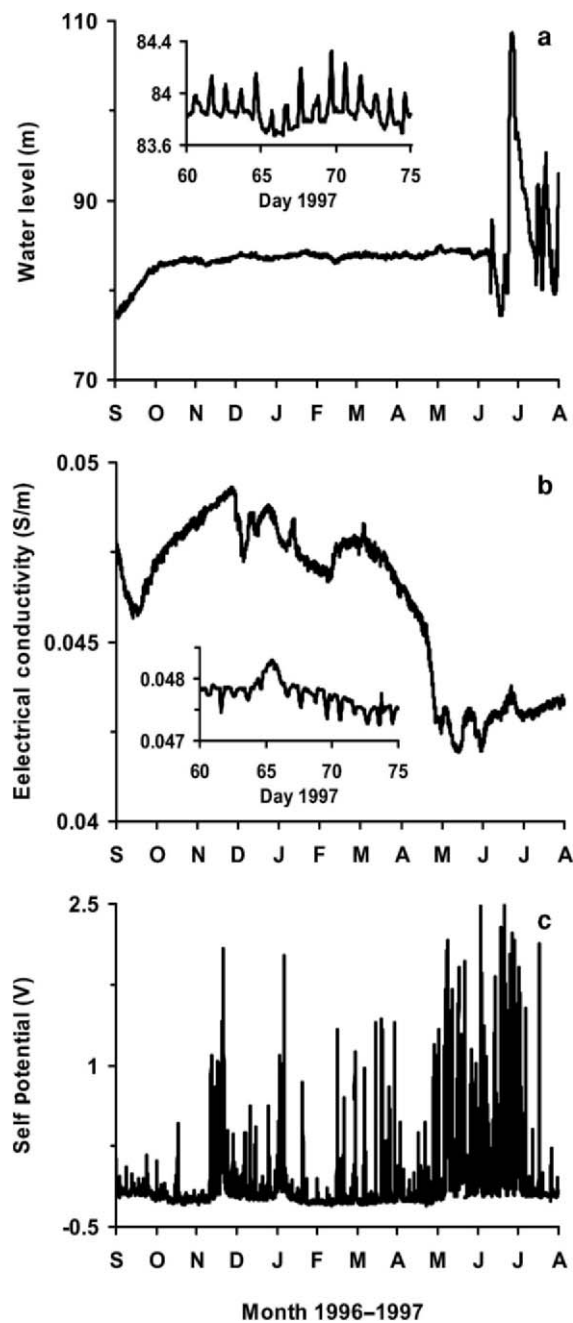


Figure 8. (a) Water pressure (in terms of equivalent borehole water level), (b) water electrical conductivity (EC), and (c) electrical self potential (SP) measured beneath Haut Glacier d'Arolla, Valais, Switzerland. Insets show pressure and EC cycles caused by earth and atmospheric tides. The largest SP peak-to-peak amplitude was ~ 2.62 V (June 1997)

and transverse to it; see above) and reaction of fresh melt waters delivered to the glacier bed with subglacial sediments. Cross-coupled flow modeling allowed mathematical separation of the two SP components, which revealed that water flow both along the subglacial channel and transverse to it contributed to the streaming potential component (Kulessa et al., 2003a), where the direction of transverse flow was found to be diurnally reversing, as expected (Hubbard et al., 1995, see above). Combination of streaming potential data with sediment hydraulic conductivity (derived from slug tests or electrical resistivity data; see below) allowed temporal variations in in-situ subglacial water flow velocities to be estimated (Kulessa et al., 2003a), which are challenging to determine by other means.

The time-lapse, subglacial electrical resistivity data were inverted in three spatial dimensions to reveal hourly changes in bulk resistivity of the subglacial sediments within the study area over two diurnal cycles (Kulessa et al., in press). The changes were generally in phase with variations in water EC. To derive sediment porosity and hydraulic conductivity from bulk resistivities, Kulessa et al. (2005) used Revil and Cathles' (1999) approach. Key to the latter is the use of the electrical formation factor to substitute *total* sediment petrophysical properties by equivalent *effective* properties, resulting in a modified version of the Kozeny–Carman–Bear equation (e.g. Freeze and Cherry, 1979, p. 351) that allows for variable clay content. The electrical formation factor was found to increase from 5.8 at the subglacial channel to 20.8 approximately 9 m away from it (Kulessa et al., 2006). Allowing for some uncertainty in the estimates of clay content, sediment porosity and hydraulic conductivity are respectively calculated to decrease from 0.34 ± 0.03 and $1.7 \pm 0.3 \times 10^{-2}$ m s^{-1} to 0.14 ± 0.02 and $2.3 \pm 1.7 \times 10^{-4}$ m s^{-1} over the same distance. Analysis of overdamped, underdamped, and critically-damped slug test data using standard hydrogeological methods confirmed that sediment hydraulic conductivity decreases away from the channel, and yielded an almost identical value of hydraulic conductivity at the channel ($1.1 \pm 0.5 \times 10^{-2}$ m s^{-1}) (Kulessa et al., 2005). It is inferred that systematic flushing of fines from the channel area (see above) causes porosity and hydraulic conductivity to be larger in its immediate vicinity than within the distributed hydrological system at some distance from it.

In summary, we find that inter-melt season subglacial SP measurements are particularly sensitive indicators of the impact of earth tides on glacier drainage. Multi-dimensional variations in the porosity and hydraulic conductivity of subglacial sediments can be estimated from inverted, time-lapse electrical resistivity data, as confirmed by slug test results. Cross-coupled flow modeling can be used to separate streaming and electrochemical components from melt season subglacial SP data. Streaming potentials are sensitive indicators of subglacial water flow direction, even where flow patterns are

spatially and temporally variable, and in combination with hydraulic conductivity estimates from electrical resistivity data can be used to estimate temporal variations in subglacial water flow velocity. Together such an integrated hydrogeophysical approach is therefore well suited to estimating subglacial hydrological properties and processes.

7.3.3.2. *Englacial Imaging at Haut Glacier d'Arolla*

Recognising the need to determine information about the structure of englacial ice Hubbard et al. (1998) carried out electrical geophysical surveys at the Haut Glacier d'Arolla, Valais, Switzerland during summer field seasons in 1996 and 1997. The specific aim of this work was to evaluate the potential of using electrical resistivity tomography to support conventional glacial hydrology studies for assessing flow pathways within the ice.

Boreholes were drilled using the pressurised, hot water system. Borehole water was replaced with saline water (0.2 kg of table salt mixed with 200 l of supraglacial water). Addition of such fluid enhances contact with the very resistive formation but leads to short-circuiting of current which must be accounted for in the forward modelling of ERT data.

Electrical resistivity tomography measurements were then conducted between pairs of 20 m long boreholes, typically 3–5 m apart. Hubbard et al. (1998) demonstrate two hydraulic configurations identified from their field studies: (i) hydraulically homogeneous ice containing only micro-porous flow pathways, characterised by vertically uniform tomograms that indicate ice resistivities on the order of $10^9 \Omega \text{ m}$; (ii) discrete, hydraulically conductive flow pathways identified as low resistivity zones that disrupt the background high resistivity field.

Figure 9 illustrates a tomogram where a discrete hydraulic pathways were inferred from the geophysical results. For this case a small englacial void was intersected at a depth of ~ 13 m during the drilling of the two boreholes (labelled 97/17 and 97/18). Hydraulic connection was apparent from observations of water table fluctuations in 97/17 as 97/18 was drilled and confirmed by borehole to borehole impulse pressure tests (see Hubbard et al., 1998). The tomogram in Figure 9 reveals a sub-horizontal zone of anomalously low resistivity between the depths of 12.5 and 14 m, coincident with the inferred englacial channel. This low resistivity zone intersect both boreholes, as expected, at a depth of ~ 13 m. In contrast, the rest of the tomogram is similar to those recorded in resistively uniform ice (see Hubbard et al., 1998), suggesting the absence of further hydraulically conductive features. Middleton (2000) offers a detailed analysis of the ERT experiments conducted at Haut Glacier d'Arolla and additional insight into near surface ice structure through additional field experiments carried out at the site using borehole to borehole radar.

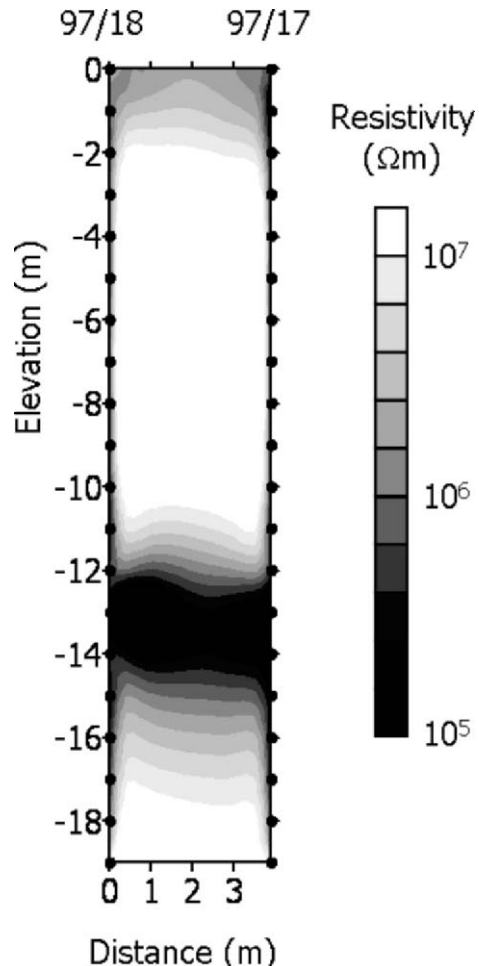


Figure 9. Electrical resistivity tomogram of englacial ice showing low resistivity zone at 13 m which coincides with hydraulic pathway inferred from borehole to borehole water pressure tests

7.4. Conclusions

Flow and transport in cold areas is complicated by the presence of ice barriers, whether they are more or less permanent or seasonally dependant. Different geophysical methods can help us to map structures which influence the water flow paths as illustrated by the case studies using transient and frequency electromagnetic soundings. The advantage of EM methods as well as GPR and capacitively coupled systems is that measurements can be conducted without grounding. Combining methods such as electromagnetic soundings (AC)

and electrical resistivity measurements (DC) can improve the interpretation of the results. Ground penetrating radar is a common method for mapping permafrost but no case-studies are presented here. The development of salt-water plumes (brines), which remain unfrozen at temperatures much lower than 0°C, has successfully been demonstrated with ER methods and is also captured well in a numerical model. The example illustrates the importance of salt concentration for the development of zones of liquid pore-water within the permafrost. Time-lapse measurements of electrical resistivity in a vertical section of a seasonally frozen unsaturated soil, illustrates the occurrence of preferential flowpaths. Measurements in the horizontal plane document the spatiotemporal variability of infiltration during snowmelt which is likely to be an important factor for the initiation of the preferential pathways. Some suggestions of how to solve the grounding problem are given in the examples and with reference to literature. Glacial hydrology plays an important role as a climate change indicator but also as a regulator. Literature references show that both GPR and seismics have been applied to study hydrological characteristics on glaciers. SP in combination with hydraulic conductivity estimates from electrical resistivity data can be used to estimate temporal variations in subglacial water flow velocity. ER tomography studies at a glacier also demonstrated the presence of englacial channels. Still there are many unsolved problems with respect to conducting hydrogeophysical experiments in frozen environment, both in terms of interpretation but also more practical issues such as grounding problems must be overcome. There are also some advantages of cold conditions, measurements can be carried out on snow, or ice surfaces which can make the data collection process faster if large areas are to be covered. Temperature and phase changes may both influence the geophysical properties and the calibration of methods is still complicated and requires several other methods for interpretation. Despite difficulties, the most common hydrogeophysical methods seem to be applicable under frozen conditions.

References

Alexeev, S.V., and L.P. Alexeeva, 2003. Hydrogeochemistry of the permafrost zone in the central part of the Yakutian diamond-bearing province, Russia. *Hydrogeol. J.*, 11, 574–581.

Anandakrishnan, S., 2003. Dilatant till layer near the onset of streaming flow of Ice Stream C, West Antarctica, determined by AVO (amplitude vs. offset) analysis, *Ann. Glaciol.*, 36, 283–286.

Anisimov, M.A., and R.U. Tankaev, 1981. Ice melting nearby hydrophilic surface. *J. Exp. Theor. Phys.*, 81, 1 (7), 217–225. (In Russian)

Arcone, S.E., A.J. Lawson, J.C. Delaney, J.C. Strasser, and J.D. Strasser, 1998. Ground-penetrating radar reflection profiling of groundwater and bedrock in areas of discontinuous permafrost, *Geophysics*, 63 (5), 1573–1584.

Atre, S.R., and C.R. Bentley, 1993. Laterally varying basal conditions under ice streams B and C, *West Antarctica*, *J. Glaciol.*, 39 (133), 507–514.

Atre, S.R., and C.R. Bentley, 1994. Indication of a dilatant bed near Downstream B Camp, Ice Stream B, *Antarctica*, *Ann. Glaciol.*, 20, 177–182.

Baker, J. M., and E.J.A. Spaans, 1997. Mechanics of meltwater movement above and within frozen soil, edited by I.K. Iskandar, E.A. Wright, J.K. Radke, B.S. Sharratt, P.H. Groenveld, and L.D. Hinzman, in *International Symposium on Physics, Chemistry, and Ecology of Seasonally Frozen Soils*, U.S. Army Cold Reg. Research and Engineering Company, Fairbanks, AK, 10-12.06., pp. 31–36.

Benn, D.I., and D.J.A. Evans, 1997. In *Glaciers and Glaciation*, edited by Hodder and Arnold, Oxford University Press, Oxford, 760 p.

Bennett, M.R., and N.F. Glasser, 1996. *Glacial Geology: Ice Sheets and Landforms*, Wiley, 376 p.

Binley, A., A. Ramirez, and W. Daily, 1995. Regularised image reconstruction of noisy electrical resistance tomography data, edited by M.S. Beck, B.S. Hoyle, M.A. Morris, R.C. Waterfall, and R.A. Williams, *Process Tomography – 1995*, in *Proceedings of the 4th Workshop of the European Concerted Action on Process Tomography*, Bergen, 6–8 April 1995, pp. 401–410.

Blake, E.W., and G.K.C. Clarke, 1999. Subglacial electrical phenomena, *J. Geophys. Res.*, 104 (B4), 7481–7495.

Blok, Yu.I., C.A. Velikin, I.A. Dobrokhotova, and I.V. Renard, 1996. Delineation of the zones of mine water burring by low frequency inductive electrical prospecting, *Geophysics*, 3, 48–50.

Boyer, E.W., G.M. Hornberger, K.E. Bencala, and D.M. McKnight, 2000. Effects of asynchronous snowmelt on flushing of dissolved organic carbon: a mixing model approach, *Hydro. Process.*, 14, 3291–3308.

Bradford, J.H., J.P. McNamara, W. Bowden, M.N. Gooseff, 2005. Measuring depth beneath peat-lined arctic streams using ground penetrating radar, *Hydro. Process.*, 19 (14), 2689–2699.

Brand, G., V. Pohjola, and R.L. Hooke, 1987. Evidence for a till layer beneath Storglaciären, Sweden, based on electrical resistivity measurements, *J. Glaciol.*, 33 (115), 311–314.

Charykova, M.V., and N.A. Charykov, 2003. *Thermodynamical Modeling of Evaporite Sedimentation*, Nauka, St. Petersburg, 262 p.

Cole, K.S., and R.H. Cole, 1941. Dispersion and absorbtion in dielectrics, *J. Chem. Phys.*, 9, 341–350.

Copland, L., and M. Sharp, 2001. Mapping thermal and hydrological conditions beneath a polythermal glacier with radio-echo sounding, *J. Glac.*, 47 (157), 232–242.

Debye P., 1929. *Polar Molecules*, The Chemical Catalogue Company, Inc., New York.

Derby, N.E., and R.E. Knighton, 1997. Frozen soil effects on depression focused water and solute movement, edited by I.K. Iskandar, E.A. Wright, J.K. Radke, B.S. Sharratt, P.H. Groenveld, and L.D. Hinzman, in *International Symposium on Physics, Chemistry, and Ecology of Seasonally Frozen Soils*, U.S. Army Cold Reg. Research and Engineering Company, Fairbanks, AK, 10-12.06., pp. 113–119.

Ershov, E.D., 1979. *Water Transport and Cryogenic Structures in Dispersive Systems*, Moscow University Press, Moscow, 213 p. (in Russian)

Feldman, G.M., 1988. *Water Movement in Thawed and Freezing Soils*, Novosibirsk, Nauka, 257 p.

Flis, M.F., G.A. Newman, and G.W. Hohman, 1989. Induced polarization effects in time-domain electromagnetic measurements, *Geophysics*, 9 (4), 514–523.

Fountain, A.G., and J.S. Walder, 1998. Water flow through temperate glaciers, *Rev. Geophys.*, 36 (3), 299–328.

Freeze, R.A., and J.A. Cherry, 1979. *Groundwater*, Prentice-Hall, Englewood Cliffs, NJ, 604 p.

French, H. K., B. Swensen, J.-O. Englund, K.-F. Meyer, and S.E.A.T.M. van der Zee, 1994. A lysimeter trench for reactive pollutant transport studies, in *Future Groundwater Resources at Risk*, edited by J. Soveri, and T. Suokko, IAHS Publication, Vol. 222, pp. 131–138.

French, H.K., and A. Binley, 2004. Snowmelt infiltration: monitoring temporal and spatial variability using time-lapse electrical resistivity, *J. Hydrol.*, 297 (1–4), 174–186.

French, H.K., and S.E.A.T.M. Van der Zee, 1999. Field scale observations of small scale spatial variability of snowmelt drainage and infiltration, *Nord. Hydrol.*, 30, 166–176.

French, H.K., C. Hardbattle, A. Binley, P. Winship, L. Jakobsen, 2002. Monitoring snowmelt induced unsaturated flow and transport using electrical resistivity tomography, *J. Hydrol.*, 267, 273–284.

French, H.K., S.E.A.T.M. Van der Zee, and A. Leijnse, 1999. Differences in gravity dominated unsaturated flow during autumn rains and snowmelt, *Hydrol. Process.* 13 (17), 2783–2800.

French, H.K., S.E.A.T.M. Van der Zee, and A. Leijnse, 2001. Transport and degradation of propylene glycol and potassium acetate in the unsaturated zone, *J. Contam. Hydrol.*, 49, 23–48.

Frolov, A.D. 1998. *Electric and Elastic Properties of Frozen Earth Materials*. Pushchino. ONTI PSC RAS. 515 p. (In Russian)

Frolov, A.D., O.P. Chervinskaya, and Yu.A. Zykova, 1997. Particularities of frozen soils electric and elastic properties, in *Proceedings of International Symposium on Ground Freezing 97*, Lulea, Sweden, pp. 385–390.

Fujita, S., S. Mae, and T. Matsuoka, 1993. Dielectric anisotropy in ice at 9.7 GHz, *Ann. Glaciol.*, 17, 276–280.

Gordon, S., M.J. Sharp, B. Hubbard, C.C. Smart, B. Ketterling, and I.C. Willis, 1998. Seasonal reorganisation of subglacial drainage inferred from measurements in boreholes, *Hydrol. Process.*, 12, 105–133.

Gorelic Ya. B., and B.S. Kulinin, 2002. Physics and modeling of cryogenic processes in lithosphere. Novosibirsk, Siberian Branch of RAS, 317 p. (in Russian)

Granger, R.J., D.M. Gray, and G.E. Dyck, 1984. Snowmelt infiltration into a frozen prairie soils. *Can. J. Earth Sci.*, 21, 669–677.

Grant, S.A., and I.K. Iskandar (eds), 2000. *Contaminant Hydrology: Cold regions modelling*, Lewis, Florida, 246 p.

Gray, D.M., R.J. Granger, and G.E. Dyck, 1985. Overwinter soil moisture changes, *Trans. Am. Soc. Agric.* 28829, 442–447.

Grechishchev, S.E., L.V. Chistodinov, and Yu. L. Shuhr, 1984. *Basis for Cryogenic Processes Modeling*, Moscow, Nauka, 230 p. (in Russian).

Hambrey, M., and J. Alean, 1992. *Glaciers*, Cambridge University Press, Cambridge, MA, 394 p.

Harbor, J., M.J. Sharp, L. Copland, B. Hubbard, P. Nienow, and D. Mair, 1997. Influence of subglacial drainage conditions on the velocity distribution within a glacier cross-section, *Geology*, 25 (8), 739–742.

Hauck, C., M. Guglielmin, K. Isaksen, and D. Vonder Muhll, 2001. Applicability of frequency-domain and time-domain methods for mountain permafrost studies, *Permafrost Periglac. Process.*, 12, 39–52.

Hauck, C., and Kneisel, 2003. Application of a capacitively coupled resistivity system for mountain permafrost studies and implications for the interpretation of resistivity values, in 8th International conf. on permafrost Ext. abstracts on current res. and newly available info. International Permafrost Association, Zurich, Switzerland, 21–25 July 2003.

Hayashi, M., G. van der Kamp, and R. Schmidt, 2003. Focused infiltration of snowmelt water in partially frozen soil under small depressions, *J. Hydrol.*, 270, 214–229.

Hinkel, K.M., J.A. Doolittle, J.G. Bockheim, F.E. Nelson, R. Paetzold, J.M. Kimble,, and R. Travis, 2001, Detection of subsurface permafrost features with ground-penetrating radar, Barrow, AK, Permafrost Periglac. Process., 12 (2), 179–190.

Hobbs, P.V. 1974. Ice physics, Clarendon, Oxford, 837 p.

Hoekstra, P., and D. McNeill, 1973. Electromagnetic probing of permafrost, in 2nd International conference on permafrost, Proceedings, National academy of sciences, Washington, DC, pp. 517–526.

Hooke, R.L., 1989. Englacial and subglacial hydrology: a qualitative review, *Arctic Alpine Res.*, 21, 221–233

Hubbard, B., and P. Nienow, 1997. Alpine subglacial hydrology, *Q. Sci. Rev.*, 16, 939–955.

Hubbard, B., A. Binley, L. Slater, , R. Middleton, and B. Kulessa, 1998. Inter-borehole electrical resistivity imaging of englacial drainage, *J. Glaciol.*, 44 (147), 429–434.

Hubbard, B., M.J. Sharp, I.C. Willis, M.K. Nielsen, and C.C. Smart, 1995. Borehole water-level variations and the structure of the subglacial hydrological system of Haut Glacier d'Arolla, Valais, Switzerland, *J. Glaciol.*, 41 (139), 572–583.

Humlum, O. and Matsuoka, N, 2004. A handbook on periglacial field methods, International Permafrost Association, The working group on Periglacial Proc. and Environment, 82 p.

Ippisch, O., 2001. Coupled transport in natural porous media, PhD dissertation, Combined Faculties for the Natural Sciences and for Mathematics of the Rupertus Carola University, Heidelberg, Germany, 123 p.

Jacoby, M., J. Dvorkin, and X. Liu, 1996. Elasticity of partially saturated frozen sand, *Geophysics*, 61 (1), 288–293.

Jansson, P.-E. 1991. Simulation model for soil water and heat conditions, Description of the SOIL model. Swedish University of Agricultural Sciences. Department of Soil Sciences. 1991;1 Communications 91:71, 165 p.

Johansen, T.A., P. Digranes, M. van Schaack, and I. Lønne, 2003. Seismic mapping and modeling of near-surface sediments in polar areas, *Geophysics*, 68 (2), 566–573

Johnsson, H. and Lundin, L.-C., 1991. Surface runoff and soil water percolation as affected by snow and soil frost, *J. Hydrol.*, 122, 141–159.

Jonscher, A.K. 1990. The “Universal” Dielectric Response: Part I, *IEEE Electr. Insul. Mag.*, 6, 2.

Kane, D.L., and J. Stein, 1983. Water movement into seasonally frozen soils. *Water Resour. Res.*, 19, 1544–1557.

King, E., J. Woodward, and A.M. Smith, 2004. Seismic evidence for a water-filled canal in deforming till beneath Rutford ice stream, West Antarctica, *Geophys. Res. Lett.*, 31, doi:10.1029/2004GL020379

Kiryukhin, V.A., N.B. Nikitina, and S.M. Sudarikov, 1989. Hydrogeochemistry of faulted regions. Nedra, Leningrad, 253 p. (in Russian).

Kozevnikov, N.O., and S.P. Nikiforov, 1995. Investigations of the fast IP process in permafrost. *Geoecology*, 2, 118–126. (In Russian)

Krylov, S.S., and Bobrov N. Yu., 1998. Anomalous electrical properties of saline permafrost in the Yamal Peninsula, North-West Siberia, from field electromagnetic survey, in Proc. of the VIIth Int. Conf. on Permafrost, Yellowknife, pp. 611–616.

Kulakov, V.V. 1990. Groundwater for water supply in Priamurie. Vladivostok, Russian Academy of Science, 152 p. (in Russian)

Kulessa, B., 2000. Geophysical borehole investigations of subglacial drainage conditions at Haut Glacier d'Arolla, Switzerland, Ph.D. thesis, University of Wales, Aberystwyth.

Kulessa, B., and B. Hubbard, 1997. Interpretation of borehole impulse tests at Haut Glacier d'Arolla, Switzerland, *Ann. Glaciol.*, 24, 397–402.

Kulessa, B., B. Hubbard, and G.H. Brown, 2003a. Cross-coupled flow modelling of coincident streaming and electrochemical potentials, and application to subglacial self-potential (SP) data, *J. Geophys. Res.*, 108 (B8), doi: 10.1029/2001JB1167.

Kulessa, B., B. Hubbard, G.H. Brown, and J. Becker, 2003b. Earth tide forcing of glacier drainage, *Geophys. Res. Lett.*, 30 (1, 1011), doi: 10.1029/2002GL015303.

Kulessa, B., B. Hubbard, and G.H. Brown, 2006. Time-lapse imaging of subglacial drainage conditions using 3-D inversion of subglacial electrical resistivity data, *J. Glaciol.*, 52 (176), 49–57.

Kulessa, B., B. Hubbard, M. Williamson, and G.H. Brown, 2005. Hydrogeological analysis of slug tests in glacier boreholes, *J. Glaciol.*, 51 (173), 269–280.

LaBrecque, D.J., M. Miletto, W. Daily, A. Ramirez, and E. Owen, 1996. The effects of noise on Occam's inversion of resistivity tomography data, *Geophysics*, 61, 538–548.

Lewis, L.M., Jr., and M.C. Grant, 1979. Relationship between discharge and yield of dissolved substances from a mountain watershed, *Soil Sci.* 128, 353–363.

Maeno, N., T. Araki, J. Moore, and M. Fakuda, 1992. Dielectric response of water and ice in frozen Soils. *Phys. and Chem. Office*, Hokkaido Univ. Press, Sapporo, Japan, pp. 381–386.

Mair, D., I. Willis, U.H. Fischer, B. Hubbard, P. Nienow, and A. Hubbard, 2003. Hydrological controls on patterns of surface, internal, and basal motion during three spring events: Haut Glacier d'Arolla, Switzerland, *J. Glaciol.*, 49 (167), 555–567.

Mair, D., P. Nienow, M.J. Sharp, T. Wohlleben, and I.C. Willis, 2002. Influence of subglacial system evolution on glacier surface motion: Haut Glacier d'Arolla, Switzerland, *J. Geophys. Res.*, 107 (B8), doi: 10.1029/2001JB000514.

Marion G.M., and Farren R. 1999. Mineral solubilities in the Na–K–Mg–Ca–C–H₂O–SO₄ system: A re-evaluation of the sulfate chemistry in the Spencer–Møller–Weare model. *Geochim. Cosmochim. Acta*, 63 (9), 1305–1318.

Middleton, R.T., 2000. Hydrogeological characterisation using high resolution electrical resistivity and radar tomographic imaging, PhD Thesis, Lancaster University, UK, 500 p.

Mironenko, V.A., and F.G. Atroschenko, 2000. Hydrogeological problems in developing the diamont-bearing deposits in Northern regions of Russia, in *Contaminant Hydrology. Cold Region Modeling*, edited by S.A. Grant and I.K. Iskandar, Lewis, Florida, pp. 65–74.

Moorman, B.J., S.D. Robinson, and M.M. Burgess, 2003. Imaging periglacial conditions with ground-penetrating radar, *Permafrost Periglac. Process.*, 14, 319–329.

Nolan, M., and Echelmeyer, K., 1999. Seismic detection of transient changes beneath Black Rapids Glacier, Alaska, U.S.A.: I. Techniques and observations, *J. Glaciol.*, 45 (149), 119–131 and in: II. Basal morphology and processes, *J. Glaciol.*, 45 (149), 132–147.

Olhoeft, G.R. 1985. Low frequency electrical properties, *Geophysics*, 50(12), 2492–2503.

Parkhomenko, E.I., 1967. Electrical properties of rocks, New York, Plenum, 314 p.

Paterson, W.S.B., 1994. *The Physics of Glaciers*, Pergamon, Oxford, 390 p.

Pelsh, A.D. (ed.), 1973. *Handbook on Solubility in Salt Systems*, Vol. 1, *Ternary Systems*, Leningrad, Khimia issue 1. pp. 1–568, issue 2, pp. 569–1070. (in Russian)

Pelton, W.H., S.H. Ward, P.G. Hallof, W.R. Sill, P.H. Nelson, 1978, Mineral discrimination and removal of inductive coupling with multifrequency IP, *Geophysics*, 43 (3), 588–609.

Petrenko, V.F. 1993. Electrical properties of ice, USA CRREL. Spec. Rep. 93–20, 659 p.

Ponomariov, V.M. 1960. Groundwater at the territories with high thickness permafrost zone. Russian Academy of Sciences Press, Moscow, 199 p.

Post, A., and E. LaChapelle, 2000. Glacier ice, University of Toronto Press, Toronto, 166 p.

Revil, A., and L.M. Cathles III, 1999. Permeability of shaly sands, *Water Resour. Res.*, 125 (3), 651–662.

Revil, A., K. Titov, C. Doussan, and V. Lapenna, 2006. Applications of the self-potential method to hydrological problems: Chapter 9 in Vereecken, H. et al. (ed.) *Applied Hydrogeophysics*, Springer, 255–291.

Reynolds, J.M., 1997. *An Introduction to Applied and Environmental Geophysics*, Wiley, Chichester, UK, 796 p.

Röthlisberger, H. 1972. Seismic exploration in cold regions, I. CRREL Monograph, Hanover, NH.

Sharma, P.V., 1997. *Environmental and engineering geophysics*, Cambridge University Press, Cambridge, MA, 475 p.

Sharp, M.J., K. Richards, I. Willis, N. Arnold, and P. Nienow, 1993. Geometry, bed topography and drainage system structure of the Haut Glacier d'Arolla, Switzerland, *Earth Surf. Proc. Land.*, 18 (6), 557–571.

Smith, A.M., 1997. Basal conditions on Rutford Ice Stream, West Antarctica, from seismic observations, *J. Geophys. Res.*, 101 (C10), 22, 749–755.

Smith, A.M., T. Murray, B.M. Davison, A.F. Clough, J. Woodward, and H. Jiskoot, 2002a. Late surge glacial conditions on Bakaninbreen, Svalbard, and implications for surge termination, *J. Geophys. Res.*, 107 (B8), doi: 10.1029/2001JB000475.

Smith, A.M., T. Murray, B.M. Davison, A.F. Clough, J. Woodward, and H. Jiskoot, 2002b. Late surge glacial conditions on Bakaninbreen, Svalbard, and implications for surge termination, *J. Geophys. Res.*, 107 (B8), DOI: 10.1029/2001JB000475.

Solomatin, V.I., 1986. Petrogenesis of subsurface ice. Novosibirsk, Nauka, 216p. (in Russian)

Stähli, M., P.-E. Jansson, and L.-C. Lundin, 1996. Preferential water flow in a frozen soil—a two domain model approach, *Hydrol. Process.*, 10, 1305–1316.

Sullivan, J.M., R. Ludwig Jr., and D.V. Repin, 2000. Permafrost and stratigraphic layer identification using a hierarchical neural network for interpretation of ground-penetrating radar, edited by S.A. Grant and I.K. Iskandar, *Contaminant Hydrology: Cold regions modelling*, Lewis, Florida, 246 pp.

Telford, W.M., L.P. Geldart, and R.E. Sheriff, 1990. *Applied Geophysics*, 2nd ed., Cambridge University Press, Cambridge, MA, 770 p.

Titov, K., V. Loukhmanov, and A. Potapov, 2000. Monitoring of water seepage from a reservoir using resistivity and self polarization methods: case history of the Petergoph fountain water supply system. *First Break* 18 (10), 431–435.

Tolstikhin, N.I., 1941. The water of frozen part of lithosphere. Gosgeolizdat, Moscow, 204 p. (in Russian)

Vaughan, D.G., A.M. Smith, , P.C. Nath, and E.L. Meur, 2003. Acoustic impedance and basal shear stress beneath four Antarctic ice streams, *Ann Glaciol.*, 36, 225–232.

Walker G.G., and K. Kawasaki, 1988. Observation of double sign reversals in transient electromagnetic central induction soundings, *Geoexploration*, 25 (3), 245–254.

Washburn, A.L., 1979. *Geocryology. A Survey of Periglacial Processes and Environments*, Edward Arnold, London.

White, M.D., and M. Oostrom, 2000. STOMP, Subsurface Transport Over Multiple Phases, version 2.0. Users guide U.S. Department of Energy and Pacific Northwest National Laboratory, Richland, Washington, 238 p.

Woo, M.-K., and P. Marsh, 1990. Response of soil moisture change to hydrological processes in a continuous permafrost environment, *Nordic Hydrol.* 21, 235–252.

Zadoroznaya, V.Yu., and V.P. Lepeshkin, 1998. IP process in multi-layered sections and interpretation of inductive soundings. *Phys. Earth*, 4, 55–61. (in Russian)

Zhao, L., D.M. Gray, and B. Toth, 2002. Influence of soil texture on snowmelt infiltration into frozen soils, *Can. J. Soil. Sci.* 82, 75–83.

Zimmerman, R.W., and M.S. King, 1986. The effect of the extent of freezing on seismic velocities in unconsnsolidated permafrost, *Geophysics*, 51 (6), 1285–1290.

8. HYDROGEOPHYSICAL APPLICATIONS IN COASTAL AQUIFERS

Mark Goldman and Uri Kafri

8.1. Introduction

In many countries all around the world, the most densely populated regions are located in coastal areas since they normally provide the best conditions for both economical development and quality of life. On the other hand, coastal zones more than other regions suffer from natural disasters such as flooding and tsunami as well as from scarcity of fresh groundwater due to seawater intrusion. The latter problem is usually caused by a violation of a delicate hydrogeological balance that exists between freshwater and seawater in coastal aquifers. In most cases, the balance is disturbed by groundwater pumping and other human activities (e.g. land drainage) that lower groundwater levels and ultimately cause seawater encroachment into coastal aquifers. Although this problem is fairly important in all coastal aquifers, it becomes crucial in arid and semi-arid regions, where precipitation is limited and groundwater thus represents the main, if not only, source of fresh water.

In order to rationally manage groundwater resources in coastal aquifers, where hydrogeological conditions are particularly dynamic, a great amount of information regarding the geometrical and hydraulic properties of the aquifer is necessary. Most of this information is provided by observation and pumping wells, however, due to their scarcity and inevitably very local character of the information they provide, the supplementary geophysical data are crucial.

Among all geophysical techniques, geoelectric, and in particular, geoelectromagnetic methods are undoubtedly the leading ones in the exploration and management of groundwater. The most successful applications of the methods reported in the literature focus mainly on the studies of geometrical features of different geohydrological targets such as the configuration of fresh-saline groundwater interface, the thickness of alluvial fill and gravel lenses over bedrock, the thickness and depth of sand and gravel lenses in till, etc. (Fitterman and Stewart, 1986; Albouy, et al., 2001; Fitterman and Labson, 2005).

Several attempts have been also made to quantitatively evaluate different hydraulic/hydrological parameters using geoelectric parameters either measured (e.g. apparent resistivities) or interpreted in terms of true physical

parameters (e.g. resistivities). The most extensive efforts were devoted to studying the relationship between the porosity and/or the pore water salinity/conductivity on one hand and the bulk electrical resistivity on the other hand (Kelly and Mareš, 1993; Yang et al., 1999). However, due to uncertainties in determining all the parameters involved in the relationship (such as the pore water and bulk electrical resistivities, clay content, specific parameters related to the type of a rock sequence, etc.), these attempts proved to be much less successful than those devoted to delineating geometrical parameters.

Among numerous relationships connecting formation (bulk) resistivity with pore-fluid resistivity and porosity, the simplest, yet the most widely used one, is the empirical Archie's equation (Archie, 1942):

$$\rho_b = \alpha \rho_w \Phi^{-m} \quad (1)$$

where ρ_b is the bulk resistivity of the rock, ρ_w is the resistivity of water within the pore space, Φ is fractional porosity of the rock (approximately representing the volume of water filling the pore space), α is the tortuosity coefficient and m is the cementation index.

Equation (1) is somewhat oversimplified and in many cases the adequate mathematical description of real microstructure of rocks and conduction mechanisms require considering additional parameters such as partial saturation, temperature, pressure, clay content, matrix conductivity, surface conductivity, anisotropy, etc. (Hermance, 1979; Mendelson and Cohen, 1982; Knight, 1991 and 1992; Bahr, 1997; Sen, 1997; Revil et al., 1998; Chinh, 2000, etc.). The consideration of more complicated relationships here is beyond of the scope of this chapter and, as a matter of fact, is unnecessary. Indeed, we propose to significantly improve the determination of only two basic parameters, namely the bulk and pore-water resistivities, which are included in all relevant relationships. Equation (1) is thus considered only as an example and as such it can even be simplified further without reducing the generality of the consideration by fixing parameters α and m . Letting $\alpha = 1$ and $m = 2$ (typical for sandstones), one obtains instead of (1):

$$\rho_w = \rho_b \Phi^2 \quad (2)$$

Provided the bulk resistivity, ρ_b , is obtained by geoelectric measurements, even in such an oversimplified case we still have one equation with two unknowns, namely ρ_w and Φ . Moreover, in reality, the bulk resistivity of rocks in many cases is determined ambiguously due to the so called equivalence problem (discussed below). Thus, to determine porosity by using geoelectric measurements one has to extensively use *a priori* information (e.g. borehole) to fix both ρ_b and ρ_w . As a result, most of the attempts to apply surface geoelectric measurements to determine hydrological parameters suffer from one common drawback: they are apparently "successful" in close proximity to boreholes, where the information is available, but might be fairly unreliable

far away from the boreholes (Goldman et al., 1988). Furthermore, even in the proximity of boreholes, the required *a priori* information provided by well logs is inevitably scale dependent and, thus, does not necessarily coincide with the required bulk geoelectric parameters (discussed below). This phenomenon, which is less pronounced in the case of granular clastic aquifers, becomes crucial for fractured/cavernous karstic or crystalline aquifers.

8.1.1. HOW TO IMPROVE DETERMINATION OF AQUIFER POROSITY?

It is proposed herein to significantly reduce the ambiguities of both hydrogeological and geoelectrical interpretations (primarily in coastal aquifers but also in all those aquifers, in which fresh groundwater is underlain by the saline one) by

- (i) using properly selected geoelectric and/or geoelectromagnetic technique(s) for the accurate detection of fresh/saline groundwater interface and by
- (ii) follow-up application of the Archie's equation (or any other relevant relationship, which includes among other parameters ρ_b , ρ_w and Φ) only to the seawater intruded portions of the aquifer.

By doing so, one can entirely eliminate one of the unknowns in the Archie's equation (ρ_w) as it is known exactly for seawater salinity (Repsold, 1989) and to significantly reduce the ambiguity in determining the other unknown (ρ_b) since by using appropriate geoelectric/geoelectromagnetic method it could be much more accurately determined within the seawater intruded portions of the aquifer (discussed below). Using Equations (1) or (2), one can then calculate the porosity of the saline water saturated portion of the aquifer. Since the location of the interface is generally invariant regarding hydraulic properties of the aquifer, one might expect that the porosity determined below the interface is adequately representative of the entire aquifer or sub-aquifer.

The described methodology is especially feasible in coastal aquifers, where ρ_w of the intruding seawater is well known and where the relatively wide distribution of the intrusion allows gathering of sufficient amount of geoelectric data to be statistically representative of the entire aquifer. In the following sections, we will describe how to select the geoelectric methods with optimum potential for mapping saline-water interfaces and then demonstrate the method of computing porosities using field examples from Israel.

8.2. The Equivalence Problem

The choice of a proper geoelectric technique is crucial for the successful application of the proposed methodology. The main requirement to the method

is the ability to accurately detect the fresh/saline interface and to determine the bulk resistivity of the aquifer below the interface. Experience gathered in Israel has shown that in most cases, the time domain electromagnetic (TDEM) method is the most appropriate choice mainly due to its excellent lateral and vertical resolutions with respect to highly conductive targets (Goldman et al., 1991) and easy employment (no ground contact or galvanic connection is necessary). However, in some specific cases, where the application of TDEM is technically limited either due to a high level of ambient EM noise (e.g. within or close to industrial areas) or because of the difficulties in assembling relatively large transmitter loops (e.g. within urban areas or due to a rough topography), DC resistivity measurements, either 1-D or 2-D, can be applied instead. Both DC resistivity approaches can be linearly employed (e.g. along streets or roads), are much less sensitive to ambient EM noise and, in addition, the 2-D resistivity imaging method provides good constraints regarding the presence of sharp lateral resistivity variations. The detailed description of both the TDEM and 2-D resistivity imaging methods is given in numerous publications including those devoted to groundwater exploration (Fitterman and Stewart, 1986; Loke, 2000). In this chapter, we will discuss only those features of the methods that are relevant to the determination of the porosity of the aquifer.

8.2.1. TDEM METHOD

The most important feature, which may significantly affect the ability of the method to quantitatively estimate the porosity, is the so called equivalence range, i.e., the range, in which geoelectric parameters may vary without noticeable variations in the measured signal. Let us consider this problem in more detail, using a typical example of the TDEM measurement (Figure 1) over the Mediterranean coastal aquifer in Israel (Goldman and Gendler, 2002).

Figure 1 shows the TDEM data collected using the Geonics EM-67 system (open squares at the left hand side) along with a family of the equivalent interpreted models at the right hand side of the figure. One of the models, shown as a solid line, represents the so called best-fit model, while the rest of the models, shown by dashed lines, are the equivalent models. The solid line connecting the data points on the left hand side represents the synthetic responses for both the best-fit and equivalent models. The difference between the responses is so small that they all appear as a single curve. In this specific example, the best-fit model provides a misfit error of approximately 1.9%, while the greatest misfit error for the shown equivalent models does not exceed 2%. Thus the maximum difference between all the synthetic responses (in the rms sense) does not exceed 0.1%, i.e., less than the overall noise level of the measurement. Therefore, in practical terms all the interpreted models are

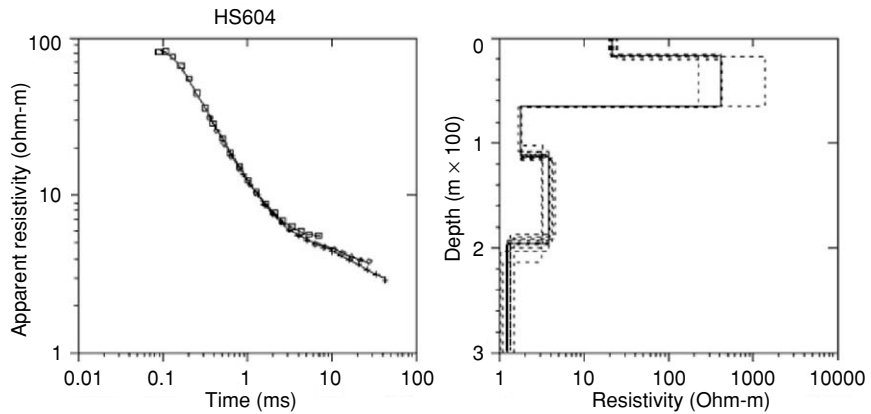


Figure 1. TDEM data collected at station HS604 (Goldman and Gendler, 2002) and the results of the interpretation including linear equivalence analysis by means of TEMIX-XL interpretation software

equally consistent with the data and cannot be distinguished without *a priori* information.

It should be noted that both the data interpretation and the equivalence analysis have been carried out using TEMIX-XL interpretation software (Interpex, 1996). Strictly speaking, the software does not provide a full (non-linear) equivalence analysis, but only the one, which is based on the use of a parameter resolution matrix (linear equivalence). Nevertheless, for illustration purposes, it is enough to consider the partial equivalence analysis as it represents the minimum equivalence range. In reality, the variations of some model parameters could be even wider than those shown in Figure 1. Some further details regarding the difference between linear and non-linear equivalence problems have been discussed by Goldman et al. (1994).

The equivalence analysis of the TDEM measurement (Figure 1) exhibits the following resistivity sequences:

Layer No.	Min ρ (Ohm-m)	Best fit ρ (Ohm-m)	Max ρ (Ohm-m)
1	19.4	21.3	24.7
2	223.0	415.0	1394.0
3	1.6	1.7	1.8
4	3.0	3.7	4.4
5	1.0	1.2	1.4

It should be noted that the appropriate depth equivalence ranges are not considered here as they are irrelevant for the following porosity estimation.

8.3. Methodology for Porosity Calculations

The TDEM data for station HS604 (Figure 1) is used to demonstrate the methodology of calculating porosity of the saline part of the aquifer. Although this specific TDEM sounding was carried out close to an observation well, our calculations will be based on the geophysical results only.

Based on the fact that bulk resistivity values below 2 Ohm-m are solely indicative of seawater intrusion into the Mediterranean coastal aquifer (Goldman et al., 1991), one can fix the location of freshwater/seawater interface at the depth of approximately 65 m. The shallow sequence from the surface to the depth of approximately 17 m exhibits moderate resistivity of approximately 21 Ohm-m. The elevation of the ground surface at the measurement site measured by a differential GPS is approximately 12.2 m and the distance from the seashore is about 1 km. This allows us to estimate the depth to the water table as approximately 11 m. Thus the upper relatively resistive layer, having a thickness of approximately 18 m, includes both the unsaturated zone and the underlying freshwater saturated part of the aquifer. No resistivity drop is observed at the depth of the water table, apparently due to the limited resolution of the TDEM method. The intermediate zone between 18 and 65 m exhibits very high resistivity (hundreds of Ohm-m) that is typical for fresh water saturated calcareous sandstone.

The very low resistivity geoelectric layer below 65 m depth is identified with seawater intrusion. Applying Equation (2), one can calculate the porosity of the seawater-intruded portion of the aquifer by using the TDEM data alone. Indeed, the salinity of the Mediterranean water is known and the fluid resistivity (ρ_w) calculated using a salinity/resistivity nomogram (Repsold, 1989) is approximately 0.18 Ohm-m. This value roughly coincides with those obtained from the Ashdod-112 water conductivity profiles (see below). Thus, according to the above specified equivalence range, the calculated porosity varies in a fairly narrow range: $\Phi = \sqrt{(\rho_w/\rho_b)}$ = 0.32 ± 3%.

When dealing with the shallow resistivity sequence, porosity calculations lead to great uncertainty due to the wide equivalence range of resistivities ρ_b . By using $\rho_w = 50$ Ohm-m, typical of the fresh waters in the area (based on both the above mentioned nomogram and the Ashdod-112 water conductivity data), the calculated porosities vary between 0.19 and 0.47 according to the equivalence range for ρ_b of the second layer.

The resistivities of the first layer, though varying in a relatively narrow equivalence range, exhibit meaningless fractional porosities (greater than one). This could be either an artifact of the TDEM inversion due to the low resolution of shallow structures or significant influence of partial saturation and clay content or both.

It is interesting to note that the suggested approach can even be used to resolve non-uniqueness in the intermediate resistivity sequence. Indeed, applying Equation (2) for $\Phi = 0.32$ and $\rho_w = 50$ Ohm-m, one obtains $\rho_b = 488$ Ohm-m that is accidentally fairly similar to the best fit resistivity value of the sequence.

The resistivity model shown in Figure 1, exhibits additional resistivity contrasts below the freshwater/seawater interface. These contrasts, which reflect the appropriate salinity variations within different sub-aquifers of the Mediterranean coastal aquifer of Israel (Goldman et al., 2004), will be discussed below in greater detail. For calculating porosity at this site, the deeper sub-aquifers are less suitable since the water salinity and, accordingly, ρ_w within the sub-aquifers can be only roughly estimated. In addition, the resolution of the TDEM method below very low resistivity layer (sea water intrusion) is somewhat deteriorated and, as a result, the equivalence range becomes wider (Figure 1). These calculations, however, will be carried out below using *a priori* borehole information to check the assumption that the porosity of different portions of the aquifer is roughly similar and does not depend on the water salinity.

Owing to the limited observational bandwidth of the conventional TDEM field systems and the inherent low sensitivity to resistive structures, the method is unable to resolve the resistivity of the shallow freshwater-saturated portion of the aquifer. Thus, the above parameter estimates for the freshwater-saturated aquifer may be different for different geoelectric methods. In order to examine the applicability of other geoelectric techniques to determine porosity of both freshwater and saline water saturated aquifers, the most sophisticated shallow-depth, high resolution geoelectric method commonly referred to as 2-D resistivity imaging (Loke, 2000), was applied at the above mentioned site.

8.3.1. 2-D RESISTIVITY IMAGING

The measurements were carried out using the Syscal-R2 multi-electrode system by Iris Instruments. The system included 64 electrodes located along the 945 m long line (inter-electrode spacing of 15 m). The observation well Ashdod-112 (as well as the TDEM central-loop sounding point for the data shown in Figure 1) is located in the middle of the line. The collected data were pre-processed using the Iris Instrument's Prosys software and then processed and interpreted using the RES2DINV package by Loke (2004). The interpreted 2-D resistivity cross-section along with the best-fit TDEM model and the borehole water conductivity profile are shown in Figure 2.

It is obvious that the TDEM resistivity model accurately represents the location of the freshwater-seawater interface and the salinity distribution below

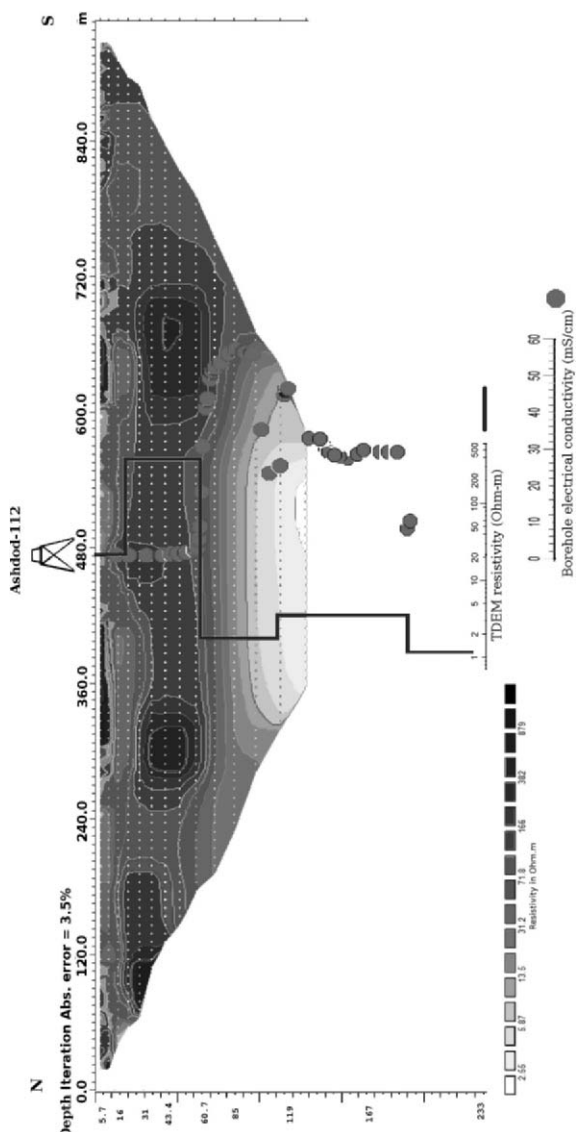


Figure 2. Comparison of the geophysical (2-D resistivity imaging and TDEM) results with direct borehole electrical conductivity measurements

the interface. According to the model, the resistivity increase below the interface represents a lowering of groundwater salinity (electrical conductivity) within deeper sub-aquifers (hydrological inversion). The resistivity drop at a depth of approximately 190 m corresponds to the base of the aquifer (Saqiye clays).

The shallow distribution of TDEM resistivities roughly corresponds to that of the 2-D resistivity model below the TDEM/borehole location (Figure 2). Both show the resistivity high at a depth of approximately 20 m. However the absolute resistivity values are fairly different in both models. The most remarkable feature of the 2-D resistivity model is the existence of extremely high lateral resistivity variations within the shallow and intermediate depth ranges. Even without the equivalence analysis (that is, by the way, unavailable in the existing 2-D inversion software), it is clear that the choice of the proper bulk resistivity value, which would adequately represent the entire freshwater saturated aquifer, is practically impossible. Within the freshwater saturated depth range between approximately 15 and 60 m, the 2-D resistivities vary roughly between 150 Ohm-m and 450 Ohm-m (Figure 2). This leads to the corresponding porosity variations between 0.33 and 0.58. Thus, the application of 2-D resistivity imaging in the freshwater saturated part of the aquifer does not significantly improve the ability of calculating porosity compared to that demonstrated by 1-D TDEM sounding within the same depth range.

Considering the 2-D resistivity model within the sea water saturated depth range, one can see that, though the depth to the interface is determined rather inaccurately, there are no significant lateral resistivity variations and the lowest absolute resistivity value is quite similar to that determined by TDEM. This means that, if 2-D resistivity imaging is applied in the coastal aquifer instead of TDEM (e.g. in urban areas, etc.), calculating porosity should be done using the lowest resistivity value irrespective of the actual depth to the interface. In the example under consideration, the interface is located at a depth of approximately 65 m, while the lowest resistivity in the 2-D model appears at a depth of approximately 120 m.

To conclude this section, we will calculate the porosity of the lower sub-aquifers using the TDEM bulk resistivity and the average salinity (electrical conductivity) measured in observation well Ashdod-112. According to Figure 2, the electrical conductivity in question is approximately 30 mS/cm. This corresponds to $\rho_w = 0.33$ Ohm-m. Applying Equation (2) for the best-fit $\rho_b = 3.7$ Ohm-m, one obtains $\Phi = 0.3$ that is quite similar to the porosity value calculated for the upper sub-aquifer. This and similar calculations support our assumption that porosities of different portions of the aquifer at a specified site are similar irrespective to the water salinity within these portions. Clearly, this assumption is only true, if the sub-aquifers were formed in a similar way.

8.4. Calibration of TDEM Measurements in Different Coastal Aquifers of Israel

During the last two decades, TDEM measurements were carried out in Israel primarily to detect saline water bodies within different aquifers and to delineate the interface between these saline bodies and the fresh ones. The studies mainly focused on the Mediterranean coastal aquifer, but some additional TDEM measurements were also performed in the coastal aquifers of the Gulf of Elat and the Dead Sea, as well as in the coastal parts of the regional carbonate Judea Group aquifer of Israel (Figure 3).

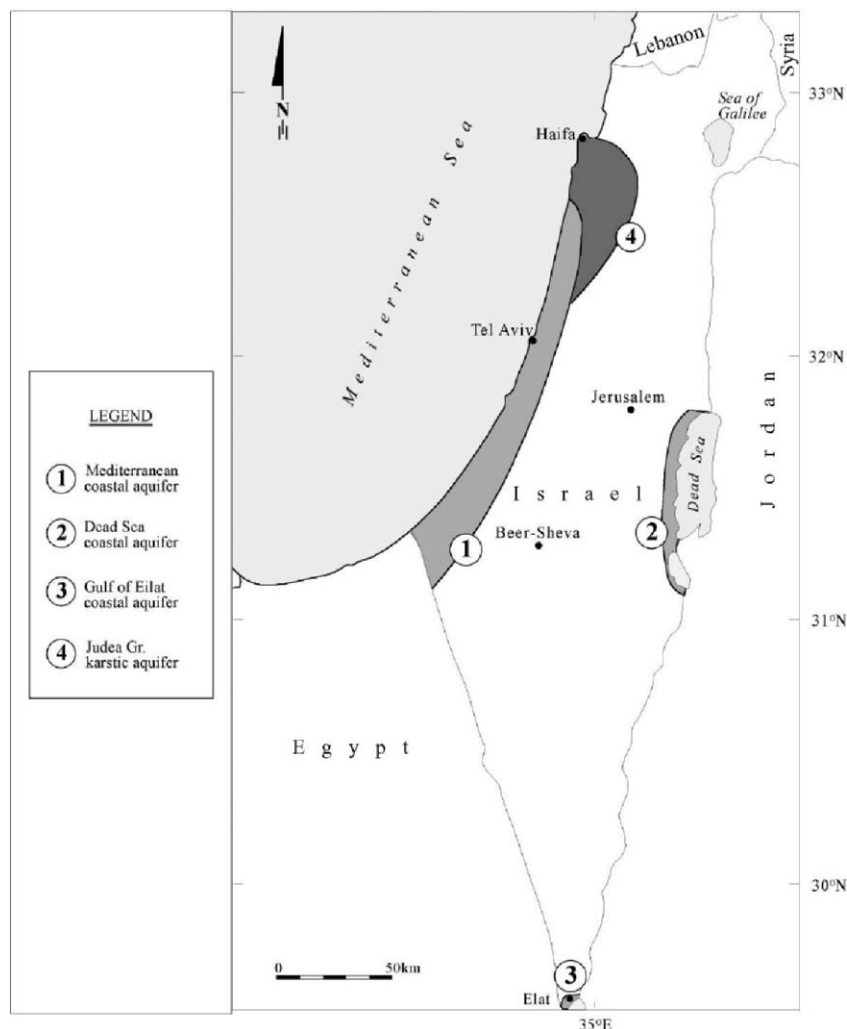


Figure 3. Schematic location map of the investigated coastal aquifers. The approximate numbers of TDEM soundings over the different aquifers are: $\varphi \sim 400$; $\kappa \sim 50$; $\lambda \sim 20$; $\mu \sim 10$

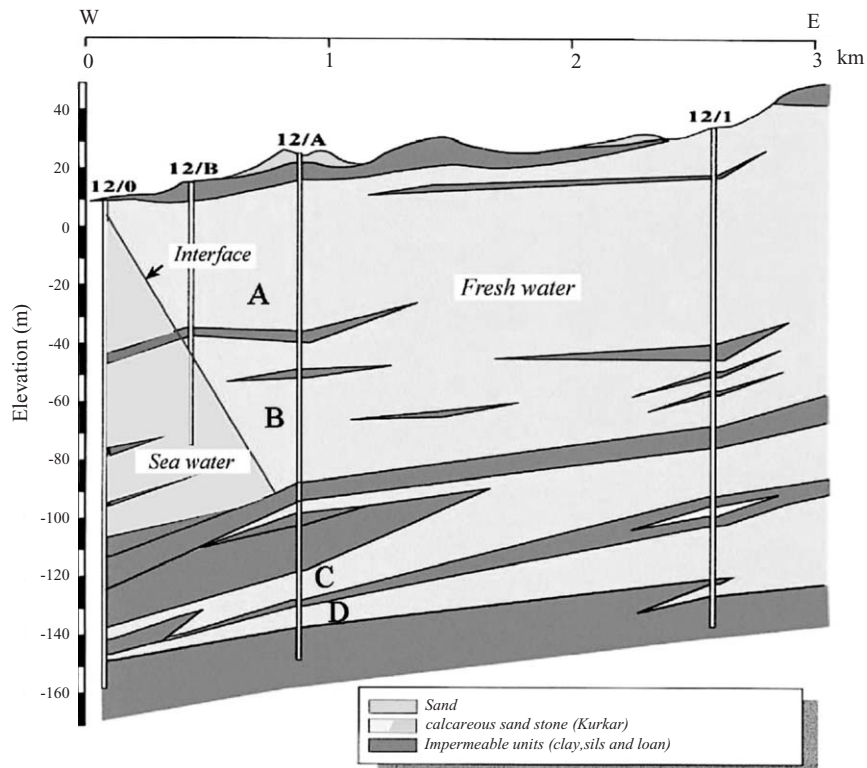


Figure 4. Typical hydrogeological cross-section of the Mediterranean coastal aquifer (in the Nizanim area). A,B,C and D designate different sub-aquifers

8.4.1. MEDITERRANEAN COASTAL AQUIFER

The Pleistocene Mediterranean coastal aquifer consists of 100 to 200 m thick calcareous sandstone and sand, which form the aquiferous part of this aquifer. Close to and within a few kilometers from the shore, the aquifer is subdivided by marine and continental clay and loam interlayers into a few (generally four) sub-aquifers customarily designated as A, B, C and D sub-aquifers (Figure 4).

The TDEM method was routinely employed to detect the intruding saline water bodies during the last fifteen years. The numerous measurements and studies (e.g. Goldman et al., 1988) found correlation between TDEM resistivities with groundwater salinities.

The studies have shown that in the overwhelming majority of cases the portions of the aquifer saturated with seawater have TDEM resistivities below 2 Ohm-m (Figure 5). Only very few measurements have shown resistivities between 2 and 3 Ohm-m and none of the measurements yielded higher resistivities (Figure 6).

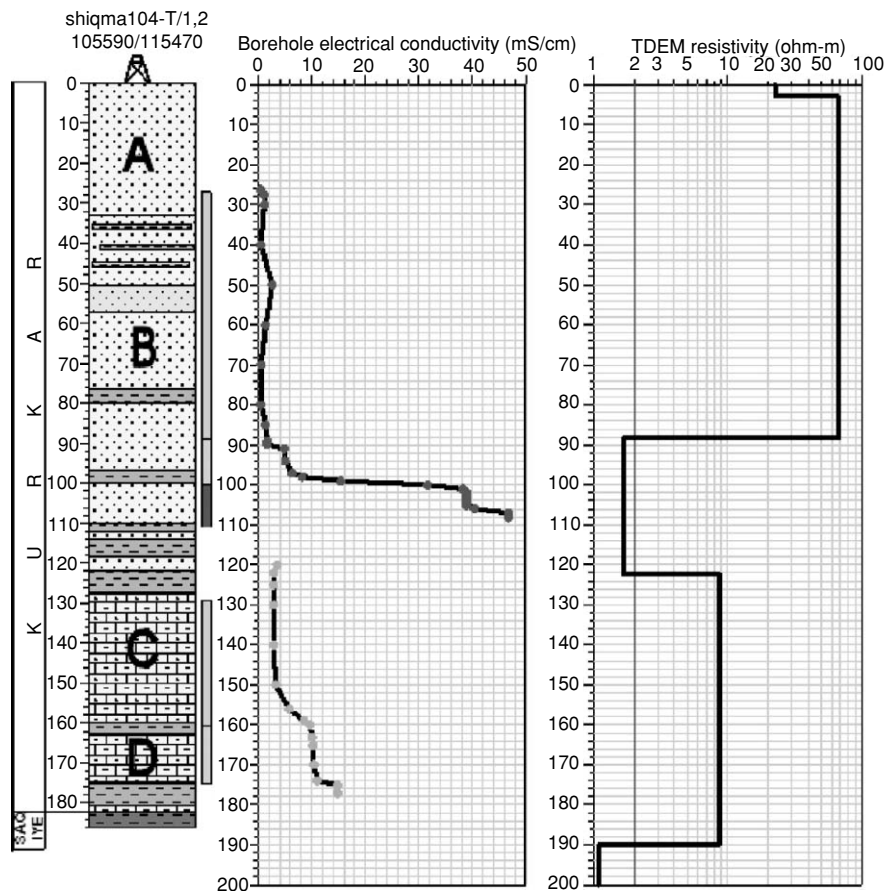


Figure 5. Comparison of the TDEM resistivities on the right with the lithological log and the groundwater conductivity profile from the adjacent Shiqma-104 well on the left. The red line on the right roughly represents the threshold resistivity value for seawater. A, B, C and D represent different sub-aquifers. The increase of the TDEM resistivity below seawater intrusion clearly indicates the existence of fresher water in the lower sub-aquifers (hydrological inversion). The location of the interface according to TDEM is somewhat higher than that in the well probably because the surface TDEM soundings were made 3 years after the well measurements

The portions of the aquifer saturated with brackish waters (e.g. within sub-aquifers C and D in Figure 5) exhibit resistivities between 3 and 10 Ohm-m, and fresh groundwater bodies show higher resistivities.

Observations from all around the world show similar resistivity values for saline water saturated rocks and, what is most important, they also show that almost any lithologies whether freshwater saturated or dry, exhibit much higher resistivities (Palacky, 1987).

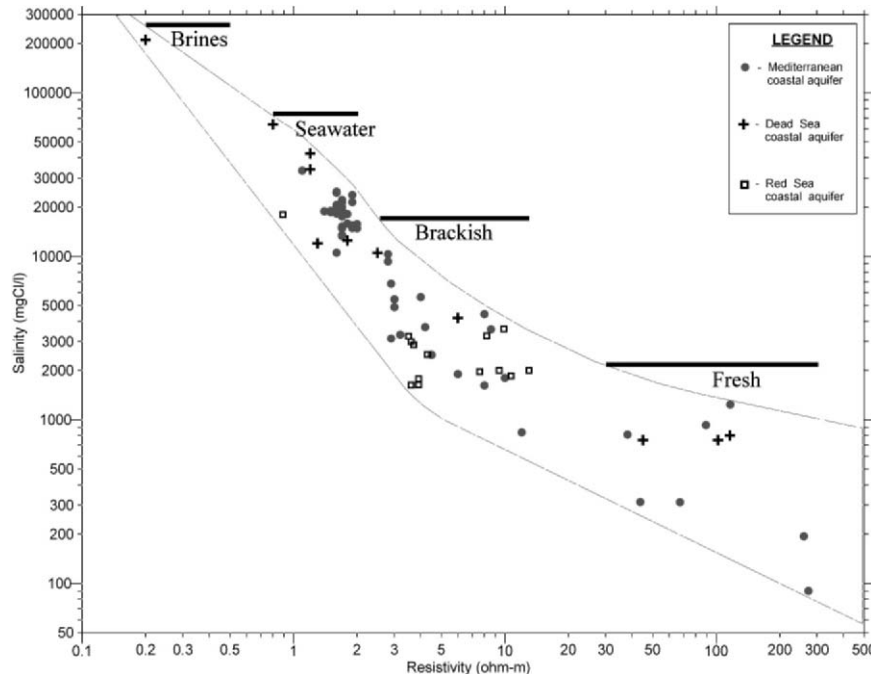


Figure 6. TDEM resistivity-borehole salinity calibration data from the Mediterranean, Dead Sea and Red Sea coastal aquifers

8.4.2. GULF OF ELAT COASTAL AQUIFER

The coastal aquifer in this region consists of coarse clastic graben fill material alternating with clay and marl beds that divide the sequence into sub-aquifers. TDEM results in this area, when correlated with groundwater salinities (Kafri et al., 2001), revealed the following: close to the shore, low resistivities (around 1 Ohm-m) could be identified with seawater intrusion into the coastal aquifer detected in boreholes. Further inland, where brackish groundwater was found in boreholes, TDEM resistivities varied between 3 and 10 Ohm-m as expected, but in some cases resistivities were found to be below 1 Ohm-m, typical of brines and in contradiction to the detected brackish groundwater. Similar phenomenon was encountered in deep sub-aquifers of the Mediterranean coastal aquifer and will be discussed below.

8.4.3. DEAD SEA COASTAL AQUIFER

The Dead Sea coastal aquifer consists of mainly Quaternary continental deposits, which fill the Dead Sea rift valley. These constitute coarse clastics

(gravel and sand) alternating with clay beds as well as lacustrine gypsum and aragonite deposits. As a result, the sequence is divided into sub-aquifers. The system is hydrologically connected to the Dead Sea, which contains brines whose concentration is ten times greater than that of normal seawater. TDEM surveys were carried out to detect the saline water bodies and the configuration of the interface between them and the overlying fresh groundwater bodies (Kafri et al., 1997; Yechieli et al., 2001). It was found that resistivities below 1 Ohm-m and mostly below 0.6 Ohm-m (sometimes even as low as 0.25 Ohm-m) are typical of the Dead Sea water intrusion either concentrated or slightly diluted.

Resistivities above 5 Ohm-m reflect any lithology whether unsaturated or saturated with fresh or brackish waters and intermediate resistivities represent mixtures between the above end members.

The results of the resistivity/salinity calibration measurements for all granular coastal aquifers of Israel are shown in Figure 6.

8.4.4. THE JUDEA GROUP CARBONATE AQUIFER

The Judea Group Cretaceous carbonate aquifer is a regional, 600–700 m thick, partly karstic aquifer, which consists mainly of limestones and dolomites. The aquifer is in places hydrologically connected to the sea and in places may host trapped seawater or brines.

The correlation TDEM measurements in this aquifer are limited in number as compared to the coastal aquifers due to the scarcity of boreholes that can be used for calibration and due to the depth to the target normally exceeding the maximum penetration depth of the common TDEM system (i.e., 500–600 m). Nevertheless, previous preliminary TDEM measurements carried out in the Mt. Carmel area not far from the sea shore, managed to detect resistivities close to 1 Ohm-m just below the fresh/seawater interface calculated using the Ghyben-Herzberg approximation (Goldman et al., 1988).

Recent deep TDEM measurements in this aquifer, showed significantly higher resistivities varying between 4 and 10 Ohm-m for possible seawater salinities (Goldman and Kafri, 2002) either measured in boreholes or assumed according to available hydrogeological information.

The Tanninim Deep well and the adjacent TDEM station N1 can serve as a good example (Figure 7). The borehole penetrated the carbonate Upper Cretaceous aquifer that is known to be connected to the sea. The top of the aquifer is located at 580 m depth and, according to the Ghyben-Herzberg relationship, the freshwater-seawater interface is expected at a depth of about 600 m. In fact, somewhat diluted seawater (17,000 mgCl/l) was detected in the well at approximately the same depth and also appears as a resistivity drop in the TDEM resistivity/depth profile.

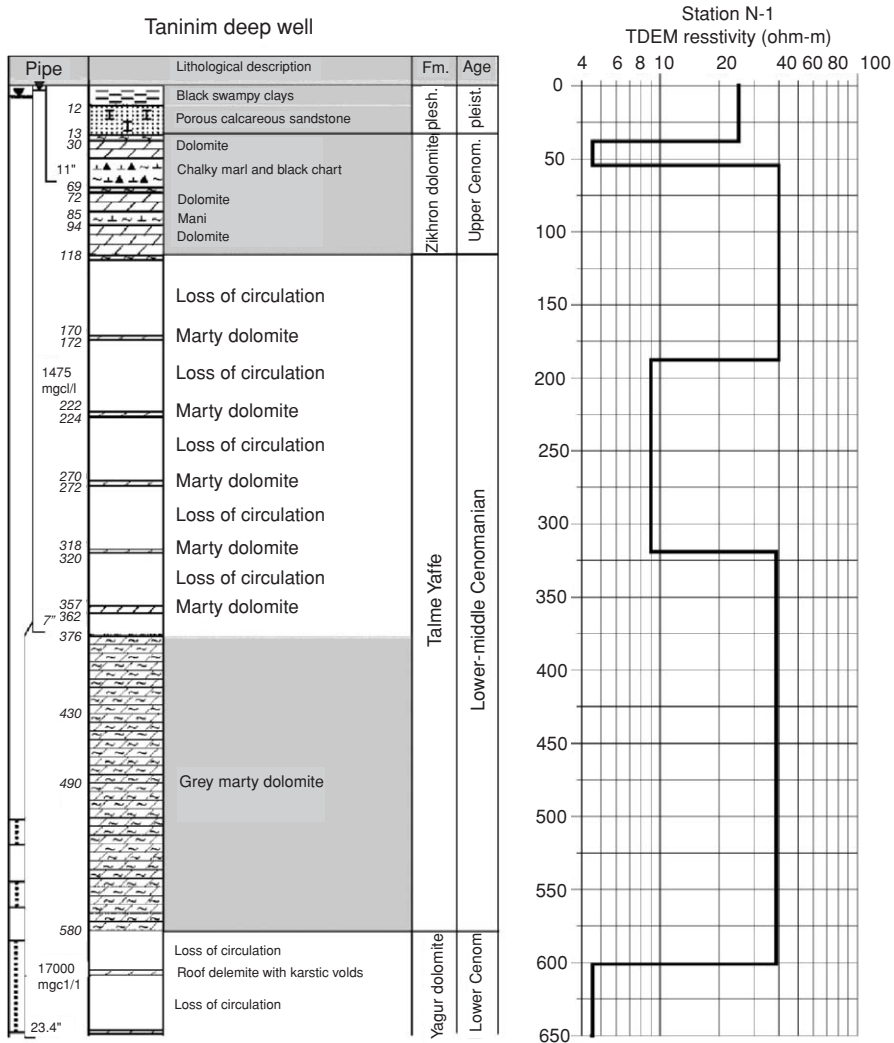


Figure 7. Comparison of the TDEM resistivities on the right with the lithological log and the groundwater chlorinity measurements from the adjacent Tanimim Deep well on the left

It should be noted that electric resistivity logs in boreholes (e.g. the Netanya-1 well), which penetrated saline water bodies, having roughly seawater salinities, also exhibited resistivities varying between 4 and 6 Ohm-m in the relevant depth intervals.

The significant difference in the observed resistivities of seawater-intruded granular clastic and karstic carbonate aquifers is discussed below.

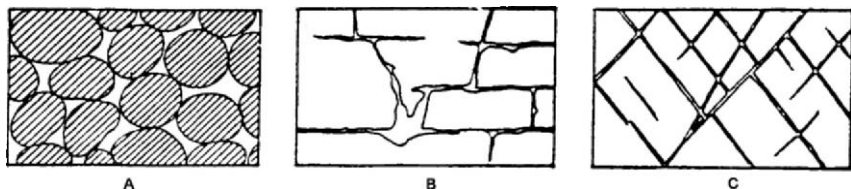


Figure 8. Diagram showing different types of rock interstices and the relation of rock texture to porosity. (A) Well-sorted sedimentary deposit having high porosity; (B) rock rendered porous by solution processes; (C) rock rendered porous by fracturing. (After Meinzer, 1942)

8.5. Discussion

8.5.1. THE POROSITY OF THE AQUIFERS IN QUESTION

The total porosity of an aquifer includes both the connected pores (or the aquifer storativity) and the unconnected pores. The total porosity is determined in a laboratory from core samples, whereas storativity is obtained from hydrological pumping interference tests, which are not available in most cases.

Two main types of aquifers exist, namely granular (Figure 8A) and those, in which porosity is mostly gained by dissolution processes (Figure 8B) and fracturing (Figure 8C).

In granular aquifers, the porosity is mostly intergranular and the aquifers are not extremely heterogeneous. Thus, a porosity value obtained from a core sample might approximately represent larger volumes of the aquifer. As far as carbonate aquifers are concerned, the conditions are usually different. Most of the hydraulic conductivity, as well as storativity are related to open fissures and solution channels and the aquifer is extremely heterogeneous. Very often an aquifer might have a double or even triple porosity system, which includes the initial matrix porosity and the secondary fissured and solution porosity. As a result, the hydraulic parameters obtained are scale dependent and often show higher parameters with increasing test radii, from a core sample to a pumping test and toward a regional study (Rover and Cherkauer, 1995; Zuber and Motyka, 1998; White, 2002). It is thus essential to know, mainly for carbonate aquifers, whether a given porosity value represents a small or a large aquifer volume. Furthermore, when a resistivity value is used, it should be taken into account whether it is obtained from a borehole log representing a small radius and thus lower porosities, or from TDEM measurements that integrate larger aquifer volumes and thus possibly representing higher porosities.

Storativity values from pumping tests and hydrological models as well as porosity values for both granular and carbonate aquifers discussed above, are summarized in Table 1.

Storativities in the coastal aquifers vary between 0.25 and 0.4 and they reflect the aquiferous portion of the sequence. It is assumed that in this portion,

TABLE 1. Storativity and porosity of granular and karstic aquifers

Aquifer	Location/basin	Storativity	Reference
Coastal (granular)	Shiqma	0.3–0.4	Sellinger and Kapuler (1972)
	Nizzanim	0.3–0.4	Sellinger and Kapuler (1973)
	Western Galilee	0.25–0.35	Sellinger and Levin (1977)
	General	0.25	Mercado (2000)
	Dead Sea	0.012	Hirsch (1975)
Judea Group (carbonate)	Naaman	0.03–0.08	Michaeli et al (1973)
	Naaman	0.06	Mercado and Ben Zvi (1983)
	Kabri	0.04	Shachnai and Goldshtoff (1978)
	Yarkon-Taninim	0.05	
	Bet Shean	0.03–0.07	Baida et al (1978)
	Mt. Carmel	0.03	Goldshtoff and Shaliv (1979)
	Na'aman	0.013	Bar Yosef et al. (1997)
	Atlit 1 (Carmel)	0.15	Mercado and Ben Zvi (1983)
	N. Oren Carmel)	0.15	Mercado and Ben Zvi (1983)
	Porosity		
Mt. Carmel reefs	Up to 0.15		Bein (1971)
	Ashqelon 3	0.15–0.20	Bein (1971)

the values are not quite similar to those of the total porosity. The situation, however, is different in the clayey aquicluial interlayers which might exhibit a high non-effective porosity that contains trapped, unflushed fluids.

The carbonate aquifer exhibits mostly storativities between 0.03 and 0.08, since the initial sedimentary (matrix) porosity is small and most of the storativity is related to secondary porosity gained by fracturing and solution. In places, like Mt. Carmel area (Figure 3, aquifer 4), where a reef facies is known in both outcrops and subcrops, the initial porosity and as a result the storativity are high, attaining a value of 0.15. In the case of the discussed carbonate aquifers one should take into account, in addition, the large aquifer volume with a small initial non-effective porosity.

8.5.2. CALCULATED VERSUS ACTUAL RESISTIVITIES

Using the derived porosities (Φ), the expected bulk resistivities (ρ) and saline groundwater resistivities (ρ_w) for different aquifers could be calculated using the Archie equation.

The ρ_w values, for the different saline potential end members, were obtained from a resistivity/salinity chart (Repsold, 1989) and they are 0.18 and 0.04 Ohm-m for Mediterranean seawater and Dead Sea brine, respectively. The ranges of porosities (Φ) used were those described above for the different aquifers. The resultant calculated ρ values for different porosities are given in Table 2. It can be seen that in the Mediterranean coastal aquifer,

TABLE 2. Bulk resistivities calculated using Archie's equation for different porosities and water resistivities and actual resistivities measured by TDEM in different aquifers. In the calculations for granular aquifers, parameter α was set 1.2 that is normally used for sands

Aquifer and saline water body	Φ	ρ_w (Ohm-m)	ρ (Ohm-m)	
			Calculated	TDEM
Coastal, granular aquifer saturated with normal seawater.	0.2	0.18	3.6	Between 1 and 2
	0.3	0.18	1.6	
	0.4	0.18	0.91	
Coastal, granular aquifer saturated with Dead Sea concentrated brine.	0.2	0.04	0.81	Between 0.2 and 0.8
	0.3	0.04	0.36	
	0.4	0.04	0.20	
Judea Group carbonate aquifer saturated with normal seawater.	0.03	0.18	200	Between 4 and 8
	0.05	0.18	72	
	0.07	0.18	37	
	0.08	0.18	28	
	0.15	0.18	8	
	0.20	0.18	4.5	
Judea Group carbonate aquifer saturated with Dead Sea concentrated brine.	0.05	0.04	16	Between 5 and 10
	0.15	0.04	1.8	

subjected to seawater intrusion, the TDEM measurements yielded resistivities between 1 and 2 Ohm-m similar to the ones shown in Table 2 for the porosity values greater than 0.3. It should be noted that in the lower part of the Mediterranean coastal aquifer the proportion of the clayey interlayers as compared to the aquiferous ones is higher. Here, in some cases where fresh waters were sampled in the aquiferous parts, TDEM resistivities were below the expected values. It is assumed that in these cases the TDEM measurements integrate both aquiferous and clayey layers with apparently trapped and unflushed saline waters, resulting in the lowering of resistivities of the entire sequence. The same phenomenon was encountered in the Gulf of Elat coastal aquifer.

In the Dead Sea coastal aquifer, where intrusion of the Dead Sea brine to the aquifer is evident, resistivities below 1 Ohm-m were measured, similar to the calculated ones (Table 2).

The situation seems to be more complicated regarding the Judea Group carbonate aquifer when intruded by seawater. The calculated resistivities for relatively low storativities (0.03–0.08) are significantly higher (between 28 and 200 Ohm-m) than those measured by TDEM and only for higher storativities (0.15–0.20) are the resistivities closer to the actual TDEM or well log resistivities.

Measurements in Mt. Carmel, near N. Oren, where high storativities were measured, yielded resistivities around 1 Ohm-m and in other places approximately between 5 and 10 Ohm-m (Goldman and Kafri, 2002) possibly due to lower storativities. It is noteworthy that in a few wildcats (Gaash 2, Netania 1 and Cesarea 3), carbonate sequences saturated with waters of seawater salinity (18,000–20,000 mgCl/l) exhibited well log resistivities between 4 and 6 Ohm-m, similar to the TDEM resistivities.

8.6. Conclusions

TDEM resistivity measurements allow improved detection of the geometry and bulk resistivity of seawater intrusion into both granular and carbonate coastal aquifers. This permits more reliable estimation of porosity of seawater-intruded parts of the aquifers, since both the bulk and the fluid resistivities are well determined in these parts. The obtained porosity, in most cases, adequately represents the entire aquifer or its major parts, since it is generally similar both above and below the freshwater/seawater interface.

Comparison of the calculated porosities and storativities obtained from pumping tests and hydrological models show generally good agreement in the granular coastal aquifers of Israel. The situation is more complicated in the carbonate karstic aquifers where both geophysical and borehole data are scarce and storativities vary over a wide range. For these aquifers, an extensive and more detailed TDEM survey is necessary to provide a sufficient amount of the resistivity constraint.

It is essential to calibrate the method in coastal granular and, more importantly, carbonate aquifers in regions where hydrological data (water levels, salinities, porosities) are available. Potential study areas, among others, exist along the Mediterranean coasts in southern Spain, southern France, Greece and the Adriatic coasts, as well as in the southern Atlantic coasts of the United States.

It is important to emphasize that although the suggested approach has been tested using only the oversimplified Archie's equation, it could be even more feasible in complicated groundwater systems including partial saturation, clay conductivity effect, etc. Such systems are described by more general equations connecting fluid and electrical properties (such as the empirical Schlumberger equation or the theoretical Clausius-Mossotti equation), the application of which requires additional a priori information (Wempe, 2000). However, in brine-saturated aquifers, in which for example the clay conductivity effect becomes insignificant (Hoyer and Spann, 1975), the amount of information required can thus be significantly reduced.

References

Albouy, Y., P. Andrieux, G. Rakotondrasoa, M. Ritz, M. Descloires, J.-L. Join, and E. Rasolomanana, 2001. Mapping coastal aquifers by joint inversion of DC and TEM soundings – three case histories, *Ground Water*, 39, 87–97.

Archie, G.W., 1942. The electrical resistivity log as an aid in determining some reservoir characteristics, *Trans. Am. Inst. Min. Met. Eng.*, 146, 54–62.

Baida, U., Y. Goldstoff, and Y. Kidron, 1978. Numerical model of the Cenomanian aquifer in the southern part of the Yarkon-Taninim basin (Beer Sheva Basin), *Tahal Rep. 01/78/08*. (in Hebrew)

Bahr, K., 1997. Electrical anisotropy and conductivity distribution functions of fractal random networks and of the crust, the scale effect of connectivity, *Geophys. J. Int.*, 130, 649–660.

Bar Yosef, Y., A. Michaeli, and S. Wolman, 1997. Hydrological planning of exploitation from the Naaman basin, *Summarizing Report, NRD Rep. NR/221/97*. (in Hebrew)

Bein, A., 1971. Rudistid reef complexes (Albian to Cenomanian) in the Carmel and the Coastal Plain, Israel, *Inst. Pet. Res. Geophys., Rep. 1051* and *Geol. Surv. Israel, Rep. OD/2/71*.

Fitterman, D.V., and M.T. Stewart, 1986. Transient electromagnetic soundings for groundwater, *Geophysics*, 51, 995–1006.

Fitterman, D.V., and V.F. Labson, 2005. Electromagnetic methods for environmental problems, in *Near-Surface Geophysics*, edited by D.K. Butler, SEG, Tulsa, pp. 295–349.

Chinh, P.D., 2000. Electrical properties of sedimentary rocks having interconnected water-saturated pore spaces, *Geophysics*, 65, 1093–1097.

Goldman, M., A. Arad, U. Kafri, D. Gilad, and A. Melloul, 1988. Detection of freshwater/seawater interface by the Time Domain Electromagnetic (TDEM) method in Israel, in *Proceedings of the 10th SWIM*, Ghent, Belgium, pp. 329–344.

Goldman, M., D. Gilad, A. Ronen, and A. Melloul, 1991. Mapping of seawater intrusion into the coastal aquifer of Israel by the time domain electromagnetic method, *Geoexploration*, 28, 153–174.

Goldman, M., A. Du Plooy, and M. Eckard, 1994. On reducing ambiguity in the interpretation of transient electromagnetic sounding data, *Geophys. Prospect.*, 42, 3–25.

Goldman, M., and M. Gandler, 2002. Detection of fresh and brackish groundwater bodies within deep sub-aquifers and mapping freshwater/seawater interface along the coastal aquifer of Israel using geophysical (TDEM) method, *Geophys. Inst. Israel Rep. 914/210(1)/02*. (in Hebrew)

Goldman, M., and U. Kafri, 2002. Integrated electromagnetic geophysical technology applied to the detection of deep fresh/saline groundwater interfaces in northern and central Israel, *Geophys. Inst. Israel Rep. 911/188/01*.

Goldshtoff, Y., and G. Shaliv, 1979. The Bet Shean basin. Calibration of a numerical model for the reconstruction of groundwater movement, *Progress Report No. 2*, *Tahal Rep. 01/79/60*. (in Hebrew)

Hermance, J.F., 1979. The electrical conductivity of materials containing partial melt, a simple model from Archie's law. *Geophys. Res. Lett.*, 6, 613–616.

Hirsch, H., 1975. Possibility for exploitation of fresh water in the Ein Tureibe – Ein Ghuweir region, *Tahal Rep. 01/75/67*.

Hoyer, W.A., and M.M. Spann, 1975. Comments on obtaining accurate electrical properties of cores, *Trans. SPWLA XVI*, paper 13.

Interpex Ltd., 1996. TEMIX XL user's manual, Interpex, Golden Co, USA.

Kafri, U., M. Goldman, and B. Lang, 1997. Detection of subsurface brines, freshwater bodies and the interface configuration in between by the Time Domain Electromagnetic (TDEM) method in the Dead Sea rift, Israel, *J. Environ. Geol.*, 31, 42–49.

Kafri, U., M. Goldman, and M. Gendler, 2001. TDEM survey to characterize groundwater salinity in the southern Arava and the Gulf of Elat coast, *Geol. Surv. Israel Rep. TR-GSI/3/2001 and GII Rep. 906/94/00.* (in Hebrew)

Kelly, W.E., and S. Mareš, 1993. Applied geophysics in hydrogeological and engineering practice, Elsevier, Amsterdam, 290 p.

Knight, R., 1991. Hysteresis in the electrical resistivity of partially saturated sandstone. *Geophysics*, 56, 2139–2147.

Knight, R., 1992. Seismic and electrical properties of sandstone at low Saturation. *J. Geophys. Res.*, 97, 425–432.

Loke, M.H., 2000. Electrical imaging surveys for environmental and engineering studies. A practical guide to 2-D and 3-D surveys, 67 pp.

Loke, M.H., 2004. RES2DINV Ver. 3.5, Rapid 2D resistivity and IP inversion using the least squares method, Geotomo Software, Accessed from www.geoelectrical.com, 90 pp.

Meinzer, O.E., 1942. Hydrology. Dover Publications, New York, 712 pp.

Mendelson, K.S., and M.H. Cohen, 1982. The effect of grain anisotropy on the electrical properties of sedimentary rocks, *Geophysics*, 47, 257–263.

Mercado, A., 2000. Hydrological examination of sea water supply to desalination plants by wells in the southern coastal plain, *Progress Report No. 1.*, Geol. Surv. Israel.

Mercado, A., and A. Ben Zvi, 1983. A preliminary hydrogeological survey in chosen areas for siting of subsurface nuclear power plants, *Tahal Rep. 04/83/11.* (in Hebrew)

Michaeli, A., M. Shaharabani, and D. Blank, 1973. Development and calibration of groundwater flow model in the Na'aman basin, *Tahal Rep. 01/73/29.* (in Hebrew)

Palacky, G.I., 1987. Resistivity characteristics of geological targets, in *Electromagnetic Methods in Applied Geophysics-Theory*, edited by M. Nabighian, Society of Exploration Geophysicists, Tulsa, OK, pp. 53–129.

Repsold, H., 1989. Well logging in groundwater development, *Int. Assoc. Hydrogeol.*, 9, 136.

Revil, A., L.M. Cathles, S. Losh, and J.A. Nunn, 1998. Electrical conductivity in shaly sands with geophysical applications. *J. Geophys. Res.*, 23, 925–23,936.

Rover, C.W. II, and D.S. Cherkauer, 1995. Scale dependency of hydraulic conductivity measurements, *Ground Water*, 33, 769–780.

Sellinger, A., and I. Kapuler, 1972. The Shiqma coastal collector; proposal for hydrological planning of the exploitation system, *Tahal Rep. HR/72/118.* (in Hebrew)

Sellinger, A., and I. Kapuler, 1973. The Nitzanim coastal collector; proposal for hydrological planning of the exploitation system, *Tahal Rep. HR/73/01.* (in Hebrew)

Sellinger, A., and M. Levin, 1977. Hydrology of the Pleistocene aquifer in the Western Galilee, *Tahal Rep. 01/77/18.* (in Hebrew)

Sen, P.N., 1997. Resistivity of partially saturated carbonate rocks with microporosity, *Geophysics*, 62, 415–425.

Shachnai, E., and Y. Goldstoff, 1978. The upper Cenomanian – Turonian aquifer of the Qeren – Kabri basin. Calibration of digital model to simulate ground water flow, *Tahal Rep. 01/77/42.*

Yang, C.-H., L.-T. Tong, and C.-F. Huang, 1999. Combined application of dc and TEM to sea-water intrusion mapping, *Geophysics*, 64, 417–425.

Yechieli, Y., U. Kafri, M. Goldman, and C.I. Voss, 2001. Factors controlling the configuration of the fresh-saline water interface in the Dead Sea coastal aquifers, *Hydrogeol. J.*, 9, 367–377.

Wempe, W.L., 2000. Predicting flow properties using geophysical data: Improving aquifer characterization, Ph.D. Thesis, Stanford University, Stanford, CA, 113 p.

White, W.B., 2002. Karst hydrology: Recent developments and open questions, *J. Eng. Geol.*, 65, 85–105.

Zuber, A., and Motyka, J., 1998. Hydraulic parameters and solute velocities in triple-porosity karstic-fissured-porous carbonate aquifers: Case studies in southern Poland, *J. Environ. Geol.*, 34, 243–250.

9. APPLICATIONS OF THE SELF-POTENTIAL METHOD TO HYDROLOGICAL PROBLEMS

A. Revil, K. Titov, C. Doussan, and V. Lapenna

9.1. Introduction

The self-potential method consists in the passive measurement of the distribution of the electrical potential at the ground surface of the Earth and in boreholes. The purpose of this method is to map the electrical potential to reveal one or several polarization mechanisms at play in the ground. In some cases, the self-potential signals are monitored with a network of non-polarisable electrodes, which provides both a better signal-to-noise ratio and the possibility to discriminate between various sources. The two main contributions to the self-potential signals are (1) the streaming potential or hydroelectric coupling (Fournier, 1989; Birch, 1993, 1998; Aubert and Yéné Atangana, 1996; Revil and Leroy, 2001) and (2) electro-chemical processes (membrane or diffusion potentials) associated with gradients of the chemical potentials of ionic species in the pore water (e.g., Sen, 1991; Naudet et al., 2003, 2004; Revil and Leroy, 2005). In the former case, the self-potential signal corresponds to the electrical field associated with the flow of ground water in a porous medium and more precisely with the drag of the excess of charge generally contained in the so-called diffuse layer in the vicinity of the mineral surface (e.g. Revil and Leroy, 2004). If the chemical potential concerns the electrons (redox potential), the transfer of electrons through an electronic conductor also generates self-potential signals in the surrounding conductive medium as discussed by Sato and Mooney (1960).

Historically, the self-potential method is the oldest of all the geophysical methods. The existence of natural polarization mechanisms in the ground is mentioned for the first time in 1830 (Fox, 1830). Like the induced polarization method, the self-potential method was initially developed to locate ore deposits (e.g., Sato et Mooney, 1960; Stoll et al., 1995; Bigalke and Grabner, 1997). In the classical model of Sato and Mooney (1960), the ore body transmits electrons between the reduced part and the oxidized part of the ground (for example when the ore body intercepts the water table).

The self-potential method also has a long history in the oil industry, especially as a downhole measurement to distinguish clean sandstones from shaly formations and oil/gas reservoirs from aquifers. In this case, the main

component of the self-potential signals is usually due to the difference of chemical potentials between the pore water of the formations and that of the drilling mud infilling the borehole. The interpretation of the self-potential logs was developed back in the 1920s and 1930s by Conrad and Marcel Schlumberger in France to locate oil and gas reservoirs in sedimentary basins (Schlumberger and Schlumberger, 1922).

In the case of the electrical signals associated with ground water flow, Poldini (1938) was one of the first to suggest the use of the self-potential method to map the pattern of ground water flow, for example in geothermal systems. However, for a long time, the measurements of the self-potentials were interpreted only in a rather qualitative way. A revolution in the analysis of self-potential signals started 25 years ago with the works by Fitterman (1978, 1979) and Sill (1983). Fitterman (1978, 1979) developed integral equations to derive the electrical and the magnetic fields associated with non-equilibrium conditions in the crust of the Earth. Sill (1983) was the first to quantify self-potential signals associated with ground water flow using generalized Darcy and Ohm coupled laws.

More recently, various authors have formulated the forward problem in terms of integral equations relating the source distribution to the signals perceived by the sensors (the electrodes) (e.g., Fournier 1989; Birch, 1993, 1998; Revil et al., 2002, 2004) using the type of analysis presented earlier by Fitterman (1978, 1979). All these improvements have renewed the interest of the scientific community for this geophysical method for hydrolocal applications, the simplest and the cheapest geophysical method but also considered as one of the most difficult to interpret because of the various sources of noises and signals. Actually, the same type of problem arises in medical imaging when dealing with electro-encephalographic signals in the study of electrophysiological activity of the brain. The remedy is to deal with the signals in the frequency domain because, most of the time, various sources of electrical signals have different frequency contents (Hauk et al., 2002). This solution is also relevant to geoelectric survey analysis (Corwin, 1990).

In this chapter, we review the applications of the self-potential method in hydrogeology including pumping tests, vadose zone transfer, ground water flow in landslides, and contaminant plumes. Other applications not discussed in this review paper concern the study of dams (e.g., Gex, 1980), CO₂ sequestration (Moore et al., 2004; Moore and Glaser, 2004), and geothermal systems (Corwin and Hoover, 1979).

9.2. Rationale of Self-Potential Signals

We consider here the fundamental mechanisms of natural polarization in the ground from a purely phenomenological point of view. We recall first some

fundamental properties of electrical properties in the quasi-static limit of the Maxwell equations. The total current density \mathbf{j} , through a porous material (expressed in A m^{-2}) corresponds to the amount of charge crossing a unit surface area of the porous body per unit time. We denote σ the electrical conductivity of the porous material (expressed in S m^{-1} and $\rho = 1/\sigma$ the electrical resistivity in $\Omega \text{ m}$). The existence of a macroscopic polarization process is intimately related to the existence of a net source current density in the ground, \mathbf{j}_s . In this situation, the total current density is equal to the sum of the conduction current (Ohm's law) plus the net source current density,

$$\mathbf{j} = -\sigma \nabla \varphi + \mathbf{j}_s \quad (1)$$

where φ is the electrical potential. Various sources of polarization of electrical charges in water-saturated porous media has been modeled by Revil and Leroy (2004) and Revil et al. (2005) using a mechanistic approach. In this approach, the local equations known to apply to each phase of the porous composite are upscaled using a volume-averaging approach. The existence of an electrical field is due to the coupling between a primary flux (for example the flow of pore water in a porous material in the case of streaming potential) and the electrical current density. As shown recently by Revil and Leroy (2004), there is a variety of mechanisms able to generate a source of current in porous materials including thermo-electric and diffusion phenomena.

In addition to Eq. (1), we need a continuity equation for the charge, which is written in the quasi-static approximation, by:

$$\nabla \cdot \mathbf{j} = 0 \quad (2)$$

The quasi-static limit of the Maxwell equations implies that the information is transmitted instantaneously between the source and the measurement sensors. By combining the current density equation with the continuity equation, the electrical potential obeys:

$$\nabla^2 \varphi = \frac{1}{\sigma} \nabla \cdot \mathbf{j}_s + \frac{\nabla \rho}{\rho} \nabla \varphi \quad (3)$$

The integration of this equation with the Green's method yields an equation giving the electrical potential at observation point \mathbf{P} outside the source volume Ω containing the source of polarization (e.g. Patella, 1997a, b):

$$\varphi(\mathbf{r}) = \frac{-1}{2\pi} \int_{\Omega} \frac{\nabla \cdot \mathbf{j}_s(\mathbf{r}')}{|\mathbf{r} - \mathbf{r}'| \sigma(\mathbf{r}')} d\mathbf{v} + \frac{-1}{2\pi} \int_{\Omega} \frac{\nabla \ln \rho(\mathbf{r}') \cdot \nabla \varphi(\mathbf{r}')}{|\mathbf{r} - \mathbf{r}'|} d\mathbf{v} \quad (4)$$

The distribution of the electrical potential is the sum of two terms. The first one is related to the source of polarization associated with the divergence

of the current density. The second term is associated with the existence of heterogeneities in the distribution of the resistivity of the porous system. This resistivity distributions modifies the streamlines of the electrical current and therefore the distribution of the electrical potential at the boundaries of the system. The two main sources of signals are associated with ground water flow (streaming potential) and redox potential. Several examples will be considered in the next sections showing the relationship between the source of polarization and self-potential anomalies observed at the ground surface.

9.3. Applications to Pumping Tests

Pumping test experiments are a standard method used to assess the hydraulic transmissivity and storativity of aquifers (e.g., Butler and Zhan, 2004). In the course of pumping tests, hydraulic heads are recorded in observation wells. The time-lapse distribution of these heads provide the information needed to determine the hydraulic conductivity and storativity around a pumping well. However this information is poorly distributed due to the high cost of piezometers and therefore the inverse problem is strongly under-determined. In other words hydrogeological data are usually not sufficient to obtain a reasonable distribution of the hydrogeological parameters of interest.

As mentioned above, self-potential signals are generated in such systems in response to ground water flow. These so-called “streaming potentials” are sensitive to hydraulic gradients. A question naturally arises about the strength of these signals and the signal-to-noise ratio required to use these signals in the inverse problem. In the case of monitoring studies, measurable values for the self-potential in field conditions correspond to a threshold of 0.2 mV (e.g. Revil et al., 2002).

Russian scientists provided the first documented observations of self-potential signals associated with pumping tests. The earliest observation of this nature was reported by Gorelik and Nesterenko (1956). These authors presented electrical potential drops versus azimuths at several stations located in the vicinity of a pumping well. They showed that the electrical field is mainly directed radially toward the well. Nearly 20 years later, Bogoslovsky and Ogilvy (1973) showed a significant positive electrical anomaly (~ 40 mV) around a pumping well during a pumping test experiment in a steady-state condition. Isopotential lines on the ground surface around a pumping well have also been presented in Chapter XI of the monograph by Semenov (1980). The self-potential response was also positive and amounted to $\sim +40$ mV (Figure 1).

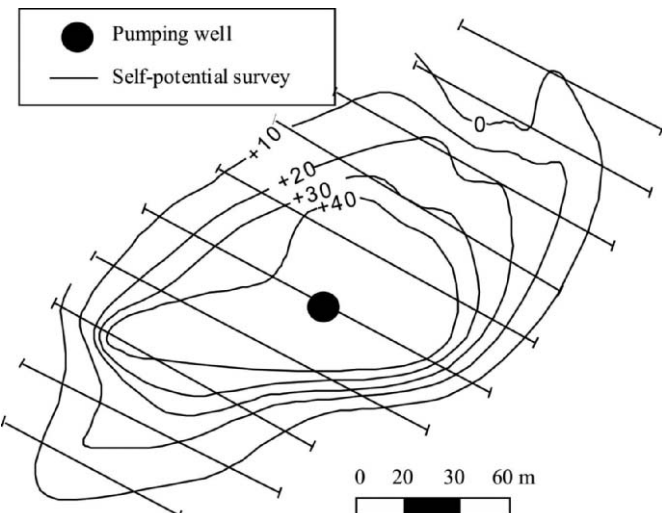


Figure 1. Self-potential map obtained in the course of a pumping test (from Semenov, 1980, p. 312)

However until the beginning of the 1980s, all the self-potential data presented in relation with pumping test experiments were reported for steady-state conditions. Murashko et al. (1981) presented the first self-potential signals obtained in the vicinity of a pumping well in transient conditions. He measured the self-potential response at three different times after the starting of the pumping test experiment. Figure 2 shows self-potential anomaly amounting +60 mV at the beginning of the experiment and also significant variations of self-potential in the course of the pumping.

As mentioned in the introduction, there are usually several sources of the self-potential signals. In the case of self-potential signals associated with pumping tests, electrochemical potentials associated with corrosion of the iron casing also takes place and frequently produces strong negative self-potential anomalies localized in the vicinity of the wells (e.g. Rizzo et al., 2004). This also offers a means to locate abandoned boreholes (e.g. Frischknecht et al., 1983). In all cases, corrosion generates negative self-potential signals in the vicinity of the wells with corroded metallic casing. In all the cases discussed above, the self-potential responses were positive and therefore they cannot be attributed to corrosion of the metallic casings.

The results discussed above were obtained by performing a self-potential survey (except in the case of Gorelik and Nesterenko, 1956). A self-potential survey is performed by using a moving electrode to scan the ground surface electrical potential, the measured potential being referenced to a fixed electrode (the so-called “reference electrode”). It is known that the standard

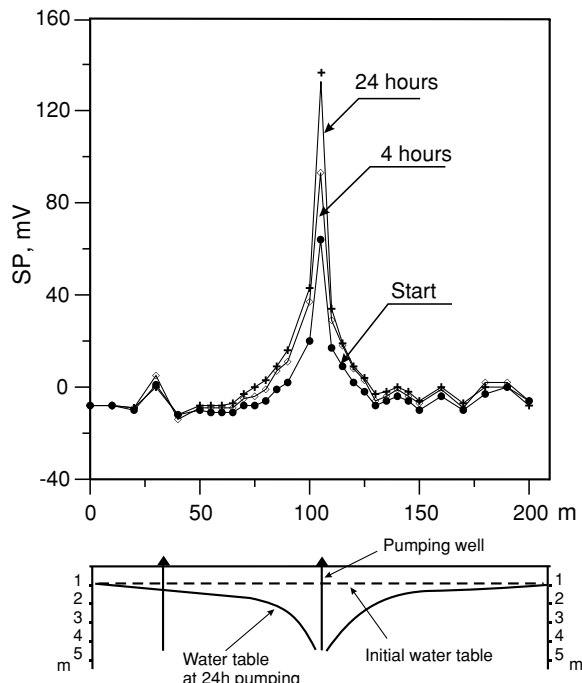


Figure 2. Electrical potential profiles obtained at different time laps after the beginning of a pumping test in a shallow aquifer at the “Polessye” test site (from Murashko et al., 1980, p. 28)

deviation of such measurements is typically ~ 5 mV for self-potential mapping. Because the anomalies discussed above were >40 mV, they correspond to high signal-to-noise ratios. A reasonable assumption is that components of self-potential that are not related to the streaming potential (e.g. the electrochemical potential of corroded casing, the membrane potential) around a pumping well do not vary in the course of pumping test experiments. Thus these components can be viewed as static signals. Therefore the self-potential distribution should be measured at least twice in time to remove the static contribution: under “no-flow” conditions when the streaming potential is not at play, and under “flow” conditions while the streaming potential arises.

The data by Bogoslovsky and Ogilvy (1973) were inverted recently to determine the position of the water table by Revil et al. (2003) and Darnet et al. (2003). However, as in the case of the data in Semenov (1980) and in Murashko et al. (1981), there is a lack of information regarding the field data described by Bogoslovsky and Ogilvy (1973) to test fully interpretation methods of these self-potential signals. Note also that inverting hydraulic heads to determine hydraulic storativity requires knowledge of the variation

of hydraulic heads with time. Recently, new data containing observations of both electrical signals and piezometric levels in the course of a pumping test experiment have been presented by Rizzo et al. (2004) and Titov et al. (2005). The experiment was carried out in an aquifer covered by a clayey aquitard. The aquifer was confined prior to the experiment and became unconfined in the course of the pumping during about four days. The field methodology followed the principles described as follows. The self-potential signals were measured using a network of fixed electrodes located at the ground surface. The observations were carried out during several minutes at quasi-steady-state conditions, and, then during 175 min after the shut down of the pump, while hydraulic heads relaxed. At the end of the experiment, the piezometric levels were considered nearly constant in the vicinity of the pumping well. The values of self-potential obtained 175 min after the shutdown of the pump were used as the temporal reference for each electrode.

The magnitude of the observed signals arrived at +12 mV in the vicinity of the pumping well, which is much larger than the noise level (few mV). The results were analyzed using a new analytical interpretation scheme based on the coupling of hydrodynamic and electrical theory. According to this scheme streaming potential signals on the ground surface obey quasi-linear relationships with hydraulic heads in the aquifer. This quasi-linear relationship

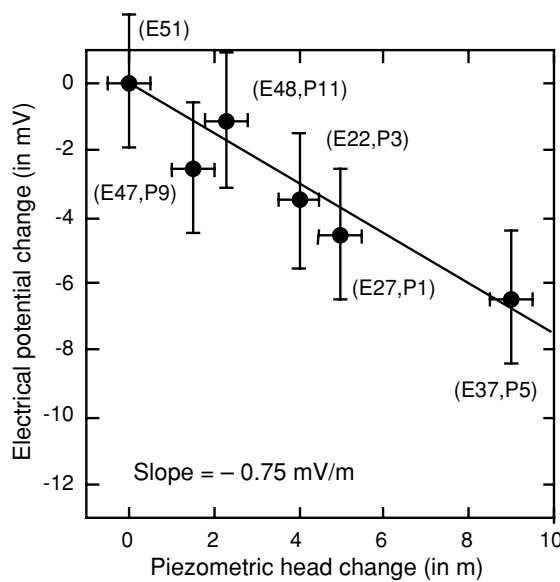


Figure 3. Self-potential change versus piezometric change during the relaxation of the phreatic surface (E_i indicates the name of the electrode i while P_j indicates the name of piezometer j). We use the electrodes close to each piezometer including the pumping well (from Rizzo et al., 2004)

was supported by experimental data (Figure 3). The slope of the relationship represents the so-called apparent voltage coupling coefficient. The apparent coefficient characterizes the sensitivity of self-potential signals to variations of the water heads at specific hydrogeological and geoelectrical settings of the pumping test experiment. Therefore it is possible to relate the time-lapse distribution of the streaming potentials to the distribution of hydraulic heads, and, then to hydraulic conductivity and storativity of an aquifer. Consequently both the hydraulic conductivity and the storativity can be assessed on the basis of electrical data. An independent estimation of the hydraulic conductivity and storativity based on the Theis equation confirms the electrically assessed values.

A numerical analysis of data by Rizzo et al. (2004) has been done on the basis of the numerical simulator GWFGEM (Ground Water Flow Geo-Electrical Mapping) (Titov et al., 2002). The GWFGEM software allows 2-D plus time forward modeling of streaming potentials in saturated media. This analysis allowed also to take in consideration the electrical resistivity distribution captured by Rizzo et al. (2004) on the basis of electrical resistivity tomography, as well as possible heterogeneities in the distribution of hydraulic conductivity and storativity in the aquifer around the pumping well. This new interpretation confirms the linear relationship observed by Rizzo et al. (2004), see Figure 4. It follows that the self-potential signals can be kriged to reconstruct, with a minimum of piezometers, the shape of the water table during the pumping tests. Preferential drainage networks, hydraulic conductivity and storativity could be inverted from this combined information.

9.4. Application to the Vadose Zone

Generally, self-potential signals existing in the vadose zone are most often considered as noise in the case of geophysical prospecting e.g. long period magneto-telluric soundings (e.g. Perrier and Morat, 2000), or in the case of cave or seepage mapping using the self-potential method, (e.g. Corwin, 1990; Vichabian and Morgan, 2002). However, growing environmental concerns during the last decades lead to greater needs in near-surface characterization and, particularly, hydrogeological parameters. In this context, self-potential was most often considered as a qualitative descriptive variable. But due to its unique sensitivity to ground water flow, recent efforts have focused to relate self-potential signals to ground water flow (e.g. Thony et al., 1997; Doussan et al., 2002; Darnet and Marquis, 2004). In this section, we review some of the applications of the self-potential method to unsaturated porous media

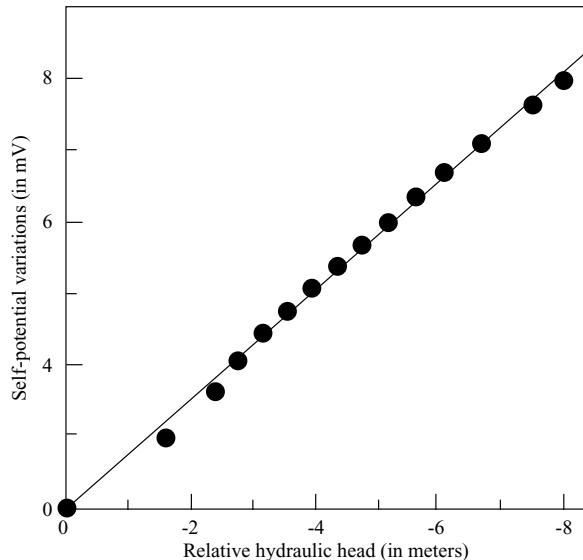


Figure 4. Modeled relationships between self-potentials and the hydraulic heads at the end of the pumping phase for the case described in Rizzo et al. (2004). The line indicates the linear trend. The value of apparent voltage coupling coefficient is -1.5 mV/m of hydraulic head

and discuss some future directions in order to get quantitative information regarding self-potential signals applied to vadose zone transfers.

9.4.1. FIELD APPLICATIONS

As stated in Section 9.3, self-potential data are usually gathered with surface electrode along profiles in order to map horizontal spatial variations and sometimes time variations of the electric signals. However, measurements of time variations of the self-potential signals along vertical profiles are also useful to determine vertical drainage in the vadose zone.

9.4.1.1. Determination of the Thickness of the Vadose Zone

Self-potential signals have often been used to estimate the thickness of the vadose zone comprised between the ground surface and the water table or an impermeable unit. The self-potential variations recorded at the soil surface are more or less proportional to the thickness of the vadose zone (Aubert et al., 2000):

$$e = H(x, y) - h(x, y) = -e_0 - \varphi(x, y)/K \quad (5)$$

where e is the thickness of vadose zone, $h(x, y)$ is the altitude of soil surface, $H(x, y)$ is the altitude of water table or impermeable layer, $\varphi(x, y)$ is the self-potential signal, e_0 the thickness of vadose zone below the self-potential reference station, and K an empirical coefficient ranging between -1 and -10 mV/m. Aubert and Yene Atangana (1996) showed that the conditions needed to check the validity of Eq. (5) are the presence of a highly resistive superficial layer overlying a deep lower resistivity layer. This linear relationship has been explained in terms of vertical infiltration in the vadose zone (Titov et al., 2002) or electrokinetic contribution due to the shape of the water table (Rizzo et al., 2004).

9.4.1.2. *Self-Potential Signals in Consolidated Rocks*

Transient self-potential signals have been observed in unsaturated consolidated rocks. Pisarenko et al. (1996) showed diurnal variations of self-potential on the surface wall of an ancient abbey made of sandstone. The diurnal self-potential variations had an amplitude of about 10 mV and were attributed to diurnal evaporation/condensation sequences driven by temperature variations and capillary rise from superficial water table up the wall. Chène et al. (1995) showed, on the same sandstone, self-potential signals reaching 50–100 mV during an upward imbibition process into an initially dry rock sample. Morat and Le Mouël (1992) made self-potential measurements on a pillar of an underground quarry of coarse limestone. They also found diurnal variations of self-potential with characteristics length scales of a few tens of cm. The self-potential variations were correlated with, but not proportional to, atmospheric pressure variations and showed an amplitude of ~ 1 mV/hPa. This effect was attributed to an electrokinetic origin. In a recent study, Nimmer and Osiensky (2002) used temporal mapping of self-potential (in conjunction with direct current injection) to follow a potassium chloride tracer plume, followed by tap water injection in an unsaturated basalt. There was some variability and noise in the self-potential data but some temporal variations were attributed to plume movement in the vadose zone and a jump of self-potential was attributed to the tracer reaching the water table.

9.4.1.3. *Self-Potential in Unconsolidated Soils*

In unconsolidated surface soils, vadose zone processes (water transfer, electrochemical reactions) were most often considered as noise in the static field of self-potential mapping. However, self-potential can bring valuable information with regards to vadose zone transfers.

9.4.1.4. *Influence of Lithology*

Ernstson and Scherer (1986) conducted an extensive study during a year and a half measuring the self-potential along profiles encompassing different

lithological units. They identified a long-wavelength spatial component of self-potential (m to some tens of m, ~ 10 mV amplitude) that they attributed to changes in underground lithology. Yene Atangana et al. (2003) mapped the self-potential of the lateritic cover of a watershed in southern Cameroon. The self-potential map indicates that the slopes show 10 to -20 mV self-potential amplitude while the valley present more negative self-potential amplitudes (-80 to -100 mV). This self-potential/altitude gradient is the opposite of what could be expected from an electrokinetic source (see discussion above). The authors found that self-potentials correlate with the clay fraction of the loose clay rich horizon of the soil investigated, with self-potential increasing with the clay percentage. This observation suggested that the measured self-potential were of electrochemical origin. Self-potential measurements could, in this case, be used to map the clay-rich zones of the investigated soils.

9.4.1.5. *Self-Potential and Soil Hydrology*

Rainfall events can produce large variations of self-potential on measurement dipoles (e.g., Perrier et al., 1997; Ernstson and Scherer, 1986). However few studies have tried to understand the link between these electric signals and hydraulic behaviour of the soil (see Lachassagne and Aubert, 1989; Thony et al., 1997; Doussan et al., 2002). Estimation of soil-water fluxes is essential in soil physics because of its direct implications in environmental, agronomical or hydrological purposes (estimation of drainage, evaporation, pollutant transfer, aquifer recharge, infiltration/runoff partition, etc.). Field methods for determining soil-water flux is classically done either by mass balance (e.g. the zero flux plane method; Vachaud et al., 1978) or direct application of Darcy's law extended for unsaturated flow. All of these methods are rather difficult to set up and manage, requiring specific equipment. In particular, hydraulic properties of soil are often difficult to obtain. A particular difficulty is that soil properties, and consequently soil-water fluxes, are highly variable in space (vertically and horizontally, e.g. hydraulic conductivity) and time (e.g. water potential). An accurate determination of water flux at different scales would require a high number of measuring sites, which is practically not feasible because of the time needed and the complexity of the measurements. As self-potential measurement would be easier to perform and based upon the fact that self-potential is sensitive to water flux in saturated porous medium, self-potential monitoring could give indications on flow direction and intensity in soils. In the studies reported here, self-potential measurement configuration differs from classical profiling or mapping because electrodes are installed in the soil at the same location but at different depths. Lachassagne and Aubert (1989) gave first measurements of self-potential and water potential (i.e., equivalent to the hydraulic head) variations at different depth, showing that self-potential variations at 25 cm depth were linked

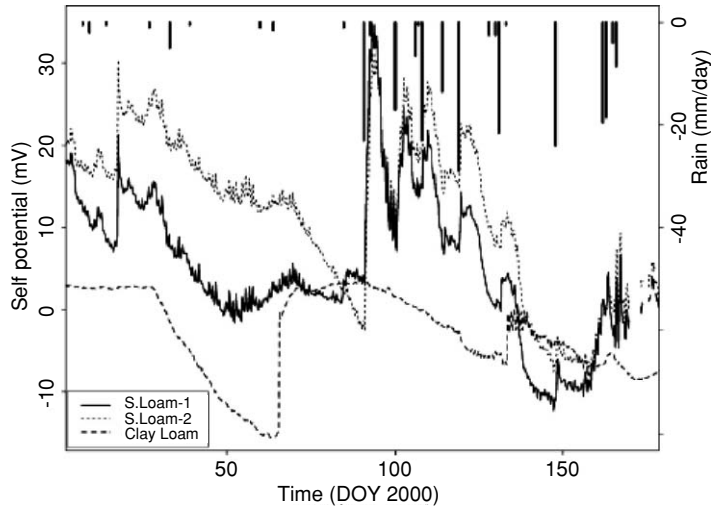


Figure 5. Time variation of the self potential between 30 and 40 cm depths (i.e., $\varphi_{40\text{cm}} - \varphi_{30\text{cm}}$, where φ is the electric potential at indicated depth) for the two measuring points sandy loam soil (S.Loam1 and S.Loam2), and in a clay loam soil. Daily rainfalls are also presented (vertical lines) (from Doussan et al., 2002)

to water potential variations. Thony et al. (1997) found, in a well equipped, cropped experimental field, a strong linear correlation ($r^2 = 0.992$) between self-potential measured at 30 and 50 cm depth and water flux at 40 cm depth following a 24 mm rainfall event. Doussan et al. (2002) showed in a long term experiment, with pedoclimatic conditions differing from Thony et al.'s (1997) experiment, that self-potential variations between 30 and 40 cm soil depth were clearly linked to both rainfall events and evaporation (Figures 5 and 6). The sign of self-potential gave the direction of water flux and self-potential magnitude was much higher in the sandy loam than in the clay loam soil. The linear self-potential – hydraulic flux relationship was weaker in this experiment ($r^2 = 0.75$ at most) compared to Thony et al. (1997) experiment and decreased with time to almost no correlation.

Taking the water saturation into account greatly improved the self-potential – hydraulic flux relationship (Figure 7):

$$u = \left(a \frac{\theta}{\theta_s} + b \right) \varphi + c \frac{\theta}{\theta_s} + d, \quad (6)$$

where φ is the self-potential, u is the flux of water, θ and θ_s are water content and saturated water content, and a, b, c, d are calibration coefficients. Equation (6) shows that the water content by itself is an important variable for relating the hydraulic flux and the self-potential signals. Equation (6) is applicable at the time scale of a single rainfall event, but its robustness decreases for long

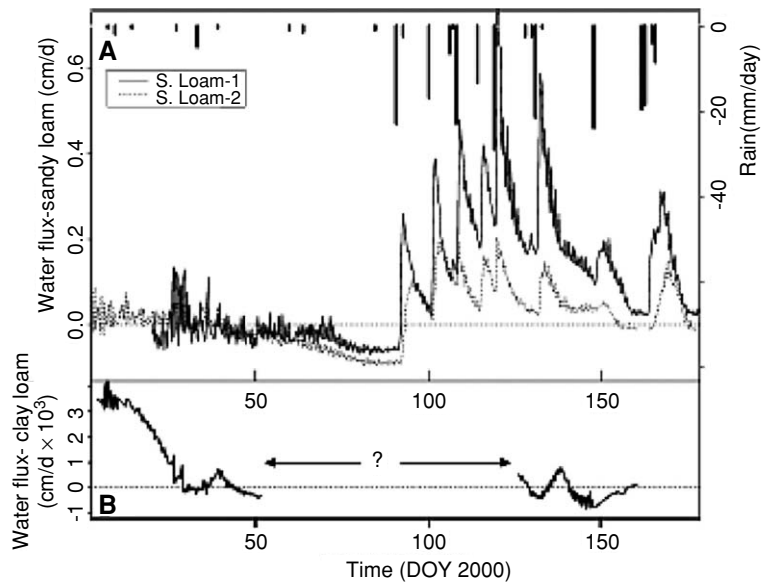


Figure 6. Calculated soil water fluxes (from measured hydraulic conductivity and hydraulic heads data) at 35 cm depth for two measuring points (S.Loam1 and S.Loam2) in a sandy loam soil (A) and in a clay loam soil (B). The “?” mark signifies that hydraulic heads could not be measured at that time and so water flux is not available. Daily rainfalls are also presented (vertical lines) (from Doussan et al., 2002)

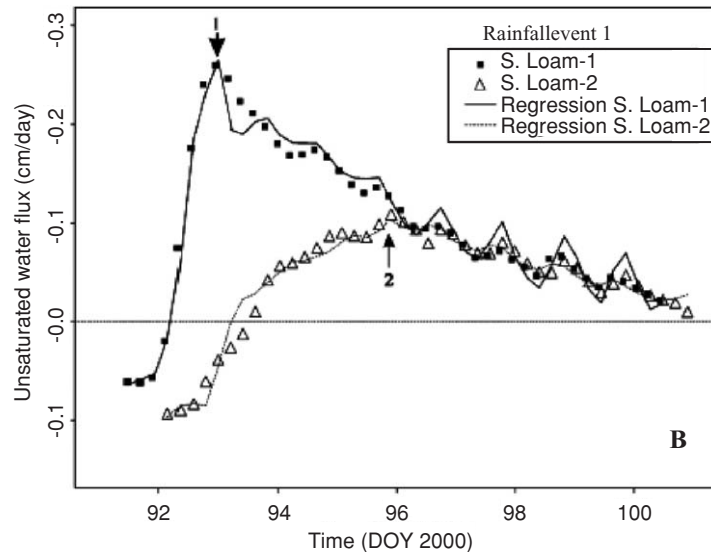


Figure 7. Comparison between the soil water fluxes calculated with the flux – self-potential relationship, Equation (6), of the main text and the field estimated water fluxes for two measuring points (S.Loam1 and S.Loam2) in a sandy loam soil for the first rainfall event (23 mm) shown Figure 6 and 7. A different fit is applied to infiltration and drainage periods. Arrows show the end of the infiltration phase and the beginning of drainage for the two measuring points (from Doussan et al., 2002)

durations (i.e., the coefficient of Eq. (6) varied between rainfalls) and could not be used for predictive purposes). The authors point out methodological problem for long-term measurement of self-potential in soil: electrodes drift, variability of the soil-electrode according to soil moisture conditions, and washing of the salt added to the mud at the basis of the electrodes at the time of installation.

Self-potential could not only be used for the estimation of infiltration, but possibly for the estimation of soil surface evaporation too. Albouy et al. (2000) present self-potential measurements along the same 3 m length profile with different depth for electrode installation (soil surface, 4 cm depth, 10 cm depth). A self-potential difference along the profile reaching 80 mV between measurement at the surface and 10 cm depth was found. Such a self-potential gradient could be attributed to soil evaporation (evapotranspiration was around 5 mm/day and a high water content gradient was measured between surface and 10 cm depth). Other sources of self-potential variations in soils are also possible, but also probably linked to electrokinetic effect: The ‘so-called’ bioelectric effect where high variations of self-potential along profiles may be induced by the vegetation, particularly trees near an open field (Ernstson and Scherer, 1986) and are characterised by short spatial wavelength (0.1–1m) with amplitude up to 150 mV. Such effect might be due to electric fields generated within trees (Morat et al., 1994) or to plant water uptake and the associated water flow in soil. Another source of self-potential spatial variations in soil can arise from soil heterogeneity. Perrier and Morat (2000) identified daily variations of self-potential from 50 m length, ~60 cm depth, dipoles. The electrical signal was correlated with temperature variations. In this study, the authors identified that the most probable source of self-potential variations was not only related to capillary flow in the vadose zone, but also to different water saturation profiles between the two electrode locations.

9.4.2. MODELLING OF SELF-POTENTIAL VARIATIONS AND UNSATURATED FLOW

Few modelling studies of self-potential variations with unsaturated flow are available, particularly for the vadose zone (Adler et al., 1997; Darnet and Marquis, 2004). The modelling relies on (1) calculation of the water flow with some version of the Darcy-Richards equation for unsaturated flow, (2) calculation of the self-potential, by integration along soil depth, the variations of the electrical potential, with the use of the coupling coefficient between electric potential and hydraulic head gradients. As for the saturated case, the modelling relating unsaturated flow and self-potential generation strongly relies on the estimation of the coupling coefficient. For example, Adler et al. (1997) considered a constant coupling coefficient to model the self-potential

daily variations of Morat and Le Mouël (1992). The self-potential amplitude of actual data could be reproduced, but not the time phase. Darnet and Marquis (2004) considered a coupling coefficient varying with water saturation due to variations of electrical conductivity with saturation. They could qualitatively describe the field data of soil water transfer of Thony et al. (1997) and Doussan et al. (2002) and showed that the self-potential was in-phase with the hydraulic head gradient. With the same type of assumptions as Darnet and Marquis (2004), Sailhac et al. (2004) developed a sensitivity analysis between self-potential and hydraulic parameters for infiltration experiments with an analytical solutions and showed that hydraulic conductivity could possibly be estimated by inversion of self-potential data.

It should be stressed that, in these modelling studies, if general trends are depicted, not all the parameters (i.e., hydraulic or electrical parameters) are available for a rigorous evaluation of the modelling assumptions and a hydro-electrical modelling validation is still lacking for the case of unsaturated flow. In particular, as shown below, the estimation of the coupling coefficient for unsaturated flow deserves further evaluation.

9.4.3. SELF POTENTIALS IN UNSATURATED CONDITIONS

Few data are available concerning self potential signals associated with unsaturated flow in porous materials. More particularly, there is almost no data concerning the coupling coefficients for unsaturated soils. Most laboratory self-potential measurements for unsaturated flow conditions were done by injecting gas in a saturated porous medium. Contradictory results emerge from the literature for the relationship between the coupling coefficient and water saturation: Morgan et al. (1989) found an increase of the coupling coefficient, relative to the saturated value, of roughly a half of an order of magnitude by introducing small quantities of air into the high pressure end of a sample of crushed granite. Sprunt et al. (1994) recorded a self-potential jump from -1.8 to -300 mV when a gas bubble (air) migrates through the core of a limestone sample, which translates into a two orders of magnitude increase in the coupling coefficient relative to full saturation. However, gas bubbles could have been trapped in the electrodes during these experiments explaining the very unstable signals they observed. Despite these uncertainties, these findings are in line with the intuitive fact that when the porous medium desaturates, the associated increase in resistivity should enhance the electrical signals.

On the other hand, Guichet et al. (2003) found, for a water saturated sand column in which argon gas was injected, a threefold, and almost linear, decrease of the coupling coefficient between 100% and 40% water saturation. No clear variation of the coupling coefficient with saturation was found when nitrogen gas was injected and the coupling coefficient was roughly constant.

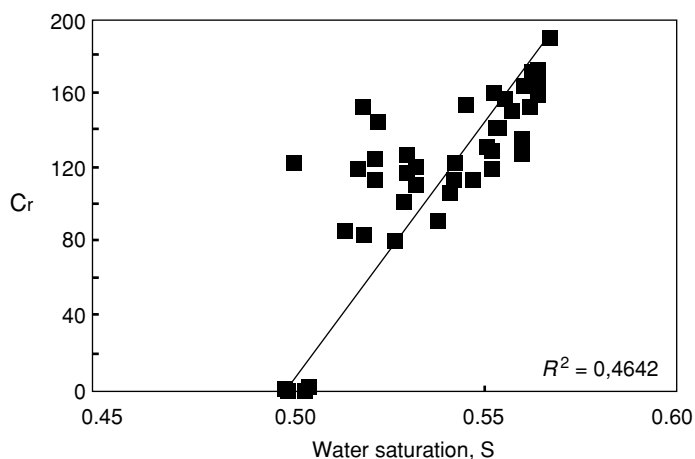


Figure 8. Variation of the relative coupling coefficient (i.e., coupling coefficient for unsaturated conditions divided by the coupling coefficient at saturation) versus water saturation. The coupling coefficient has been estimated from the field data obtained by Doussan et al. (2002)

Revil and Cerepi (2004) also found for dolomite core samples a decrease of the coupling coefficient with saturation using pressurized nitrogen gas in Richards type pressure cells tests. The coupling coefficient was decreased by a factor between 3 and 5 at 50% saturation, relative to the full saturation value, and was nearly zero at 40% saturation. This latter water saturation value was interpreted as the irreducible water saturation at which the water phase becomes immobile.

The field data of Doussan et al. (2002) showed an effective coupling coefficient decreasing trend with water saturation (Figure 8). However, on the narrow range of saturation observed (0.50–0.57) the coupling coefficient is increased by up to two orders of magnitude relative to the coupling coefficient measured in the laboratory on disturbed soil samples at saturation ($C = -2.2\text{mV}/0.1\text{ MPa}$).

Theoretical expressions of the coupling coefficient variations with saturation were derived by Revil et al. (1999) and Revil and Cerepi (2004). Experimental data can be found in Doussan et al. (2002), Guichet et al. (2003) and Revil and Cerepi (2004). The equation derived by Revil and Cerepi (2004) including a new model for electrical conductivity which does not rely on the extended version of Archie's law for unsaturated rock. It predicts a decrease of the coupling coefficient with saturation and was found to give a good agreement with experimental data obtained with dolomite by Revil and Cerepi (2004).

Other published sets of measurements deal with injection of steam into glass capillaries and rock samples heated or not (Moore and Glaser, 2004 and

references cited therein). An increase of the coupling coefficient was shown in this situation, up to two orders of magnitude, compared to one phase flow. As evaporation is basically a vapour phase transfer of water, these measurements tend to show that the evaporation process could be identified by self-potential measurements.

In the light of the preceding discussion, there is a clear need to get more experimental data relating self potential and unsaturated water flow in porous media. This is particularly true for soils, with realistic flow conditions, for which almost no data are available in a controlled environment. Such data with new insights in the theory are highly needed if one wants to get a quantitative use of electric signals in the vadose zone.

9.4.4. PROSPECTIVES

Clearly, self-potential measurements and monitoring can bring useful information about vadose zone processes. For example, spatial variations of soil lithology, such as clay content, could be investigated with self-potential mapping. However, other reliable methods (e.g. electrical resistivity tomography) already exist for this purpose. The most promising applications of self-potential for the vadose zone rely on the estimation of hydrodynamic behaviour (flux, hydraulic gradients, hydraulic conductivity) due to the sensitivity of self-potential to water flux. However, practical and theoretical problems need to be addressed in order to get quantitative information from self-potential signals. From a practical point of view, the microstructure of soils varies over time and they are chemically aggressive media. An electrode design and implantation, which minimise electrode drift and noise (such as varying soil-electrode contact) are presently needed for long term monitoring in soils. Perrier and Pant (2005) present a methodological study which could be adapted to soil studies. From a theoretical point of view, new self-potential data in unsaturated flows should be obtained in controlled environments in order to assess theoretical bases. Without such data and theoretical interpretations, self-potential interpretation for unsaturated flow will remain empirical and qualitative. Field assessment of water flux and self-potential signal should also be carried out, with the same level of accuracy for electrical and hydraulic processes, in order to test the practicability of self-potential monitoring with a sound theoretical basis. In particular, the way temperature and chemistry variations (during infiltration for example) influence the self-potential response during flow should be assessed.

Other uses of self-potential, which have not been specifically investigated, could be tested for vadose zone processes: evaporation (because of a seemingly sensitive coupling coefficient to water vapour transfer), geochemistry and more particularly redox processes or solute transfer. Both these processes

could significantly affect the electrical signal, but should be discerned from the electrokinetic response.

9.5. Applications to Landslides

Landslides are responsible for thousands of deaths and injuries each year and enormous economic losses around the world (Hutchinson et al., 2003). The impact on society is enormous. Every year, landslides produce damage in urban areas and in other man-made structures such as bridges, highways, electric power lines, railroads and underground pipes. The complex dynamics of the landslides require a wide range of observations at various scales, including geological and soils mapping, topographic data, climatic and meteorological parameters, and geophysical surveys. Nowadays, the scientific community is paying great attention to the emerging role of new technologies for Earth observation in the study and monitoring of natural and man-made hazards. In particular, near surface geoelectrical techniques (self-potential and electrical resistivity) are extremely promising technologies for landslide monitoring and to reconstruct the geometry of the landslide body (lateral extension and thickness), the identification of the sliding surfaces between the landslide body and the underlying bedrock and the hydrological characterisation of the site (Bogoslovsky and Ogilvy, 1977; McCann and Forster, 1990; Bruno and Marillier, 2000; Hack, 2000; Mauritsch et al., 2000).

Geoelectrical methods show a high spatial resolution, relatively fast field data acquisition and low costs appearing as the natural counterpart of the near-surface seismic reflection in the study of hydrogeological phenomena (Sharma, 1997; Steeples, 2001, and reference therein). The self-potential method can give relevant information in the study of the groundwater flows, in the estimation of the water-table depth, and in the detection of the space and time-dependent changes of water content. In the following subsections, the first and more interesting results from the application of the self-potential technique to the study of landslide areas in Southern Italy are presented.

9.5.1. SELF-POTENTIAL SURVEY OF GIARROSSA LANDSLIDE

The mapping of the self-potential anomalies was mainly used for delineating the boundaries of the landslides and the main features of groundwater circulation system. The distance between the measurement stations was 50 m. In addition, a moving dipole, with a length of 20 m, has been used to estimate the electrical field along a selected profile, using the starting point as a reference for the self-potential profile. In a second step, the self-potential

values could be also inverted using a 2D probability tomography technique proposed by Patella (1997). The inversion problem consists of recovering the most probable discretised charge distribution which is responsible for the measured self-potential field. The tomographic algorithm is based on the cross-correlation between a theoretical scanner function and the observed electrical field along the profile. The cross-correlation integral gives an estimate of the charge occurrence probability (COP) function which represents the probability of finding electrical charge accumulation in each point of a cross section along the profile.

The Giarrossa landslide is located close to the city of Potenza (Figure 9) and is one of the greatest mass movements of the whole Lucanian Apennine. On December 1976, following relentless heavy rain, the entire landslide mobilised, causing serious damage to suburban areas, communications and roads (Polemio and Sdao, 1998). Now the landslide is inactive, although there are local reactivations in the accumulation zones. The landslide is approximately 2700 m long, about 60–420 m wide and with an upper elevation of 1215 m near Poggi S. Michele and 790 masl (meters above sea level) near Fiumara Malamogliera. It has a mean inclination of about 9°. The landslide involved the Argille Varicolori formations, that area being composed of intensively tectonised, fissured clays shales, clay and mudstones, locally including disarranged blocks and layers of lapideous rocks, such as marls, calcarenites or limestones.

Figure 10 summarises the main geomorphological features of the landslide and shows the location of the geological and geophysical surveys. The source area of the earth flow is very wide and can be described as a multiple and retrogressive transrotational slide. The main scarp, at an elevation of about 1215–1200 masl is semicircular in plan and concave in longitudinal section. The thickness of the disturbed material is in the order of 35–40 m. The flow track of the landslide, which is probably placed on a pre-existing drainage line is approximately 960 m. The depth of the sliding surface varies between 20 and 30 m. The accumulation zone is about 1,050 m wide, with a mean inclination of 7°. The toe material blocked the bed of Fiumara Malamogliera, thereby splitting it into channels that currently border the slide mass. The thickness of material displaced varies from about 10 m in the lateral zones to 25–30 m in the central zones of the accumulation.

In the frame of a geophysical survey planned for studying the Giarrossa landslide, two self-potential maps have been carried out in different climatic conditions (April and September) and many 2D self-potential tomograms have been obtained measuring the electrical field on the Earth surface along profiles transversely oriented respect to the slide (Gallipoli et al., 2000; Lapenna et al., 2003).

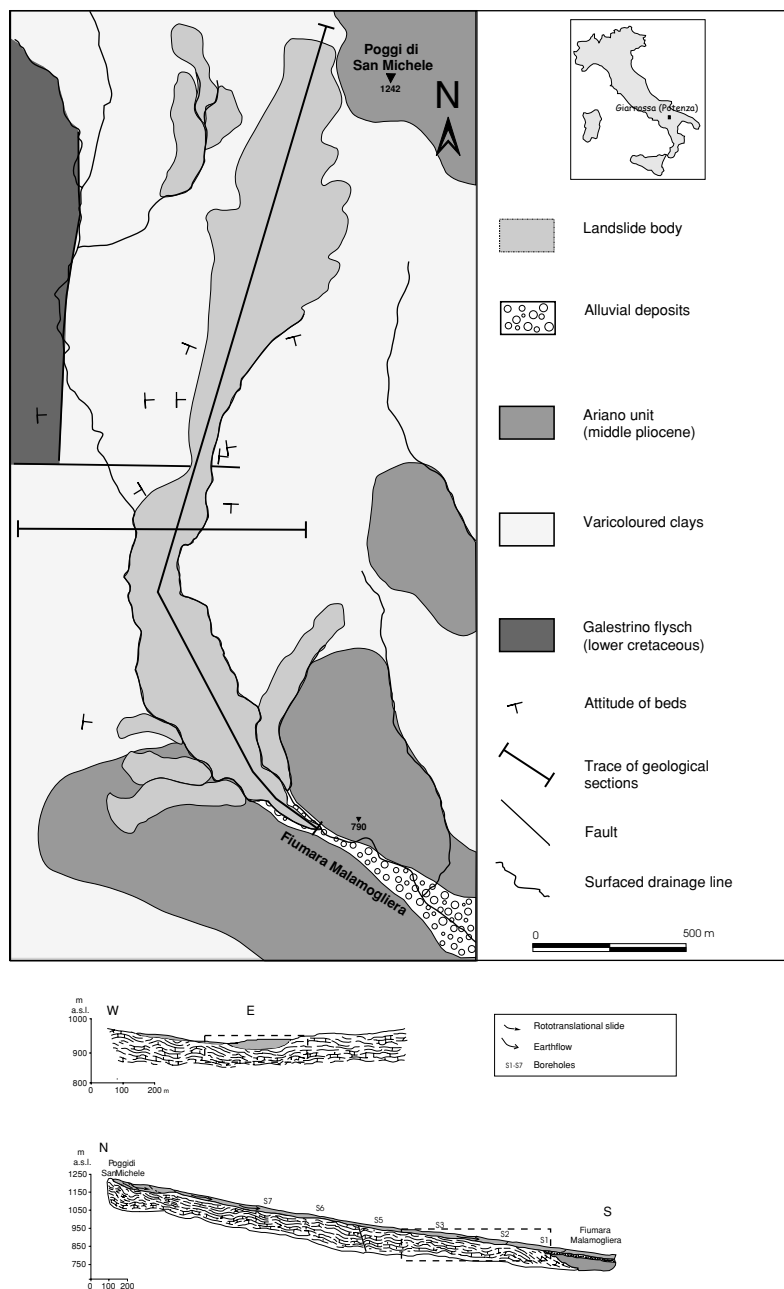


Figure 9. Geological map of the Giarossa area (Southern Italy) and (a) transversal and (b) parallel geological sections. Sliding surface is mapped on the basis of interpretation of the geological studies (from Gallipoli et al., 2000)

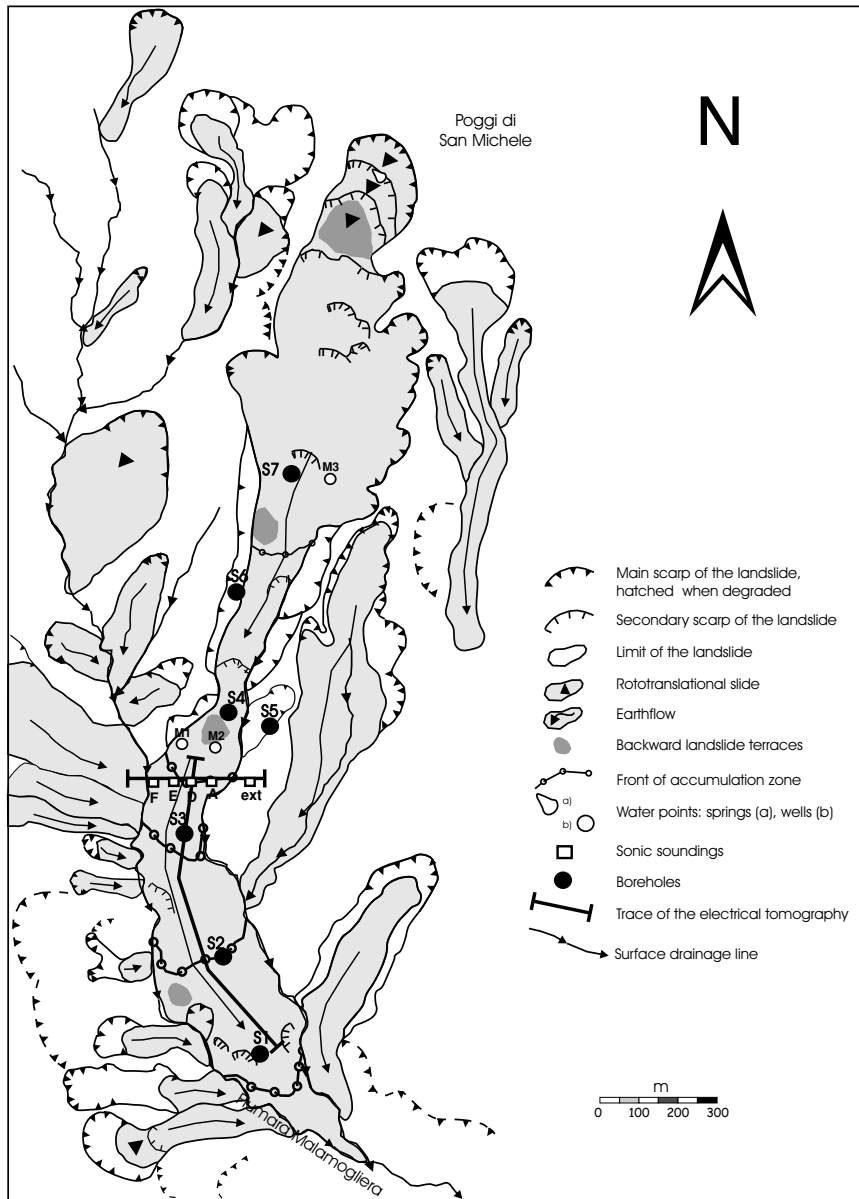


Figure 10. Geomorphologic map of the Giarossa landslide showing location of geological and geophysical surveys (from Gallipoli et al., 2000)

Figure 11 shows the two self-potential map surveys. Both self-potential maps show a wide electrical potential anomalies, predominantly negative in the source zone and positive in the accumulation zone, in part due to the so-called topographic effect often observed in mountainous areas (Sharma,

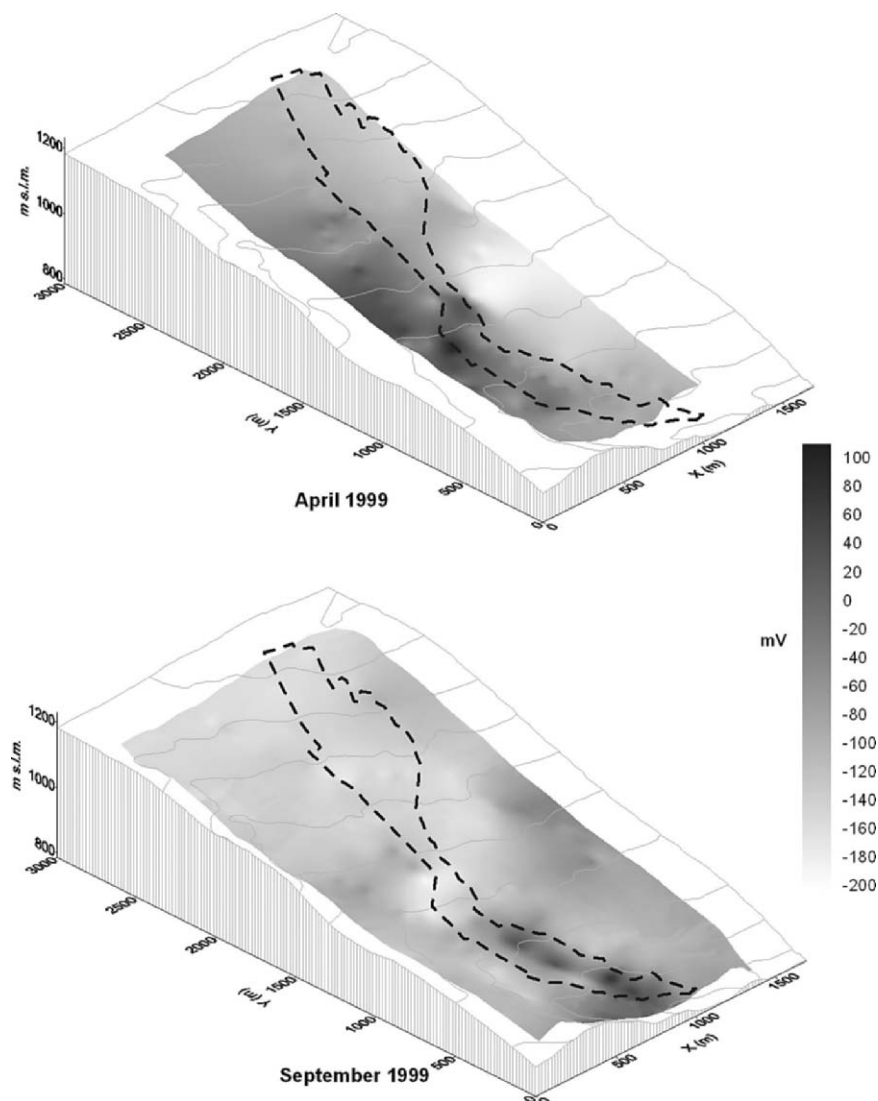


Figure 11. Maps of SP anomalies relative to the areal survey carried out in April 1999 (above) and September 1999 (below). The SP values change in a range from -200 to 100 mV and the dashed line represents contour of slide (from Lapenna et al., 2003)

1997). Moreover, strong self-potential horizontal gradients from negative to positive self-potential values are reduced and moved toward the toe of the landslide in the September map. According to the electrokinetic theory, these anomalies can be the result of the movement of ground water from the source zone to the accumulation zone within the landslide body. The reduction and

migration downwards of the positive self-potential area in the September map could reflect the lowering of the water level inside the landslide body after the dry summer period. In the source area a quite uniform negative electrical potential is present, indicative of weak groundwater movement, while in the accumulation area a clear separation is noted between the negative and positive self-potential. Moreover, strong self-potential horizontal changes from negative to positive self-potential values geometrically delimit the accumulation zone of the landslide. Such configuration could be associated with water infiltration from the surrounding in-situ terrain into the disturbed material, which, being reworked, has a lower density. The clear separation, indicative of the dynamics of the underground waters, suggests that the accumulation area is most at risk of remobilisation.

In Figure 12 a comparison is shown between the self-potential tomography, the ERT image and the geological section carried out along the profile CC' (see Figure 10). The ERT shows a weak resistivity contrast between a relatively high-resistivity zone ($>30 \Omega m$) and a relatively low-resistivity zone ($< 20 \Omega m$) in the central part at depth of about 25–30 m. The low resistivity zone has a lens shape, which is likely to be associated with a high clayey content and high saturated levels in the landslides, as observed in the boreholes. The deep relatively high resistive zone is considered to reflect the in-situ rock head which is not involved in the landslide. The shallow high-resistive nuclei may be associated with intercalations within the disturbed material. It is worth noting that the low-resistivity zone is limited on both sides of the landslide.

9.5.2. SELF-POTENTIAL SURVEY OF VARCO D'IZZO LANDSLIDE

The Varco d'Izzo landslide is located close to Potenza town (Southern Italy) and was one of the most dangerous mass movements of the whole Lucanian Apennine Chain. It is an active rototranslational slide, i.e., complex mass movement occurring dominantly on a partly planar and partly curved detachment, that evolved into an earthflow (Cruden and Varnes, 1996). The landslide is approximately 1400 m long, about 130–140 m wide and extends between 850 and 620 m (Basento river) and has a mean inclination of about 10° (Figure 13). In the area, the structurally complex clayey-marly terrains are referred to as the shale Varicolori (Upper Cretaceous-Lower Oligocene) outcrop. They are composed of intensively fractured shales and mudstones, which locally include disarranged blocks, and layers of lapideous rocks including marls, calacarenitic rocks, and limestones.

Geological and geomorphologic in situ surveys, aerial photo analyses and data interpretation from direct soundings allowed us to define the limits of the landslide body and to estimate the thickness of its displaced material for different sectors of landslide. In Figure 14 the main geomorphologic

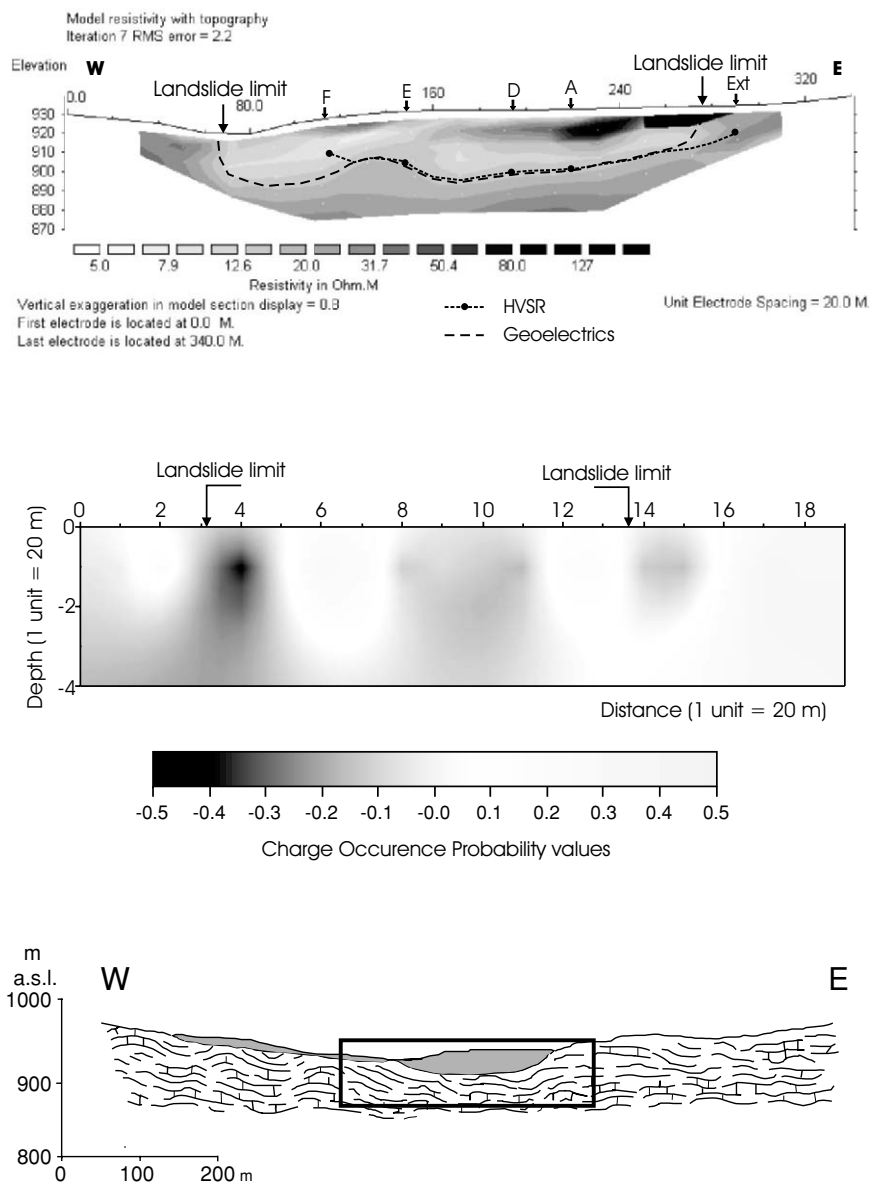


Figure 12. Comparison between electrical resistivity tomography (above), self-potential tomography (middle) and geological cross-section (below). The yellow dots shows the depths estimated with seismic methods (HVSR techniques) and the dashed lines the shape of the sliding surface reconstructed combined geophysical and geological data (from Lapenna et al., 2003)

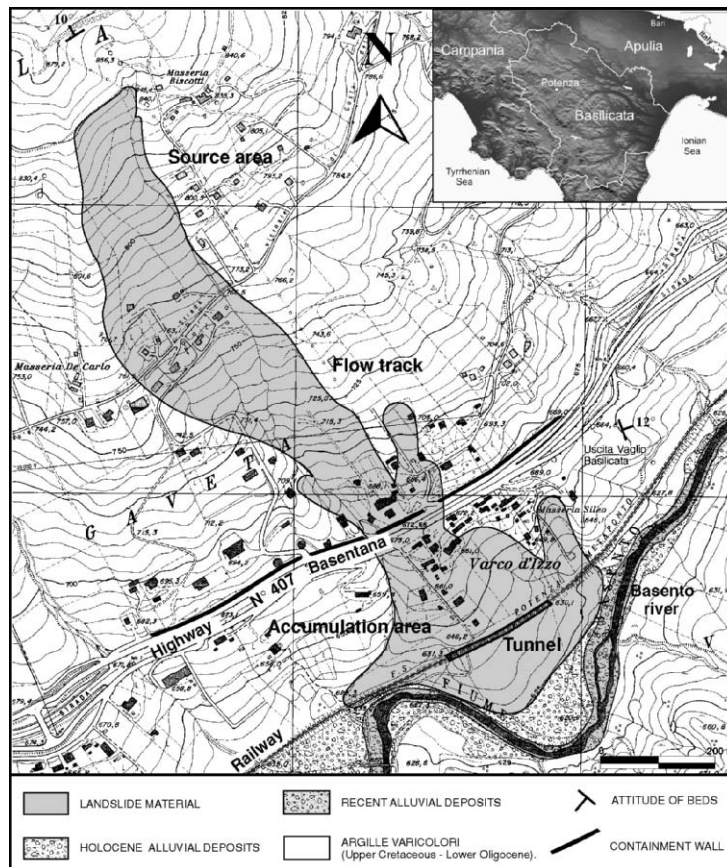


Figure 13. Location and geological map of the Varco d'Izzo landslide in the Basilicata region (Southern Apennine, Italy). The landslide develops entirely in the clayey material of the Varicolori Formation and, in the accumulation zone, it partly covers recent alluvial deposits (from Perrone et al., 2004)

features of the landslide, along with the location in which the geologic and geophysical surveys were carried out, have been summarised (Perrone et al., 2004; Lapenna et al., 2005).

The source area of the mass movement is a rototranslational slide showing an inclination mean of about 16° . It is approximately 300 m long, about 100–150 m wide and extends from 885 to 820 m a.s.l. The flow track of the landslide is approximately 700 m long and, on average, its inclination is 12° . The thickness of the sliding material varies from 15 to 25 m. The zone of accumulation is the widest part of the landslide (about 500 m) and is 350 m long. It shows an inclination of 8° . The toe material has diverted the Basento riverbed. The thickness of the displaced material, as shown by the borehole

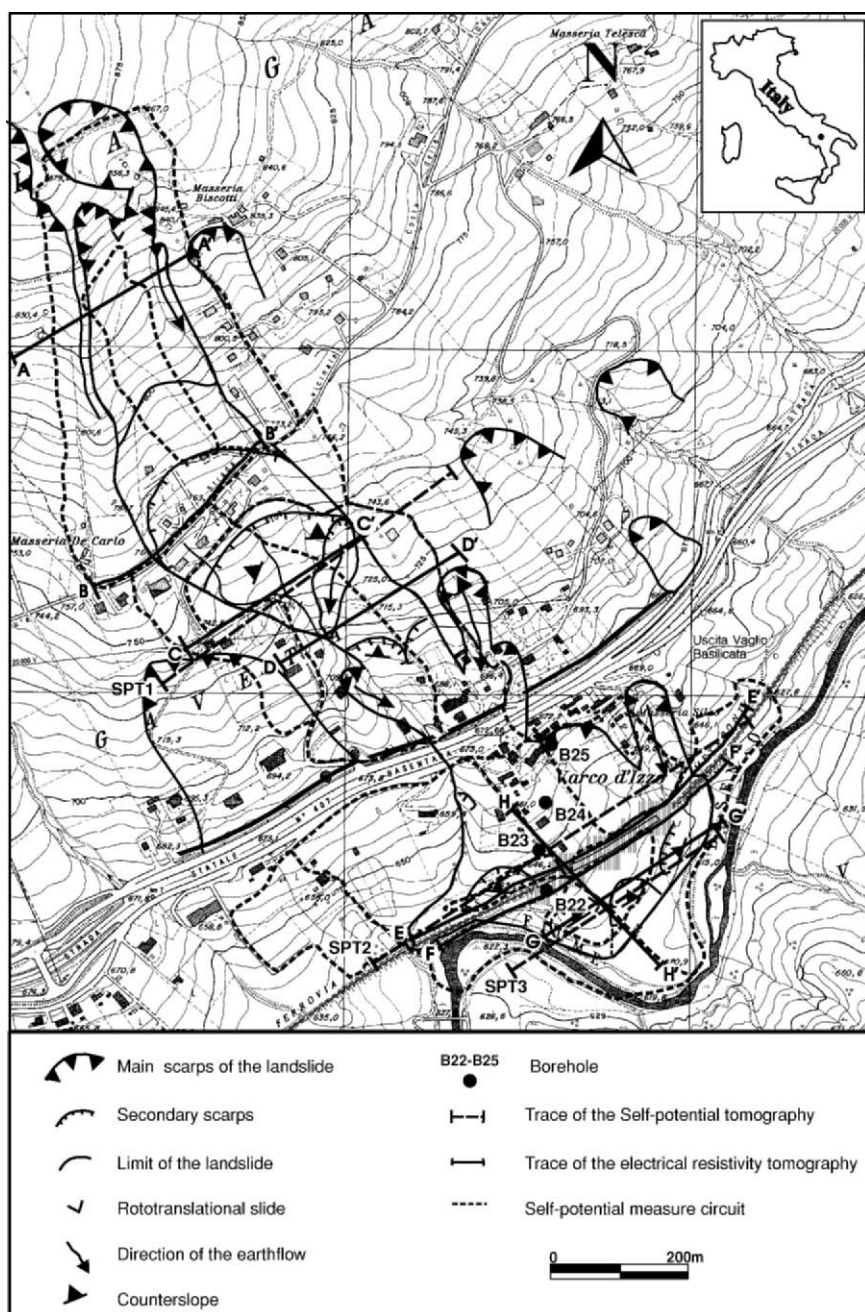


Figure 14. Geomorphologic map of the Varco d'Izzo landslide with location of the geological and geophysical surveys. SP mapping was carried out on the entire landslide body; seven electrical resistivity tomographies profiles were performed transversal to the landslide and only one longitudinal; self-potential profiles were carried out transversal to the landslide body (from Perrone et al., 2004)

data, varies from approximately 13 m in the upper zone to 32 m in the lower zone.

A preliminary inspection of the electrical resistivity images (Figure 15) allows us to identify small variability of electrical resistivity for values lower than $150 \Omega \text{ m}$. In particular, the very low resistivity values ($< 10 \Omega \text{ m}$) observed in the middle part of the resistivity tomograms could be associated to the landslide body which is characterised by a high content of clayey material and water. Geochemical and mineralogical analyses show that the Argille Varicolori formation is characterised by the presence of illite-smectite mixed layer clays showing a high cationic exchange capacity that could notably reduce the resistivity values to a limiting value as low as $0.1 \Omega \text{ m}$ (Keller and Frischknecht, 1966; Cavalcante et al., 2003). The relative high resistivity zones on the slides and at the bottom of the slide may indicate compact rocks not involved in the landslide, the estimated thickness varies from less than 10 m up to 40 m.

The self-potential map shows a spatial pattern characterised by slightly negative self-potential values in the source area, a positive zone in the flow track area and a strong self-potential negative zone in the accumulation area of the slide (Figure 16). The self-potential negative value in the source area are probably due to water infiltration in the detachment zone. The self-potential positive zone in the flow track may be due to the containment walls and drainage structures, built for the SS 407 Basentana road, that prevent groundwater from flowing into the accumulation area, which in turn produces an accumulation and excess of positive electrical charges. On the other hand, the self-potential negative sector in the accumulation zone, which seems to follow the slide outline perfectly, may be explained by a groundwater flow towards the Basento River having an excess of positive electrical charges.

9.5.3. FURTHER DEVELOPMENTS

The results of the geophysical surveys carried out for the study of two complex rototranslational landslides (Giarrossa and Varco d'Izzo) located in Southern Italy allow us to evaluate the abilities of the geoelectrical techniques. Electrical Resistivity Tomography can be considered as a suitable and powerful method for the geometrical reconstruction of the landslide bodies and the Self-potential techniques give significant results in describing the main pattern of the subsurface fluid flows. The high-resolution of the electrical resistivity tomograms is a key to illuminate sliding surfaces, separating layers characterised by a relatively low resistivity contrast in the presence of a complex hydrogeological environment. The integration of geoelectrical results with other geological, geomorphological and borehole data can be considered an

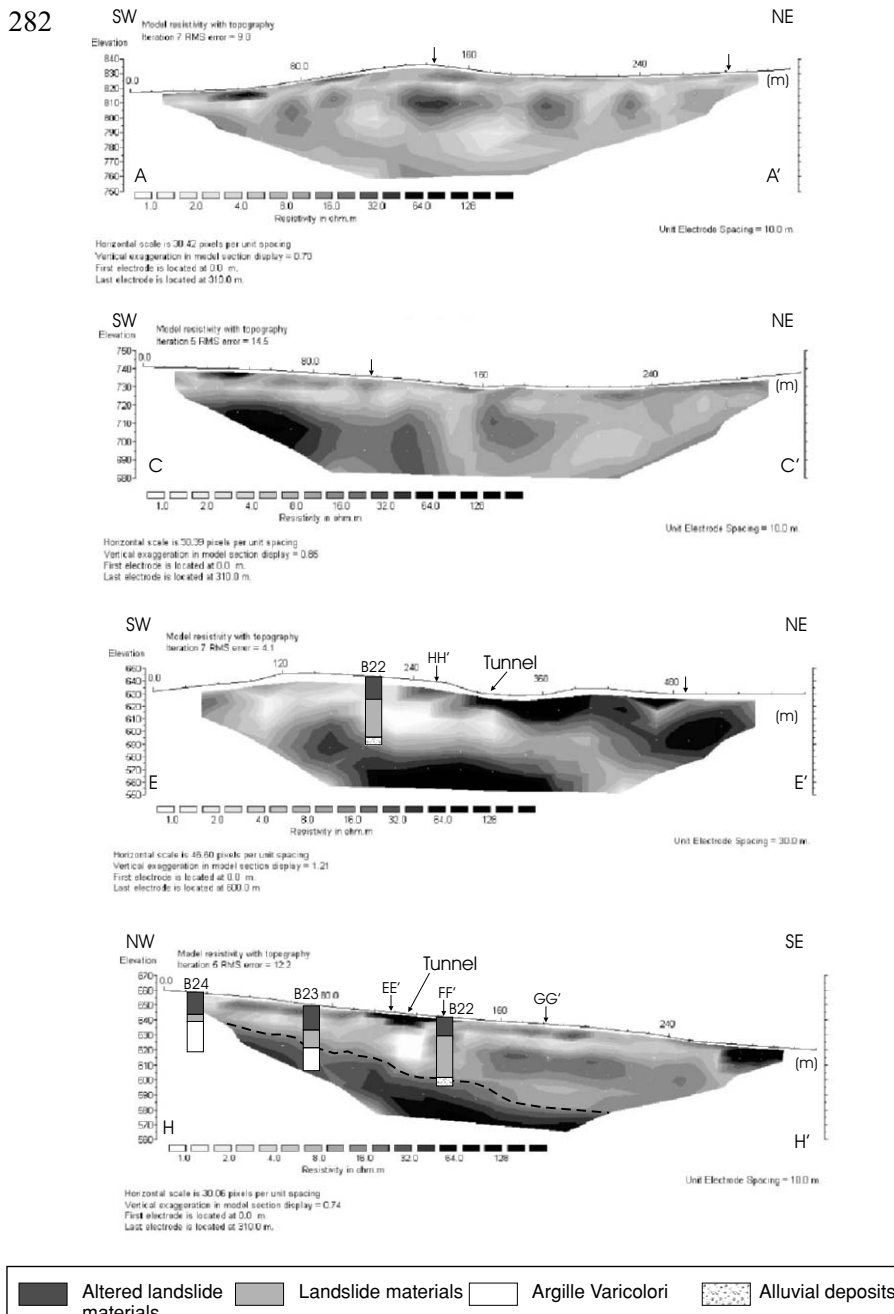


Figure 15. Dipole-dipole electrical resistivity tomographies carried out perpendicular (AA', CC' and EE') and parallel (HH') to the direction of the landslide body. We adopted the same colour palette for all the electrical sections. The red arrows indicate the lateral limits of the landslide as derived from geomorphological observations. The data coming from boreholes B22, B23 and B24 are also included. The dashed red line represents the interpreted sliding surface in the accumulation zone of the landslide body (from Perrone et al., 2004). The resistivity tomographies were obtained with the software RES2DINV by Loke and Barker (1996)

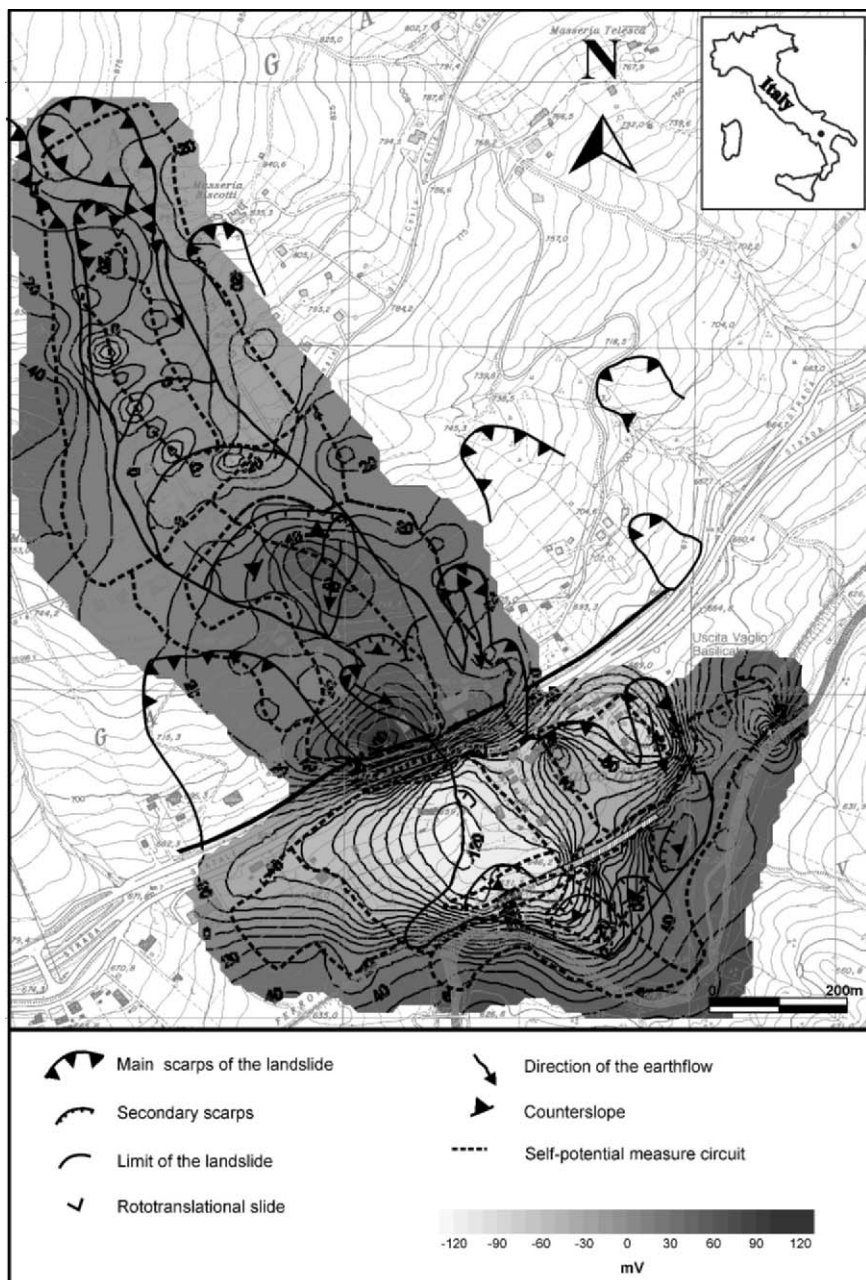


Figure 16. Map of the self-potential anomaly measured at the ground surface. Red zones are positive values, whereas blue zones are negative values (from Perrone et al., 2004)

optimal approach for the investigation of landslides in areas with complex geology.

In the near future, the development of monitoring system able to measure the time-dependent changes of the self-potential values along selected profiles will disclose the way for the time-lapse analysis of the self-potential images. These new technique could help us to better understand the time-dynamics of the geoelectrical parameters in connection with meteorological conditions and identify zones of likely instability due to a high water content. A prototype of this monitoring self-potential system has been installed in the accumulation zone of the Varco d'Izzo landslide (Colangelo et al., 2005). The measuring station is equipped with a multi-electrode system connected to electrical no-polarizable probes, a multimeter, a modem GPRS, a TDR (Time Domain Reflectometry) to estimate the soil moisture and a system to measure meteo-climatic parameters, as soil temperature, humidity and rain content. A GPRS modem allows the remote control of the station. Every 15 min the data are pre-processed, filtered and sent to the following web site www.seleta.it/cnr/self-potential/1slide.htm where it is possible to read the measurements of all the probes installed on the landslide body.

9.6. Applications to Contaminant Plumes

Despite the long history of the self-potential method, its application to the study of contaminant plumes has been very recent. Weigel (1989) has realized a monitoring of the self-potential signals with a network of 256 electrodes in the purpose to delineate a contaminant plume. He observed a correlation between the self-potential signals (approximately -40 mV) and the extent of the contaminant plume. The contamination comes from dissolved salts from a repository and the electrical potential is observed to be small in areas where the salinity is high.

Hämmann et al. (1997) have performed a self-potential survey in the vicinity of a landfill in Switzerland. Self-potential anomalies observed were associated with contaminant plumes with negative anomalies of -30 mV and positive anomalies of $+50$ mV to $+75$ mV for other type of wastes. Nyquist and Corry have observed a self-potential anomaly of -50 mV associated with the presence of an anaerobic contaminated domain in the soil. Self-potential anomalies have also been evidenced over hydrocarbon contaminated areas. For example Perry et al. (1996) and Vichabian et al. (1999) showed a correlation between negative self-potential signals and an hydrocarbon contaminant plume in the ground. Sauck et al. (1998) have obtained positive self-potential signals delinetaing an LNAPL (Light Non-Aqueous Phase Liquid) contaminant plume in the ground. Other examples include the works

by Buselli and Lu (2001), Nimmer and Osiensky (2002) and Béhaegel et al. (2004).

A contaminant plume in the ground is typically a thermodynamic system out of equilibrium. There are several sources of self-potential signals. They are (1) diffusion potentials associated with concentration gradients, (2) redox potentials associated with a gradient in the electroactivity of the electrons, and (3) streaming potential associated with ground water flow. Naudet et al. (2003, 2004) were the first to investigate the quantitative relationship between the self-potential signals and geochemical parameters prevailing in a contaminant plume.

The contaminant plume studied by Naudet et al. (2003) was associated with the landfill of Entressen located in Provence, in the South of France. This is the municipal landfill of the city of Marseille and the largest open-air landfill in Europe. The conclusions reached by Naudet et al. (2003, 2004) were the following (1) the self-potential method can be used to delineate a contaminant plume rich in organic matter, the strength of the anomalies can reach several hundreds of millivolts; (2) the contaminant plume behaves as a natural geobattery and the electrical signals are proportional to the variations of the redox potential; (3) the self-potential signals can be analyzed quantitatively with a minimum of in situ measurements of the redox potential to calibrate the linear relationship observed between the self-potential signals and the in situ redox potentials. Bacteria play likely a critical role in the process of the geobattery because they participate directly to the transfer of the electrons at the edge of the contaminant plumes where most of the bio-mass is located and where there are sharp variations in the gradient of the redox potential. Precipitation of metallic particles at the boundaries of the plume play a role similar to that described by ore bodies in the model of Sato and Mooney (1960). Timm and Möller (2001) have also proposed the existence of self-potentials anomalies associated with gradient of the redox potential in soils containing metallic sulfides.

9.7. Development of Tomographic Algorithms

The forward problem correspond to the computation of the self-potential at all points of the system under consideration. For that purpose it is necessary to account for (1) the various sources of current density corresponding to different mechanisms of polarization (e.g. streaming potential and redox potentials), and (2) the distribution of the electrical conductivity of the system. For streaming potentials, the hydroelectric problem can be partially decoupled because the influence of the electrical field upon the Darcy velocity (electroosmosis) is truly negligible in most cases (Sill, 1983). This implies that the

hydraulic problem can be solved first and its solution used to compute the sources of current and then the distribution of the electrical field.

The inverse problem consist in using the measured distribution of the electrical potential (e.g. measured at the ground surface and in boreholes) to find the geometry of the source body, i.e., the distribution of the source current density, which can in turn be used to characterize the thermodynamic state of the system and how far it is from thermodynamic equilibrium. For example in the case of the streaming potential, the source of current can be inverted to recover the shape of the water table or the distribution of the redox potential in contaminant plumes.

There are several possibilities to do self-potential tomography. A family of methods concerns the use of algorithms associated with self-potential spectral analysis in the Fourier domain or with the wavelet or intercorrelation functions (e.g., Gibert et Pessel 2001; Revil et al., 2001; Iuliano et al., 2002). The drawback of these methods is that they cannot distinguish between primary and secondary sources of electrical potential, which also means that one of the current challenge in the self-potential tomography in hydrogeophysics is how to include the information related to the electrical resistivity distribution in self-potential tomography.

Based on the preliminary works by Fournier (1989), Birch (1993, 1998), Revil et al. (2003) have investigated the self-potential signals associated with the piezometric surface of an unconfined aquifer as discussed above in Section 9.3. The principal limitation of these methods concerns the inclusion of electrical resistivity, induced polarization and self-potential data. A joint inversion of these data would be extremely useful with some additional constraints added by in situ measurements (redox potential, salinity, piezometric heads) in a set of boreholes. Recent progresses in the development of tomographic algorithms in medical imaging to locate the source of epilepsy and electro-physiological activity of the brain (e.g. Michel et al., 2004) could represent a breakthrough for self-potential tomography.

9.8. Concluding Statements

The self-potential method has a long history (over 150 years). However, quantitative analysis of this method is fairly recent. Self-potential signals have initially been considered using phenomenological relationships before the underlying physics was developed. A mechanistic theory of self-potential signals can be obtained from by volume-averaging local equations as shown recently by Pride (1994) and Revil et al. (2005). At the macroscopic scale, self-potential theory has been formulated in terms of integral relationships linking the source distribution with the self-potential signals recorded at a set

of electrodes (or magnetometers). Very recently, these integral relationships have been used to formulate the inverse problem to locate the source of these signals inside a geological structure. This is called self-potential tomography. In the quasi-static limit of the Maxwell equations, self-potential tomography can be performed with algorithms developed for electroencephalography due to the similarity between these two methods. These improvements imply a bright future for the self-potential method because of the high number of applications in hydrogeology that can be foreseen, its good signal-to-noise ratio, and a good understanding of the underlying physics.

References

Adler, P.M., J.F. Thovert, C. Jacquin, P. Morat, and J.L. Le Mouël, 1997. Electrical signals induced by the atmospheric pressure variations in unsaturated media. *Comptes Rendus De l'Académie Des Sciences Série II, Fascicule a, Sciences de la Terre et des Planètes*, Vol. 324, pp. 711–718.

Albouy, Y., S. Cabrera, C. Camerlynck, M. Dietrich, C. Doussan, N. Florsch, S. Garambois, S. Hautot, L. Jouniaux, E. Marmet, M. Menviell, H. Perroud, D. Rousset, L. Szarka, and P. Tarits, 2000. PNRH Géophysique – Hydrologie 99: Un premier compte rendu des expérimentations menées sur le site INRA d'Avignon, Colloque PNRH 2000, Toulouse, May 16–17, 19–143.

Atangana, J.Q.Y., B. Nyeck, D. Bitom, and H. Robain, 2003. Self-potential anomalies in the lateritic cover of the Nsimi watershed in southern Cameroon: Origin and influence of electrical and granulometric parameters. *J. Appl. Geophys.*, 54, 85–96.

Aubert, M., and Q.Y. Atangana, 1996. Self-potential method in hydrogeological exploration of volcanic areas. *Ground Water*, 34, 1010–1016.

Aubert, M., I.N. Dana, and A. Gourgaud, 2000. Internal structure of the Merapi summit from self-potential measurements. *J. Volcanol. Geotherm. Res.*, 100, 337–343.

Béhaegel, M., J.-C. Gourry, and J.-F. Girard, 2004. Geophysical measurements on an ancient coking plant contaminated by tar, GU 1st General Assembly, Nice, 25–30 April 2004, Poster HS17-1FR2P-0110 (session EGU04-A-01783).

Bigalke, J., and E.W. Grabner, 1997. The geobattery model: A contribution to large scale electrochemistry, *Electrochem. Acta*, 42, 3443–3452.

Birch, F.S., 1993. Testing Fournier's method for finding water table from self-potential, *Ground Water*, 31, 50–56.

Birch, F.S., 1998. Imaging the water table by filtering self-potential profiles, *Ground Water*, 36, 779–782.

Bogoslovsky, V.A., and A.A. Ogilvy, 1977. Geophysical methods in the investigations of landslides, *Geophysics*, 42, 562–571.

Bogoslovsky, V.A., and A.A. Ogilvy, 1973. Deformation of natural electric fields near drainage structures, *Geophys. Prospect.*, 21, 716–723.

Bruno, F., and F. Marillier, 2000. Test of high-resolution seismic reflection and other geophysical techniques on the Boup Landslide in the Swiss Alps, *Surv. Geophys.*, 21, 333–348.

Buselli, G., and K. Lu, 2001. Groundwater contamination monitoring with multichannel electrical and electromagnetic methods, *J. Appl. Geophys.*, 48, 11–23.

Butler, J.J., and X. Zhan, 2004. Hydraulic tests in highly permeable aquifers, *Water Resour. Res.*, 40, W12402, doi: 10.1029/2003WR002998.

Cavalcante, F., S. Fiore, G. Piccareta, and F. Tateo, 2003. Geochemical and mineralogical approaches to assessing provenance and deposition of shales: A case study. *Clay Miner.*, 38, 383–397.

Chène, G., C. Brunjail, N. Aouaissia-Abdallah, and G. Bastian, 1995. Détection de flux hydriques dans les géomatériaux par mesure de polarisation spontanée, in *Proceedings Journées détude sur les milieux poreux et transferts dans les structures du génie civil et de l'habitat, janvier 1995*, Société Française des Thermiciens, Vol. 1–9.

Colangelo, G., J. Heinicke, U. Koch, V. Lapenna, G. Martinelli, and L. Telesca, 2005. Results of gas flux records in the seismically active area of Val d'Agri (Southern Italy). *Annals Geophys.*, 48 (1), 55–63.

Corwin, R.F., 1990. The self-potential method for environmental and engineering applications, in *Geotechnical and environmental Geophysics*, vol.1: Reviews and tutorial, edited by S.H. Ward, Society of Exploration Geophysics, Tucson, pp. 127–145 .

Corwin, R.F., and D.B. Hoover, 1979. The self-potential method in geothermal exploration, *Geophysics*, 44 (2), 226–245.

Cruden, D.M., and D.J. Varnes, 1996. Landslide types and processes and mitigation, in *Landslides – investigation and mitigation*, edited by A.K. Turner and R.L. Schuster, Transportation Research Board, Spec. Rep. 247, National Academy of Sciences, Washington, DC, pp. 36–75.

Darnet, M., G. Marquis, and P. Sailhac, 2003. Estimating aquifer hydraulic properties from the inversion of surface streaming potential anomalies, *Geophys. Res. Lett.*, 30, 1679, doi: 10.1029/2003GL017631.

Darnet, M., and G. Marquis, 2004. Modelling streaming potential (SP) signals induced by water movement in the vadose zone, *J. Hydrol.*, 285, 114–124.

Doussan, C., L. Jouniaux, and J.L. Thony, 2002. Variations of self-potential and unsaturated water flow with time in sandy loam and clay loam soils. *J. Hydrol.*, 267, 173–185.

Ernstson, K., and U. Scherer, 1986. Self-potential variations with time and their relation to hydrogeological and meteorological parameters, *Geophysics*, 51, 1967–1977.

Fitterman, D.V., 1978. Electrokinetic and magnetic anomalies associated with dilatant regions in a layered earth, *J. Geophys. Res.*, 83, 5923–5932.

Fitterman, D.V., 1979. Calculations of self-potential anomalies near vertical contacts, *Geophysics*, 44, 195–205.

Fournier, C., 1989. Spontaneous potentials and resistivity surveys applied to hydrogeology in a volcanic area: Case history of the Chaîne des Puys (Puy-de-Dôme, France), *Geophys. Prospecting*, 37, 647–668.

Fox, R.W., 1830. On the electromagnetic properties of metalliferous veins in the mines of Cornwall, *Philosoph. Transact. Royal Soc.*, 130, 399.

Frischknecht, F.C., L. Muth, R. Grette, T. Buckley, and B. Kornegay, 1983. Geophysical methods for locating abandoned wells, U.S. Geol. Surv. Open-File Report 83-702.

Gallipoli, M., V. Lapenna, P. Lorenzo, M. Mucciarelli, A. Perrone, S. Piscitelli, and F. Sdao, 2000. Comparison of geological and geophysical prospecting techniques in the study of a landslide in Southern Italy. *Eur. J. Environ. Eng. Geophys.*, 4, 117–128.

Gex, P., 1980. Phénomènes d'électrofiltration liés à quelques sites de barrages, *Bull. Soc. Vaud Sci. Nat.*, 357 (75), 39–50.

Gibert, D., and M. Pessel, 2001. Identification of sources of potential fields with the continuous wavelet transform: Application to self-potential profiles, *Geophys. Res. Lett.*, 28, 1863–1866.

Gorelik, A.M., and I.P. Nesterenko, 1956. Metod potentsialov elektrofiltratsii pri opredelenii radiusa depressionnoi voronki v khode otkachki iz skvazhini. (Method of electro-filtration potential in the determination of radius of the depression cone during a pumping test from borehole, in russian), *Izvestia Akad. Nauk SSSR, Ser. Geofiz. (Solid Earth Physics)*, 11, 1361–1363.

Guichet, X., L. Jouniaux, and J.-P. Pozzi, 2003. Streaming potential of a sand column in partial saturation conditions, *J. Geophys. Res.*, 108, 2141, doi: 10.1029/2001JB001517.

Hack, R., *Geophysics for slope stability*, 2000. *Surv. Geophys.*, 21, 423–448.

Hämmann, M., H.R. Maurer, A.G. Green, and H. Horstmeyer, 1997. Self-potential image reconstruction: Capabilities and limitations, *J. Environ. Eng. Geophys.*, 2, 21–35.

Hauk, O., A. Keil, T. Elbert, and M.M. Müller, 2002. Comparison of data transformation procedures to enhance topographical accuracy in time-series analysis of the human EEG, *J. Neurosci. Methods*, 113, 111–122.

Hutchinson, D.J., R. Harrap, M. Diederichs, M. Villeneuve, and N. Kjelland, 2003. Geotechnical rule development for ground instability assessment using intelligent GIS and networked monitoring sensors. 3rd Canadian Conference on Geotechnique and Natural Hazards. Edmonton, Alberta, Canada, June 9 and 10.

Iuliano, T., P. Maudiello, and D. Patella, 2002. Looking inside Mount Vesuvius by potential fields integrated probability tomographies, *J. Volcanology Geothermal Res.*, 113, 363–378.

Keller, G.V., and F.C. Frischknect, 1966. Electrical methods in Geophysical Prospecting, Pergamon, Oxford, p. 517.

Lachassagne, P., and M. Aubert, 1989. Etude des phénomènes de polarisation spontanée (PS) enregistrées dans un sol lors de transferts hydriques verticaux, *Hydrogéologie*, 1, 7–17.

Lapenna, V., P. Lorenzo, A. Perrone, S. Piscitelli, E. Rizzo, and F. Sdao, 2003. High-resolution geoelectrical tomographies in the study of the Giarrossa landslide (Potenza, Basilicata). *Bull. Eng. Geol. Environ.*, 62, 259–268.

Lapenna, V., P. Lorenzo, A. Perrone, S. Piscitelli, E. Rizzo, and F. Sdao, 2005. 2D electrical resistivity imaging of some complex landslides in the Lucanian Apennine chain, Southern Italy, *Geophysics*, 70 (3), B11–B18.

Loke, M.H., and R.D. Barker, 1996. Rapid least-squares inversion of apparent resistivity pseudosections by a quasi-Newton method. *Geophys. Prospect.*, 44, 131–152.

Mauritsch, H.J., W. Seiberl, R. Arndt, A. Romer, K. Schneiderbauer, and G.P. Sendlhofer, 2000. Geophysical investigations of large landslides in the Carnic region of southern Austria. *Eng. Geol.*, 56, 373–388.

McCann, D.M., and A. Forster, 1990. Reconnaissance geophysical methods in landslide investigations, *Eng. Geol.*, 29, 59–78.

Moore, J.R., S.D. Glaser, H.F. Morrison, and G.M. Hoversten, 2004. The streaming potential of liquid carbon dioxide in Berea sandstone, *Geophys. Res. Lett.*, 31, L17610, doi: 10.1029/2004GL020774.

Moore J.R., and S.D. Glaser, 2004. Laboratory observation of an advancing boiling front in a porous medium and correlation to self-potential measurements, in *Proceedings 29th Workshop on Geothermal reservoir engineering*, Stanford University, Stanford, CA, January 26–28.

Morat P., and J.M. Le Mouël, 1992. Signaux électriques engendrés par des variations de contrainte dans des roches poreuses non saturées, *Compt. Rend. Acad. Sci. Sér.*, 2, 315, 955–963.

Morat P., J.L. Le Mouël, and A. Granier, 1994. Electrical Potential on a Tree – a Measurement of the Sap Flow, *Compt. Rend. Acad. Sci. Sér. III – Sci. Vie, Life Sci.*, 317, 98–101.

Morgan, F.D., E.R. Williams, and T.R. Madden, 1989. Streaming potentials properties of Westerly granite with applications, *J. Geophys. Res.*, 94, 12449–12461.

Murashko, A.M., B.K. Khasenevich, and P.I. Firsuk, 1981. Vremennie recomendatsii po premeneniu geofisicheskikh metodov pri iziskaniyakh dlia meliorativnogo stroitel'stva v usloviakh BSSR. (Recommendations for use of geophysical methods for investigations for amending construction in BSSR, in Russian), Belnii MVH, Minsk, p. 51.

Naudet, V., A. Revil, E. Rizzo, J.-Y. Bottero, and P. Bégassat, 2004. Groundwater redox conditions and conductivity in a contaminant plume from geoelectrical investigations, *Hydrol. Earth Syst. Sci.*, 8 (1), 8–22.

Naudet, V., A. Revil, J.-Y. Bottero, and P. Bégassat, 2003. Relationship between self-potential (SP) signals and redox conditions in contaminated groundwater, *Geophys. Res. Lett.*, 30 (21), 2091, doi: 10.1029/2003GL018096.

Nimmer R.E., and J.L. Osiensky, 2002. Direct current and self-potential monitoring of an evolving plume in partially saturated fractured rock. *J. Hydrol.*, 267, 258–272.

Patella, D., 1997a. Introduction to ground surface self-potential tomography. *Geophys. Prospect.*, 45, 653–681.

Patella, D., 1997b. Self-potential global tomography including topographic effects, *Geophys. Prospect.*, 45, 843–863.

Perrier, F., and P. Morat, 2000. Characterization of electrical daily variations induced by capillary flow in the non-saturated zone. *Pure Appl. Geophys.*, 157, 785–810.

Perrier, F., and S.R. Pant, 2005. Noise reduction in long-term self-potential monitoring with travelling electrode referencing. *Pure Appl. Geophys.*, 162, 165–179.

Perrier, F.E., G. Petiau, G. Clerc, V. Bogorodsky, E. Erkul, L. Jouniaux, D. Lesmes, J. Macnae, J.M. Meunier, D. Morgan, D. Nascimento, G. Oettinger, G. Schwarz, H. Toh, M.J. Valiant, K. Vozoff, and O. Yazici-Cakin, 1997. A one-year systematic study of electrodes for long period measurements of the electric field in geophysical environments. *J. Geomagn. Geoelectr.*, 49, 1677–1696.

Perrone, A., A. Iannuzzi, V. Lapenna, P. Lorenzo, S. Piscitelli, E. Rizzo, and F. Sdao, 2004. High-resolution electrical imaging of the Varco d'Izzo earthflow (Southern Italy). *J. Appl. Geophys.*, 56 (1), 17–29.

Perry, J.W., C.H. Corry, and T. Madden, 1996. Monitoring leakage from underground storage tanks (UST) using spontaneous polarization method, SEG (extended abstract).

Pisarenko, D., P. Morat, and J.-L. Le Mouel, 1996. On a possible mechanism of sandstone alteration: Evidence from electric potential measurements, *Comptes-Rendus De L'Académie Des Sciences Série II Fascicule a-Sciences De La Terre et des Planètes*, Vol. 322, pp. 17–24.

Poldini, E., 1938. Geophysical exploration by spontaneous polarization methods, *Mining Mag.*, London, 59, 278–282, 347–352.

Polemio, M., and F. Sdao, 1998. Heavy rainfalls and extensive landslides occurred in Basilicata, southern Italy, in 1976, in *Proc. 8th Int. Cong. EEGS*, Vancouver, Canada, pp. 1849–1855.

Pride, S.R., 1994. Governing equations for the coupled electromagnetics and acoustics of porous media, *Phys. Rev. B*, 50, 15678–15696.

Revil, A., P. Leroy, and K. Titov, 2005. Characterization of transport properties of argillaceous sediments. Application to the Callovo-Oxfordian Argillite, *J. Geophys. Res.*, 110, B06202, doi: 10.1029/2004JB003442.

Revil A., and A. Cerepi, 2004. Streaming potential in two-phase flow condition, *Geophys. Res. Lett.*, 31(11), L11605, doi:1029/2004GL020140.

Revil, A., and P. Leroy, 2001. Hydroelectric coupling in a clayey material, *Geophys. Res. Lett.*, 28 (8), 1643–1646.

Revil, A., and P. Leroy, 2004. Governing equations for ionic transport in porous shales, *J. Geophys. Res.*, 109, B03208, doi : 10.1029/2003JB002755.

Revil, A., V. Naudet, and J.D. Meunier, 2004. The hydroelectric problem of porous rocks: Inversion of the water table from self-potential data, *Geophys. J. Int.*, 159, 435–444.

Revil, A., V. Naudet, J. Nouzaret, and M. Pessel, 2003. Principles of electrography applied to self-potential electrokinetic sources and hydrogeological applications, *Water Resour. Res.*, 39 (5), 1114, doi: 10.1029/2001WR000916.

Revil, A., D. Hermite, M. Voltz, R. Moussa, J.-G. Lacas, G. Bourrié, and F. Trolard, 2002. Self-potential signals associated with variations of the hydraulic head during an infiltration experiment, *Geophys. Res. Lett.*, 29 (7), 1106, doi: 10.1029/2001GL014294.

Revil, A., P.A. Pezard, and P.W.J. Glower, 1999. Streaming potential in porous media: 1. Theory of the zeta potential. *J. Geophys. Res.*, 104, 20021–20031.

Revil, A., H. Schwaeger, L.M. Cathles, and P.D. Manhardt, 1999. Streaming potential in porous media 2. Theory and application to geothermal systems, *J. Geophys. Res.*, 104, 20033–20048.

Rizzo, E., B. Suski, A. Revil, S. Straface, and S. Troisi, 2004. Self-potential signals associated with pumping-test experiments, *J. Geophys. Res.*, 109, B10203, doi: 10.1029/2004JB003049.

Sailhac, P., M. Darnet, and G. Marquis, 2004. Electrical streaming potential measured at the ground surface: Forward modelling and inversion issues for monitoring infiltration and characterizing the vadose zone, *Vadose Zone J.*, 3, 1200–1206.

Sato, M., and H.M. Mooney, 1960. The electrochemical mechanism of sulfide self-potentials, *Geophysics*, 25 (1), 226–249.

Schmutz, M., Y. Albouy, R. Guerin, O. Maquaire, J. Vassal, J.J. Schott, and M. Descloitres, 2000. Joint electrical and Time domain electromagnetism (TdEM) data inversion applied to the Super Sauze earthflow (France), *Surv. Geophys.*, 21, 371–390.

Schlumberger, C., M. Schlumberger, and E.G. Leonardon, 1934. A new contribution to subsurface studies by means of electrical measurements in drill holes, *Trans. AIME*, 110.

Sekihara, K. et al., 1997. Noise covariance incorporated MEG-MUSIC algorithm: A method for multiple-dipole estimation tolerant of the influence of background brain activity, *IEEE Trans. Biomed. Eng.*, 44, 839–849.

Semenov, A.S., 1980. Elektrorazvedka metodom estestvennogo elektricheskogo polia (Electrical prosel-potential ecting with the natural electric field method, 2nd edn., In Russian), Nedra, Leningrad, p. 445.

Sen, P.N., 1991. Correspondence between membrane potential and conductivity, *Geophysics*, 56 (4), 461–471.

Sharma, P. S., 1997. Environmental and Engineering Geophysics, Cambridge University Press, Cambridge, MA.

Sill, W., 1983. Self-potential modeling from primary flows, *Geophysics*, 48, 76–86.

Sprunt, E.S., T.B. Mercer, and N.F. Djabarrah, 1994. Streaming potential from multiphase flow. *Geophysics*, 59, 707–711.

Steeple, D.W., 2001. Engineering and environmental geophysics at the millennium, *Geophysics*, 66, 31–35.

Stoll, J., J. Bigalke, and E.W. Grabner, 1995. Electrochemical modelling of self-potential anomalies, *Sur. Geophys.*, 16, 107–120.

Thony, J.L., P. Morat, G. Vachaud, and J.L. Le Mouél, 1997. Field characterization of the relationship between electrical potential gradients and soil water flux. *Comptes Rendus De L'Académie Des Sciences Série II, Fascicule a, Sciences de la Terre et des Planètes*, Vol. 325, pp. 317–321.

Timm, F., and P. Möller, 2001. The relation between electric and redox potential: An evidence from laboratory to field experiments, *J. Geochem. Explor.*, 72, 115–127.

Titov, K., A. Revil, P. Konasovsky, S. Straface, and S. Troisi, 2005. Numerical modeling of self-potential signals associated with a pumping test experiment, *Geophys. J. Int.*, 162, 641–650.

Titov, K., Y. Ilyin, P. Konosavski, and A. Levitski, 2002. Electrokinetic self-potential spontaneous polarization in porous media: petrophysics and numerical modelling, *J. Hydrol.*, 267, 207–216.

Vachaud, G., C. Dancette, M. Sonko, and J.L. Thony, 1978. Méthodes de caractérisation hydrodynamique in situ d'un sol non-saturé. Application à deux types de sols du Sénégal en vue de la détermination du bilan hydrique. *Ann. Agron.*, 29, 1–36.

Vichabian, Y., and F.D. Morgan, 2002. Self potentials in cave detection, *The Leading Edge*, September, pp. 866–871.

Vichabian, Y., P. Reppert, and F.D. Morgan, 1999. Self-Potential Mapping of Contaminants. In *Proceedings of the symposium on the application of Geophysics to Engineering and Environmental Problems*, pp. 14–18.

Weigel, M., 1989. Self-potential surveys on waste dumps, in *Theory and Practice in Detection of subsurface Flow Phenomena*, Lecture Notes in Earth Sciences, vol. 27, G.-P. Merkler et al. (Eds.), *Detection of Subsurface Flow Phenomena*, Springer, Heidelberg, Germany, pp. 109–120.

Xu, X.L., B. Xu, and B. He, 2003. An alternative subspace approach to EEG dipole source localization, *Phys. Med. Biol.*, 49, 327–343.

10. ENGINEERED BARRIERS FOR POLLUTANT CONTAINMENT AND REMEDIATION

Lee Slater and Andrew Binley

10.1. Introduction

10.1.1. GENERAL CONCEPTS

Engineered barriers for pollutant containment and remediation present unique opportunities and challenges for geophysical investigation. Three fundamental issues pertain to all engineered barriers placed in the subsurface: (1) is the structure located in the ground according to the engineer design specifications? (2) does the barrier effectively perform its intended function? (3) how does design performance degrade over time? Issues 2 and 3 also pertain to engineered barriers placed on the ground surface.

The objectives of this chapter are to (1) identify the engineered barriers for pollutant containment and remediation that are amenable to geophysical investigation (2) define the geophysical properties of such structures (3) discuss their unique geometry and implications for geophysical imaging, and (4) review the geophysical research so far performed to characterize the geometry and performance of such structures. This review reveals that geophysical technologies have to date seen limited use in investigations of engineered barriers for pollutant containment and remediation. However, given the increasing use of barriers in the containment and treatment of contaminants, novel applications of geophysical methods are anticipated.

10.1.2. TYPES OF ENGINEERED BARRIERS

Engineered barriers for pollutant containment and remediation can be separated into containment structures and flow-through structures. A containment structure is designed to contain and limit spreading of a substance. Surface pollutant containment structures include *storage tanks*, primarily used to store chemicals. Subsurface pollutant containment structures are used to contain chemical wastes and contaminants. They can be divided into *walls* and *floors* as well as *caps*, used to isolate the subsurface from chemical and fluid input from above. Flow-through structures are designed to redirect flow of groundwater through an artificial media for treatment and ultimate remediation. The most common flow through treatment structure is

the *permeable reactive barrier (PRB)* that is used to remediate contaminated groundwater.

The investigation of engineered barriers for pollutant containment and remediation in the ground is complicated as it is essential not to damage the structure. Containment structures punctured by invasive probing methods will leak; invasive probing of flow through structures will generate flow bypass pathways. Geophysical methods may play an important role by non-invasively providing information on the physical and chemical state of such engineered barriers.

Applications of geophysical technologies to the study of engineered barriers for pollutant containment and remediation fall within the following categories (1) verification that design specifications are met during installation (2) characterization of variation in the physical properties of the barrier, (3) monitoring of liquids (leaks) through containment barriers, and (4) evaluation/monitoring of geochemical processes occurring in flow through reactive barriers. Geophysical methods can also assist in the characterization of a site prior to installation of a barrier. The focus of this chapter is novel applications of geophysics to the investigation of engineered pollutant containment and remediation barriers that have developed over the last ten years in response to demands to better manage contaminated land. Consequently, geophysical studies of dams used to contain water flow (see for example, Bogoslovsky and Ogilvy, 1970, 1972) are excluded from this chapter. Furthermore, as geophysical site characterization of native soils is well described in numerous texts, the pre-installation characterization issues (where geophysical methods may play an important role) are not covered here.

10.2. Geophysical Investigation of Engineered Structures

10.2.1. GEOPHYSICAL PROPERTIES OF ENGINEERED STRUCTURES

The ability of geophysical methods to characterize and/or monitor an engineered barrier depends on the contrast in geophysical properties between the barrier and native geology. Geophysical characterization of engineered barriers is facilitated by the fact that the construction material will likely display strong geophysical contrasts with native soil. Barriers designed to contain fluids are constructed of impermeable material such as electrically conductive grouts or electrically resistive man-made fibers. Leaks through barriers tend to generate distinct electrical anomalies due to the channeling of water, solute and electrical current through a small area at the leak location. Permeable reactive barriers are composed of reactive media not typically found in significant concentrations in native soils. Zero valent iron is the most common

PRB material. The addition of a large amount of iron to the subsurface will profoundly modify the electrical and magnetic properties of the earth.

10.2.2. IMAGING OF ENGINEERED STRUCTURES

Surface geophysical measurements tend to lack the image resolution required to determine barrier features at a spatial scale of interest (an exception is in the investigation of caps discussed in Section 10.3.4). Cross-borehole or bore-hole to surface tomographic imaging methods are instead required to obtain the image resolution needed to determine useful information on the structure and performance of engineered barriers. In addition to visualization and characterization of the engineered structure itself, engineered barriers provide other interesting imaging opportunities. Firstly, it may be possible to image variation in the internal composition, or the flow of material escaping from, a containment structure. Here time-lapse geophysical imaging may indirectly yield valuable information on the presence and location of flaws in engineered structures due to the loss of volume of the contained fluid. Such geophysical investigation of engineered structures is also included here.

Engineered structures also generate unique boundaries in the subsurface. First, the geometry of the barrier is determined by the design specifications and is therefore theoretically known *if one assumes that the design specifications are met in construction*. Second, man-made barriers are typically characterized by very sharp boundaries between the native geology and the emplaced material. These issues pose challenges for the incorporation of *a priori* information in the imaging of engineered structures. One challenge is whether to specify the geometry of the barrier in the inversion. Accurate incorporation of this *a priori* information might improve efforts to image variation in the internal composition of a barrier material or a process occurring in the barrier. However, what if the installation procedure did not faithfully match the design specifications? In this case, incorrect *a priori* information could easily lead to artifacts in the images. If the objective of a geophysical investigation is to verify the installation then perhaps no *a priori* information should be used to constrain the inversion.

It is common practice in geophysical imaging to add a roughness penalty to the objective function of the inverse algorithm (de Groot-Hedlin and Constable, 1990). This constitutes inclusion of *a priori* information whereby it is most typically assumed that the subsurface is characterized by smooth contrasts in physical properties. This smoothness criterion is inappropriate for imaging the exterior structure/geometry of barriers. In this case, an inversion algorithm that produces sharp (rough) contrasts may be more appropriate (de Groot-Hedlin and Constable, 2004). However, imaging of variations in the internal composition of a barrier material might require specification of both

TABLE 1. Leakage rates (in $1 \text{ ha}^{-1} \text{ day}^{-1}$) through a 1 mm HDPE geomembrane (after Giroud and Bonaparte, 1989)

Flow Path	Water depth above geomembrane (m)				
	0.003	0.03	0.3	3	30
Permeation	0.0001	0.01	1	100	300
Pinhole	0.01	0.1	1	10	100
Small hole	100	300	1000	3000	10000
Large hole	3000	10000	30000	100000	300000

sharp (to define the edge of barrier) and smooth (to describe changes in the interior of the barrier) contrasts. This presents a challenging inversion problem not addressed in the published literature to date.

10.3. Containment Structures

10.3.1. GEOMEMBRANE LANDFILL LINERS AND CAPS

In most modern landfills synthetic liners are used to protect the waste from leaking out and entering the environment. In addition, once the landfill is complete, caps are often placed above the landfill to minimize infiltration into the system. These man-made liners and caps, often made from high density polyethylene (HDPE) geomembranes, will degrade eventually with time and naturally are prone to damage throughout the working life of the waste facility. Consequently, it is essential that techniques are available to determine the quality of the barrier once emplaced and periodically assess the integrity of the barrier and locate possible leaks. Giroud and Bonaparte (1989) estimate leakage rates through common defects in a typical landfill liner, as shown in Table 1. The potential for high mass flux of contaminants into aquifers is clearly significant and reliable methods are required to assess damage to liners during the working life of a landfill and also post-closure.

Geomembrane leak location methods have been established based on injecting electrical current through the liner into the surrounding soil and then, using pairs of electrodes above the liner, high potential gradients, associated with current leakage, may be identified. The methods are based on the original work conducted at Southwest Research Institute, USA. Para (1988) and Para and Owen (1988) discuss some of the original concepts of this approach. Figure 1a illustrates the principles behind this method. An electrical current is passed through the leak in the liner (or cap) and the voltage difference across a roving pair of electrodes is measured along transects. Figure 1b shows the typical signal associated with a leak. Mobile systems are now used routinely for

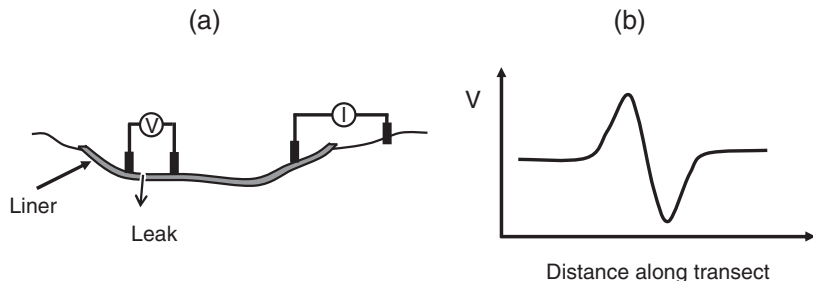


Figure 1. (a) Schematic of electrical leak detection approach. (b) Typical dipole voltage response of leak

quality assurance testing following liner installation (see for example, Laine, 1991). In some cases double liners are installed for added protection. The electrical leak detection approach may still be applied to assess damage to the upper liner by inserting the grounded electrode between the two layers rather than outside the facility. This is easily achieved as such double liner systems are constructed with access ports to monitor fluids between the two liners.

Mobile electrical leak location methods rely on good electrical contact of the voltage electrodes. This is achieved, prior to addition of waste, by conducting the survey on the thin layer of sand (or similar material) placed on top of the liner for protection. These mobile methods have also been used during the active life of landfill systems by conducting surveys on top of the waste (for example, Laine et al., 1997; Colucci et al., 1999). However, the method has limited sensitivity when applied over significant thicknesses of waste and this has led to the development of under-liner systems, installed prior to liner placement. These have the added advantage of more continuous monitoring without the reliance of high labor effort needed for mobile surveys. Permanent under-liner electrode arrays have been installed at a number of landfill sites to allow long term monitoring of leakage. Frangos (1992, 1997) documented one of the earliest demonstrations of such an approach. Others have reported similar studies, for example, Nosko (1996) and White and Barker (1997). These systems are generally based on a square grid of point electrodes, typically several meters apart, installed just below the liner. Voltage differences may be measured across different combinations of pairs of electrodes whilst injecting current between an electrode placed within the landfill and one outside. For geomembrane cap integrity monitoring, the electrode array may be placed above the cap. Figure 2 shows the results of a grid survey carried out over part of an active waste site documented in Laine et al. (1997). In this study an array of electrodes was installed on the surface of the waste. Current was injected between an electrode placed between the geomembranes of the double liner and a 'return electrode' on the surface (away from the measurement grid).

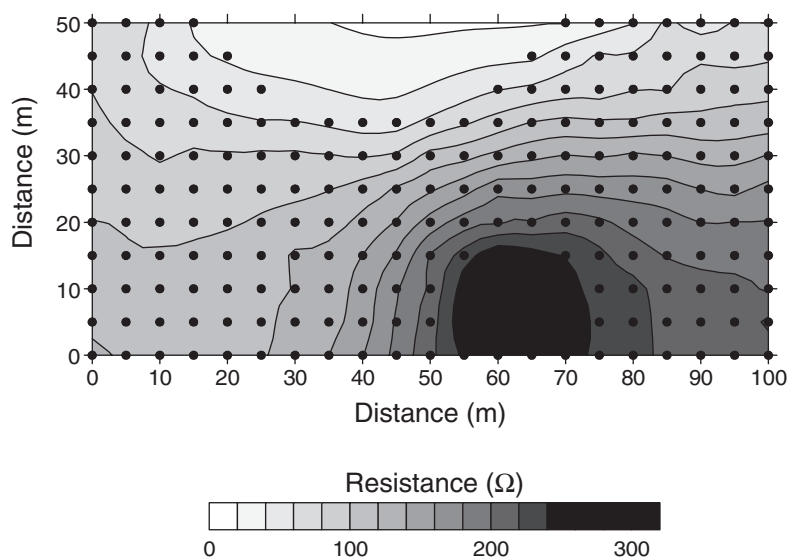


Figure 2. Results of leak location survey carried out on the surface of an active industrial waste landfill after Laine et al. (1997). The symbols show the location of the grid of electrodes. Results are expressed in terms of resistance (difference in voltage between each electrode and a fixed remote electrode relative to electrical current injected through the liner). High resistances are associated with electrical leakage through the liner. The map shows clearly the location of a single leak, confirmed later by excavation in the waste

Voltages were then measured on a 5 m by 5 m grid of electrodes relative to a remote reference electrode. The results show clearly the resistance anomaly associated with electrical leakage through the liner. This was later confirmed by excavation in the waste. Note that the geophysical signal associated with the leak is dispersed over a large area – this is caused by the significant thickness of waste at the site (in this case approximately 3 m).

As in the case of mobile systems, electrical isolation of the barrier is needed. Edges of the liner must be modified, where appropriate, to ensure no lateral electrical current leakage. This may be particularly problematic during the life of the landfill as access routes for disposal will be in place. Materials used for electrodes and connecting wires must be suitable to ensure no deterioration due to overburden pressure and, more importantly, the harsh chemical environment caused by landfill leachate. As a result, permanent electrode arrays are not an inexpensive option in landfill construction.

The permanent approach can be expensive to implement and is clearly not applicable in existing sites, where retrofitting is not an option. A tomographic variant of traditional, permanently installed electrical leak location methods was first proposed by Binley et al. (1997). In this approach electrical potentials are collected around the perimeter of the site, either inside or outside of the landfill (see Figure 3), and then, with suitable inverse methods, the locations

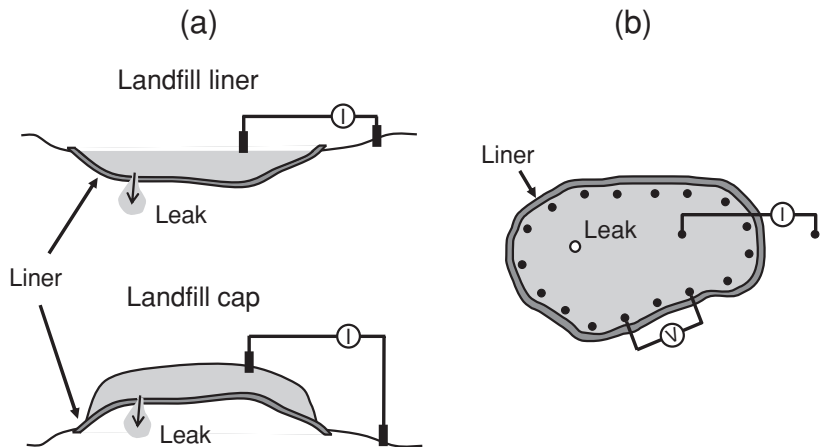


Figure 3. Schematic of electrical leak detection approach using perimeter electrodes for liner or cap integrity assessment, after Binley et al. (1997). (a) Vertical section. (b) Plan view

of leaks in the geomembrane are computed that best satisfy the measured data. Binley et al. (1997) and Binley et al. (1999) demonstrate application of the approach to a number of field sites.

Commissioned by the UK Environment Agency, Bishop (2002) compiled an extensive review of electrical leak location methods for testing geomembranes. From this report it is clear that little is understood about the reliability of permanent monitoring systems. Several applications have used single test leaks to demonstrate success without assessing how multiple leaks in the system may degrade the overall performance. The effect of leakage of current through boundaries and the impact of subsoil heterogeneity on the performance of leak location systems have also been neglected in these applications. More alarming perhaps is that no attempt appears to be made in any industrial systems to assess the uncertainty in leak location. Binley and Daily (2004) recently attempted to address these issues by examining laboratory models of liner and cap systems with grid and perimeter based measurements. Their results indicate that the identification of single leaks is relatively straightforward, however, the ability to distinguish multiple leaks with grid or perimeter based arrays, particularly in heterogeneous subsurface environments, is non-trivial and further investigation into the reliability of these methods is required.

10.3.2. WASTE TANKS AND STORAGE PONDS

Many stored wastes have a high electrical conductivity relative to native soil water and thus resistivity imaging has been used in a number of studies to reveal leakage from surface and subsurface tanks and ponds. These methods rely on assessing temporal changes in the subsurface resistivity to monitor

contaminant plumes and therefore rely on measurements collected prior to any leakage in order to make a reliable assessment of changes in the subsurface.

Van et al. (1992) illustrate how conventional resistivity measurements may be effectively used to monitor changes in the subsurface due to leakage from a 55 acre evaporation pond in Nevada, USA. In this case study the pond overlies a relatively high resistive vadose zone, thus enhancing the contrast of the plume arising from leakage from the pond. Ramirez et al. (1996) discuss the use of cross-borehole electrical imaging to detect changes in resistivity beneath a 15 m diameter mock steel underground storage tank in Hanford, Washington, USA. The US Department of Energy has over 300 underground storage tanks, within sites such as Hanford, storing a total of nearly 400,000 m³ of high-level waste (Ramirez et al., 1996). Monitoring of these tanks is usually performed through liquid level detectors and, externally, by borehole monitoring. These methods are limited in their sensitivity and are unable to locate exactly where the leak (or leaks) exist. In addition, the tank waste is often a mixture of solid and liquid material, making quantification of leaks from liquid level detection unreliable.

In 1994 the US Department of Energy funded a series of experiments on a mock tank at the Hanford site in order to evaluate the potential of various geophysical methods for detection of leaks from the tank. The scaled tank was buried in the ground and instrumented with pipework to allow controlled leaks of non-hazardous tracers from specific locations under the tank base. Ramirez et al. (1996) show the results from electrical imaging using electrodes installed in boreholes surrounding the tank. The results demonstrate the effectiveness of this method, despite the close proximity of the electrically conductive tank shell, for detecting leak volumes of several cubic meters. However, the leak tracer used was highly conductive (0.3 S/m) and thus the bulk resistivity contrast in the subsurface was high (note, however, that this tracer was much less saline than the liquids stored in the operational tanks).

The experiment of Ramirez et al. (1996) benefited from the use of background (prior to leak) measurements. Under operational conditions such background conditions will be affected by previous leakage from the tank and possibly from neighboring tanks. In 2002 a more realistic experimental program was carried out at the Hanford mock tank site, as described in Daily et al. (2004a). In this experiment 54 m³ of brine was released from the tank over a 110 day period. A series of 13 releases of different rates and from different locations was made over this period. Daily and colleagues collected electrical imaging data each day, using electrode arrays installed in boreholes surrounding the tank. Autonomous data collection minimized labor overheads. Datasets were processed daily, without any knowledge of the leak status and inferred conditions reported (leak or no leak). Figure 4 shows an example 3-D image of change in resistivity (over a 24 hour period) beneath the tank due to leakage of

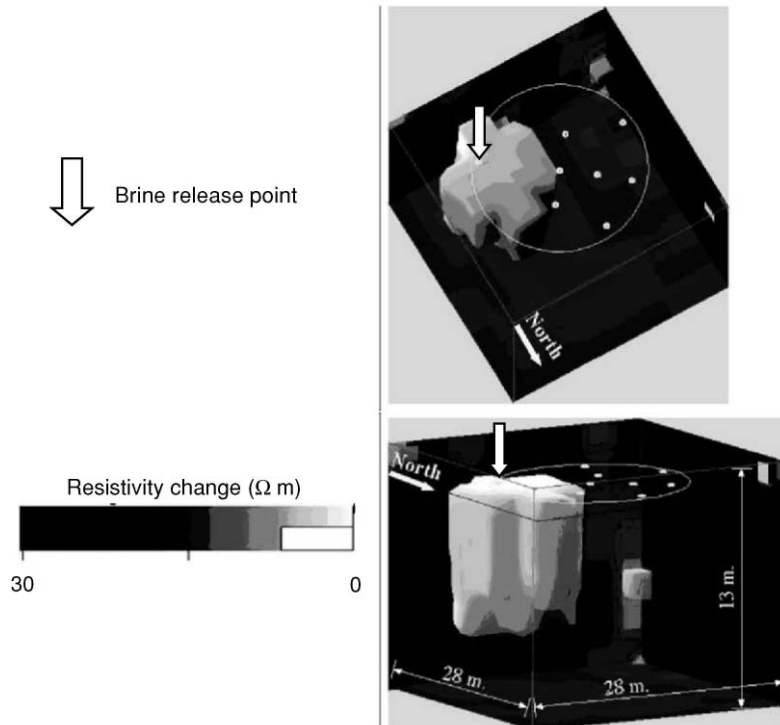


Figure 4. Images showing changes in resistivity on one day during 2002 leak monitoring experiment at Hanford, USA. The upper image is a top view and the lower image a side view with the tank footprint and fluid release points superimposed. The isosurface defines the volume where the resistivity changed by more than 10 Ohm m. Modified from Daily et al. (2004b)

brine. The experiment of Daily et al. (2004a) was thus a real (and rare) trial of geophysical applications to engineered barriers. The 'blind' test successfully estimated the leak status 57% of the time, although Daily et al. (2004a) show additional post-processing steps that increase this performance.

10.3.3. CONTAINMENT BARRIERS

Containment barriers are designed to prevent or slow the movement of groundwater and isolate contaminants. Vertical barriers are constructed of impermeable material such as grouts or man-made fibers. The floor of the barrier may be a low permeability geologic layer or a constructed wall. The location of the barrier, its thickness and integrity are all design specifications that may or may not be achieved during the installation procedure. Performance evaluation focuses on the location of leaks due to construction flaws (short term assessment) or the degradation in the integrity of the barrier

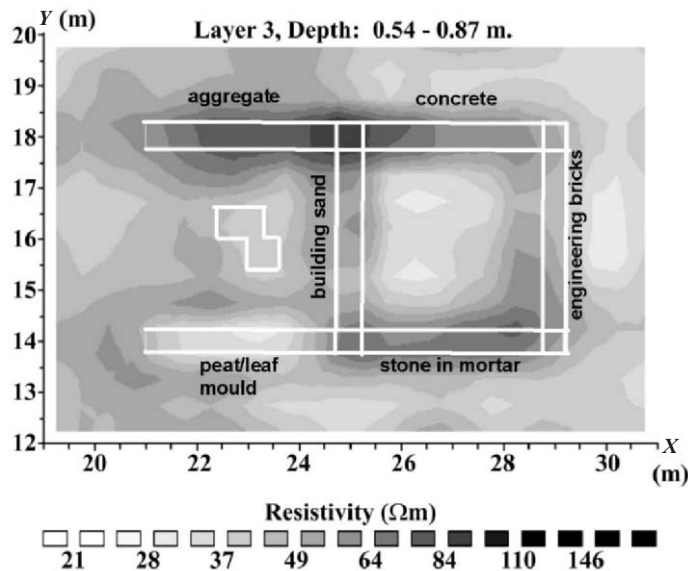


Figure 5. Resistivity image of seven wall materials buried between 0.4–1.0 m depth. Image shows the result for 0.61–0.87 m depth obtained from 3D modeling/inversion. The white frame outlines the walls (modified from Chambers et al., 2002)

resulting in leaks (long term assessment). The desired lifespan of such containment barriers is typically thirty years (Majer, 2006).

Few geophysical investigations of vertical barriers are reported in the published literature. Chambers et al. (2002) describe 3D surface electrical imaging of numerous wall materials (concrete, engineering bricks, stone/mortar, aggregates, building sand and a peat/leaf mould) emplaced at a test site. Although these materials do not constitute containment barriers, their results showed that the geometry of 0.4 m high vertical walls buried at 0.6 m depth could be well resolved using a large number of four electrode measurements (Figure 5). The investigation of vertical barriers below 1 m depth with surface electrical methods is of limited practical value due to the poor resolution away from the surface-placed electrodes.

Daily and Ramirez (2000) describe cross-borehole electrical resistivity imaging experiments during installations of two prototypes of engineered barriers: (1) a thin-wall vertical grout barrier and (2) a thick-wall viscous polymer barrier composed of colloidal silica. Ground penetrating radar tomography and zero-offset profiling was also performed on the thin thin-wall barrier (Pellerin et al., 1998). Electrical measurements were obtained before and immediately after installation of these barriers. The conductivity contrast due to the installation of the viscous polymer barrier was high enough that this structure could be directly imaged with resistivity measurements; in contrast,

the thin-wall grout barrier was only resolved by imaging the difference in resistivity resulting from the barrier emplacement. Daily and Ramirez (2000) successfully imaged conductive anomalies that they interpreted in terms of the spatial extent of the barrier material resulting from the injection procedure.

The thin-wall barrier was formed from a grout-bentonite mix that was injected into the formation from a lance as it was withdrawn from the subsurface. The procedure was repeated to produce a series of overlapping panels that penetrated a clay aquitard, forming the floor. Figure 6a shows a plan view

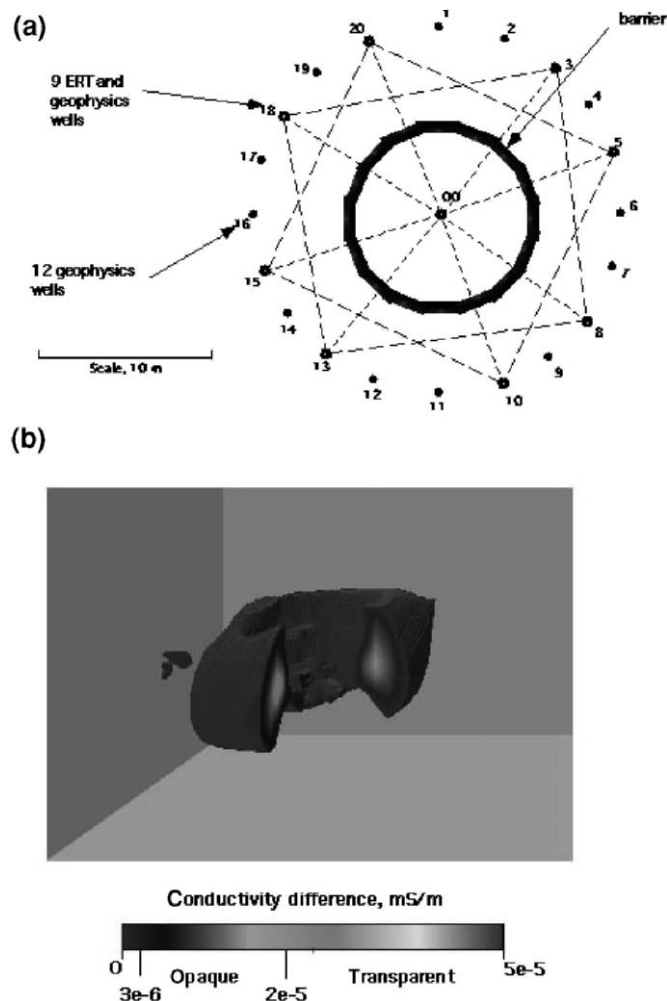


Figure 6. (a) Plan view of the prototype thin wall barrier showing location of nine electrode arrays used for electrical imaging. Dashed lines indicate electrode pairs used to collect ERT data. (b) 3D image of this barrier after the removal of artifacts associated with the electrode arrays. A quadrant is removed to show the containment zone inside the barrier (modified from Daily and Ramirez, 2000)

of the geometry of the barrier and nine resistivity imaging wells whereas Figure 6b shows the 3D image of this barrier obtained by the authors. The authors state the image resolution was about 1 m so details and flaws smaller than this are not resolved. This barrier was also resolvable from GPR attenuation tomograms (Pellerin et al., 1998).

Daily and Ramirez (2000) also conducted a resistivity imaging experiment to investigate the containment performance of the prototype thin-wall grout barrier investigated in their study. They monitored the changes in electrical resistivity associated with the release of saltwater that they injected into the containment region. This experiment is similar to the leak detection methods described in Section 10.3.2. Post-experiment excavation of this barrier showed that the changes in electrical resistivity coincided with small defects in the barrier that could not be directly resolved from imaging the barrier itself. Unfortunately, such an experiment would not be appropriate on an active barrier as it would induce contaminant spreading (Daily and Ramirez, 2000).

10.3.4. CAPS

Caps are surface engineered barriers designed to limit recharge and bio-intrusion of buried wastes. Geomembrane caps were discussed in Section 10.3.1 as they are identical in construction to landfill liners. Here we consider caps constructed of natural materials that share more common characteristics with containment barriers (Section 10.3.3). Although they may form a critical component of long-term management of buried wastes, application of such surface barrier technology remains largely unproven at the field scale (Ward and Gee, 1997). Being at the ground surface, caps are readily accessible to high-resolution, surface-based geophysical methods. Geophysical measurements may be capable of detecting flaws that occur in construction. However, the primary issues with caps relate to post-installation performance. Increases in porosity and permeability as a result of the development of post-construction cracks will jeopardize performance. Geophysical methods may be able to directly detect such features. Alternatively, monitoring of the fluxes of moisture through the cap that develop with reduced cap performance might be performed with geophysical methods.

Monitoring of caps may be best achieved through long-term, spatially continuous measurements of near-surface moisture conditions over a range of spatial scales (Majer, 2006). Caps are generally larger structures than containment barriers, necessitating rapid, non intrusive data acquisition techniques that do not impair the integrity of the surface of the cap. Surface ground penetrating radar and electromagnetic methods are often used to evaluate moisture content in the vadose zone (see for example, Sheets and Hendrickx, 1995; Huisman et al., 2003). Majer (2006) suggests that variations in moisture

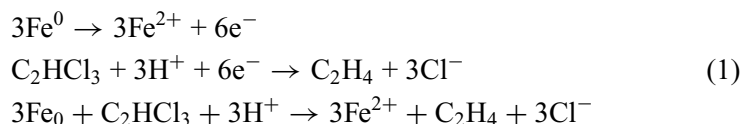
content within a cap will exert the primary control on electrical conductivity as variations in the pore water conductivity and cap texture are small.

Ward and Gee (2001) describe geophysical measurements on a prototype cap constructed at the US Department of Energy's Hanford site. The prototype barrier is a vegetated capillary barrier containing eight layers of natural materials with a total thickness of 4.4 m. This test barrier was instrumented with a drainage monitoring system and access holes for moisture content measurements using neutron probe, capacitance probe and time domain reflectometry techniques. Surface terrain conductivity (EM31 and EM38) and GPR measurements were recorded over a ten-month period in 2001. Interpretation of the terrain conductivity measurements was limited by the relatively small size of the dataset although the authors did conclude that the methods show potential for rapid monitoring of moisture content changes in caps. GPR surface wave velocities were converted to moisture content estimates and showed good correlation with neutron probe data. The variation in moisture content across the barrier was not sufficiently validated with control data to reach firm conclusions on the value of the method. Ward and Gee (2001) concluded that monitoring of moisture content in caps will improve if site-specific or cap material-specific relationships between geophysical properties (dielectric permittivity, electrical conductivity) and moisture content are identified.

10.4. Permeable Reactive Barriers

10.4.1. BACKGROUND

The permeable reactive barrier is an engineered structure designed to remediate contaminated groundwater flowing through it. The reactive material of the barrier participates in a redox reaction with the contaminant, resulting in the conversion of the contaminant into inorganic, non-toxic compounds. The reactive iron (Fe^0) barrier is the most established PRB technology for the *in situ* remediation of chlorinated solvents, as well as heavy metals (Gilham and O'Hannessin, 1994). As an example, degradation of trichloroethylene (TCE) by Fe^0 is generally assumed to result in ethene and chloride as the primary end products (Gavaskar et al., 1998),



Over forty Fe^0 barriers are currently operative in the United States. Concern exists regarding long-term (decade scale) performance reduction as a result of oxidation and precipitation at the zero valent iron (Fe^0) surface

(Gavaskar et al., 1998), as well as clogging of the pore space (Mackenzie et al., 1999). In addition, there is evidence that many PRBs installed at sites across North America failed to meet design performance criteria. Technologies are therefore needed to (a) non-invasively image and verify that Fe^0 barriers meet the design specifications, and (b) monitor and provide warning of performance reduction, permitting remedial measures and minimizing increased contaminant concentrations at locations down-gradient from the barrier.

10.4.2. LABORATORY STUDIES

Granular reactive iron has very distinct geophysical properties. Electronic conduction in iron results in high electrical conductivity relative to near surface geological formations. The electrical conductivity of iron is $1 \times 10^7 \text{ S/m}$ (Carmichael, 1989) whereas that of near surface earth materials is typically less than 1 S/m . Iron also has very high magnetic susceptibility. Endres et al. (2000) investigated the electrical and magnetic properties of granular reactive iron mixed with sand. Laboratory measurements, reproduced in Figure 7, illustrate the dependence of electrical conductivity and magnetic susceptibility on the volume of granular iron. Note that the conductivity of the 100%

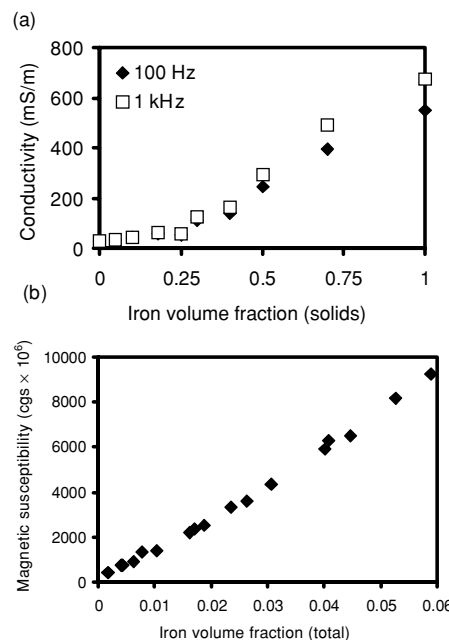


Figure 7. (a) Electrical conductivity of sand-granulated iron mixtures with varying iron content of solids. Mixtures were saturated with 0.01 M KCl solution. (b) Magnetic susceptibility of iron mixtures as a function of total volumetric content (reproduced from Endres et al., 2000)

granular iron sample is much less than the electrical conductivity of iron as electronic conduction in a highly porous granular medium compared to a pure iron rod, for example, is relatively small. Electrode polarization at the iron-fluid interface also makes the PRB an induced polarization target (Slater et al., 2005). Finally, iron has seismic properties distinctly different to most near surface earth materials. The acoustic velocity in iron is 5900 m/s (McIntire, 1991) whereas it is typically less than 2500 m/s in near surface unconsolidated sediments.

Slater et al. (2005) conducted laboratory measurements on samples of zero valent iron mixed with Ottawa sand to investigate the sensitivity of resistivity and induced polarization measurements to the volume of Fe^0 , surface area of Fe^0 and electrolyte chemistry. Figure 8 shows the dependence of conduction

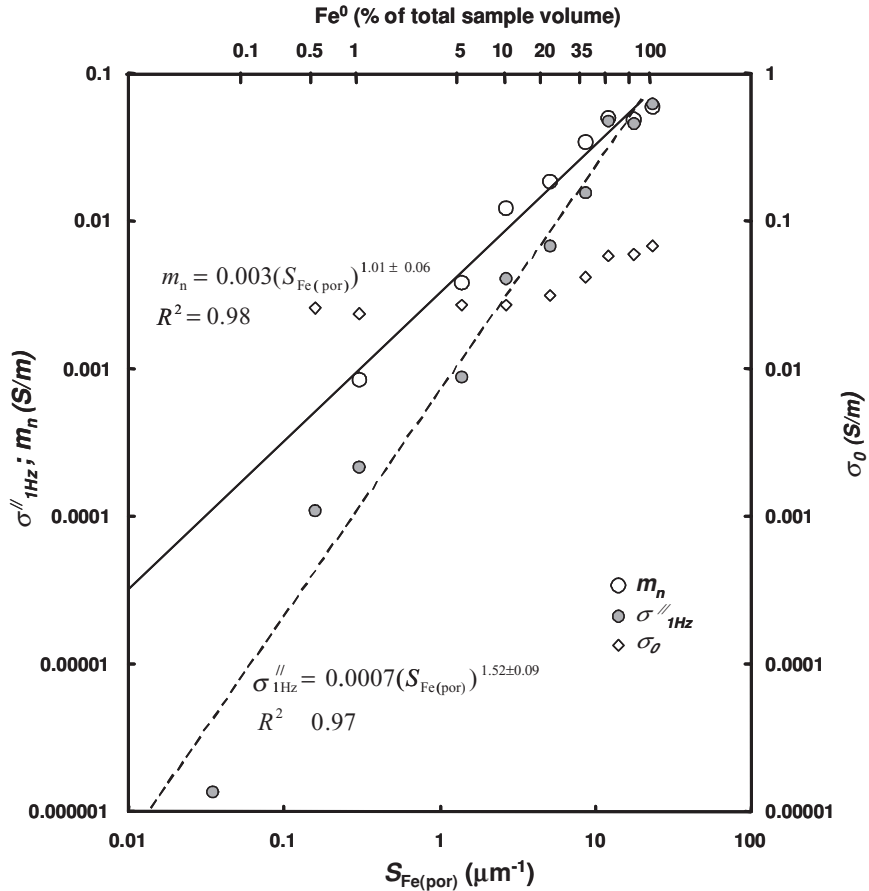


Figure 8. Dependence of polarization (m_n , σ'' at 1 Hz) and conduction (σ_0) parameters on the surface area of reactive Fe^0 per unit pore volume ($S_{\text{Fe}(\text{por})}$) and percentage Fe^0 concentration for Ottawa sand- Fe^0 mixtures (modified from Slater et al., 2005)

and polarization parameters on the surface area of Fe^0 to pore volume ratio ($S_{\text{Fe(por)}}$) and Fe^0 percentage concentration for homogenized Ottawa sand- Fe^0 mixtures. Two induced polarization parameters are shown; the normalized chargeability (m_n) is a global estimate of the polarization obtained from frequency dependent electrical measurements between 0.1 and 1000 Hz whereas the imaginary conductivity is the polarization at 1 Hz. Both polarization parameters show a very strong (linear correlation coefficient $R_2 > 0.96$), power law dependence on $S_{\text{Fe(por)}}$ whereas the conductivity is insensitive to the Fe^0 concentration below 20% Fe^0 by volume. The conductivity increases with Fe^0 concentration above 20% Fe^0 by volume when electronic conduction becomes significant in the sample, consistent with the study of Endres et al. (2000) shown in Figure 7. The surface area of reactive material is a critical design parameter determining the performance of a PRB. These results therefore suggest that induced polarization is a promising technology for evaluating the performance of reactive Fe^0 in a PRB.

Slater et al. (2005) also considered the sensitivity of electrical measurements to precipitation reactions occurring on the reactive metal surface. Figure 9 shows the changes in the spectral electrical response (in terms of phase angle) induced by forced precipitation of iron hydroxides and iron carbonates onto the Fe^0 surface. Their results show an increase in the magnitude of the

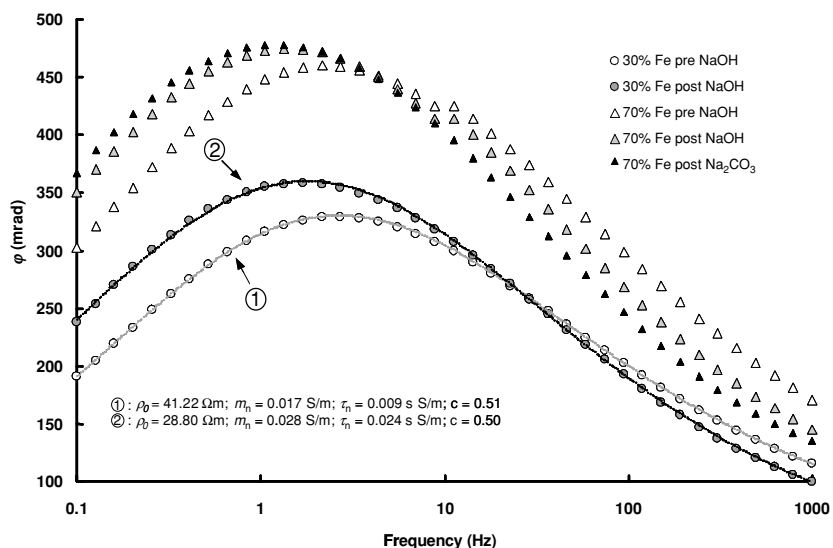


Figure 9. Change in electrical measurements (0.1–1000 Hz) in response to precipitation of iron hydroxides and iron carbonates onto the Fe^0 surface. Results are shown for a 30% and 70% by volume Fe^0 -Ottawa sand sample (from Slater et al., 2005)

polarization and the time constant characterizing the polarization peak. They interpreted this response as a result of an increase in iron mineral-fluid surface area and grain size due to the formation of iron hydroxides and iron carbonates. Although these results demonstrate that the effects of precipitation are discernible from induced polarization measurements, the experiments were not representative of field conditions. Analysis of aging PRBs shows that precipitation and clogging primarily occurs along a thin section of the structure on the inflow face (Phillips et al., 2000). This indicates that any electrical response to precipitation/clogging occurring in currently active PRBs is likely to be localized and small.

10.4.3. FIELD STUDIES

Joesten et al. (2001) conducted cross-hole GPR imaging of pilot-scale testing of a hydraulic fracture method of PRB installation in unconsolidated sediments at depth. They also conducted numerical modeling of cross-hole radar pulses to assist interpretation of the barrier structure from the radar data. Design specifications called for installation of two iron walls 5 m apart, 12 m long and at a depth of 24–37 m. Application of GPR was based on the large reduction in transmitted wave amplitude associated with emplacement of conductive iron. Cross-hole radar amplitude measurements between fourteen boreholes were combined to define variability in cross-sectional amplitude attenuation along the length of the two walls (Figure 10). Contour plots defined irregularly shaped walls about 8 m wide. Small scale structure was tentatively interpreted as stringers of iron possibly attributable to iron particles moving into higher permeability formations. The absence of ground truth data limited the value of this study for evaluating the effectiveness of geophysical imaging of PRBs.

Slater and Binley (2003) describe an application of electrical imaging at a PRB installation in Kansas City, Missouri. This PRB was constructed as a continuous 40 m long, 1.8 m wide trench (Figure 11a). The first 1.8 m of the trench was filled with 100% granular Fe^0 , the base being in contact with bedrock. The remainder of the trench was filled with 0.6 m of Fe^0 and 1.2 m of sand as per the depiction in Figure 11a. The thicker lower unit was designed to compensate for the higher flow-through velocities associated with hydraulically conductive basal gravel resting on the bedrock. This L-shaped structure was a good target for testing the ability of electrical imaging to resolve the *in situ* structure of a PRB and compare the result with the design specifications. Figure 11b shows the result of a 3D inversion of an electrical resistivity dataset (4620 measurements) taken between four wells. These wells were placed in a square arrangement with two upstream of the barrier and two

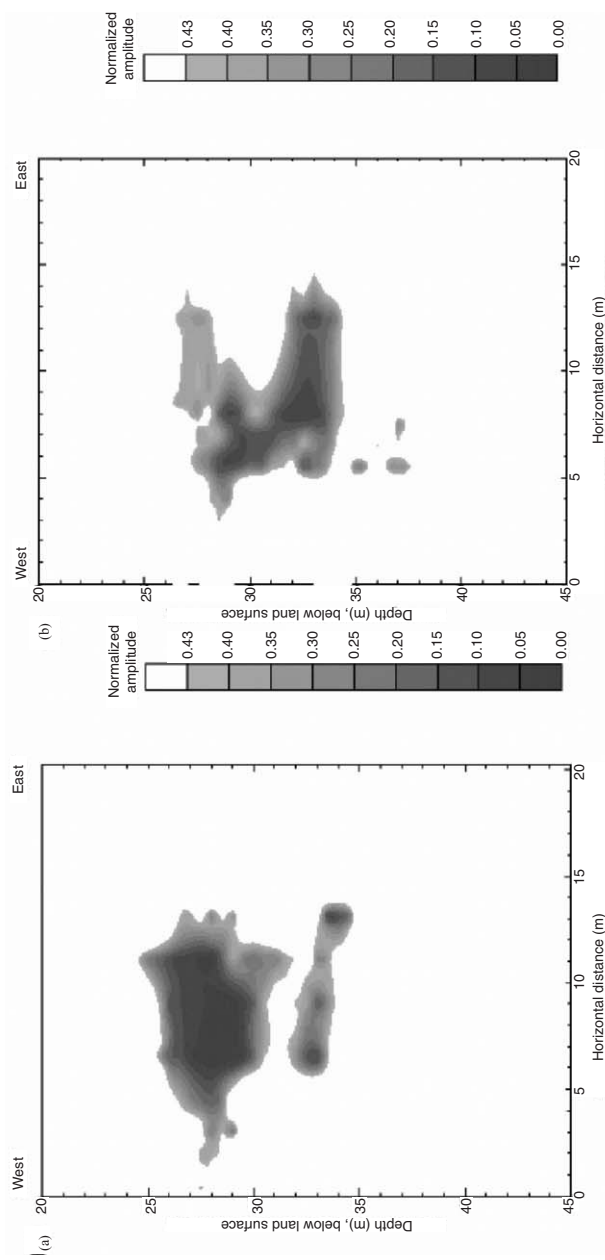


Figure 10. Cross-well GPR amplitude imaging of the two reactive walls installed at Massachusetts Military Reservation. Normalized amplitudes less than 0.43 were modeled as indicative of the presence of iron (from Joesten et al., 2001). The performance of the grout injection was not verified with ground truth data so the significance of these images is uncertain

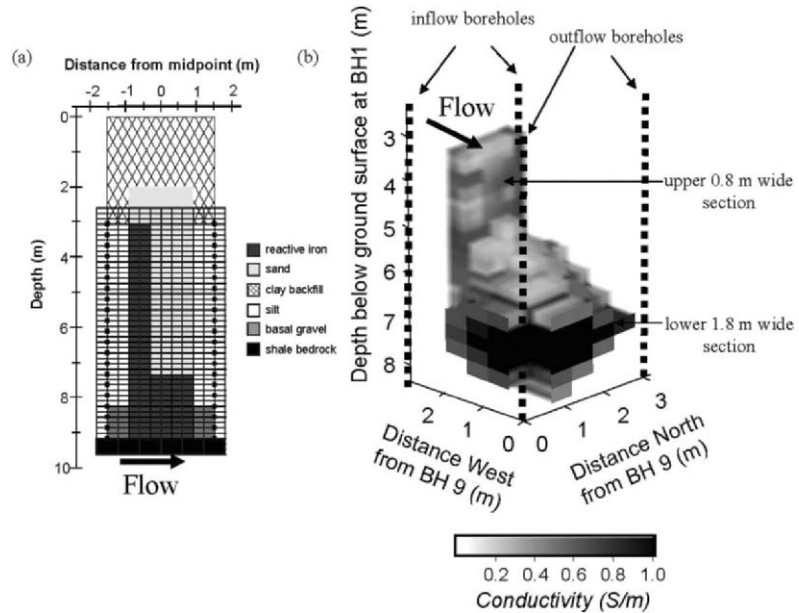


Figure 11. (a) Cross-sectional geometry of the granular Fe^0 PRB at Kansas City showing design geometry of the barrier, geology, electrode locations and the finite element mesh used for image reconstruction in this plane (b) Result of 3D inversion of electrical resistivity measurements between four boreholes in a square arrangement. Upper (0.8 m wide) and lower (1.6 m wide) sections annotated. Flow direction shown in both (a) and (b). Modified from Slater and Binley (2003)

downstream of the barrier. The spacing between wells on the square was 3 m. The imaging well resolves the barrier geometry with an approximate optimal resolution of 0.3 m (the size of the inverted elements in the image). However, this inversion was smoothness-constrained; it may be possible to improve upon this image with a regularization method more appropriate for sharp boundaries as discussed in Section 10.2.2.

Slater and Binley (2003) also collected induced polarization measurements at the Kansas City site. Figure 12 shows the 2D resistivity and IP inversions obtained between two wells spaced 3 m apart. The white outline shows the location of the PRB based on the design specifications. Figure 12a shows the inverted real conductivity, Figure 12b shows the inversion of the phase angle, being a measure of the polarization magnitude relative to the conduction magnitude, whereas Figure 12c shows the calculated imaginary conductivity that represents a direct measure of the polarization. In this example the imaginary conductivity image shows some improvement in resolving the PRB structure (assuming the in situ structure meets the design specifications) over the real conductivity image. However, Slater and Binley (2003)

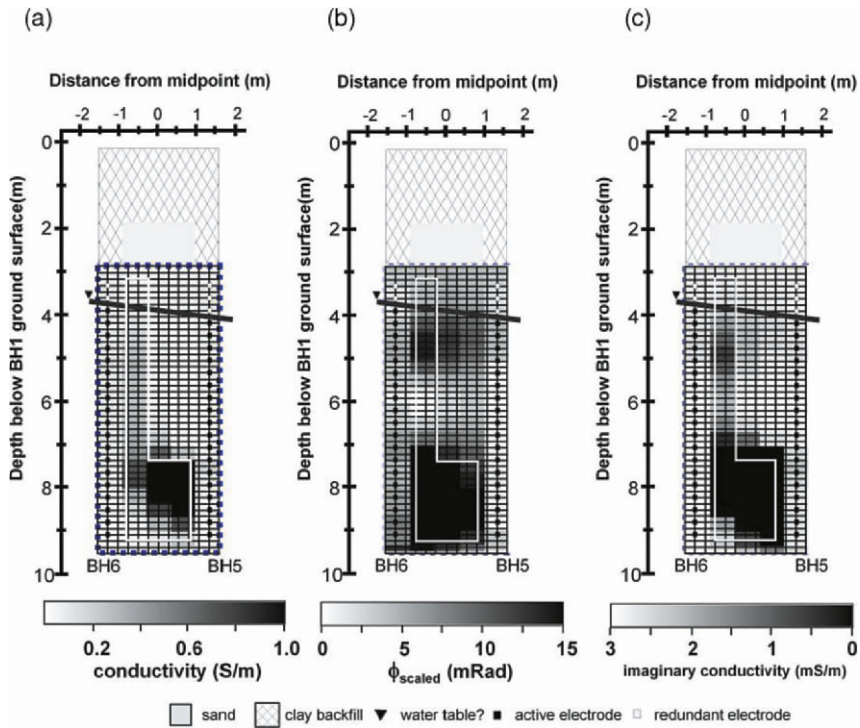


Figure 12. 2D electrical images of the permeable reactive barrier at the Kansas City site (a) real conductivity (b) phase angle (c) imaginary conductivity. The PRB outline based on the design specifications is shown by the white line. Figures modified from Slater and Binley (2003)

showed other datasets where the induced polarization measurements produced a poorer representation of the PRB structure than the resistivity measurements. The relatively high noise associated with the induced polarization data obtained in this study limited this assessment of the use of induced polarization to study PRBs.

The Kansas City PRB is permanently instrumented with electrode arrays to permit detection of changes in the electrical images of the structure that might indicate precipitation and clogging. This monitoring experiment was initiated in January 2003. Results obtained to date show no evidence for a measurable effect such as that observed in the laboratory. Figure 13 shows the differences in measured resistivity and phase for the data comprising the primary image plane located in a section of the barrier where the contaminant plume under remediation is concentrated. The data are remarkably consistent and suggest that any changes discernible from electrical imaging will occur over larger time scales than this two year duration.

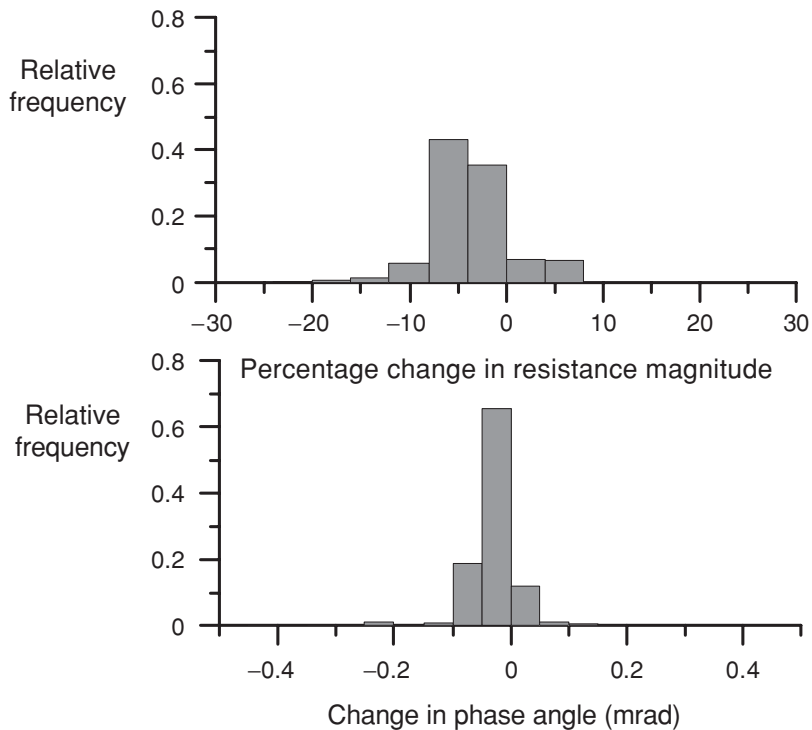


Figure 13. Changes in cross-borehole electrical measurements on a PRB between July 2003 and March 2004

10.5. Conclusions

Engineered barriers present unique opportunities for novel geophysical research. The most significant achievements to date have occurred with the detection of leaks through geomembrane liners and from waste ponds/storage tanks using electrical resistivity methods. Although this is a successful technology, research is still needed to further evaluate the effectiveness of the method as imaging changes in resistivity beneath a barrier in order to infer leakage suffers from a number of aspects. Firstly, in order to detect changes it is essential that background data (preferably under 'no leak' conditions) are available. Secondly, leaks from barriers may also be from a relatively small discharge, making resistivity contrasts undetectable, but still significant from the potential pollution threat.

Geophysical investigations of containment barriers, caps and flow-through barriers, in contrast, are few. The published studies primarily describe application of electrical based (resistivity, electromagnetic, ground penetrating radar and induced polarization) methods due to the strong resistivity, permittivity

and low-frequency polarization anomalies associated with the structures and active processes. The magnetic signatures of metallic PRBs and the seismic signatures of bentonite/grout barriers have not been investigated despite the apparent obvious potential.

Exploitation of geophysical technologies for the verification and monitoring of these structures will require changes in current installation practice. For example, the application of electrical resistivity to leak detection from geomembrane liners has advanced with the installation of geophysical monitoring equipment beneath landfills (e.g. Frangos, 1997; White and Barker, 1997). Installation of geophysical sensors proximal to, or inside, engineered barriers during construction would encourage similar achievements with high-resolution cross-hole geophysical technologies. Caps are largely excluded from this criterion as geophysical methods are readily placed in contact with the cap surface provided they cause no damage.

Geophysical imaging is often more effective when a background dataset is obtained prior to changes occurring in the subsurface. With respect to engineered barriers, this will require data acquisition prior to the installation of a structure. Again, this procedure has been adopted in novel landfill liner monitoring systems. The barrier, or leaks occurring through it, can be reconstructed from changes in geophysical properties relative to the background condition. Daily and Ramirez (2000) effectively utilized this approach in the investigation of prototype containment barriers. Ideally, boreholes for geophysical data acquisition would be drilled prior to any subsurface disturbance to permit acquisition of a representative background data set (Majer, 2006). For example, boreholes could be drilled immediately upgradient and downgradient of the planned barrier location. These recommendations are again contingent upon changes in current installation practice.

Geophysical tracer tests, where permissible, have considerably improved geophysical characterization of solute transport processes in natural soils (see for example, White, 1998; Daily et al., 1992). Geophysical monitoring of an injected tracer (for example, a conductive brine) may also aid in the detection of flaws in storage tanks prior to filling with a contaminant. A similar procedure might be followed to investigate weaknesses in caps. Daily and Ramirez (2000) successfully applied this method to the investigation of a prototype containment barrier. However, they note that a liquid tracer test is not appropriate for investigating operative barriers as the hydraulic gradients induced will encourage contaminant spreading. They did speculate on the use of a geophysically detectable gas tracer that would avoid mobilization of the contaminant. Such novel imaging approaches may ultimately improve the capabilities of geophysical technologies in barrier investigations.

Engineered barriers installed in the subsurface are complex dynamic systems requiring enhanced communication between design engineer and

geophysicist in order to fully exploit geophysical monitoring applications (Majer, 2006). Barrier technologies are continuously under development. For example, PRB technologies based on novel reactive media, such as suspensions of hydrocarbon degrading microbes, are currently being field-demonstrated (Kalin, 2004). Recent studies suggest that evidence for subsurface microbial activity is discernible from geophysical measurements (see Atekwana et al., this volume). Geophysical methods may therefore provide non-invasive solutions to monitoring of engineered microbial-induced remediation processes at contaminated sites. New technologies for the injection of highly conductive grout (such as pressure jetting) are also being developed and will require innovative verification tools. The application of geophysical methods to engineered barriers is clearly in its infancy. Given increased efforts to manage contaminated land across the globe, “barrier-geophysics” will likely form a growing sub-section of near surface geophysics.

References

Atekwana, E., D. Werkema, and E. Atekwana, 7. Biogeophysics: Impact of biological processes on geophysical properties, this volume.

Binley, A., and W. Daily, 2004. The performance of electrical methods for assessing the integrity of geomembrane liners in landfill caps and waste storage ponds, *J. Environ. Eng. Geophys.*, 8, 227–237.

Binley, A., W. Daily, and A. Ramirez, 1999. Detecting leaks from waste storage ponds using tomographic methods. First World Congress on Industrial Process Tomography, Buxton, Greater Manchester, April 14–17, 1999, pp. 6–13.

Binley, A., W. Daily, and A. Ramirez, 1997. Detecting leaks from environmental barriers using electrical current imaging, *J. Environ. Eng. Geophys.*, 2, 11–19.

Bishop, I., 2002. Electrical leak location testing of geomembranes, Environment Agency R&D Technical Report P1-419/TR, Environment Agency, Bristol, UK, 120 p.

Bogoslovsky, V.A., and A.A. Ogilvy, 1970. Application of geophysical methods for studying the technical status of earth dams, *Geophys. Prospect.*, 18, 758–773.

Bogoslovsky, V.A., and A.A. Ogilvy, 1972. Natural potential anomalies as a quantitative index of the rate of seepage from water reservoirs, *Geophys. Prospect.*, 18, 261–268.

Carmichael, R.S., 1989. *Practical Handbook of Physical Properties of Rocks and Minerals*, CRC, Boca Raton, FL, p. 373.

Chambers, J.E., R.D. Ogilvy, O. Kuras, J.C. Cripps, and P.I. Meldrum, 2002. 3D electrical imaging of known targets at a controlled environmental test site, *Environ. Geol.*, 41, 690–704.

Colucci, P., G.T. Darilek, D.L. Laine, and A. Binley, 1999. Locating landfill leaks covered with waste, in *Proceedings of Sardinia '99: 7th International Waste Management and Landfill Symposium*, CISA, Cagliari, Italy, October 4–8, 1999, pp. 137–140.

Daily, W., and A. Ramirez, 2000. Electrical imaging of engineered hydraulic barriers, *Geophysics*, 65, 83–94.

Daily, W., A. Ramirez, and A. Binley, 2004a. Remote monitoring of leaks in storage tanks using electrical resistance tomography: Application at the Hanford Site, *J. Environ. Eng. Geophys.*, 9, 11–24.

Daily, W., A. Ramirez, A. Binley, and D. LaBrecque, 2004b. Electrical resistance tomography, *The Leading Edge*, 23, 438–442.

Daily, W., A. Ramirez, D. LaBrecque, and J. Nitao, 1992. Electrical resistivity tomography of vadose water movement, *Water Resour. Res.*, 28, 1429–1442.

De Groot-Hedlin, C., and S. Constable, 1990. Occam's inversion to generate smooth, two-dimensional models from magnetotelluric data, *Geophysics*, 55, 1613–1624.

De Groot-Hedlin, C., and Constable, S., 2004. Inversion of magnetotelluric data for 2D structure with sharp resistivity contrasts, *Geophysics*, 69, 78–86.

Endres, A.L., S.D. Piggott, and J.D. Redman, 2000. Characterization of reactive treatment zones containing granulated iron using induction logging, in *Proceedings of the 7th International Symposium on Borehole Geophysics for Minerals, Geotechnical and Groundwater Applications*, Mineral and Geotechnical Logging Society, Golden, CO, pp. 1–8.

Frangos, W., 1992. Electrical detection of leaks in lined waste disposal ponds, Unpublished M.Sc. thesis, University of Utah, 78 p.

Frangos, W., 1997. Electrical detection of leaks in lined waste disposal ponds, *Geophysics*, 62, 1737–1744.

Gavaskar, A.R., N. Gupta, B.M. Sass, R.J. Janosy, and D. O'Sullivan, 1998. Permeable Reactive Barriers for Groundwater Remediation, Batelle, Columbus, Ohio.

Gilham, R.W., and S.F. O'Hannisin, 1994. Enhanced degradation of halogenated aliphatics by zero valent iron, *Ground Water*, 32, 958–967.

Giroud, J.P., and A. Bonaparte, 1989. Leakage through liners constructed with geomembranes – Part 1, *Geomembrane Liners, Geotextiles and Geomembranes*, Vol. 8, pp. 27–67.

Huisman, J.A., S.S. Hubbard, J.D. Redman, and A.P. Annan, 2003. Measuring soil water content with ground penetrating radar: A review, *Vadose Zone J.*, 2, 476–491.

Joesten, P.K., J.W. Lane, Jr., J.G. Savoie, and R.J. Versteeg, 2001. Application of borehole-radar methods to image two permeable reactive-iron walls at the Massachusetts Military Reservation, Cape Cod, Massachusetts, in *Proceedings of the Symposium on the Application of Geophysics to Engineering and Environmental Problems (SAGEEP)*, March 4–7, 2001, Denver, CO, 10 p.

Kalin, R.M., 2004. Engineered passive bioreactive barriers: Risk-managing the legacy of industrial soil and groundwater pollution, *Curr. Opin. Microbiol.*, 7, 227–238.

Laine, D.L., 1991. Analysis of pinhole seam leaks located in geomembrane liners using the electrical location method: Case histories, in *Proceedings of Geosynthetics '91 Conference*, Atlanta, GA, Feb. 26–28, 1991, pp. 239–253.

Laine, D.L., A.M. Binley, and G.T. Darilek, 1997. How to locate leaks under waste, *Geotechnical Fabrics Report*, Vol. 15, pp. 34–36.

Mackenzie, P.D., D.P. Horney, and T.M. Sivavec, 1999. Mineral precipitation and porosity losses in granular iron columns: *J. Hazard. Mater.*, 68, 1–17.

Majer, E.L., 2006. Airborne and surface geophysical method verification, Chap. 4, in Title currently unknown, edited by C. Chien, H. Inyang, and L.G. Everett, *Barrier Systems for Environmental Contaminant Containment and Remediation*, pp. 375, CRC Press, Boca Raton, FL.

McIntire, P., 1991. Nondestructive Testing Handbook, 2nd Edn., Vol. 7, Ultrasonic Testing ASNT 1991.

Nosko, V., 1996. Underliner electrode rapid reading damage detection system – SENSOR DDS, in *Geosynthetics: Applications Design and Construction*, edited by M.B. de Groot, G. den Hoedt, and R.J. Termaat, Balkema, Rotterdam, The Netherlands, pp. 691–695.

Para, J.O., 1988. Electrical response of a leak in a geomembrane liner, *Geophysics*, 53, 1445–1452.

Para, J.O., and T.E. Owen, 1988. Model studies of electrical leak detection surveys in geomembrane-lined ponds, *Geophysics*, 53, 1453–1458.

Pellerin, L., D. Reichhardt, T. Daley, F. Gilbert, S. Hubbard, E. Majer, J. Petersen, W. Daily, and A. Ramirez, 1998. Verification of subsurface barriers using integrated geophysical techniques, in *Proceedings of the Symposium on the Application of Geophysics to Environmental and Engineering problems (SAGEEP)*, Environmental & Engineering Geophysical Society, pp. 635–644.

Phillips, D.H., B. Gu, D.B. Watson, Y. Roh, L. Liang, and S.Y Lee, 2000. Performance evaluation of a zerovalent iron reactive barrier: Mineralogical characteristics, *Environ. Sci. Technol.*, 34, 4169–4176.

Ramirez, A., W. Daily, A. Binley, D. LaBrecque, and D. Roelant, 1996. Detection of leaks in underground storage tanks using electrical resistance methods, *J. Environ. Eng. Geophys.*, 1, 189–203.

Sheets, D.K., and J.M.H. Hendrickx, 1995. Noninvasive soil water content measurement using electromagnetic induction, *Water Resour. Res.*, 31, 2401–2409.

Slater, L., and A. Binley, 2003. Evaluation of permeable reactive barrier (PRB) integrity using electrical imaging methods, *Geophysics*, 68, 911–921.

Slater, L., J. Choi, and Y. Wu, 2005. Electrical properties of iron-sand columns: Implications for induced polarization investigation and performance monitoring of iron-wall barriers, *Geophysics*, 70, G87–G94.

Van, G.P., S.K. Park, and P. Hamilton, 1992. Use of resistivity monitoring systems to detect leaks from storage ponds, in *Proceedings of the Symposium on the Application of Geophysics to Engineering and Environmental Problems*, EEGS, Chicago, pp. 629–647.

Ward, A.L., and G.W. Gee, 1997. Performance evaluation of a field-scale surface barrier, *J. Environ. Qual.*, 26, 694–705.

Ward, A.L., and G.W. Gee, 2001. The application of electromagnetic techniques to cover performance monitoring: Milestone A1-3 interim report on Hanford barrier monitoring, Pacific Northwest National Laboratory, Richland, WA.

White, C.C., and R.D. Barker, 1997. Electrical leak detection system for landfill liners: A case history, *Ground Water Monit. and Rem.*, 17, 153–159.

White, P.A., 1988. Measurement of ground-water parameters using salt-water injection and surface resistivity, *Ground Water*, 26, 179–186.

11. GEOFLECTIONAL CHARACTERIZATION OF COVERED LANDFILL SITES: A PROCESS-ORIENTED MODEL AND INVESTIGATIVE APPROACH

Maxwell Meju

11.1. Introduction

Landfill sites commonly use the space available in disused quarries or special purpose-built structures but not all past landfill operations were adequately controlled or documented such that the site boundaries, and the type and volume of fill are unknown in some old covered landfill sites. Even in controlled sites, the final form and depth extent of the landfill may not conform to those indicated in the original plan submitted to the regulatory authorities during the application for a site license. Thus, a significant amount of work is required in order to accurately define the relevant parameters of a covered landfill site. Our hydrogeophysical interest in landfill sites lies in assessing the pollution threat they pose since they may contain hazardous substances.

In conventional geophysical investigation of landfill sites, the usual goals are to determine the geometrical characteristics (size and shape) of the repository and the physiochemical properties of the infill. Of the several non-invasive geophysical methods used in landfill studies, the electrical and electromagnetic (EM) methods are the most popular owing to their inherent ability to detect changes related to variations in fluid content, chemical composition and temperature in the subsurface, and the minimum capital and labor outlay required to use them in small-scale surveys (Whiteley and Jewell, 1992; Meju 2000). Since the presence of saline fluids in the ground enhances its ability to conduct electrical current, it is possible to locate a leachate plume by measuring the resistivity distribution in the subsurface. The main ground resistivity measurement techniques employed in landfill studies are the direct current (dc) resistivity and/or induced polarization (IP) methods (e.g. Barker, 1990; Ross et al., 1990; Carpenter et al., 1990, 1991; Meju, 2000; Weller et al., 2000) and transient electromagnetic (TEM) methods (e.g. Buselli et al., 1990, 1992); but the radiofrequency magnetotelluric (RMT) method (e.g. Tezkan et al., 1996) and self potential (SP) method (e.g. Naudet et al., 2003, 2004) are rapidly emerging as powerful tools for landfill investigations (see also Chapter 9).

The focus of this chapter is on the development and application of a consistent process-oriented geoelectrical framework for investigating old non-engineered landfill sites where the necessary record of operations is no longer available or never existed, as in the case of unauthorized dumping grounds. The adopted approach draws from concepts in geotechnics and contaminant biogeochemistry, and stresses the complex geometry of landfill sites, the heterogeneous material compositions, and the attendant biogeomorphic-cum-biogeochemical processes in landfill environments. The analogy between landfill waste decomposition processes and weathering of geological materials permits the development of a conceptual geoelectrical model for old covered landfill sites (Meju, 2000). The geochemical observations that leachate properties vary consistently with age (e.g. Farquhar, 1989; DoE, 1996) and the observations that some geoelectrical and hydrochemical parameters of leachate are interrelated (e.g. Meju, 2000; Naudet et al., 2003), suggest the possibility of predicting fill-age and hydrochemical properties using geoelectrical information (e.g. Meju, 2000, 2002). Practical examples will be used to illustrate the various aspects of the proposed conceptual geoelectrical model.

11.2. Landfill Processes and Geoelectrical Signature

To understand how the attendant processes in landfill environments can influence our geoelectrical measurements, it is instructive to examine the consistent features of models derived from geological, geotechnical, biological and biogeochemical observations on landfills and rock weathering that can be adopted as the basic building blocks for any geoelectrical model for landfill sites. Three main features of landfill sites (complex geometry, heterogeneous material composition, and complex biogeomorphic processes in harsh environmental conditions) are adapted into a simple geoelectrical model in this section.

11.2.1. CHARACTERISTICS OF LANDFILL SITES

11.2.1.1. *Structure of Landfill Sites*

The old non-contained landfill sites come in various shapes, sizes and depths, many being located in disused quarries, opencast coal mines or other convenient holes in the ground. They may be situated above, below or astride the regional water table. In some landfill sites, a lining of relatively impermeable material may be present, or the waste may be in direct contact with granular or crystalline geological materials. In landfill capping, a soil cover layer is required when returning the site to agricultural or amenity use and steep sided cover systems are often incorporated in the cover design (see Figure 1) to maximize the landfill capacity (Hall and Gilchrist, 1995). The cover system may

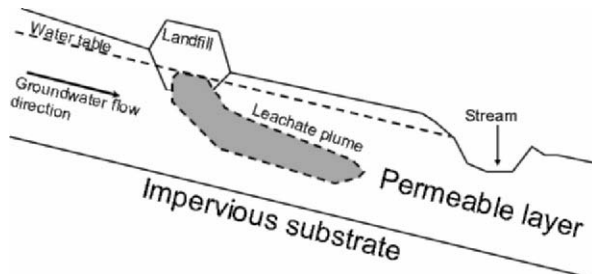


Figure 1. Geometry of an old covered landfill site. The landfill cover may be a domed cap or have a steeply-sloping side. A basal liner may be absent or breached allowing a 3-D contaminant plume to migrate downgradient from the site

be multi-layered or single-layered in some old landfills. There may be basal floor slopes to promote leachate drainage to sumps but it can be expected that many pre-regulation landfill sites may have inadequate basal containment and leachate collection systems; there will also be cases where the landfill bottom is neither graded nor lined. Landfills generally range in thickness from about 3 to 40 m.

11.2.1.2. *Nature and Characteristics of Landfill Wastes*

Landfill deposits are characterized by complex material composition, non-uniform compaction within each layer, non-uniform decomposition process, non-uniform settlement and varying pore fluid composition (Fang, 1995). The deposits may be intermixtures of domestic and industrial wastes, soils and exhumed geological materials (see Table 1). The composition of urban waste will vary from community to community, from country to country (Table 1), and from season to season (Fang, 1995).

The wastes in old landfill sites may not be as well compacted as in modern regulated landfill practice and will thus have substantial internal permeability. They will in general consist of degradable and non-degradable materials (food and garden wastes, ashes, paper, textiles, plastics, metals, building waste, mill tailings, organic liquids etc) but it is their chemical composition that is important when assessing their potential for groundwater pollution (Meju, 2000). Since landfills are a complex mixture of anthropogenic deposits, their physical properties would show a wide range of variation. The published electrical resistivity of solid waste and contaminated substrate range from 1.5 Ωm to ca. 20 Ωm (e.g. Knight et al., 1978; Laine et al., 1982; Everett et al., 1984; Carpenter et al., 1991; Meju, 2000) with the associated leachate being highly conductive (Whiteley and Jewell, 1992; Meju, 2000).

TABLE 1. Composition (percentage by weight) of typical municipal solid wastes (Meju, 2000)

Types	New York City, USA	Osaka, Japan	Zagreb, Croatia	Meruelo, Spain	Ankara, Turkey	Beijing, China
Food and garden/ Organic wastes*	19.3	17.7	23.3*	52.0*	50.8*	45
Paper, paper board	58.8	37.1	20.5	21.9	8.9	5
Metal	7.6	5.5	2.4	3.2	1.2	1
Glass	8.6	12.3	7.3	4.1	1.4	1
Wood	2.5	2.5	1.1	2.4	—	
Textiles, rugs	0.8	4.0	3.8		1.4	
Rubber, leather, (bones ^b , wood*)	0.8	0.3	2.6 ^b			1*
Plastic	0.8	15.2	10.8	8.3	2.1	1
Earth, ash, cinder				1.4	32.4	
Construction rubble			28.2		1.8	
Others				6.7		46

Data compiled from Sowers (1968); Yamamura (1983); Kovacic et al. (1995); Sanchez-Alciturri et al. (1995) and Wasti (1995). The superscripts refer to original classifications at data sources.

11.2.1.3. Formation and Migration of Landfill Leachate and Biogas

Degradable domestic waste will decompose into organic and/or inorganic soils plus other byproducts depending on its chemical composition. Initially, it undergoes a short-term process of mechanical decomposition and settlement causing its physical properties to change (Fang, 1995). Owing to the heterogeneous nature of the usually organic-rich domestic waste, the distribution of settlement will be non-uniform (Fang, 1995) and often leads to severe fracturing of the top seal of the landfill cover. The top seal is then highly vulnerable to erosion and infiltration of rainwater and snow-melts. Long-term physical, chemical (notably hydrolysis, hydration, carbonation, oxidation and solution) and microbial degradation processes lead to the dissolution or deterioration of landfill materials, gas generation and production of leachate. Initially, the microbial degradation of landfill waste occurs under aerobic conditions. As the oxygen becomes depleted by the microbial activity, anaerobic conditions rapidly set in and the biodegradation of organic materials becomes anaerobic. Methane gas is generated bacterially from the abundant organic materials under the prevailing anaerobic conditions.

Infiltrating rainwater, groundwater, or other liquids disposed of within the wastes will dissolve some soluble mineral constituents of the landfill once the absorbent or field capacity of the fill is exceeded and free drainage of water can occur. This leaching process may remove the common mineral elements or the bonding materials causing changes in matrix cement or the

TABLE 2. Typical changes in leachate concentrations with age of landfill waste

Leachate parameter	Age of waste			
	0–5 years	5–10 years	10–20 years	>20 years
TDS	10000–25000	5000–10000	2000–5000	<1000
pH	5–6	6–7	7–7.5	7.5
BOD	10000–25000	1000–4000	50–100	<50
COD	15000–40000	10000–20000	1000–5000	<1000
Ammoniacal N	500–1500	300–500	50–200	<30
Total P	100–300	10–100		<10
Chloride	1000–3000	500–2000	100–500	<100
Sulphate	500–2000	200–1000	50–200	<50
Calcium	2000–4000	500–2000	300–500	<500
Sodium + potassium	2000–4000	500–1500	100–500	<100
Magnesium + iron	500–1500	500–1000	100–500	<100
Zinc + aluminium	100–200	50–100	10–50	<10
Alkalinity (CaCO_3)	10000–15000	1000–6000	500–2000	<500
σ_w	1500–4000	750–1500	200–950	<200

The hydrochemical data are from Farquhar (1989) and Birks and Eyles (1997). The fluid conductivity (σ_w) data have been compiled from numerous published sources as well as long-term measurements in monitoring boreholes in landfill sites in northwest England by a regional council (T. Hodson, personal communication, 2004, 2005) and SITA (UK) Ltd. (2004; I. Thomson, personal communication, 2004). Conductivities are in mS/m, pH is in the standard unit and the other quantities are in mg/l. TDS, total dissolved solids. BOD, biological oxygen demand. COD, chemical oxygen demand. N, nitrogen. P, phosphorous.

ion concentration within the landfill-porewater system and hence significant physical property changes. The resulting liquid (termed leachate) is rich in fungi, bacteria, inorganic salts and organic matter; but the compositional trend may be water and dissolved inorganic salts, water and dissolved organic wastes and organic fluids, or simply organic acids depending on the availability of solvent and solute types in the leached mass. The composition of the leachate will change as the waste in the landfill ages (Farquhar, 1989). The leachate from a young landfill may be characterized by high levels of organic acids, ammonia and total dissolved solids (TDS), but as much of the biodegradable mass is broken down with time, the concentrations of these parameters will decrease in the leachate produced from the ageing landfill (see Table 2).

Within the landfill, this liquid may collect in various areas (e.g. perched saturated zones) or mound at the bottom of the landfill. This leachate starts seeping as soon as enough hydrostatic head is developed. Biochemically controlled exothermic reactions are known to cause higher groundwater temperatures in leachate (MacFarlane et al., 1983) and because of the ingress of leachate from the upper leached zones, the temperature in the lower portion of the landfill is often significantly higher than elsewhere in the leached section

(Fang, 1995). Consequently, there are higher bacterial activities and higher ion exchange reactions in the lower parts of the landfill as time progresses. These microbial-chemical decomposition reactions may cause significant changes to the existing pore fluids (and to the substrate if the fill is in direct contact with geological materials).

On passing through the base of the landfill, the metal ions in solution may be removed from the aqueous phase by ion exchange, sorption or precipitation onto the substrate (especially if clayey). However, metal ions can be sorbed preferentially onto the surface of colloidal particles and may by-pass the natural attenuation processes as the leachate seeps into the substrate (Dearlove, 1995). Initially, on entering the anaerobic groundwater system in the substrate, the organic material in the leachate is slowly biodegraded forming more acids which may react with aquifer materials (cf. Bennett and Siegel, 1987) with attendant changes in the fluid chemistry near the water table. In this deoxygenated environment, inorganic materials in the leachate may be dissolved in the groundwater. The dispersing leachate extends laterally and vertically as it sinks towards the bottom of the substrate forming a 3-D contaminant plume which may be steeply dipping (Figure 1). The amount of groundwater contamination resulting from this invasion will depend on the hydrogeology of the area and the attenuation capacity of the substrate material. It may be effectively diluted and dispersed by groundwater in highly permeable geological formations with high flow rates. Given enough time in less permeable formations, or with slowly moving groundwater, the plume (laden with inorganic salts) may enhance mineralization of groundwater (Meju, 2000). Since it is a moving and continuously evolving 3-D feature, it will in time be dispersed over a sizeable area, possibly with distinct compositional zoning.

11.2.2. A CONCEPTUAL PROCESS-ORIENTED GEOFIELD MODEL

The observable geoelectrical response of landfill sites will vary in relation to significant changes in the chemistry of subsurface pore fluids. It follows that a conceptual resistivity model can be developed that is consistent with the above biogeomorphic and hydrochemical considerations. It can be expected that surface layers of landfill waste may experience rapid aerobic decomposition whilst the bulk of the waste at depth may have only been partially decomposed under anaerobic conditions thus leading to different physical properties. For a leachate-generating landfill in contact with granular substrate, the interactions between the invading leachate and substrate material may cause geochemical alterations of substrate depending on its buffering and cation exchange capacities.

The relevant conceptual model is shown in Figure 2. Several zones are recognized in this generalized model. The top soil and clay cap (i.e., zones

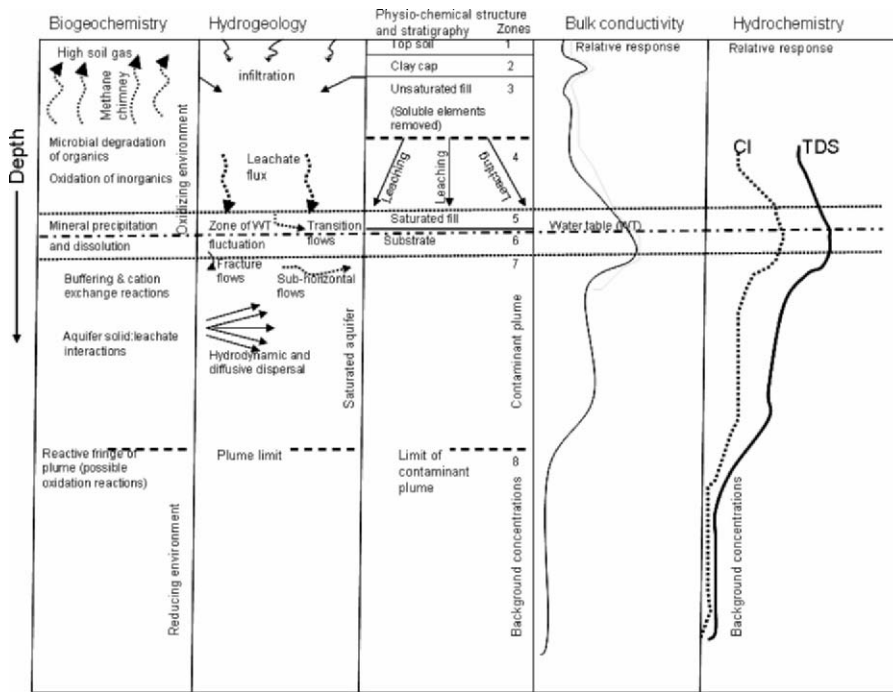


Figure 2. A conceptual resistivity model for old landfill sites with leachate generation and migration into groundwater system in granular substrate and environs (after Meju, 2000). Note the expected conductivity variation with changes in hydrochemistry down the section

1 and 2) form the uppermost confining layers. The resistivity of the top soil will vary from region to region and with season but the usually 0.3 to 1 m thick clay cap will in general be relatively conductive. Landfill sites are notorious for high levels of soil gas (principally methane and carbon-dioxide). Fractured clay caps would also allow gas migration. The geoelectrical signatures of zones 1 and 2 will be affected by seasonal changes. In wet seasons, infiltrating water may drive out gas thus lowering its bulk resistivity. Conversely, rising vapors in the dry periods will drive out soil moisture with attendant increase in bulk resistivity. The degree to which these changes are detectable will depend on the nature of the materials in zones 1 and 2. For instance, the influx of gas into pore spaces in some clays may cause appreciable resistivity increases (if water or leachate is displaced) but not so for a highly resistive dry sandy topmost layer. If these cover materials are iron-rich, it is conceivable that the rising methane and sulfur-dioxide in landfills may lead to the formation of a pyritic geochemical alteration halo (Meju, 2000) akin to the so-called 'sulfide chimney' found in iron-rich sediments overlying fractured hydrocarbon reservoirs (e.g. Oehler and Sternberg, 1982, 1984; Ostrander et al., 1983) which might be detectable in 3-D or time-lapse geoelectrical

surveys. This will be an important source of SP and IP anomalies in landfill sites.

The clay cap is underlain by a zone of pervasive leaching of landfill waste and residual products (i.e., zone 3 in Figure 2). This is the top part of the landfill waste where oxygen and bacterial supply is abundant (and will thus decompose quicker than the deeper parts). The bulk resistivity of this oxidized zone will show a relative increase with time (as the organics for microbial degradation become depleted in supply, oxidation of inorganics tends towards completion and much of the soluble elements have been removed). The leaching of clay minerals from the original landfill-soil mixture would leave behind the non-degradable fill material and siliceous geomaterial with average soil/rock grains of larger size fraction (cf. Witmer et al., 1984) and of relatively higher resistivity than the parent landfill material (Meju, 2000). It may thus be relatively resistive in comparison with the clay cap and the underlying zone of incomplete waste decomposition (i.e., zone 4). However, the rate of water flux through zone 3 will affect its eventual resistivity characteristics – it will be more resistive for fast flows in comparison to slow fluxes which will cause lower resistivities.

The lower part of the waste deposit contains a zone dominated by relatively immature leaching and therefore exhibits relatively low bulk resistivities (zone 4 in Figure 2). For landfill resting on highly impermeable substrate, leachate mounding may occur in the basal part of the waste deposits rendering it the most electrically conductive part of the entire landfilled section. However, if the landfill rests directly on a relatively permeable substrate saturated with groundwater, fluctuations in the water table may occur within a section encompassing the basal part of the landfill (zone 5) and the uppermost part of the substrate (zone 6) as indicated in Figure 2.

The mineral salts and organic material leached from the fill materials will be deposited near the water table depending on the local hydrogeological and Eh-pH conditions causing an increase in total dissolved solids or mineralization (and therefore electrical conductivity) and other chemical parameters in the pore water. Due to water table fluctuations, the zone of deposition or mineral enrichment may extend from the basal part of the landfill into the upper part of the subjacent geological formation or may lie well below the base of the landfill depending on the permeability, fluid saturation, groundwater flow and dispersion characteristics of the substrate and the mobilities of the ions in solution. Below the water table, the leachate mixes with groundwater and reacts with substrate material (cf. Bennet and Seigel, 1987) forming a relatively conductive plume (zone 7). Beyond the plume, the uninvaded substrate (zone 8) will have background values of TDS and electrical conductivity.

The main tenet of this model is that vertical profiles of the TDS and electrical conductivity will peak near the water table and tail-off in either direction

outside the zone of mineral enrichment. It can be expected that this zone will have a discernible conductivity signature on geoelectrical soundings in leachate-bearing landfill environments. For unsaturated substrate in contact with leachate-generating landfill deposits, the leachate will advance with the infiltrating water and displace the air or residual connate water in the pore spaces of the substrate. This displacement will cause a decrease in the resistivity of sandy or fractured carbonate formations but the effects may not be geoelectrically appreciable in some clayey substrate. If the unsaturated section were thick enough, the rate of advance of the leachate front (and hence the depth location of the zone of maximum leachate concentration) will depend on the buffering and cation exchange capacities of the substrate. For instance, calcite-rich sands may attenuate the leachate better than dominantly siliceous sands (e.g. DoE, 1996) with consequent differences in the position of occurrence of leachate-related geoelectrical conductors in unsaturated substrates.

There is support for this conceptual resistivity model from borehole studies at several landfill sites in different parts of the world. Birks and Eyles (1997) examined the hydrochemical data from long-term (1984–1994) monitoring of the Beverly landfill site in Canada. The sampling points in each monitoring well were placed at two levels (1–4 m and 10–12 m) below the water table (see Birks and Eyles, 1997, Figure 2). These workers found that the shallower monitors showed higher conductivities (and chloride concentrations) than deep monitors but interpreted this as indicative of leachate dilution with downward migration or preferential flow in the shallower parts of the aquifer. Analysis of the composition of leachate from a 3–5 year old fill at Lucas Heights in Sydney showed that heavy metals, iron and manganese attain maximum values just below a water intersection in a borehole (see Knight et al., 1978, Figure 8).

Geoelectrical depth soundings over landfill sites clearly show evidence of the proposed resistivity zoning. In Figure 3 are shown representative apparent resistivity sounding curves from old covered landfill sites in different geological, climatic and geoenvironmental settings. All the curves are of the minimum or H-type and exhibit a characteristic W-shaped response pattern. The curves show clear evidence of resistivity zoning in accord with the proposed conceptual model (Figure 2). It was clearly demonstrated elsewhere (Meju, 2000) that the depth location of these zones are in good agreement with borehole data. From Figure 3, it is obvious that measurements incorporating dense sampling with half-electrode array lengths of 0.1 to 10 m are necessary for resolving the full signature of zones 1 to 4 in the typical landfill site. The most conductive segment of each sounding curve corresponds to the saturated basal section of the landfill and/or leachate-invaded substrate (zone 4). Note, however, that an apparently highly resistive terminal segment of a sounding curve at a landfill site (as exhibited by the curves shown in this

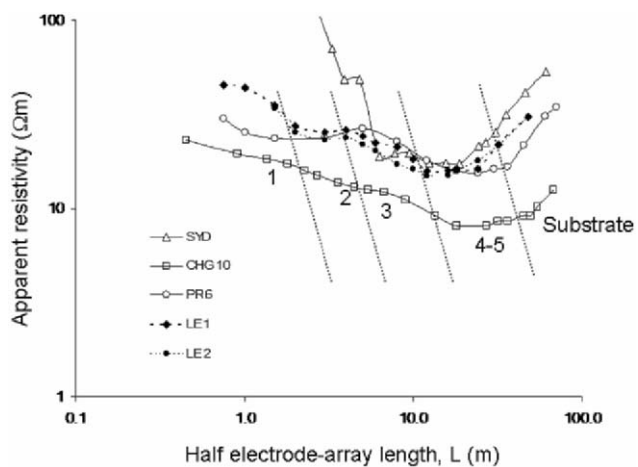


Figure 3. Typical sounding curves from landfill sites in different geographical and climatic settings. Note the classical skewed W-shape of the curves which is consistent with the conceptualized conductivity zoning at depth (zones 1 to 5). Sounding curves prefixed by LE and PR come from England, SYD is from Australia (Knight et al., 1978) and CHG from the USA (Carpenter et al., 1991)

figure) may not always be indicative of a resistive nature for the substrate but instead may be due to 3-D distorting influences of the typically complex site geometry especially when the expanding electrodes occupy positions outside the actual confines of the landfill site.

11.3. Implications for Geoelectrical Investigation of Landfill Sites

11.3.1. PREDICTION OF RELATIONSHIPS BETWEEN HYDROGEOLOGICAL, HYDROCHEMICAL AND GEOELECTRICAL PARAMETERS

The chemical parameters and age of fill are important components of any hydrogeophysical characterization of landfill sites. Fluid electrical conductivity is usually taken as a measure of the total dissolved salts in groundwater by hydrogeochemists while chloride content is used as a conservative leachate indicator parameter in water sample studies since, apart from dilution, it undergoes very little chemical or biological change in the groundwater system (Baedecker and Apgar, 1984). The relationship between fluid conductivity and TDS and between fluid conductivity and chloride content in leachate plumes emanating from some landfill sites is shown in Figure 4. Note the apparent relationship between the various parameters. It would be expected that if similar relationships obtain for bulk resistivity and TDS

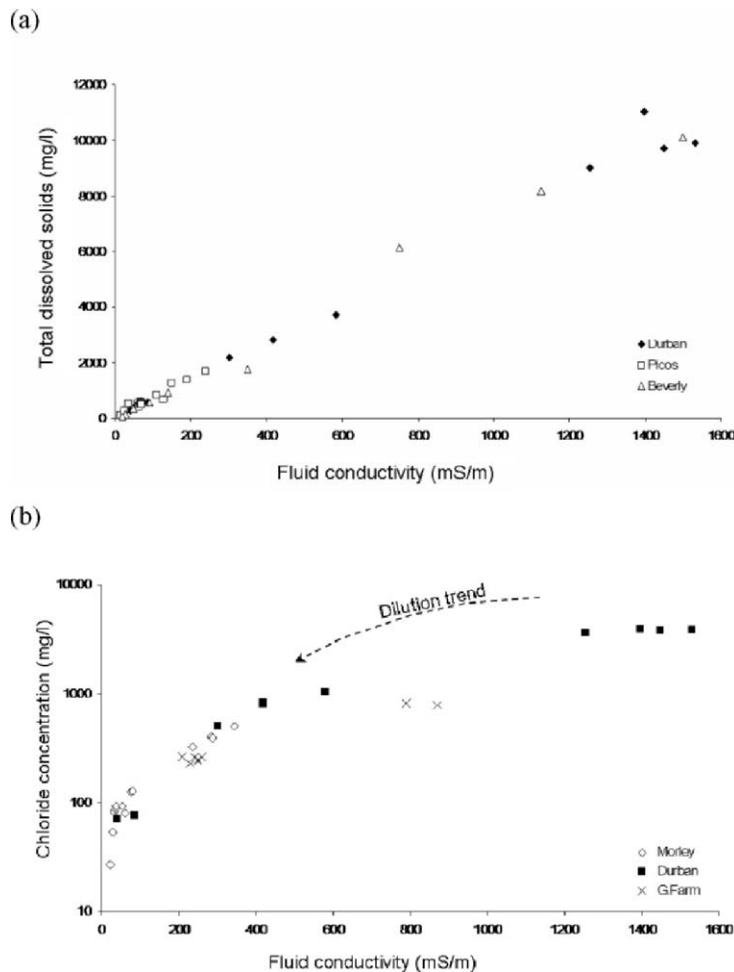


Figure 4. Relationship between the electrical conductivity of leachate and its TDS content (a) and chloride concentration (b). The data come from Durban landfill site in South Africa (Bell and Jermy, 1995), Beverly landfill site in Canada (Birks and Eyles, 1997), a contaminated aquifer near Picos in northeast Brazil (Meju, 2000) and from the Grange Farm landfill site in northwestern England (T. Hodson, personal communication, 2004).

or fluid conductivity, then it will be possible to predict compositional trends in hydrochemical parameters (such as TDS and chloride content) from surface geoelectrical soundings (e.g. Buselli et al., 1990; Meju, 2000). However, despite the good correlation observed between fluid conductivity in boreholes and geoelectrical models from analysis of surface measurements in different environments (cf. Ebraheem et al., 1990; Meju, 2000; Naudet et al., 2004), there is as yet no unequivocal relationship between

bulk conductivity and hydrochemical parameters for use in the general medium.

Variations in the composition of fills of different ages have been noted by several workers (see e.g. Knight et al., 1978). However, from a geoelectrical viewpoint, an important development in geochemical characterization of landfill leachates is the observation that these variations are consistent with age (e.g. Farquhar, 1989; DoE, 1996) as can be seen in Table 2. If the approximate concentrations of the relevant hydrochemical parameters can be predicted, empirically or theoretically from geoelectrical measurements, it follows that one can, at least at a conceptual level, predict the age range of a given saturated fill using the information furnished by surface and/or borehole geoelectrical measurements. This provides a basis for geoelectrical forensics (Meju, 2000). The main problem that will bedevil such an approach is the fact that there are three main sources that contribute to the observed leachate composition – infiltrating groundwater or rain, waste deposits and ambient geological materials.

Accurate mapping of the electrical conductivity and redox potential of groundwater is important in delineating the shape of a contaminant plume (Naudet et al., 2004). Three-dimensional geoelectrical imaging is now well established (e.g. Zhang et al., 1995; Weller et al., 2000; Herwanger et al., 2004) and can provide information on the mineralization of the leachate impacted groundwater. It is emerging that the redox potential (EH) of an aquifer contaminated by leachate (see Chapter 9) can be reliably predicted using the SP method (Naudet et al., 2003, 2004). A map of redox potential in an aquifer is indicative of biodegradation of organic matter and of concentrations of redox-active components (Naudet et al., 2004).

11.3.2. CHARACTERIZATION OF COVER AND INTERNAL STRUCTURE OF LANDFILLS

Engineered barriers are treated in Chapter 10. Here, we are concerned mostly with identifying the key elements of our conceptual model in old covered landfill sites which may or may not have special purpose-built caps or basal liners. A 5-step investigative approach for landfill sites can be proposed that is consistent with the above concepts.

11.3.2.1. *Desk Study*

The analysis of historical documents (town development plans and topographic maps) and any available geotechnical reports for the area of study is a vital first step in site investigation. It can furnish much of the necessary information to address some pressing problems. Host rock geology and possible physical property contrasts can be gleaned from desk study. A good

knowledge of the underlying geology is important as it is undesirable for the fill to be in contact with permeable geological materials. The presence of geological structures (e.g. faults or fractures) that will permit fluid flow or lead to structural instability is also undesirable (but these can be mapped using 3D geoelectrical surveys).

11.3.2.2. *Development of Exploration Model*

This second phase defines the site constraints and boundary conditions (natural and gradational or anthropogenic and abrupt) and thence a site-specific exploration model that is consistent with geotechnical, biological, geological and physico-chemical considerations. Site-specific model development involves posing the problem with the attendant constraints in a form that can be addressed using the chosen geoelectrical methods. In general, the main elements of a closed landfill site are the site boundaries (which are typically irregular), buried near-vertical rock faces in disused hard-rock quarries, dome-shaped or tabular cap, depth locations and dips of the layers of waste and sealing materials, the integrity of the sealing zones, the position of access roads or buried bund walls, and the presence of high levels of hazardous gases, leachate (or corrosive chemicals in the case of industrial waste disposal sites) or perched groundwater bodies. Particular attention should be paid to accurately mapping any leachate or gas seepages and the associated geochemical alteration haloes, the presence and intensity of fracturing of the capping layer, and the degree of anisotropy or heterogeneity.

11.3.2.3. *Survey Design, Execution and Data Quality Control*

The third phase involves the design and execution of a geoelectrical survey to define the cap and internal structure of the landfill site. The geoelectrical methods should be selected to define the various parts of the above model and with data quality and integrity as key considerations. Obviously the various methods would respond differently to specific aspects of this model which would suggest that an integrated approach is the best option. In designing and executing surveys to investigate covered landfill sites, it may be necessary to combine geoelectrical measurements with some other geophysical technique (such as seismic refraction) but electrical and electromagnetic (EM) methods must be seen as a necessary combination. Background noise and physical property contrasts at the site are important physical constraints since high background noise may reduce the accuracy of the geophysical measurements and thus lead to poor model resolution. The background noise and expected physical property contrasts would help in determining whether the sensitivities of the available geophysical instrumentation are adequate for the given problem. It is possible to determine the methods that have optimum potential

for target definition by forward modeling studies. This can also be achieved by a site reconnaissance survey.

The sampling interval should be sufficiently high to define the key structural features (and in particular, the thin clay cap) as well as give a representative range of results for the typically variable waste materials. Since landfill environments are inherently three-dimensional (3-D), a dense 3-D network of observational stations and small vertical sampling intervals would normally be required. However, the degree of ground variability in well-compacted sites may be such that densely sampled 2-D profiles may provide useful constraints. In some situations, spot soundings may also be used to quickly assess whether the elements of the proposed model (resistive top-soil and conductive clay cap, resistive unsaturated fill and conductive saturated fill) can be sensed. For example, the cap over the landfill site could consist of a 0.3–1 m clay layer and 0.5–1 m topsoil. To adequately image this, one would require electrode array lengths starting from less than 1 m and increasing arithmetically, not logarithmically as in traditional depth soundings (cf. Figure 3).

11.3.2.4. *Data Homogenization and Integration*

Data integration is necessary to reduce interpretation uncertainty in landfill investigations. It provides a basis for assessing the consistency, completeness and sufficiency of electrical and electromagnetic field data, and hence their suitability for combined interpretation. It is very important to eliminate subjectivity and achieve comparability between the various techniques in landfill site investigations. The apparent resistivity data from TEM and in-line 4-electrode dc resistivity (Schlumberger, Wenner and dipole-dipole) arrays may be compared using the space-time relation (Meju, 2005)

$$t = 0.5\pi\mu\sigma L^2 \quad (1)$$

or equivalently, $L = 711.8\sqrt{t\rho}$ meters where the transient time t is in seconds (s), μ is the magnetic permeability (taken to be equal to that of free-space, $\mu_0 = 4\pi \times 10^{-7} \Omega\text{sm}^{-1}$), L is one half the electrode array length (i.e., the distance from the centre of the array to an outermost electrode), and $\rho(=1/\sigma)$ is apparent resistivity (in Ωm). Similarly, the scaling relation for RMT and dc resistivity arrays is (Meju, 2005)

$$T = 2\pi\mu\sigma L^2 \quad (2)$$

or $L = 355.9\sqrt{T\rho}$ meters where T is the RMT period in seconds. It follows that for a given depth sounding data (apparent resistivity versus time or frequency) from time-domain or frequency-domain EM experiments, one may estimate the half-electrode array length for the appropriate in-line 4-electrode configuration that will yield the equivalent relative information and vice versa, making for easy comparison of data from EM and electrical resistivity

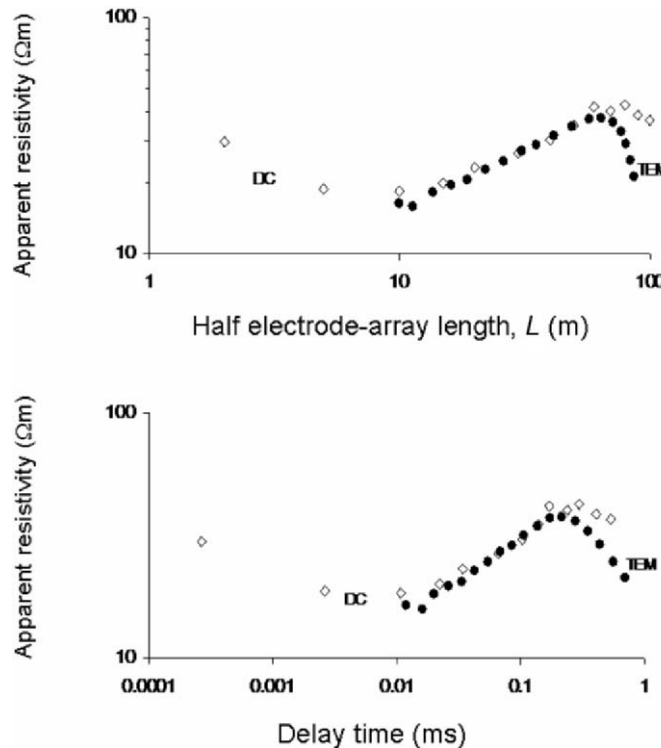


Figure 5. Equivalent presentation of Schlumberger DC resistivity and TEM sounding data from the Ledburn Road landfill site in Leighton Buzzard in the UK. The same data are presented as a function of half the electrode array length in the top plot and as a function of transient time in the bottom plot. The TEM data were acquired using the Geonics TEM47 equipment and a base frequency (repetitive rate) of 237 Hz. Note that the poorly sampled dc measurements for $L = 1$ to 10 m (3 points per decade) will severely limit the geoelectrical resolution of the landfill cap

methods. Dc resistivity and TEM sounding data from an old covered landfill site are presented in Figure 5 using Equation (1) for comparison. Both data sets are compatible and may thus be jointly interpreted in terms of the subsurface resistivity structure.

The above space-time relations are also useful for determining vertical data coverage (i.e., depth sampling) and for identifying spurious effects or static shifts in electrical sounding curves (Meju, 2005). In Figure 5, the overlap between the dc resistivity and TEM sounding data is obvious; the shallow-depth corresponding to half the dc electrode array length is only sampled by the dc data. Electrical static shift is a galvanic problem caused by a build-up of charges around small-size 3-D bodies in the near-surface and manifests in log domain as a vertical shift of the apparent resistivity sounding curves

(Spitzer, 2001). This can be identified and corrected using multi-geometry TEM data (Meju, 2005). The inversion of statically-shifted sounding curves will lead to erroneous resistivities (Meju, 2005) and has implications for consistency in geoelectrical prediction of leachate properties or groundwater quality.

Static shift is a common problem in RMT surveys (employing both magnetic and electric field measurements) but can be solved by 3-D joint inversion for the subsurface resistivity and static shift parameters (e.g. Sasaki and Meju, 2006). Static shifts in dc resistivity occur for the Schlumberger array where the inner electrodes are almost fixed; the soundings show obvious constant shifts just like RMT soundings. Thus, if we interpret Schlumberger data in terms of 1D or 2D models, the results can be seriously affected by static shifts. However, the static effects for 3D inversions may not be as serious as for 1D and 2D inversions, because static effect is absorbed in the near-surface structure to some extent. A more common problem related to near-surface heterogeneity is spatial undersampling (or spatial aliasing) in landfill surveys. The only solution to this problem is reducing electrode spacings such as done in 'high-density' electrical surveys employing the pole-pole or pole-dipole array in geotechnical and environment applications.

11.3.2.5. *Model Identification and Appraisal*

The final phase provides an appropriate physico-chemical solution to the given problem, based on site-constrained analysis of the geoelectrical field data (and for added value, the definition of future monitoring requirements). The appropriate interpretative schemes are determined by the dimensionality characteristics of the site but the available computational platform will often dictate what interpretative tools are ultimately selected and applied to the recorded field data. It is important, especially for gas reservoir or leachate level tracking, to accurately map the unsaturated and saturated fill (i.e., zones 3 and 4); their boundary should be well resolved in joint electrical and EM inversion. It is also important to correctly identify whether the cover system is multi-layered or single-layered and the presence of steeply sloping cover systems. A landfill site with a domed or steeply sloping impermeable undisturbed cover system ('clay cap') over relatively permeable gas-generating waste might constitute a good trap (as well-known in petroleum geology) for hazardous gases (e.g. methane and carbon-dioxide). If the integrity of the sealing zones in a landfill site has been breached (e.g. by natural or man-made disturbance), then hazardous substances can escape into the air or into the groundwater system and thus the pollution potential of the site rests mainly on the nature and amount of emitted fluids and the surrounding geology. Thus, the identification of fluid migration pathways, subsurface leachate accumulations and their possible concentration must be seen as important deductive goals.

11.4. Discussion and Conclusion

11.4.1. PREDICTION OF HYDROCHEMICAL PARAMETERS FROM GEOELECTRICAL DATA

It has long been known that the chemical composition of leachate varies with age (Farquhar, 1989). In this chapter, a new compilation of the available data on the electrical conductivity of leachate samples appears to support this geochemical trend (Table 2). Other studies (e.g. Naudet et al., 2004) show that there is a good correlation between the electrical resistivity determined by 3-D geoelectrical analysis and the conductivity of leachate impacted groundwater measured in boreholes. Recently, the relation between electric and redox potential has been established (Timm and Moller, 2001; Naudet et al., 2003). There is thus a good basis for using geoelectrical information to predict hydrochemical parameters in ideal landfill environments. A conceptual geoelectrical model has been described in this chapter for characterizing old, covered landfill sites. The model integrates consistent concepts in geotechnics, geomicrobiology, geochemistry and rock weathering in an effort to develop a unifying framework for landfill studies employing electrical and electromagnetic geophysical methods. The resistivity sounding curves over landfill sites in different geographical regions are consistent with this model. The elements of the model can be easily tested in practical settings. It is stressed that the reliability of any geoelectrical predictions depends on the uniqueness of the reconstructed resistivity distribution for the given landfill site. The use of joint electrical and electromagnetic data for landfill resistivity characterization or integrated surface and borehole resistivity imaging is highly recommended for improved model identification.

11.4.2. EMERGING METHODS AND FUTURE CHALLENGES

Non-contained landfill sites generating leachate pose a threat to groundwater aquifers, and there is a need for reliable non-intrusive methods for tracking the depth distribution of leachate at such sites. The key questions of topical interest in landfill research are: (i) Can we deduce the concentration of total dissolved solids in a leachate plume or the age of leachate-formation from remote geophysical measurements, and how accurate are the predictions in comparison with the hydrochemical data from direct measurements on samples from existing boreholes? (ii) Can we use geoelectrical measurements to accurately predict the redox potential in leachate-contaminated groundwater (Timm and Moller, 2001; Naudet et al., 2003) on a routine basis, and what are the implications for non-invasive monitoring of biodegradation of organic matter? (iii) Can dynamic variations in the physical properties of the host

aquifer, as are expected to occur during the passage of a leachate front or during the remediation of a polluted landfill environment, be monitored using a non-invasive geoelectrical approach?

There is every indication that electrical conductivity is the physical property most affected by fluid or thermal variations in the subsurface. It is thus possible to locate and monitor contaminant plumes in landfill sites using surface/borehole electrical and electromagnetic geophysical measurements and advanced tomographic image reconstruction. Landfill leachate plumes typically show marked zoning at depth, for example, in chloride and TDS concentrations. Given that variations in electrical conductivity in the invaded substrate are known to correspond with changes in the total dissolved solids and/or chloride concentration in such environments, it is possible to predict some hydrochemical parameters and fluid migration patterns from accurate electrical conductivity models of the subsurface and time-lapse studies. Electromagnetic (TEM and RMT) and electrical resistivity/IP methods are now used, either singly or in combination, to characterize old covered landfill sites. However, the complexity of landfill environments requires combined surface and borehole measurements and the development of realistic joint 3D inversion of electromagnetic (especially TEM) and electrical (especially IP) data. Coupling this with 3D streaming potentials calculation (Revil et al., 1999) should provide better constraints on fluid migration processes in landfill environments. This should be seen as a major challenge for hydrogeophysical characterization of landfill sites. If developed, the penetration and resolving power of the combined approach will permit a major leap in our ability to accurately characterize the electrical conductivity structure and flow regimes in the top 100 m. Developing and applying joint three-dimensional geoelectrical and seismic travel-time imaging (compare Gallardo and Meju 2003, 2004; Gallardo et al., 2005) should also be considered a top priority in time-lapse hydrogeophysical characterization of landfill environments.

Acknowledgements

The constructive reviews of Andrew Binley and Andreas Weller improved this chapter.

References

Baedecker, M.J., and M.A. Apgar, 1984, Hydrochemical studies at a landfill in Delaware, in *Groundwater Contamination*, edited by J. Bredehoeft, National Academy Press, Washington, DC, pp.127–138.

Barker, R.D., 1990. Improving the quality of resistivity sounding data in landfill studies, in *Geotechnical and Environmental Geophysics*, edited by S.H. Ward, Vol. 1, Society of Exploration Geophysicists, pp. 245–251.

Bell, F.G., and C.A. Jermy, 1995. A seepage problem associated with an old landfill in the greater Durban area, in *Waste Disposal by Landfill-GREEN'93*, edited by R.W. Sarsby, A.A. Balkema, Rotterdam, The Netherlands, pp. 607–614.

Bennett, P.C., and D.I. Siegel, 1987. Increased solubility of quartz in water due to complexing by organic compounds, *Nature*, 326, 684–686.

Birks, J., and C.A. Eyles, 1997. Leachate from landfills along the Niagara Escarpment, in *Environmental Geology of Urban Areas*, edited by N. Eyles, Geological Association of Canada, Chap. 24, pp. 347–363.

Buselli, G., C. Barber, G.B. Davis, and R.B. Salama, 1990. Detection of groundwater contamination near waste disposal sites with transient electromagnetic and electrical methods, in *Geotechnical and Environmental Geophysics*, Vol. II, edited by S.H. Ward, SEG, Tulsa, OK, pp. 27–39.

Buselli, G., G.B. Davis, C. Barber, M.I. Height, and S.H.D. Howard, 1992. The application of electromagnetic and electrical methods to groundwater pollution problems in urban environments, *Explor. Geophys.*, 23, 543–556.

Carpenter, P.J., S.F. Calkin, and R.S. Kaufmann, 1991. Assessing a fractured landfill cover using electrical resistivity and seismic refraction techniques, *Geophysics*, 56, 1896–1904.

Carpenter, P.J., R.S. Kaufmann, and B. Price, 1990. Use of resistivity soundings to determine landfill structure, *Ground Water*, 28, 569–575.

Dearlove, J.P.L., 1995. Geochemical interaction processes between landfill clay liner materials and organo-metallic landfill leachate, in *Waste Disposal by Landfill-GREEN'93*, edited by R.W. Sarsby, A.A. Balkema, Rotterdam, The Netherlands, pp. 409–414.

DoE, 1996. Long-term monitoring of non-contained landfills: Burnstump and Gorsethorpe on the Sherwood Sandstone, edited by K. Lewin, C.P. Young, N.C. Blakey, P. Sims, and P. Reynolds, Department of the Environment, U.K., Published Report CWM 139/96.

Ebraheem, M.W., E.R. Bayless, and N.C. Krothe, 1990. A study of acid mine drainage using earth resistivity measurements, *Ground Water*, 28, 361–368.

Everett, L.G., L.G. Wilson, and E.W. Hoyleman, 1984. Vadose zone monitoring for hazardous waste sites: Pollution Technology Review, vol. 112, Noyes Data Corporation, New Jersey, 358 p.

Fang, H.Y., 1995. Engineering behaviour of urban refuse, compaction control and slope stability analysis of landfill, in *Waste Disposal by Landfill-GREEN'93*, edited by R.W. Sarsby, A.A. Balkema, Rotterdam, The Netherlands, pp. 47–72.

Farquhar, G.J., 1989. Leachate: Production and characterisation, *Can. J. Civ. Eng.*, 16, 317–325.

Gallardo, L.A., and M.A. Meju, 2003. Characterisation of heterogeneous near-surface materials by joint 2D inversion of dc resistivity and seismic data, *Geophys. Res. Lett.*, 30 (13), 1658–1661.

Gallardo, L.A., and M.A. Meju, 2004. Joint two-dimensional dc resistivity and seismic traveltime inversion with cross-gradients constraints, *J. Geophys. Res.*, 109, B3, B03311, doi: 10.1029/2003JB002716.

Gallardo, L.A., M.A. Meju, and M.A. Flores-Perez, 2005. A quadratic programming approach for joint image reconstruction: Mathematical and geophysical examples, *Inverse Prob.*, 21, 435–452.

Hall, C.D., and A.J.T. Gilchrist, 1995. Steeply sloping lining systems – stability considerations using reinforced soil veneers, in *Waste Disposal by Landfill-GREEN'93*, edited by R.W. Sarsby, A.A. Balkema, Rotterdam, The Netherlands, pp. 427–431.

Herwanger, J.V., C.C. Pain, A. Binley, C.R.E. de Oliveira, and M. Worthington, 2004. Anisotropic resistivity tomography, *Geophys. Int.*, 158, 409–425.

Knight, M.J., J.G. Leonard, and R.J. Whiteley, 1978. Lucas Heights solid waste landfill and downstream leachate transport – a case study in environmental geology, *Bull. Int. Assoc. Eng. Geol.*, 18, 45–64.

Kovacic, D., D. Mayer, and I. Muhovec, 1995. Geotechnical characteristics of Zagreb waste disposal site and possibilities of its reclamation, in *Waste Disposal by Landfill-GREEN'93*, edited by R.W. Sarsby, A.A. Balkema, Rotterdam, The Netherlands, pp. 543–547.

Laine, D.L., J.O. Parra, and T.E. Owen, 1982. Application of an automatic earth resistivity system for detecting groundwater migration under a municipal landfill: In: *Proc. NWWA Conf. on Surface and borehole geophysical methods in groundwater investigations*, Feb. 12–14, 1982, pp. 34–51.

MacFarlane, D.S., J.A. Cherry, R.W. Gillham, and A. Sudicky, 1983. Migration of contaminants in groundwater at a landfill: A case study, *J. Hydrol.*, 63, 1–29.

Meju, M.A., 1996. Joint inversion of TEM and distorted MT soundings: Some effective practical considerations, *Geophysics*, 61, 56–65.

Meju, M.A., 2000. Geoelectrical investigation of old/abandoned, covered landfill sites in urban areas: Model development with a genetic diagnosis approach, *J. Appl. Geophys.*, 44, 115–150.

Meju, M.A., 2002. Environmental geophysics: Conceptual models, challenges and the way forward, *The Leading Edge*, 21 (5), 460–464.

Meju, M.A., 2005. Simple relative space-time scaling of electrical and electromagnetic depth sounding arrays: Implications for electrical static shift removal and joint DC-TEM inversion with the most-squares criterion, *Geophys. Prospect.*, 53, 463–479.

Naudet, V., A. Revil, and J.-Y. Bottero, 2003. Relationship between self-potential (SP) signals and redox conditions in contaminated groundwater, *Geophys. Res. Lett.*, 30 (21), 2091, Doi: 10.1029/2003GL018096.

Naudet, V., A. Revil, E. Rizo, J.-Y. Bottero, and P. Begassat, 2004. Groundwater redox conditions and conductivity in a contaminant plume from geoelectrical investigations, *Hydrol. Earth Syst. Sci.*, 8 (1), 8–22.

Oehler, D. Z., and B.K. Sternberg, 1984. Seepage-induced anomalies, “false” anomalies, and implications for electrical prospecting, *Am. Assoc. Pet. Geol. Bull.*, 68 (9), 1121–1145.

Oehler, D. Z., and B.K. Sternberg, 1982. Induced polarization for hydrocarbon exploration: Geochemical/geological interpretation, in *Technical program abstracts and biographies, 52nd Annual International Society of Exploration Geophysicists Meeting and Exposition*, Dallas, TX, pp. 445–448.

Ostrander, A.G., N.C. Carlson, and K.L. Zonge, 1983. Further evidence of electrical anomalies over hydrocarbon accumulations using CSAMT: Expanded Abstracts and Biographies, in *53rd Annual International Society of Exploration Geophysicists Meeting and Exposition*, Las Vegas, pp. 60–63.

Revil, A., H. Schwaeger, L.M. Cathles, and P.D. Manhardt, 1999. Streaming potentials in porous media: 2. Theory and application to geothermal systems, *J. Geophys. Res.*, 104, 20,033–20,048.

Ross, H.P., C.E. Mackelprang, and P.M. Wright, 1990. Dipole–dipole electrical resistivity surveys at waste disposal study sites in Northern Utah, in *Geotechnical and Environmental*

Geophysics, edited by S.H. Ward, Vol. 2, Society of Exploration Geophysicists, Tulsa, USA, pp. 145–152.

Sanchez-Alciturri, J.M., J. Palma, C. Sagaseta, and J. Canizal, 1995. Mechanical properties of wastes in a sanitary landfill, in *Waste Disposal by Landfill-GREEN'93*, edited by R.W. Sarsby, A.A. Balkema, Rotterdam, The Netherlands, pp. 357–363.

Sasaki, Y., and M.A. Meju, 2006. Three-dimensional joint inversion for magnetotelluric and static shift distributions in complex media, *J. Geophys. Res.*, 111, xxxxxx, doi: 10.1029/2005JB004009 (in press).

Sowers, G.F., 1968. Foundation problems in sanitary landfill, *J. Sanit. Eng. Div. Proc. ASCE*, 94 (1), 207–210.

Spitzer, K., 2001. Magnetotelluric static shift and direct current sensitivity, *Geophys. J. Int.*, 144, 289–299.

Tezkan, B., M. Goldman, S. Greinwald, A. Hordt, I. Muller, F.M. Neubauer, and G. Zacher, 1996. A joint application of radiomagnetotellurics and transient electromagnetics to the investigation of a waste deposit in Cologne (Germany), *J. Appl. Geophys.*, 34, 199–212.

Timm, F., and P. Moller, 2001. The relation between electric and redox potential: An evidence from laboratory to field experiments, *J. Geochem. Explor.*, 72, 115–127.

Wasti, Y., 1995. Municipal plans for solid waste disposal in Turkey, in *Waste Disposal by Landfill-GREEN'93*, edited by R.W. Sarsby, A.A. Balkema, Rotterdam, The Netherlands, pp. 195–203.

Weller, A., W. Frangos, and M. Seichter, 2000. Three-dimensional inversion of induced polarization data from simulated waste, *J. Appl. Geophys.*, 44, 67–83.

Whiteley, R.J., and C. Jewell, 1992. Geophysical techniques in contaminated lands assessment: Do they deliver? *Explor. Geophys.*, 23, 557–565.

Witmer, K.A., J. Volk, and D. Naik, 1984. Low-cost ground improvement technique for landfill area, in *Proceedings of Low-cost and Energy Saving Construction Materials*, pp. 497–516.

Yamamura, K., 1983. Current status of waste management in Japan, *Waste Manage. Res.*, 1, 1–15.

Zhang, J., R.L. Mackie, and T.R. Madden, 1995. 3-D resistivity forward modelling and inversion using conjugate gradients, *Geophysics*, 60 (5), 1313–1325.

12. CHERNOBYL-BORN RADIONUCLIDES: GROUNDWATER PROTECTABILITY WITH RESPECT TO PREFERENTIAL FLOW ZONES

Vyacheslav M. Shestopalov, Yuriy F. Rudenko, Alexander S. Bohuslavsky,
and Volodymir N. Bublias

12.1. Introduction

A significant increase of technogenous load on the environment caused by aerosol fallout of heavy metals consisting of industrial atmospheric injections and automobile exhaust gases, wide use of pesticides and fertilizers in agriculture, as well as the threat of radioactive contamination as a result of nuclear weapons tests and danger of nuclear war have led to apprehensions of the possible contamination of shallow groundwater that occurs over wide areas and intensively used for the water supply of villages, small settlements and farms.

The necessity of groundwater protectability assessments was acknowledged and implemented in several countries – France, Czechoslovakia, Germany, USA, USSR, etc. in 1960–1990 (Aller et al., 1987; Rosen, 1994; Rundquist et al., 1991).

Most methodologies of groundwater protectability assessments accounted for the protective role of the unsaturated zone, its thickness and lithologic composition. Later (Belousova and Galaktionova, 1994; Zektser, 2001; Pashkovsky, 2002), the protective capability of soils was also considered. For protectability determination, either conventional numbers, or the “arrival time” of the contamination front were used.

The Chernobyl disaster resulted in radioactive contamination of soils over huge areas, and soon after the accident, for the first 1–5 years, initial traces of groundwater contamination by Chernobyl-born radionuclides were revealed. Soon after the catastrophe, the problem of groundwater protectability in radioactively contaminated areas became of the greatest practical importance (Baryakhtar et al., 1997).

In spite of a large number of research studies on the formation of groundwater resources (Shestopalov, 1979, 1981), and processes of exogenic contaminant migration into the subsurface hydrosphere (Lukner and Shestakov, 1988; Mironenko et al., 1988; Mironenko and Rumynin, 1999; Pashkovsky, 2002; Schnoor, 1992), not enough attention has yet been paid to preferential pathways of groundwater flow and migration.

The very low degree of study of different types of preferential flow zones (PFZ) in the upper geological medium during regional research is related, first of all, to their prevailing relatively small dimensions as compared to the total research area.

In groundwater resource assessments, insufficient attention to zones with abnormally high vertical water exchange leads to the “reliability reserve” of calculated forecast resources, and therefore it is justified in view of diminishing expenses for research. However, when studying possible groundwater contamination, such approaches may lead to significant underestimates of predicted risks, as compared to their real values.

Meanwhile, the presence of permeability anomalies in the structure of the geological environment is one of its main features controlled by the structural-geodynamic heterogeneity and regularities of regional development, as well as by related exogenic processes.

The concept of preferential flow of solutes in heterogeneous soils has been described at least since Lawes et al. (1882). Later on, observations of finger-like infiltration pathways in aeolian sands during heavy rainfalls were made by Gripp (1961) in Germany and Lyall (1969) in Canada. Raats (1973) and Phillip (1975) explained these phenomena with unstable wetting front theories.

It is worth noting that research into preferential infiltration and migration pathways was initiated in most cases by agricultural practice, including problems of groundwater contamination with pesticides and nitrates (Shuford et al., 1977; Parlange et al., 1988). For this reason, most authors mainly described soils down to a depth of 0.3–1 m, and the preferential flow phenomenon was associated with heterogeneity of the soil pore space, or macropore flow (Bouma, 1981; Beven and Germann, 1982), and heterogeneous finger-like moisture distribution in layered soils (Glass et al., 1989; Baker and Hillel, 1990). Some authors described preferential flow through the unsaturated zone to a depth of 5–10 m and more (Kung, 1990; Singh and Kanwar, 1991). Significant efforts were devoted to the theoretical and modeling aspects of the problem (Hillel and Baker, 1988; Nieber et al., 1993; Nieber, 1996).

All the contributions mentioned above described the preferential flow phenomena and their possible mechanisms on the detailed scale of soil sections, local sites, etc., and no attention was paid to the regional aspects of the problem. In particular, questions related to the preferential transport of groundwater contaminants were not taken into account in regional assessments of groundwater vulnerability and protectability (Aller et al., 1987; Vrba and Zaporozec, 1994; Rosen, 1994; Rundquist et al., 1991; Belousova and Galaktionova, 1994; Goldberg, 1983; Zektser, 2001; Pashkovsky, 2002).

In the present work, based on the results of field observations of groundwater contamination with Chernobyl-born ^{137}Cs and ^{90}Sr performed in the Chernobyl Exclusion zone (CEZ) and Kyiv conurbation during the post-accidental period, an attempt is made to account for vertical preferential flow and downward migration of radionuclides in corresponding preferential flow zones in the upper geological medium. In this connection, the questions of regional-scale groundwater protectability and vulnerability assessments are considered in detail.

12.2. Chernobyl-Born Radionuclides in the Geological Environment

According to the results of numerous previous studies (Borzhilov, 1989; Baryakhtar et al., 1997), it was supposed that radioactive contamination coming to the soil surface by atmospheric fallout is concentrated in the upper soil layer, and its lower boundary gradually deepens with time. It is obvious that different-scale heterogeneities of the geological medium, as well as relief variability, result in the existence of various preferential pathways of water infiltration and radionuclide migration from the contaminated soil into the groundwater. Such pathways are distinguished from the average “background” geological medium by the intensity of the migration process, as determined by different velocities of downward radionuclide migration from the upper soil layers into unsaturated zone and groundwater aquifers.

The fact of the penetration of Chernobyl ^{137}Cs and ^{90}Sr into relatively deep groundwater aquifers has been demonstrated by numerous groundwater sampling data obtained from the main aquifers in the Chernobyl and Kyiv regions (Shestopalov et al., 1992, 1997). Depending on hydrogeological conditions and the technogenous situation (water intake operation, etc.), Chernobyl-related groundwater contamination by ^{137}Cs and ^{90}Sr is presently observed at different concentrations in practically all regions where surface contamination initially occurred. According to sampling data obtained in 1992–1997 (over 700 ^{137}Cs and 500 ^{90}Sr samples taken from wells in the Kyiv and Chernobyl regions except for the immediate vicinity of Chernobyl Nuclear Power Plant (NPP)), in the groundwater of the main aquifers in the Kyiv region used for the water supply the concentrations reach 100 mBq/dm³ and more (Table 1).

The areal distribution of ^{137}Cs and ^{90}Sr concentrations in groundwater of the upper Quaternary aquifer (depths to 30 m) within the Kyiv region as plotted for 1996 is shown in Figure 1.

In the Quaternary aquifer, the maximum groundwater contamination with ^{137}Cs is observed in the northern part of the region showing good correlation with surface contamination density, which increases as it approaches

TABLE 1. Concentrations of ^{137}Cs and ^{90}Sr in groundwater of Kyiv regional aquifers given as percentage of total samples in the aquifer for given concentration ranges

Aquifer (age)	Depth interval, m	^{137}Cs , mBq/dm 3				^{90}Sr , mBq/dm 3		
		<10	10–50	51–150	>150	<10	10–50	>50
Quaternary	2–20	41%	44%	11%	4%	53%	42%	5%
Eocene	45–65	43%	45%	9%	3%	74%	21%	5%
Cenomanian- Callovian	80–150	50%	36%	8%	6%	80%	20%	–
Bajocian	200–300	51%	36%	7%	6%	75%	24%	1%

the Chernobyl NPP. For ^{90}Sr , which is characterized by its higher migration ability as compared to ^{137}Cs , relatively high concentrations in groundwater were found not only in the northern part of the region, but also around Kyiv City where the depression cone generated by intensive exploitation of groundwater of deeper (Cenomanian-Callovian and Bajocian) aquifers has led to increased recharge intensity of the Quaternary aquifer and related downward migration of radionuclides.

At the end of eighties, measurable concentrations of the short-lived isotope ^{134}Cs (half-life period = 2 years) were discovered in the valley of the Desna River in the groundwater of several artesian wells springing from the Eocene aquifer (depth 40–60 m) in the close vicinity of Kyiv. In this case, it is clear that the technogenous hypothesis of penetration of the radionuclide by annular well-casing space is of low probability, and that there is no other way of its penetrating to the aquifer than vertical downward migration from the contaminated surface in the corresponding groundwater recharge area. This fact indicates, first, the Chernobyl-related origin of the contamination. Secondly, in order to penetrate to such depths, the downward velocity of the radionuclide transport should amount to 10–15 m/year or even more.

Such high velocities testify to the existence of the preferential vertical flow and transport pathways in the upper sedimentary cover, probably related to disintegration zones of neotectonic activity. Facial, mineralogical and granulometric heterogeneities of the covering deposits are also of great importance. Consequently, the discovering of radioactive isotopes and other contaminants of undoubtedly surface sources (radionuclides and pesticides) is evidence of the existence of PFZ in the upper geological environment.

In 1996–1998, a series of determinations was performed of ^{137}Cs solid-phase concentrations in core samples from specially drilled boreholes of depths down to 100 m within the Kyiv conurbation area. These measurements showed noticeable contamination of deposits with concentrations from

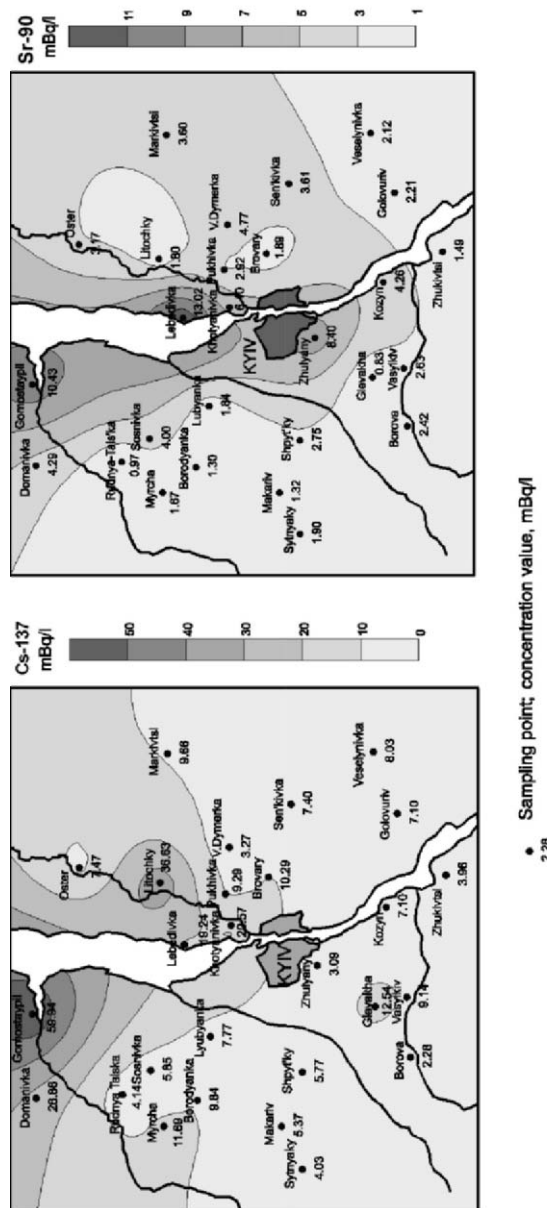


Figure 1. Distribution of ^{137}Cs (left) and ^{90}Sr (right) concentrations in Quaternary aquifer in the Kyiv conurbation, 1996

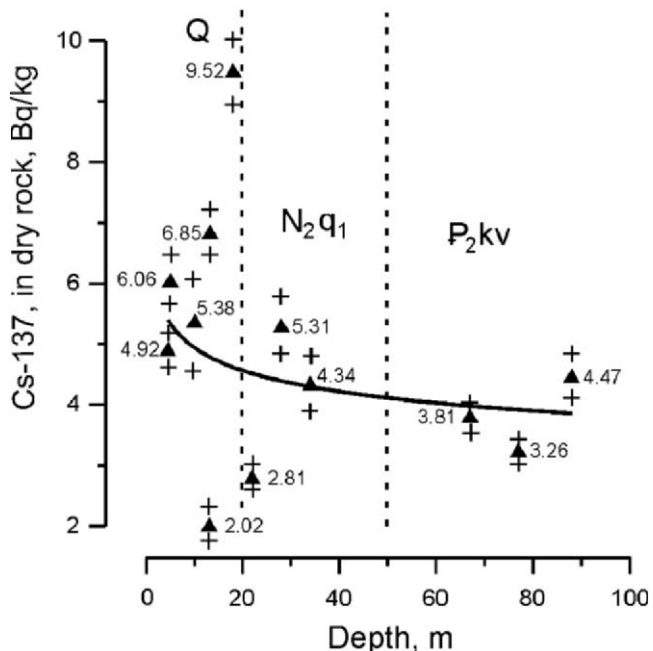


Figure 2. Content of ^{137}Cs (Bq/kg) in core samples from a borehole at the southern margin of Kyiv City (Teremki). Crosses show possible error range; curve shows logarithmic approximation of vertical concentration distribution; Q – Quaternary deposits; $\text{N}_{2\text{q}1}$ – Neogene deposits; $\text{P}_{2\text{kv}}$ – Paleogene deposits

1 to 10 Bq/kg (Shestopalov, 2002). The corresponding vertical concentration plotted against depth (logarithmic fit) for one of these boreholes (south-west part of Kyiv conurbation) is shown in Figure 2.

A series of ^{137}Cs solid-phase concentration measurements in core material from the Quaternary boreholes was also performed in the CEZ. A corresponding typical vertical concentration profile is shown in Figure 3 (Chistogalovka village, borehole 188/4, depth 30 m).

Along with a core sample study, several series of deposit samples were analyzed that had been taken from the lower part of the Kyiv marl bed (depth 80 m) during tunnel driving in the course of constructing the Kyiv subway. The results of ^{137}Cs content determinations are shown in Figure 4. The solid-phase concentration of the radionuclide varies from 0.2 to 2.7 Bq/kg increasing along the section in the direction of the Syrets creek valley characterized by increased permeability of the deposits formed. Previously an increased content of pesticides had also been discovered at this location (Shestopalov, 1988).

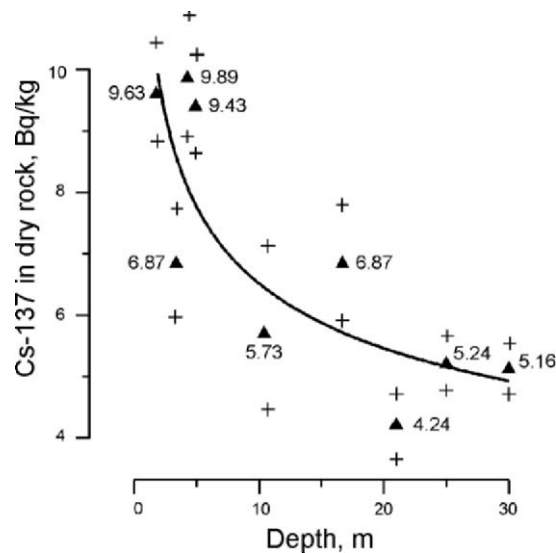


Figure 3. Vertical distribution of ^{137}Cs solid-phase obtained by core samples from borehole No 188/4 (CEZ, Chistogalovka village). Crosses show range of possible measurement errors

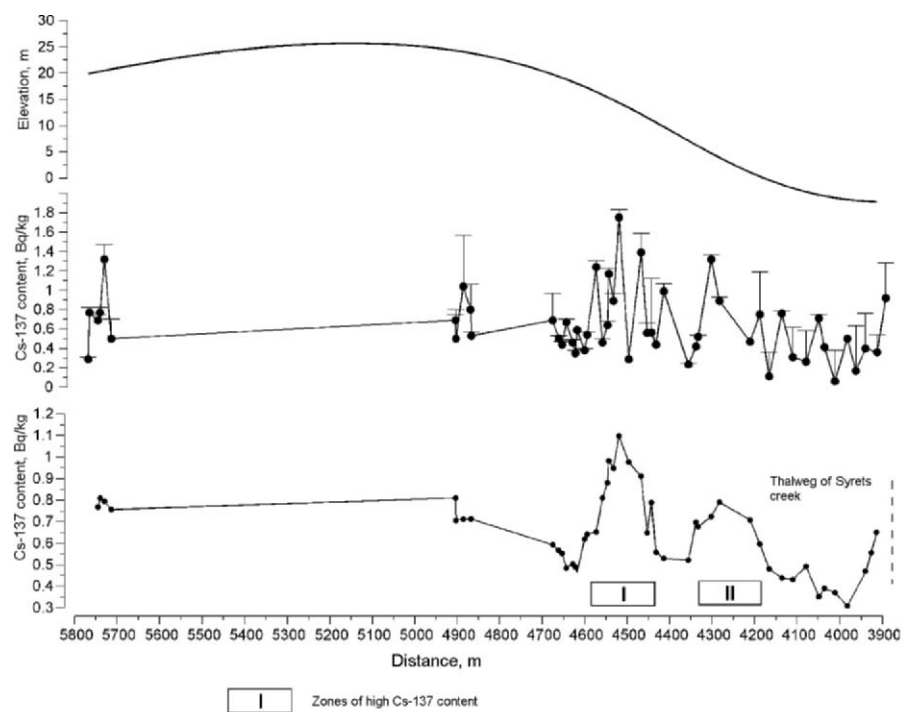


Figure 4. Distribution of ^{137}Cs (Bq/kg) in Kyiv marls (depth 80 m) plotted by sampling data obtained during drilling of tunnels for Kyiv subway between “Zoloti Vorota” and “Dorogozhichi” stations. Upper curve shows variation of the relief

From the viewpoint of mass balance, physico-chemical and modeling considerations, the revelation of measurable ^{137}Cs concentrations in liquid and solid phases at such depths is an interesting fact requiring the implementation of additional field and modeling studies.

The only possible explanation for these observation results is the existence of PFZs of different dimension ranges with preferential vertical pathways of downward radionuclide migration characterized by specific values of migration and geochemical parameters in the geological medium, as compared to the background areas.

12.3. PFZ Typification

A series of studies during last few decades were devoted to various types of preferential flow phenomena differentiated by their physical mechanisms. They include: macropore flow (Bouma, 1981; Beven and Germann, 1982; Singh and Kanwar, 1991), gravity-driven unstable flow (Hill, 1952), heterogeneity-driven flow (Kung, 1990), oscillatory flow (Prazak et al., 1992). All the above-mentioned cases of preferential flow have relatively small scale ranging from 10^{-2} to 10 m (Nieber, 2001). As a larger-scale process, the depression-focused recharge should be mentioned, with characteristic dimensions from 10^{-1} to 10^3 m. This type of flow is well known to hydrogeologists, and has been studied experimentally (Lissey, 1971) and theoretically (Nieber et al., 1993).

Helling and Gish (1991) used representations described earlier by Landon (1984) and proposed a general classification of the pore space and pore functions, including dimensions from 10^{-4} to 10^4 mm. Greenland (1977) showed that pores with dimensions of less than 10^{-1} m mainly have the function of joint capacity.

PFZ typification in the geological medium may be done with respect to: 1) genesis and corresponding degree of involvement of stored water exchange zones; 2) morphometry (surface, vertical section); 3) degree of activity; 4) degree of involvement of elements of the water exchange geosystem; 5) direction and character of development.

By means of morphometric indexes, they may be classified into megazones (subregional) with dimensions ranging within 10–100 km, macrozones – 1–10 km, mesozones – 0.3–1 km, nanozones – 1–10 m, picozones – 0.1–1 m, femtozones – < 0.1 m. The megazones are usually contoured in the large-scale studies.

In the medium and detailed-scale studies, the smaller forms such as macro-, meso- and microzones with dimensions from 10 to 10^4 m, can be contoured and studied in detail.

Nano- and pico-forms (and smaller) are usually not reflected, or only weakly distinguished in the relief. Their heterogeneity is determined by the character of sedimentogenesis and diagenesis of rocks and soils, and the influence of geo-biocenoses.

According to their genesis, the PFZs may be classified into two large groups: exogenic and endogenic. The first are related to peculiarities of erosion, glacial, karst, suffusion processes, influence of biocenoses and technogenic disturbances on the structure of the soil layer and unsaturated zone. The second are determined by the character of the distribution and development of geodynamic stresses of the earth's crust and lithofacial peculiarities of deposits. Because of the long-term influence of endogenic factors, they often lead to the appearance and imposition of exogenous processes on the endogenous formation of the PFZ. As a result, in many cases it is possible to distinguish a third group of zones – of mixed genesis, formed under the influence of internal and external forces, but with the leading role played by endogenic stresses and processes. The presence of endogenic geodynamic factors in the formation of PFZs determines their maximum depth range (hundreds and thousands of meters). Endogenic lithofacial factors of PFZ formation usually determine their lower depths (mainly meters and tens of meters). Even smaller depths are characteristic of the exogenic PFZs (usually within one meter). By means of morphometric peculiarities, PFZ may be classified into plane – to linear, round; in section – to window-like, vein-like, fracturing, elementary (filled or not filled), etc.

By filtration and migration activity, PFZs can be subdivided into hyper-active with more than a ten-fold increase of filtration and migration processes as compared to background sites; very active – with a 5- to 10-fold increase of these processes as compared to background values; medium-active (2–5 times higher than background); and low-active (<2 times higher than the background). It is worth noting that the filtration and migration activities, depending on the deposit composition and migrant type, may not correlate. In addition, they can vary in time under the influence of natural and technogenic impacts determining variations of the water exchange intensity and ingress into the aquifer system of different substances, including contaminants.

By the involvement of elements of the hydrogeological system (soil, unsaturated zone, upper groundwater, deep confined aquifers and aquitards), it is possible to distinguish the following PFZ types: 1) through – with complete or high involvement of the main water exchange geosystem elements; 2) meso-deep with involvement of soils, unsaturated zone and one or two aquifers; 3) subsurface (aeration) – with involvement of soil, unsaturated zone, and possibly part of the upper aquifer (in the case of a thin unsaturated zone); 4) soil – located within the soil cover. By evolution, one can distinguish stable, progressing, and degrading PFZs.

As an example of a picozone in sedimentary granular rock, a result can be mentioned obtained by sampling of sandy soils with low humus content taken from a pit of dimensions 1×1.1 m with a sampling frequency grid of 10×10 cm (Shestopalov et al., 2001). The samples were analyzed for soil concentration of ^{90}Sr , soil humidity and mechanic composition. The distribution of ^{90}Sr concentration in soil did not correspond to the average front of the radionuclide concentration and distribution of the moisture content. This example shows the complexity of the soil structure and mechanisms of the radionuclide migration in it. In medium-scale and large-scale studies, such zones are not usually considered.

In hard rock massifs, the macro-, nano-, and picozones of increased permeability related to fracturing are also known. However, their role as zones of preferential flow and mass exchange is usually assessed only integrally.

12.4. Studying Depression-Related PFZs

Our research is concentrated on the study of micro- and mesozones of preferential flow (70–500 m in diameter) represented in the present relief as closed depressions of different shapes. They occur frequently in the relief of plain areas, and are found in Ukraine, Poland, Germany, Russia, Canada, and many other countries.

Studies of the micro- and mesozones of the depression type were made at several stationary, specially equipped observation plots within the CEZ and Kyiv region (Shestopalov, 2001). As a methodological background, morphogenetic principles of study were used, consisting in revealing, on the one hand, the morphometric characteristics of depressions, and, on the other hand, their genetic properties – conditions, processes, and formation factors, as well as the present state, position, and significance in the landscape structure. For the determination of the qualitative and quantitative characteristics of the most mobile and representative component of the migration process – the liquid phase solutions containing dissolved or suspended matter – hydrophysical and chemical methods were used enabling the water-solute regime, flow rate and balance of pore liquid to be controlled in natural and laboratory conditions. The degree of transformation of rocks in the PFZ was determined by the morphological characteristics of rocks, their chemical, mineralogical, and granulometric composition, and by variation of the structure of elementary rock particles.

The structural peculiarities of the area were studied using materials from aerospace image decoding. This method is based on the idea that the present and most recent tectonic movements are “inherited” from the historical development stages of the earth’s crust. In such a way, the principal

components of present landscape (relief, hydrographic network, lithological composition of Quaternary deposits, soil-plant cover, etc.) should inherit (as an approximation) the main features of the internal structure of the geological environment.

12.4.1. COMPLEX GEOPHYSICAL STUDIES

Existence of a definite areal zonality in the present state of the earth crust's was revealed in the last few decades as a result of the appearance of essentially new research methods, in particular, direct methods of natural stress measurement in the geological rock massif (Shtengelov, 1979). This work provides evidence of the existence of very complicated geodynamic structure related to the presence of tectonic stress deformations. For this reason, in order to clarify the structural peculiarities and geodynamic state of the PFZ, as well as the probable pathways of groundwater flow and contamination, we used a complex of geophysical methods including georadar (depth to 10 m), short-impulse electromagnetic (depth to 500 m), seismoacoustic (depth to 50 m), and gas-emanation profiling (Shestopalov, 2001, 2002). The results of the georadar and emanation profiling for the typical depression, "Stary Shepelichi," are shown in Figure 5.

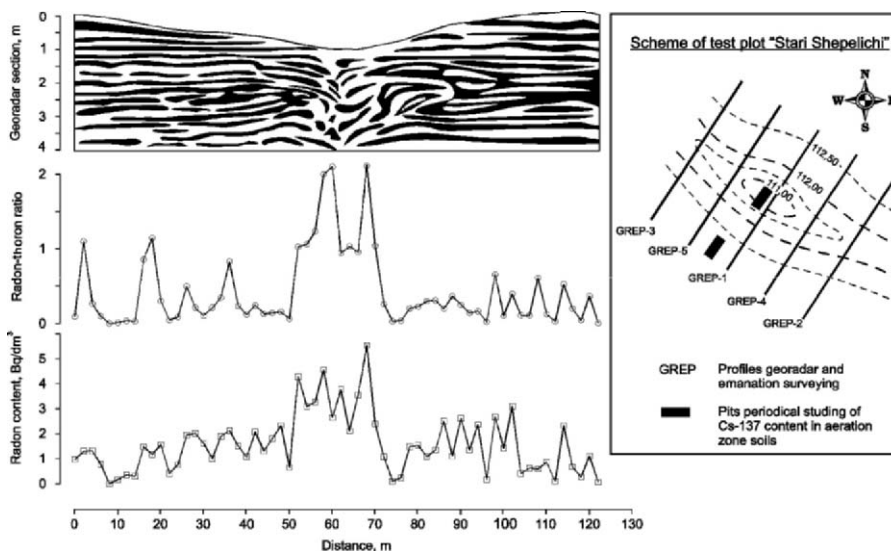


Figure 5. Results of complex geophysical research (georadar GREP-1 profile), relief, radon content, radon-thoron ratio) at specially equipped observation plot "Stary Shepelichi" (close to the CEZ)

The *georadar* observations were performed using the "SIR-2" equipment (antenna operating at 300 MHz frequency) with a continuous survey along parallel profiles spaced 5 m apart and 2 m between piquets. The signal processing was accomplished using the special "RADAN" program. The material obtained is of a qualitative character depicting structural peculiarities of the section under study and revealing zones with disturbed (disintegrated) deposit structure. Figure 5 shows the profile for the central section GREP-1 across the depression.

The structure of disintegration zones and some of their anomalous properties (degree of fragmentation) are well traced using the detailed *emanation profiling* – determination of the content of radioactive gases radon (^{222}Rn) and thoron (^{220}Tn) in the gas samples taken in the subsurface layer (sampling depth 1 m). The radioactive emanations of radon and thoron are released from radium isotopes dispersed in sedimentary rocks. The method is used for revealing geodynamical zones where free gases move by diffusion and convection in covering deposits from zones of tectonic disintegration. Such zones reach the surface. The half-live periods of radon and thoron are 3.8 days and 54 s, respectively. With respect to the calculated velocities of these gases, the depth of emanation formation cannot be more than 10 m for radon and 0.5 m for thoron. In order to analyze the gas samples obtained, the alpha-beta analyzer of the NC-4286 gamma-spectrometer was used. In Figure 5, the two plots are shown for the radon concentration and the radon-thoron ratio. During previous studies (Shestopalov, 1988), the latter was found to be a good index of the presence of disintegration zones and intensity of geodynamic processes in the underlying geological medium.

The results of the complex geophysical studies performed show the presence of disintegration zones in deposits of central active parts of the depressions studied.

The infiltration rate and volume of water infiltrating through the unsaturated zone were studied using the hydrophysical and thermodynamic methods by observing the data of suction pressure, hydraulic conductivity and moisture content at definite depths.

Field and laboratory methods were used to study the migration of the Chernobyl-born radionuclides. Field work included measurements of the exposure dose with a field gamma radiometer. For the qualitative and quantitative characterization of radionuclide migration soil sampling for radionuclide content was performed in different morphological elements of the depressions. The soil samples were taken along the horizontal and vertical profiles with a degree of detail corresponding to the complexity of the relief. The radionuclide content in groundwater was studied by data obtained by sampling in the regime wells.

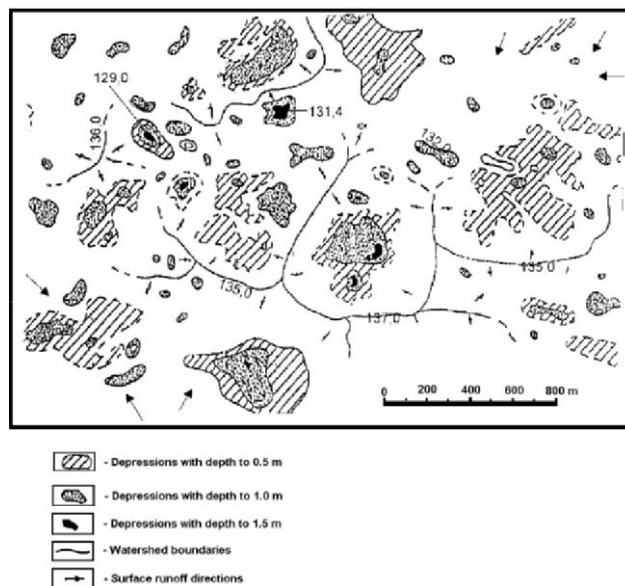


Figure 6. Location scheme of depressions for a typical sandur plain area of the CEZ

It is obvious that the majority of depressions are genetically related to main landscape types, and appeared as the result of different exogenic processes. For example, in floodplains falcated depressions occur widely and are associated with ancient river courses. Within the first floodplain terrace there is a prevalence of round shallow depressions of suffosion and deflation-suffosion origin. In sandur plains, complex (of irregular form in plane) mainly polygenetic depressions occur (Figure 6). Characteristic of moraine uplands are round, oval, often deep glacial-suffusion depressions, as well as runoff gullies formed by processes of finite moraine development.

As a result of implementation of a complex geophysical research, it was found that all depressions studied are associated with tectonically disintegrated zones having deep structural roots. The geophysical data show good correlation with data of remote observation (aerial photography) revealing the correspondence of depression locations to tectonic disintegration zones. Data from remote observations also confirm the correspondence of the majority of depressions to linear geodynamic zones (Figure 7).

Depressions serve as local bases of erosion and runoff. They form local catchments of surface water accumulating in the central lowest parts of depressions. It is found that a depression system may capture up to 60–80% of surface runoff within interfluvial plain areas, in view of the fact that this runoff is formed only during spring snow melt and intensive rainfalls. The

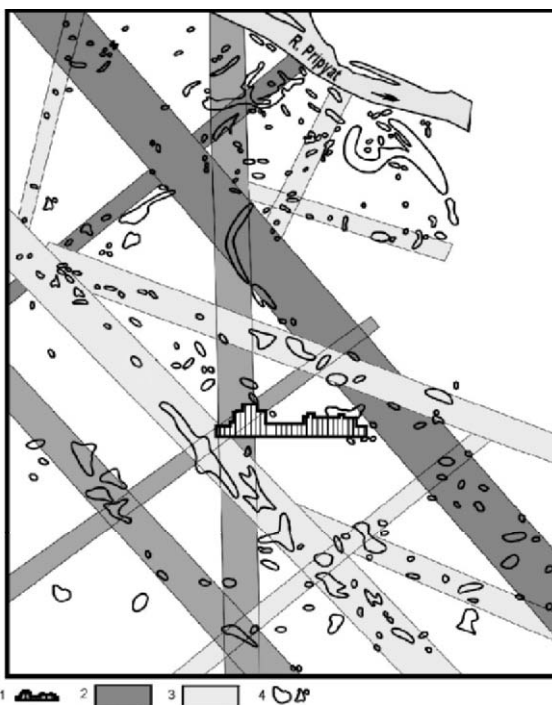


Figure 7. Scheme of correlation between the depression microrelief and geodynamic zones in the area adjacent to the Chernobyl NPP: 1 – Chernobyl NPP; 2 – geodynamic zones revealed by geophysical methods; 3 – geodynamic zones located by data from aerospace image decoding; 4 – depressions

structure of soils in depressions is of a complicated character (Figure 8). The following concentric zones are distinguished in the types of developing depressions under consideration according to the characteristics of vertical flow activity: central active (1), central passive (2), near-border active (3), slope (4,5), and background.

The central and near-border active zones are related to paleocryogenic rock disturbances and retain traces of the most active rock leaching and movement of the most mobile substances from the upper to lower layers of unsaturated zone until they reach the groundwater table. Characteristic of this zone is absence or minimum concentrations of easily soluble minerals, degraded aggregate rock structure, presence of ferruginous seams (goethite, hydrogoethite), which due to their vertical texture indicate comparatively high activity of hydrogenic geochemical processes in the active zones (see Figure 8, layer B, zones 1,3).

Studies of groundwater level variation show that during low-water periods depression cones are formed in the active central parts of some depressions.

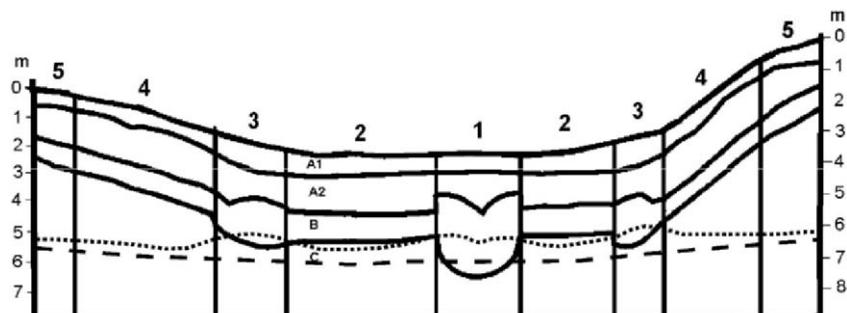


Figure 8. Complex scheme of geological section (160-m wide) across a characteristic depression (Lyutezh observation plot, northern part of Kyiv region) with morphological-lithostratigraphic depression elements: Layers: A1, A2- sod-meadow (zones 1,2) and sod-podzolic (zones 3-5) soils; B-ferruginous seams, C-sands of different granularity and loamy sands. Concentric zones: 1 – central active; 2 – central passive; 3 – near-border active; 4, 5 – slope. Dashed line shows long-term average groundwater level; dotted line – groundwater level in summer period after rainfall

In other depressions, a spreading cupola is formed under active zones during intensive rainfall in the summer period (Figure 8). These phenomena give evidence of the existence, on the one hand, of higher permeability of deposits in the central parts of depressions and good conditions of water discharge, and, on the other hand, of intensive downward flow of water through central parts of depressions into the groundwater.

According to data from regime observations and results of balance assessments, a significant part of surface runoff water within the depressions infiltrates into the groundwater. While the average infiltration rate in the background areas ranges from 50–200 mm/year, in the depressions it reaches 700 mm/year (Shestopalov, 2001, 2002).

Accumulation of the surface runoff in depressions leads to increased vertical transport of radionuclides and other contaminants both in a soluble form and also sorbed by suspended soil particles in the active zones of depressions. The soil particles accumulate in soils of depression bottoms and under defined conditions (increased leaching during periods of intensive downward flow) move downward into the aquifer. It was found that the radionuclide concentration and migration rate in the active zones of depressions is several times higher than at background sites. Studies of the variation of ^{137}Cs and ^{90}Sr concentrations in the deposits of unsaturated zone in depressions during the period 1987–2002 have shown (Shestopalov, 2001): 1) intensive transport of radionuclides proceeds from the water catchment area of depressions into their active parts; 2) accumulation of radionuclides proceeds with periodical intensity in soils of depression bottoms that leads to 2–4 times higher radioactive contamination of soils as compared to background sites; 3) relatively fast washout

of radionuclides to underlying unsaturated deposits and groundwater; 4) the intensity of horizontal and vertical transport of radionuclides in depressions depends on the intensity of atmospheric precipitation; 5) contamination of deposits in depressions proceeds to greater depths compared to background sites.

12.5. Groundwater Protectability and Vulnerability Assessment

12.5.1. GENERAL CONSIDERATIONS

Serious drawbacks in present assessments of groundwater protectability and vulnerability from surface contamination can be explained by their disregarding some important hydrodynamic and transport processes which have been revealed by recent hydrogeological studies.

Having taken the experimental results for concentrations of such radioisotopes as ^{137}Cs and ^{90}Sr and their slow downward migration in the upper soil layers from soil science, many hydrogeologists treated these results as final, taking no account of the difference between approaches of soil science and hydrogeology. With respect to the study of radionuclide transport, in most cases soil scientists have the objective of studying the exchange of contaminants in the “soil-plant” system, and for this reason their assessments of the intensity and depth of the transport processes are quite satisfactory for their purpose. In many such studies of the behavior of Chernobyl-born radionuclides, they use the concept of the contamination front inside the soil layer, which for a series of radionuclides, including ^{137}Cs , in most cases still has not arrived at the lower soil boundary. In such studies, diffusion models are often used, without any assessment of the advection transport component. Within the scope of their studies, until recently soil scientists were thus right to ignore the fact that in the course of their downward migration a significant part of the radioactive contaminants have already left the soil layer, passed through the unsaturated zone, and contaminated the underlying upper and even deeper confined aquifers to different degrees.

Hydrogeologists, generally accepting the fact of groundwater contamination by radionuclides migrating from the surface, in their assessments continue to use the previous traditional methodologies which do not analyze the disagreement between the results of such assessments and data from observations. The reason for this disagreement consists in disregarding the heterogeneity of the soil and geological medium, existence in the geological medium of the complicated network of preferential moisture flow and transport pathways whose characteristic dimensions vary from millimeters and centimeters to kilometers, involving disturbances of different origin: variations of microorganism activity, dead plant roots, wormholes, micro- and macro-erosion processes, disintegration lineaments of geological medium related to variations of the stress deformation regime, tectonic movements, etc.

It is obvious that in contrast to most problems of soil science, the hydrogeologist, in the course of assessing groundwater protectability and vulnerability, must not only accept the existence of such preferential flow and transport pathways, but also take them into account.

It is clear, however, that quantification of the real input of the preferential flow pathways and zones in total groundwater contamination is a complicated problem which cannot be solved on the basis of general qualitative consideration either of the whole hierachic system of preferential pathways, or each separate element of this system.

Only implementation of special field and experimental research including hydrogeophysical methods (GPR, ERT, ...) enables us to solve this problem taking account of the integral effect of preferential flow pathways on the state of groundwater contamination.

By concentrating their efforts only on achieving the apparent accuracy of accounting for soil properties, lithological differences, and unsaturated zone thickness without any consideration of the role of the overall system of preferential pathways, hydrogeologists inevitably come to erroneous assessments.

It is worth noting that the accuracy of assessments of these two different blocks of field data should be commensurate. Their existing disparity should be balanced and gradually overcome by obtaining additional observation data on preferential migration pathways in the course of future research.

Groundwater *protectability* is taken to mean the complex barrier function of the upper geological medium above the groundwater table – the soil layer and unsaturated zone – for a definite groundwater contaminant, determined by degree of development of both hydraulic (presence of layers with low hydraulic conductivity) and geochemical (presence of deposits or their fractions with high sorption capacity) barriers. Groundwater protectability is a characteristic of covering deposits not related to specific contamination, the intensity and distribution over the given area.

By groundwater *vulnerability* we mean the potential (or forecast) groundwater contamination with a definite pollutant. It is determined not only by the hydraulic and geochemical permeability of soil and unsaturated zone layers, but also depends on the intensity of the contamination source (in our case – the degree of soil contamination).

These concepts are in agreement with representations by Belousova and Galaktionova (1994), Zektser (2001), and other authors.

From our viewpoint, the general algorithm of a realistic methodology of groundwater protectability and vulnerability assessment must be the following:

1. Conducting experiments and observations of real contamination of groundwater and deposits in typical elements of the geological medium (soil, unsaturated and saturated zones, aquifers and aquitards).

2. Modeling assessment of obtained results, assessment of model parameters.
3. Interpolation and extrapolation of parameters in the course of area regioning by typical soils, lithological and thickness characteristics of the unsaturated zone, presence of the macro-scale PFZ makes it possible to distinguish by regioning (depressions, system of gullies and ravines, large lineaments of strain deformation, etc.).
4. Quantitative assessment of groundwater protectability by calculation of possible groundwater contamination relative to possible (conventional) soil contamination, and regioning of the studied area by this index.
5. Assessment of groundwater vulnerability of the studied area for a specific contaminant, as dependent on the real or forecast contamination density. More realistic assessments can be achieved for concentration of a radionuclide in the soil pore water, or its exchangeable form, rather than its total amount in the soil.

Regional groundwater flow and radionuclide transport modeling with an account of the PFZs and their related radionuclide migration pathways reflects not their isolated, but also some integral effect. Consequently, the modeling parameters obtained should also be considered as general, relative to some equivalent quasi-homogeneous conditions of the medium, and may be extrapolated to other areas, if there is accepted similarity of typical sites and areas to which the data are extrapolated. The more precise validation of such similarity is a problem for further research.

In most recommendations for groundwater protectability assessment it is proposed to use the characteristic arrival time t_A of the contamination front movement from the surface $z = 0$ to the upper groundwater table at depth $z = M_A$. In the case of a conservative contaminant migrating at groundwater flow downward velocity (infiltration) w , this time can be assessed from the balance equation (Mironenko and Rumynin, 1990):

$$wt_A = \int_0^{M_A} \theta(z) dz, \quad (1)$$

where $\theta(z)$ -volumetric humidity, which can be expressed through the full moisture capacity θ_m , saturated field moisture capacity θ_0 , and hydraulic conductivity k by the formula:

$$\theta = \theta_0 + (\theta_m - \theta_0) \sqrt{\frac{w}{k}} \quad (2)$$

If account is to be taken of the equilibrium sorption, then the vertical downward migration velocity u of a contaminant can be described by relations

$$u = \frac{w}{n}, \quad n = \theta \left(1 + \frac{K_d \cdot \delta}{\theta} \right), \quad (3)$$

where n – effective porosity related to the distribution coefficient K_d , humidity θ , and rock solid matrix density δ .

The above approach of “arrival time” implies the existence of the distinguished front of the contaminant with a given concentration, at a definite depth at every moment in time. Below this front the medium is considered as clean. It is obvious that such a model takes no account of the area heterogeneity of hydraulic conductivity that leads to vertical longitudinal dispersion of the contaminant front, caused by the existence of PFZs on different scales – from macropores of different origin to area zones of fast downward migration related to depressions and geodynamical zones. The larger the study area, the greater the size of heterogeneities and discontinuities of geological medium which should be taken into account, and the assessed groundwater protectability of the area is determined by their total “openness.”

12.5.2. MODELING ASSESSMENT APPROACH

In connection with the aspects stated above, we propose a more feasible approach to the problem considered, based on the modeling assessment of vertical radionuclide migration calibrated for typical representative (key) sites of the study area. The model is based on the solution of the initial-boundary problem for a 1D differential equation describing vertical (downward) convection-dispersion transport in a quasi-homogeneous porous medium in saturated-unsaturated conditions taking account of equilibrium sorption and irreversible (radioactive) decay:

$$\frac{\partial}{\partial z} \left[D(z) \frac{\partial c}{\partial z} - w c \right] - \lambda c = n \frac{\partial c}{\partial t}, \quad (4)$$

$$c(0, t) = c_0 e^{-\lambda t}, \quad \left. \frac{\partial c}{\partial z} \right|_{z=L} = 0, \quad (5)$$

where c – sought concentration of the contaminant in liquid phase, w – infiltration, $D(z)$ – dispersion coefficient, n – effective porosity, λ – decay constant for a given contaminant (radionuclide): $\lambda = \ln(2)/T$, (T – half-life period).

The initial-boundary problem, Equations (4, 5), is solved numerically for selected representative vertical profiles corresponding to typical subregions of the area under study characterized by similar vertical flow-transport parameters determined from observation data (infiltration w , effective porosity n) and in the course of the inverse problem solution (dispersion coefficient D). The preliminary regioning of the area for contouring such subregions is performed during the expert assessment by analogy, based on the analysis of maps for unsaturated zone thickness, types of soils, intensity of infiltration, geological composition, and hydrogeological characteristics of the upper unconfined aquifer. The time period of the modeling forecast for a given contaminant

corresponds to the time during which significant contamination of the upper groundwater could occur. For ^{90}Sr and ^{137}Cs , according to available observation data and results of preliminary modeling, the half-life period (30 years) in most cases satisfies this requirement.

During the inverse problem solution for determining the dispersion coefficient $D(z)$ the data of groundwater sampling were used for ^{137}Cs concentrations at typical (representative) sites of contaminated area of the CEZ and Kyiv region (Shestopalov, 2001). The dispersion coefficient obtained by this “implicit” calibration procedure should to some extent implicitly account for flow and transport heterogeneities of the geological medium of the representative site.

In the result of modeling for each typical profile, the dimensionless relative (as a percentage of the initial surface value c_0) vertical concentration distribution is plotted for a given forecast period, and using such plots, the forecast liquid-phase concentration of the radionuclide (Bq/dm^3) at the depth of the groundwater table can be approximately assessed for a given location within the corresponding typical subregion.

The areal distribution of the forecast dimensionless concentration at the depth of the groundwater table (percentage of initial surface concentration, or soil pore solution) obtained by such a procedure is a measure of the groundwater protectability. It can be refined by more detailed zoning by introducing zonal coefficients corresponding to the available literature data for lithological structure and thickness of the unsaturated zone, etc. For example, in the case of alternating sands and clays or loams, the resultant vertical downward migration velocity will be determined by low-permeable strata of clays and loams, as compared to sands. Consequently, the assessed protectability of the area should be increased accordingly.

A question of special importance is accounting for the PFZs associated with depressions on a more detailed scale, by contouring separate depressions and their groups. Because of its great importance for the groundwater protectability assessment with respect to radionuclides, this question requires special attention, and it is discussed below in detail.

Let us consider the application of the above approach for an assessment of possible groundwater contamination by ^{137}Cs within the Kyiv province area of the Dnieper basin. To this end, we performed a preliminary regioning of the area into 3 landscape types: 1) southern areas of chernozem and loess-like loams; 2) central (region of Kyiv) areas of loamy and sod-podzolic soils and sandy-loamy composition of the unsaturated zone; 3) northern and north-western Polesye areas of 1st and 2nd Dnieper floodplain terraces and sandur plains.

For each of these typical areas we obtained representative vertical model distributions of the relative concentration (as a percentage of the initial surface

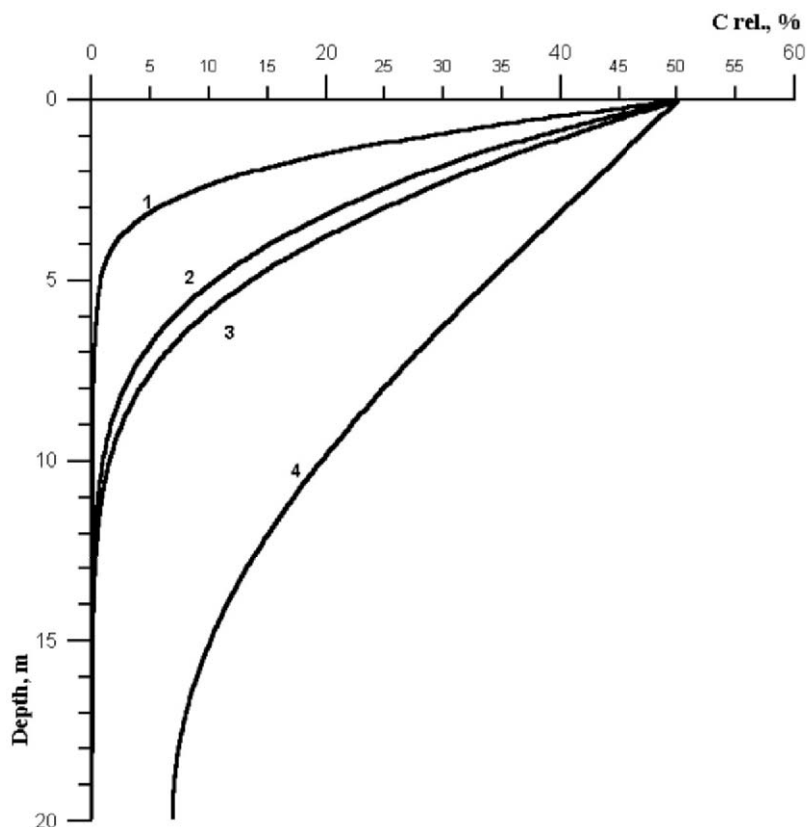


Figure 9. Characteristic modeling plots of ^{137}Cs for 30-year (1 half-life time) relative ground-water concentration (% of initial surface concentration in liquid phase) against depth at typical areas of Dnieper basin: 1 – territories of chernozem and loess-like soils; 2 – territories of sod-podzolic soils and loamy-sandy composition of unsaturated zone; 3 – territories of floodplain terraces and sandur plains; 4 – typical depression of floodplain terraces and sandur plains

concentration taken as 100%) down to a depth of 20 m (upper part of the Quaternary aquifer) for the 30-year period corresponding to maximum contamination of geological medium within this depth interval.

The vertical distributions of relative concentration obtained for the above three representative types of area are shown in Figure 9 (curves 1,2,3 respectively). Characteristic concentrations of ^{137}Cs for the 1st type (areas of chernozem and loess-like soils) appear to be 1–2 orders of magnitude lower than corresponding concentrations for type 2, where observed upper ground-water concentrations vary from several hundreds to 0.1 Bq/dm³. Plots 2 and 3 are close together, which can be explained by the relatively close sandy-loamy composition structure of the unsaturated zone in these two subregions.

However, in correlation with the surface contamination density, the observed ^{137}Cs concentrations at the depth of the groundwater table for subregion 3 are much higher as compared to subregion 2, reaching 3–10 Bq/dm³.

The calculated characteristic profiles for the above three typical areas are used to prepare the preliminary (“background”) groundwater protectability and vulnerability maps for ^{137}Cs within the Dnieper basin by the following general procedure:

1. Zone the studied area into the 3 above types;
2. Using the maps of unsaturated zone thickness, take values of relative concentration (in %) from the corresponding plots (Figure 9) at the depth of the groundwater table of the Quaternary aquifer with necessary degree of resolution for drawing the resulting map;
3. Draw the resulting map of the relative concentration (in percent) at the groundwater table depth, reflecting conditions of groundwater protectability;
4. Using the data for real concentrations of the radionuclide in soil pore solution (or other characteristic surface concentrations in an exchangeable form) it is possible to approximately assess the absolute predicted concentration of the radionuclide (in Bq/dm³) at the groundwater table by recalculating the relative concentration taken from the protectability map to the absolute values. The resultant map will reflect the background groundwater vulnerability of the upper aquifer.

In order to obtain the refined groundwater protectability and vulnerability maps accounting for the depression-related PFZ, similar modeling was performed using data for typical depressions within the CEZ and Kyiv region. A typical vertical profile of dimensionless concentration for the case of floodplain areas (subregion 3) is shown by curve 4 in Figure 9.

12.5.3. ACCOUNTING FOR DEPRESSION-RELATED PFZs

For a more detailed assessment of possible vertical and lateral transport of radionuclides ingressing into the upper Quaternary aquifer through the isolated depression, a separate 3D model was also developed based on observation data obtained at a specially equipped observation plot “Stary Shepelichi” within the CEZ, belonging to subregional type 3 (sandur plain of the second floodplain terrace). The model includes the local watershed of the depression with an area of 450 × 400 m, and involves 2 stored aquifers (Quaternary and Eocene to a depth of 70 m). The result of the ^{137}Cs dimensionless concentration (relative to the initial surface value taken as 1) is shown in Figure 10. The figure shows the depression contours, the model finite-difference grid, and concentric zones of different hydraulic conductivity. The control section is

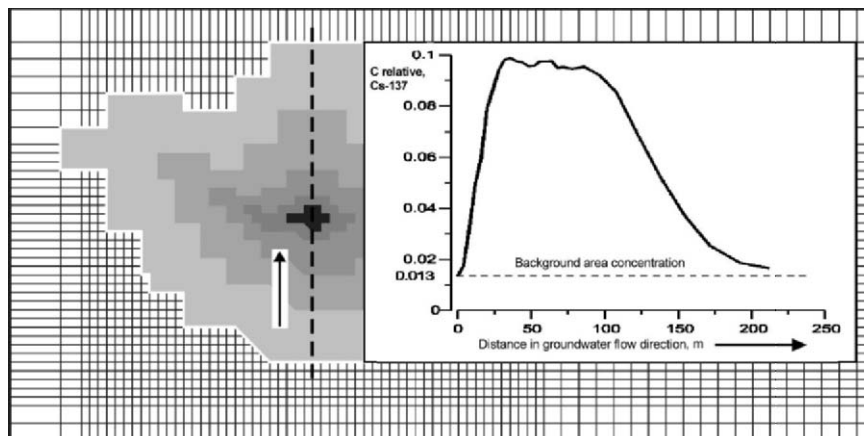


Figure 10. Scheme of the modeled area of the isolated depression (observation plot “Stary Shepelichi,” close to CEZ, subregion type 3), and result of modeling prediction of relative ^{137}Cs concentration in the Quaternary aquifer (depth 25 m) for 30-year time period

taken across the depression center (vertical dashed line) in the groundwater flow direction (indicated by arrows). The inserted plot shows the resultant relative concentration at a depth of 25 m (upper Quaternary aquifer) along the section. The maximum relative concentration reaches 0.08, which is about 6 times higher than the corresponding background value (horizontal dashed line) out of the depression border. The lateral spread of the contamination plume during the forecast period is insignificant on the horizontal scale, remaining within the depression watershed area. This is explained by relatively low horizontal flow gradients for the area studied. The result enables a conclusion to be drawn about possibility of making simplified balance assessments for this area type, based on the calculation of the total share of depressions in the areal infiltration balance for the upper aquifer, using cartographic materials for the occurrence of depressions occurrence.

To this end, a cartographic analysis of depression occurrence was performed using topographic maps on the scales of 1:50000, 1:20000, and of separate local areas on a scale of 1:10000. The analysis shows that the number of contoured depressions per unit area increases significantly with increasing detail of the map. However, even the less detailed scale of 1:50000 enabled more than 2000 depressions to be discovered per standard map sheet on a scale of 1:50000. As a result of the sheet-by-sheet calculation of the depression area on this scale, the map was drawn of the relative occurrence of depressions (in % per unit area) for the studied territory of the Kyiv region, shown in Figure 11. According to this scheme, the areal share of depressions increases from 0% in the southern part to 10–15% in the north-eastern part of the region.

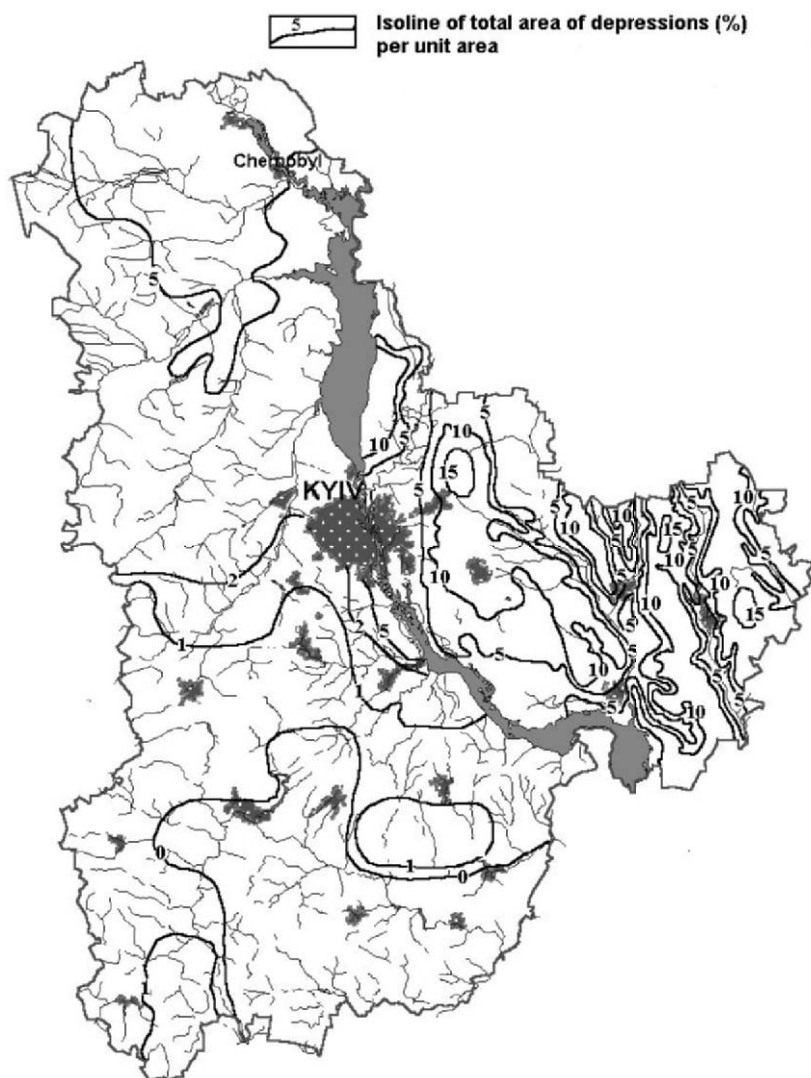


Figure 11. Scheme of depression occurrence (% of depression area per 1 km²) for the studied area of the Dnieper basin (Kyiv region) obtained as a result of cartographic analysis on a scale of 1:50000

Returning to the PFZ typification given above, it is worth noting that the depression-related PFZ characteristic of plain areas described here, along with gullies and ravines characteristic of the dissected relief, range in linear dimension from 10 to 10³ m, so they belong to the type of meso- and microzones. The PFZs with dimensions of 10³–10⁵ m (macro- and megazones) are taken into account in the course of preliminary area zoning on a scale of 1:50000,

and in part on a scale of 1:20000. PFZs with dimensions ranging from 10^{-2} to 10 m (femto-, pico- and nano-zones) are in most cases implicitly taken into consideration by the groundwater sampling procedure.

Based on the above modeling assessments and areal occurrence (percentage) of the depression-related PFZs, the resultant groundwater contamination accounting for background area and depressions can be assessed by the following balance calculations.

Let $F_s = F_b + F_a$ (m^2) be the overall area of the studied watershed, where F_b and F_a are, respectively, total areas of background sites and PFZs (depressions); W_a (m/day), C_a (Bq/m^3) and W_b , C_b – average groundwater infiltration and contaminant concentration at the groundwater table depth of the background and PFZ areas, respectively. Then the balance equations determining the total average infiltration recharge of the studied area W_s and resultant average contaminant concentration C_s have the form:

$$W_s F_s = W_b F_b + W_a F_a, \quad (6)$$

$$C_s W_s F_s = C_b W_b F_b + C_a W_a F_a, \quad (7)$$

and the sought resultant concentration C_s is found by the formula:

$$C_s = \frac{C_a W_a F_a + C_b W_b F_b}{W_a F_a + W_b F_b} \quad (8)$$

Equation (8) is written for the average liquid-phase contaminant concentrations in units of contaminant mass or activity per unit volume (Bq/m^3). However, it is also valid for relative concentrations c_s , c_a , c_b , if they are determined as a part or percentage of the same value, for example, initial surface concentration at background area C_b^0 of each assessed subregion. Equation (8) can be used for an assessment of the relative resultant concentration c_s for each subregion for which the previous steps of analysis have been performed.

12.5.4. MAPPING GROUNDWATER ^{137}Cs PROTECTABILITY AND VULNERABILITY FOR KYIV PART OF DNIPEPER BASIN

Finally, the proposed procedure of refinement of the previously drawn “background” groundwater protectability and vulnerability maps leads to the following:

1. According to the available data on unsaturated zone thickness, the interval of the groundwater table depth is determined by the necessary resolution step for the area studied, and its average weighted assessment is taken. Separately from the account of typical morphological and hydrogeological

characteristics, the similar average assessment of the groundwater table depth is performed for depressions within each subregion.

2. According to typical vertical plots, the relative concentration of the radionuclide (see Figure 9) for background sites (c_b) and depressions (c_a) is taken (in % of initial surface background concentration) for each site at its average groundwater table depth.
3. For each site, the data are tabulated for the annual average infiltration recharge at background areas (W_b) and in depressions (W_a) obtained by observation data at reference plots, and the relative total area of depressions assessed by the map (see Figure 11).
4. Using Equation (8), the assessment of the resultant average relative concentration c_s of the contaminant ingressing into the groundwater table is performed for each subregion for which the previous steps of analysis have been performed.
5. The areal distribution of relative concentration obtained in percent is a characteristic of groundwater *protectability* for the forecast period. We performed the assessment for ^{137}Cs for the forecast time period of 30 years. However, similar assessments can be implemented for any soluble groundwater contaminant.
6. The groundwater *vulnerability* mapping is based on the data for the actual (or calculated) concentration of the contaminant in the contamination source (land surface). In our case the role of the contamination source is played by the soil pore solution which gradually infiltrates into the unsaturated zone and deeper into the upper groundwater aquifer. However, the available data on the soil pore solution concentration are very scarce. For this reason, for further calculations we used the “conservative” assessment of the share of migrationally active (soluble) forms of ^{137}Cs in the total soil contamination. Calculation of this value is performed on the basis of the available data on surface contamination distribution by recalculating the relative concentration taken from the protectability map to the absolute concentration values. The areal distribution of the radionuclide concentration determined in this way (for example, in kBq/m^2) will characterize the groundwater vulnerability of the given area.

In accordance with the methodology described above, for the studied area of the Dnieper basin (Kyiv region) we drew the groundwater protectability map for ^{137}Cs for the forecast time of 30 years. It is shown in Figure 12. The different zones on the map correspond to the percentage of the migrationally active soluble part of the surface contamination with the radionuclide in soils. As can be seen from the map, the measurable groundwater contamination takes place at the groundwater table depth almost everywhere within the studied area. However, the vulnerability characterized by the relative concentration is

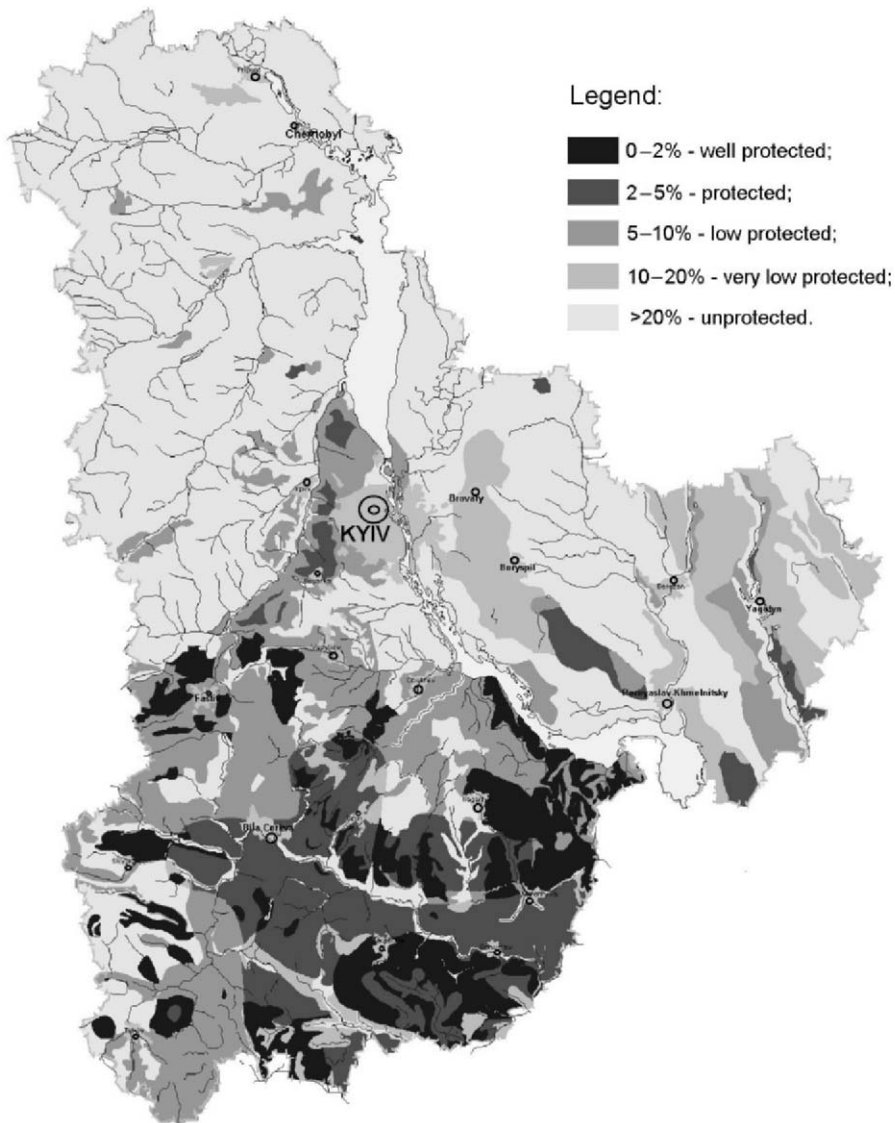


Figure 12. Scheme of assessed groundwater protectability for contamination by ^{137}Cs of the Dnieper basin area within the Kyiv region obtained by assessment of possible contamination during a 30-year forecast period, in percent of initial contamination

different in different regions corresponding to the accepted gradations (0–2, 2–5, 5–10, 10–20, and 20–50% of the soluble part of the radionuclide in soils).

The corresponding drawn groundwater vulnerability map is shown in Figure 13, characterizing the areal distribution of the radionuclide ingress into the upper Quaternary aquifer per unit area of the groundwater table.

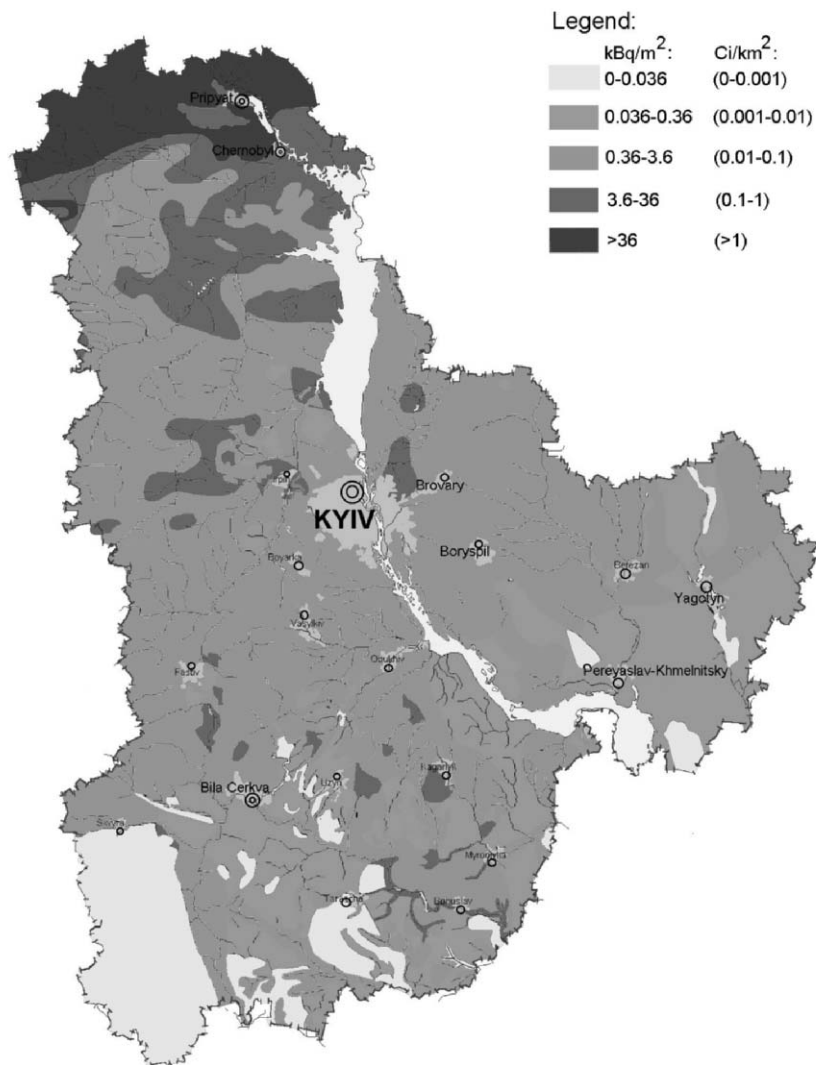


Figure 13. Scheme of assessed groundwater vulnerability by ^{137}Cs of the Dnieper basin area within Kyiv region for a 30-year forecast period

12.6. Results and Discussion

The concepts of groundwater protectability based mainly on the barrier role of soil and unsaturated zone, related to data on their composition and thickness, require serious revision.

Even in course of medium- and large-scale mapping it is necessary to account for the results of more detailed observation and special regional studies

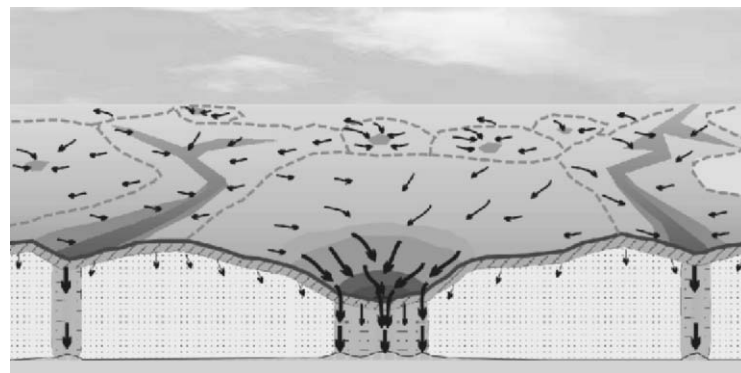


Figure 14. Scheme of groundwater recharge and contamination by subvertical preferential flow zones

on revealing and assessing the system of elements of relatively fast flow and migration which differ according to size, frequency of occurrence, and activity. It is necessary to aim to implement the principle of successively reducing conservativeness in assessments of groundwater protectability or vulnerability in the course of the transition from larger scales to smaller scales of study. The implementation of this principle means the necessity of accounting for the main risks related to the appearance of all possible anomalous sites, zones, and elements of fast migration. Decreasing conservativeness in such an approach is achieved by more detailed research leading to the possibility not only of increasing but also successively diminishing the modeling risks of the contamination danger. Only such an approach makes it possible to avoid negative ecological consequences related to insufficiently grounded optimistic forecasts in the planning of economic activities and different protection measures. A wide range of data on groundwater contamination by pesticides, radionuclides, different organic contaminants, heavy metals, etc., along with the given favorable assessments of groundwater protectability, confirm the above statement.

The concept described above of subvertical zones of preferential preferential flow and contaminant transport associated with meso- and microzones of preferential flow related to closed round and linear depression forms of the relief is illustrated in Figure 14.

The relative role of these PFZs in the total groundwater infiltration recharge and contamination by radionuclides migrating from the surface, as follows from the results obtained, is very significant.

According to the above balance consideration based on Equations (6,7), the share of depressions in total groundwater contamination can be determined by the ratio $\eta = C_a W_a F_a / C_s W_s F_s$, which in view of Equation (7) and after

dividing the numerator and denominator by the same value $C_b W_b F_s$, gives:

$$\eta = \frac{\sigma c_a W_{a/b}}{1 - \sigma + \sigma c_a W_{a/b}}, \quad (9)$$

where $c_a = C_a/C_b$; $W_{a/b} = W_a/W_b$.

According to the mapping data presented above (Figure 11), the area part $\sigma = F_a/F_s$ covered by depressions within the floodplain areas of the studied region often reaches 10% ($\sigma = 0.1$). According to observation data and modeling, the background infiltration rate at corresponding sites W_b reaches 100 mm/year, and its value in the depressions is $W_a = 700$ mm/year (Shestopalov, 2001).

According to the modeling result given above (for ^{137}Cs) for a typical depression of the floodplain terrace, the assessed relative concentration at the depth of the groundwater table within the typical depression area is 6 times higher than in the background area (Figure 10), that is $c_a = 6$. Then, substituting these values into the obtained Equation (9), one can find the upper assessment $\eta \approx 0.82$, so that the share of anomalous depressions in the total influx of the radionuclide (^{137}Cs) into the groundwater may exceed 80%.

Using Equation (9) and vertical profiles obtained above for relative ^{137}Cs concentrations in depressions and background areas for the sandur plain subregion and floodplain terraces (plots 3,4, Figure 9), the values of the PFZ/background concentration ratio c_a were calculated as dependent on the groundwater table depth (or thickness of the unsaturated zone). Further, taking the ratio $W_{a/b} \cong 6$, according to the average assessments given above for the studied area (600 and 100 mm/year for W_a and W_b respectively), plots were drawn of the relative share of depressions in the groundwater contamination η against the groundwater table depth Z , for 3 different areal percentages of depressions per unit area (Figure 11): $\sigma = F_a/F_s$: 1%, 5%, and 10%. Corresponding plots are shown in Figure 15.

It is seen from the figure that with increasing thickness of unsaturated zone, the relative input of depressions in total groundwater contamination increases from 3–30% to 80–100%. For areas with unsaturated zone thicknesses exceeding 15 m, penetration of ^{137}Cs into the upper groundwater aquifer proceeds almost entirely (by 90% and more) by means of depressions.

In view of the typification of anomalous zones described above, we performed an analysis of only one type of PFZ – microzones associated in most cases with relatively closed round or elongated depressions. However, even among the microzones other forms of appearance occur – fractures, linear disintegration zones, microdepressions, etc. They also need to be studied according to their anomalous properties and degree of their influence on the integral assessment of properties of the geological environment, first of all, with respect to different ecological aspects.

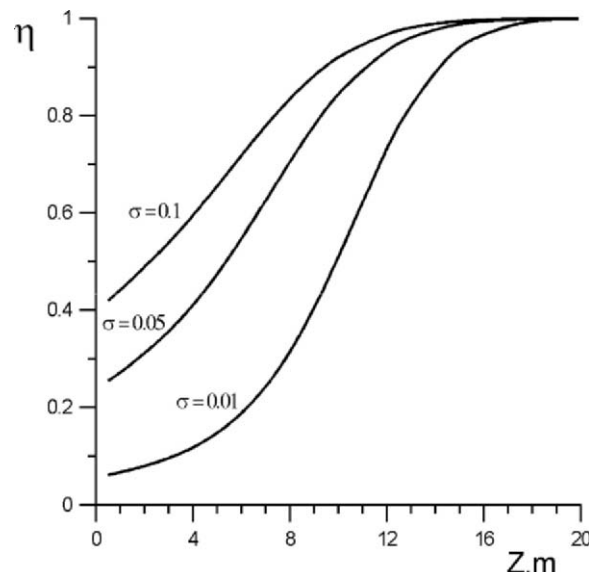


Figure 15. Assessed dependence of the relative input of depressions assessed by Equation (9) in total groundwater contamination (parts of 1) on the groundwater table depth Z for different area percentages of depressions $\sigma = F_a/F_s$

Concerning the depressions themselves, different aspects appear feasible for their study thus accounting for the following.

In the hydrogeological aspect, their importance is determined by possible significant input in the formation of natural and exploitable groundwater resources while increasing, at the same time, their vulnerability.

In regions characterized by the absence of groundwater resources of acceptable quality, or in zones of accidents, depressions play a positive ecological role consisting in faster deepening of surface contaminants and their conservation in the geological environment. In such a way, depressions facilitate the rehabilitation of contaminated areas.

In agriculture, depressions mainly play a negative role. Under the influence of the plain runoff they concentrate different contaminants, which leads to a higher contamination of agricultural produce.

In construction work, depressions cause significant difficulties as characterized by significantly modified engineering-geological properties and active geodynamic processes that may influence the stability of constructions.

Special high attention to PFZ, and depressions in particular, should be paid in the course of constructing very hazardous objects such as nuclear power plants, chemical plants, repositories for radioactive and toxic wastes, etc.

The example of Chernobyl NPP definitely confirms this statement. In the region of this NPP, according to aerospace image data, landscape and

topographic maps, the geodynamic zones are revealed (see Figure 7) manifesting themselves in the present landscape (relief, soils, vegetation). It is worth noting that elongated chains of most depressions correspond to stretching of geodynamic zones related to peculiarities of the geological structure of the crystalline base.

During the period of construction of the Chernobyl NPP (beginning of the 70s) the area of the operation site was covered by sand and leveled. In 1986, the depression forms appeared again and were concentrated along lines of ancient and present geodynamic zones giving evidence of their continuing activity.

Undoubtedly, active geodynamic zones related to the more frequent occurrence of depressions should be taken into account during construction of the "New Safe Confinement" of the Chernobyl Power Unit 4 for reliable isolation from the environment for at least 100 years to come.

12.7. Conclusions

The available data of groundwater contamination with Chernobyl-born radionuclides (^{137}Cs and ^{90}Sr) within the CEZ and Kyiv region have proven the reality of measurable concentrations of these radioisotopes not only in the soil solutions and upper groundwater, but practically in regional aquifers down to a depth of 100 m and more. Experimental and modeling studies have shown that groundwater contamination mainly enters the upper groundwater aquifer by subvertical preferential pathways of different scales and activities.

The depression-related PFZs, which occur widely in floodplain terraces of the Dnieper and Ukrainian Polesye region, have been studied in detail. Their role in the penetration of Chernobyl-born radionuclides through the soil-unsaturated zone barrier into the aquifer system is very important, although it is different for different parts of the area studied.

An experimental study of radionuclide distribution in deposits and groundwater also revealed the influence of other types of preferential flow zones on the total contamination of the geological environment.

As a result, a conclusion was drawn about the insufficiency of considering only the lithological and thickness parameters of the unsaturated zone, and the necessity of considering the preferential flow zones in order to obtain a more reliable assessment of possible groundwater contamination and protectability.

A new concept has been proposed for the assessment of groundwater protectability and vulnerability based on field experimental assessments and modeling.

Application of this methodology enabled maps to be drawn of groundwater protectability and vulnerability for ^{137}Cs within the Kyiv region of the Dnieper basin giving consideration to preferential flow zones.

It was found that the relative role of depression-type PFZs in the formation of groundwater contamination by radionuclides increases with increasing unsaturated zone thickness. On the whole, the depressions significantly diminish the protection potential of the soil-unsaturated zone barrier as assessed without giving any consideration to the distribution and influence of the depressions.

In order to implement the proposed methodology of groundwater protectability assessment in hydrogeological practice, it is necessary to perform special field work at reference sites for typical areas and to test the methodology at detailed-scale sites (map scales 1:50000 – 1:10000).

The research undertaken demonstrates the necessity of performing a complex range of special research including hydrogeophysical methods aimed to study and assess the subvertical

zones of preferential flow and contaminant migration from soils into the geological environment.

Within the boundaries of the area studied, the vertical downward migration of radionuclides appears to be an important process which promotes the autorehabilitation of contaminated areas by increasing the depot function of the geological environment. The activity, development direction, and stability state of these processes should be studied with increasing degrees of detail in order to increase the reliability of forecasts and develop appropriate environment protection measures.

The research performed provides evidence for the necessity of assessing not only the protectability and vulnerability of the upper groundwater, but of deep confined aquifers, including first of all regions of intensive groundwater exploitation. This research is necessary for optimizing the groundwater exploitation regime and increasing groundwater ecological safety, typification and regioning of areas by the assessed risk of aquifer contamination, development of measures for optimizing the technogenous influence on the area, and assessment of possible remediation measures for contaminated areas.

References

Aller, L., T. Bennet, J.H. Lehr, R.J Petty, and G. Hackett, 1987. DRASTIC: A standardized system for evaluating ground water pollution potential using hydrogeologic settings. US Environmental Protection Agency, Ada, EPA/600/2-87-036.

Baker, R.S., and D. Hillel, 1990. Laboratory tests of a theory of fingering during infiltration into layered soils. *Soil Sci. Soc. Am. J.*, 54, 20–30.

Baryakhtar, V.G., V.I. Kholosha, and D.M. Grodzinsky (eds), 1997. Chernobyl Catastrophe. National Academy of Sciences of Ukraine. Ukrainian Ministry for the Protection of the Population (?) from Chornobyl NPP Accident Consequences, Editorial House of Annual Issue “Export of Ukraine,” Ministry of Health, Kyiv, 576 p.

Belousova, A.P., and O.B. Galaktionova, 1994. On the methodology of assessment of natural groundwater protectability from radioactive contamination, //Vodnye Resursy, Vol. 21, No 3, Moscow, pp. 340–345. (In Russian)

Beven, K., and P. Germann, 1982. Macropores and water flow in soils, Water Resour. Res., 18 (5), 1311–1325.

Borzilov, V.A., 1989. Physical-mathematical modeling of processes determining the carrying out of long-lived radionuclides from watersheds in 30-km zone of Chernobyl NPP. //Meteorology and Hydrology, Vol. 1, Moscow, pp. 5–13. (In Russian)

Bouma, J., 1981. Soil morphology and preferential flow along macropores. Agr. Water Manage., 3, 235–250.

Gees, R.A., and A.K. Lyall, 1969. Erosion sand columns in dune sand, Cape Sable Island, Nova Scotia, Canada. Can. J. Earth Sci., 6, 344–347.

Glass, R.J., T.S. Steenhuis, and J.-Y. Parlange, 1989. Mechanism for finger persistence in homogeneous, unsaturated, porous media: Theory and verification, Soil Sci., 148, 60–70.

Goldberg, V.M., 1983. Natural and technogenic factors of groundwater protectability, Bull. Moscow Soc. Nat. Invest., 2, 103–110. (In Russian)

Greenland, D.J., 1977. Soil drainage by intensive arable cultivation: Temporary or permanent? Phil. Trans. R. Soc. (Lond.), B281, 193–208.

Gripp, K., 1961. Ueber Werden und Vergehen von Barchanen an der Nordsee-Kueste Schleswig-Holsteins, Berlin, Germany, Zeitsch. fuer Geomorphol., Neue Folge, Bd., 5, 24–36.

Helling, C.S., and T.J. Gish, 1991. Physical and chemical processes affecting preferential flow, Preferential Flow, in Proceedings of the National Symposium, December 16–17, 1991, Chicago, Illinois, edited by N.J. Gish and A. Shirmohammadi, American Society of Agricultural Engineering (ASAE), pp. 77–86.

Hill, S., 1952. Channeling in packed columns, Chem. Eng. Sci., 1, 247–253.

Hillel, D., and R.S. Baker, 1988. A descriptive theory of fingering during infiltration into layered soils, Soil Sci., 146, 51–56.

Kung, K.-J.S., 1990. Preferential flow in a sandy vadose zone. 1. Field observation. 2. Mechanism and implications. Geoderma, 46, 51–71.

Landon, J.R. (ed), 1984. Booker Tropical Soil Manual. Booker Agricultural International Ltd., London, 450 p.

Lawes, J.B., J.H. Gilbert, and R. Warington, 1882. On the amount and composition of the rain and drainage water collected at Rothamsted, Williams Clowes and Sons, Ltd., London, 167 p. Originally published in J. R. Agric. Soc. Engl., XVII (1881), 241–279, 311–350; XVIII (1882), 1–71.

Lissey, A., 1971. Depression-focused transient groundwater flow patterns in Manitoba, The Geological Association of Canada, Special Paper No. 9, pp. 333–341.

Lukner, L., and V.M. Shestakov, 1988. Modeling Groundwater Migration, Nedra, Moscow.

Mironenko, V.A., E.V. Molsky, and V.G. Rumynin, 1988. Studying Groundwater Contamination in Mining Regions, Nedra, Leningrad.

Mironenko, V.A., and V.G. Rumynin, 1990. Assessment of protection properties of the unsaturated zone (as applied to groundwater contamination), Eng. Geol., 2, 3–18. (In Russian)

Mironenko, V.A., and V.G. Rumynin, 1999. Problems of Hydro-geo-ecology, Vol. 3, Moscow State University, Moscow.

Nieber, J.L., C.A.S. Tosomeen, and B.N. Wilson, 1993. Stochastic-mechanistic model of depression-focused recharge, Hydrologic Investigation, Evaluation, and Ground Water Modeling, edited by Y. Eckstein and A. Zaporozec, in Proceedings of Industrial and

Agricultural Impacts on the Hydrologic Environment, The Second USA/CIS Joint Conference on Environmental Hydrology and Hydrogeology, pp. 207–234.

Nieber, J.L., 1996. Modeling finger development and persistence in initially dry porous media. *Geoderma*, 70, 209–229.

Nieber, J.L., 2001. The relation of preferential flow to water quality, and its theoretical and experimental quantification. Preferential Flow. Water Management and Chemical Transport in the Environment. in Proceedings of the 2nd International Symposium, January 3–5, 2001, Honolulu, American Society of Agricultural Engineers (ASAE), pp. 1–9.

Parlange, J.-Y., T.S. Steenhuis, R.J. Glass, T.L. Richards, N.B. Pickering, W.J. Waltman, N.O. Bailey, M.S. Andreini, and J.A. Throop, 1988. The Flow of Pesticides Through Preferential Paths in Soils, Cornell University, Ithaca, NY, N.Y. *Food Life Sci. Q.*, 18 (1, 2), 20–23.

Pashkovsky, I.S., 2002. Principles of assessment of groundwater protectability from contamination. //Present problems of hydrogeology and hydromechanics, St. Petersburg State University, St. Petersburg, pp. 122–131.

Phillip, J.R., 1975. Stability analysis of infiltration, *Soil Sci. Soc. Am. Proc.*, 39, 1042–1049.

Prazak, J., M. Sir, F. Kubik, J. Tywoniak, and C. Zarcone, 1992. Oscillation phenomena in gravity-driven drainage in coarse porous media, *Water Resour. Res.*, 28, 1849–1855.

Raats, P.A.C., 1973. Unstable wetting fronts in uniform and nonuniform soils, *Soil Sci. Soc. Am. Proc.*, 37, 681–685.

Rosen, L., 1994. A study of the DRASTIC methodology with emphasis on Swedish conditions, *Ground Water*, 32, 278–285.

Rundquist, D.C., A.I. Peters, L. Di, D.A. Rodekohr, R.L. Ehrman, and G. Murray, 1991. Statewide groundwater-vulnerability assessment in Nebraska using the DRASTIC/GIS Model, *Geocarto Int.*, 2, 51–58.

Schnoor, J.L. (ed), 1992. Fate of pesticides and chemicals in the environment, Wiley , 436 p.

Singh, P., and R.S. Kanwar, 1991. Preferential solute transport through macropores in large undisturbed saturated columns, *J. Environ. Qual.*, 20, 295–300.

Shestopalov, V.M., 1979. Formation of Exploitation Groundwater Resources of Platform Structures of Ukraine, Naukova Dumka, Kiev, 214 p.

Shestopalov, V.M., 1981. Natural Groundwater Resources of Platform Artesian Basins of Ukraine, Naukova Dumka, Kiev.

Shestopalov, V.M. (ed), 1988. Water Exchange in Hydrogeological Structures of Ukraine. Methods of Water Exchange Study, Naukova Dumka, Kiev, 272 p.

Shestopalov, V.M., V.V. Gudzenko, Y.F. Rudenko, and A.S. Boguslavskij, 1992. Combined analysis, modelling and forecast of long-term underground water contamination inside the Chernobyl Fallout influenced zone, in *Hydrological Impact of Nuclear Power Plant Systems*, International Hydrological Programme, UNESCO Chernobyl Programme, Paris.

Shestopalov, V.M., V.V. Goudzenko, Yu.F. Rudenko, V.N. Bublias, and A.S. Boguslavsky, 1997. Assessment and forecast of groundwater and rock contamination within the Kyiv industrial agglomeration influenced by Chernobyl fallout, in Proceedings of the XXVII IAH Congress on Groundwater in the Urban Environment, Nottingham, UK, September 21–27, 1997, Vol. 1, Problems, Processes and Management, PA.A.Balkema, Rotterdam, Brookfield, pp. 171–174.

Shestopalov, V.M., V.A. Kashparov, Yu. A. Ivanov, and I.M. Bogdevich, 2001. Migration pathways of “Chernobyl” radionuclides in landscapes. 15 years of Chernobyl Catastrophe. Experience of overcoming. Chernobylinterinform, Kyiv, pp. 96–117.

Shestopalov, V.M. (ed), 2001. Water Exchange in Hydrogeological Structures of Ukraine. Water Exchange and Chernobyl Catastrophe, Vol. 1, 2, Institute of Geological Sciences, Radioenvironmental Center, Kyiv, 630 p. (In Russian).

Shestopalov, V.M. (ed), 2002. Chernobyl Disaster and Groundwater, A.A.Balkema/Lisse/Abingdon/Exton(Pa)/Tokyo, 289 p.

Shtengelov, E.S., 1979. Some questions of Pliocene-Quaternary separation of continental crust, Bull. Moscow Soc. Nat. Invest., Geol. Sect., 262, 3-14.

Shuford, J.W., D.D. Fritton, and D.E. Baker, 1977. Nitrate nitrogen and chloride movement through undisturbed field, Soil J. Environ. Qual., 6, 255-259.

Vrba, J., and A. Zaporozec, 1994. Guidebook on mapping groundwater vulnerability, Int. Assoc. Hydrogeol., 16.

Zektser, I.S., 2001. Groundwater as a Component of the Environment, Nauchnyi Mir, Moscow, 327 p. (In Russian)

INDEX

a priori 3, 9, 10, 16–20, 24, 29, 62, 102, 152, 234, 235, 237, 239, 251, 295
acoustic 140, 164, 169, 182, 209, 307
acquisition 15, 16, 22, 89, 92, 99, 100, 103, 109, 111, 118, 141, 142, 146, 147, 272, 304, 314
amplitude 142, 164, 169, 182, 208, 221, 222, 264, 265, 268, 269, 309, 310
anisotropy 12, 140, 234, 331
antenna 21, 22, 33, 34, 80, 81, 88–90, 93, 94, 98–100, 102–104, 107, 127, 128, 132, 141, 147, 185, 208, 211, 352
apparent resistivity 11, 45, 46, 206, 207, 221, 233, 237, 327, 332, 333
aquifer 1, 2, 4–7, 15, 24, 30–32, 34, 35, 45–49, 61, 75, 98, 102, 117–119, 123–126, 128, 132–137, 139, 142, 145, 181, 182, 200, 214–216, 233, 235, 236, 238, 239, 241–251, 255, 258, 260–262, 265, 286, 296, 324, 327, 329, 330, 335, 336, 343–345, 349, 350, 355–357, 359, 361–363, 366, 367, 370, 370, 372, 373
Archie's law 14, 47, 48, 77, 82, 126, 147, 184, 270
artefact 110
attenuation 24–26, 85, 127, 142–145, 172, 174, 182, 208, 209, 304, 309, 324
bacteria 25, 161, 164, 172, 174, 178–182, 187, 285, 323
Bayesian 3, 20, 22, 24, 25, 35, 46, 57
bedrock 2, 11, 89, 91, 94–96, 140, 161, 198, 208, 209, 220, 221, 233, 272, 309, 311
bioelectric effect 268
biofilm 165–170, 178, 180–182, 186, 189
biogeochemical 6, 7, 161, 179, 320
biogeophysics 161, 162, 189, 190
bio-physicochemical 165, 186
bioremediation 183, 186
borehole 1, 4, 12, 15, 16, 22, 23, 25, 26, 29, 31–34
boundary 2, 12, 48, 49, 51, 53, 57, 61, 62, 69, 75, 79, 81, 96, 119, 125, 136, 196, 197, 211, 214, 219, 258, 272, 285, 295, 299, 311, 319, 331, 334, 343, 356, 359, 373
breakthrough curve 122, 128, 130, 131, 142–144
brines 199, 213–216, 226, 245, 246, 249–251, 300, 314
bulk electrical conductivity 61, 85, 125, 133, 150, 162, 174, 175, 183, 184, 217, 218
calibration 5, 14, 29, 67, 69, 77, 81, 84, 85, 103, 108, 111, 127, 135, 136, 138, 141, 218, 226, 242, 245, 246, 266, 360
capacitively-coupled systems 202, 207, 225
capillary 31, 88, 108, 199, 264, 268, 270, 305
carbonate aquifers 246, 248–251
casing 100, 146, 259, 260, 344
cementation 5, 82, 126, 166, 168, 170, 189, 234
chargeability 207, 211, 212, 308
Chernobyl Exclusion zone (CEZ) 7, 343, 347, 348, 351, 353, 360, 362, 363, 372
clay content 16, 84, 97, 111, 177, 223, 234, 238, 271
cokriging 3, 24, 46, 47, 51–54
cokriging weights 52, 53
Cole-Cole 211, 212
common 17, 18, 21, 22, 28, 71, 81, 85, 88, 89, 122, 127, 133, 141, 200, 217, 226, 234, 246, 293–296, 304, 322, 334
complex refractive index method (CRIM) 13, 14, 29, 82–84, 101, 106, 107, 127, 148
concentration 4, 7, 25, 26, 28, 32, 48, 61, 62, 71, 117–122, 125–129, 132, 135, 138, 142–145, 147–151, 162–164, 170, 172, 174, 176, 177, 181, 184, 199, 215, 217, 218, 226, 246, 285, 294, 306–308, 323, 327, 329, 330, 334–336, 343–346, 348, 350, 352, 354–356, 358–363, 365, 366, 370, 372
conditional mean 46, 48, 50, 51, 55, 57
conditional variance 65
conditioning 3, 25, 35, 48, 57, 62, 63

conduction 126, 150, 172, 180, 234, 257, 306–308, 311
 contamination 2–4, 7, 175, 185, 187, 189, 213, 284, 324, 341–344, 351, 355–358, 360–363, 365–367, 369–373
 continuum models 121
 convection-dispersion equation 121, 128
 convection-dispersion model 123, 128, 130, 135
 correlation 15, 18, 31, 33, 34, 37, 52, 58, 64, 181, 187, 221, 243, 246, 266, 284, 305, 308, 329, 335–343, 353, 354, 362
 correlation structure 12, 15, 19, 25, 29, 49, 53, 58, 64
 covariance 12, 18, 19, 47, 49, 52–56, 58, 152
 cross borehole 4, 106, 107, 109, 130, 145, 146, 295, 300, 302, 313
 cross-correlation 52, 56, 273
 cross-covariance 52–55
 crosshole surveys 22
 crystalline 140, 235, 320, 372
 damping 12, 132
 data fit 18, 19, 31
 dc resistivity 6, 16, 45, 79–81, 96, 97, 99, 174, 175, 177, 202, 203, 207, 236, 319, 332
 depth of investigation 19, 85, 98, 111
 deterministic 12, 16, 17, 50, 59
 dielectric constant 13, 14, 21–23, 81, 83, 95, 106, 127, 145, 147–149, 212
 dielectric permittivity 79, 81, 83, 85, 125, 127, 150, 166, 204, 205, 208, 305
 diffusion 120–123, 255, 257, 285, 352, 356
 dipole-dipole array 332
 direct mapping 3, 10, 20, 21, 24, 37, 38
 discretization 12, 37, 69, 121, 128
 disintegration zones 344, 352, 353, 360
 dispersion 94, 95, 119–124, 142, 150, 204–207, 211–213, 326, 359, 360
 dispersivity 120, 122, 126, 129–131, 138, 151
 disturbance 1, 314, 334, 349, 354, 356
 Dnieper basin 7, 360–362, 364–368, 372
 drainage 7, 78, 86, 88, 196, 201, 209, 213, 219–223, 262, 263, 265, 267, 273–275, 281, 305, 321, 322
 dynamic 4, 76, 79, 80, 85, 103–105, 125, 128, 233, 314, 335
 effective dispersion 124
 effective porosity 119, 249, 359
 Einstein convention 53
 elastic moduli 5, 166, 169, 170, 182, 189
 electric current 45, 46, 48–50, 52, 55, 58, 67, 68, 171, 172
 electric potential 45, 46, 48–55, 60, 67, 68, 266, 268
 electrical conductivity 3, 5, 14, 16, 48–55, 57–59, 61–63, 72, 79–83, 85, 107, 111, 125, 133, 137, 145, 150, 162, 169, 172, 174, 175, 178, 183, 184, 189, 204, 208, 211, 215, 217, 218, 221, 222, 240, 241, 244, 257, 269, 270, 285, 299, 305–307, 326–330, 335, 336
 electrical double layer 82, 166, 172, 174, 179, 181, 187
 electrical imaging 128, 300–303, 309, 312
 electrical methods 12, 88, 302
 electrical properties 81, 126, 165, 172, 174, 175, 178, 187, 189, 205, 207, 211, 212, 251, 257
 electrical resistivity tomography 3, 4, 29, 45–52, 55, 67, 69, 71, 76, 77, 96, 106, 109, 111, 128–140, 145–147, 149, 152, 217, 218, 224, 262, 271, 277, 278, 280–282, 303, 314
 electrode array 47, 96, 109, 130, 146, 297, 298, 300, 303, 312, 327, 332, 333
 electrode spacing 80, 87, 136, 239, 334
 electrography 6
 electrokinetic 181, 264, 265, 268, 272, 276
 electromagnetic induction 79, 81, 97
 electromagnetic soundings 5, 204, 206, 211, 225
 electromagnetic methods 6, 72, 80, 304
 ensemble 49, 50
 equivalence problem 234, 235, 237
 equivalent transport models 128, 151
 equivalent transport parameters 128
 erosion 322, 349, 353, 356
 electrical resistivity tomography (ERT) 1, 4, 29, 43, 46–52, 55, 57–67, 69, 71, 76, 77, 96, 109, 111, 128–141, 145–147, 149, 152, 217, 218, 224, 262, 271, 277, 280–282, 303
 estimation 3, 9, 11, 13, 14, 16–18, 20–22, 24, 25, 28–30, 34, 37, 38, 46–48, 52, 55, 57, 65, 66, 79, 91, 100, 111, 125,

151, 152, 237, 251, 262, 265, 268, 269, 271, 272

exponent 78, 82, 83, 126, 203

facies 16, 249

fault 196, 197, 274, 331

first order approximation 54

floodplain terraces 7, 353, 360–362, 370, 372

flow equation 122

flowmeter 25, 35

flow velocity 2, 121, 122, 126, 130, 138, 139, 223, 224, 226

formation factor 5, 15, 82, 83, 166, 170, 171, 189, 223, 350

fracture delineation 34

fractured media 4, 120

frozen soils 195, 197, 198, 200, 202, 204, 216, 217, 219

fundamental 2, 9, 20, 36, 37, 81, 118, 256, 257, 293

gamma 100, 101, 147, 352

gather 33, 90, 98, 141, 147

geochemical characterization 25, 330

geochemistry 271, 335

geodynamic zones 352–354, 359, 372

geoelectrical methods 272, 331

geoelectrical signature 320, 325

geoelectrical soundings 327, 329

geoelectromagnetic methods 233, 235

geology 45, 75, 162, 284, 294, 295, 311, 331, 334

geomembranes 296, 297, 299, 304, 313, 314

geophysical imaging 110, 111, 118, 128, 130, 134, 135, 150, 151, 293, 295, 309, 314

geostatistic 12, 24

geostatistical parameterization 12, 16, 124

glacial 99, 161, 162, 195, 199, 209, 216, 224, 226, 349, 353

glacier 5, 195, 198, 200, 201, 204, 209, 219–224, 226

grain size 78, 120, 184, 309

granular aquifers 117, 132, 133, 248, 250

granular media 119, 307

gravity 108, 198, 221, 348

ground penetrating radar (GPR) 3, 4, 21, 22, 24, 25, 28, 29, 31, 33, 34, 71, 76, 77, 79, 81, 84, 85, 88–95, 97–102, 105, 107, 109–111, 127, 128, 130, 132, 133, 140, 141, 145–147, 150, 162, 174, 185, 186, 195, 202, 207, 208, 225, 226, 302, 304, 305, 309, 310, 313

groundwater contamination 2, 3, 7, 185, 324, 341–343, 356–358, 360, 366, 369–373

groundwater flow 31, 38, 41, 118, 134, 138, 181, 258, 272, 281, 285, 326, 341, 351, 358, 363

groundwater resource assessments 342

Hanford site 22, 300, 305

head 11, 24, 46, 47, 78, 98, 107, 122, 197, 200, 261, 263, 265, 268, 269, 277, 323

heterogeneity 4, 25, 31, 36, 47, 86, 117, 118, 121, 124, 125, 129, 130, 136, 139, 144, 145, 213, 258, 262, 268, 299, 331, 334, 342–344, 348, 349, 356, 359, 360

homogeneous 45, 57, 58, 67, 68, 86, 94, 123, 124, 128, 129, 135, 224, 358, 359

hydraulic conductivity 4, 6, 46, 47, 78, 258, 260–263, 265

hydraulic head 9, 11, 24, 46, 47, 78, 258, 260–263, 265

hydraulic parameters 31, 33, 34, 63, 102, 104, 248, 265, 267, 268, 269

hydraulic tomography 47

hydrocarbons 5, 117, 162, 164, 171, 174, 175, 181, 183–188, 284, 315, 325

hydroelectric coupling 255

hydrogeological site characterization 9, 11

hydrogeophysical parameter estimation 9–11, 13, 16, 20, 21, 30, 37, 38

hydrogeophysics 2, 7, 16, 18, 20, 37, 38, 57, 90, 109, 146, 152, 195, 286

hydrological inversion 241, 244

hydrology 2, 4, 46, 75, 140, 195, 200, 201, 209, 216, 224, 226, 265

ill-conditioned 19, 55

ill-posed 12, 132

imaginary conductivity 178–181, 187, 188, 308, 311, 312

imaging 6, 8, 60, 72, 96, 97, 108, 109, 111, 118, 125, 128–130, 132–135, 141, 146, 150–152, 224, 236, 239, 240, 241, 256, 286, 293, 295, 299, 300, 302–304, 309–314, 330, 335, 336

impedance 60, 104, 138, 209

indicator 10, 35, 69, 223, 226, 228
 induced polarization 5, 38, 79–81, 111, 151, 166, 174, 177, 186–188, 212, 216, 255, 286, 307–309, 311–313, 319
 infiltration 4, 5, 33, 63, 64, 69, 80, 86–88, 90, 91, 93, 97, 99–102, 198, 200, 216, 217, 219, 226, 264, 267–269, 277, 281, 296, 322, 342, 343, 352, 355, 358, 359, 363, 365, 366, 369, 370
 information sharing 28
 integration methods 3, 10, 20, 24, 25, 28–30, 36–38
 interface 15, 22, 80, 81, 86, 91, 94, 100, 104, 119, 126, 150, 172, 177, 181, 184, 187, 209, 233, 235, 236, 238, 239, 241, 242, 244, 246, 251, 307
 inverse approach 57
 inversion 3, 6, 7, 10, 12, 16, 17, 19–24, 28–31, 33–38, 46, 48, 57–59, 61–63, 65, 68, 69, 71, 77, 88, 90, 95, 99, 103, 104, 110, 128, 133, 136, 138–143, 145, 147, 150, 152, 217, 238, 241, 244, 269, 273, 286, 295, 296, 302, 309, 311, 334, 336
 inverse problem 3, 11, 12, 15, 18, 19, 26, 46–48, 50, 59, 151, 152, 258, 286, 287, 359, 360
 joint inversion 3, 7, 10, 20, 21, 30, 33, 36–38, 61, 286, 334
 karstic 4, 110, 235, 246, 247, 249, 251
 Krauthausen test site 4, 133, 134
 Kyiv conurbation 343–346
 landfill 6, 164, 182, 186, 284, 285, 296–299, 304, 314
 landfill liners 6, 296, 299, 304, 314
 landslides 6, 91, 256, 272–282, 284
 leachate 117, 164, 186, 298, 319–331, 334–336
 leak location methods 296–299
 leaks 6, 294, 296, 299–302, 313, 314
 light non-aqueous phase liquid (LNAPL) 117, 83–185, 284
 likelihood 25, 49
 linear regression 14, 25
 magnetic field 138, 188, 256
 mass balance 110, 119, 123, 132, 214, 265
 maximum a posteriori (MAP) estimate 19, 33, 57
 mean 12, 14, 24–26, 28, 34, 46, 48–52, 54–56, 58, 67, 68, 71, 78, 120, 123, 129, 130, 134–138, 196, 273, 287, 289
 measurement 33, 45, 58, 61, 68, 75, 77, 80, 83–85, 87, 90, 98, 118, 123, 125, 130, 132, 151, 181, 207, 211, 217, 236–238, 255, 257, 265, 268, 272, 319, 351
 measurement error 10, 24, 29, 35, 38, 66, 128, 132, 347
 measurement support volume 9, 143, 150
 microbial growth 164–166, 168–170, 173, 177, 178
 microbial processes 161, 163, 165, 168, 174, 177, 178, 181, 183, 186, 189, 190
 microbiology 162, 189
 microorganisms 162–165, 167–169, 171, 183, 186, 356
 migration of contaminants 61
 mineral weathering 166, 170, 172, 175, 186, 187, 189
 mixing processes 123, 124
 model norm 18
 moisture content 3, 4, 47, 48, 57, 63–66, 69, 71, 76, 77, 90, 97, 101, 102, 105, 111, 145–148, 304, 305, 350, 352
 moment 4, 51, 122–124, 128, 130, 131, 139, 212, 359
 monitoring 3, 4, 6–8, 22, 31, 33, 47, 48, 54, 63, 66, 67, 69, 76, 80, 84, 85, 90, 91, 97–100, 102, 105, 109, 111, 124, 125, 127, 133–135, 138, 139, 146, 175, 182, 187, 197, 207, 212, 213, 258, 265, 271, 272, 284, 294, 295, 299–301, 304, 305, 312, 314, 315, 323, 327, 334, 335
 Monte Carlo methods 10, 17, 35
 Monte Carlo simulation 132
 multiple offset gather (MOG) 33, 98, 99, 147
 neutron probes 22, 23, 218, 305
 non-aqueous phase liquids 117, 183, 284
 nonlinear relation 3, 47, 55, 57
 non-stationary 10, 13, 15, 28
 non-unique 10, 13, 35, 72
 non-uniqueness 10, 17, 111, 150, 239
 nuclear magnetic resonance (NMR) 79, 166, 188, 189

numerical 47, 48, 52, 53, 55, 57, 58, 61, 66, 80, 107, 128, 130, 132, 140, 144, 146, 200, 214, 226, 262, 309

objective function 10, 17–19, 38, 295

Occam inversion 19, 203

offset 22, 33, 89–94, 107, 147, 302

optimization 10, 17, 46, 54

organic acids 165, 166, 170, 175, 323

parameterization 10, 12, 15–17, 38, 78, 121

peak 120, 142, 143, 183, 221, 222, 309, 326

period 90, 103, 109, 135, 138, 141, 147, 176, 179, 200, 217, 262, 277, 300, 305, 325, 332, 343, 344, 352, 354, 355, 359–361, 363, 366–368, 372

permafrost 5, 195–197, 199, 202–204, 206, 208–216, 226

permeability 11, 14–16, 24, 25, 30–36, 38, 139, 140, 147, 163, 169, 170, 208, 301, 304, 309, 321, 326, 332, 342, 346, 350, 355, 357

permeability structure 25, 30, 139

permeable reactive barriers 6, 294, 295, 305, 307–309, 311–313, 315

perturbation 49–52

pesticides 1, 200, 341, 342, 344, 346, 369

petroleum 30, 76, 79, 81, 162, 164, 175, 183, 187, 334

petrophysical models 13, 14, 34, 35, 127, 132, 146, 150, 151

petrophysical relationship 10, 13–16, 20, 21, 24, 28, 29, 31, 35–38, 76, 77, 84, 97, 110, 111, 118, 126, 128, 132, 151

piezometric 261, 286

pilot points (PP) 33

point measurements 3, 46, 57, 62, 63

pore water velocity 120, 150

porosity 2, 5, 13, 14, 78, 82–84, 106, 119, 120, 126, 143, 162, 166, 168–172, 177, 182, 213, 215, 223, 234–239, 241, 248–251, 304, 359

preferential flow 31, 97, 117, 204, 217, 218, 327, 342, 343, 348, 350, 369, 373

preferential flow zone (PFZ) 7, 341–343, 369, 372

pressure 1, 31, 47, 75, 78, 79, 98, 121, 12, 197, 201, 205, 220–222, 224, 225, 234, 264, 269, 270, 298, 315, 352

prior information 16, 19, 46, 57, 68

primary information 49

prior knowledge 19, 48, 56, 68

profiling 4, 80, 81, 88, 99, 133, 146, 209, 265, 302, 351, 352

protectability (of groundwater) 7, 341–343, 356–360, 362, 365–369, 372, 373

pumping test 6, 248, 251, 256, 258–262

radio-magnetotellurics 4, 6, 133, 138, 139, 319, 332, 334, 336

radon 351, 352

random 12, 14, 25, 33, 35, 49, 57, 58, 61, 63, 64

ray-based tomography 22, 29

real conductivity 178, 183, 187, 311, 322

realization 29, 31, 32, 34, 49, 50

redox processes 6, 186, 231

reflection 21, 22, 79, 80, 85, 88–90, 104, 106, 144, 162, 185, 186, 208, 209, 232

refraction 16, 79, 80, 88, 89, 91, 100, 140, 331

regolith 161–164

regularization 11, 12, 15, 18, 56, 57, 103, 132, 142, 311

relaxation 188, 205, 206, 212, 261

remediation 6, 7, 34, 102, 117, 189, 293, 294, 305, 312, 315, 336, 373

representative elementary volume 119, 120

resistivity 3–6, 11, 15, 16, 19, 45–50, 55, 57–65, 67–71, 76, 79–82, 96, 97, 99, 106–111, 126, 128, 137, 138, 140, 145–151, 166, 174, 175, 177, 183, 195, 202–207, 210–212, 216, 217, 219–221, 223–226, 233, 234, 236–241, 243–251, 257, 258, 262, 269, 271, 272, 277, 280–282, 286, 299–304, 307, 309, 311–314, 319, 321, 324–328, 332–336

resolution 7, 9, 28, 29, 37, 46, 60, 66, 71, 76, 77, 80, 84, 85, 98, 103, 109, 111, 130, 132, 133, 139, 142, 145, 150, 151, 203, 236–239, 272, 295, 302, 304, 311, 331, 333, 362, 365

Richards equation 77–79, 101, 104, 107, 122

roughness 18, 19, 166, 168–170, 295

runoff 4, 200, 265, 353, 355, 371

saline 133, 140, 141, 145–147, 150, 196, 197, 199, 209–211, 214, 215, 224, 233,

235, 236, 238, 239, 242–244, 246, 247, 249, 250, 300, 319
 salinity 97, 111, 127, 147, 148, 150, 196, 202–205, 211, 213–216, 234, 235, 238, 239, 241, 245, 246, 249, 251, 284, 286
 sampling 1, 17, 25, 50, 57, 62, 71, 75, 79, 84, 86, 90, 93, 98, 103, 118, 125, 133, 135, 143, 195, 218, 327, 332, 333, 347, 350, 352, 360, 365
 Sandur plains 353, 360–362, 370
 sandstones 4, 83, 99–101, 105–109, 146, 147, 203, 208, 234, 238, 243, 247, 255, 264
 saturation 13, 14, 31, 33, 34, 76, 78, 79, 81–83, 91, 126, 148, 162, 171, 218, 219, 221, 234, 238, 251, 266, 268–270, 326
 seawater intrusion 5, 233, 238, 244, 245, 250, 251
 secondary information 24, 49, 55, 57, 65
 second-order stationarity 49
 sedimentary 12, 16, 126, 212, 248, 249, 256, 344, 350, 352
 seismic reflection 90, 209, 272
 self potential 5, 6, 8, 38, 145, 174, 171, 186, 192, 195, 204, 222, 255–269, 271–273, 278, 280, 281, 283–287, 319
 sensitivity matrix 54, 55
 sensors 59, 60, 67, 107, 147, 256, 257, 314
 sequential successive linear estimator (SSLE) 3, 47, 48, 51, 55–59, 62, 63, 65, 66, 68, 71
 shallow 1, 6, 7, 76, 77, 80, 84, 86, 90, 91, 94, 96–98, 117, 145, 146, 161–164, 189, 197, 200, 203, 207, 212, 238, 239, 241, 260, 277, 341, 353
 simulation 10, 32, 34, 37, 61, 64, 68, 101, 102, 108, 130, 132, 212
 skip one array 61
 slowness 15, 22, 31, 32, 34
 snowmelt 97, 145, 198, 200, 204, 216, 217, 219, 226
 soil layer 22, 90, 91, 94, 95, 117, 343, 349, 356
 soil moisture 4, 77, 128, 208, 268, 284, 325
 solute concentration 4, 71, 117, 119–122, 125, 127–129, 132, 142, 145, 147–151, 366
 solute flux 119, 120, 122, 123
 solute plumes 61, 120, 122–124, 128, 129, 133, 145, 150
 solute transport 4, 5, 111, 117, 118, 123–126, 128, 129, 132, 133, 136, 139, 145, 146, 150, 152, 195, 199, 214, 217, 219, 271, 314
 sorption 120, 324, 357–359
 spatial moments 122, 128
 state variables 2, 5, 11, 33, 36, 37, 125, 126
 static shift 106, 333, 334
 steady state 47, 86, 101, 141, 164, 258, 259
 stochastic process 49–51
 storage tanks 145, 164, 293, 300, 313, 314
 storativity 6, 248, 249, 258, 260, 262
 stream tube model 129–131, 138, 151
 streaming potential 6, 204, 223, 255, 257, 258, 260–262, 285, 286, 336
 subsurface barriers 293
 successive linear estimator (SLE) 3, 45, 47, 52, 55
 surface 1, 2, 4, 5, 8, 16, 22, 45, 47, 64, 66, 69, 70, 75–77, 80–86, 88–92, 94, 96–99, 101, 108, 109, 117, 119, 122, 126, 127, 130, 133, 135, 137, 138, 140, 145, 147, 150, 161–164, 166, 168–172, 177, 178, 181, 185, 187, 189, 196–200, 208, 209, 211, 216–221, 224, 234, 238, 242, 255, 257–259, 261–264, 268, 272–275, 278, 282, 283, 286, 293, 295, 297–299, 302, 304–311, 314, 315, 324, 329, 330, 333–336, 343, 344, 348, 352, 353, 355, 356, 358, 360–362, 365, 366, 369, 371
 survey 9, 15, 38, 45, 46, 48–50, 52, 55, 57, 58, 60–65, 67, 71, 72, 97, 98, 103, 135, 138, 218, 219, 251, 256, 259, 272, 273, 276, 277, 284, 297, 298, 331, 332, 352
 synthetic 3, 15, 29, 30, 33, 37, 58, 61, 63, 64, 129, 136, 236, 296
 system properties 11, 12, 14–16, 19, 24, 28–30, 33, 36, 38
 temperature 5, 66, 79, 97, 111, 126, 168, 195–199, 202–205, 208, 209, 214, 215, 216, 219, 226, 234, 264, 268, 271, 284, 319, 323
 temporal moments 4, 122–124, 128, 130

texture 5, 111, 117, 151, 166, 168, 170, 177, 189, 198, 211, 248, 305, 354

thermal 120, 197–199, 214, 336

Tikhonov regularization 11, 12

time domain electromagnetic (TDEM) 5, 80, 236–248, 250, 251

time domain reflectometry (TDR) 4, 76–78, 81–88, 90, 91, 111, 195, 218, 284, 305

time lapse 4, 22, 31, 34, 48, 76, 80, 83, 90, 92, 97, 99, 102, 111, 118, 126–128, 133, 136–138, 140–142, 145, 146, 195, 202, 219, 221, 223, 226, 258, 262, 284, 326, 336

time-lapse imaging 97, 128, 295

tomogram 25, 28, 29, 31, 35, 98, 128, 130, 142, 143, 145, 148, 149, 151, 224, 225, 273, 281, 304

tomography 3, 4, 6, 19, 23, 29, 34, 45–47, 52, 55, 60, 72, 76, 80, 96, 106, 109, 128, 130, 132, 140, 143, 146, 150, 203, 217, 224, 226, 262, 271, 273, 275, 277, 278, 281, 286, 287, 302

Topp equation 86

tortuosity 5, 82, 120, 122, 166, 170, 234

total dissolved solids (TDS) 126, 127, 174, 175, 323, 326, 328, 329, 335, 336

tracer breakthrough 126, 135–138, 142

tracer experiments 35, 105, 107, 122, 125, 126, 133, 134, 136–138, 141

transient electromagnetic (TEM) 6, 204, 206, 211–213, 319, 332–334, 336

transmission 45, 49, 50, 52, 55, 56, 58, 59, 61, 67, 68, 79, 80, 98, 99, 106, 107, 130, 147

transmitter 22, 88, 89, 96, 98, 99, 103, 133, 138, 147, 204, 207, 217, 236

transport models 118, 121, 122, 126, 128, 135, 140, 150, 151

transport process 4, 5, 25, 61, 117–119, 121, 124, 125, 128, 132, 133, 150, 152, 163, 314, 356

transport properties 117, 118, 125, 128, 150, 151

transverse 120, 129, 223, 273

time-lapse monitoring 80, 90

uncertainty 13, 14, 17, 20, 24, 39, 33, 35, 37, 38, 46, 47, 51, 54, 57, 59–61, 65, 71, 110, 145, 223, 234, 238, 269, 299, 332

unconsolidated 81, 91, 161, 187, 198, 220, 264, 307, 309

unsaturated 3, 4, 63, 75, 77–81, 98, 99, 101, 105, 106, 114, 118, 119, 122, 145, 146, 150, 163, 164, 187, 188, 197, 200, 208, 213, 226, 238, 246, 262, 264, 265, 267–271, 332, 334, 341–343, 349, 350, 352, 354–362, 365, 366, 368, 370, 372, 373

update 47

vadose zone 1, 2, 4, 6, 13, 21, 22, 30, 31, 47–49, 57, 63, 75–77, 79–81, 84, 96–99, 105, 108, 109, 111, 119, 122, 132, 145, 146, 256, 262–264, 268, 271, 300, 302, 365–369, 371–373

variance 12, 24, 25, 46, 49, 54, 58, 65, 66, 68, 120, 122, 124

vertical electrical sounding (VES) 96, 211

vertical radar profiling (VRP) 4, 99, 102–106

vulnerability (of groundwater) 7, 8, 342, 343, 356–358, 362

volumetric water content 21, 23, 76–78, 80, 81, 83, 85–91, 94–97, 99–102, 104, 105, 107, 109, 119, 120, 122, 125, 127, 132, 150, 198, 202, 209, 217, 219, 266, 268, 272, 284

water flux 78, 120–122, 265–267, 271, 326

water salinity 111, 127, 147, 148, 234, 239, 241

water saturation 13, 14, 31, 33, 81–83, 126, 148, 162, 175, 218, 221, 266, 268–270

watershed 265, 362, 363, 365

wellbore 9, 22, 23

well-conditioned 19

well-posed 11, 12, 17, 18, 36, 71

zero-offset profile (ZOP) 33, 98, 107, 302

zonation 11, 12, 16, 30, 31, 35, 80